5163

NUREG/CR-5163
EGG-2541

Power Burst Facility (PBF) Severe Fuel Damage Test 1-4 Test Results Report

Prepared by D.A. Petti, Z.R. Martinson, R.R. Hobbins, C.M. Allison,
E.R. Carlson, D.L. Hagrman, T.C. Cheng, J.K. Hartwell
K. Vinjamuri, L.J. Seifken

Idaho National Engineering Laboratory
EG&G Idaho, Inc.

Prepared for
U.S. Nuclear Regulatory
Commission

READEX FICHE best copy available

Y 3.N88:25/

AVAILABILITY NOTICE

Availability of Reference Materials Cited in NRC Publications

Most documents cited in NRC publications will be available from one of the following sources:

1. The NRC Public Document Room, 2120 L Street, NW, Lower Level, Washington, DC 20555
2. The Superintendent of Documents, U.S. Government Printing Office, P.O. Box 37082, Washington, DC 20013-7082
3. The National Technical Information Service, Springfield, VA 22161

Although the listing that follows represents the majority of documents cited in NRC publications, it is not intended to be exhaustive.

Referenced documents available for inspection and copying for a fee from the NRC Public Document Room include NRC correspondence and internal NRC memoranda; NRC Office of Inspection and Enforcement bulletins, circulars, information notices, inspection and investigation notices; Licensee Event Reports; vendor reports and correspondence; Commission papers; and applicant and licensee documents and correspondence.

The following documents in the NUREG series are available for purchase from the GPO Sales Program: formal NRC staff and contractor reports, NRC-sponsored conference proceedings, and NRC booklets and brochures. Also available are Regulatory Guides, NRC regulations in the *Code of Federal Regulations*, and *Nuclear Regulatory Commission Issuances*.

Documents available from the National Technical Information Service include NUREG series reports and technical reports prepared by other federal agencies and reports prepared by the Atomic Energy Commission, forerunner agency to the Nuclear Regulatory Commission.

Documents available from public and special technical libraries include all open literature items, such as books, journal and periodical articles, and transactions. *Federal Register* notices, federal and state legislation, and congressional reports can usually be obtained from these libraries.

Documents such as theses, dissertations, foreign reports and translations, and non-NRC conference proceedings are available for purchase from the organization sponsoring the publication cited.

Single copies of NRC draft reports are available free, to the extent of supply, upon written request to the Office of Information Resources Management, Distribution Section, U.S. Nuclear Regulatory Commission, Washington, DC 20555.

Copies of industry codes and standards used in a substantive manner in the NRC regulatory process are maintained at the NRC Library, 7920 Norfolk Avenue, Bethesda, Maryland, and are available there for reference use by the public. Codes and standards are usually copyrighted and may be purchased from the originating organization or, if they are American National Standards, from the American National Standards Institute, 1430 Broadway, New York, NY 10018.

DISCLAIMER NOTICE

This report was prepared as an account of work sponsored by an agency of the United States Government. Neither the United States Government nor any agency thereof, or any of their employees, makes any warranty, expresed or implied, or assumes any legal liability of responsibility for any third party's use, or the results of such use, of any information, apparatus, product or process disclosed in this report, or represents that its use by such third party would not infringe privately owned rights.

NUREG/CR-5163
EGG-2542
R3

Power Burst Facility (PBF) Severe Fuel Damage Test 1-4 Test Results Report

Manuscript Completed: February 1989
Date Published: April 1989

Prepared by
D.A. Petti, Z.R. Martinson, R.R. Hobbins, C.M. Allison,
E.R. Carlson, D.L. Hagrman, T.C. Cheng, J.K. Hartwell,
K. Vinjamuri, L.J. Seifken

Idaho National Engineering Laboratory
Managed by the U.S. Department of Energy

EG&G Idaho, Inc.
P.O. Box 1625
Idaho Falls, ID 83415

Prepared for
Division of Systems Research
Office of Nuclear Regulatory Research
U.S. Nuclear Regulatory Commission
Washington, DC 20555
NRC FINS A6305, A6321
Under DOE Contract No. DE-AC07-761D01570

ABSTRACT

A comprehensive evaluation of the Severe Fuel Damage (SFD) Test 1-4 performed in the Power Burst Facility (PBF) at the Idaho National Engineering Laboratory is presented. Test SFD 1-4 was the fourth and final test in an internationally sponsored light water reactor severe accident research program, initiated by the U. S. Nuclear Regulatory Commission. The overall technical objective of the test was to contribute to the understanding of fuel and control rod behavior, aerosol and hydrogen generation, and fission product release and transport during a high-temperature, severe fuel damage transient.

A test bundle, comprised of 26 previously irradiated (36,000 MWd/MtU) pressurized water-reactor-type fuel rods, 2 fresh instrumented fuel rods, and 4 silver-indium-cadmium control rods, was surrounded by an insulating shroud and contained in a pressurized in-pile tube. The experiment consisted of a 1.3-h transient at a coolant pressure of 6.95 MPa in which the inlet coolant flow to the bundle was reduced to 0.6 g/s while the bundle fission power was gradually increased until dryout, heatup, cladding rupture, and oxidation occurred. With sustained fission power and heat from oxidation, temperatures continued to rise rapidly, resulting in zircaloy and control rod absorber alloy melting, fuel liquefaction, material relocation, and the release of hydrogen, aerosols, and fission products. The transient was terminated over a 2100-s time span by slowly reducing the reactor power and cooling the damaged bundle with argon gas.

A description and evaluation of the major phenomena, based upon the response of on-line instrumentation, analysis of fission product and aerosol data, postirradiation examination of the fuel bundle, and calculations using the SCDAP/RELAP5 computer code, are presented.

FIN No. A6305—PBF Severe Fuel Damage PIE and Analysis
FIN No. A6321—PBF Fission Product Behavior

EXECUTIVE SUMMARY

The Severe Fuel Damage Test 1-4 (SFD 1-4) was conducted in the Power Burst Facility (PBF) at the Idaho National Engineering Laboratory (INEL) on February 7, 1985. The test was the last in a series of four in-pile tests performed in the PBF as part of an internationally sponsored[a] light water reactor (LWR) severe fuel damage research program initiated by the U.S. Nuclear Regulatory Commission (NRC). The objective of the program was to develop a data base and models to enable predictions of (a) the overall response of the fuel rods, control rods, and associated spacer grids; (b) the rate of hydrogen generation from the interaction of steam with the fuel, cladding, and core components; and (c) the rate, magnitude, and chemical forms of fission products and aerosols released from the core for the range of conditions encountered in severe accidents. In addition, the data are being used to aid in resolving some of the outstanding NRC safety issues related to severe reactor accidents.

The SFD 1-4 test train incorporated a fuel bundle and a simulated upper plenum. The test bundle was comprised of 26 1.0-m-long BR-3 fuel rods previously irradiated to 36,000 MWd/MtU, 2 fresh instrumented fuel rods, and 4 control rod guide tubes, each containing a stationary silver-indium-cadmium control rod. The bundle was housed in an insulated shroud that allowed steam boiloff from a liquid pool at a rate between 0.6 and 1.3 g/s. During the transient, a small flow of argon was introduced into the bundle to stabilize system pressure and ensure the transport of hydrogen, aerosols, and fission products from the bundle. The upper plenum located above the fuel bundle region provided a flow path to the sampling and monitoring system. A portion of the upper plenum was heated and housed a deposition rod which contained 40 deposition coupons to characterize fission product and aerosol deposition in the plenum during the experiment.

The entire effluent from the test bundle—consisting of superheated steam, hydrogen, fission products, and aerosols—was routed through the upper plenum to a sampling and monitoring system containing a variety of instrumentation. Isotopic fission product concentrations in the effluent were obtained by on-line gamma-ray spectrometers, while general fission product release levels were measured by an array of gross radiation monitors. The aerosol number concentration in the effluent line was determined using an optical turbidity meter. The effluent line hydrogen concentration was monitored on-line by a thermal conductivity analyzer. A variety of samples was collected, including effluent steam and liquid grab samples, collection tank samples, deposition coupons, and effluent line sections.

The transient phase of the test consisted of a 1.3-h-long nuclear transient which simulated a small-break, loss-of-coolant accident without emergency core cooling (S_2D) in a commercial pressurized water reactor (PWR). Bundle boildown, dryout, heatup, control rod absorber alloy melting, cladding rupture, and oxidation occurred as the bundle fission power was slowly increased to 27 kW. The bundle fission power was maintained at 27 kW for 223 s; and temperatures rose rapidly, resulting in zircaloy melting, fuel liquefaction, and material relocation and interaction, along with hydrogen, aerosol, and fission product release. The SFD 1-4 bundle was cooled slowly through a gradual power decrease and increased argon flow through the bundle. The bundle and upper plenum were kept dry in an inert environment until the test train was removed from the test loop. The overall test behavior is summarized here in terms of specific severe accident phenomena.

Zircaloy Oxidation, Hydrogen Generation, and Melt Progression

The transient was initiated, starting at an initial equilibrium temperature of 750 K, by increasing the bundle power to produce a heatup rate of 0.37 K/s from 800 to 1200 K. The power was then increased further to obtain an average heatup rate of 1.6 K/s from 1200 to 1600 K. An increasing oxidation rate accelerated the heatup rate to >2 K/s, with a maximum heatup rate of ~ 10 K/s measured just prior to thermocouple failure at ~ 1900 K.

The oxidation front started at the bundle midplane, then propagated upward, downward, and later radially outward to the shroud liner. Heatup and oxidation of the zircaloy in the lower bundle regions consumed essentially all of the incoming steam, resulting in steam-starved conditions during most of the high-temperature transient. After nearly complete oxidation of the lower bundle regions over an $\sim$200-s time span, the oxidation front moved upward again to the higher power mid-bundle elevations (0.4 to 0.6 m), where rapid oxidation produced temperatures of $\sim$2800 K. The total amount of hydrogen generated during the experiment was 86 ± 12 g, equivalent to 32% oxidation of the zircaloy exposed to high temperatures.

---

[a] Partners in the program include Belgium, Canada, Federal Republic of Germany, Finland, Italy, Japan, Netherlands, American Institute of Taiwan, Republic of Korea, Spain, Sweden, Switzerland, United Kingdom, and United States Nuclear Regulatory Commission.

The damage progression in the bundle was a result of control rod melting and relocation, zircaloy oxidation, and fuel liquefaction. Posttest examination revealed four distinct damage regions in the bundle. The upper portion of the bundle consisted of a rubble bed of unclad fuel fragments. Partial fuel pellets and the remnants of fuel dissolution remained in the mid-bundle region. Molten zircaloy and liquefied fuel accumulated in the lower bundle; and metallic melts, consisting of zircaloy, stainless steel, and control rod alloy material, resided at the lower spacer grid near the bottom of the bundle. A total of $\sim$18% of the fuel liquefied during the transient.

Hot effluent hydrogen, produced by extensive zircaloy oxidation in the low and mid-bundle regions, apparently carried enough sensible heat to cause melting of most of the zircaloy in the upper bundle regions (0.7 to 0.9 m). The molten zircaloy relocated to the mid-bundle region, and the declad fuel in the upper bundle formed a rubble bed. Molten zircaloy relocation from the upper bundle region and continued oxidation in the middle of the bundle drove fuel temperatures above 2800 K and caused significant UO_2 dissolution. Fuel material in the mid-bundle region relocated to the lower third of the bundle between 2300 and 2900 s. The relocated material was not totally oxidized because it dissolved previously oxidized cladding and a significant amount of fuel in the lower bundle. Peak bundle temperatures were estimated to be at least 2800 K in about 25% of the bundle where most of the damage occurred, about 2200 K in the upper bundle debris bed region, and below 1700 K in the lower bundle region where metallic melts accumulated. Melt relocation decreased the available flow area by 70% in the lower bundle region, with a maximum flow area reduction of 87% at the bottom of the bundle.

The instrumented control rod failed early in the test at 1170 K because of a weld defect that resulted in waterlogging and excessive internal pressure during the heatup. The other three non-instrumented control rods failed at a temperature of $\sim$1700 K, corresponding to the melting point of the control rod stainless steel cladding (1720 K). The alloy located above the elevation of cladding failure drained rapidly out of the rod. As the bundle continued to heat up, upper portions of the empty control rod guide tube melted and relocated downwards. Posttest examination indicated that 83% of the control rod material relocated and froze near the lower spacer grid at 0.08 m in the bundle, and much of the remaining control rod material had relocated to the lower plenum. The control rod alloy and molten stainless steel interacted with zircaloy in the bundle during and following relocation but did not interact significantly with fuel. Control rod material that relocated to the lower regions of the bundle was reheated by relocating ceramic melts long after initial control rod failure, causing additional vaporization of control rod alloy materials, especially cadmium. The principal effects of the control rods were the generation of cadmium aerosol and the formation of metallic melts that solidified at low elevations in the bundle, producing a lower crust that caused a significant reduction in the flow area.

Test SFD 1-4 indicates that melt progression in a severe accident is inherently incoherent. Axial and temporal temperature gradients in the SFD 1-4 bundle and the presence of different materials with different melting points caused large spatial and temporal variations in melt relocation behavior. The bundle was at high temperatures and melt relocation occurred for several minutes in Test SFD 1-4, continuing well after the power descent had begun, as evidenced by the 1080- to 1440-s duration of hydrogen production, aerosol generation, and fission product release. Thicknesses of alternating metal and oxide layers low in the bundle suggest multiple relocation events at 5- to 60-s intervals. In addition, relocated material of different compositions and melting points observed in the lower bundle indicate that several discrete melt relocation events occurred. These melts include: ceramic $(U,Zr)O_2$ (melting point $\sim$2800 K), zircaloy (melting point $\sim$2200 K), stainless steel (melting point $\sim$1700 K), and Ag-In-Cd (melting point $\sim$1120 K).

The melt progression phenomena observed in Test SFD 1-4 reveal parallels to those more fully developed in the TMI-2 accident which was terminated at a later stage. The debris bed of fuel fragments in the upper bundle is similar to the upper debris bed in TMI-2. The high-temperature U-Zr-O melt in the lower bundle is a precursor to the molten pool in TMI-2. The accumulation of metallic melts (Ag-In-Cd, zirconium, stainless steel) near the bottom of the bundle is a precursor of the metallic lower crust found in TMI-2.

Fission Product Release

Fission product release was affected by changes in fuel morphology and isotopic half-life in Test SFD 1-4. Very little noble gas release was measured below 1500 K. The noble gas fractional release rate increased four orders of magnitude as bundle temperatures were driven above 2100 K by oxidation of the zircaloy cladding and then remained generally constant during the high-temperature portion of the transient. The effect of changes in fuel morphology, such as liquefaction and dissolution, on the rate of fission product release was difficult to detect due to the integral nature of the test. Elevated releases were measured during the cooldown phase of the transient.

Integral releases of the noble gases ranged from 23 to 52%. Total bundle releases for iodine and cesium were 24 and 51%, respectively, whereas only 3% of the bundle inventory of tellurium was released. Most of the released iodine, cesium, and tellurium was deposited in the test train, upper plenum, and effluent line. Iodine and cesium were later washed from system surfaces during flushing operations and measured in the collection tank. System flushing removed very little of the deposited tellurium. Lesser amounts of the low-volatility fission products (strontium, barium, lanthanum, europium, and cerium) were released during the experiment.

Releases of long-lived volatile fission product species were greater than those of short-lived species. The release fractions for ^{85}Kr and stable xenon and krypton isotopes were $\sim$0.5, yet the average release of seven short-lived noble gases was $\sim$0.35. This difference in release is believed to be related to the morphology of the fuel and the location of the fission products in the fuel prior to release. More long-lived than short-lived species reside at grain boundaries from which release is relatively fast during heatup because of the interconnected porosity in the high-burnup fuel. Release is much slower for the short-lived species, because more of the inventory is in the fuel grain and must diffuse to the grain boundaries prior to release.

Calculations of fission gas release were performed using CORSOR, FASTGRASS, and Booth-type release models to provide additional insight into the physical phenomena governing fission product release during Test SFD 1-4. Calculated release rates from all the models were in good agreement with those measured on heatup in Test SFD 1-4. CORSOR calculations were in much better agreement with the heatup release from high-burnup fuel in Test SFD 1-4 than with the heatup release measured from low-burnup fuel in Test SFD 1-1. The Booth model, that used the diffusion coefficient correlation derived from Oak Ridge National Laboratory fission product release tests with similar high-burnup fuel, provided the best agreement with the release measured during heatup. The agreement indicates that very little difference should be expected between in-pile and out-of-pile experiments for releases from high-burnup fuel during heatup. FASTGRASS calculations indicated that release rates on heatup for short- and long-lived species should be different; however, these differences should diminish once significant fuel dissolution occurs. All three models overpredicted the measured releases during the high-temperature portion of the test, when significant fuel liquefaction and dissolution occurred; and all of the models failed to account for the sustained releases measured during the cooldown phase of the test.

Fission Product and Aerosol Deposition and Transport

Aerosol generation in Test SFD 1-4 was continuous during the high-temperature portion of the experiment and was strongly coupled to melt progression phenomena in the bundle. The vaporization of Ag-In-Cd control rod material, tin release due to zircaloy oxidation, volatile fission product release, possible release of loose particulates from the shroud (ZrO_2) insulation cavity, and ceramic melt relocation and interaction with control rod material all contributed to the aerosol source exiting the SFD 1-4 bundle.

Measurements indicate that at least 13 g of aerosol material were released from the bundle—$\sim$5 g of cadmium, 0.4 g of silver, and 0.2 g of indium, at least 4 g of tin, and 3.5 g of zirconium. Although these values represent a small fraction of the bundle inventory of these materials, their mass was sufficient to produce a very dense aerosol during the entire high-temperature portion of the transient.

Chemical equilibrium calculations indicate that the dominant forms of cesium and iodine in the effluent were cesium iodide and cesium hydroxide, with some elemental cesium at high temperatures. Because of the high concentrations of cesium and iodine released from the high-burnup fuel and the low release of silver, no hydrogen iodide and no silver iodide were predicted to form. The dominant form of tellurium released from the bundle was calculated to be tin telluride. These results are consistent with posttest system flushing results that indicate most of the iodine and cesium deposition was easily removed by water, whereas very little of the deposited tellurium was removed. The reducing environment resulted in silver, cadmium, and tin being released in their elemental form.

Distinct mechanisms governed aerosol behavior in different parts of the SFD 1-4 upper plenum. Vapor condensation and aerosol nucleation were the dominant mechanisms immediately above the fuel bundle. Upon exiting the bundle, silver and tin, because of their low volatility, condensed and formed aerosols near the top of the bundle. The high temperatures above the bundle and the high vapor pressures of cadmium, cesium hydroxide, and cesium iodide prevented these materials from condensing onto aerosols and system surfaces until they reached the lower tip of the deposition rod ($\sim$800 K), whereupon they condensed very rapidly on the tin and silver aerosols and the downstream surfaces of the deposition rod. The presence of significant quantities of ^{137}Cs on the cadmium aerosol deposits and the results of fission product and aerosol transport calculations indicate that the aerosol generated in Test SFD 1-4 provided a large mobile surface on which volatile fission products could condense. Below 700 K, $>95\%$ of the volatile fission products remaining in the effluent were transported as an aerosol.

Once the aerosol moved further downstream, aerosol agglomeration, deposition, and settling governed its behavior in the heated portion of the upper plenum. Cohesive deposits of cadmium were observed on the horizontal surfaces of most of the deposition rod. This deposition was caused by turbulent deposition of particles $>25\ \mu$m due to wakes and eddies, gravitational settling, and/or flow of liquid condensate (e.g., cesium hydroxide, cadmium) from vertical to horizontal surfaces on the deposition rod. Significant attenuation of the larger-sized aerosols occurred in the heated upper plenum because of the filtering effect of the 20 horizontal surfaces of the deposition rod.

As the aerosol entered the unheated portion of the upper plenum, the cooler wall temperatures caused some evaporation of cadmium, cesium hydroxide, and cesium iodide from the aerosol to the wall, leaving a small ($<1\ \mu$m) tin-rich aerosol which entered the aerosol monitor. A fine yet dense aerosol was continuously measured 10 m downstream of the bundle at the aerosol monitor. The aerosol measured by filtered samples near the monitor was predominantly tin and cadmium, with small amounts of silver, zirconium, and fission products. The diameter of average mass of the aerosol at the turbidity monitor ranged from 0.4 to 1.0 μm, and the number concentration varied between 5×10^7 and 2×10^8 p/cm^3 during the test.

SCDAP/RELAP5 Calculations

SCDAP/RELAP5-MOD1 analyses of Test SFD 1-4 were made to help determine the probable damage progression history, to evaluate the importance of uncertainties in measured test boundary conditions and modeling assumptions on the calculated bundle behavior, and to define needed modeling improvements. In general, the code calculations accurately represented the bundle transient behavior. Calculated fuel, control rod, and shroud temperatures agreed well with the measurements until the thermocouples failed. The calculated peak bundle temperatures reached during the transient were representative of those determined from metallurgical estimates. The combination of the SCDAP/RELAP5 analyses, on-line measurements, and metallurgical examination provided a consistent scenario of the bundle behavior.

A series of sensitivity studies indicate that the uncertainties in test boundary conditions and modeling assumptions contributed about equally to the uncertainties in the calculations but had minor impact upon the interpretation of the bundle response and code validation. Comparisons of the calculations with test data and the sensitivity calculations have pointed out the need for additional improvements related to melt porosity, ceramic melt solidification, and fuel dissolution. A new fuel dissolution model, incorporated as a result of these analyses, made a significant improvement in the prediction of fuel liquefaction, relocation, and fission product release. These comparisons also made a substantial impact on the validation of SCDAP/RELAP5 by confirming that many of the models developed from other experiments or basic physics are applicable to severe accident conditions.

Impact

The results of Test SFD 1-4 have been applied to outstanding severe accident and source term issues related to (a) melt progression, (b) Ag-In-Cd control rod behavior, (c) hydrogen generation and zircaloy oxidation, (d) fission product release, (e) fission product chemical form, and (f) fission product and aerosol transport.

Test SFD 1-4 has provided data that have significantly improved the understanding of early-phase PWR melt progression related to the thresholds and mechanisms of material relocation, Ag-In-Cd control rod behavior, zircaloy oxidation in an intact geometry, and the extent of hydrogen generation after molten zircaloy relocation and blockage formation.

Information gained from Test SFD 1-4 has been used to address several source term issues. Fission product releases have been used to address questions related to differences between out-of-pile and in-pile release measurements and the adequacy of fission product release models. Fission product and aerosol transport behavior has helped define fission product chemical forms, dominant aerosol sources, and the impact of aerosols on fission product deposition and transport in a PWR severe accident.

The data obtained from Test SFD 1-4 strengthen the in-vessel PWR severe accident and source term behavior data base, and the improved understanding of specific phenomena can be used to reduce uncertainty in the results of probabilistic risk assessments of nuclear power plants.

ACKNOWLEDGMENTS

The authors are extremely appreciative of the organizations that have contributed to this program. It has taken about five years from conception of Severe Fuel Damage Test 1-4 to the issuance of this report; and the planning, execution, and analysis are a credit to all those individuals involved. The project required a wide range of disciplines and, within EG&G Idaho, Inc., engaged groups from severe accident research, engineering, reactor physics, PBF facility and technical support, test train assembly, data acquisition and reduction, Test Reactor Area hot cells and radiation measurements laboratory, and code development. Thanks go to J. D. Abrashoff, for the RAFFLE calculations; to B. G. Schnitzler and M. L. Takata, for the ORIGEN2 calculations; M. L. Carboneau, for the CORSOR and FASTGRASS calculations; C. E. White, for the VAPOR and Booth calculations; and G. S. Reilly, for the ETRA analysis. In addition, sincere appreciation goes to C. S. Olsen, for assistance in the metallographic examination; B. A. Pregger, for the SEM examinations; D. H. Meikrantz, L. A. Weinrich, M. W. Huntley, and G. L. Bourne, for the retained fission product radiochemical work; and R. D. McCormick, for instrument evaluations.

Other organizations have also participated in this collaborative program. The test train hardware was designed and fabricated by Battelle Pacific Northwest Laboratories; neutron radiography was performed by Argonne National Laboratory-West; Westinghouse Idaho Nuclear Company, Inc., performed chemical analysis; and Dr. J. Rest, of Argonne National Laboratory-East, provided FASTGRASS code consultation.

The careful and thorough reviews of this document by Drs. D. Olander, A. W. Cronenberg, and P. Hofmann are greatly appreciated. Special thanks go to G. S. Reilly, C. E. White, G. Jones, L. Hatcher, and D. H. Schwieder for providing the exemplary graphics, and to N. L. Wade, for excellent editing of the report.

Finally, D. J. Osetek is recognized for his contributions to the management of the SFD Program since its inception, including test specifications, hardware design, data acquisition, and results reporting.

CONTENTS

ABSTRACT iii

EXECUTIVE SUMMARY iv

ACKNOWLEDGMENTS ix

1. INTRODUCTION 1

2. SYSTEM DESCRIPTION 4

   2.1 The Facility 4

   2.2 Fuel Bundle and Test Train Design 4

   2.3 Effluent Sampling and Monitoring System 10

3. TEST CONDUCT 19

   3.1 Power Calibration Phase 19

   3.2 Long-Lived Fission Product Inventory Generation Phase 19

   3.3 Short-Lived Fission Product Inventory Generation Phase 19

   3.4 Bundle Boildown Phase 19

   3.5 High-Temperature Transient Phase 22

   3.6 Cooldown 23

   3.7 Posttest Activities 24

4. OVERVIEW OF THE SFD 1-4 TRANSIENT 25

   4.1 Test Boundary Conditions 25

      4.1.1 Rationale 25
      4.1.2 Coolant Pressure 25
      4.1.3 Coolant Flow Rate and Steam Interface Level 25
      4.1.4 Bundle Power 27
      4.1.5 Heat Loss Rate Measurement 28

   4.2 Experiment Scenario 30

      4.2.1 Initial Heatup 30
      4.2.2 Oxidation, Hydrogen Generation, and Melt Progression 32
      4.2.3 Control Rod Behavior 33
      4.2.4 Fission Product Release 34
      4.2.5 Aerosol Generation and Transport Behavior 35

5. BUNDLE HEATUP, OXIDATION, AND MELT PROGRESSION BEHAVIOR 37

5.1 Bundle Thermal Response 37

5.1.1 Fuel Rod and Shroud Temperatures 37
5.1.2 Effluent Temperature 44
5.1.3 Effluent Flow 50

5.2 Zircaloy Oxidation and Hydrogen Generation 50

5.2.1 Hydrogen Generation Rate 53
5.2.2 Collection Tank Hydrogen Results 54
5.2.3 Postirradiation Examination Oxidation Results 54
5.2.4 Summary 56

5.3 Fuel Behavior 56

5.3.1 Overview of Bundle Damage 57
5.3.2 Upper Bundle Region 57
5.3.3 Mid-Bundle Region 67
5.3.4 Lower Bundle Region 67
5.3.5 Lower Spacer Grid Region 75

5.4 Control Rod Behavior 75

6. FISSION PRODUCT RELEASE AND RETENTION BEHAVIOR 90

6.1 ORIGEN2 Inventory Calculations 90

6.2 Measurements and Analysis 90

6.2.1 Gross Radiation Monitor Responses 90
6.2.2 Fractional Release Rates Determined from the Effluent Grab Samplers 94
6.2.3 Fission Product Release Rates from the On-Line Spectrometer Data 94
6.2.4 Integral Release Data 98
6.2.5 Retained Fission Product Results 102

6.3 Model Comparisons 106

6.3.1 FASTGRASS Calculations 107
6.3.2 CORSOR Calculations 111
6.3.3 Booth Diffusional Calculations 112

6.4 Summary 118

7. FISSION PRODUCT AND AEROSOL TRANSPORT BEHAVIOR 119

7.1 Aerosol Measurements 119

7.2 Deposition Measurements and Analysis 119

7.2.1 Deposition Measurements 128
7.2.2 Integral Deposition Estimates 135

7.3 Aerosol Generation, Deposition, and Transport Behavior 137

7.3.1 Boundary Conditions 137
7.3.2 Aerosol Nucleation and Vapor Condensation Behavior 140
7.3.3 Aerosol Settling and Deposition 141
7.3.4 Aerosol Evaporation and Fine Aerosol Transport 146
7.3.5 Analysis of Aerosol Monitor Results 146

7.4 Fission Product and Aerosol Transport Analysis 148

7.4.1 Analysis Technique 150
7.4.2 Analysis Results 151
7.4.3 Conclusions from the PULSE Analysis 166

7.5 Aerosol Behavior Summary 167

7.5.1 Aerosol Generation 167
7.5.2 Aerosol Formation, Deposition, and Transport Summary 169

8. SCDAP/RELAP5 ANALYSES 171

8.1 Description of the SCDAP/RELAP5 Model 171

8.2 Results of SCDAP/RELAP5 Best-Estimate Calculations 175

8.2.1 Temperatures 175
8.2.2 Hydrogen Production 179
8.2.3 Changes in Bundle Geometry 179
8.2.4 Fission Product Release 179

8.3 Results of Sensitivity Calculations 188

8.4 Discussion 191

8.4.1 Damage Progression History 196
8.4.2 Influence of Uncertainties in Test Conditions and Modeling Assumptions 197
8.4.3 Model Improvements 198

9. IMPACT OF TEST SFD 1-4 ON SEVERE ACCIDENT ISSUES 199

9.1 Melt Progression 199

9.2 Zircaloy Oxidation and Hydrogen Generation 199

9.3 Ag-In-Cd Control Rod Behavior 200

9.4 Fission Product Release 200

9.5 Fission Product Chemical Form 200

9.6 Fission Product and Aerosol Deposition and Transport 200

9.7 Summary 200

10. SUMMARY AND CONCLUSIONS 201
10.1 Thermal Behavior 201
10.2 Zircaloy Oxidation and Hydrogen Generation 202
10.3 Melt Progression 202
10.4 Control Rod Behavior 203
10.5 Fission Product Release 203
10.6 Fission Product and Aerosol Transport Behavior 204
10.7 SCDAP/RELAP5 Analysis 204
10.8 Impact 205
11. REFERENCES 206
APPENDIX A—SYSTEM DESIGN FOR TEST SFD 1-4 .... A-1
APPENDIX B—INSTRUMENTATION AND SAMPLER DESCRIPTION, LOCATION, AND PERFORMANCE B-1
APPENDIX C—TEST SFD 1-4 DATA QUALIFICATION, UNCERTAINTIES, AND DATA PLOTS C-1
APPENDIX D—BUNDLE POWER RESULTS D-1
APPENDIX E—HYDROGEN MEASUREMENTS E-1
APPENDIX F—COOLANT LEVEL MEASUREMENTS F-1
APPENDIX G—FISSION PRODUCT RELEASE AND RETENTION MEASUREMENTS AND ANALYSIS G-1
APPENDIX H—FISSION PRODUCT AND AEROSOL BEHAVIOR ANALYSIS METHODS H-1
APPENDIX I—POSTIRRADIATION EXAMINATION RESULTS I-1
APPENDIX J—SCDAP/RELAP5 ANALYSIS MODEL J-1

FIGURES

1. Cutaway view of the Power Burst Facility reactor 5
2. Cross-sectional diagram of the SFD 1-4 test train and fuel bundle region 6
3. Axial diagram of the SFD 1-4 test train and effluent line with deposition rod 7

4. Axial schematic of the SFD 1-4 fuel bundle region 8

5. Schematic of a portion of the SFD 1-4 deposition rod 11

6. Layout diagram of the SFD 1-4 fission product sampling and monitoring system 12

7. Schematic of the SFD 1-4 sampling and monitoring system 12

8. SFD 1-4 aerosol monitor spool piece 14

9. Diagram of the SFD 1-4 aerosol monitor fiber-optic probe 14

10. Schematic of the SFD 1-4 effluent line up to the condenser 18

11. SFD 1-4 bundle nuclear power history during power calibration and fuel conditioning phases (zero time 13:30 h, Jan. 13, 1985) 23

12. Bundle coolant pressure during Test SFD 1-4 26

13. Bundle inlet steaming rate and steam interface level during Test SFD 1-4 28

14. Bundle nuclear power during Test SFD 1-4 29

15. Power transferred to the bypass coolant during Test SFD 1-4 29

16. Fission power, power to bypass coolant, steam oxidation power, power to effluent, and net bundle power during Test SFD 1-4 30

17. Neutron radiograph of the SFD 1-4 bundle 31

18. Scenario of events for Test SFD 1-4 32

19. Cladding temperatures at 0.39, 0.54, and 0.74 m for Test SFD 1-4 fuel rod 3B 38

20. Cladding temperatures at 0.39, 0.54, and 0.74 m for Test SFD 1-4 fuel rod 4D 38

21. Average cladding temperature ramp rate for Test SFD 1-4 fuel rods 3B and 4D at 0.39, 0.54, and 0.74 m 39

22. SFD 1-4 shroud inner liner temperatures at 270 degrees at 0.35, 0.50, and 0.70 m 40

23. SFD 1-4 shroud inner liner temperature ramp rate at 270 degrees at 0.35, 0.50, and 0.70 m 40

24. Bundle pressure, shroud outer wall temperature, and shroud meltthrough detector signals during the time of shroud liner failure in Test SFD 1-4 41

25. Comparison of measured cladding and fuel centerline temperatures at 0.39 m for Test SFD 1-4 rod 3B 42

26. Comparison of measured cladding and fuel centerline temperatures at 0.39 m for Test SFD 1-4 rod 4D 42

27. Axial temperature profile of fuel rod cladding temperatures at selected times during the Test SFD 1-4 transient 43

28. SFD 1-4 shroud midwall temperatures at 0.50, 0.70, and 0.91 m 43

29. SFD 1-4 shroud midwall temperatures at 0.50 m at 0, 90, 180, and 270 degrees 44

30. SFD 1-4 shroud meltthrough detector and midwall temperature responses 45

31. Steam temperatures within the SFD 1-4 bundle at 0.54 and 0.99 m 45

32. Test SFD 1-4 steam temperature at 0.54 m, average cladding temperature at 0.54 m, and average shroud inner liner temperature at 0.50 m 46

33. Steam temperatures above the SFD 1-4 bundle at 1.14 m at 30, 210, and 330 degrees 46

34. Steam temperatures above the SFD 1-4 bundle at 1.54, 2.35, and 3.36 m 47

35. Test SFD 1-4 effluent line wall temperatures at 1.84, 2.29, 2.83, and 3.40 m 47

36. Test SFD 1-4 deposition coupon temperatures at 1.57, 2.38, and 3.40 m at 45 degrees 48

37. Test SFD 1-4 steam and coupon temperatures at 2.35 and 2.38 m, respectively 48

38. Comparison of Test SFD 1-4 steam temperatures at 1.14 and 1.54 m and the deposition coupon temperature at 1.57 m 51

39. Response of the flow meter measuring liquid flow into the condenser during Test SFD 1-4 51

40. Response of the flow meter measuring gas flow into the condenser during Test SFD 1-4 52

41. Argon inlet flow and the gas and liquid flow from the SFD 1-4 bundle during the latter part of the transient 52

42. Hydrogen generation rate and cladding temperatures from rod 3B in Test SFD 1-4 53

43. Integral hydrogen generation in Test SFD 1-4 54

44. Zircaloy retention and oxidation fraction for solid zircaloy components 55

45. Oxidation fraction of zircaloy-bearing melts 55

46. Photograph of multiple oxide layers in melt at 0.17 m 56

47. Posttest distribution of open flow area, intact fuel, and control rod alloy material 58

48. Minimum peak temperature of in-place and relocated materials 59

49. Bundle cross section at 0.85 m 60

50. Partially oxidized metallic melt between two fuel fragments at 0.85 m 61

51. Photomicrographs showing oxidized and previously molten inner liner at 0.85 m 62

52. Photomicrograph showing fuel microstructure typical of the 0.85-m elevation 63

53. Bundle cross section at 0.74 m 64

54. Unetched photomicrographs showing attack of UO_2 by previously metallic melt in pellet crack at 0.74 m 65

55. Photomicrograph showing oxidized and previously molten inner liner at 0.74 m 66

56. Bundle cross section at 0.54 m 68

57. Photomicrograph showing microstructure in reacted portion of rod 5A fuel pellet at 0.54 m 69

58. Secondary electron image and X-ray dot map showing wide grain boundaries filled with iron oxide in reacted region of fuel rod 5A at 0.54 m 70

59. Bundle cross section at 0.39 m 71

60. Bundle cross section at 0.25 m 72

61. Normalized fission chamber output, indicating melt relocation events during Test SFD 1-4 73

62. SEM photomicrograph showing ceramic melt with metallic inclusions at 0.25 m 73

63. SEM photomicrograph showing ceramic and metallic phases in melt at 0.25 m 74

64. SEM photomicrograph at control rod position 2B at 0.25 m showing mixture of UO_2 and silver 74

65. Bundle cross section at 0.17 m 76

66. Photomicrograph of metallic melt between rods 5C, 6B, and 6C at 0.17 m 77

67. Bundle cross section at 0.08 m 78

68. Photomicrograph showing melt attack on cladding at 0.08 m 79

69. Photomicrograph showing containment of molten control material by oxide of dissolved guide tube in control rod position 2B at 0.08 m 80

70. Bundle cross section at 0.02 m 81

71. Photomicrograph of melt penetration of guide tube in control rod position 2B at 0.02 m 82

72. Photomicrograph showing relocation of Ag-In-Cd control rod material within and outside of control rod position 5B at 0.02 m 83

73. Bundle cross section at −0.09 m 84

74. Cladding temperatures for control rod 5E at 0.39 and 0.74 m during Test SFD 1-4 85

75. Cladding temperature for control rod 5E at 0.39 m, internal rod pressure, and coolant pressure during Test SFD 1-4, indicating the time that the instrumented control rod failed 86

76. Average inlet coolant temperature during failure of the control rods in Test SFD 1-4 86

77. Calculated control rod internal pressure as a function of temperature 87

78. Pressure and cladding temperature of control rod 5E during the three boildowns prior to the Test SFD 1-4 high-temperature transient 87

79. Normalized fission chamber output at the time of suspected control rod failure during Test SFD 1-4 89

80. Schematic of the SFD 1-4 sampling and monitoring system with locations of the four on-line gamma spectrometers noted 92

81. Response of SFD 1-4 effluent line ion chambers on the main floor and in Cubicle 13 92

82. Gamma activities at the SFD 1-4 steamline (Cubicle 13), liquidline, and gasline NaI(Tl) gross gamma-ray detectors 93

83. SFD 1-4 delayed neutron monitor (BF_3 type) response 94

84. Fractional release rates of noble gases determined from the gaseous portion of the SFD 1-4 unfiltered and filtered effluent samples 96

85. Selected isotopic concentrations at the SFD 1-4 mainfloor gamma-ray spectrometer 97

86. Selected isotopic concentrations at the SFD 1-4 steamline gamma-ray spectrometer 97

87. Comparison of fractional release rate from the on-line gamma spectrometers and the grab samples 99

88. Best-estimate noble gas fractional release rate in Test SFD 1-4 99

89. Comparison of FASTGRASS-calculated and measured noble gas release rates in Test SFD 1-4 with key events noted 109

90. Schematic comparison of FASTGRASS-modeled and actual liquefaction process 110

91. Comparison of CORSOR-predicted and measured noble gas release rates in Test SFD 1-4 112

92. Comparison of Booth base-case-calculated and measured noble gas release rates in Test SFD 1-4 115

93. Booth temperature sensitivity results using $a = 10\ \mu m$ 116

94. Booth "a" sensitivity results using the SCDAP/RELAP5 best-estimate temperature distribution 117

95. Aerosol monitor response in Test SFD 1-4 from the 1-cm path detector 120

96. Aerosol monitor response in Test SFD 1-4 from the 4-cm path detector 120

97. Aerosol monitor response in Test SFD 1-4 from the 1-cm path detector with filtered effluent sampling times indicated 121

98. SEM photomicrographs of SFD 1-4 effluent filters FEF-1 and FEF-2 123

99. SEM photomicrographs of SFD 1-4 effluent filters FEF-3 and FEF-4 124

100. SEM photomicrographs of SFD 1-4 effluent filters FEF-5 and FEF-6 125

101. Photographs of materials removed from SFD 1-4 effluent filter FEF-6 (a) and examined by SEM (b and c) 126

102. Photograph of the cohesive deposit (SD-12) found at coupon holder 12 128

103. A comparison of ^{137}Cs deposition on vertical and horizontal surfaces of the SFD 1-4 deposition rod 129

104. A comparison of ^{131}I deposition on vertical and horizontal surfaces of the SFD 1-4 deposition rod 129

105. A comparison of ^{129}I deposition on vertical and horizontal surfaces of the SFD 1-4 deposition rod 130

106. A comparison of ^{127m}Te deposition on vertical and horizontal surfaces of the SFD 1-4 deposition rod 130

107. A comparison of ^{90}Sr deposition on vertical and horizontal surfaces of the SFD 1-4 deposition rod 131

108. A comparison of ^{140}Ba (^{140}La) deposition on vertical and horizontal surfaces of the SFD 1-4 deposition rod 131

109. A comparison of ^{154}Eu deposition on vertical and horizontal surfaces of the SFD 1-4 deposition rod 132

110. A comparison of ^{244}Cm deposition on vertical and horizontal surfaces of the SFD 1-4 deposition rod 132

111. Silver deposition profile in the SFD 1-4 upper plenum 133

112. Cadmium deposition profile in the SFD 1-4 upper plenum 133

113. Tin deposition profile in the SFD 1-4 upper plenum 134

114. Zirconium deposition profile in the SFD 1-4 upper plenum 134

115. Schematic of the upper plenum geometry from the top of the active fuel to the top of coupon holder 2 138

116. Vapor pressures of potential aerosol sources 140

117. Vapor condensation and aerosol formation behavior of tin in the SFD 1-4 upper plenum 142

118. Vapor condensation and aerosol formation behavior of tin, silver, cadmium, and cesium iodide in the SFD 1-4 upper plenum 142

119. Settling velocity versus particle size for aerosols in the SFD 1-4 upper plenum 144

120. Inviscid flow calculations of the impaction efficiency for particles around a cylinder and a sphere 145

121. Streamlines for flow past a circular cylinder 146

122. Aerosol behavior in the heated and unheated portions of the SFD 1-4 upper plenum 147

123. Aerosol number concentration at the SFD 1-4 aerosol monitor 148

124. Diameter of average mass of the aerosol 149

125. Aerosol mass concentration 149

126. Calculated mole fraction of the dominant cesium chemical species at thermochemical equilibrium for the base-case conditions at temperatures between 900 and 2100 K 151

127. Comparison of calculated and measured aerosol mass density at the monitor for three calculations 152

128. Comparison of calculated and measured aerosol number concentration at the monitor for three calculations 153

129. Comparison of calculated and measured geometric mean diameter (GMD) of the aerosol at the monitor for three calculations 154

130. Calculated aerosol mass density at the heat shield and at the monitor 156

131. Calculated aerosol number density at the heat shield and at the monitor for the best-estimate calculation 157

132. Calculated aerosol size of a slug of effluent at ∿2800 s as a function of location for three calculations 158

133. Calculated distribution of cesium hydroxide and cesium iodide in the vapor and as an aerosol in a slug of effluent at ∿2800 s for three calculations 160

134. Calculated distribution of cadmium in the vapor and as an aerosol in a slug of effluent at ∿2800 s for three calculations 161

135. Comparison of calculated and measured surface concentrations of cesium for three calculations 163

136. Comparison of calculated and measured surface concentrations of cadmium for three calculations 164

137. Comparison of calculated and measured surface concentrations of tin for three calculations 165

138. SCDAP/RELAP5 representation of the SFD 1-4 test train and bundle 172

139. Bundle fission power used for the SCDAP/RELAP5 calculation 173

140. Axial power profile used for the SCDAP/RELAP5 calculation 173

141. Steam and argon inlet temperature and flow rate histories used for the SCDAP/RELAP5 calculation 174

142. Measured and calculated two phase fluid-steam interface 176

143. Comparison of measured and calculated steaming rates 176

144. Calculated cladding temperatures for the SFD 1-4 bundle 177

145. Calculated shroud inner liner temperatures for the SFD 1-4 bundle 178

146. Comparison of measured (rod 3B) and calculated cladding temperatures 180

147. Comparison of measured and calculated coolant temperatures 181

148. Comparison of measured and calculated shroud inner liner temperatures 182

149. Comparison of measured and calculated shroud midwall temperatures 183

150. Comparison of measured and calculated shroud outer wall temperatures 184

151. Comparison of metallurgically estimated and calculated peak fuel temperatures 185

152. Comparison of the measured and calculated hydrogen generation rate with the calculated steam starvation limit 185

153. Comparison of the measured and calculated fuel and melt cross-sectional area 187

154. Calculated volatile fission product release 189

155. Variation in calculated cladding temperature at 0.40 m with variations in test conditions 193

156. Variation in calculated cladding temperature at 0.40 m with variations in modeling assumptions 194

157. Variation in calculated cladding temperature at 0.55 m with variations in test conditions 194

158. Variation in calculated cladding temperature at 0.55 m with variations in modeling assumptions 195

159. Variation in calculated cladding temperature at 0.74 m with variations in test conditions 195

160. Variation in calculated cladding temperature at 0.74 m with variations in modeling assumptions 196

A-1. Cross-sectional diagram of the SFD 1-4 test train and fuel bundle region A-3

A-2. Axial schematic of the SFD 1-4 fuel bundle A-8

A-3. Axial diagram of the SFD 1-4 test train and effluent line with deposition rod A-12

A-4. Schematic of fission product deposition rod A-13

A-5. Layout diagram of the SFD 1-4 fission product sampling and monitoring system A-14

A-6. Schematic of the SFD 1-4 sampling and monitoring system A-14

A-7. Schematic of the SFD 1-4 aerosol monitor spool piece A-16

A-8. Diagram of the SFD 1-4 aerosol monitor fiber-optic probe A-16

A-9. Schematic of the SFD 1-4 effluent line up to the condenser A-17

B-1. Cross sections of the Test SFD 1-4 shroud and test bundle, indicating instrumentation between the 1.429- and 0.457-m elevations, with DARS parameter numbers in square brackets B-12

B-2. Cross sections of the Test SFD 1-4 shroud and test bundle, indicating instrumentation between the 0.393- and 0.363-m elevations, with DARS parameter numbers in square brackets B-13

B-3. Schematic of axial locations of SFD 1-4 test train instrumentation, with DARS parameter numbers in parentheses B-14

B-4. Schematic of the SFD 1-4 test train coolant system, pressure control system, and effluent sampling and measuring system B-16

D-1. Axial power distribution for an intact, water-filled SFD 1-4 bundle D-6

D-2. Axial power distribution for an intact, partially steam-filled SFD 1-4 bundle D-7

D-3. Axial power distribution for an intact, steam-filled SFD 1-4 bundle D-7

D-4. SFD 1-4 bundle material distribution used for the reactor physics calculations D-9

D-5. Axial power distribution of steam-filled SFD 1-4 bundle before and after control rod material relocation D-10

D-6. Transient SFD 1-4 bundle power history D-12

E-1. Measured H_2 monitor response in Test SFD 1-4 .... E-6

E-2. Schematic of the geometry used in the effluent transit analysis for Test SFD 1-4 .... E-8

E-3. Flow rates of steam, argon, and nitrogen input to the effluent transit analysis for Test SFD 1-4 .... E-10

E-4. Preliminary and best-estimate hydrogen monitor data for Test SFD 1-4 .... E-12

E-5. Preliminary and best-estimate hydrogen generation rates in the bundle for Test SFD 1-4 .... E-12

E-6. Mole fraction of steam, hydrogen, and argon exiting the bundle in Test SFD 1-4 .... E-13

E-7. Modified steaming rate for Test SFD 1-4 .... E-14

E-8. Integral hydrogen production in Test SFD 1-4 .... E-15

E-9. Transit time from bundle exit to separator inlet for Test SFD 1-4 .... E-16

E-10. Transit time to various locations in the effluent sampling and monitoring system for Test SFD 1-4 .... E-16

E-11. Transit time through the gas line versus time at the separator for Test SFD 1-4 .... E-18

E-12. Transit times calculated from spectrometer isotopic ratios from Test SFD 1-4 .... E-19

E-13. A comparison of the measured and calculated transit times for Test SFD 1-4 .... E-20

E-14. The effect of a ±5% change in the measured hydrogen concentration on the hydrogen generation rate for Test SFD 1-4 .... E-21

E-15. The effect of a ±5% change in the measured hydrogen concentration on the integral hydrogen generation rate for Test SFD 1-4 .... E-21

E-16. The effect of doubling the input steaming rate on the predicted hydrogen generation rate for Test SFD 1-4 .... E-22

E-17. The effect of a 15% change in total transient time on the hydrogen generation rate for Test SFD 1-4 .... E-23

E-18. The hydrogen generation rate for Test SFD 1-4 and its uncertainty envelope E-23

F-1. Steam interface level and steaming rate during Test SFD 1-4 .... F-4

G-1. Activity of ^{90}Sr as a function of exposure for BR-3 B300 and B500 series irradiations G-6

G-2. Activity of ^{95}Nb as a function of exposure for BR-3 B300 series irradiation G-7

G-3. Activity of ^{95}Nb as a function of exposure for BR-3 B500 series irradiation G-7

G-4. Activity of ^{106}Ru as a function of exposure for BR-3 B300 and B500 series irradiations G-8

G-5. Activity of ^{110m}Ag as a function of exposure for BR-3 B300 and B500 series irradiations G-8

G-6. Activity of ^{125}Sb as a function of exposure for BR-3 B300 and B500 series irradiations G-9

G-7. Activity of ^{127m}Te as a function of exposure for BR-3 B300 series irradiation G-9

G-8. Activity of ^{127m}Te as a function of exposure for BR-3 B500 series irradiation G-10

G-9. Activity of ^{129}I as a function of exposure for BR-3 B300 and B500 series irradiations G-10

G-10. Activity of ^{134}Cs as a function of exposure for BR-3 B300 and B500 series irradiations G-11

G-11. Activity of ^{137}Cs as a function of exposure for BR-3 B300 and B500 series irradiations G-11

G-12. Activity of ^{144}Ce as a function of exposure for BR-3 B300 and B500 series irradiations G-12

G-13. Activity of ^{154}Eu as a function of exposure for BR-3 B300 and B500 series irradiations G-12

G-14. Activity of ^{155}Eu as a function of exposure for BR-3 B300 and B500 series irradiations G-13

G-15. Ratio of gram ^{235}U equivalent to total grams uranium G-13

H-1. Silver, indium, and cadmium release rate predictions from VAPOR (base-case calculation) H-9

H-2. Modified temperature at Node 2 used for the VAPOR reheat calculation H-10

H-3. Silver, indium, and cadmium release rate predictions from VAPOR, accounting for reheat H-10

H-4. Mole fractions of steam, hydrogen, and argon; and total molar flow rate H-13

H-5. Gas temperature in the heat shield cone used in the fission product and aerosol transport analysis H-13

H-6. Wall temperature in the heat shield cone (1 through 4) and heat shield tube (5) used in the fission product and aerosol transport analysis H-14

H-7. Wall temperatures of the deposition rod (6 through 11) used in the fission product and aerosol transport analysis H-14

H-8. Wall temperature of effluent line (12 through 14) and aerosol monitor (15 through 17) used in the fission product and aerosol transport analysis H-15

H-9. Fission product fractional release rate used in the fission product and aerosol transport analysis H-16

H-10. Calculated mole fraction of the dominant cesium chemical species at thermochemical equilibrium for the base-case conditions at temperatures between 900 and 2100 K H-20

H-11. Source rates of cadmium, cesium hydroxide, and cesium iodide to the heat shield used in the fission product and aerosol transport analysis H-20

H-12. Source rates of tin vapor and tin aerosol to the heat shield used in the fission product and aerosol transport analysis H-21

I-1. Axial gross gamma scan of the SFD 1-4 test train posttest I-4

I-2. Comparison of the posttest gamma scan from test bundle SFD 1-4 with calculated burnup profile (from irradiation in the BR-3 reactor prior to PBF operation) I-4

I-3. Overall axial neutron radiographs of the Test SFD 1-4 bundle, showing relative locations of sections I-6

I-4. Comparison of pretest and posttest unreacted fuel distribution I-9

I-5. Comparison of pretest and posttest flow area distribution I-9

I-6. Posttest distribution of zircaloy components in the SFD 1-4 bundle I-10

I-7. Distribution of different melts in the SFD 1-4 bundle I-10

I-8. Cross-sectional area of oxidized zircaloy components in the SFD 1-4 bundle I-14

I-9. Cross-sectional area of molten zircaloy in the SFD 1-4 bundle that was oxidized I-15

I-10. Pre- and posttest axial fuel distribution in the SFD 1-4 bundle I-15

I-11. Pre- and posttest axial control rod material distribution in the SFD 1-4 bundle I-16

I-12. Minimum peak temperature of in-place and relocated materials I-16

I-13. SFD 1-4 bundle cross section at 0.85 m I-17

I-14. Partially oxidized metallic melt between two fuel fragments at 0.85 m I-18

I-15. Photomicrographs showing oxidized and previously molten inner liner at 0.85 m I-19

I-16. Zirconium-oxygen equilibrium phase diagram (Ref. I-3) I-20

I-17. Photomicrograph showing fuel microstructure typical of the 0.85-m elevation I-22

I-18. SFD 1-4 bundle cross section at 0.74 m I-23

I-19. Unetched photomicrographs showing attack of UO_2 by previously metallic melt in pellet crack at 0.74 m I-24

I-20. Photomicrograph showing oxidized and previously molten inner liner at 0.74 m I-25

I-21. Unetched photomicrograph showing dissolution of ZrO_2 insulation by molten zircaloy at 0.74 m I-26

I-22. Unetched photomicrograph showing UO_2 fuel microstructure at 0.74 m I-27

I-23. SFD 1-4 bundle cross section at 0.54 m I-28

I-24. Photomicrograph showing microstructure in reacted portion of rod 5A fuel pellet at 0.54 m I-29

I-25. Secondary electron image and X-ray dot map showing wide grain boundaries filled with iron oxide in reacted region of fuel rod 5A at 0.54 m I-30

I-26. Secondary electron image showing fuel microstructure in unreacted region of fuel rod 5A at 0.54 m I-31

I-27. Secondary electron image showing microstructure of reacted fuel in the center of the bundle at 0.54 m I-31

I-28. Fe_3O_4—ZrO_2 phase diagram (Reference I-4) I-32

I-29. Photomicrograph showing melt/fuel interaction at the bundle periphery, rod 6C, at 0.54 m I-33

I-30. SFD 1-4 bundle cross section at 0.39 m I-34

I-31. Photomicrograph showing melt attack on fuel in rod 3B at 0.39 m I-35

I-32. Photomicrograph showing melt interaction with fuel in rod 3C at 0.39 m I-36

I-33. Photomicrographs showing effects of fuel etch on ceramic melts at 0.39 m I-37

I-34. Photomicrograph showing microstructure of reacted/melted fuel in center of rod 6B at 0.39 m I-38

I-35. Photomicrograph showing fuel microstructure in unreacted portion of rod 6B at 0.39 m I-38

I-36. SFD 1-4 bundle cross section at 0.25 m I-39

I-37. Melt interactions with fuel and control rods at 0.25 m I-40

I-38. SEM photomicrograph showing ceramic melt with metallic inclusions at 0.25 m I-42

I-39. SEM photomicrograph showing ceramic and metallic phases in melt at 0.25 m I-42

I-40. SEM photomicrograph at control rod position 2B at 0.25 m showing mixture of UO_2 and silver I-43

I-41. Photomicrograph showing eutectoid transformation at 1770 K in ZrO_2 in the oxidized cladding of fuel rod 1C at the periphery of the bundle at 0.25 m I-43

I-42. Photomicrograph showing fuel unreacted with melt and with grain boundary shattering at 0.25 m I-44

I-43. Photomicrograph showing the attack of molten zircaloy on ZrO_2 in the oxidized liner at 0.25 m I-44

I-44. Photomicrograph showing the equiaxed α-zircaloy microstructure in the saddle at 0.25 m I-45

I-45. Photomicrograph showing the hydriding (about 150 ppm) in the saddle at 0.25 m I-45

I-46. SFD 1-4 bundle cross section at 0.17 m I-46

I-47. Photomacrograph showing molten zircaloy attack on oxidized cladding and bundle insulation, locations 1B and 1C, at 0.17 m I-48

I-48. Photomacrograph showing metallic melt between rods 5C, 6B, and 6C at 0.17 m I-49

I-49. Photomicrograph of metallic melt attacking oxidized cladding on rod 6C at 0.17 m I-50

I-50. Backscattered electron image and x-ray dot maps of a sample of metallic melt between rods 5C, 6B, and 6C at 0.17 m I-51

I-51. Photomicrograph showing multiple oxide layers in melt at 0.17 m I-56

I-52. Ceramic melt between rods 3F and 4F at 0.17 m I-57

I-53. Photomicrograph showing unetched fuel microstructure near the periphery of rod 5C at 0.17 m I-59

I-54. Photomicrograph showing unetched fuel microstructure near the center of rod 5C at 0.17 m I-60

I-55. Composite photomicrograph of the fuel structure in rod 3E showing grain boundary separation in the outer ring of the fuel, large equiaxed grains in the inner ring, and metallic material relocated and frozen in the central void at 0.17 m I-61

I-56. Photomicrographs showing the cladding at control rod position 5F, as polished, at 0.17 m I-62

I-57. Photomicrograph showing the heat-affected region in the saddle at 0.17 m I-63

I-58. Photomicrograph showing hydriding typical of the saddle at 0.17 m I-64

I-59. SFD 1-4 bundle cross section at 0.08 m I-65

I-60. Photomicrograph showing damage in the vicinity of control rod position 5E at 0.08 m I-66

I-61. Photomicrograph showing molten control material contained by the ZrO_2 shell of the oxidized guide tube at 0.08 m I-66

I-62. Photomicrograph showing oxides on materials that have interacted with the melt at 0.08 m I-67

I-63. Photomicrograph showing prior β-zircaloy microstructure of unreacted liner at 0.08 m I-67

I-64. Photomicrograph showing melt attack on cladding at 0.08 m I-69

I-65. Photomicrograph showing containment of molten control material by oxide of dissolved guide tube in control rod position 2B at 0.08 m I-70

I-66. Photomicrograph showing melt in fuel cracks in rod 3C at 0.08 m I-71

I-67. SFD 1-4 bundle cross section at 0.02 m I-72

I-68. Photomicrograph of melt penetration of guide tube in control rod position 2B at 0.02 m I-73

I-69. Photomicrograph showing relocation of Ag-In-Cd control rod material within and outside of control rod position 5B at 0.02 m I-74

I-70. Photomicrograph showing equiaxed α-zircaloy microstructure typical of fuel rod cladding at 0.02 m I-76

I-71. Photomicrograph showing equiaxed α-zircaloy microstructure typical of the liner at 0.02 m I-76

I-72. Photomicrograph showing equiaxed α-zircaloy microstructure typical of the saddle at 0.02 m I-77

I-73. Photomicrograph showing fuel grain size of 18.4 μm in rod 6B at 0.02 m I-77

I-74. SFD 1-4 bundle cross section at −0.09 m I-78

I-75. Photomicrographs showing two-phase melt between rods 3C and 3D at −0.09 m I-79

I-76. Photomicrographs of multiphase melt surrounded by oxide layer between rods 3F and 4F at −0.09 m I-80

TABLES

1. The PBF severe fuel damage test series 2

2. SFD 1-4 bundle characteristics 9

3. Sample system component dimensions for Test SFD 1-4 15

4. SFD 1-4 sequence of events 20

5. SFD 1-4 effluent line temperatures (K) 49

6. Fission chamber response during control rod failure 89

7. ORIGEN2 inventories of selected radionuclides 91

8. Fractional release rates from the gas portion of the effluent line grab samplers 95

9. Comparison of noble gas release fractions based on various measurements 101

10. Best-estimate release fractions for reactive fission products in Test SFD 1-4 102

11. Composition and identification of core bore samples analyzed for retained fission product content 103

12. Estimated fission product retention percentages 104

13. Comparison of CORSOR-calculated fission product release and Test SFD 1-4 data 112

14. Arrhenius parameters for diffusion coefficients used in the Booth release model for Test SFD 1-4 114

15. Description of Booth release calculations 114

16. Calculated release fractions using the Booth model 115

17. Radioisotopic and elemental analysis of effluent sample filters 121

18. Aerosol composition based on the effluent sample filter results (wt.%) 122

19. Results of particle size analysis of effluent filters 127

20. Material deposition in the SFD 1-4 sampling system 136

21. Comparison of pre- and postflush collection tank and effluent system release fractions 136

22. System geometry for the SFD 1-4 upper plenum and deposition rod 138

23. Thermal-hydraulic conditions in the SFD 1-4 upper plenum 139

24. Source rates and melting points of bundle materials used in the aerosol analysis 140

25. Models included in the SFD 1-4 fission product transport analysis 150

26. Measured and calculated aerosol composition at 11.7 m 162

27. Calculated and measured key events 186

28. Sensitivity studies on test conditions 190

29. Sensitivity studies on modeling assumptions 191

30. Summary of results from sensitivity studies 192

31. Relative variation in predicted test results for the variation in test conditions and modeling assumptions 193

A-1. Nominal design characteristics for unirradiated fuel rods for Test SFD 1-4 .... A-4

A-2. Nominal design characteristics for irradiated fuel rods for Test SFD 1-4 .... A-4

A-3. Summary of irradiated fuel rod characteristics for Test SFD 1-4 .... A-5

A-4. Control rod design characteristics for Test SFD 1-4 .... A-7

A-5. Sample system component dimensions for Test SFD 1-4 .... A-9

B-1. Test SFD 1-4 instrumentation identification and data channel recording B-4

B-2. Test SFD 1-4 instrumentation performance B-21

C-1. DARS data qualifications C-6

C-2. Time spans for various phases of Test SFD 1-4 .... C-15

C-3. List of microfiche DARS data plots C-17

D-1. Test SFD 1-4 ratio of bundle power to reactor power as a function of coolant density D-6

D-2. Test SFD 1-4 measured and calculated ratio of bundle to reactor power D-8

D-3. Test SFD 1-4 axial pointwise control rod material distribution D-8

D-4. Test SFD 1-4 axial histogram of control rod material used in RAFFLE calculation D-8

D-5. Calculated Test SFD 1-4 transient bundle power D-11

E-1. Test SFD 1-4 collection tank mass and gamma spectroscopy results E-3

E-2. Test SFD 1-4 collection tank contents based on results from mass and gamma spectroscopy E-3

E-3. Test SFD 1-4 collection tank contents corrected for air in-leakage E-4

E-4. Comparison of Test SFD 1-4 collection tank and benchmarking results E-6

E-5. Volumes of the effluent sampling and monitoring system for Test SFD 1-4 .... E-9

E-6. Temperatures of the effluent line in Test SFD 1-4 (K) E-11

G-1. ORIGEN2 inventories of selected radionuclides G-4

G-2. Comparison of measured and calculated BR-3 isotopic ratios G-5

G-3. Comparison of measured and calculated isotopic activities from BR-3 rod I-887 .... G-5

G-4. Fractional release rates from the gas portion of the effluent line grab samplers G-15

G-5. Preflush collection tank gas sample results G-17

G-6. Preflush collection tank liquid sample results G-17

G-7. Collection tank gas recirculation measurements and release fractions prior to bundle flushing G-18

G-8. Collection tank liquid recirculation measurements and release fractions prior to bundle flushing G-19

G-9. Noble gas release fractions based on integration of the on-line gamma spectrometer results G-20

G-10. Results of integrating the liquidline spectrometer data G-21

G-11. Results of postflush collection tank liquid grab samples G-22

G-12. Collection tank liquid recirculation measurements and release fractions after flushing operations G-23

G-13. Radioanalytical results for the SFD 1-4 core bore samples G-24

G-14. Sample specific burnup estimates derived from indicator ratios G-26

G-15. Estimated fission product retention percentages G-28

G-16. BR-3 fuel rod design characteristics G-32

G-17. Average burnup and rod average peak linear power for the BR-3 rods used in Test SFD 1-4 .... G-32

G-18. Comparison of calculated and stated burnups for BR-3 rods G-32

G-19. Normalized average linear power required to achieve rod average burnup G-33

G-20. Peaking factors for BR-3 irradiation cycles G-33

G-21. Irradiation history for the PBF steady-state irradiations G-33

G-22. Axial power profile during the PBF irradiations G-33

G-23. Summary of model and input detail for the transient FASTGRASS calculation G-35

H-1. Test SFD 1-4 geometrical input to the VAPOR code H-9

H-2. Comparison of SFD 1-4 control rod material release fractions with the VAPOR code H-11

H-3. System dimensions and wall materials H-12

H-4. Initial inventories H-16

H-5. Principal species of the I-Cd-Ag-H-O system H-17

H-6. Initial conditions for Test SFD 1-4 thermochemical calculations H-18

H-7. Free energies of formation used in the SOLGAS analysis H-19

I-1. Measured cross-sectional area of bundle components (cm^2) I-8

I-2. ICP results I-12

I-3. Average composition of molten material I-13

I-4. Percent of intact zircaloy components that are oxidized I-14

I-5. Hydriding in the zirconium saddle I-47

J-1. Description of the SCDAP model J-4

PBF SEVERE FUEL DAMAGE TEST 1-4 TEST RESULTS REPORT

1. INTRODUCTION

The light water reactor (LWR) accident at Three Mile Island Unit 2 (TMI-2)[1] in 1979 resulted in core damage beyond the limits associated with design-basis loss-of-coolant accidents. At the time of the TMI-2 accident, the severe fuel damage and melt progression data base for the assessment of risk and consequences from a nuclear reactor accident was very limited. Therefore, the U.S. Nuclear Regulatory Commission (NRC) initiated an internationally sponsored[a] severe fuel damage (SFD) research program[2] to develop a data base and models to enable prediction of: (a) the overall response of the core and associated structures; (b) the rate of release of fission products, their chemical forms, and characteristics of transport and deposition in the primary system; (c) the rate of hydrogen generation from the interaction of coolant with the fuel, cladding, and reactor structure; and (d) the coolability of the damaged fuel following reflood. A significant portion of the program, encompassing both experimental and model development aspects, was undertaken at the Department of Energy's (DOEs) Idaho National Engineering Laboratory (INEL).

The major test program at the INEL consisted of a series of four SFD experiments performed in the Power Burst Facility (PBF). Each experiment consisted of a transient in which the test fuel bundle inlet coolant flow was reduced and the nuclear power was increased, until high temperatures in the bundle typical of severe accidents were achieved.

Peak temperatures approached fuel melting in all the tests. Parameters that were varied during the four experiments included the heatup rate, coolant inlet flow rate, cooldown rate, fuel rod burnup, and the presence of control rod material. The objectives of the SFD test series were to obtain data on LWR fuel bundle behavior, hydrogen generation, and the release, transport, and deposition of fission products. In addition to these general objectives, the fourth test in the series, Test SFD 1-4, was designed to study silver-indium-cadmium (Ag-In-Cd) control rod and aerosol behavior in severe reactor accidents.

The principal test conditions for the SFD series are summarized in Table 1. Results from the Scoping Test, Test SFD 1-1, and Test SFD 1-3 are found in References 3, 4, and 5, respectively. The data from the PBF tests are being combined with those from other integral and separate-effects tests and the TMI-2 core examination to facilitate identification of key phenomena and processes, development of deterministic models, and definition of hydrogen and fission product source terms. The data from Test SFD 1-4 are also being used to address outstanding NRC severe accident issues relating to core melt progression, hydrogen generation, fission product release and retention, aerosol generation and transport, and control rod behavior in severe reactor accidents.

Test SFD 1-4 was the fourth and final large-scale SFD experiment performed in PBF. A comprehensive report of Test SFD 1-4 is provided in this document, including an evaluation of the on-line instrumentation, postirradiation examination results, and fission product and aerosol measurements. This report also presents test analyses and best-estimate computer code predictions of the major phenomena that were used to help interpret the test results.

Descriptions of PBF, the test train and fuel bundle configuration, the fission product and hydrogen sampling and monitoring system, and the on-line instrumentation are given in Section 2. A summary of the test conduct, including the fuel conditioning, power calibration, and fission product inventory generation phases, is provided in Section 3. Section 4 presents an overview of Test SFD 1-4, including boundary conditions and the scenario of events that occurred during the high-temperature transient. The next three sections address various test phenomena in more detail.

---

[a] Sponsors of the program include Belgium, Canada, Federal Republic of Germany, Finland, Italy, Japan, Netherlands, Republic of Korea, Spain, Sweden, Switzerland, United Kingdom, American Institute of Taiwan, and the United States Nuclear Regulatory Commission.

Table 1. The PBF severe fuel damage test series

Test (date completed)	Bundle Description	Nominal Inlet Flow Rate (g/s)	Approximate Steam Production Rate (g/s)	Approximate Heating Rate Prior to Rapid Oxidation[a] (K/s)	Cooldown Procedure
SFD-ST (Oct 28, 1982)	32 fresh rods	16	16	0.1 to 0.15	Reactor scram, 16 g/s reflood increasing to ~30 g/s after 4 min. Whole bundle at saturation temperature ~8 min after scram.
SFD 1-1 (Sept 8, 1983)	32 fresh rods	0.6	0.7 to 1.0	0.46 between 800-1300 K 2.9 between 1300-2000 K	Power reduction and argon assisted cooldown over 20 min prior to 17 g/s reflood.
SFD 1-3 (Aug 3, 1984)	26 irradiated rods 2 fresh rods 4 guide tubes	0.6	0.6 to 2.4	0.5 below 1200 K 1.9 above 1200 K	Power reduction and argon assisted cooldown over at least 50 min. No reflood.
SFD 1-4 (Feb 7, 1985)	26 irradiated rods 2 fresh rods 4 Ag-In-Cd control rods in guide tubes	0.6	0.6 to 1.3	0.4 between 800-1200 K 1.6 between 1200-1600 K	Power reduction and argon assisted cooldown over at least 50 min. No reflood.

---

a. The heating rate was extremely rapid and driven by the metal-water reaction above ~1500 to 2000 K (depending on axial location) in SFD-ST, and about 1600 K in the other three tests.

Bundle heatup, oxidation, and melt progression behavior are discussed in Section 5. Fission product release and retention results are examined in Section 6. Fission product and aerosol transport behavior is described in Section 7.

Analysis of Test SFD 1-4 was performed with the SCDAP/RELAP5 code[6] to help understand the experiment in terms of the system boundary conditions, the bundle temperature response, cladding ballooning and oxidation, and meltdown. Results of these analyses are reported in Section 8. The impact of Test SFD 1-4 results on outstanding severe accident and source term issues is presented in Section 9. Section 10 summarizes major findings and conclusions. Appendices A through J contain information important to the development of the report and of interest to those who wish to pursue independent analyses.

2. SYSTEM DESCRIPTION

The PBF reactor and Test SFD 1-4 test train, fuel bundle, and fission product and hydrogen sampling and monitoring system are briefly described in Sections 2.1 through 2.4. The nominal design characteristics of the fuel rods, bundle, and the effluent sampling and monitoring system are provided in Appendix A. The instruments used during the experiment are itemized, and their performance is evaluated in Appendix B.

2.1 The Facility

The PBF reactor (shown in Figure 1) consists of a driver core and a central flux trap contained in an open-tank reactor vessel. An independent pressurized water coolant loop can provide a wide range of thermal-hydraulic conditions within the flux trap test space.

The PBF core is a right-circular annulus, 1.3 m OD and 0.91 m in length, enclosing the vertical flux trap, which is 0.21 m in diameter. The core was designed for both steady-state and power burst operation. The core contains eight control rods for reactivity control during steady-state operation and four transient rods for dynamic control during rapid reactivity transients. Each of the control and transient rods consists of a stainless steel canister containing a cylindrical annulus of boron carbide and is operated within an air-filled shroud.

An in-pile tube (IPT) fits in the central flux trap region to contain the test train assembly. The IPT is a thick-walled (0.20 m OD, 0.15 m ID), Inconel-718,[a] high-strength tube designed to contain the steady-state operating pressure and any pressure surges from test fuel rod failures. Test transient phenomena, such as cladding failure, gross fuel melting, fuel-coolant interactions, fuel failure propagation, fission product release, or metal-water reactions, can be safely contained by the IPT without damage to the driver core.

2.2 Fuel Bundle and Test Train Design

The SFD 1-4 bundle assembly, shown in Figures 2 and 3, consisted of 28 zircaloy-clad fuel rods and 4 zircaloy guide tubes that each contained a stainless-steel-clad, Ag-In-Cd control rod. The rods were arranged in a 6-x-6 array without the four corner rods. The rod positions in the bundle assembly were designated by number-letter combinations, as shown in Figure 2. The fuel bundle location in the test train is shown in Figure 3. Twenty-six of the fuel rods were previously irradiated in the Belgian BR-3 reactor,[a] where they attained a rod average burnup of 36,000 MWd/MtU. These irradiated rods were discharged from the BR-3 reactor either in April 1978 or September 1980.

Two fresh fuel rods (positions 3B and 4D, Figure 2) were fabricated specifically for Test SFD 1-4 so that instruments could be incorporated into the rods. Instrumentation for each fresh rod consisted of three cladding thermocouples (axially distributed on the inside of the cladding), one centerline fuel thermocouple, and a pressure switch designed to respond at a specific pressure level to indicate cladding failure. The as-fabricated enrichment of the irradiated rods was 5.76% ^{235}U, while the effective enrichment at 36,000 MWd/MtU was $\sim$3.6%. The fresh rods were enriched to 2.9%. The active fuel length of the irradiated rods was 1.0 m, with the axial midplane centered at the PBF core midplane. The fresh fuel rods had an active length of 0.914 m, with the upper end of the fuel column located at the same elevation as the upper end of the irradiated rods. Elevations of various bundle components are shown in Figure 4. Design characteristics of the fuel rods are presented in Appendix A, while Table 2 summarizes the overall test bundle characteristics.

Four simulated pressurized water reactor (PWR) control rods were located in bundle locations 2B, 5B, 2E, and 5E, with no provision for withdrawal. The control rod located in bundle position 5E was instrumented in the same manner as the fresh fuel rods. The absorber material was an alloy composed of 80% silver-15% indium-5% cadmium by weight. The Ag-In-Cd alloy slugs were enclosed in a Type-304 stainless steel tube with stainless steel end plugs. The overall length of all control rods' absorber material was 0.957 m. Zircaloy-4 guide tubes were fastened to the bottom support plate to position each control rod. A small amount of

---

[a] Mention of specific products and/or manufacturers in this document implies neither endorsement or preference nor disapproval by the U.S. Government, any of its agencies, or EG&G Idaho, Inc., of the use of a specific product for any purpose.

[a] The BR-3 reactor is a small PWR test reactor with an active length of 1.0 m.

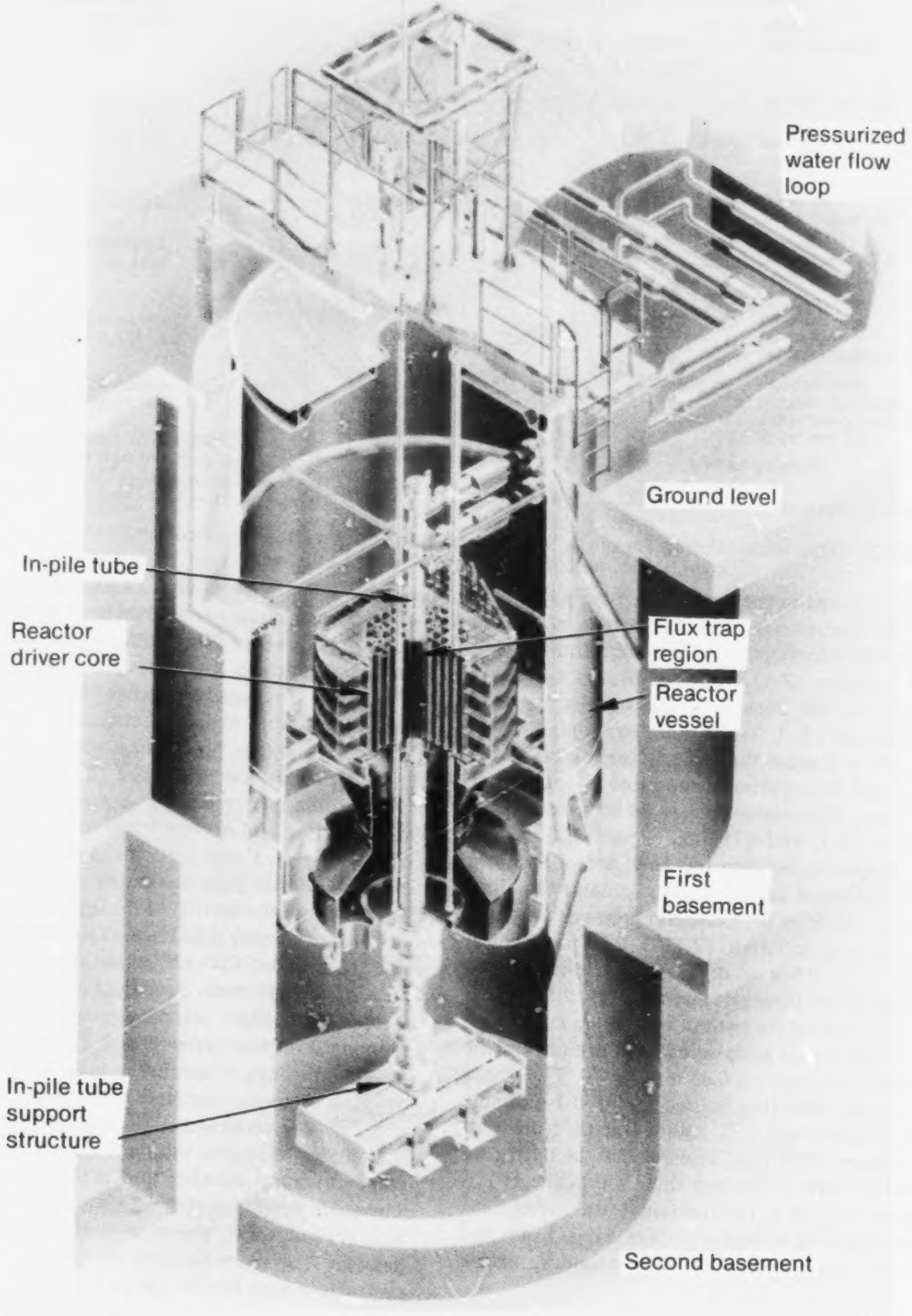
Pressurized water flow loop
Ground level
In-pile tube
Reactor driver core
Flux trap region
Reactor vessel
First basement
In-pile tube support structure
Second basement
7-3200

Figure 1. Cutaway view of the Power Burst Facility reactor.

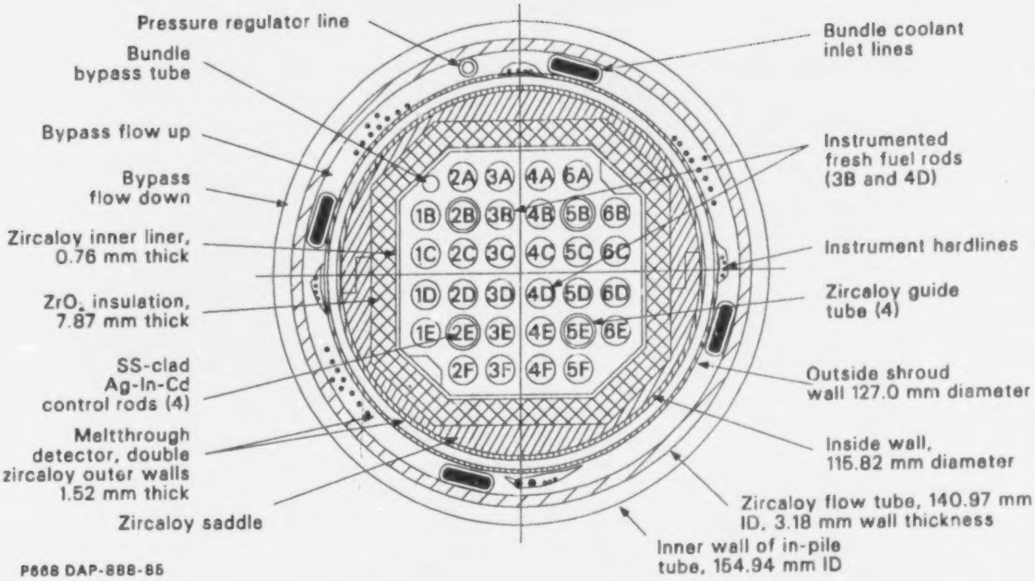
Pressure regulator line
Bundle bypass tube
Bypass flow up
Bypass flow down
Zircaloy inner liner, 0.76 mm thick
ZrO2 insulation, 7.87 mm thick
SS-clad Ag-In-Cd control rods (4)
Meltthrough detector, double zircaloy outer walls 1.52 mm thick
Zircaloy saddle
P868 DAP-888-85
Bundle coolant inlet lines
Instrumented fresh fuel rods (3B and 4D)
Instrument hardlines
Zircaloy guide tube (4)
Outside shroud wall 127.0 mm diameter
Inside wall, 115.82 mm diameter
Zircaloy flow tube, 140.97 mm ID, 3.18 mm wall thickness
Inner wall of in-pile tube, 154.94 mm ID
2A 3A 4A 5A
1B 2B 3B 4B 5B 6B
1C 2C 3C 4C 5C 6C
1D 2D 3D 4D 5D 6D
1E 2E 3E 4E 5E 6E
2F 3F 4F 5F

Figure 2. Cross-sectional diagram of the SFD 1-4 test train and fuel bundle region.

coolant flowed in the gap between the guide tube and the control rod cladding. Details of control rods and guide tubes are given in Appendix A.

A zirconia (ZrO_2) bundle bypass tube was located in the corner of the bundle between rods 2A and 1B. It was intended to maintain a separate flow channel through the fuel region in the event that the experiment produced extensive flow blockage. The outside and inside diameters of the tube were 6.35 and 4.75 mm, respectively.

The spacing between fuel rods and control rod tubes in the test assembly was maintained by three Inconel spacer grids. Each grid provided a square-pitch spacing pattern of 12.75 ± 0.25 mm (typical of a 17 x 17 PWR array). Respective elevations of the tops of the three grids were 0.1129, 0.5109, and 0.9572 m above the bottom of the fuel in the PBF core.[a] The spacer grids were 39.7 mm high, and the Inconel thickness was 0.43 mm.

The test train that housed the SFD 1-4 bundle was designed and built by the Pacific Northwest Laboratory (PNL) and assembled at the INEL. An elevation view of the test train within the IPT is shown in Figure 3. The fuel bundle was surrounded by an insulated shroud to minimize heat losses and provide structural integrity. The shroud insulation consisted of a 7.6-mm layer of high-density ZrO_2 fiberboard material sandwiched between inner and outer zircaloy walls. The zirconia insulation, which had a higher density than that used in Tests SFD-ST and SFD 1-1, reduced the radial heat loss through the shroud wall and, consequently, the power required to attain high temperatures. Specially shaped zircaloy pieces (termed the saddles) were placed around the insulation to provide support for the insulation and zircaloy inner liner. The shroud insulating region was pressurized with argon gas from a line that passed through the IPT closure head and into the bottom of the insulating shroud.

Another zircaloy tube (termed the inside shroud wall) surrounded the saddles and was welded into position at both ends. Four dual-conductor, insulated thermocouple cables were spirally wrapped around the outside of the shroud. Heatup or imminent meltthrough of the shroud inner wall could be detected by measurement of the insulation resistance between conductors. An outside shroud wall surrounded the cable wrap and served as the primary structural member and pressure boundary. The cable wrap, together with the inside and outside shroud walls, constituted the meltthrough detector. The space between the shroud walls was pressurized with helium gas to 0.49 MPa, and the pressure was monitored during the test. A rupture of either cavity wall would have resulted in a measured pressure increase.

---

[a] All elevations in this report will be referenced to the bottom of the PBF driver core active fuel stack.

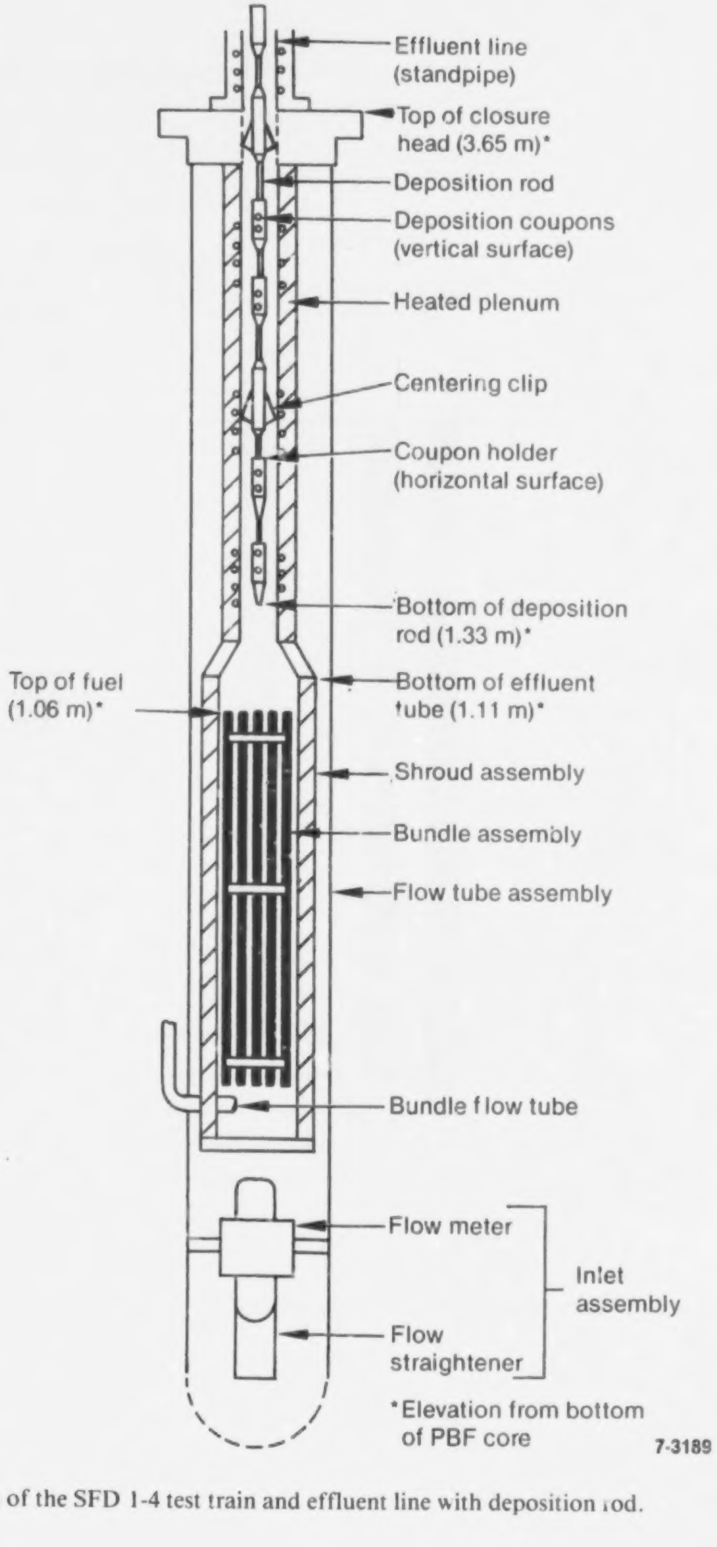
Effluent line (standpipe)
Top of closure head (3.65 m)*
Deposition rod
Deposition coupons (vertical surface)
Heated plenum
Centering clip
Coupon holder (horizontal surface)
Bottom of deposition rod (1.33 m)*
Top of fuel (1.06 m)*
Bottom of effluent tube (1.11 m)*
Shroud assembly
Bundle assembly
Flow tube assembly
Bundle flow tube
Flow meter
Inlet assembly
Flow straightener
*Elevation from bottom of PBF core
7-3189

Figure 3. Axial diagram of the SFD 1-4 test train and effluent line with deposition rod.

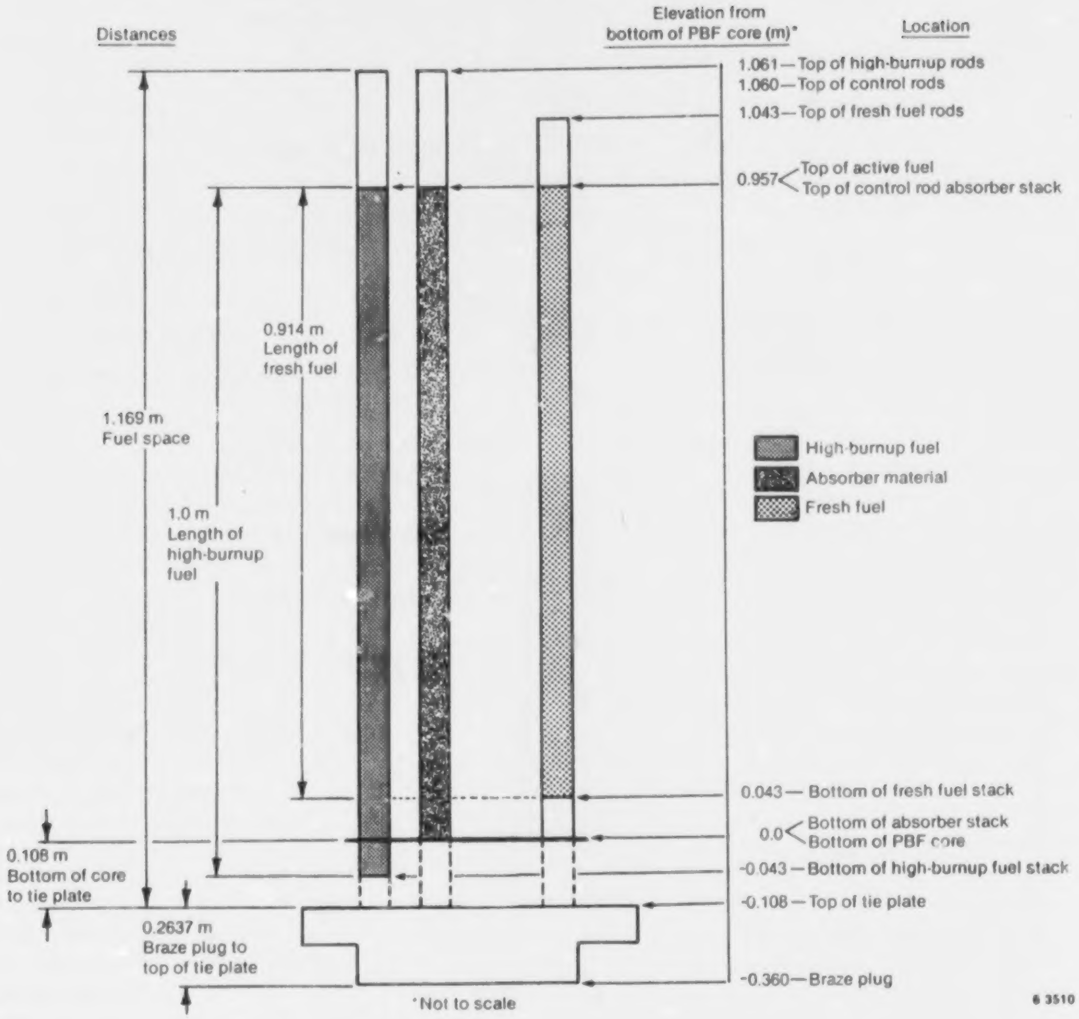
Distances
Elevation from bottom of PBF core (m)*
Location
1.061—Top of high-burnup rods
1.060—Top of control rods
1.043—Top of fresh fuel rods
0.957 Top of active fuel
Top of control rod absorber stack
0.914 m Length of fresh fuel
1.169 m Fuel space
1.0 m Length of high-burnup fuel
High-burnup fuel
Absorber material
Fresh fuel
0.043— Bottom of fresh fuel stack
0.0 Bottom of absorber stack
Bottom of PBF core
-0.043—Bottom of high-burnup fuel stack
-0.108—Top of tie plate
-0.360—Braze plug
0.108 m Bottom of core to tie plate
0.2637 m Braze plug to top of tie plate
*Not to scale
6 3510

Figure 4. Axial schematic of the SFD 1-4 fuel bundle region.

Table 2. SFD 1-4 bundle characteristics

Parameter	Value
Unirradiated Fuel Rods:	
Number of rods	2
Fuel material	UO_2 sintered pellets
Pellet enrichment	2.9 wt.% ^{235}U
Fuel density	95% TD
Cladding material	Zircaloy-4
Fuel rod OD	9.63 mm
Cladding ID	8.43 mm
Pellet OD	8.27 mm
Fuel rod length	914.4 mm
Pretest burnup	Zero
Irradiated Fuel Rods:	
Number of rods	26
Fuel material	UO_2 sintered pellets
Pellet enrichment	5.76 wt.% ^{233}U
Fuel density	95% TD
Cladding material	Zircaloy-4
Fuel rod OD	9.5 mm
Cladding ID	8.24 mm
Pellet OD	8.04 mm
Fuel rod length	1000 mm
Pretest burnup	29,200 to 41,700 MWd/MtU
Control Rods:	
Number of rods	4
Absorber material	80% silver/15% indium/5% cadmium
Absorber density	10.16 g/cm^3
Cladding material	Stainless steel
Guide tube material	Zircaloy-4
Overall rod length	1.169 m
Absorber OD	7.65 mm
Cladding ID	8.89 mm
Cladding OD	9.70 mm
Guide tube ID	11.43 mm
Guide tube OD	12.24 mm
Bundle Inventory:	
UO_2	14.87 kg
Zircaloy	6.12 kg
Silver-indium-cadmium	1.72 kg
Stainless steel	0.49 kg
Inconel	0.28 kg

Inlet flow to the bundle was provided by a line entering through the closure head assembly. The flow from this line was divided into four small lines that extended through the bypass region to the bottom of the test train and into the interior of the test train inlet assembly. Flow passed upward through the test bundle and into the effluent line. The effluent line extended up through the IPT closure head to external piping, which split into two branches. One branch was connected to the sample collection system piping, and the other was connected to the PBF loop piping. The latter branch was used for preconditioning flow only and contained a check valve, an isolation valve, and a flow meter. During the transient, a low-flow injection pump provided a pretest calibrated bundle flow of 0.6 g/s.

A simulated upper plenum above the fuel incorporated a thermal radiation shield to reduce heat transfer through the noninsulating shroud area and provided a direct flow path to the effluent line. Between the radiation shield and the IPT head, electrical heaters were used to establish a known temperature gradient through the upper plenum and to inhibit steam condensation in the effluent line during the transient.

A deposition rod, shown in Figures 3 and 5, was mounted in the plenum region above the fuel bundle and extended from 1.33 to 5.6 m above the bottom of the PBF core fuel. Forty removable deposition coupons were mounted along the rod to characterize fission product and aerosol deposition in the test. Thermocouples were positioned on the rod to measure the effluent steam and coupon surface temperatures at three axial elevations. The effluent line was designed to simulate the thermal conditions in a LWR upper plenum during a severe accident and to allow the deposition rod to be removed after the experiment while preventing any water from entering the test train or contacting the deposition rod. After the experiment was completed, the effluent line, including the section housing the deposition rod, was backfilled with nitrogen and kept above saturation temperature until the water was removed from the IPT.

The test train incorporated a variety of instrumentation to measure the response of the entire system to the severe fuel damage conditions produced in the bundle. The test train was instrumented to measure fuel rod cladding inside surface temperatures (6), fuel centerline temperatures (2), rod internal pressure (2), control rod centerline temperature (1), control rod cladding temperature (3), control rod internal pressure (1), shroud temperatures (24), water and steam temperature (28), coolant flow rates (4), coolant pressure (6), relative neutron flux (10), total fluence (4), plenum wall temperature (8), deposition wall temperature (3), steam tube heater temperature (8), and meltthrough of the shroud. Appendix B provides a brief description of these devices and detailed tables and diagrams identifying each instrument, its location, and its performance, as well as the plant and the effluent sampling and monitoring system instrumentation description.

2.3 Effluent Sampling and Monitoring System

Effluent from the SFD 1-4 test bundle was characterized by a remotely controlled sampling and monitoring system. Figure 6 is a layout diagram showing the position of the major components in the system relative to the reactor. Figure 7 is a schematic diagram that illustrates the flow path through the various components. The effluent sampling and monitoring system consisted of a long, 6.35-mm-dia pipe that directed the effluent flow past a series of on-line instruments and grab samples into a large collection tank.

The effluent line was shielded with lead, heat-traced, and insulated up to the condenser (with the exception of an uninsulated region at the steamline detector viewing position), in an attempt to minimize condensation and maintain effluent temperatures above the saturation temperature (644 K) for pure steam at 6.9 MPa along the length of the line. Thermocouples were positioned at various locations along the line to measure effluent line temperatures.

Upon exiting the upper plenum, the effluent flow passed the first of four gamma spectrometers. All four gamma spectrometers, termed the mainfloor, steamline, gasline, and liquidline for the respective portions of line they viewed, used a shielded intrinsic germanium detector and a variable aperture collimator between the effluent line and the detector to permit on-line remote adjustment of the gamma flux incident on the detector crystal during the experiment.

Immediately downstream of the mainfloor spectrometer, the effluent line passed in front of an on-line aerosol monitor. A specially designed aerosol monitor was fabricated and installed in the effluent line for monitoring aerosol concentrations during Test SFD 1-4. Aerosol concentrations were measured by projecting a light beam across the effluent stream and recording the beam attenuation

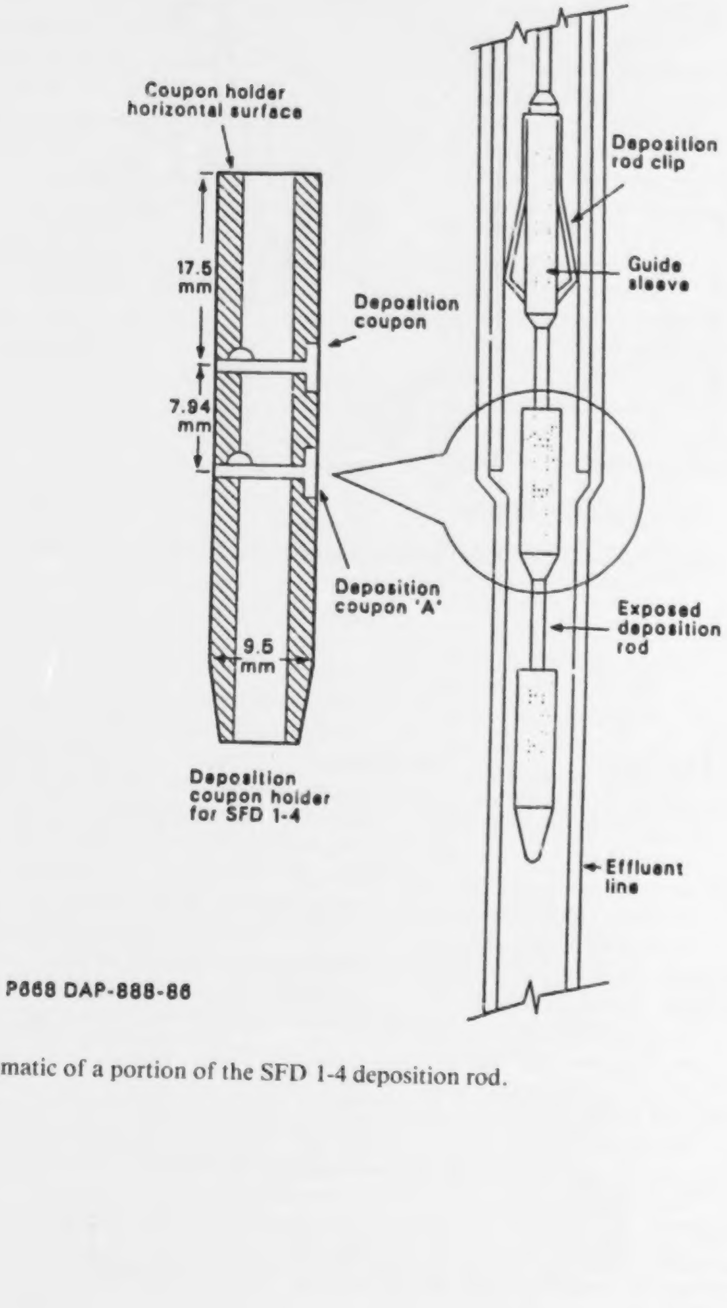
Coupon holder horizontal surface
17.5 mm
7.94 mm
9.5 mm
Deposition coupon
Deposition coupon 'A'
Deposition coupon holder for SFD 1-4
Deposition rod clip
Guide sleeve
Exposed deposition rod
Effluent line
P868 DAP-888-86

Figure 5. Schematic of a portion of the SFD 1-4 deposition rod.

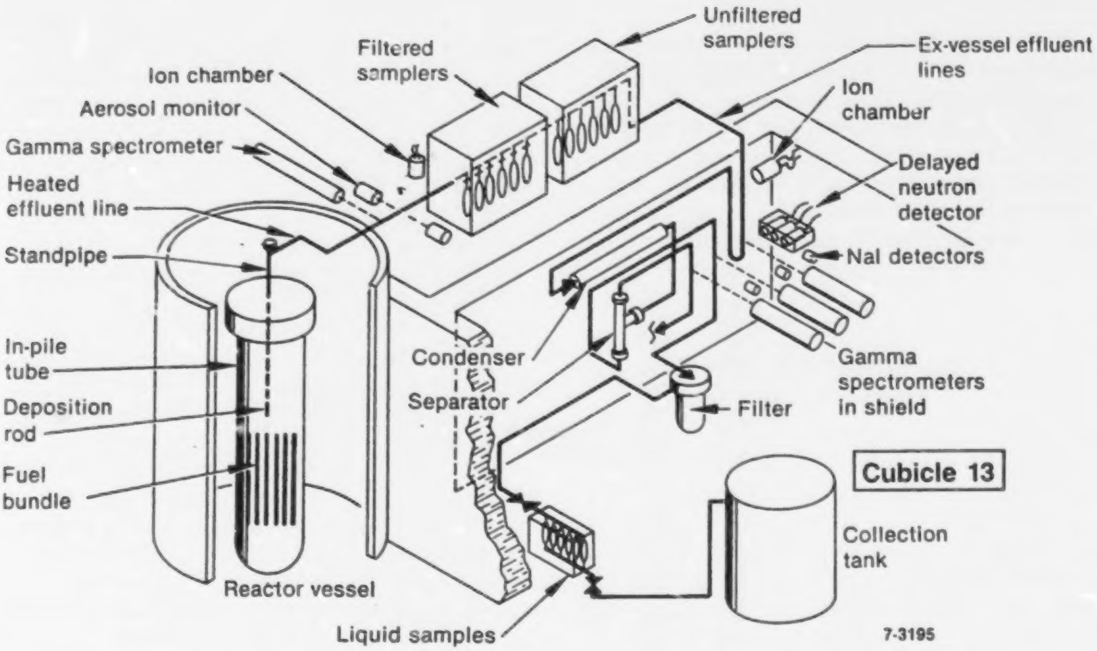
Unfiltered samplers
Filtered samplers
Ex-vessel effluent lines
Ion chamber
Aerosol monitor
Ion chamber
Gamma spectrometer
Delayed neutron detector
Heated effluent line
NaI detectors
Standpipe
In-pile tube
Condenser
Gamma spectrometers in shield
Separator
Filter
Deposition rod
Fuel bundle
Cubicle 13
Collection tank
Reactor vessel
Liquid samples
7-3195

Figure 6. Layout diagram of the SFD 1-4 fission product sampling and monitoring system.

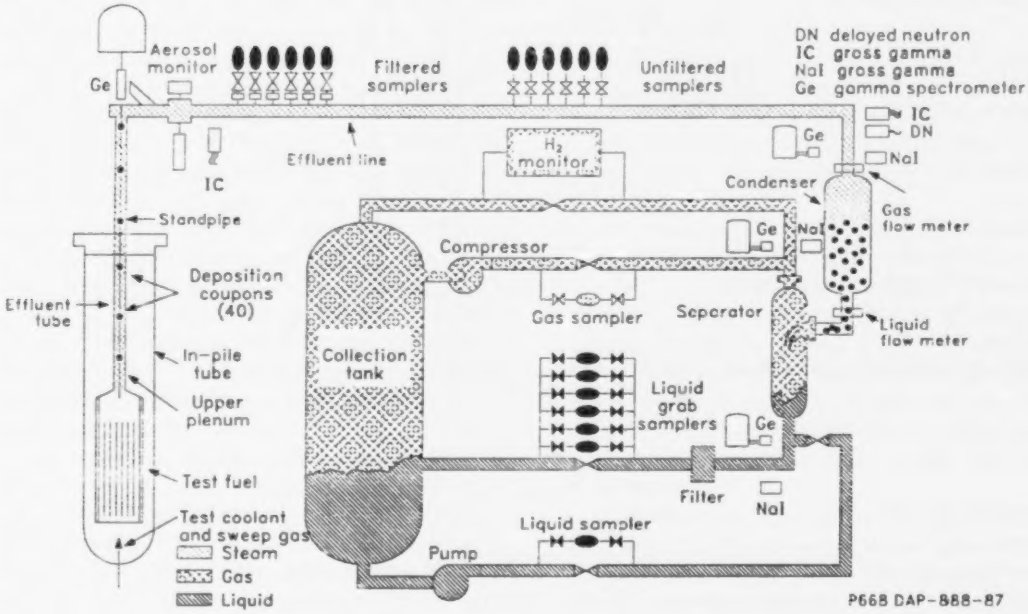
Aerosol monitor
Ge
Filtered samplers
Unfiltered samplers
DN delayed neutron
IC gross gamma
NaI gross gamma
Ge gamma spectrometer
IC
DN
NaI
Ge
H2 monitor
IC
Effluent line
Condenser
Standpipe
Gas flow meter
Ge
NaI
Compressor
Deposition coupons (40)
Effluent tube
Gas sampler
Separator
Liquid flow meter
In-pile tube
Collection tank
Liquid grab samplers
Ge
Upper plenum
Test fuel
Filter
NaI
Test coolant and sweep gas
Liquid sampler
Pump
Steam
Gas
Liquid
P668 DAP-888-87

Figure 7. Schematic of the SFD 1-4 sampling and monitoring system.

as aerosols passed through the light path. Fiber optics were used to transmit and receive the light beam. A special aerosol monitor spool piece (shown in Figure 8) was designed and tested under high-temperature and high-pressure conditions (560 K, 7 MPa) for this application. The spool piece provided for two different light beam path lengths (1 and 4 cm) to monitor different ranges of particle concentration. The monitor also incorporated four fiber-optic probe assemblies (shown in Figure 9) with spinel windows to protect the optical fibers from the high-pressure steam environment. A nitrogen gas purge was maintained through pinholes to reduce the buildup of aerosols on the protective windows. Details of its design and operation are found in Reference 7.

After exiting the aerosol monitor, the effluent line passed the first of two ion chambers and a series of six filtered and six unfiltered effluent samplers. These samplers were designed to be actuated remotely at different times during the test to obtain grab samples of the effluent. The grab samples, along with the deposition coupons in the simulated upper plenum, were analyzed posttest to determine fission product and aerosol behavior in the effluent line throughout the experiment.

The effluent line was then routed past the second ion chamber, a delayed neutron monitor (moderated BF_3 tube-type), a NaI gross gamma detector, and the steamline spectrometer before entering the condenser. Two flow meters were used to measure flow into and out of the condenser. A paddle wheel flow meter was mounted in the effluent line just upstream of the condenser to measure the flow rate during the transient and the liquid flow rate during the posttransient operations. A heated-wall-type flow meter was mounted in the line immediately downstream of the condenser to measure the liquid flow rate during pretest fuel bundle leakage measurements.

Upon leaving the condenser, the flow entered the separator where the entrained gas was separated from the liquid. To reduce the transit time and to ensure transport of fission products in the liquid line downstream of the separator, a dilution water flow of 30 g/s was added at the separator inlet. The liquid that drained from the separation vessel was measured using an orifice differential pressure-type flow meter. The condensed liquid then flowed past the liquidline spectrometer, a NaI gross gamma detector, and through a particulate filter. A pressure transducer was located across the particulate filter bypass to indicate if the filter was being bypassed. Downstream of the particulate filter there was a manifold with six flow-through liquid samplers to take samples of condensed coolant. The coolant finally passed through a level control valve and then into the collection tank.

Nitrogen gas was bled into the separator at a constant flow rate (1.13 g/s) to ensure fission product and hydrogen transport out of the separator gas space, to provide control of the back-pressure in the system, and to dilute the hydrogen concentration below 70% to present monitor saturation. The gaseous effluent, consisting of both the gases separated from the bundle effluent and the nitrogen carrier gas, was routed through a pressure control valve. The pressure control system regulated the gas flow through the pressure control valve to maintain a fixed differential pressure between the bypass and the separator. The effluent gas then traveled past a NaI gross gamma detector and the gasline gamma spectrometer. A continuous fraction of the gas (3.3 cm^3/s) was diverted through a parallel-path pipe to a Beckman Model 7C thermal conductivity gas analyzer. This analyzer determined the concentration of hydrogen in the effluent by measuring the conductivity of the gas passing through the detector cell and comparing it to a reference gas of known conductivity. All of the gaseous effluent then entered the collection tank. The pressure of the tank was monitored with a pressure transducer.

An argon sweep gas system introduced gas at the bottom of the bundle during and following the transient to stabilize the bundle pressure, to transport fission products through the sample system, and to cool the bundle following the transient while keeping the fission product deposition rod dry. Nitrogen gas was used after the test to pressurize the bundle and keep the deposition rod dry until the IPT was pumped dry. Remote sampling and monitoring of the collection tank gas and liquid contents was facilitated after the test by recirculation systems that pumped the tank contents through in-line samplers and past the gamma spectrometers. Quantitative details of the sample system geometry are given in Table 3 and in Figure 10.

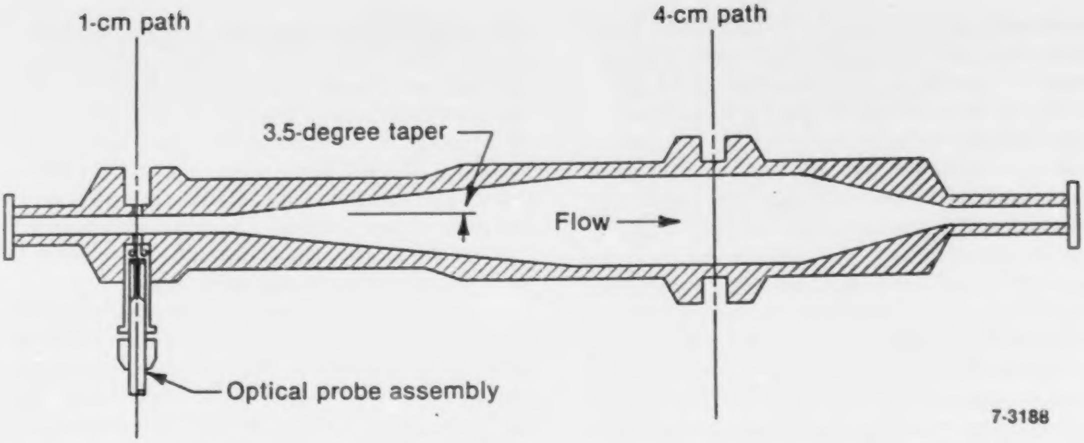
1-cm path
4-cm path
3.5-degree taper
Flow
Optical probe assembly
7-3188

Figure 8. SFD 1-4 aerosol monitor spool piece.

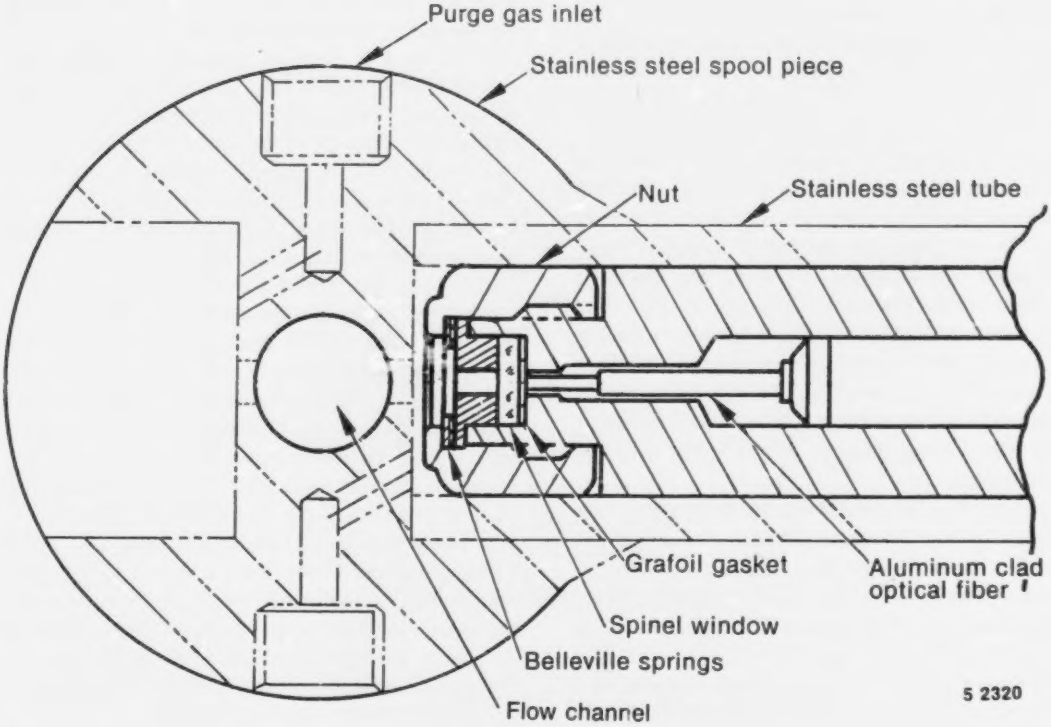
Purge gas inlet
Stainless steel spool piece
Nut
Stainless steel tube
Grafoil gasket
Aluminum clad optical fiber
Spinel window
Belleville springs
Flow channel
5 2320

Figure 9. Diagram of the SFD 1-4 aerosol monitor fiber-optic probe.

Table 3. Sample system component dimensions for Test SFD 1-4

Component Number	Component Description	Inside Diameter (m)	Length (m)	Cumulative Length (m)	Volume (m^3)	Cumulative Volume (m^3)	Surface Area (m^2)	Cumulative Surface Area (m^2)
1	Fuel space	8.13 E − 02	1.17	1.06	6.50 E − 03	6.50 E − 03	3.01 E − 01	3.01 E − 01
1A	High-burnup fuel rods (26)	9.50 E − 03	1.13	—	1.96 E − 03	—	8.23 E − 01	1.12 E + 00
1B	Fresh fuel rods (2)	9.50 E − 03	1.00	—	1.48 E − 04	—	6.23 E − 02	1.19 E + 00
1C	Instrumented control rod (1)	1.22 E − 02	1.06	—	1.19 E − 04	—	3.88 E − 02	1.23 E + 00[a]
1D	Noninstrumented control rods (3)	1.22 E − 02	1.06	—	3.74 E − 04	3.90 E − 03[b]	1.22 E − 01	1.35 E + 00[a]
2	Space above fuel	8.13 E − 02	0.05	1.11	3.25 E − 04	4.23 E − 03	6.13 E − 04	1.35 E + 00
3	Heat shield cone	9.09 E − 02	0.03	1.14	8.36 E − 05	4.31 E − 03	7.13 E − 03	1.36 E + 00
4	Heat shield cone to tip of deposition rod	2.22 E − 02	0.19	1.33	7.35 E − 05	4.38 E − 03	1.32 E − 02	1.37 E + 00
5	Tip of deposition rod to closure head	2.22 E − 02	2.32	3.65	7.88 E − 04	5.17 E − 03	2.28 E − 01	1.60 E + 00
6	Deposition rod	4.78 E − 03	4.17	—	2.00 E − 04	4.97 E − 03	1.17 E − 01	1.71 E + 00
7	Closure head to end of standpipe	2.22 E − 02	1.85	5.50	6.84 E − 04	5.66 E − 03	1.39 E − 01	1.85 E + 00
8	Standpipe to 90° bend	2.22 E − 02	0.11	5.61	4.26 E − 05	5.70 E − 03	7.67 E − 03	1.86 E + 00
9	90° bend to top of deck plates	2.22 E − 02	0.75	6.36	2.90 E − 04	5.99 E − 03	5.23 E − 02	1.91 E + 00
10	Top of deck to transition #1	2.22 E − 02	0.76	7.12	2.94 E − 04	6.28 E − 03	5.30 E − 02	1.97 E + 00
11	Transition #1 to main floor gamma spectrometer	8.48 E − 03	3.49	10.61	1.97 E − 04	6.48 E − 03	9.30 E − 02	2.06 E + 00
12	Aerosol spool	Variable (0.01 − 0.04)	0.72	11.33	4.38 E − 04	6.92 E − 03	6.00 E − 02	2.12 E + 00

Table 3. (continued)

Component Number	Component Description	Inside Diameter (m)	Length (m)	Cumulative Length (m)	Volume (m^3)	Cumulative Volume (m^3)	Surface Area (m^2)	Cumulative Surface Area (m^2)
13	Aerosol spool to filtered effluent samples	8.48 E − 03	1.22	12.55	6.89 E − 05	6.99 E − 03	3.25 E − 02	2.15 E + 00
14	Filtered effluent samples to unfiltered samples	8.48 E − 03	4.05	16.60	2.29 E − 04	7.22 E − 03	1.08 E − 01	2.26 E + 00
15	Unfiltered effluent sample outlet to 90° bend	8.48 E − 03	4.88	21.48	2.75 E − 04	7.49 E − 03	1.30 E − 01	2.39 E + 00
16	90° bend to Cubicle 13 penetration	8.48 E − 03	0.51	21.99	2.92 E − 05	7.52 E − 03	1.38 E − 02	2.40 E + 00
17	Cubicle 13 penetration to transition #2	8.48 E − 03	1.10	23.09	6.20 E − 05	7.58 E − 03	2.92 E − 02	2.43 E + 00
18	Transition #2 to steamline spectrometer	6.20 E − 03	8.15	31.24	4.60 E − 04	8.04 E − 03	1.59 E − 01	2.59 E + 00
19	Steamline spectrometer to condenser	6.20 E − 03	0.41	31.65	1.24 E − 05	8.05 E − 03	7.99 E − 03	2.60 E + 00
20	Condenser	3.86 E − 03	2.44	34.09	2.86 E − 05	8.08 E − 03	3.00 E − 02	2.63 E + 00
21	Condenser to separator	6.22 E − 03	1.83	35.92	5.56 E − 05	8.14 E − 03	3.60 E − 02	2.66 E + 00
Gasline								
22	Separator	9.20 E − 02	0.35	36.27	2.39 E − 03	1.05 E − 02	3.10 E − 01	2.97 E + 00
23	Separator exit to delay coil	6.22 E − 03	1.10	37.37	3.34 E − 05	1.06 E − 02	2.98 E − 02	3.00 E + 00
24	Delay coil	1.02 E − 02	18.30	55.67	1.50 E − 03	1.21 E − 02	5.87 E − 01	3.59 E + 00
25	Delay coil to gasline spectrometer	6.22 E − 03	4.43	60.10	1.35 E − 04	1.22 E − 02	1.07 E − 01	3.70 E + 00

Table 3. (continued)

Component Number	Component Description	Inside Diameter (m)	Length (m)	Cumulative Length (m)	Volume (m^3)	Cumulative Volume (m^3)	Surface Area (m^2)	Cumulative Surface Area (m^2)
Gasline (continued)								
26	Gasline spectrometer to hydrogen monitor	6.22 E − 03	4.96	65.06	1.51 E − 04	1.23 E − 02	1.29 E − 01	3.83 E + 00
27	Hydrogen monitor to collection tank	6.22 E − 03	9.35	74.41	2.84 E − 04	1.26 E − 02	2.98 E − 01	4.13 E + 00
Liquidline								
22	Separator	9.20 E − 02	0.35	36.27	2.39 E − 03	1.11 E − 02	3.10 E − 01	3.02 E + 00
28	Line to delay coil	6.22 E − 03	0.34	36.61	1.02 E − 05	1.11 E − 02	6.56 E − 03	3.03 E + 00
24	Delay coil	1.02 E − 03	18.30	54.91	1.50 E − 03	1.26 E − 02	5.87 E − 01	3.61 E + 00
29	Line to liquidline spectrometer	6.22 E − 03	3.05	57.96	9.26 E − 05	1.27 E − 02	5.60 E − 02	3.67 E + 00
30	Line to filters	6.22 E − 03	3.35	61.31	1.02 E − 04	1.28 E − 02	6.56 E − 02	3.74 E + 00
31	Filters (3)	1.27 E − 01	0.64	61.95	1.22 E − 02	2.50 E − 02	1.24 E + 00	4.98 E + 00
32	Line to liquid samples	6.22 E − 03	1.83	63.78	5.56 E − 05	2.51 E − 02	1.14 E − 01	5.09 E + 00
33	Line to collection tank	6.22 E − 03	18.3	82.08	5.56 E − 04	2.56 E − 02	3.57 E − 01	5.45 E + 00

---

a. Includes the surface area of the zircaloy guide tubes.

b. Void volume = 1 − 1A − 1B − 1C − 1D.

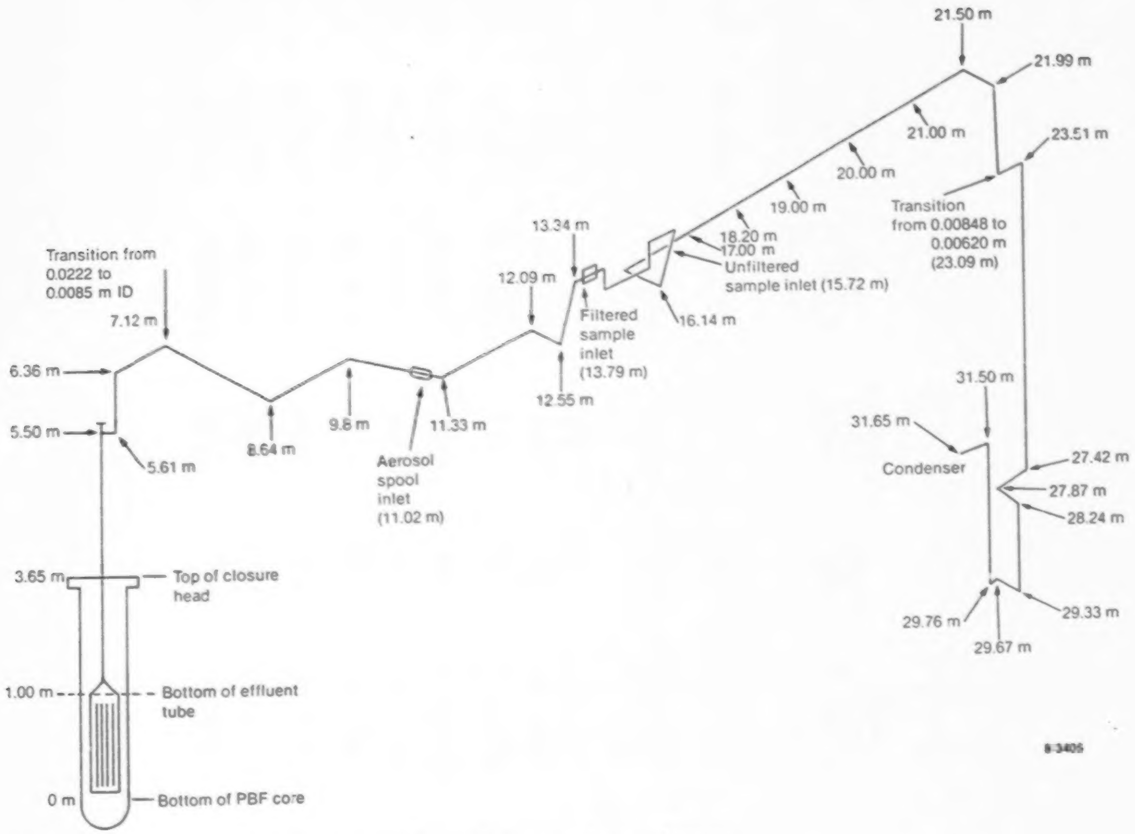
21.50 m
21.99 m
21.00 m
23.51 m
20.00 m
19.00 m
Transition from 0.00848 to 0.00620 m (23.09 m)
13.34 m
18.20 m
17.00 m
Unfiltered sample inlet (15.72 m)
Transition from 0.0222 to 0.0085 m ID
12.09 m
7.12 m
Filtered sample inlet (13.79 m)
16.14 m
6.36 m
31.50 m
12.55 m
31.65 m
9.8 m
11.33 m
5.50 m
27.42 m
Condenser
8.64 m
5.61 m
Aerosol spool inlet (11.02 m)
27.87 m
28.24 m
3.65 m
Top of closure head
29.76 m
29.33 m
29.67 m
1.00 m
Bottom of effluent tube
8-3405
0 m
Bottom of PBF core

Figure 10. Schematic of the SFD 1-4 effluent line up to the condenser.

3. TEST CONDUCT

This section describes the complete sequence of operations for Test SFD 1-4. Sections 3.1 through 3.6 describe each phase of the test sequence: power calibration measurements, a lengthy long-lived fission product inventory generation phase, a 14-day shutdown, two 8-h low-power (85 kW) operations to produce a short-lived fission product inventory, a coolant boildown, the high-temperature transient, a slow cooldown in argon gas, and bundle isolation in pressurized nitrogen gas until the deposition rod was removed. Fission product effluent samples were taken at intervals during the transient. A discussion of posttest activities is given in Section 3.7. A chronological summary of the event sequence is provided in Table 4.

3.1 Power Calibration Phase

The power calibration phase consisted of two slow power ramps to intercalibrate the fuel bundle power with the PBF reactor nuclear power for single-phase liquid coolant conditions at reactor powers of 10, 12, and 26 MW. The maximum bundle power attainable at 26 MW of reactor power was about 146 kW (5.2 kW/m average rod power) at bundle inlet coolant conditions of 518 K, 7.83 MPa, and 1.35 L/s flow rate. The maximum fuel centerline temperature for these conditions was about 740 K. The ratio of the thermally measured bundle power to the thermally measured reactor power was 5.7 kW/MW. This measured value averaged about 15% lower than that calculated. Details of the power calibration phase are presented in Appendix D. The computed bundle power history during the power calibration phase is shown in Figure 11.

3.2 Long-Lived Fission Product Inventory Generation Phase

After the two power calibration ramps were completed, the bundle was operated for a total of ∿178 h at powers ranging from 135 to 150 kW until a cumulative bundle irradiation energy of 26 MWh had been generated. The purpose of this long steady-state power operation was to increase the intermediate- and long-lived fission product inventories in the fuel to optimum values for measurement during the transient. The coolant inlet conditions for this phase were 518 K, 7.8 MPa, and ∿1.3 L/s.

3.3 Short-Lived Fission Product Inventory Generation Phase

After a 14-day shutdown during which preparations for the high-temperature transient were completed, the bundle was operated at ∿85 kW for 8 h to regenerate short- and intermediate-lived fission products. Because of a reactor control rod operational problem, however, the high-temperature transient had to be postponed. One day later, after the problem was rectified, a second short-lived fission product generation phase was conducted. Bundle inlet coolant conditions were 532 K, 7.0 MPa, and 1.36 L/s flow rate. At the end of the 8-h operation, the reactor power was decreased to ∿1 kW.

3.4 Bundle Boildown Phase

At the start of the bundle boildown phase, the bundle inlet coolant conditions were adjusted to 532 K and 7.0 MPa. A coolant mass flow rate of 0.6 g/s (0.76 mL/s) was established, with bundle outlet flow going into the effluent sampling and monitoring system. The effluent line and upper plenum electrical heaters were turned on to maintain temperatures above saturation. The sweep gas system was activated with nitrogen gas flowing for ∿30 min to purge any coolant from the effluent line downstream of the bundle. The sweep gas system was then switched to argon gas for the remainder of the boildown phase. The bundle power was slowly increased to ∿5 kW to boil the coolant away in the bundle region. An equilibrium level at about 0.24 m was established for the two-phase steam interface level, with a bundle power of ∿2.9 kW. The bundle outlet steam temperature was about 750 K (saturation coolant temperature at 7.0 MPa is ∿559 K), and cladding temperatures were about 775 K. The bundle pressure was about 0.02 MPa greater than the bypass pressure to minimize the possibility of bypass coolant leaking into the bundle.

Table 4. SFD 1-4 sequence of events

Event	Time (h:min:s)	Test Time[a] (s)	Date
Power calibration			
Initiated nuclear operation for core power and bundle power measurements	21:30:00	—	01/13/85
Completed first power ramp to 146-kW bundle power and 26-MW reactor power	07:24:00	—	01/14/85
Completed second power ramp to 146 MW	10:02:00	—	01/14/85
Long-lived fission product inventory buildup phase			
Initiated reactor operation	19:44:00	—	01/14/85
Completed operation (26.1 MWh bundle energy)	20:53:00	—	01/22/85
Completed final preparations for transient	—	—	02/05/85
Short-lived fission product buildup phase			
Initiated reactor operation	15:42:00	—	02/05/85
Completed 8-h operation at 85-kW bundle power.	00:49:00	—	02/06/85
First boildown			
Initiated boildown, bundle flow at 0.6 g/s; water level indication; problems with reflooded bundle to terminate	03:43:00	—	—
Second boildown			
Initiated boildown by increasing reactor power; steam and plenum heaters on	06:38:00	—	—
Bundle power at 2.5 kW, two-phase level at 0.2 m	07:58:00	—	02/06/85
Unlatched control rod indicated; shut down reactor, reflooded bundle	09:14:00	—	—
Second short-lived fission product generation			
Initiated reactor operation	00:46:00	—	02/07/85
Completed 8-h operation at 85-kW bundle power	09:43:00	—	—

Table 4. (continued)

Event	Time (h:min:s)	Test Time^a (s)	Date
Third boildown			
Increased bundle power to 1 kW, steam and plenum heaters on	18:12:00	—	—
Initiated nitrogen gas purge	18:20:00	—	—
Started to reduce nitrogen gas purge	18:38:00	—	—
Initiated argon gas sweep	18:40:00	—	—
Initiated reactor power increase	18:49:00	—	—
Turned off argon gas sweep	19:07:00	—	—
Turned on argon gas sweep to 0.26 g/s to eliminate system pressure oscillations	19:42:00	—	—
Bundle power at 3 kW, two-phase level at 0.2 m	19:54:00	—	—
High-temperature transient			
Reached equilibrium conditions; two-phase level at 0.24 m, bundle power at 2.7 kW, inlet temperature at $\sim$532 K, bundle inlet pressure at 6.9 MPa, cladding temperature at 720 to 775 K	20:30:00	00	—
Initiated bundle power ramp at rate of $\sim$0.005 kW/s	20:31:00	60	—
Turned off argon gas sweep	20:41:40	700	—
Turned on argon gas sweep to 0.26 g/s, bundle pressure decreased by 0.03 MPa	20:42:05	725	—
Bundle temperature at 1000 K, bundle power at 8.5 kW, ramp rate at 0.005 kW/s	20:48:35	1115	—
Bundle temperature at 1200 K, bundle power at 9.6 kW, increased ramp rate to 0.024 kW/s, pressure reset to 6.7 MPa	20:56:10	1570	—
Instrumented control rod (5E) failed, control rod temperature at $\sim$1170 K,	20:58:28	1708	02/07/85
System pressure spike of 0.4 MPa	20:58:32	1712	—
Onset of rapid heatup declared; bundle power at 16.3 kW	21:01:18	1878	—
Remaining three control rods failed, no pressure increase	21:02:05	1925 to 1975	—

Table 4. (continued)

Event	Time (h:min:s)	Test Time[a] (s)	Date
Shroud inner liner failed	21:02:26	1946	—
Argon flow increased to 0.58 g/s	21:02:46	1966	—
Start of power hold at $\sim$27 kW	21:09:30	2370	—
End of power hold, power decreased at rate of -0.05 kW/s	21:13:14	2594	—
Bundle power at 1 kW	21:23:00	3180	—
Started to increase argon gas sweep flow rate	21:24:40	3280	—
Bundle power at 0.5 kW	21:25:00	3300	—
Turned off bundle injection pump	21:27:36	3456	—
Argon gas sweep flow rate at 1.9 g/s	21:27:55	3475	—
Initiated reactor shutdown	21:48:00	4680	—
Reactor shutdown	21:49:00	4740	—
Switched bundle sweep gas from argon to nitrogen	22:40:00	7800	—

---

a. Zero test time is defined as 20:30:00 on February 7, 1985.

3.5 High-Temperature Transient Phase

The high-temperature transient was initiated at 2031 h on February 7, 1985. (Zero time on all data plots in this report corresponds to 2030 h.) The bundle inlet coolant conditions were $\sim$532 K and 6.95 MPa. The bundle temperature, as indicated by the average of the six fuel rod cladding thermocouples, increased from $\sim$800 K to $\sim$1200 K at a rate of 0.37 K/s by increasing the bundle power at a rate of $\sim$0.005 kW/s. After 1570 s, when the peak bundle temperature was $\sim$1200 K, the following two actions were taken:

1. The pressure in the shroud insulator region was increased from 5.23 to 6.7 MPa and then maintained at $\sim$0.2 MPa less than the bundle pressure.
2. The bundle power ramp rate was increased to $\sim$0.024 kW/s to obtain an average cladding temperature ramp rate of $\sim$1.6 K/s from 1200 to 1600 K.

The instrumented control rod (5E) ruptured at $\sim$1708 s due to high internal pressure. The coolant pressure spike of about 0.4 MPa was measured after the control rod failed at an indicated cladding temperature of $\sim$1170 K. The instrumented control rod had become waterlogged prior to the transient

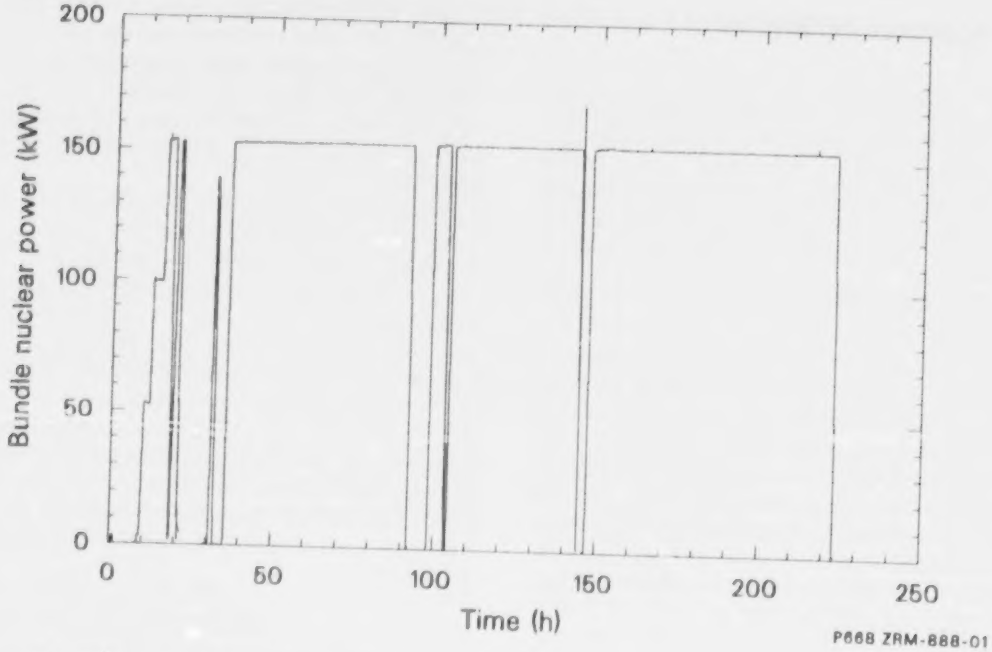

Figure 11. SFD 1-4 bundle nuclear power history during power calibration and fuel conditioning phases (zero time 13:30 h, Jan. 13, 1985).

due to a defect in the cladding end plug or instrumentation welding. The other three noninstrumented control rods did not fail until 1927 to 1978 s. At 1927 s, the estimated control rod cladding temperature was ~1700 K, based on the centerline thermocouple in the failed control rod (5E).

After the onset of rapid heatup was identified at 1878 s, the bundle power was increased to 27 kW at a rate of 0.02 kW/s and then held approximately constant at 27 kW for 223 s (from 2369 to 2592 s). At 1946 s, the shroud inner zircaloy liner failed (as planned) and the shroud pressure momentarily decreased by ~0.15 MPa over a 40-s time interval. The argon gas sweep system flow rate was manually increased from 0.26 to 0.58 g/s when the bundle pressure decreased. All of the fuel rod thermocouples formed new junctions and/or failed during the heatup phase of the transient (maximum measured temperature was 2280 K), so that maximum temperatures had to be determined from posttest metallurgical examination. Elevated fuel rod temperatures caused a variety of changes in the fuel and cladding microstructures. These changes included grain growth, phase transformation, porosity redistribution, oxidation, cladding melting, UO_2 dissolution, and the solidification of melts. Since most of these phenomena leave characteristic patterns in the resulting microstructures of the various phases, these microstructures can be compared with those obtained in well-defined out-of-pile experiments and peak temperatures and environmental conditions can be estimated. A maximum temperature of 2800 K was determined from such metallographic indicators.

3.6 Cooldown

After the 223-s power hold, the bundle power was decreased at a rate of −0.05 kW/s to about 1 kW (3180 s). An increase in the argon gas flow rate was initiated at 3280 s; the bundle injection pump was turned off at ~3456 s; and, at 4740 s, the reactor was shut down by inserting the reactor control rods, thus terminating the nuclear operation portion of the test. The argon gas sweep continued for another 51 min, followed by a nitrogen gas sweep for an additional hour. The test train was kept dry by pressurized nitrogen following bundle cooldown.

3.7 Posttest Activities

A radiation survey of the reactor building and the associated sample system and effluent lines was taken after the test on February 11, 1985, before flushing the effluent line. In addition, the gas and liquid contents of the collection tank were recirculated past the respective on-line gamma spectrometers.

The deposition rod was removed from the test train on March 27, 1985, and delivered to the hot cell on April 17, 1985, where it was gross and spectral gamma-scanned. Deposition coupons and coupon holders were removed from the rod for radiochemical analysis. Temporary lines were installed after deposition rod removal to facilitate washing of the effluent line and bundle. Soluble deposits in the effluent line and bundle were washed to the collection tank in three separate operations. On May 15, 1985, the effluent line was flushed with demineralized water. On May 16 and May 23, 1985, both the bundle and the entire effluent line were washed, using demineralized water. Following each flush, the collection tank liquid contents were recirculated past the liquidline gamma spectrometer to measure isotope-specific activities.

Radionuclides deposited in the effluent line were measured in-situ both before and after system flushing using a mobile gamma-ray spectrometer. The detector signal output was processed by the same fission product detection system that supported the on-line spectrometers during Test SFD 1-4. In-situ gamma spectral measurements of the various sections of the effluent lines were made both before and after flushing with water. The deposition rod was removed from the test train and shipped to the hot cell. Filtered and unfiltered grab samples, in-line liquid grab samples, collection tank liquid and gas samples, and the PBF loop liquid samples were removed and processed for analysis.

4. OVERVIEW OF THE SFD 1-4 TRANSIENT

An overview of Test SFD 1-4 is presented in this section. The test boundary conditions that directly affected the test results are first discussed. Then, summaries of the important phenomena relating to bundle heatup, oxidation, hydrogen generation, and melt progression; control rod behavior; and fission product and aerosol release and transport are presented. Detailed discussions of these phenomena are given in Sections 5, 6, and 7.

4.1 Test Boundary Conditions

This section discusses the rationale used to establish the system boundary conditions for Test SFD 1-4 and presents measurements of coolant pressure, coolant flow rate, single-phase steam interface level, and bundle power.

4.1.1 Rationale. A RELAP5 analysis[8] of a small break loss-of-coolant accident without emergency core cooling (S_2D) in a commercial PWR served as a basis for establishing test boundary conditions for Test SFD 1-4. The analysis predicted that a PWR core would become completely uncovered by about 1.5 h after shutdown because of the boiloff of primary coolant by decay heat. Within 2 h, the zircaloy cladding in the top half of the core would be melted and some fuel would be liquefied by the molten zircaloy. Between 1.5 to 2 h, the inlet steam mass flow rate through the upper half of the core would be about 4 kg/s, the primary pressure (which is slowly decreasing) would average ∿6.9 MPa, and the core decay power would average ∿1.3% of full power. For Test SFD 1-4, test fuel fission power had to be used instead of fission product decay heat to simulate this accident because of the significant radial heat losses inherent in a small-scale experiment. Test fuel rod linear heat rating was determined for the above accident scenario by correcting for experiment heat losses at higher temperatures. Steam flow through the PBF bundle was scaled down from the large PWR value on the basis of total fuel rod length to a coolant inlet flow rate of 0.6 g/s. System pressure was fixed at 6.95 MPa. Finally, an effort was made to maximize the length of fuel rods uncovered when the temperature exceeded 1000 K by boiling away the coolant at a rate faster than the supply rate.

4.1.2 Coolant Pressure. The bundle coolant pressure was controlled by back-pressurizing the effluent line at the separator (see Figure 7) with a constant flow of nitrogen gas into the separator and regulating the release rate of gases from the separator into the collection tank. Bundle pressure (shown in Figure 12) was automatically controlled at 6.95 ± 0.05 MPa through the transient, except at ∿1712 s, after the instrumented control rod failed, and at 1946 s, when the shroud inner liner failed.

4.1.3 Coolant Flow Rate and Steam Interface Level. The methods used to determine the bundle inlet flow rate and the steam interface level from test measurements are discussed in this section. Coolant inlet flow was provided by a positive displacement injection pump that was calibrated to deliver water at 0.6 g/s. The inlet coolant was heated to 532 K as it passed through four small-diameter tubes that traversed the IPT bypass coolant region prior to entering the lower plenum. The bypass coolant flow during the test was maintained at ∿2.6 L/s. Before the transient, a non-nuclear leakage measurement was performed. The liquid flow meter downstream of the condenser in the effluent line indicated an outlet flow of only 0.5 g/s, implying that about 20% of the coolant was leaking out of the system. Subsequent measurements showed that the outlet flow rate was independent of the bypass-to-bundle pressure differential between −0.2 to +0.2 MPa. Thus, leakage to or from the bypass region was believed to be insignificant. In addition, no evidence of leakage from the effluent line was found prior to or after the test. It was therefore concluded that the flow meter reading was erroneous and the test train was actually leak-free.

The two-phase/single-phase steam interface level during the high-temperature transient was determined from a fission chamber system developed for the SFD test series. Eight small uranium fission chambers were located on the shroud outer wall at elevations of 0.05, 0.25, 0.51, and 0.83 m at the 90-degree azimuth and at −0.05, 0.15, 0.35, and 0.67 m at the 270-degree azimuth. Because these fission chambers are predominately sensitive to thermal neutrons, their electrical output changed dramatically when the coolant, which acts as a neutron moderator, changed from a two-phase mixture to single-phase steam. The effect of variable reactor power was removed by dividing each fission chamber output by the reactor power.

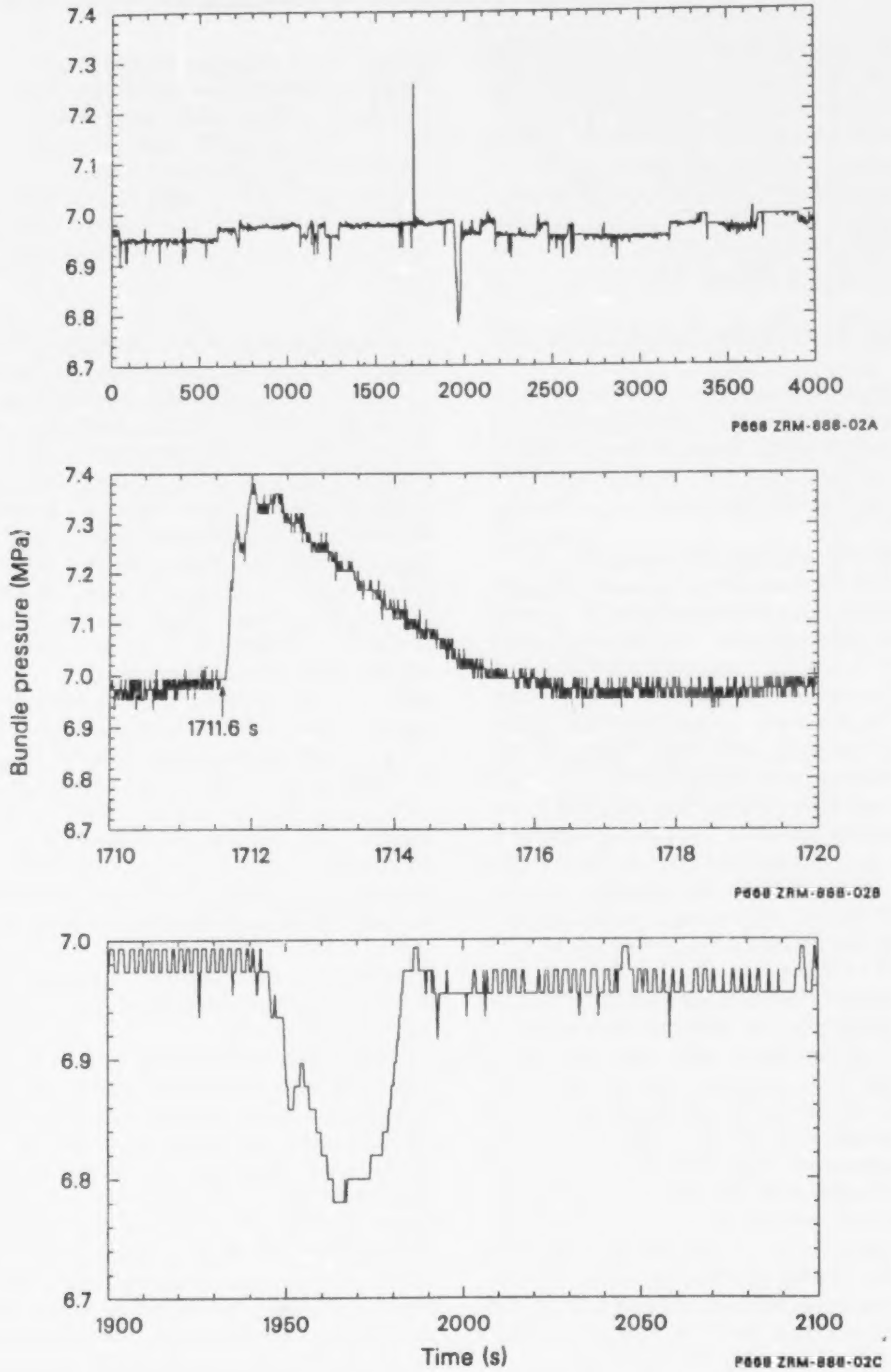

Figure 12. Bundle coolant pressure during Test SFD 1-4.

The interface level measurement, shown in Figure 13, was obtained from the fission chamber data and had an estimated uncertainty of ±0.02 m. The measurement was verified by comparing cladding thermocouple dryout times with the fission chamber level data during the boildown phase. The steam interface level could be measured by the fission chambers until ∿1712 s, about the time that the instrumented control rod failed. The steam interface level was about 0.02 m at this time. Control rod material relocation at 1712 s and between 1927 to 1978 s decreased the output of the lower fission chamber significantly and prevented further measurement of the steam interface level by this method.

From 1712 s until the shroud liner failed at 1946 s, the steam interface level was deduced from the measurement of the differential pressure across the bundle. The differential pressure measurement could not be used after ∿1946 s because of an increased argon gas flow rate that caused the bundle differential pressure to increase above the usable range. At 1946 s, the steam interface level was at about the zero reference level (bottom of PBF core fuel which was 0.043 m above the bottom of the irradiated fuel rods).

The steaming rate was calculated from the steam-interface level and the lower plenum flow area (32.1 cm^2). A plot of the steaming rate is also shown in Figure 13. The interface level dropped quickly during the boildown, causing the bundle steaming rate to vary between 0.6 and 1.3 g/s during the early phase of the transient. Based on the pump calibration, the steam flow rate entering the bundle was estimated to be accurate to within ±0.06 g/s up to 1946 s.

The data from the separator outlet flow meter were analyzed to benchmark the inlet bundle flow. Flow out of the separator included both the bundle outlet flow and the dilution flow (added directly to the separator to improve operation of the system and reduce delay times through the liquid line). A dilution flow of 33.1 g/s was measured after the transient by the separator flow meter. Subtraction of the dilution flow from the total separator flow yielded the bundle inlet flow minus any loss due to hydrogen generation or temporary holdup in the system. Because the bundle injection flow rate (0.6 g/s) was only about 2% of the total separator flow, the uncertainty in determining the bundle flow rate in this manner was relatively large. The average bundle outlet flow, derived from the separator flow meter between −555 and 1060 s, was 0.88 g/s. This value is about 20% higher than the bundle inlet flow of 0.72 g/s based on the single-phase steam interface level data over the same time interval. Considering the expected error in the separator flow meter data, a discrepancy of 20% in the two methods seems reasonable.

Beyond 1946 s, the steam interface could not be measured accurately. However, the bundle hydrogen generation rate was used to estimate a minimum steaming rate from the lower coolant plenum. The estimated minimum steaming rate is considered to be close to the actual flow rate in the experiment, since very little steam would be expected to exit the bundle in this steam-starved experiment. The minimum steam flow rate is also shown in Figure 13. The results indicate that during the high-temperature transient the steaming rate increased above the nominal value of 0.6 g/s, indicating a falling liquid level in the bundle.

4.1.4 Bundle Power. The bundle power could not be measured directly during the high-temperature transient because of thermal nonequilibrium conditions. The bundle power was therefore determined from the measured thermal reactor power and the reactor physics calculated ratio of bundle power to thermal reactor power, termed the figure of merit (FOM). The bundle power and the axial power profile were functions of the bundle coolant density, reactor control rod position, and the control material distribution in the bundle.

To estimate the effect of changes in coolant density on the FOM, three different geometries were used in the reactor physics calculations: a completely water-filled bundle; a partially water-filled bundle with steam above 0.2 m; and a completely steam-filled bundle. The bundle thermal power was measured with water-filled conditions to verify the accuracy of these calculations. The FOM was found to be 11% to 17% higher than that measured at three different power levels. Therefore, the FOMs for the partially and completely steam-filled intact bundle configuration were decreased correspondingly to account for the observed variance.

A reactor physics calculation was also made to estimate the effect of the control rod material relocation (between 1927 and 1978 s) on the FOM. The measured posttest distribution of control material was used to model the degraded bundle configuration. The results indicated that the power in the upper bundle should have increased, whereas the power in the lower portion of the bundle should have decreased. The net effect was that the overall bundle power decreased only about 3% following

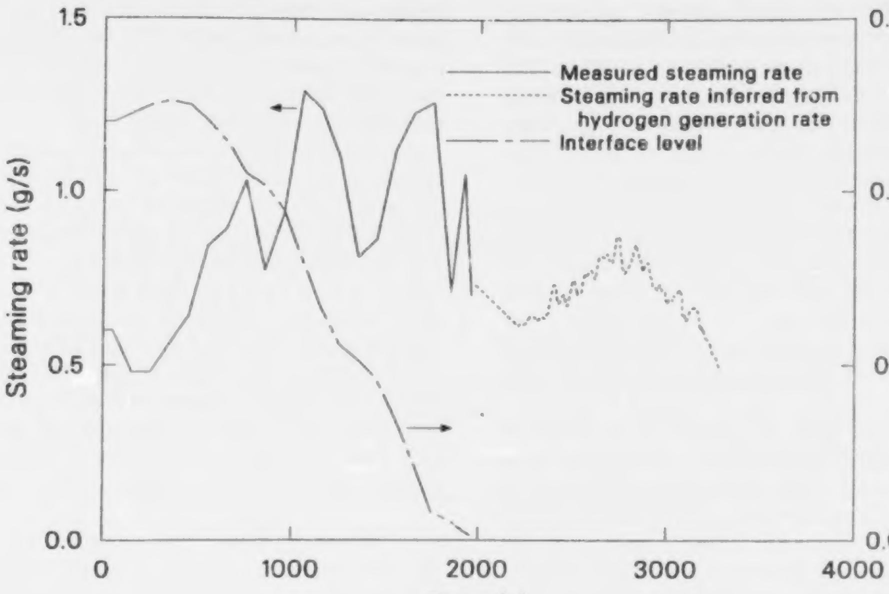

P666 DAP-888-88

Figure 13. Bundle inlet steaming rate and steam interface level during Test SFD 1-4.

control rod relocation. The small decrease is due to the fact that the relocated control material in the lower bundle region was generally distributed uniformly across the bundle cross section, and a relatively small amount of homogenized material is more effective as a neutron absorber than a larger amount in the original rod-like geometry. The effects of fuel relocation were not included in the calculation because of the small quantity of relocated material and the uncertainty in the time of relocation.

The bundle power time history, as determined from the reactor thermal power and the FOM calculations (interpolated for the appropriate coolant density and reactor control rod conditions), is shown in Figure 14. The bundle power was increased gradually during the course of the transient to a maximum of 27.1 kW to compensate for higher heat losses from the bundle as the temperature increased. The estimated uncertainty of the bundle power is ± 15% prior to control rod relocation and ± 20% afterwards. Further details of the bundle power calculations are found in Appendix D.

4.1.5 Heat Loss Rate Measurement. The energy balance of the bundle, and consequently the temperature reached during the transient, was determined largely by the effectiveness of the insulated shroud walls. Due to the transient nature of the test, thermal equilibrium was never achieved, thus preventing direct measurement of the time-dependent shroud conductivity. The rate of heat loss from the shroud was estimated by measuring the temperature rise of the coolant flowing in the bypass region. Three of the four pairs of differential thermocouples that were located at −0.31 and 1.14 m were used to measure the bypass coolant temperature rise. (The fourth pair indicated temperatures about 25% higher than the average of the other three thermocouples and failed completely from 2000 to 2100 s. Thus, data from this thermocouple pair were disregarded.) The calculated heat loss rate to the bypass coolant (shown in Figure 15) was corrected for direct neutron and gamma heating of the bypass coolant and shroud. Note that the bypass power increased significantly at ~2600 s, indicating probable deterioration of the shroud insulation. The three bypass temperature rise measurements varied from their average by ~14%. The uncertainty in the bypass coolant temperature rise measurement was relatively large (~25%) because of the small increase in the differential temperature (5 K).

The net bundle power, shown in Figure 16, was determined from the sum of the fission heating and

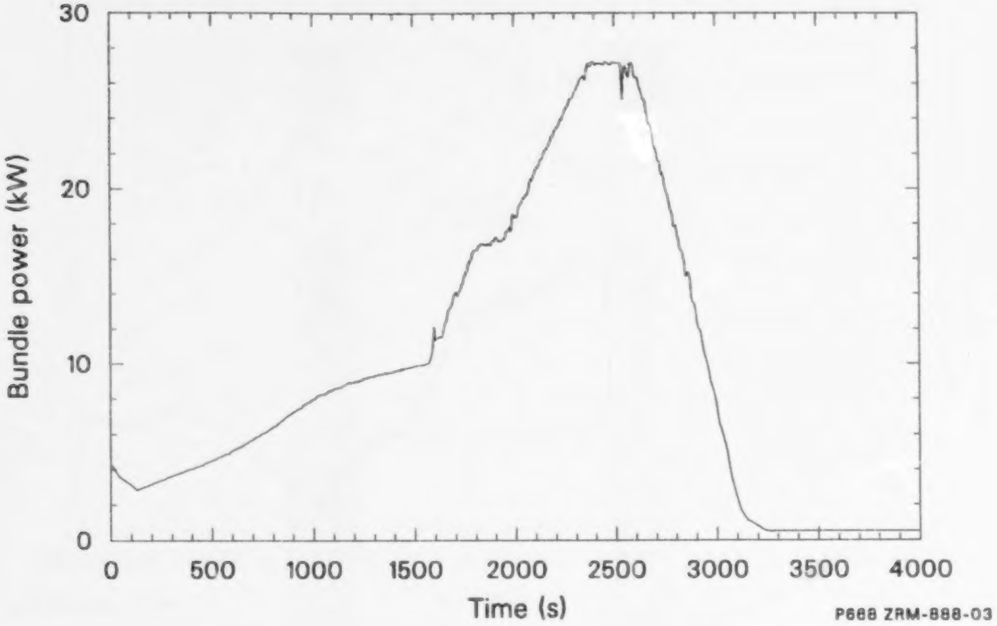

Figure 14. Bundle nuclear power during Test SFD 1-4.

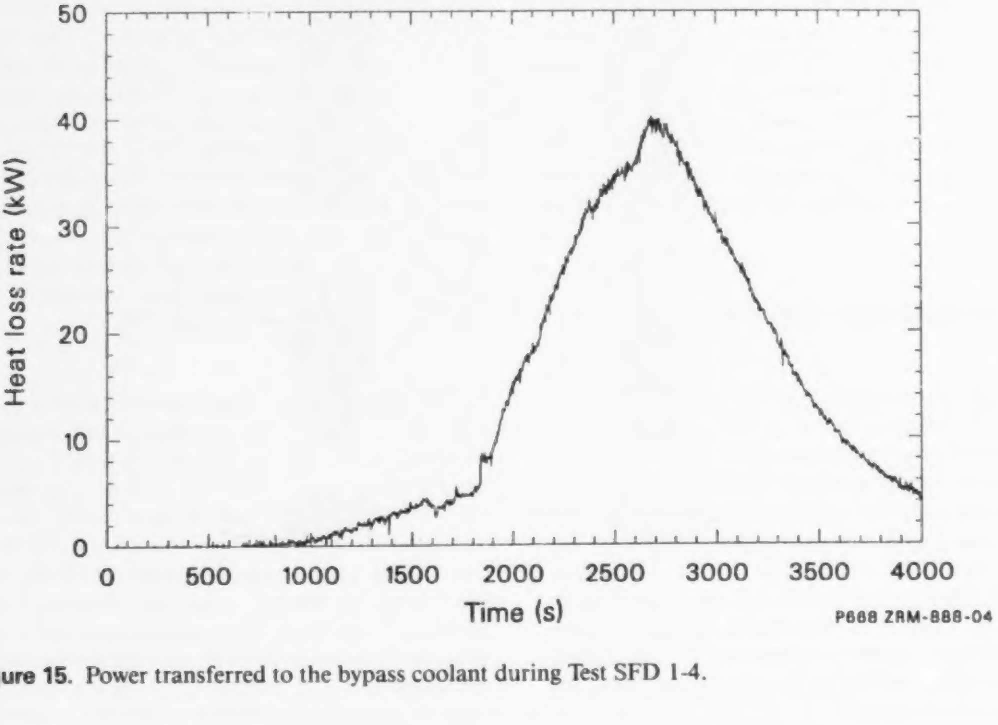

Figure 15. Power transferred to the bypass coolant during Test SFD 1-4.

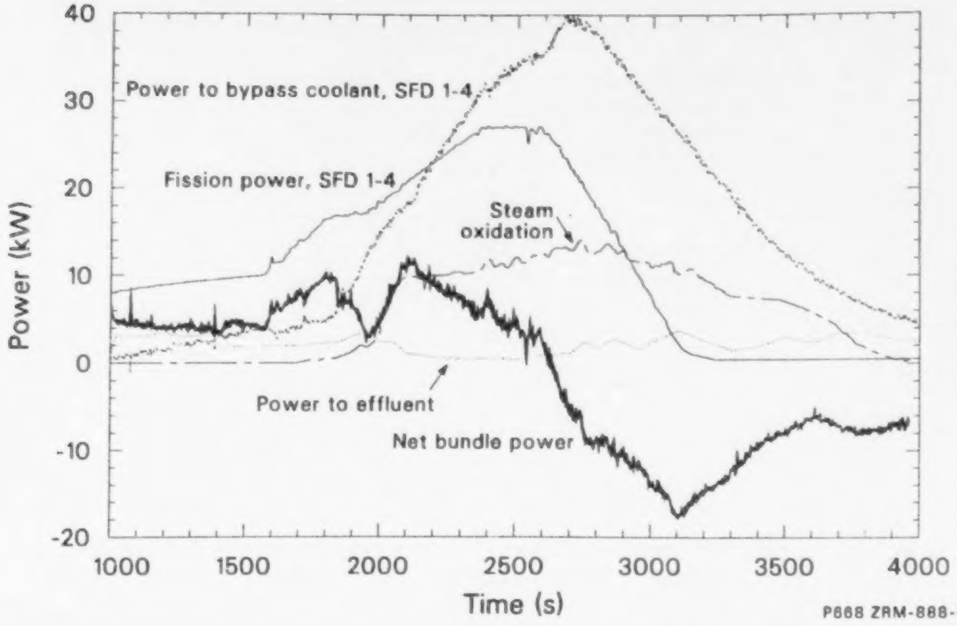

Figure 16. Fission power, power to bypass coolant, steam oxidation power, power to effluent, and net bundle power during Test SFD 1-4.

steam oxidation minus the power lost to the bypass coolant and to the effluent. The steam oxidation power is based on the hydrogen generation rate discussed in Section 5. The power lost to the steam was calculated by SCDAP/RELAP5, as discussed in Section 8. The negative net bundle power at maximum temperature implies that the power lost to the bypass coolant is not accurate because of the large uncertainties in the measured heat loss and the slight timing delay due to the thermal inertia of the shroud.

4.2 Experiment Scenario

A neutron radiograph of the posttest SFD 1-4 bundle is shown in Figure 17. The radiograph and postirradiation examination indicate four distinct regions of bundle damage. The upper portion of the bundle consisted of a rubble bed of unclad fuel fragments. Partial fuel pellets and remnants of dissolved fuel remained in the mid-bundle region. Molten zircaloy and liquefied fuel accumulated in the lower portion of the bundle. Metallic melts, consisting of zircaloy, stainless steel, and control rod material, resided at the spacer grid near the bottom of the bundle.

A discussion of the scenario of events that led to this damage state and produced the resultant fission product and aerosol release and transport behavior is presented in this section. This best-estimate experiment scenario is based on extensive analysis of the on-line instrumentation, fission product and aerosol measurements and analysis, postirradiation examination data, and SCDAP/RELAP5 results. The scenario is discussed in five parts: (a) initial heatup; (b) oxidation, hydrogen generation, and melt progression behavior; (c) control rod behavior; (d) fission product release; and (e) aerosol behavior. A synopsis of the event scenario is shown in Figure 18.

4.2.1 Initial Heatup. The high-temperature transient was initiated with an equilibrium cladding temperature of ~750 K, 2.9 kW of fission power, and the steam interface level at 0.24 m. The steaming rate was ~0.6 g/s, and an argon sweep gas of 0.26 g/s was flowing through the bundle. At 60 s, the bundle power was increased at a rate of 0.005 kW/s to produce a bundle average heatup rate of 0.37 K/s from 800 to 1200 K. At 1180 s, the bundle power was at 8.8 kW; and the average bundle temperature (as measured by the six cladding thermocouples) was ~1000 K. At 1570 s, when the

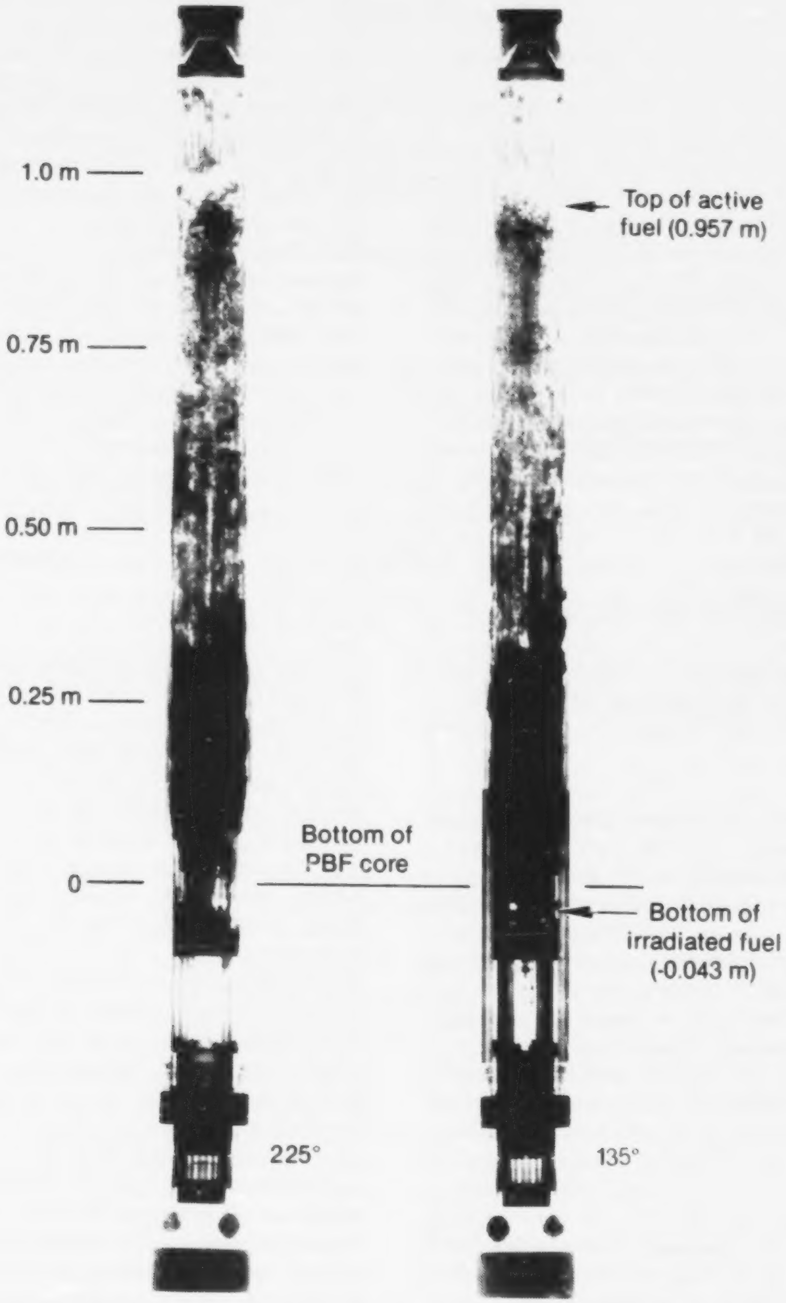
1.0 m
Top of active fuel (0.957 m)
0.75 m
0.50 m
0.25 m
Bottom of PBF core
0
Bottom of irradiated fuel (-0.043 m)
225°
135°

Figure 17. Neutron radiograph of the SFD 1-4 bundle.

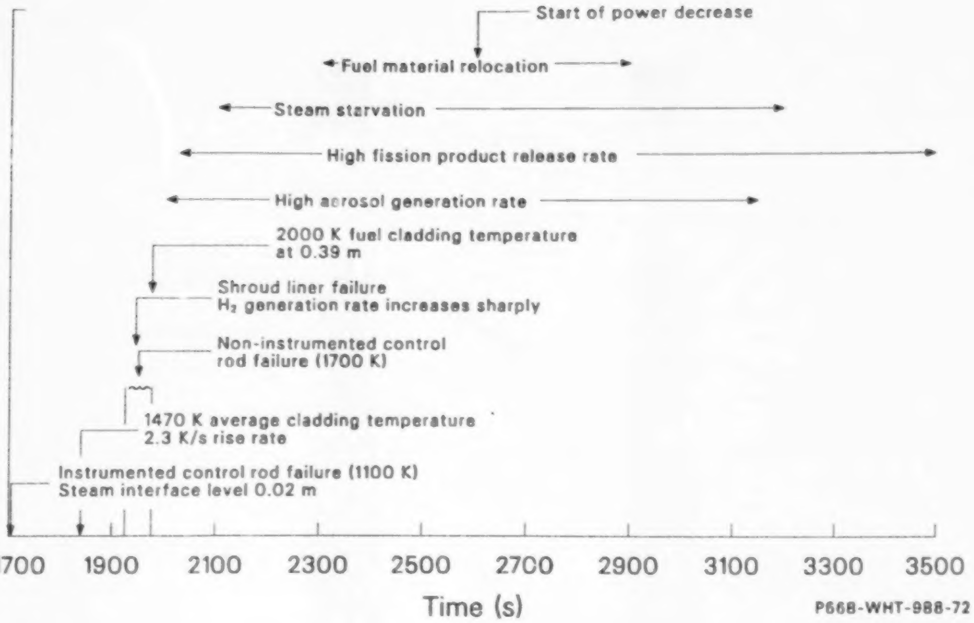

Figure 18. Scenario of events for Test SFD 1-4.

peak bundle temperature was 1200 K and the power was 10.5 kW, the power ramp rate was increased to obtain an average heatup rate of 1.6 K/s from 1200 to ~1600 K.

4.2.2 Oxidation, Hydrogen Generation, and Melt Progression. At 1838 s, an increasing oxidation rate accelerated the bundle heatup. The highest heatup rates measured for the six cladding thermocouples just prior to failure at ~1950 s averaged ~9.2 K/s at temperatures ranging between 1800 and 1990 K. At 1946 s, the shroud zircaloy inner liner failed from oxidation (as expected). Posttest examination indicated that the inner liner failure resulted in local double-sided oxidation and, later, degradation of the ZrO_2 insulation from material relocation and interaction. Thermocouples on the outer surface of the liner lagged the cladding thermocouples by about 550 s at 1000 K. The time lag had decreased to 100 s at 1946 s when the liner failed at a temperature of ~1470 K, indicating increased oxidation of the liner and heat transfer to the liner from radiation.

The oxidation front started at the bundle midplane and propagated first upward and then downward, based on the slight lag in the response of the cladding thermocouples in the lower third of the bundle, and later radially outward to the shroud liner. Extensive oxidation and heatup continued in the lower elevations. The longest surviving thermocouple (0.39 m on rod 3B) indicated a temperature of 2000 K when it failed at 1976 s. The hydrogen generation rate indicated total consumption of the nominal inlet flow (0.6 g/s) at about 2100 s. This steam starvation suggests that oxidation was probably limited to lower elevations during this time and that zircaloy in the middle and upper bundle regions had stopped oxidizing due to a lack of steam. Posttest examinations indicated almost complete oxidation of the cladding at the 0.17- and 0.25-m elevations. Maximum temperature of the original material in this region was estimated to be about 2200 K based on limited zircaloy melting. About 16% of the cladding was oxidized at the 0.08-m elevation; and the lower spacer grid was unmelted prior to the arrival of relocating materials, suggesting a temperature less than 1700 K.

Following nearly complete oxidation of intact zircaloy in the lower regions of the bundle (requiring about 200 s), the oxidation front moved upward again to the higher-power mid-bundle elevations (0.4 to 0.6 m), where rapid oxidation produced very high temperatures. The hydrogen generation rate increased slightly during the high-temperature portion of the experiment (2100 to 2500 s), indicating an enhanced steaming rate and a falling liquid level in the bundle. The hot hydrogen produced in the mid-bundle region heated the upper portions of the bundle (>0.7 m) to melting with very little concurrent oxidation. Little cladding oxidation and essentially no fuel dissolution were observed in the upper elevation samples examined posttest. Thus, it is believed that as the cladding in the upper elevation exceeded the zircaloy melting point, it relocated to the middle portion of the bundle and dissolved much of the fuel there. Upon zircaloy relocation, the declad fuel in the upper bundle formed a debris bed. The very low oxygen content of the cladding, combined with possible ballooning, would tend to reduce the wettability of the UO_2 by zircaloy, resulting in very little interaction in the upper bundle. The total amount of hydrogen generated during the test was 86 ± 12 g, which corresponds to oxidation of 32% of the total zircaloy exposed to high temperatures.

The relocation of molten zircaloy from the upper bundle to the high-power region and the rapid oxidation in the mid-bundle region produced very high temperatures and significant materials interactions. Posttest examination revealed no metallic zircaloy in the mid-bundle region and significant interaction with the fuel. Remnants of previously molten ceramic $(U,Zr)O_2$ material were found at the 0.39- and 0.51-m elevations, indicating temperatures above 2800 K.

Between 2300 and 2900 s, there were several indications of fuel material relocating away from the high-power region. Starting at 2300 s, the fission chamber data indicated probable fuel material relocation away from the 0.5-m elevation. Temperatures recorded by thermocouples above the bundle and in the shroud midwall at the 0.5-m elevation and the heat loss to the bypass increased rapidly at 2600 s, even though the fission power was decreasing after 2592 s. In addition, the hydrogen generation rate peaked at about 2700 s into the experiment. Posttest examination indicated that much of the fuel at the 0.39- and 0.51-m elevations was either missing or had interacted heavily. The material that relocated to the lower bundle region was at high temperature and interacted significantly with in-place material there. The relocated material between 0.15 and 0.30 m in the bundle was at least above the $Zr-ZrO_2$ eutectic temperature (2170 K) because it had dissolved some oxidized cladding in the lower bundle. The large amount of relocated material at 0.25 m completely dissolved the inner four fuel rods and resulted in the production of molten ceramic $(U,Zr)O_2$, indicating temperatures above 2800 K.

A second peak in the aerosol monitor signal suggests that relocating melts caused the vaporization of control materials, especially cadmium, at about 2900 s. There was posttest evidence of such interactions at the 0.25-m elevation, where liquefied fuel relocated onto control materials, and at the 0.08-m elevation, where metallic melts (zircaloy and stainless steel components) relocated onto the control rod lower stubs.

The core melt progression during Test SFD 1-4 was an incoherent process. Multiple relocation events occurred over an extended period of time because of the spatial and temporal temperature gradients in the bundle, the variety of materials in the test, their widely different melting points, and their potential for interaction.

The extended durations (600 to 1440 s) of hydrogen generation, aerosol generation, and fission product release and the fact that these processes extended 60 to 900 s beyond the beginning of the power descent indicate that the bundle was at high temperatures for an extended period and that melt relocations occurred over an ∿480- to 600-s interval. There is evidence of alternating metal and oxide layers at the 0.17-m elevation, suggesting multiple relocation events at 5- to 60-s intervals. In addition, relocated materials of different compositions and different melting points were observed in the lower bundle, indicating that several melt relocation events took place. These melts include: ceramic $(U,Zr)O_2$ (melting point ∿2800 K), zircaloy (melting point ∿2200 K), stainless steel (melting point ∿1700 K), and Ag-In-Cd (melting point ∿1120 K).

The melt progression phenomena observed in Test SFD 1-4 reveal parallels to those more fully developed in the TMI-2 accident which was terminated at a later stage.[9] The rubble bed of fuel fragments in the upper bundle is similar to the TMI-2 debris bed. The high-temperature U-Zr-O melt in the lower bundle is a precursor to the large molten pool in TMI-2. The accumulation of metallic melts (Ag-In-Cd, zirconium, stainless steel) near the bottom of the bundle is a precursor of the metallic lower crust found in TMI-2.

4.2.3 Control Rod Behavior. The instrumented control rod (rod 5E) failed at 1708 s because of a weld defect that resulted in waterlogging and excessive internal pressure during the heatup. The control rod cladding temperature was 1170 K at the 0.39-m elevation at the time of failure. A system pressure spike of 0.4 MPa occurred at 1712 s as the molten control rod material entered the lower plenum, and the lower plenum coolant temperature increased ~8 K from heating by the molten alloy. At 1768 s, aerosols were detected downstream at the monitor.

Fission chamber data indicate that between 1927 and 1978 s the three other noninstrumented control rods failed at a temperature of ~1700 K, about the melting point of the stainless steel control rod cladding (1720 K). At 2040 s, the aerosol monitor indicated the presence of large amounts of aerosol in the effluent line. A second increase of 5 K in the temperature of the lower plenum water from ~1900 to 2100 s indicated that some of the alloy entered the lower plenum; however, no pressure spike was generated. It is believed that the alloy located above the cladding failure elevation drained rapidly out of the rod. As upper portions of the empty control rod cladding reached melting, the stainless steel relocated downwards. When portions of the rod below the failure location exceeded the melting point of stainless steel, the molten alloy and stainless steel also interacted with the zircaloy guide tube and relocated. Fission chamber data suggest that most of the control rod relocation was complete by 2200 s. Reactor physics calculations indicate that this relocation and dispersal of control rod material significantly suppressed the power in the lower bundle regions. However, the overall bundle power only decreased slightly because the power in the upper regions increased.

Posttest examination indicates that although a significant quantity (17%) of the neutron absorber alloy had relocated to the lower plenum, most of the remaining control rod material relocated near the lower spacer grid location at the 0.08-m elevation. Most of the control rod alloy was found outside of the zircaloy guide tubes; however, there was evidence that molten material from above had relocated down the former zircaloy guide tube locations. The relocated material at and below 0.08 m contained control rod alloy that was close to the as-fabricated Ag-In-Cd ratio (80/15/5 wt.%), whereas above 0.08 m some depletion of the constituents of the alloy occurred, as indicated by deviations from the as-built ratio. The metallic relocated material at and below 0.17 m contained zircaloy and stainless steel components in a multitude of compositions formed with each other and control rod alloy components. The numerous interactions indicate that the control rod alloy and molten stainless steel interacted with zircaloy during and following relocation. The relocated material that collected at the lower spacer grid (after some oxidation of the zircaloy had taken place) dissolved most of the remaining metallic zircaloy and Inconel but did not interact with the fuel. Based on the thicknesses of oxide layers present in this melt, the time intervals between relocation events were on the order of 5 to 60 s.

Ag-In-Cd control rod materials were heated (and vaporized) by relocating melts long after the initial control rod failure and relocation of control rod materials. Results from the aerosol samples taken late in the experiment (after 2900 s) indicated the presence of cadmium. The principal effects of Ag-In-Cd control rods appear to be the generation of cadmium aerosol and the formation of metallic melts that freeze at low elevations in the core and produce a lower crust. The influence of control rods on UO_2 liquefaction was minimal. The melt progression affects the timing and magnitude of aerosol generation.

4.2.4 Fission Product Release. Gap release of fission products following ballooning and rupture of the fuel rod cladding was very difficult to detect in Test SFD 1-4, because the fuel rods failed over a relatively long time interval, producing a reduced fission product concentration in the effluent sampling line as compared with simultaneous rupturing of all the rods. Noble gas release began at ~1700 s (~1500 K). The noble gas fractional release rate increased four orders of magnitude between 1800 and 2100 s as bundle temperatures were driven above 2100 K. Between 2100 and 3000 s, significant liquefaction and dissolution is thought to have occurred. However, the effect of such changes in fuel morphology on the rate of fission product release was difficult to detect, since the noble gas fractional release rate was generally constant during this time. Beyond 3000 s, the noble gas fractional release rate decreased somewhat but remained elevated during the remainder of the transient.

Integral releases of the noble gases ranged from 23 to 52%. Releases of iodine and cesium were 24 and 51%, respectively, whereas only 3% of the bundle inventory of tellurium was released. Most of the released iodine, cesium, and tellurium was deposited within the bundle and sampling system. Iodine and cesium were later washed from system surfaces during flushing operations and measured in the collection tank. System flushing removed very little of the deposited tellurium. Lesser amounts of the low-volatility fission products (strontium, barium, lanthanum, europium, and cerium) were released during the experiment.

Comparison of the integral release data indicates that the releases of long-lived noble gas species were greater than those of short-lived species. The release fractions for ^{85}Kr and stable xenon and krypton isotopes were ~0.5, yet the average release of seven short-lived noble gases was ~0.35. This difference in release is believed to be related to the morphology of the fuel and the location of the fission products in the fuel prior to release.[10] A higher proportion of the long-lived species (relative to short half-lived species) reside at grain boundaries from which release is relatively fast during heatup because of the interconnected porosity in the high-burnup fuel. For the short-lived species, release is slower because more of the inventory is in the fuel grain and must diffuse to the grain boundaries prior to release.

4.2.5 Aerosol Generation and Transport Behavior. Aerosol generation in Test SFD 1-4 was continuous during the high-temperature portion of the experiment and was strongly coupled to melt progression phenomena. Many phenomena occurred simultaneously during Test SFD 1-4, all of which contributed to aerosol formation. The aerosol monitor signal, data from the deposition coupons, and results from the effluent filters indicate that the vaporization of Ag-In-Cd control rod material, tin release due to zircaloy oxidation, volatile fission product release, possible release of loose particulates from the shroud (ZrO_2) insulation cavity, and ceramic melt relocation and interaction with control rod material all contributed to the aerosol source exiting the SFD 1-4 bundle.

Measurements indicate that at least 13 g of aerosol material were released from the bundle—~5 g of cadmium, 0.4 g of silver, 0.2 g of indium, at least 4 g of tin, and 3.5 g of zirconium. Although these values represent a small fraction of the bundle inventory of these materials, their mass was sufficient to produce a very dense aerosol during the entire high-temperature portion of the transient.

Vapor-phase chemical equilibrium calculations indicate that the dominant forms of cesium and iodine in Test SFD 1-4 were cesium iodide and cesium hydroxide, with some elemental cesium at high temperatures. Because of the high concentrations of cesium and iodine released from the high-burnup fuel and the low release of silver, no hydrogen iodide and no silver iodide were predicted to form. The dominant form of tellurium released from the bundle was believed to be tin telluride. These results are consistent with posttest system flushing results that indicate most of the iodine and cesium deposition was easily removed by water, whereas very little of the deposited tellurium was removed. The reducing environment during the high-temperature transient resulted in silver, cadmium, and tin being released in their elemental form.

Calculations indicate that distinct mechanisms governed aerosol behavior in different parts of the SFD 1-4 upper plenum. Vapor condensation and aerosol nucleation were the dominant mechanism in the heat shield area immediately above the fuel bundle. Upon exiting the bundle, silver and tin, because of their low volatility, condensed and formed aerosols in the upper bundle end cap region. For cadmium and cesium iodide, the high temperatures above the bundle and the high vapor pressures of these materials prevented vapor condensation from occurring until they reached the lower end of the deposition rod (~800 K), whereupon they condensed on the tin and silver aerosols and the downstream surfaces of the deposition rod. These materials would be expected to condense very rapidly on the aerosol seeds to produce a relatively mature aerosol. The presence of significant quantities of ^{137}Cs on the cadmium deposits and the results of fission product and aerosol transport calculations indicate that the aerosol generated in Test SFD 1-4 provided a large mobile surface on which volatile fission products could condense. Below 700 K, >95% of the volatile fission products were transported as an aerosol.

Once the aerosol moved further downstream, aerosol agglomeration, deposition, and settling governed its behavior in the heated upper plenum. Very little evaporation and/or condensation of the volatile species (i.e., cadmium and cesium iodide) would be expected because the upper plenum was heated to a uniform temperature of 800 K. However, the aerosol concentration was probably high enough that agglomeration was occurring during transport, causing the aerosol size to increase. Deposition data in the heated upper plenum for almost all measured species indicate that the aerosol was large enough to cause different deposition patterns on the vertical and horizontal surfaces. Cohesive deposits of material were observed on the horizontal surfaces of most of the coupon holders. SEM photographs indicate that the particles on horizontal surfaces were agglomerates ranging in size between 25 and 250 μm, whereas those on the vertical surfaces were <20 μm. This enhanced deposition on horizontal surfaces was caused by deposition of particles >25 μm from wakes and eddies, gravitational settling, and/or flow of liquid condensate (e.g., cadmium, cesium hydroxide) from the vertical surfaces to the horizontal surface. Significant attenuation of the larger-sized aerosols occurred in the heated upper plenum because of the filtering effect of the 20 coupon holders of the deposition rod.

Elemental analysis of the solid deposits on the horizontal surfaces of the deposition rod indicates that the aerosol was predominantly cadmium. Yet, the aerosol that entered the aerosol monitor was found to be >50% tin. In addition, the cesium deposition data indicate a significant decrease in deposition in the unheated upper plenum relative to the heated upper plenum. This change in the chemical composition of the aerosol is a result of the relatively cold walls in the unheated upper plenum. As the aerosol entered the unheated portion of the upper plenum, the cooler wall temperatures (~600 K) caused some of the volatile components of the aerosol, like cadmium and cesium iodide, to evaporate from the aerosol and condense on the wall. Thus, most of the cesium deposition on the downstream surface of the deposition rod is due to vapor condensation of volatile species of cesium, like cesium iodide and cesium hydroxide, and/or deposition of fine aerosol particles.

A fine, yet dense, aerosol was continuously monitored 10 m downstream of the bundle at the aerosol monitor. The aerosol measured at the monitor was predominantly tin and cadmium, with small amounts of silver, zirconium, and fission products. The diameter of average mass of the aerosol at the aerosol monitor ranged from 0.4 to 1.0 μm, and the number concentration varied between 5×10^7 and 2×10^8 p/cm^3 during the transient.

Additional details of the on-line test data, metallurgical examination, fission product and aerosol release and transport, computer modeling, and conclusions are given in the remaining sections.

5. BUNDLE HEATUP, OXIDATION, AND MELT PROGRESSION BEHAVIOR

Information relating to bundle heatup, oxidation, and melt progression behavior in Test SFD 1-4 is presented in this section. The thermal response of the bundle is analyzed in Section 5.1. Hydrogen generation and zircaloy oxidation behavior is discussed in Section 5.2. In Section 5.3, postirradiation examination results relating to fuel behavior in Test SFD 1-4 are described. Control rod behavior in the experiment, as inferred from the on-line instrumentation and postirradiation examination, is summarized in Section 5.4.

5.1 Bundle Thermal Response

Measurements of fuel rod, shroud, and effluent temperatures and effluent flow have been used to determine the bundle thermal response described in this section.

5.1.1 Fuel Rod and Shroud Temperatures. Various thermocouples were used to measure the temperature response of the bundle and shroud. Because it was not practical to install instruments on the 26 highly irradiated fuel rods, only the two unirradiated rods were instrumented with temperature and internal pressure monitors. These two rods, located in grid positions 3B and 4D, were each instrumented with three cladding inner surface thermocouples, one centerline fuel thermocouple, and a pressure switch device to detect cladding rupture. The cladding thermocouples consisted of tungsten-rhenium thermal elements, insulated with high purity beryllium oxide and sheathed in zircaloy which was lined internally with a thin layer of tantalum. Although the tungsten-rhenium thermocouples were capable of measuring temperatures to 2500 K, the useful range in steam was considerably less because of oxidation, electrical shunting, and mechanical failures.

Five thermocouples were attached to the outer surface of the inner zircaloy liner at the 90- and 270-degree orientations (two each at 0.35 m, two each at 0.5 m, and one at 0.7 m). Seven additional midwall thermocouples were located near the outer surface of the insulation at the 0-, 90-, 180-, and 270-degree orientations (four each at 0.5 m, two each at 0.7 m, and one at 0.91 m). Eight thermocouples (four each at 0.35 m, two each at 0.50 m and 0.70 m) were used to measure the temperature on the outer surface of the outside shroud wall (in the bypass coolant region). Thermocouples at both the inner liner and the outer shroud wall were welded in place, but the midwall thermocouples were simply embedded into the fiberboard insulation and held in place by contact pressure of the saddle. The large radial temperature gradient through the insulation, combined with uncertainty in the radial location of the shroud midwall thermocouples, resulted in some early thermocouple failures and significant measurement errors.

The six cladding and two fuel centerline thermocouples provided reliable qualified data as a group up to 1838 s (1470 K average temperature). Between 1838 and 1976 s, the six cladding thermocouples became unreliable and failed, although an erratic signal continued to be produced. The five shroud inner liner thermocouples provided qualified data as a group up to 1950 s. These thermocouples became unreliable and failed between 1950 and 2040 s. Because the location of the virtual thermocouple junction(s) was unknown and shunting had reduced the electrical output, the data plots have been stopped at the time of suspected thermocouple failure. Data plotted beyond the solid vertical lines in the following figures were qualified as trend.

The small number of cladding and liner thermocouples combined with relatively early failure of the thermocouples limited the interpretation of the bundle thermal on-line data during the high-temperature portion of the experiment. The fuel rod cladding inner surface temperatures are shown in Figures 19 and 20. Plots of the average cladding temperature ramp rate at each elevation as a function of temperature are shown in Figure 21.

Prior to 60 s, the bundle was essentially at steady state with an equilibrium cladding temperature of ~750 K. The bundle temperature (as indicated by the average of the six cladding thermocouples) increased from 800 K to ~1200 K at a rate of 0.37 K/s. After reaching 1200 K at 1570 s, the bundle power ramp rate was increased to obtain an average temperature ramp rate of ~1.6 K/s up to ~1600 K. Above 1600 K, an increasing oxidation rate accelerated the temperature ramp rate. Maximum rates of 8 to 10 K/s were attained prior to thermocouple failure. The thermocouples at 0.74 and 0.54 m on both rods 3B and 4D indicated

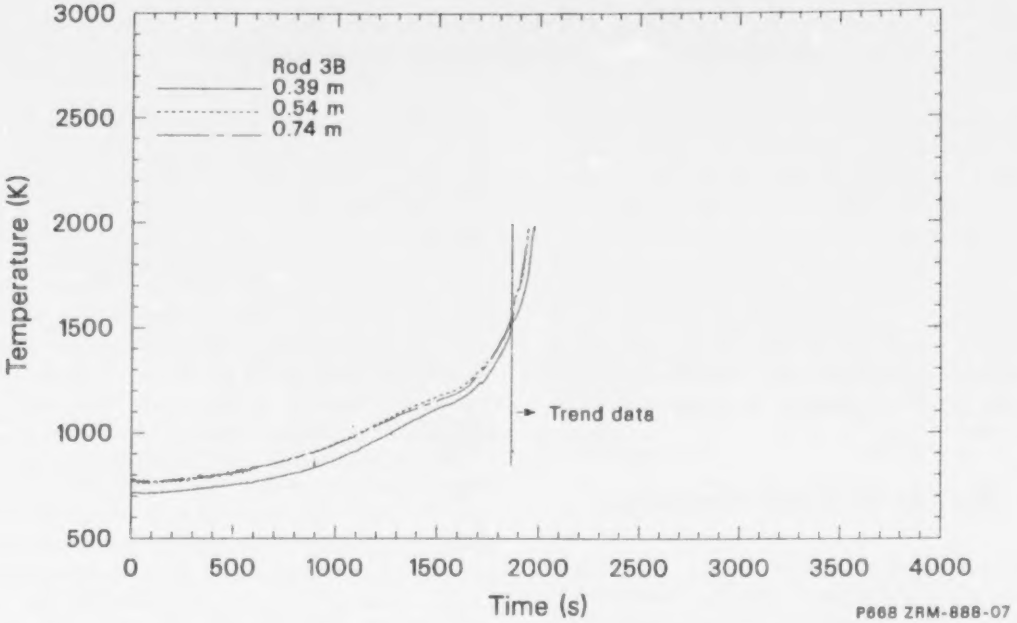

Figure 19. Cladding temperatures at 0.39, 0.54, and 0.74 m for Test SFD 1-4 fuel rod 3B.

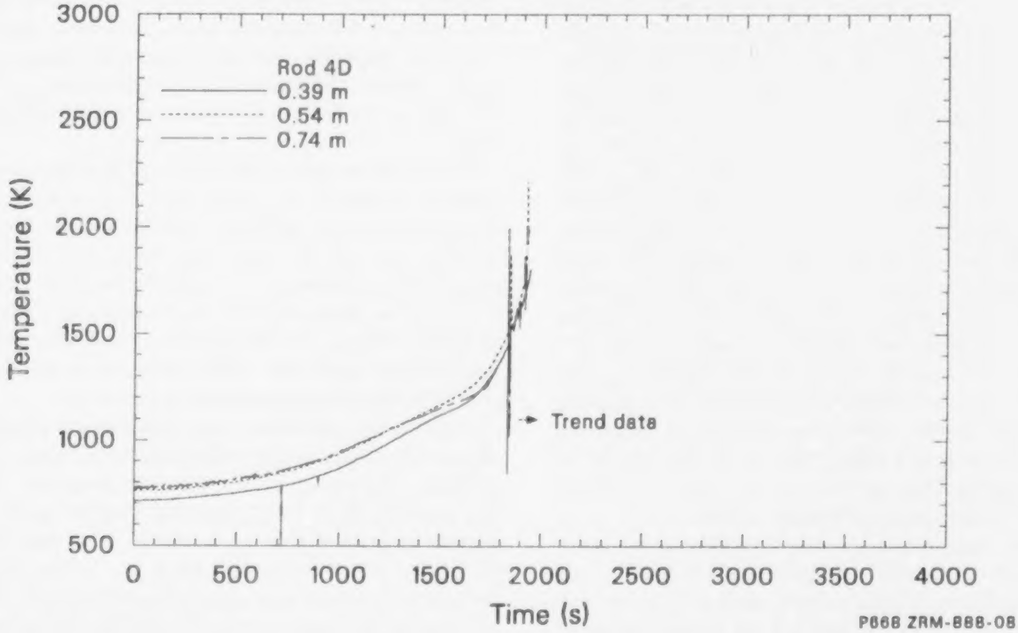

Figure 20. Cladding temperatures at 0.39, 0.54, and 0.74 m for Test SFD 1-4 fuel rod 4D.

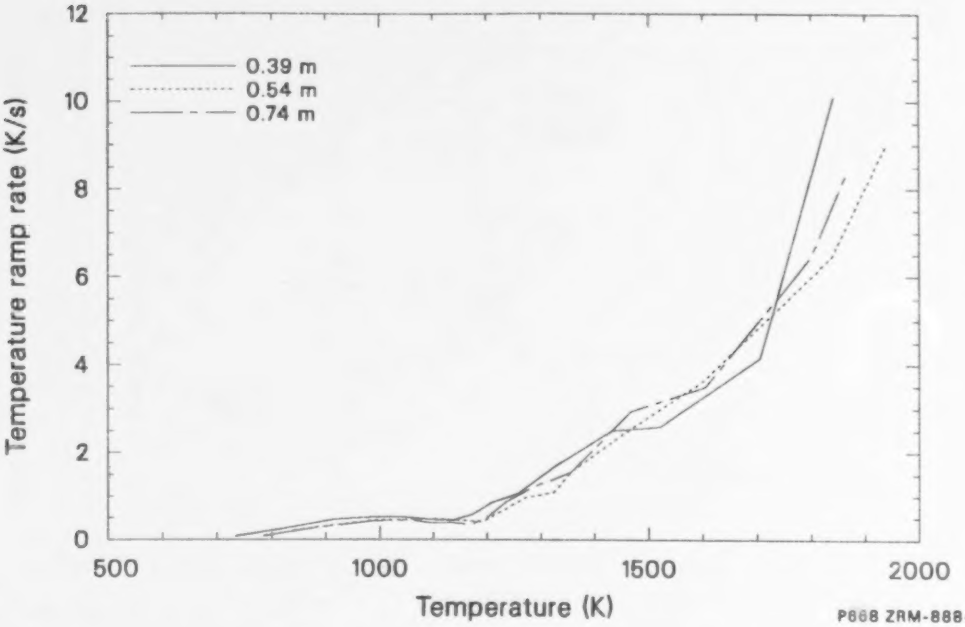

P668 ZRM-888-27

Figure 21. Average cladding temperature ramp rate for Test SFD 1-4 fuel rods 3B and 4D at 0.39, 0.54, and 0.74 m.

nearly identical heatup rates (6.5 K/s) during the last 50 s prior to thermocouple failure. The temperature and ramp rate (4.1 K/s max) at 0.39 m lagged behind the upper thermocouple traces until ∿1700 s when the ramp rate increased to ∿10 K/s and the thermocouple finally failed. The maximum cladding temperatures measured were ∿2000 K.

The three shroud inner liner temperature measurements at 270 degrees at elevations of 0.35, 0.50, and 0.70 m are shown in Figure 22; and the corresponding temperature ramp rates are shown in Figure 23. The average shroud inner liner temperature ramp rate was 0.26 K/s (from 665 to 945 K) during the same time that the cladding temperature ramp rate was 0.37 K/s (from 800 to 1200 K). During the time the cladding temperature ramp rate was 1.6 K/s (from 1200 to 1600 K), the shroud inner liner rate was 1.2 K/s (from 945 to 1240 K). Peak inner liner temperature ramp rates of 7 K/s were attained prior to shroud liner thermocouple failure. Maximum shroud liner temperatures were measured at the 0.35-m elevation until temperatures exceeded 1100 K, after which time they were recorded by the thermocouple at the 0.50-m elevation.

The shroud inner liner temperature at 0.50 m lagged the fuel rod cladding temperatures at 0.54 m by about 550 s at 1000 K. At the time of liner failure at 1946 s and 1470 K, the time lag between the cladding and liner temperatures had decreased to 100 s, indicating increased oxidation and radiation heat transfer from the bundle. The shroud inner liner had oxidized and failed as expected at ∿1946 s, as shown in Figure 24 by the rapid decrease in the bundle pressure. The inner liner was not designed as a primary pressure boundary, but its failure did allow bundle steam and hydrogen to mix with argon gas from the insulator region. The bundle coolant pressure dropped by about 0.2 MPa as the pressure in the bundle and insulator regions equalized. The argon sweep gas flow rate was manually increased from 0.26 to 0.58 g/s at 1966 s to counteract the decrease in bundle pressure when the inner liner failed. Replacement of the argon gas in the insulator with steam and hydrogen caused an increase in the conductivity of the ZrO_2 insulation material, slightly higher shroud outer wall temperatures, and an increased rate of heat loss to the bypass coolant. The shroud meltthrough detector signals responded to local heating as well as overall (global) heating of the inside shroud wall. The

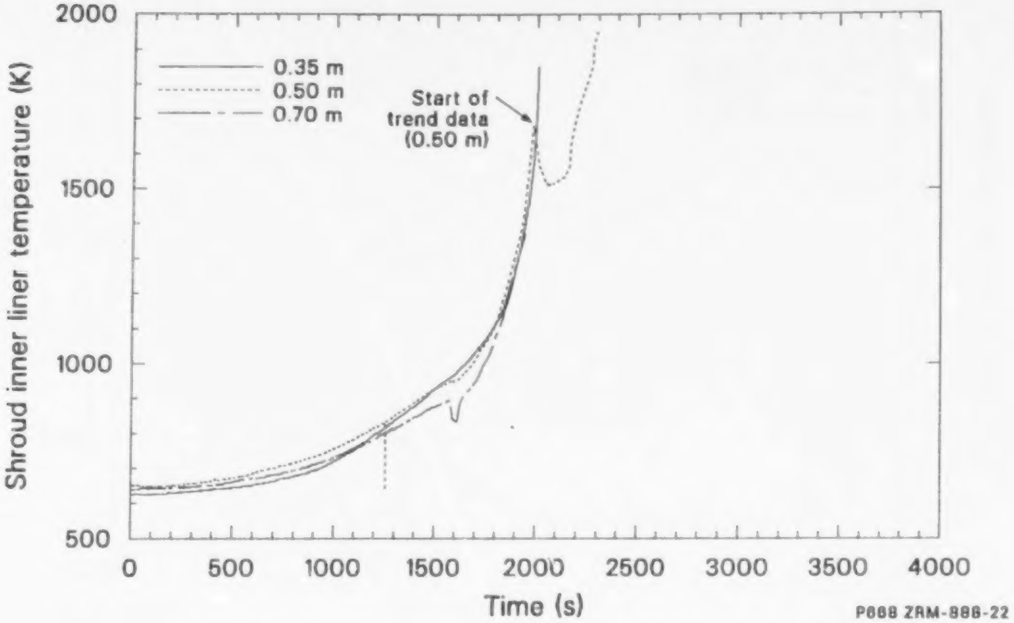

Figure 22. SFD 1-4 shroud inner liner temperatures at 270 degrees at 0.35, 0.50, and 0.70 m.

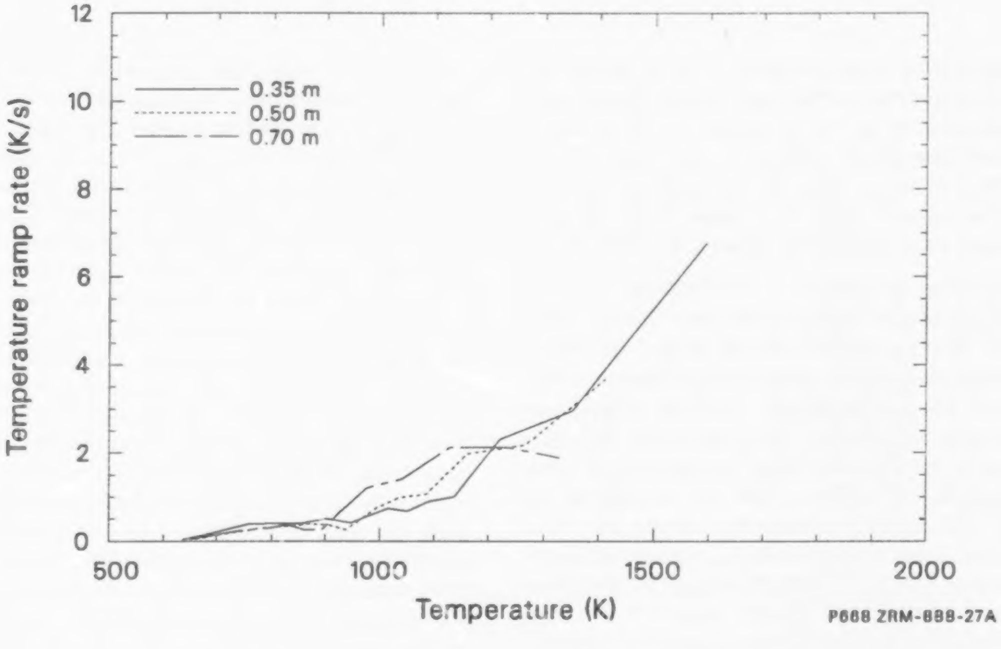

Figure 23. SFD 1-4 shroud inner liner temperature ramp rate at 270 degrees at 0.35, 0.50, and 0.70 m.

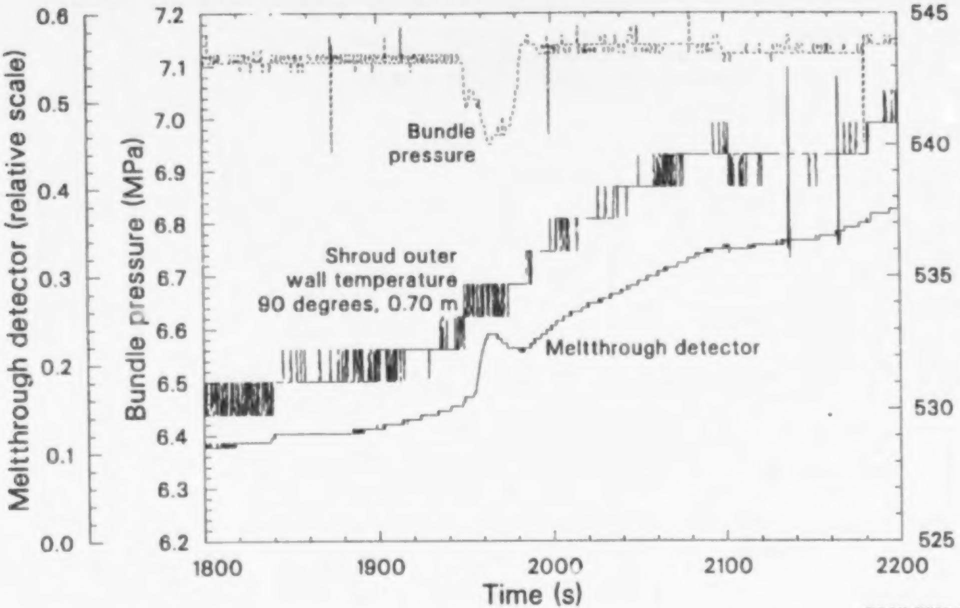

Figure 24. Bundle pressure, shroud outer wall temperature, and shroud meltthrough detector signals during the time of shroud liner failure in Test SFD 1-4.

change in the shroud meltthrough detector signal (also shown in Figure 24) was probably caused by steam and hydrogen entering the shroud insulation region.

A slight temperature gradient existed between the fuel and cladding of the instrumented fuel rods in Test SFD 1-4. Figure 25 compares the cladding temperature and the fuel centerline temperature histories for rod 3B at 0.39 m. Tabulated data indicate that the fuel centerline temperature exceeded the cladding temperature by less than 15 K up to ~1480 K (maximum qualified temperature) at 1859 s. After that time, oxidation caused the cladding temperature to exceed the fuel temperature by up to 70 K, until the cladding thermocouple failed at ~2000 K. The maximum fuel centerline temperature measured prior to failure at 2054 s was 2200 K. Data from rod 4D, shown in Figure 26, also indicate that the fuel temperature exceeded the cladding temperature at 0.39 m by less than 10 K up to the maximum qualified temperature (1465 K). The maximum fuel centerline temperature measured prior to failure at 1980 s was ~2280 K.

A plot of the axial distribution of the measured fuel rod cladding temperatures and liner temperatures at several selected times during the transient is shown in Figure 27. These measurements indicate that the axial temperature gradient was <100 K along the bundle during the early portion of the transient.

Based on the temperature response of the bundle, the oxidation front evidently started at about the bundle midplane and propagated first upward and then downward and later radially outward to the shroud liner. Oxidation in the lower regions eventually consumed essentially all of the available steam flowing through the bundle as the lower bundle temperature increased. After nearly complete oxidation at the lower bundle regions, the oxidation front moved upward again to the higher mid-bundle elevations (0.4 to 0.6 m), where rapid oxidation produced temperatures above ~2800 K.

The responses of the shroud midwall thermocouples at the 180-degree orientation at 0.5, 0.70 and 0.91 m are shown in Figure 28. The azimuthal variation in the shroud temperature at 0.50 m is shown in Figure 29. (The midwall thermocouples are mounted on the outer surface of the insulator.) The data generally indicate that significant axial and azimuthal gradients in the shroud midwall temperatures existed after oxidation became significant.

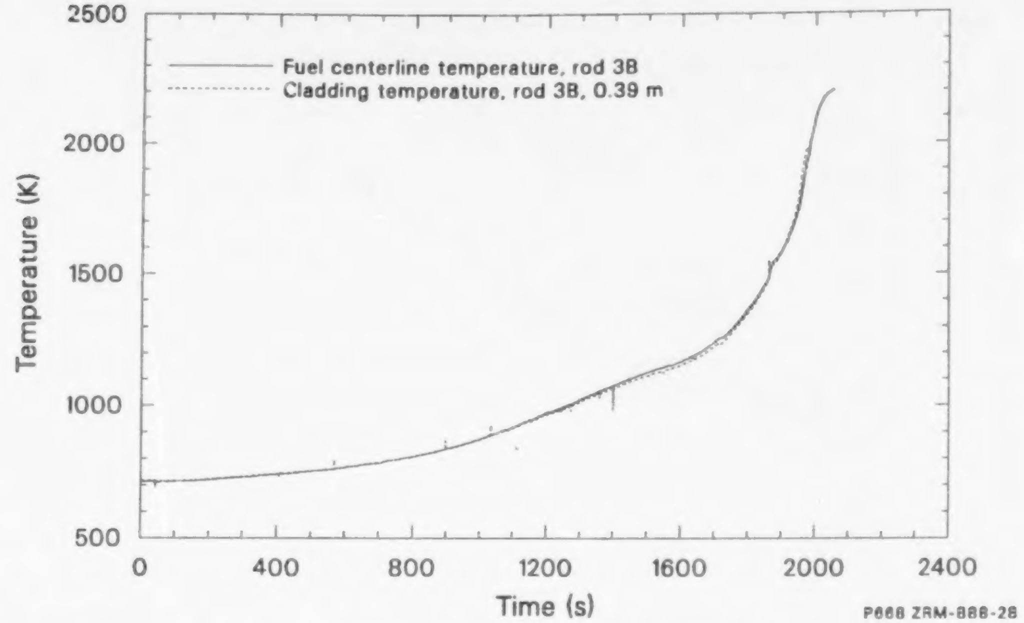

Figure 25. Comparison of measured cladding and fuel centerline temperatures at 0.39 m for Test SFD 1-4 rod 3B.

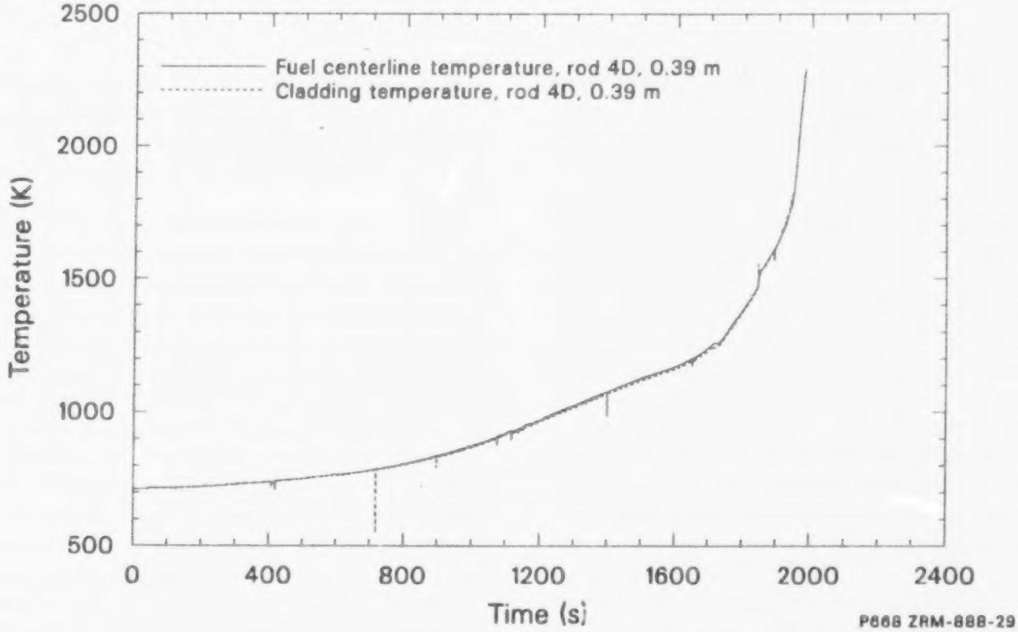

Figure 26. Comparison of measured cladding and fuel centerline temperatures at 0.39 m for Test SFD 1-4 rod 4D.

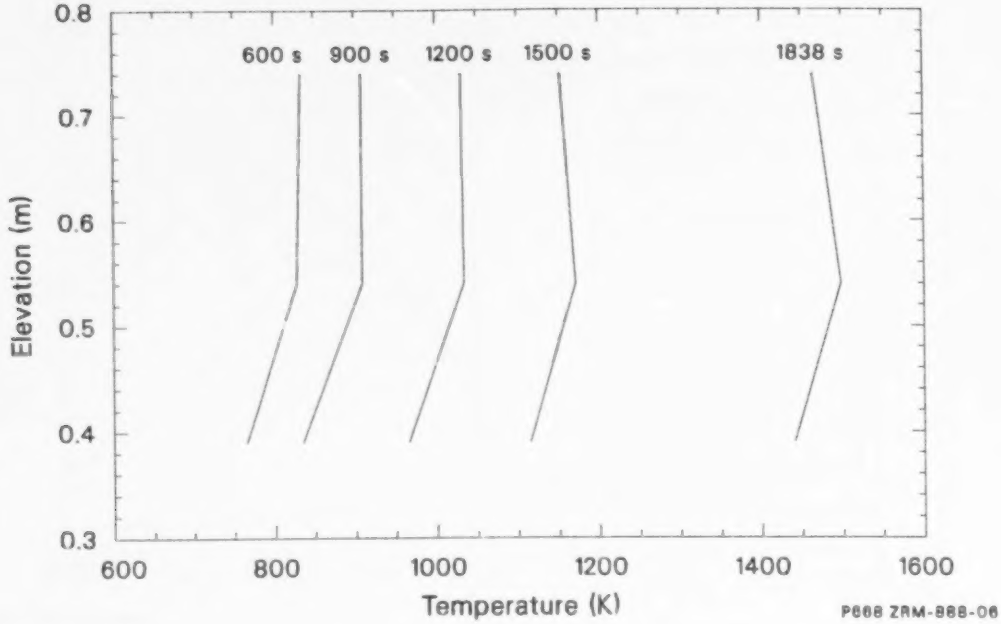

Figure 27. Axial temperature profile of fuel rod cladding temperatures at selected times during the Test SFD 1-4 transient.

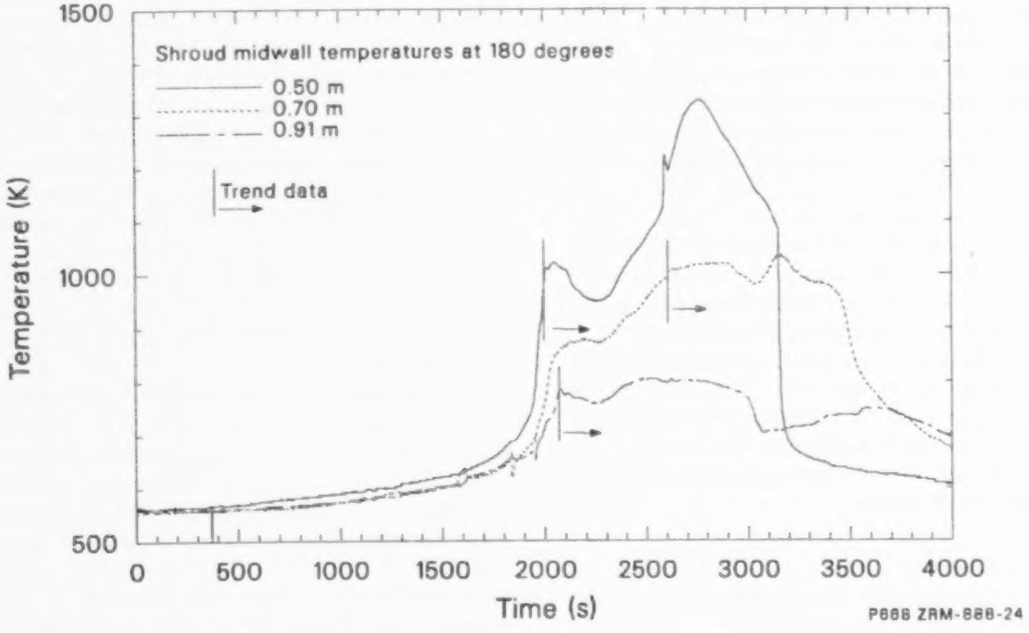

Figure 28. SFD 1-4 shroud midwall temperatures at 0.50, 0.70, and 0.91 m.

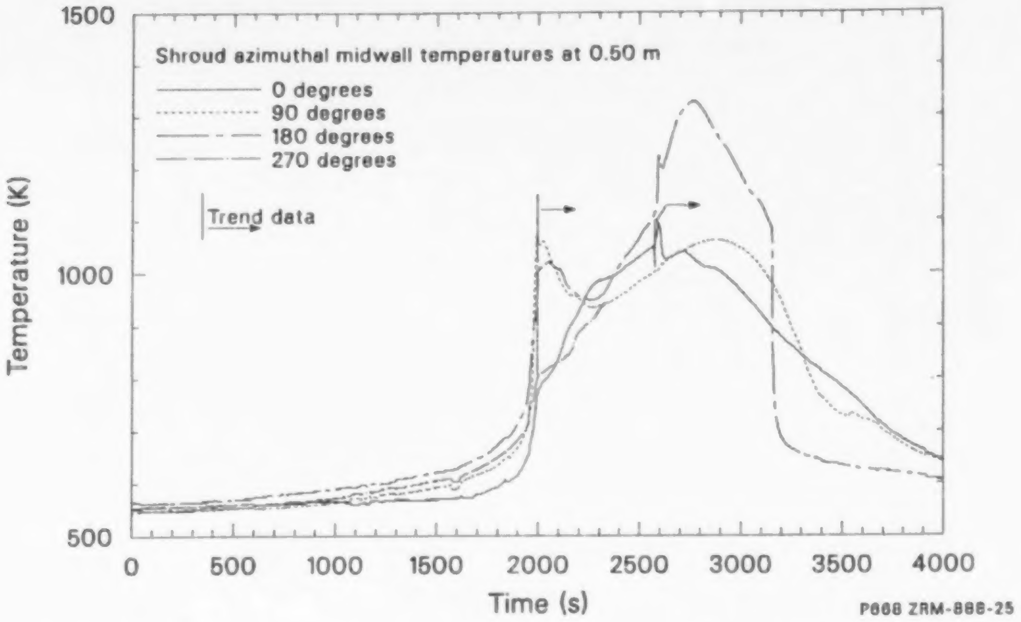

Figure 29. SFD 1-4 shroud midwall temperatures at 0.50 m at 0, 90, 180, and 270 degrees.

The midwall thermocouple data (qualified up to ~2000 s) indicated maximum temperatures in the range of 800 to 1100 K. The trend data after 2000 s indicate that the bundle remained hot for several hundreds of seconds following the power reduction from 2592 to 3180 s. As shown in Figure 30, the output of one of the shroud meltthrough detectors increased significantly at about 2600 s. The increased temperature indicated by the shroud meltthrough detector and midwall thermocouples also correlates to increases in the fission chamber response at 0.51 m, hydrogen generation in the bundle, effluent steam temperatures above the bundle, and the rate of heat loss to the bypass (see Figure 15) measured at that time. These increases are probably the result of degradation of the shroud insulation caused by interaction with molten material in the bundle and subsequent relocation from the mid-bundle region.

5.1.2 Effluent Temperature. Steam temperatures, shown in Figure 31, were measured with two thermocouples located near the periphery of the bundle at 0.54 and 0.99 m. A comparison of the cladding temperature at 0.54 m, the steam temperature at 0.54 m, and the shroud inner liner temperature at 0.50 m is shown in Figure 32. The temperatures maintained their relative position with respect to each other until the steam thermocouple failed. The exit steam temperatures, shown in Figure 33, were measured with three thermocouples at the 1.14-m elevation. Steam temperatures were also measured at elevations of 1.54, 2.35, and 3.36 m, as shown in Figure 34. The effluent line was electrically heated and insulated from 0.27 m above the bundle to the condenser. In addition, a portion of the upper plenum region was heated by three sets of electrical heaters. The lower set of heaters was automatically regulated at 800 K, the middle set at 750 K, and the upper set at 700 K. Temperatures of the effluent line, shown in Figure 35, were measured at elevations of 1.84, 2.29, 2.83, and 3.40 m.

The deposition rod, with attached coupons, was centrally located within the upper plenum from about 1.33 to 5.5 m. The coupon temperatures at elevations of 1.57, 2.38, and 3.40 m (at 45-degree orientation) are shown in Figure 36. All of the temperatures were above saturation during the high-temperature transient, thus preventing steam condensation. The temperature histories of the coupon and steam near 2.3 m are shown in Figure 37.

The temperature of various portions of the effluent line, as measured by thermocouples installed at intervals along the outer wall of the effluent line outside of the IPT, are presented in Table 5. The saturation temperature of pure steam at the

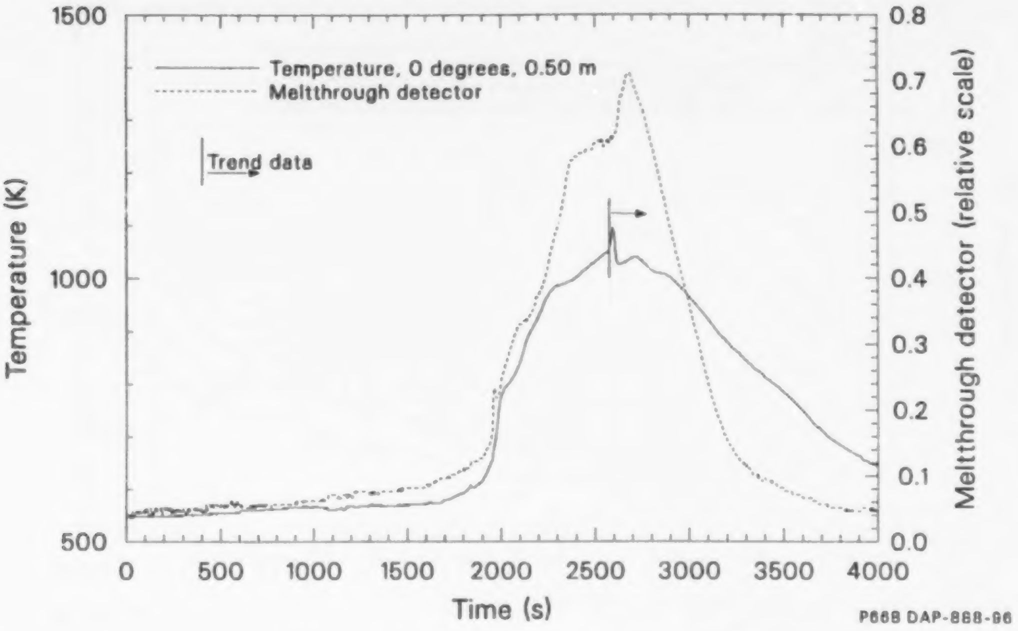

Figure 30. SFD 1-4 shroud meltthrough detector and midwall temperature responses.

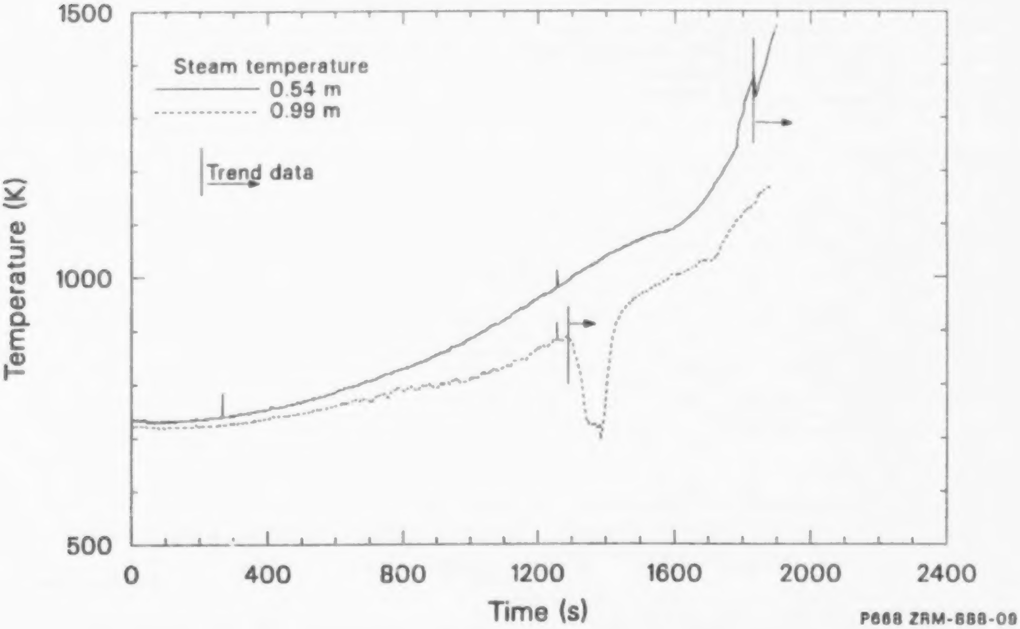

Figure 31. Steam temperatures within the SFD 1-4 bundle at 0.54 and 0.99 m.

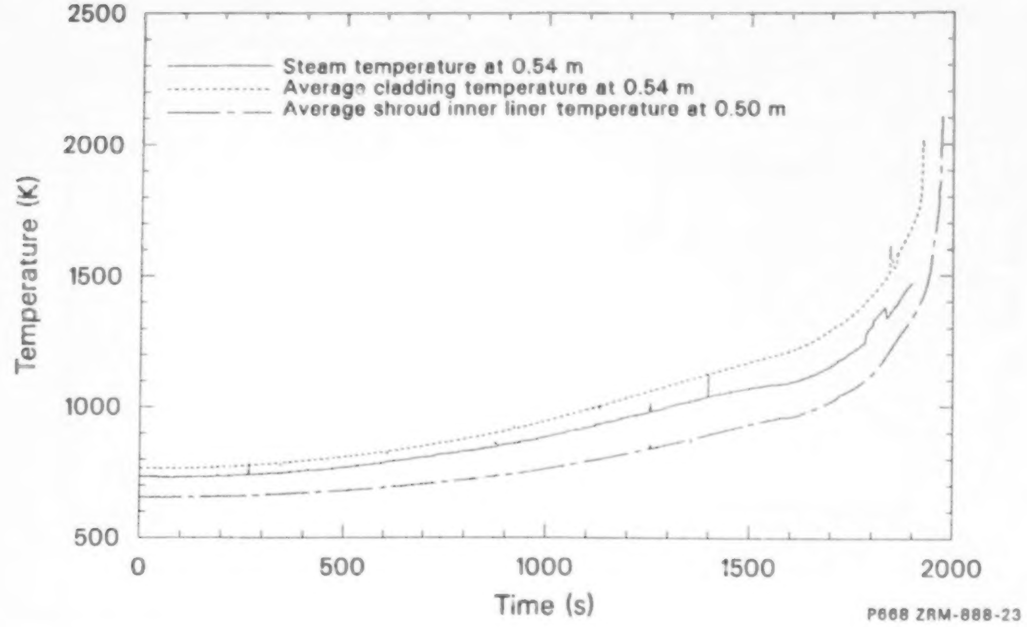

Figure 32. Test SFD 1-4 steam temperature at 0.54 m, average cladding temperature at 0.54 m, and average shroud inner liner temperature at 0.50 m.

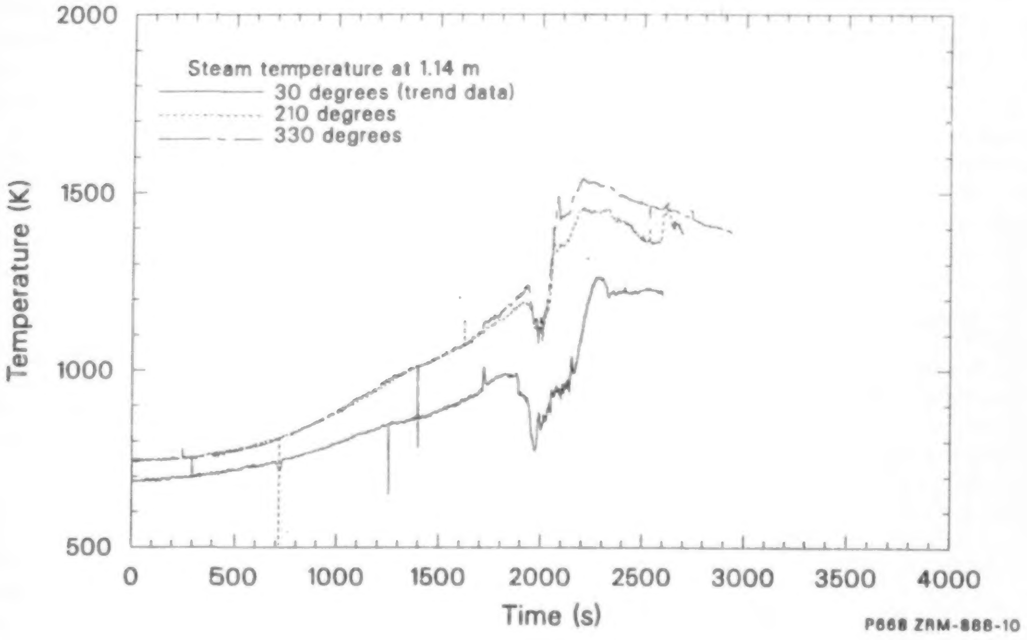

Figure 33. Steam temperatures above the SFD 1-4 bundle at 1.14 m at 30, 210, and 330 degrees.

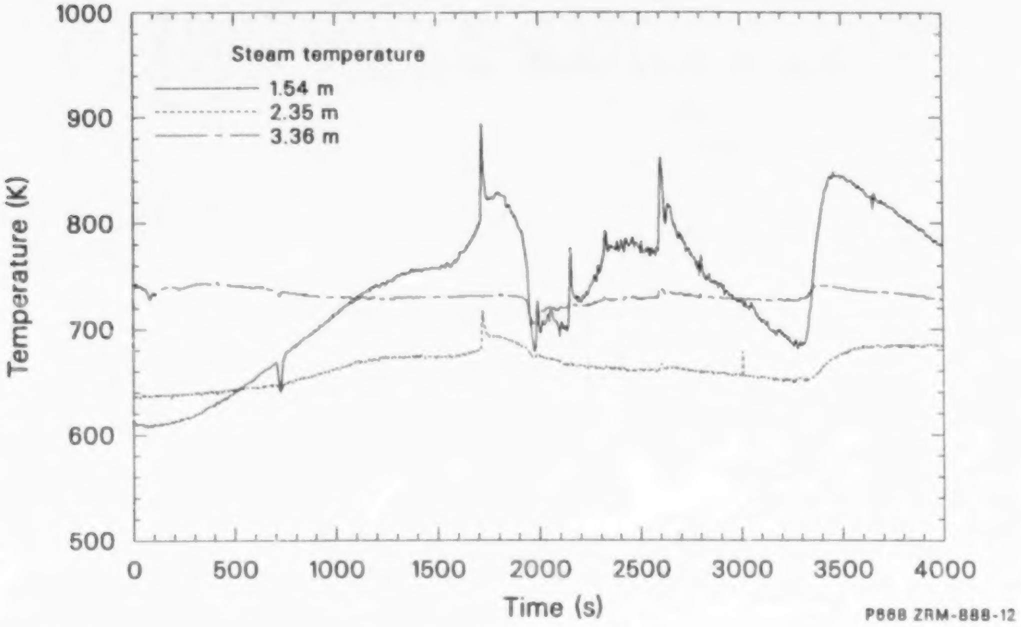

Figure 34. Steam temperatures above the SFD 1-4 bundle at 1.54, 2.35, and 3.36 m.

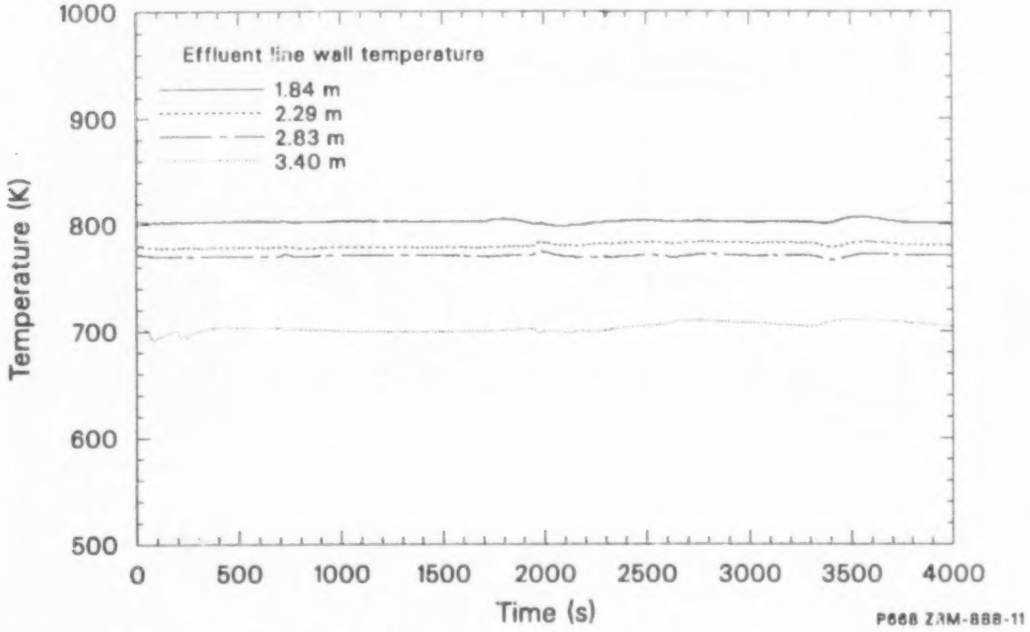

Figure 35. Test SFD 1-4 effluent line wall temperatures at 1.84, 2.29, 2.83, and 3.40 m.

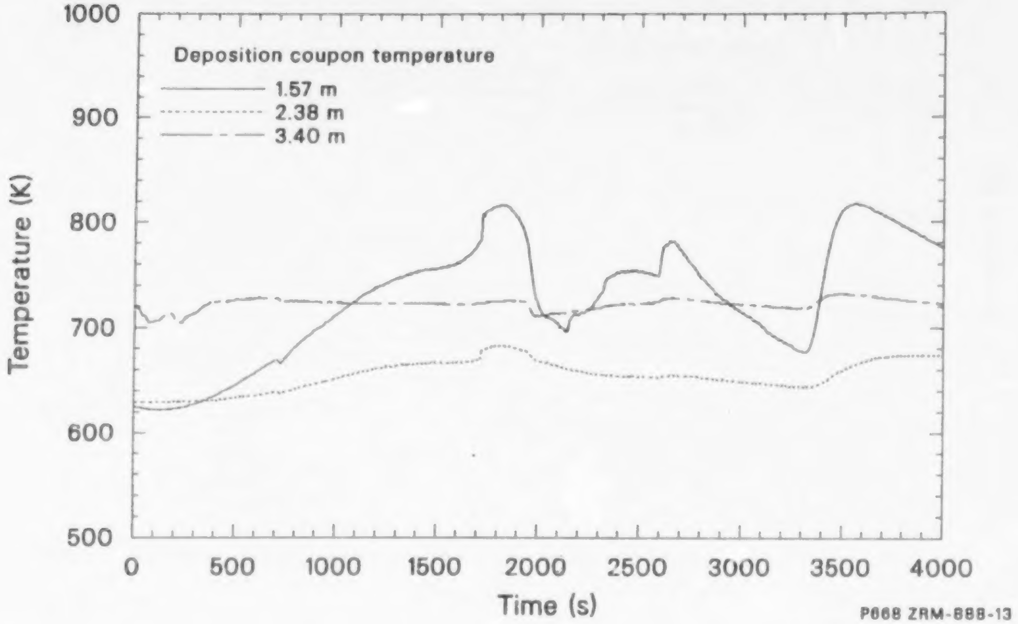

Figure 36. Test SFD 1-4 deposition coupon temperatures at 1.57, 2.38, and 3.40 m at 45 degrees.

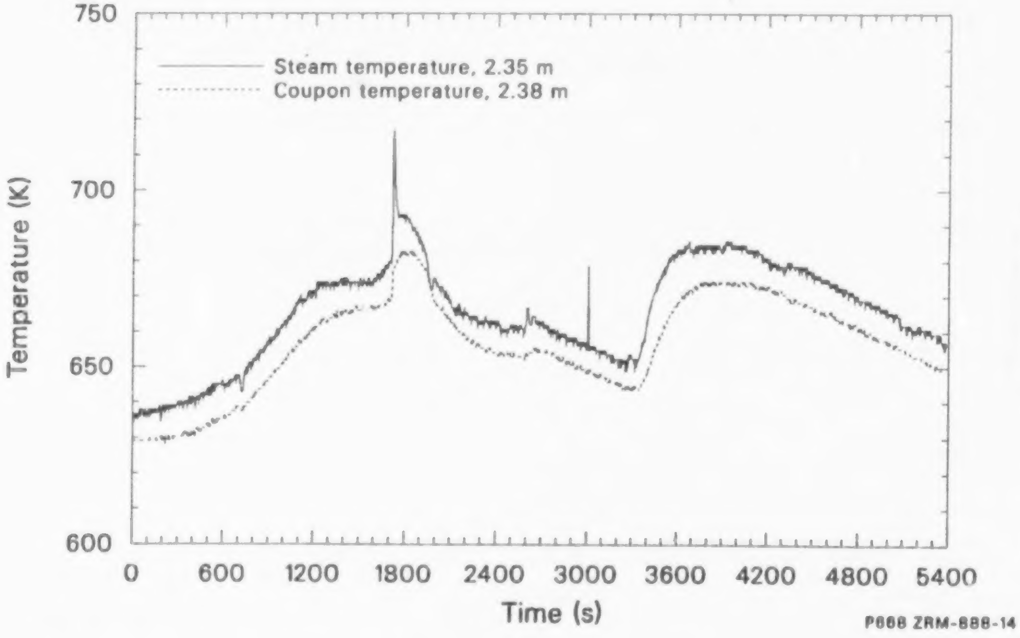

Figure 37. Test SFD 1-4 steam and coupon temperatures at 2.35 and 2.38 m, respectively.

Table 5. SFD 1-4 effluent line temperatures (K)

Time (s)	Above Closure Head (3.65)[a]	Top of Standpipe (5.50)[a]	Inlet to Aerosol Monitor (10.61)[a]	Middle of Aerosol Monitor (11.02)[a]	Outlet of Filtered Effluent Samples (13.90)[a]	Outlet of Unfiltered Effluent Samples (16.60)[a]	Bend Before Cubicle 13 (21.50)[a]	Before FPDS in Cubicle 13 (23.09)[a]	Condenser Outlet (34.09)[a]
0	595	673	578	582	589	410	509	511	511
300	606	678	580	585	589	442	512	512	512
600	607	678	580	585	589	442	512	512	512
900	628	668	578	581	588	517	515	515	515
1200	636	668	589	589	589	533	528	524	525
1500	629	678	589	589	517	528	524	522	522
1800	623	679	580	589	589	522	528	522	517
2100	578	688	595	595	595	505	546	558	505
2400	655	687	595	595	589	494	567	589	497
2700	580	685	602	603	592	480	588	612	494
3000	573	683	601	601	589	455	600	633	500
3300	622	673	606	606	651	400	623	650	505
3600	640	673	606	606	600	400	606	645	522

---

a. Distance from bottom of the PBF core (m).

nominal bundle pressure of 6.95 MPa is about 559 K. Note that the measured effluent line temperatures are generally below the saturation temperature. Evidently steam condensed in most of the line until significant hydrogen was produced. The effects of this condensation are included in the sample transit time presented in Appendix E.

Examination of the responses of the upper plenum thermocouples can provide some insight into events occurring in the bundle. Figure 38 is an overlay of steam temperatures measured at 1.14 and 1.54 m and the deposition coupon temperature measured at 1.57 m. Concurrent increases in these three temperatures are evident:

1. At ~1712 s, when the uninstrumented control rod failed (see Section 5.4), resulting in control rod material relocation to the lower plenum and steam production;
2. At 1966 s, when the argon sweep gas flow rate was increased to 0.58 g/s; and
3. At 3280 s, when the argon sweep gas flow rate was increased to 1.9 g/s to cool the bundle.

The increased temperatures were probably caused by increased oxidation heating due to a higher steam flow through the bundle. The enhanced steam flow was a result of material relocating to the water-filled lower plenum and a higher evaporation rate due to increases in the argon flow.

Between 2100 and 2900 s, the responses of the coupon and steam temperatures near 1.5 m show the effects of melt progression on partial flow blockage and steam flow in the bundle. Between 2100 and 2300 s, the temperature near 1.5 m increased, indicating general heatup of the bundle and effluent, followed by a leveling-off of the thermocouple responses between 2300 and 2600 s. The coupon and steam temperature increases at 2600 s correlate with the increases in fission chamber responses, shroud midwall temperatures, meltthrough detector response, hydrogen generation, and heat loss to the bypass. All of these measurements suggest that material was relocating, exposing hot unoxidized surfaces to steam and producing additional hydrogen. Beyond 2600 s, the effluent temperatures decreased because of the power reduction.

5.1.3 Effluent Flow. Two flow meters were installed in the effluent line of the sampling and monitoring system. The response of the liquid flow meter downstream of the condenser is shown in Figure 39. A gas flow meter, located upstream of the condenser, measured the steam and noncondensible gas flow rate, as shown in Figure 40. Although both flow meters functioned during the transient, the data can only be regarded as trend because of instrument calibration problems with noncondensible gas flow through both flow meters.

Prior to hydrogen generation, the liquid flow meter indicated an average flow rate of ~0.6 cm^3/s, in good agreement with the 0.56 cm^3/s of injected coolant flow rate. At the start of the power hold at 2370 s, when essentially all of the inlet coolant rate was being transformed to hydrogen, the gas flow meter indicated a flow of ~42 cm^3/s (including ~10.8 cm^3/s of argon sweep gas flow). (The gas flow rates are for conditions of 6.9 MPa and 600 K.) The posttest hydrogen analysis indicated a hydrogen flow rate of ~27 cm^3/s at this time, leaving a net flow discrepancy of 4.4 cm^3/s, which was either instrument error or equivalent to an unreacted steam flow of ~0.1 g/s.

The gas and liquid flow and the argon inlet flow from 3000 to 11000 s after the transient are shown in Figure 41. After the argon flow rate was increased to 1.9 g/s starting at 3280 s to maintain the bundle pressure at 6.9 MPa and the bundle injection pump was secured at 3456 s, the indicated liquid flow rate out of the condenser increased to the instrument rated limit of 3.33 cm^3/s from ~3510 to 8300 s. The flow meter signal is not believed to be accurate because of the large argon flow, but the large signal is believed to indicate that condensed coolant in the effluent line and coolant in the lower plenum region was being evaporated and expelled in the time interval from 3510 to 9500 s. The liquid flow meter signal dropped to zero at 9500 s, well before the sweep gas flow was reduced at 10600 s, indicating that the lower plenum was depleted of water coolant.

5.2 Zircaloy Oxidation and Hydrogen Generation

Three different types of measurements were made to characterize zircaloy oxidation and hydrogen generation in Test SFD 1-4. An on-line hydrogen monitor was used to determine the hydrogen generation rate in the bundle. A collection tank sample was taken posttest to measure the integral hydrogen generation from the experiment.

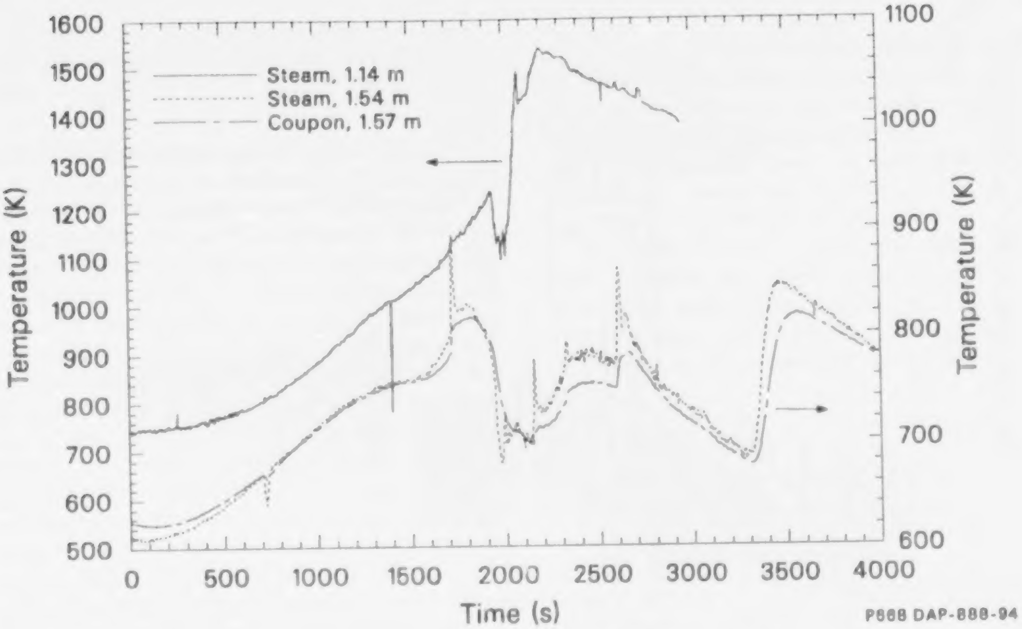

Figure 38. Comparison of Test SFD 1-4 steam temperatures at 1.14 and 1.54 m and the deposition coupon temperature at 1.57 m.

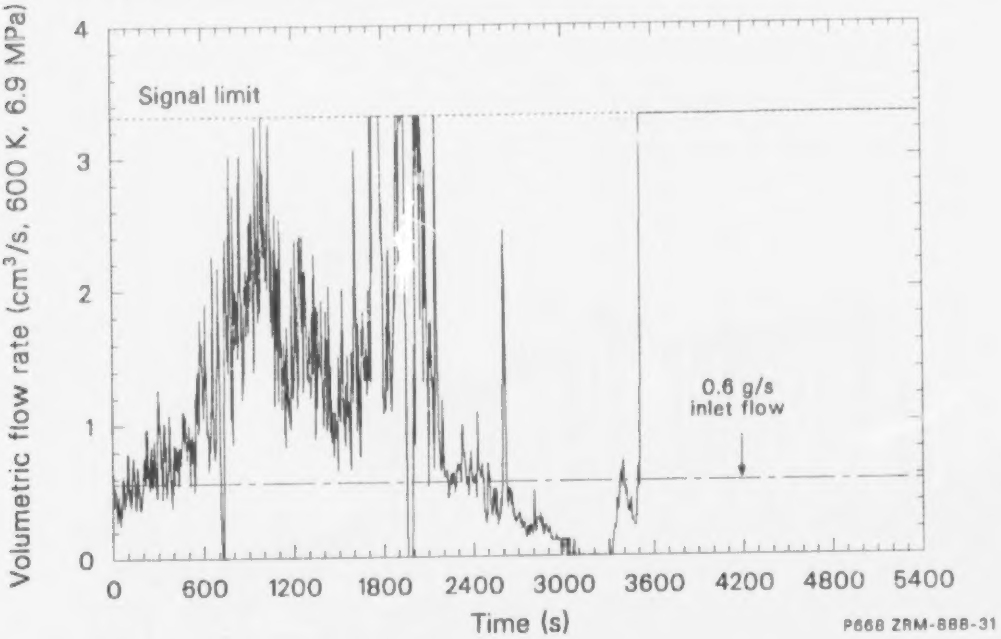

Figure 39. Response of the flow meter measuring liquid flow into the condenser during Test SFD 1-4.

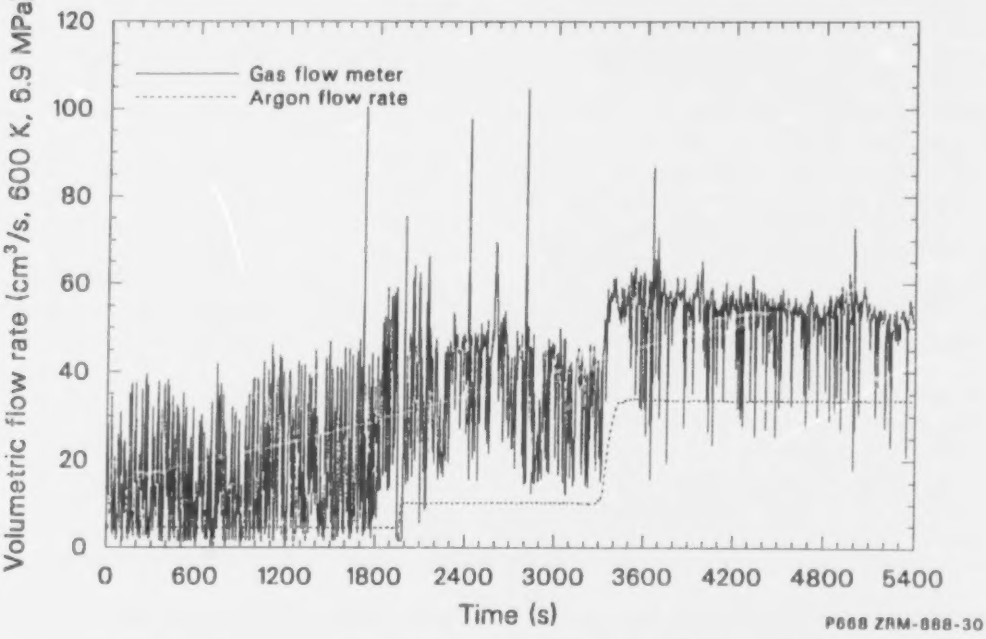

Figure 40. Response of the flow meter measuring gas flow into the condenser during Test SFD 1-4.

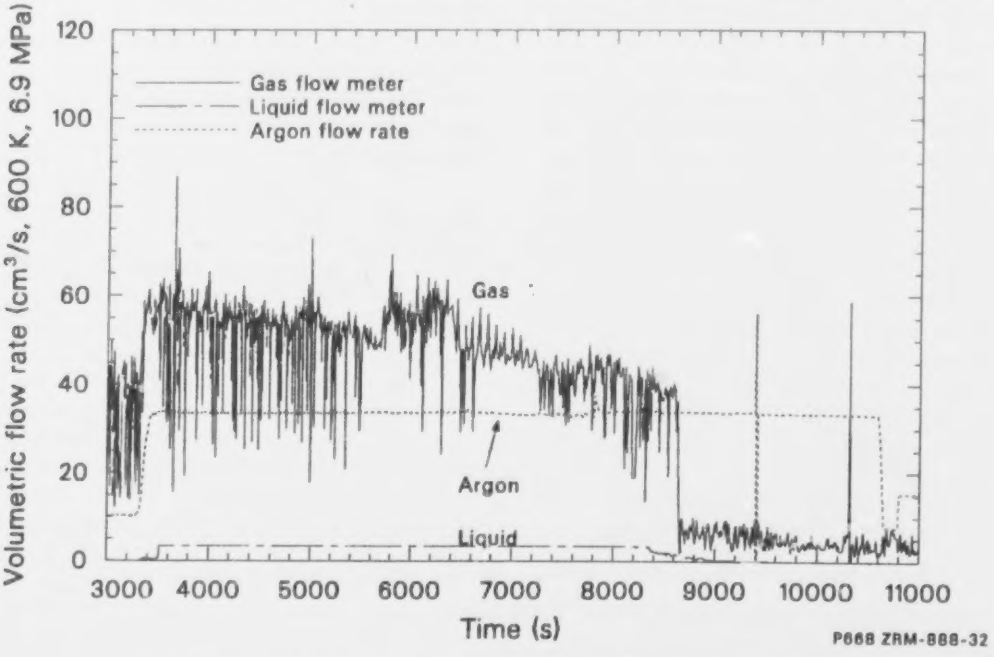

Figure 41. Argon inlet flow and the gas and liquid flow from the SFD 1-4 bundle during the latter part of the transient.

Postirradiation examination was used to determine the extent of oxidation in the debris samples examined.

5.2.1 Hydrogen Generation Rate. The hydrogen generation rate in the bundle, as determined from the on-line monitor response and the effluent transit analysis (discussed in Appendix E), is plotted in Figure 42, together with the cladding temperatures from rod 3B. The temperatures increased rapidly in response to rapid oxidation; however, the corresponding rise in the hydrogen generation rate curve was delayed by ∿150 s. Two explanations are possible to describe this behavior. First, examination of the results of the effluent transit analysis (see Appendix E) indicates that the delayed response may be the result of the transit analysis assumption of perfect mixing in the separator and in the bundle. The effluent transit analysis assumes that gas flows out of the bundle and separator represent the average concentration in those volumes. When hydrogen was first generated in Test SFD 1-4, the bundle and separator volumes were probably not instantly well mixed. As a result, the well-mixed assumption in the model is rather poor at the start of the transient, which results in the calculated generation rate being biased low prior to ∿2000 s. Second, the solution of hydrogen in zircaloy located in the steam-starved region high in the bundle and its subsequent release due to movement of the oxidation front upward and bundle cooldown in argon may also have contributed to the delay in the hydrogen measurement.

By ∿2000 s, the calculated hydrogen generation rate increased very rapidly, then leveled off at 0.07 g/s by 2100 s, indicating that all of the 0.6 g/s of steam input into the bundle was consumed. The hydrogen generation rate increased during the high-temperature portion of the transient, peaked at a value of 0.095 g/s at ∿2700 s, and continued above 0.07 g/s well into the cooldown phase of the transient. Between 2300 and 3100 s, the hydrogen generation rate exceeded that possible from total consumption of the nominal inlet flow of 0.6 g/s (0.067 g/s H_2), indicating an enhanced steaming rate because of a falling liquid level in the bundle (see Figure 13). Beyond 3280 s, water is believed to have entered the hydrogen monitor following the increase in argon flow, causing a spurious monitor signal. As a result, the actual concentration of

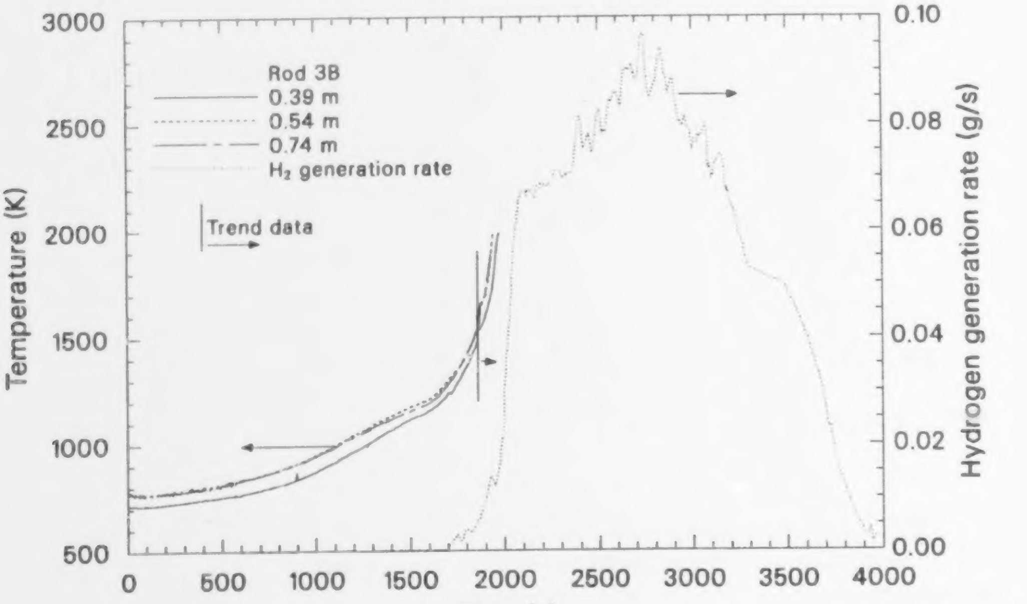

P888 DAP-888-89

Figure 42. Hydrogen generation rate and cladding temperatures from rod 3B in Test SFD 1-4.

hydrogen in the effluent at that time is unknown, causing the generation rate to be highly uncertain. The raw data have been corrected in an attempt to represent a best-estimate upper bound on the generation rate during that time period. Details are found in Appendix E. The integral hydrogen generation is plotted in Figure 43. The integral up to 3280 s is 98 ± 5 g. Integration of the generation rate from 328[illegible] to the end of the transient yields an additional 23 g. This 23 g is considered to be an upper estimate of the hydrogen generated late in Test SFD 1-4. As a result, the hydrogen generation from integration of the on-line monitor is 98 (+28/−5) g.

5.2.2 Collection Tank Hydrogen Results. The collection tank was the receptacle for the test effluent, and a sample of the gas space was taken posttest. Mass spectrometer data, corrected for pressure losses in the tank and air in-leakage during hot cell processing (see Appendix E), indicate that 86 ± 12 g of hydrogen were generated during Test SFD 1-4. Results of benchmarking the quantities of nitrogen, argon, and ^{85}Kr in the tank against other measurements and/or calculations indicate that the sample was representative of the contents of the tank. Consequently, the collection tank value of 86 ± 12 g represents the best estimate of hydrogen generation in Test SFD 1-4. This mass of hydrogen corresponds to ~32% oxidation of the zircaloy exposed to high temperatures.

5.2.3 Postirradiation Examination Oxidation Results. Metallographic cross sections of the SFD 1-4 bundle were examined posttest to determine the extent and nature of bundle component oxidation. Figures 44 and 45 are plots of zircaloy retention (fraction remaining recognizable) and oxidation fraction for solid zircaloy components (fuel rod cladding, control rod guide tube, inner liner) and previously molten zircaloy-bearing melts as a function of elevation in the bundle. The extent of oxidation was determined by visual examination of the amount of ZrO_2 relative to the amount of metallic zircaloy.

Figure 44 indicates that very little oxidation occurred above 0.7 m and below 0.08 m in the bundle. Apparently not enough steam was available in the upper bundle, and the lower bundle was not hot enough to cause significant oxidation in these regions. Almost all of the remaining solid zircaloy in the bundle from 0.17 to 0.54 m was totally oxidized.

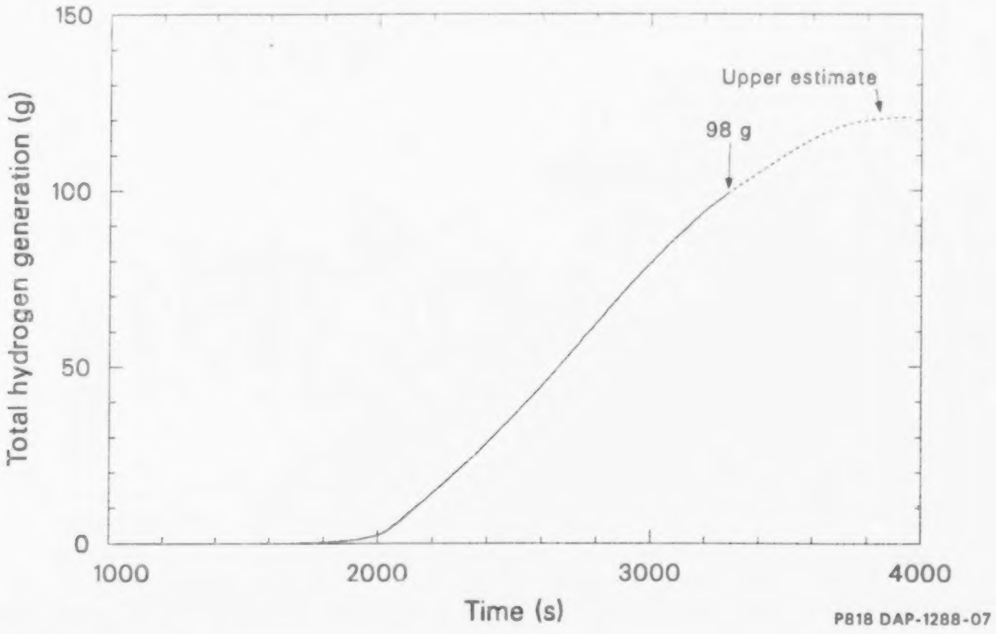

Figure 43. Integral hydrogen generation in Test SFD 1-4.

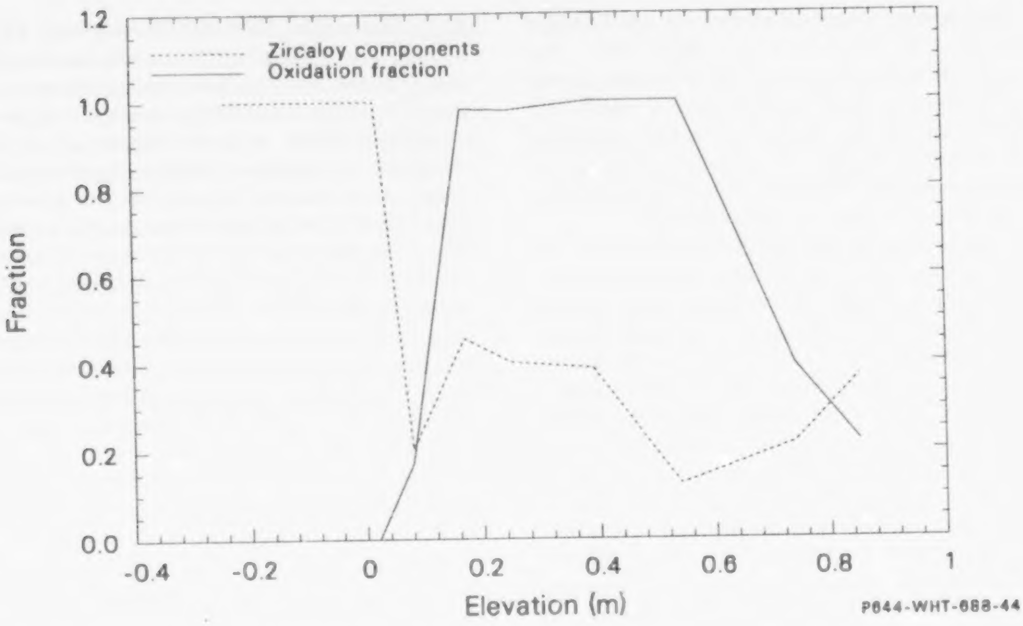

Figure 44. Zircaloy retention and oxidation fraction for solid zircaloy components.

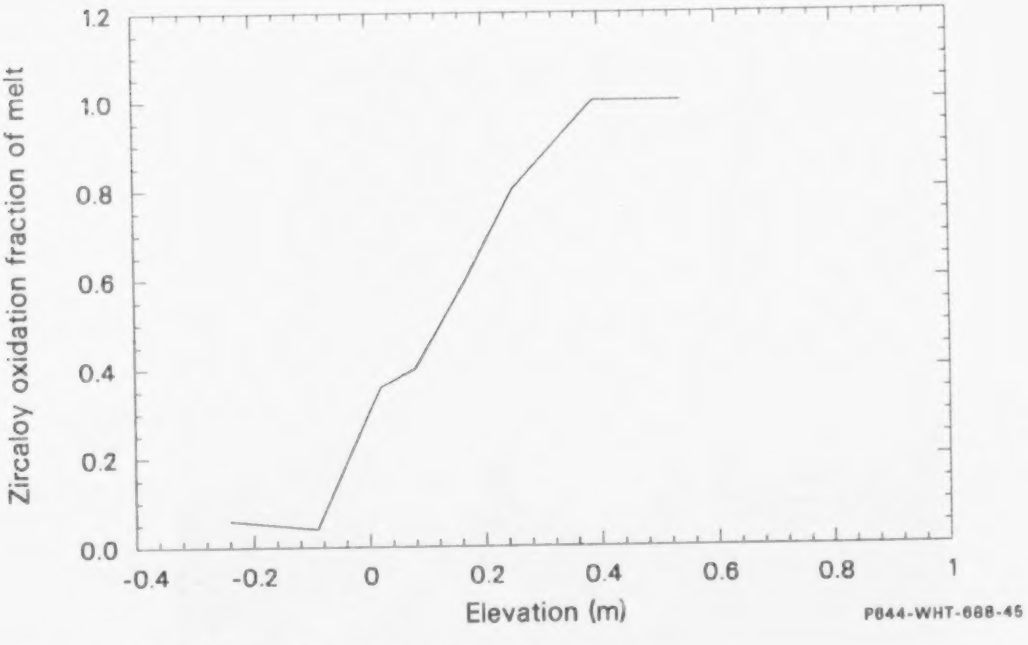

Figure 45. Oxidation fraction of zircaloy-bearing melts.

The oxidation fraction of the melt debris in Test SFD 1-4 is presented in Figure 45. The once-molten zircaloy in the middle portion of the bundle between 0.39 and 0.54 m was totally oxidized, based on its ceramic appearance. However, the oxidation fraction of once-molten zircaloy in the lower bundle decreased with elevation, as the melts were more metallic in character.

Examination of the metallographic cross sections also indicates that zircaloy continued to oxidize during and following relocation. Figure 46 is a high-magnification photograph of multiple oxide layers in the melt at 0.17 m. Oxides were formed on relocated melts that experienced partial oxidation until they were cut off from steam by additional melts relocating to the same region at later times. This behavior was observed in several regions low in the bundle at varying temperatures. These observations are an indication of the incoherent nature of the melt progress process. Materials of different melting points from regions with varying temperatures relocated at different times. Oxides were formed on the relocated melts and trapped by subsequent melt arrivals. The thicknesses of these trapped oxides suggest melt relocations at intervals varying from 5 to 60 s.

5.2.4 Summary. Examination of all of the hydrogen generation/zircaloy oxidation data from Test SFD 1-4 indicates that zircaloy oxidation continued at a high rate (100% consumption of available steam) during the high-temperature transient. Oxidation of zircaloy-containing melts occurred during and following relocation. The incoherent nature of the melting and relocation process during the test resulted in continual relocation of hot molten metal from steam-starved regions high in the bundle to steam-rich regions low in the bundle where oxidation could take place. The best estimate of total hydrogen generated in Test SFD 1-4 is 86 ± 12 g, which corresponds to 32% oxidation of the bundle zircaloy exposed to high temperatures.

5.3 Fuel Behavior

The behavior of the fuel materials during the melt progression in Test SFD 1-4 is described in this section. An overview of the bundle damage is first presented, followed by more detailed descriptions of the fuel behavior and melt progression that occurred in the bundle.

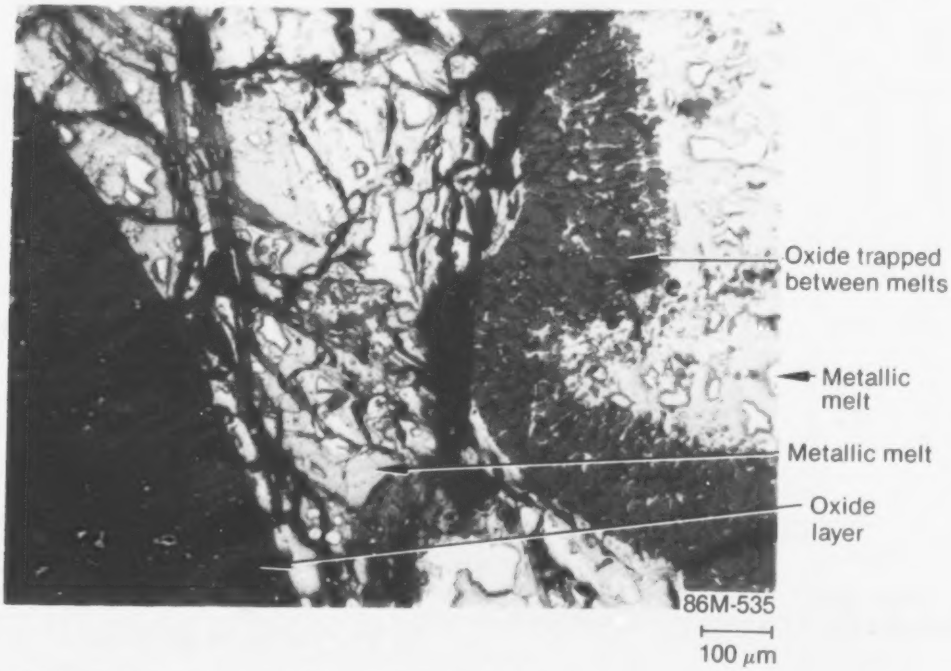

Figure 46. Photograph of multiple oxide layers in melt at 0.17 m.

5.3.1 Overview of Bundle Damage. The overall posttest condition of the bundle is depicted in the neutron radiograph in Figure 17. The radiograph indicates relocation of material downward from the top of the bundle and an accumulation mainly in the lower portion of the bundle down to the lower spacer grid. The materials that have the greatest neutron absorption cross section, and therefore contribute most to the opacity in the neutron radiograph, are the control materials and the fuel. As a result, the location of these materials is most apparent in the radiograph.

Metallographic examination of the bundle along with the neutron radiograph revealed four distinct damage regions in the bundle. The upper fueled region of the bundle was a rubble bed of fuel fragments, extending from about 0.95 m down to 0.60 m. The mid-bundle region between 0.60 and 0.30 m was severely damaged, but partial fuel pellets in more of a rod-like geometry and the remnants of dissolved fuel remained. Molten ceramic materials accumulated in the lower bundle between 0.30 and ∿0.17 m. Metallic melts, consisting of zircaloy, stainless steel, and control rod material, resided at and below the lower spacer grid; and some metallic material relocated to the lower tie plate, beneath the fueled region of the core.

Metallography, elemental spectroscopy, and chemical analyses were performed on selected samples in the SFD 1-4 bundle to quantify the degree of bundle damage in terms of the nature and extent of materials interactions, peak temperatures reached, posttest flow blockage, and the oxidation state of the materials. Details of the methods and evaluation techniques used and the results of the optical, SEM, and elemental chemical analyses are provided in Appendix I. The posttest distributions of open flow area, fuel, and control material, as determined by metallography and elemental analysis, are plotted, along with their pretest values, in Figure 47. Minimum peak temperatures of in-place (resident throughout the test) and relocated materials are plotted in Figure 48. These temperatures were estimated from microstructural and chemical information in conjunction with appropriate phase diagrams and past experience.[3,4,11] Based on the amount of intact fuel observed posttest, a total of ∿18% of the fuel was estimated to have liquefied during the transient. The results of these analyses are used in the detailed descriptions of bundle damage in the following sections.

5.3.2 Upper Bundle Region. Two separate cross sections of the bundle, taken through the rubble bed in the upper bundle region, were examined. The cross section taken at 0.85 m is shown in Figure 49. The cross section contains fragments of UO_2 fuel pellets without the presence of zircaloy cladding and control materials. The loss of cladding, control rods, and insulation resulted in an increase of 35% in the flow area. Remnants of molten cladding are present, as depicted in Figure 50; but most of the cladding has melted and relocated downward, leaving the fuel pellets unconstrained and allowing the pellets to crumble into fragments determined by the crack pattern developed during the BR-3 irradiation. This crack pattern is consistent with the cracking normally exhibited by high-burnup fuel and is also apparent in cross sections at lower elevations in the bundle where the pellets are still intact. The little remaining zircaloy was only partially oxidized and exhibited very little interaction with the UO_2 fuel fragments, as can be seen in Figure 50.

Analysis of the oxidation of the remnant of molten zircaloy in Figure 50 and of the microstructure of the liner (Figure 51) indicates that the bundle was steam-starved at this elevation during a large segment of the high-temperature transient. The fuel microstructure in this region shows grain sizes in the range 15 to 20 μm and zones of both intragranular and intergranular porosity (Figure 52). These circumferential zones or bands of differing porosity distribution in the fuel are seen in unreacted areas throughout the bundle and are of unknown origin. The grain sizes in unreacted areas throughout the bundle range from 15 to 25 μm and are similar to those measured after BR-3 irradiation and before the SFD 1-4 transient (13 μm for low-power rods and 26 μm for high-power rods). The lack of grain growth in the SFD 1-4 transient is likely related to pinning of the grain boundaries by the porosity in this high-burnup fuel. No metallographic evidence of fuel oxidation to UO_{2+x} (e.g., U_4O_9 precipitates) was observed.

As is evident in Figure 53, the second bundle cross section in the rubble bed at 0.74 m is similar to that at the 0.85-m elevation. Only a small amount of the metallic melt flowed into cracks in the fuel and began to interact with the UO_2. Figure 54 shows that this material has been largely oxidized by interaction with the fuel and steam, with the exception of some regions that contain metals more resistant to oxidation, such as nickel or silver. The relocation of cladding, control rods, and insulation from this elevation created a flow area that is 24% greater than that of an intact geometry. The microstructure of the liner (Figure 55)

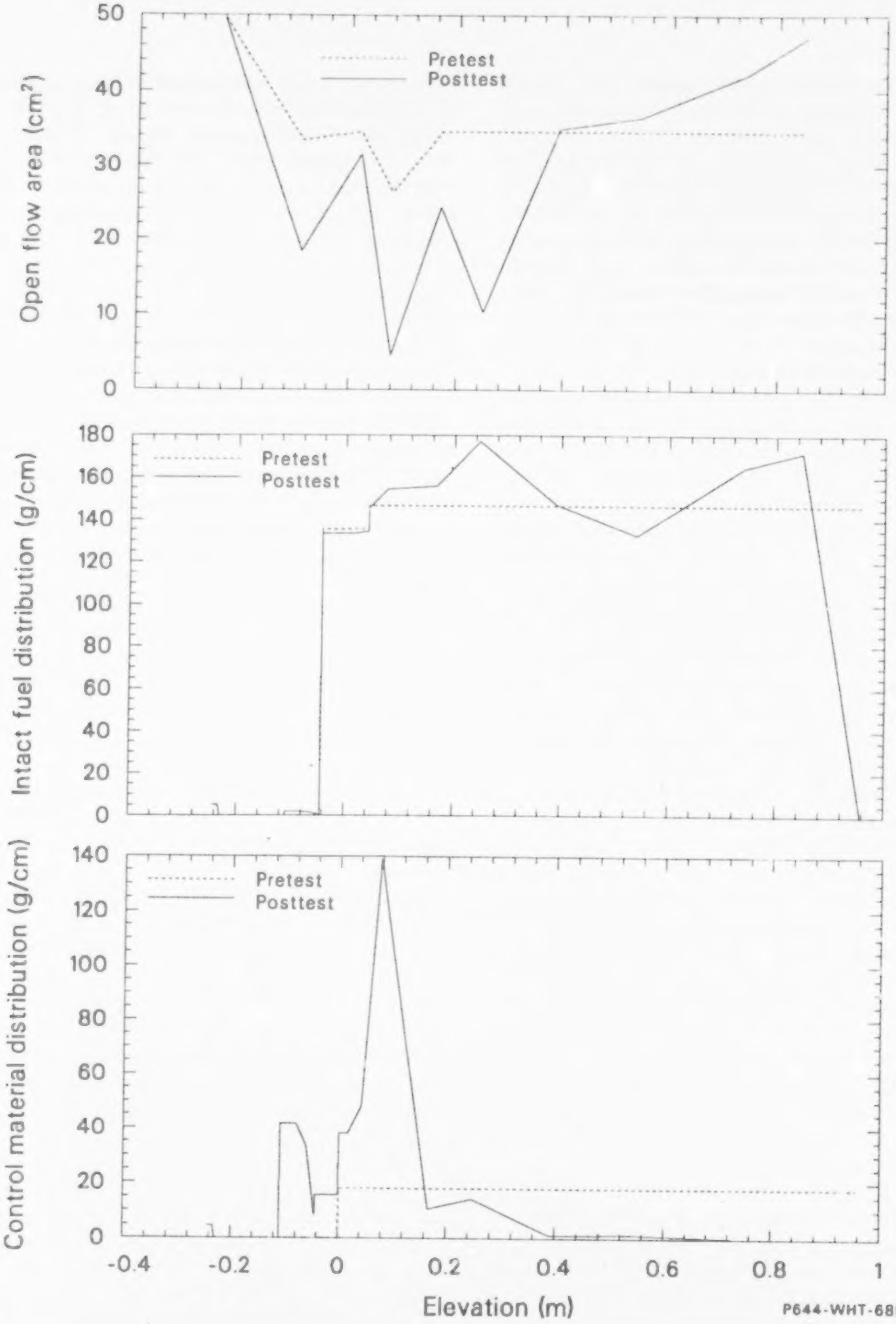

P644-WHT-688-42A

Figure 47. Posttest distribution of open flow area, intact fuel, and control rod alloy material.

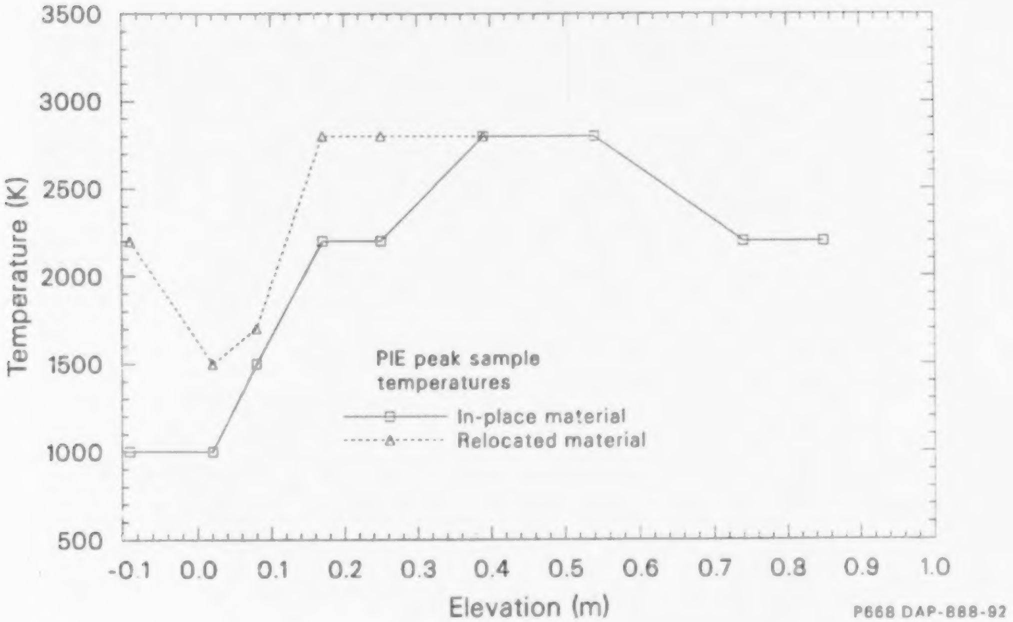

Figure 48. Minimum peak temperature of in-place and relocated materials.

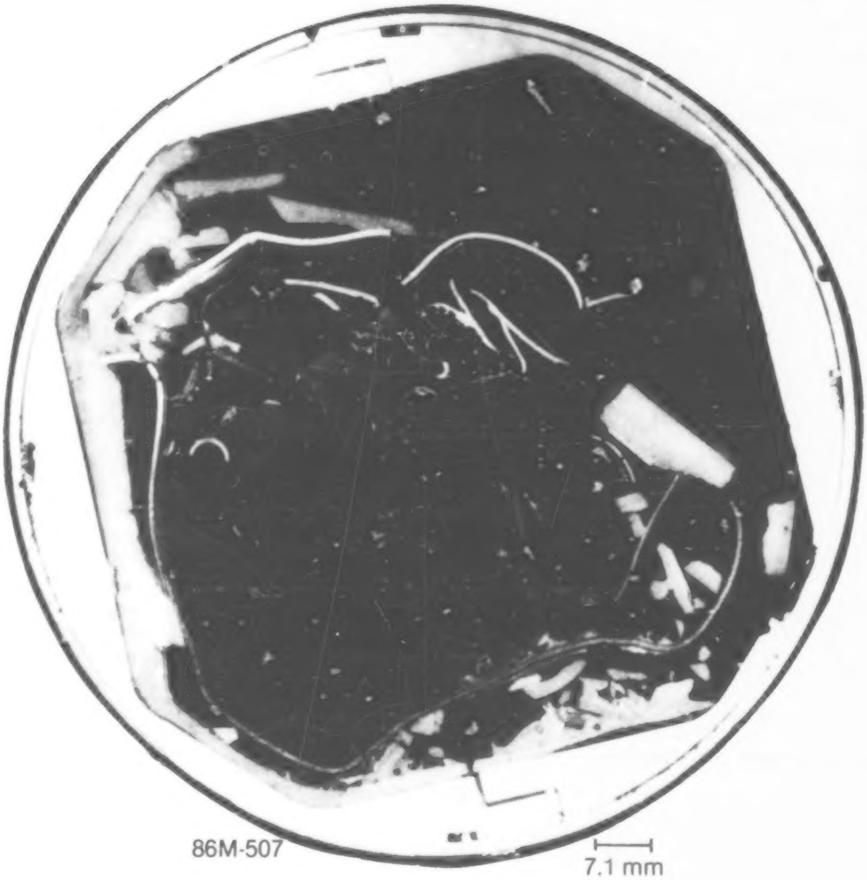
86M-507
7.1 mm

Figure 49. Bundle cross section at 0.85 m.

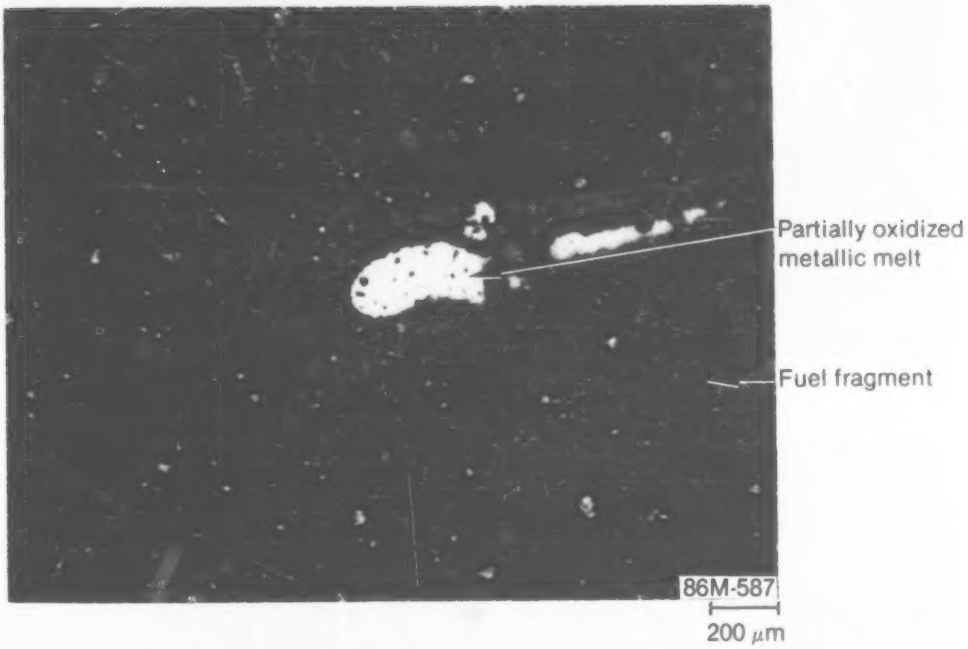
Partially oxidized metallic melt
Fuel fragment
86M-587
200 μm

Figure 50. Partially oxidized metallic melt between two fuel fragments at 0.85 m.

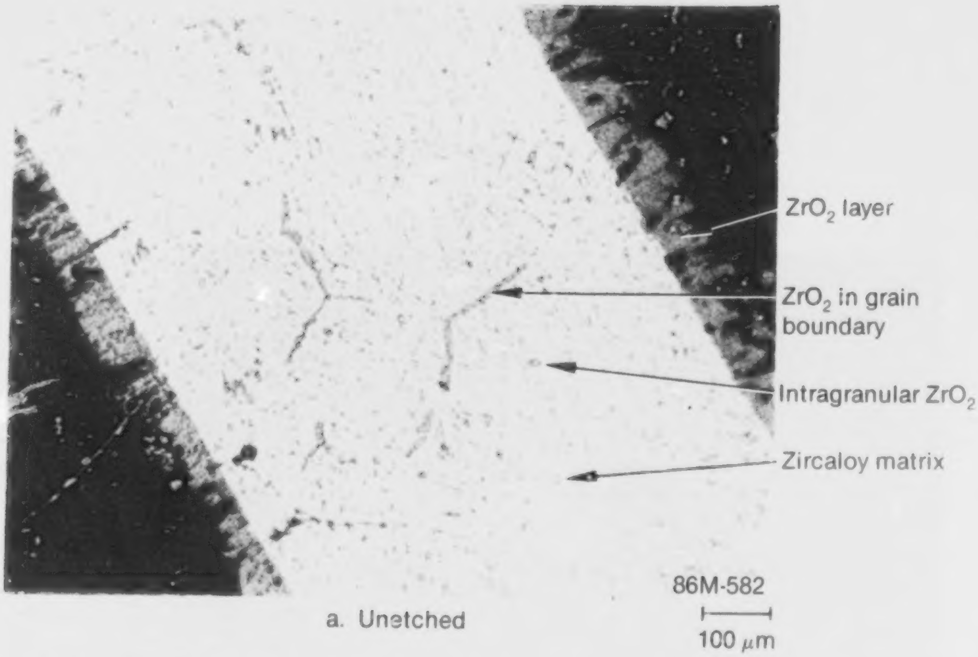
ZrO$_2$ layer
ZrO$_2$ in grain boundary
Intragranular ZrO$_2$
Zircaloy matrix
86M-582
100 μm

a. Unetched

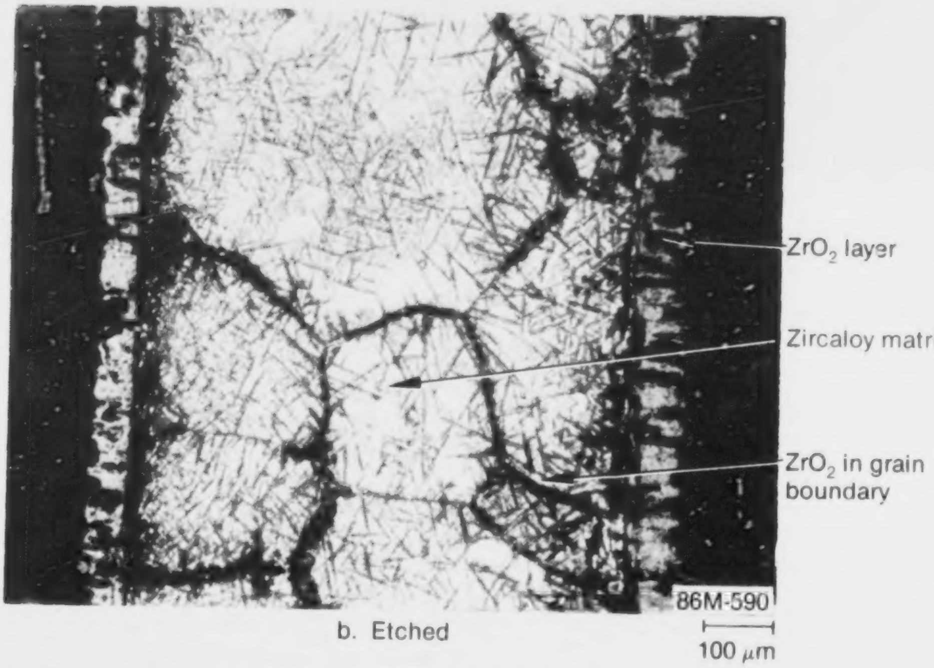
ZrO$_2$ layer
Zircaloy matrix
ZrO$_2$ in grain boundary
86M-590
100 μm

b. Etched

Figure 51. Photomicrographs showing oxidized and previously molten inner liner at 0.85 m.

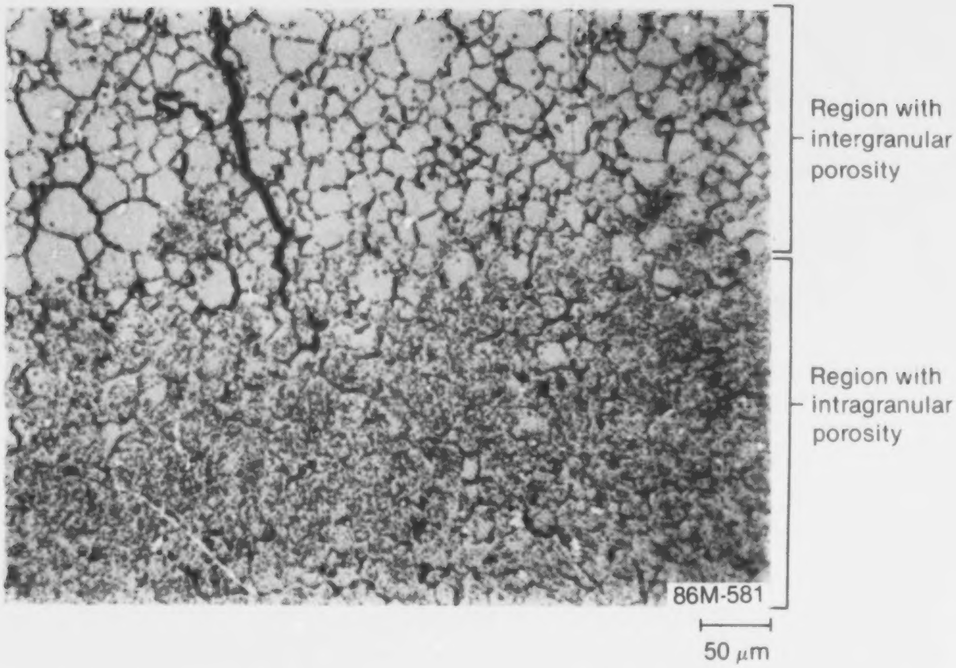
Region with intergranular porosity
Region with intragranular porosity
86M-581
50 μm

Figure 52. Photomicrograph showing fuel microstructure typical of the 0.85-m elevation.

best copy available

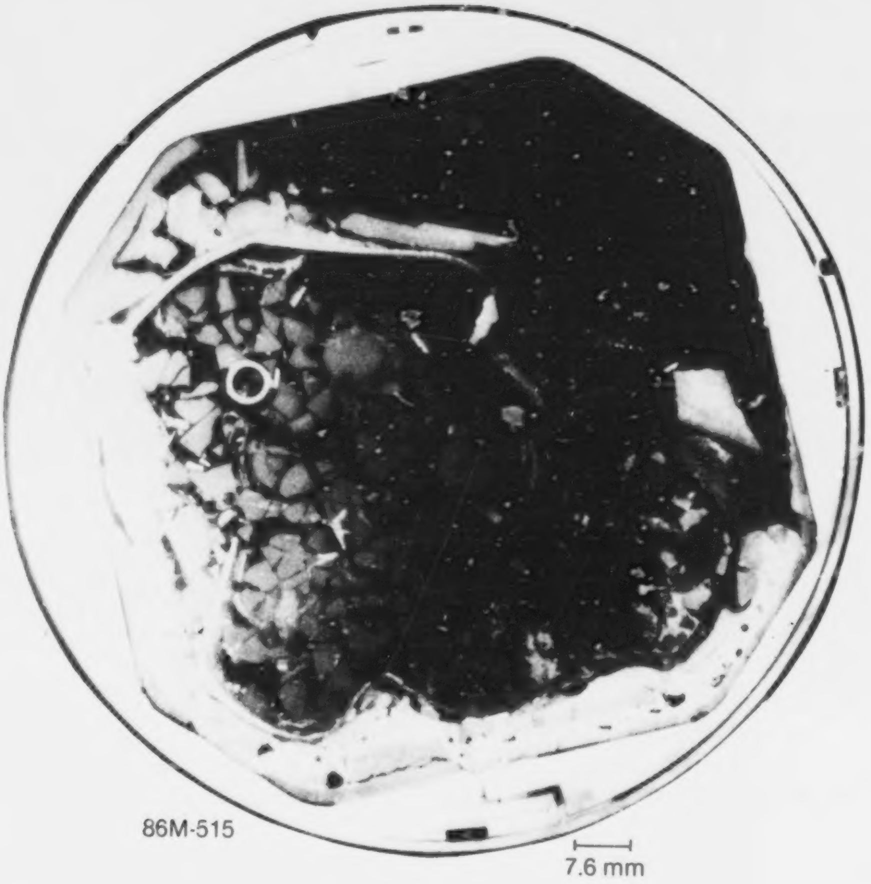
86M-515
7.6 mm

Figure 53. Bundle cross section at 0.74 m.

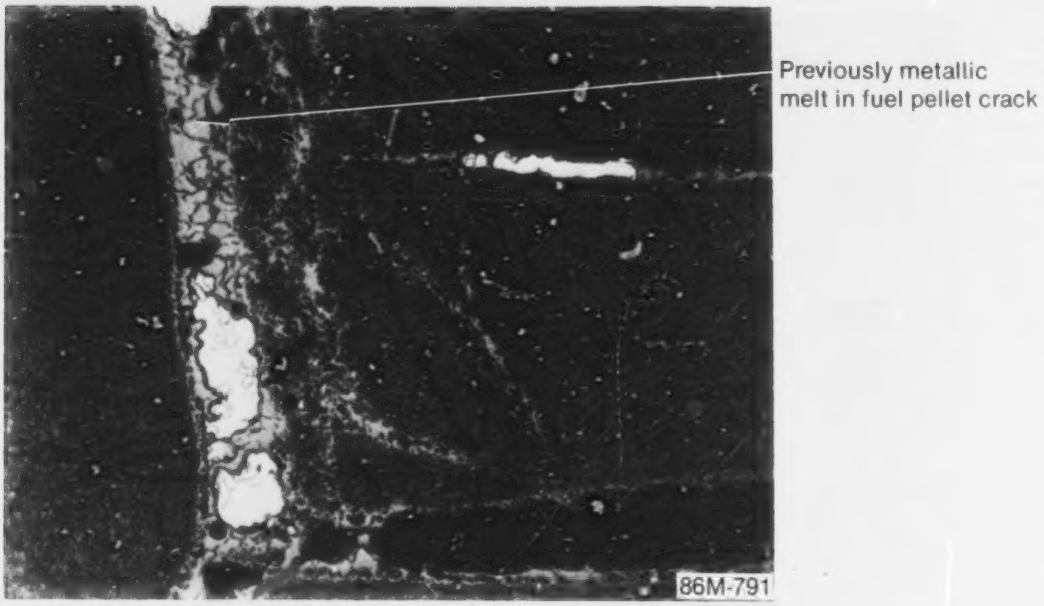
Previously metallic melt in fuel pellet crack
86M-791
200 μm

a. Low magnification

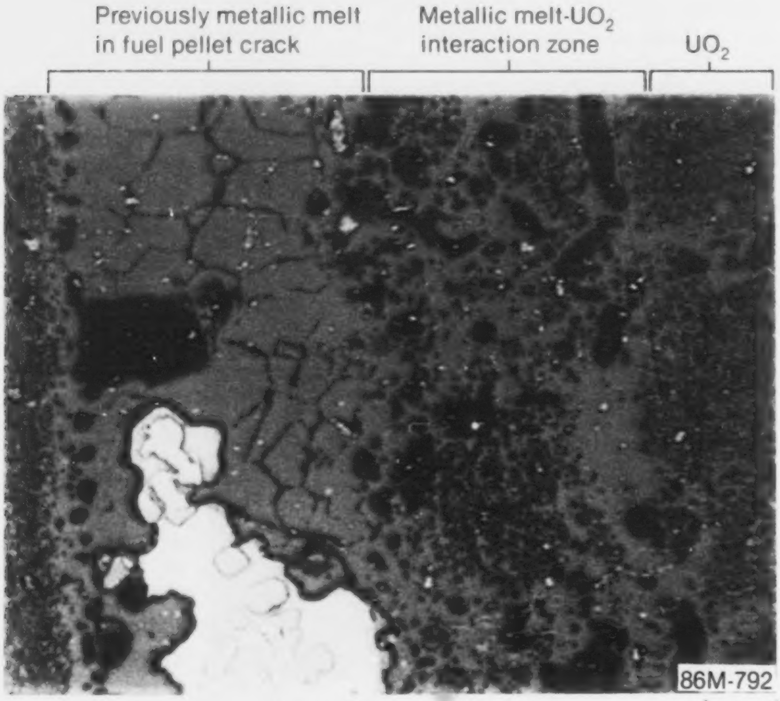
Previously metallic melt in fuel pellet crack
Metallic melt-UO$_2$ interaction zone
UO$_2$
86M-792
50 μm

b. Higher magnification

Figure 54. Unetched photomicrographs showing attack of UO$_2$ by previously metallic melt in pellet crack at 0.74 m.

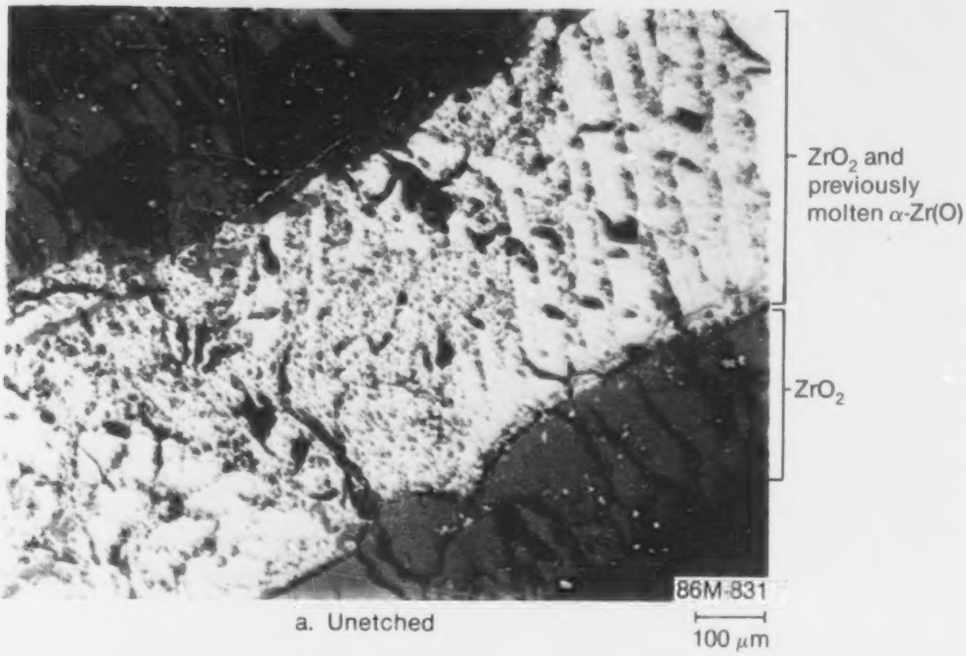
ZrO$_2$ and previously molten α-Zr(O)
ZrO$_2$
86M-831
100 μm

a. Unetched

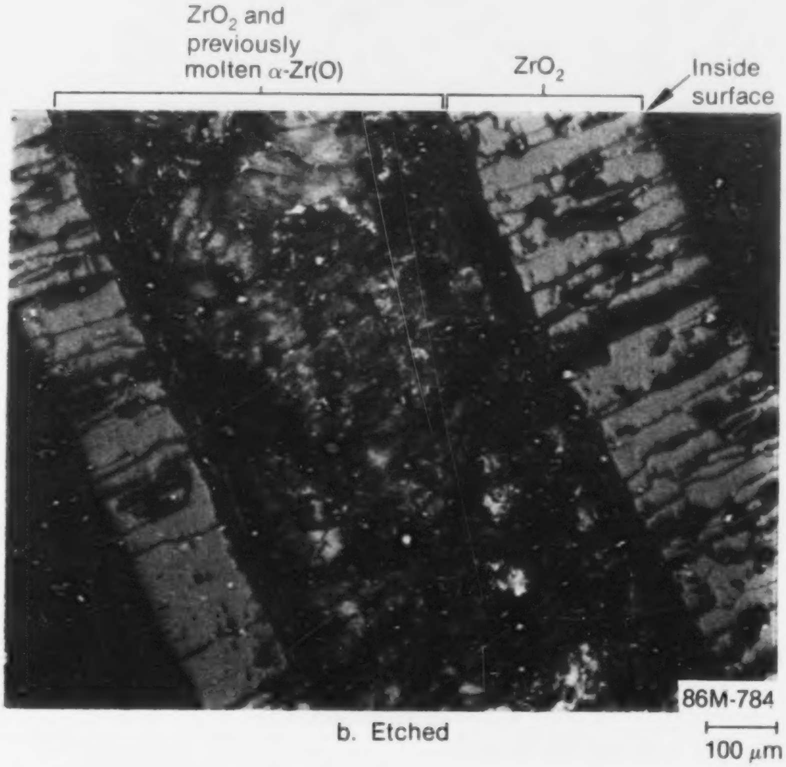
ZrO$_2$ and previously molten α-Zr(O)
ZrO$_2$
Inside surface
86M-784
100 μm

b. Etched

Figure 55. Photomicrograph showing oxidized and previously molten inner liner at 0.74 m.

indicates that it was molten. Analysis of the oxide layers indicates that this region of the rubble bed, as well as the higher elevation cross section, was steam-starved for a long portion of the high-temperature transient. Peak temperatures in the upper bundle region were at ∼2200 K based on cladding melting.

5.3.3 Mid-Bundle Region. Two cross sections that contained fuel pellets in somewhat of a rod-like geometry were examined in the severely damaged region between 0.6 to 0.3 m. The cross section at 0.54 m shown in Figure 56 indicates that the damage changed from loose fuel fragments in the rubble bed in the upper bundle to strongly reacted fuel debris. Material from the four control rods is missing at this elevation. Only about 10% of the cladding and liner remain, and this remaining zircaloy is totally oxidized to ZrO_2. It also appears that some of the liquefied fuel has relocated away from this elevation. The net result of the damage progression in this region is an increase in the flow area of about 7% compared with an intact bundle geometry. The fuel debris remaining at this elevation has reacted with molten zircaloy and transition metal oxides, such as Fe_3O_4, to form liquid ceramic phases, some of which remain attached to the debris. Examples of this previously molten material are presented in Figures 57 and 58. Metal ingots are present in the photomicrograph of Figure 57. An elemental x-ray dot map in Figure 58 revealed iron in the grain boundaries. The effect of iron oxide eutectics on the liquidus temperature of $(U,Zr)O_2$ is analyzed in Appendix I, and the effect is negligible for the compositions measured in the debris. The minimum temperature required for the formation of the liquefied fuel debris found at the 0.54-m elevation is 2800 K.

The bundle cross section at 0.39 m (Figure 59) is similar to that at 0.54 m except that a more intact fuel rod geometry exists at the bundle periphery and zircaloy oxide shells of two control rod guide tubes remain. Liquefied fuel relocated away from this elevation, but some liquefied debris appears to have relocated to this elevation from above as well. The net result is a flow area virtually unchanged from that of an intact bundle geometry. More of the zircaloy cladding and liner remain at this elevation than at 0.54 m; but, as in the cross section at 0.54 m, it is fully oxidized. Small amounts of control materials were measured in the liquefied debris at this elevation and also at 0.54 m. The minimum temperature for the formation of the molten ceramic debris in the mid-bundle region is 2800 K.

5.3.4 Lower Bundle Region. In the lower bundle region extending from 0.30 to ∼0.17 m, two cross sections were examined. The bundle cross section at the 0.25-m elevation (Figure 60) experienced an influx of metallic and ceramic melts from above and a depletion of control materials, zircaloy, and structural materials. The net accumulation of materials caused a 70% reduction in flow area at this elevation relative to intact bundle geometry. The metallic melts arrived after complete oxidation of the zircaloy present at this elevation and caused considerable dissolution of ZrO_2 and UO_2. The ceramic melts also arrived after oxidation of the zircaloy at this elevation, but they did not interact with the ZrO_2. Temperatures were in the range from 1900 to 2200 K before hot melts with temperatures up to 2800 K relocated to this elevation.

Data from the fission chambers located on the shroud outer wall indicated the timing of fuel relocation to the lower bundle region. As shown in Figure 61, the normalized output of the fission chambers located at the 0.51-m elevation increased dramatically between 2300 and 2600 s, and those at 0.35 and 0.25 m began to increase slightly. The increases probably indicate that fuel material was relocating from the mid-bundle region, since control rod absorber material should have relocated well before that time (see Section 5.3). The outputs of the fission chambers at 0.15, 0.05, and −0.05 m decreased slightly at this time, indicating the relocation of fuel material to the lower bundle regions. Other instrumentation in the experiment also registered changes during this period, indicating that material was relocating in the bundle. Temperatures recorded by thermocouples in the shroud midwall at 0.5 m (Figures 28 and 29) and above the bundle (Figure 34) increased. The heat loss to the bypass (Figure 15), the shroud meltthrough detector response, and the hydrogen generation rate in the bundle (Figure 42) also increased.

The microstructure of a melt that is principally ceramic $(U,Zr)O_2$ with small metallic inclusions is shown in Figure 62. Elemental analysis of the inclusions indicate that they are primarily alloys of zirconium and other metals, such as tin, from zircaloy and iron, nickel, and chromium from stainless steel. By comparison, the microstructure of a melt in which the ceramic phase is less dominant is more complex. Several metallic phases make up a large portion of the melt along with some undissolved UO_2 particles, as is shown in Figure 63. In addition, some control materials were trapped in the melts in this region as is demonstrated in Figure 64,

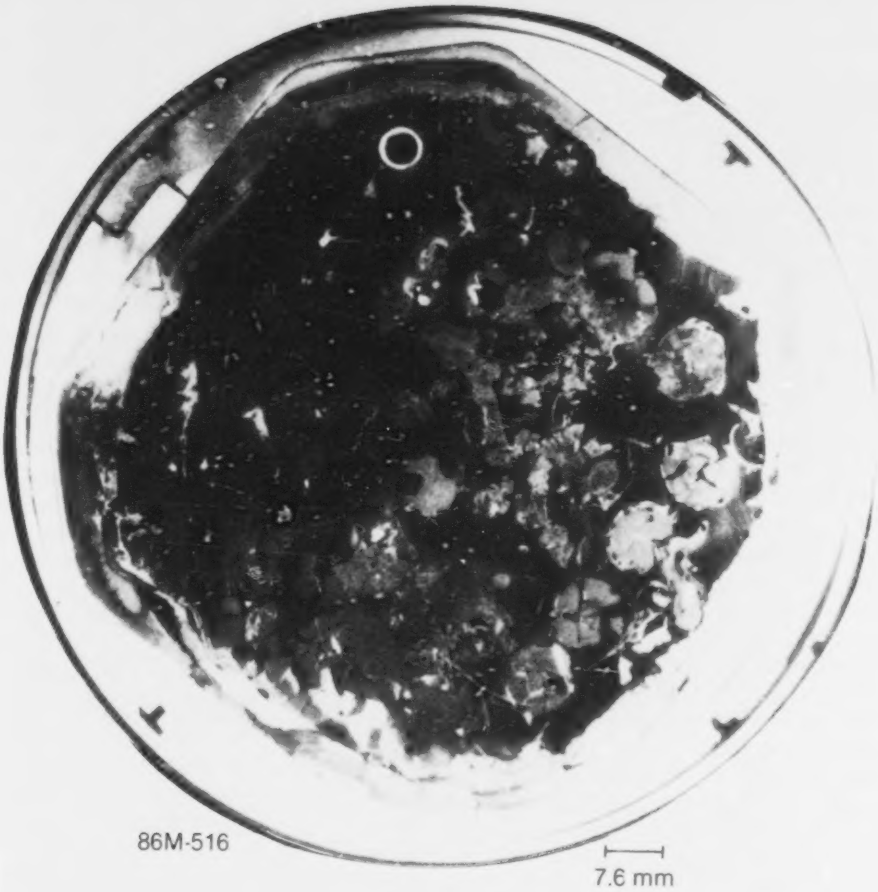
86M-516
7.6 mm

Figure 56. Bundle cross section at 0.54 m.

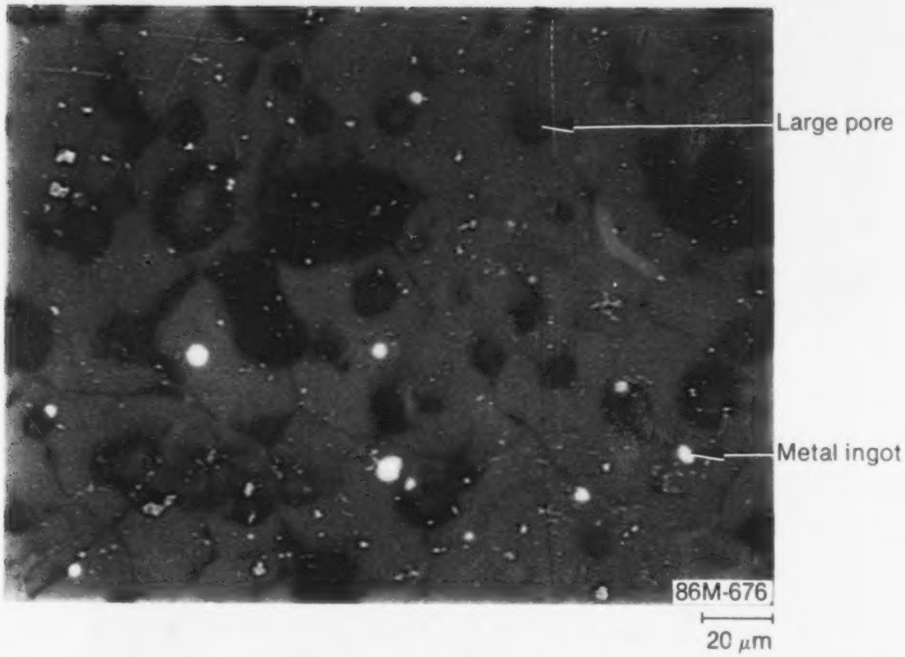
Large pore
Metal ingot
86M-676
20 μm

Figure 57. Photomicrograph showing microstructure in reacted portion of rod 5A fuel pellet at 0.54 m.

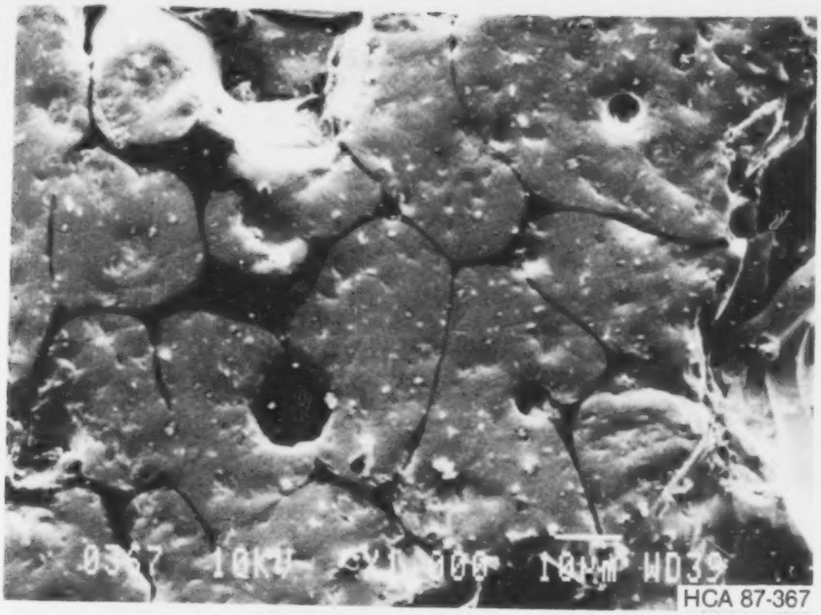
0367 10KV X1,000 10μm WD39
HCA 87-367
10 μm

a. Secondary electron image

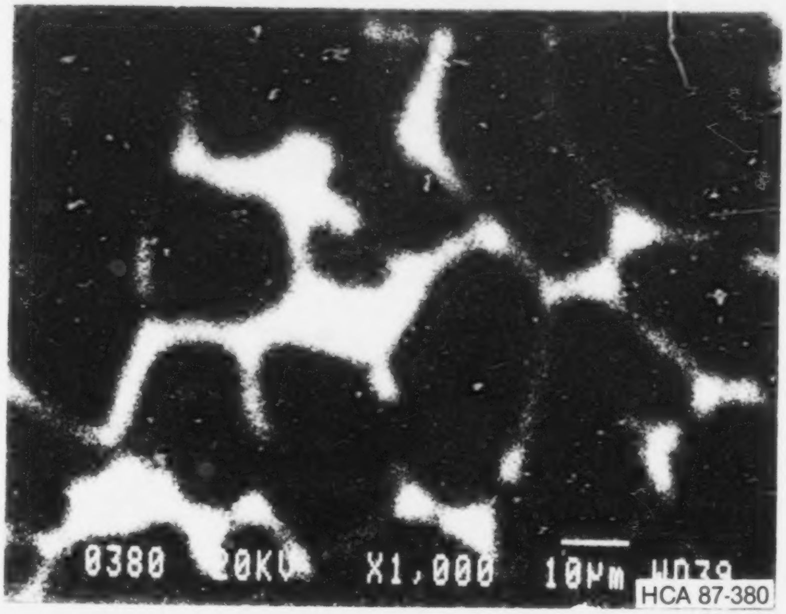
0380 20KV X1,000 10μm WD39
HCA 87-380
10 μm

b. X-ray dot map of iron

Figure 58. Secondary electron image and X-ray dot map showing wide grain boundaries filled with iron oxide in reacted region of fuel rod 5A at 0.54 m.

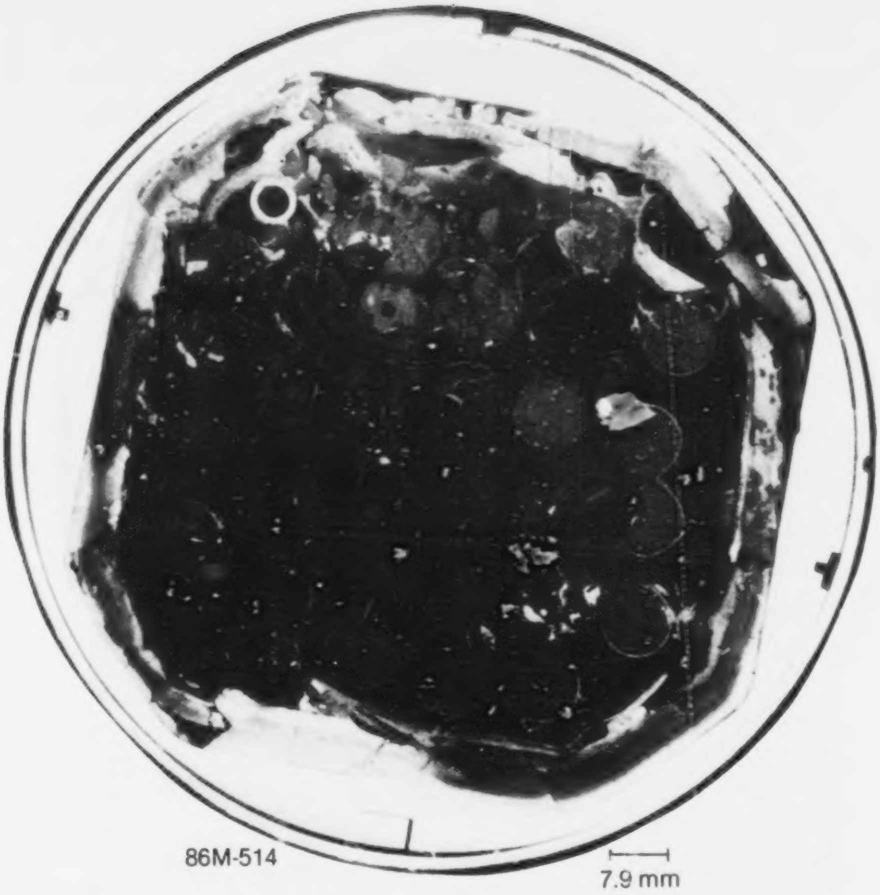
86M-514
7.9 mm

Figure 59. Bundle cross section at 0.39 m.

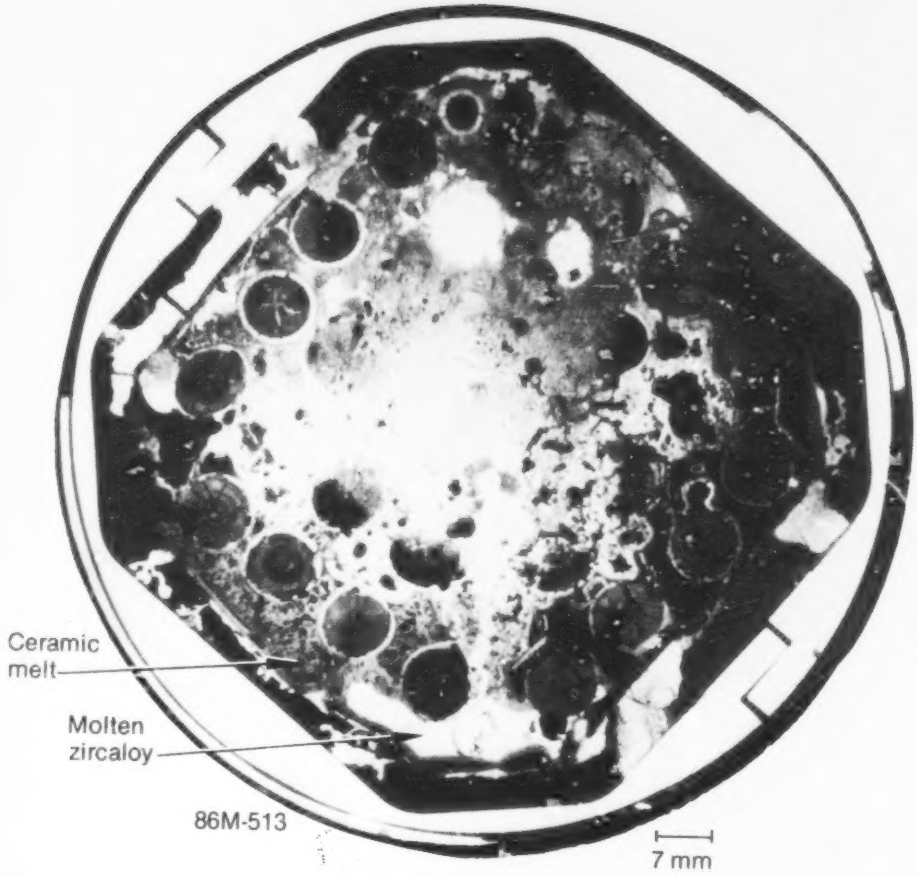
Ceramic melt
Molten zircaloy
86M-513
7 mm

Figure 60. Bundle cross section at 0.25 m.

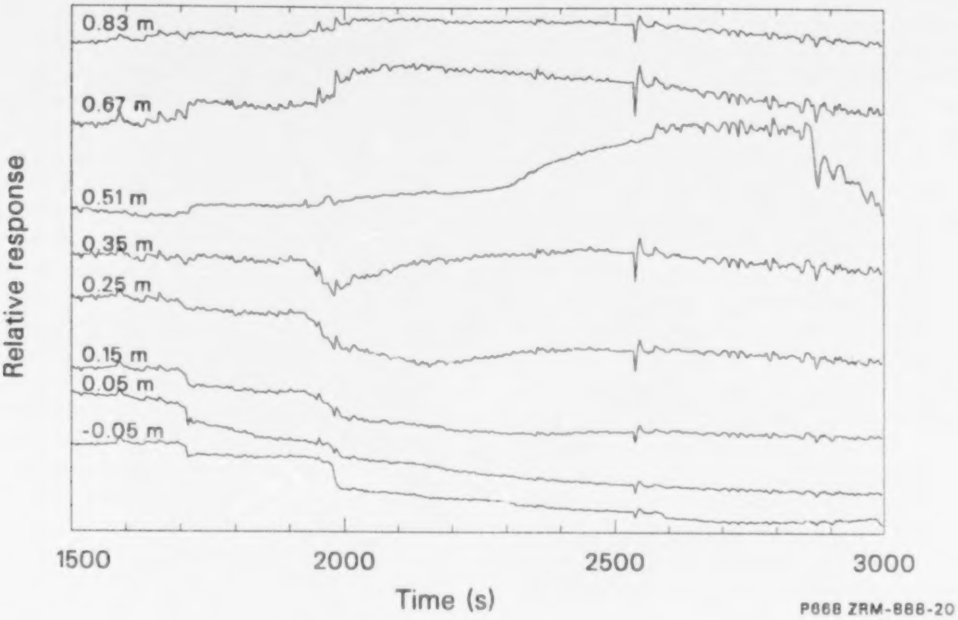

Figure 61. Normalized fission chamber output, indicating melt relocation events during Test SFD 1-4.

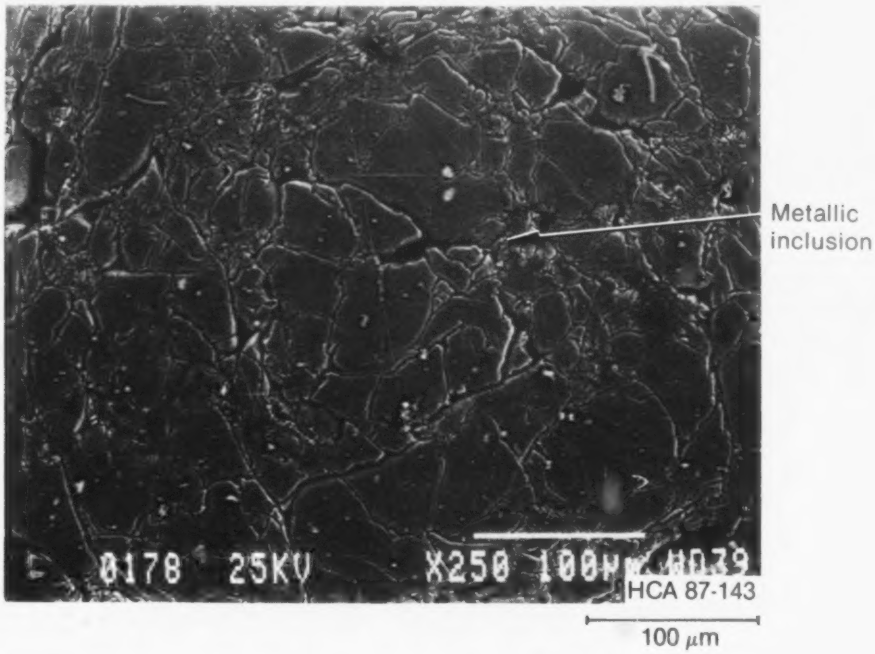
Metallic inclusion
0178 25KV X250 100μm WD39
HCA 87-143
100 μm

Figure 62. SEM photomicrograph showing ceramic melt with metallic inclusions at 0.25 m.

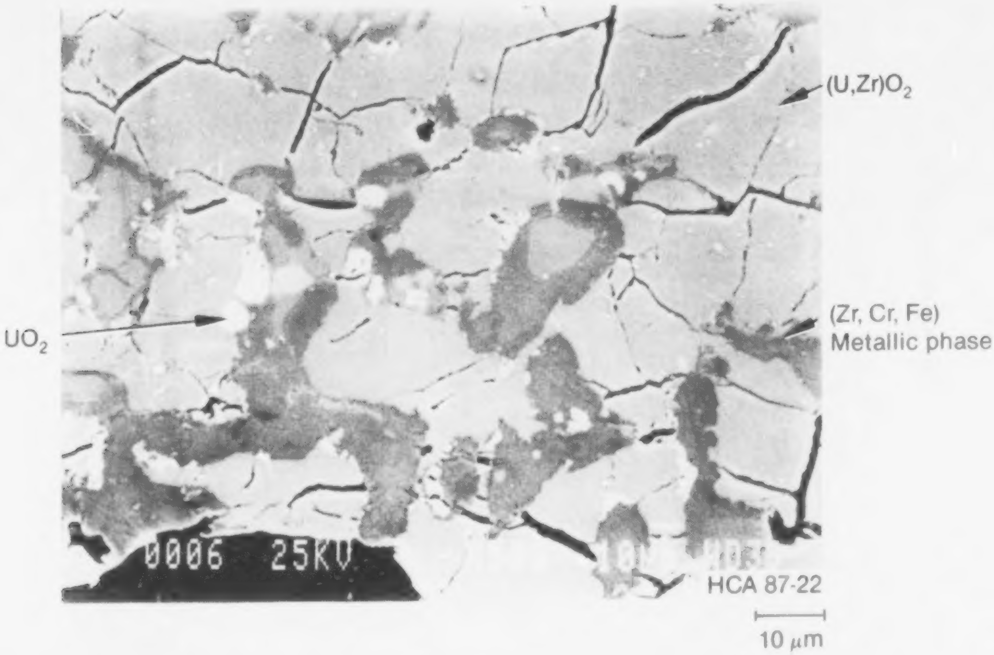
(U,Zr)O$_2$
UO$_2$
(Zr, Cr, Fe)
Metallic phase
0006 25KV
HCA 87-22
10 μm

Figure 63. SEM photomicrograph showing ceramic and metallic phases in melt at 0.25 m.

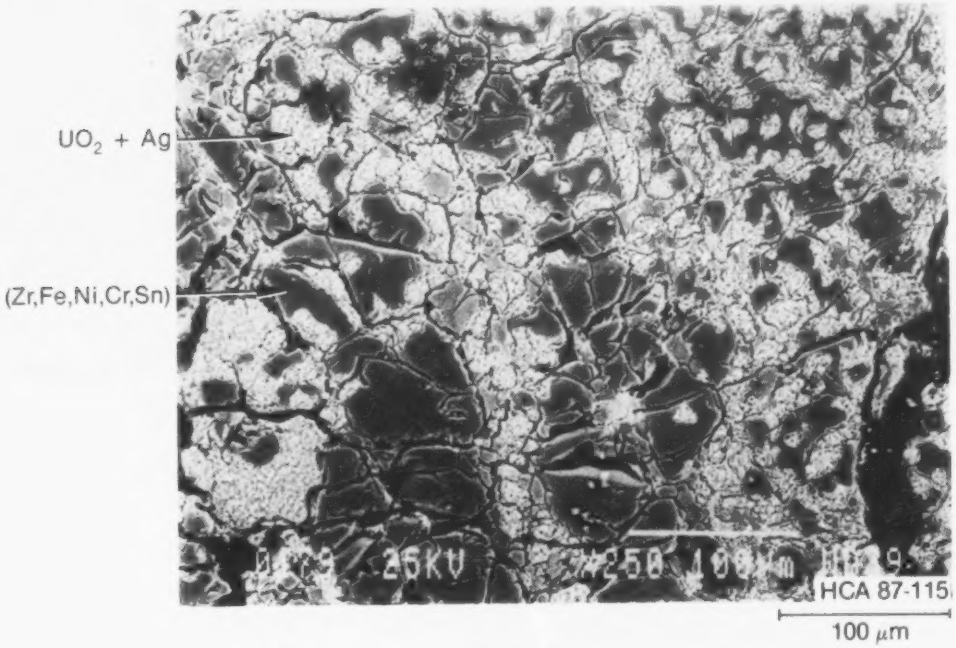
UO$_2$ + Ag
(Zr,Fe,Ni,Cr,Sn)
25KV
100μm
HCA 87-115
100 μm

Figure 64. SEM photomicrograph at control rod position 2B at 0.25 m showing mixture of UO$_2$ and silver.

which shows the structure of an intimate mixture of silver and UO_2 in the vicinity of control rod 2B.

The bundle cross section at 0.17 m (Figure 65) also experienced an influx of metallic and ceramic melts from above and a depletion of control and structural materials. The relocation of melts to this elevation from above was less extensive than at the 0.25-m elevation. This was the lowest elevation to which ceramic melt relocated. All but one of the 28 fuel rods are present in roughly their as-assembled locations in the bundle. All four control rods are missing, although oxidized shells of two of the zircaloy guide tubes remain at two positions. The net accumulation of materials caused a 30% reduction in the flow area relative to intact bundle geometry. The melts relocated to this elevation after oxidation of the zircaloy remaining there was complete. The metallic melts interacted with ZrO_2 on cladding, liner, and in the insulation, but little dissolution of UO_2 occurred. It is estimated that temperatures reached 2200 K before melts of temperatures up to 2800 K relocated to this elevation. Some control materials were found in the melts at this elevation.

The complex makeup and structure of the melts in this region are illustrated by the example in Figure 66. A variety of metallic and ceramic phases are present, including silver, indium, cadmium particles; a complex metallic phase containing zirconium, iron, nickel, chromium, uranium, silver, and indium; undissolved fragments of UO_2; and $(U,Zr)O_2$ ceramic particles. Because there appears to have been no dissolution of fuel at this elevation, the uranium-bearing material probably relocated to this elevation from above.

5.3.5 Lower Spacer Grid Region. The metallographic cross section at the 0.08-m elevation (Figure 67) reveals that the lower spacer grid collected a considerable amount of metallic debris. The metallic melt was primarily zircaloy and control material but contained stainless steel components as well. The metallic melt interacted with the fuel rod cladding, the control rod guide tubes, and the Inconel spacer grid, but did not attack the UO_2 fuel or ZrO_2 layers on the cladding or guide tubes.

An example of relocated melt attacking zircaloy fuel rod cladding but not ZrO_2 is shown in Figure 68. Presumably the melt had penetrated the cladding oxide through a crack or by chemical attack at a higher elevation where the temperature was higher. The control alloy had melted but was retained in the vicinity of the control rods in three of the four positions. An example of the retention of molten control material by the oxide on the guide tube is shown in Figure 69. The temperature before arrival of the melt was probably in the neighborhood of 1500 K; after melt arrival, the temperature was probably in the range of 1600 to 1700 K. The flow area was reduced by 87% relative to that of an intact bundle geometry.

The cross section at the 0.02-m elevation (Figure 70) exhibited a low temperature, about 1000 K, and received an influx of metallic melt that chemically attacked and penetrated three of the four zircaloy guide tubes but did not penetrate the stainless steel control rod cladding. Silver, indium, and cadmium, from molten control alloy above, relocated and froze within the control rods at this elevation. Examples of these interactions and relocations are shown in Figures 71 and 72.

The cross section at -0.09 m is below the fueled region of the bundle; but, as can be seen in Figure 73, metallic melts relocated and froze in this region without interaction with the structures. The accumulation of relocated melts reduced the flow area in this region by about 48% relative to that of the undisturbed bundle geometry at this elevation. A variety of melts relocated to this region, including a mixture of zircaloy with components of control materials and stainless steel, unreacted molten zircaloy, and other melts that were not identified.

In summary, the melt progression phenomena that produced the damage observed in Test SFD 1-4 reveal parallels to those more fully developed in the TMI-2 accident which was terminated at a later stage.[9] The rubble bed of fuel fragments in the upper bundle region is similar to the debris bed in TMI-2. The high-temperature U-Zr-O melt that relocated from mid-bundle to the lower bundle is a precursor to the molten pool in TMI-2. The accumulation of metallic melts (Ag-In-Cd, zirconium, stainless steel) near the bottom of the bundle is a precursor of the metallic lower crust found in TMI-2.

5.4 Control Rod Behavior

One of the four control rods in the test bundle (5E) was instrumented with two operable cladding inner surface thermocouples, a centerline thermocouple, and an internal pressure transducer. The control rod cladding temperature (shown in Figure 74) increased at about 0.32 K/s from 750 to 1100 K (over the same time interval that the average fuel rod cladding temperature increased by 0.37 K/s). The control rod cladding temperatures at 0.39 and 0.74 m were generally about 60 K less

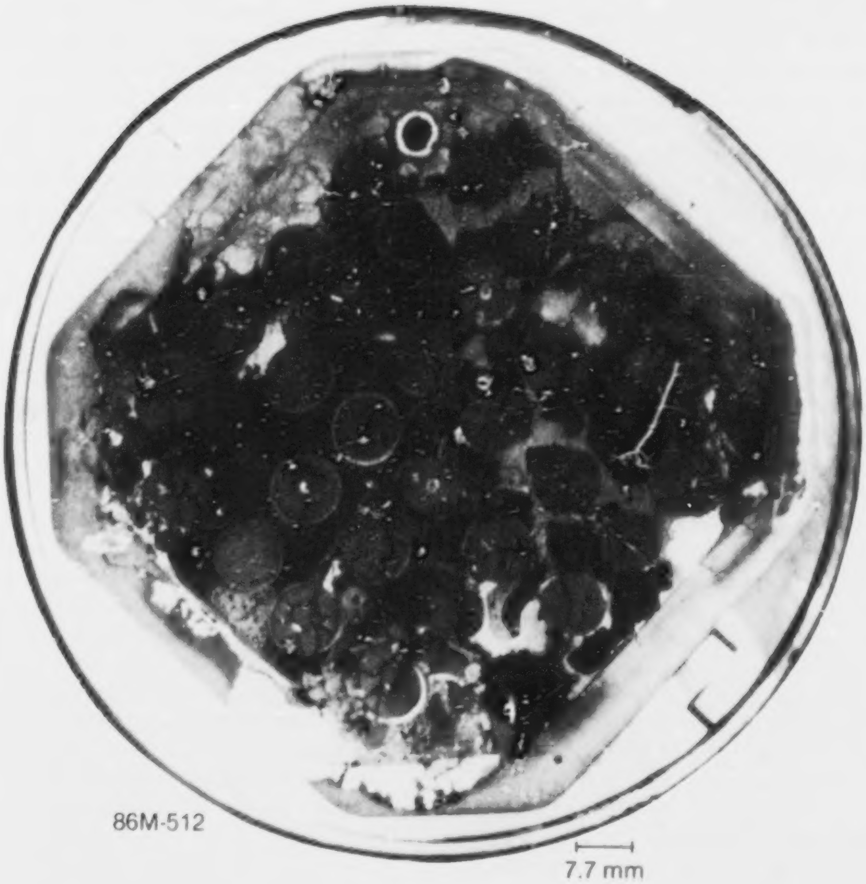
86M-512
7.7 mm

Figure 65. Bundle cross section at 0.17 m.

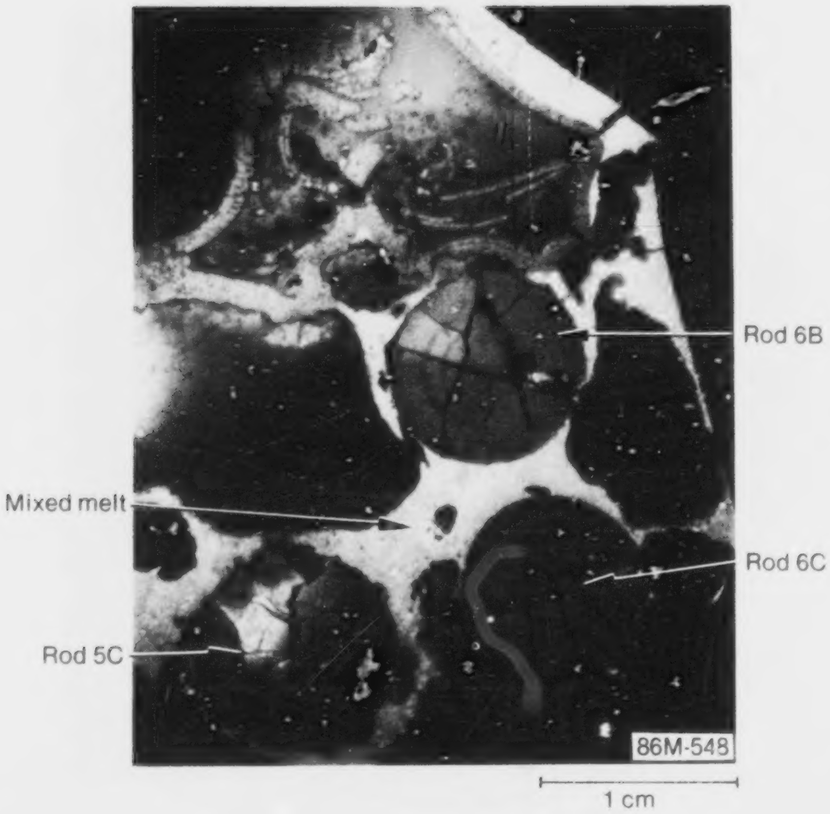
Rod 6B
Mixed melt
Rod 6C
Rod 5C
86M-548
1 cm

Figure 66. Photomicrograph of metallic melt between rods 5C, 6B, and 6C at 0.17 m.

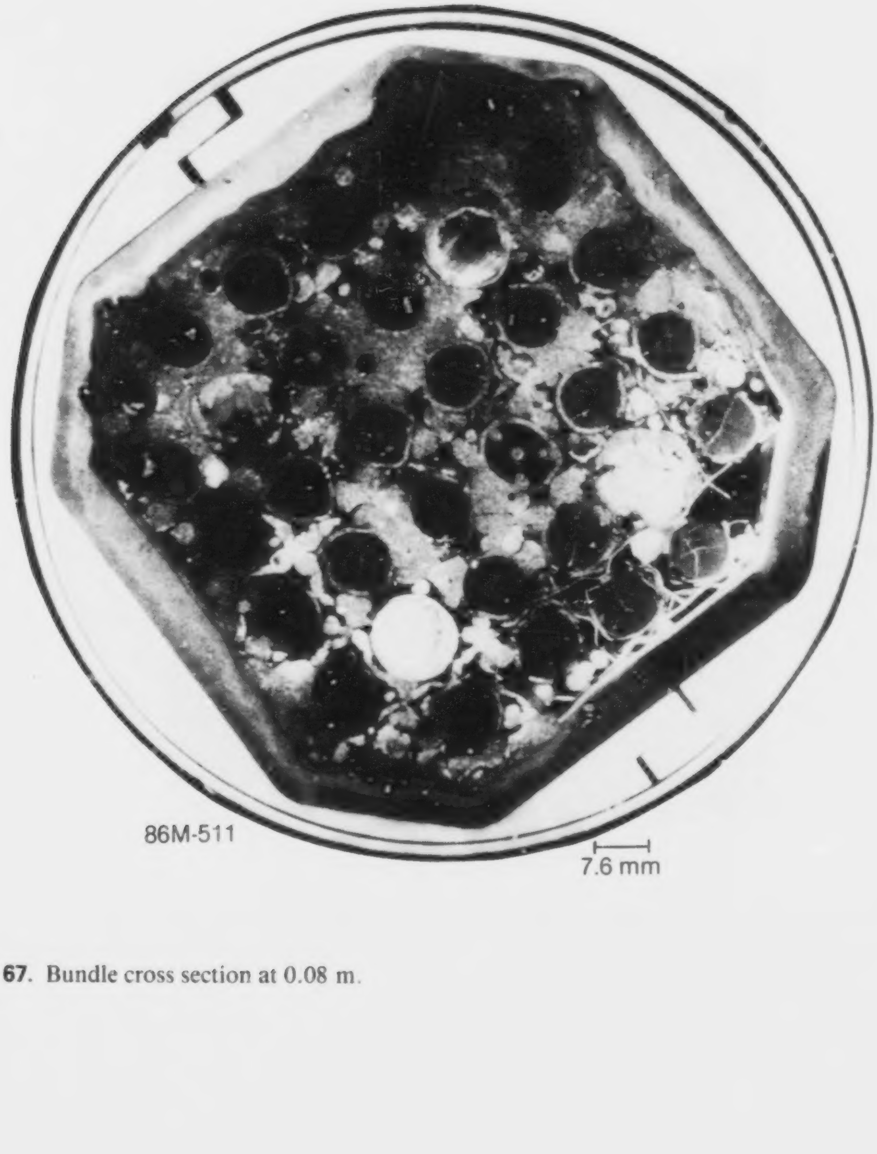
86M-511
7.6 mm

Figure 67. Bundle cross section at 0.08 m.

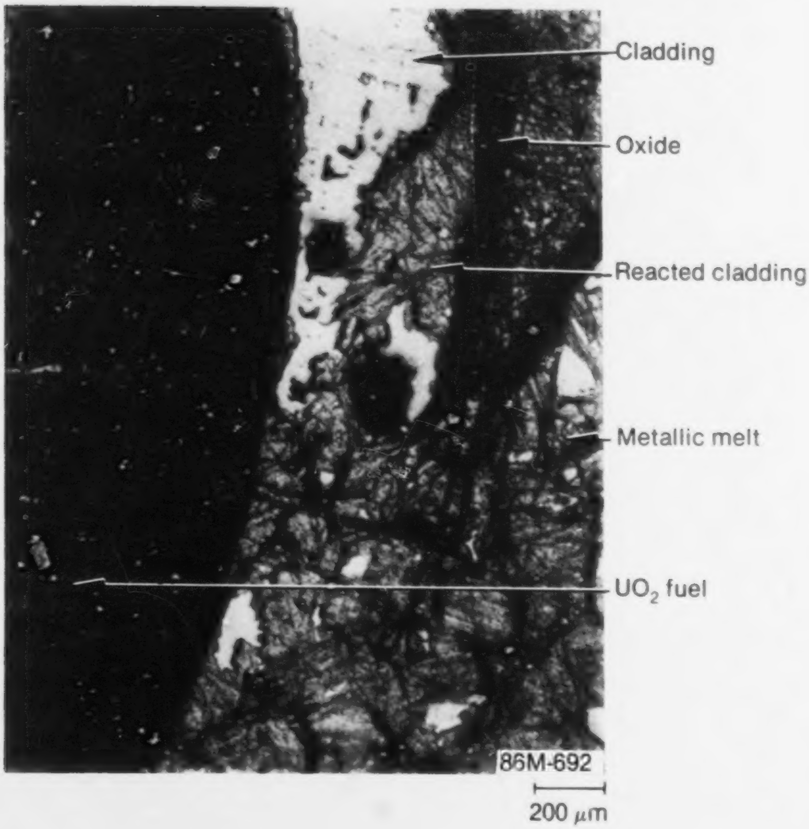
Cladding
Oxide
Reacted cladding
Metallic melt
UO$_2$ fuel
86M-692
200 μm

Figure 68. Photomicrograph showing melt attack on cladding at 0.08 m.

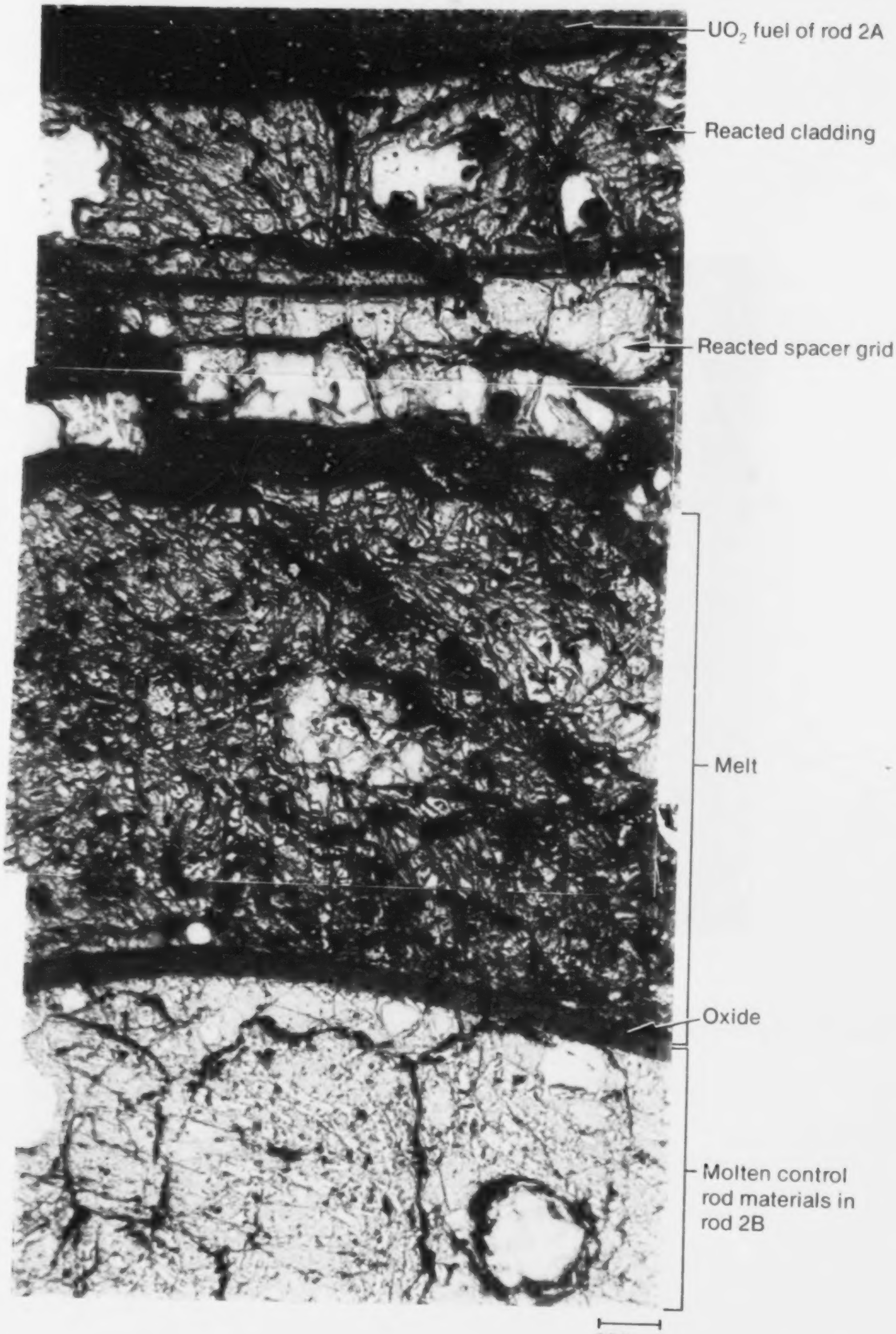
UO_2 fuel of rod 2A
Reacted cladding
Reacted spacer grid
Melt
Oxide
Molten control rod materials in rod 2B
200 μm

Figure 69. Photomicrograph showing containment of molten control material by oxide of dissolved guide tube in control rod position 2B at 0.08 m.

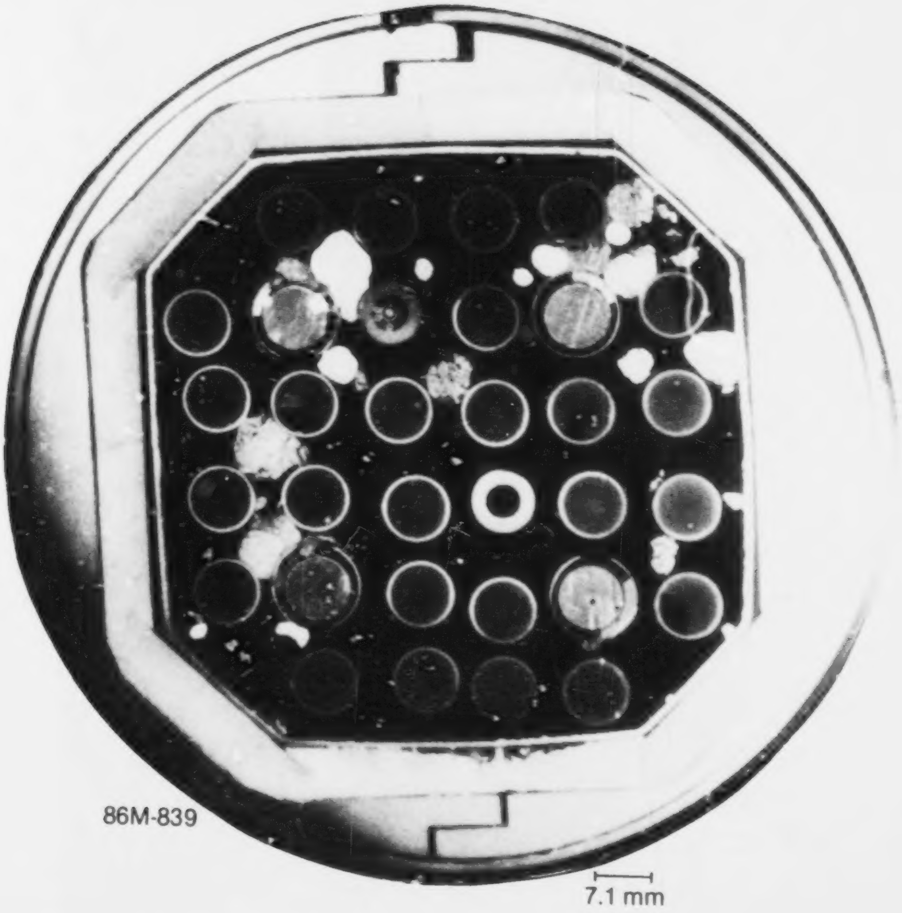
86M-839
7.1 mm

Figure 70. Bundle cross section at 0.02 m.

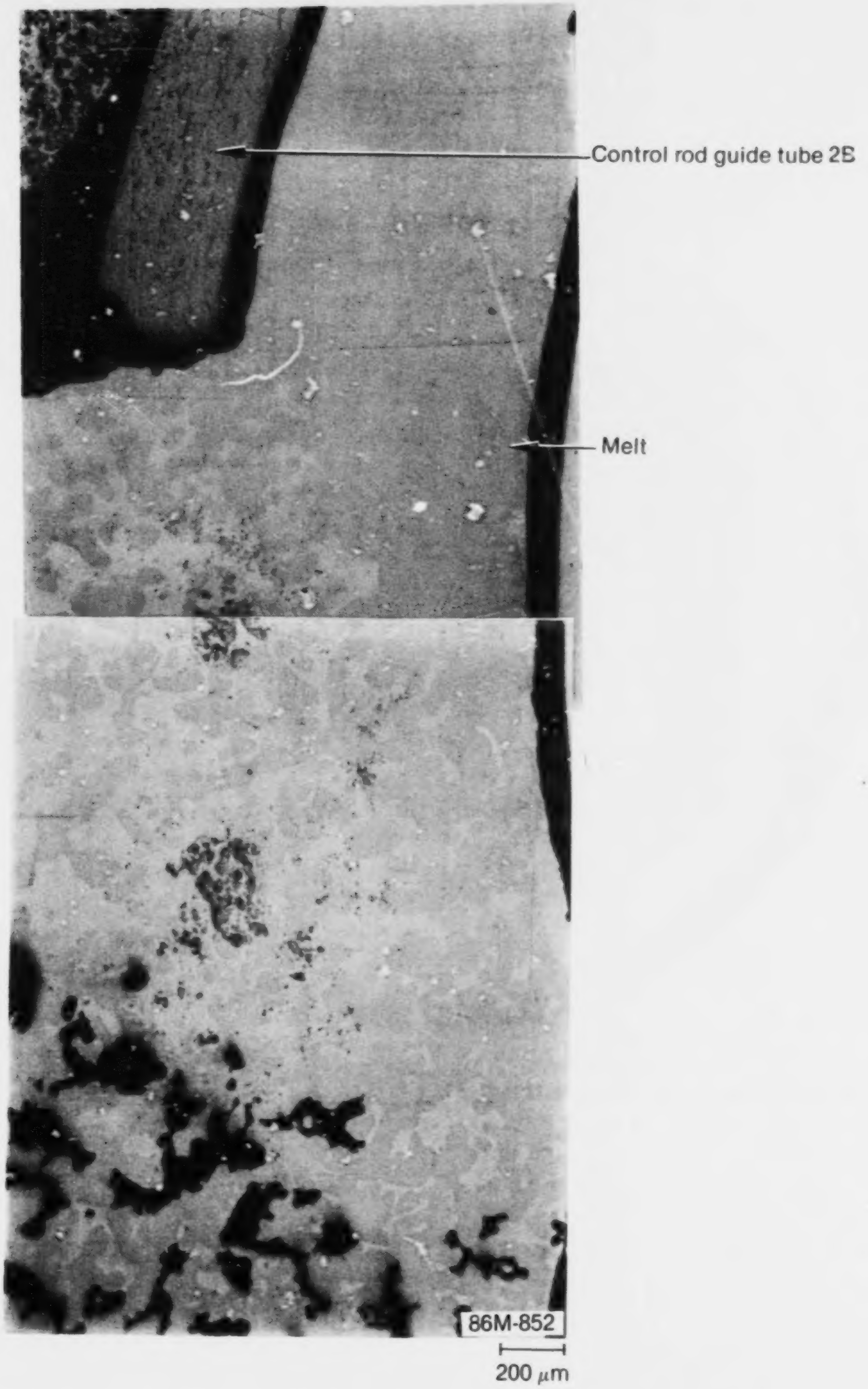
Control rod guide tube 2B
Melt
86M-852
200 μm

Figure 71. Photomicrograph of melt penetration of guide tube in control rod position 2B at 0.02 m.

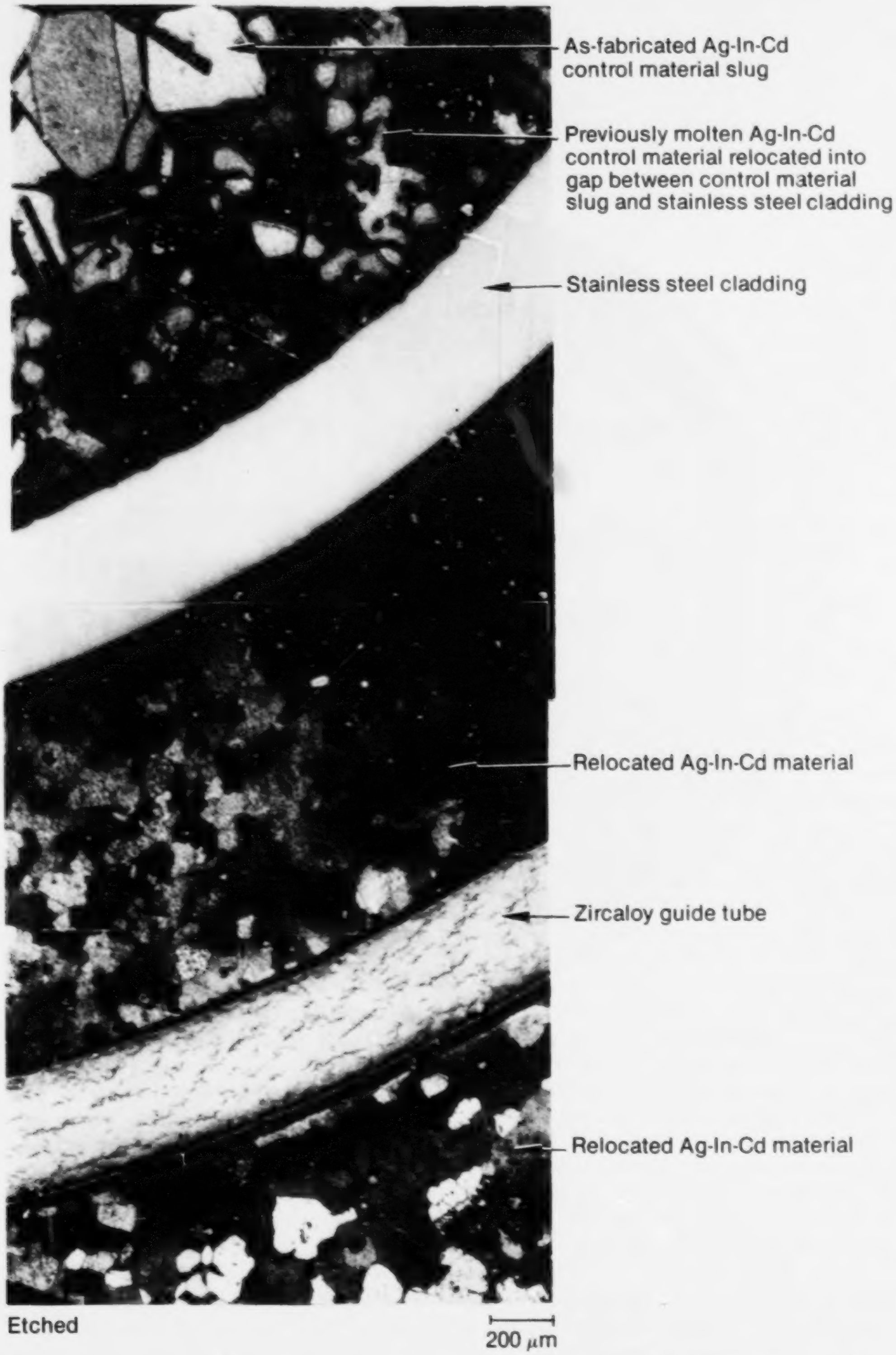
As-fabricated Ag-In-Cd control material slug
Previously molten Ag-In-Cd control material relocated into gap between control material slug and stainless steel cladding
Stainless steel cladding
Relocated Ag-In-Cd material
Zircaloy guide tube
Relocated Ag-In-Cd material
Etched
200 μm

Figure 72. Photomicrograph showing relocation of Ag-In-Cd control rod material within and outside of control rod position 5B at 0.02 m.

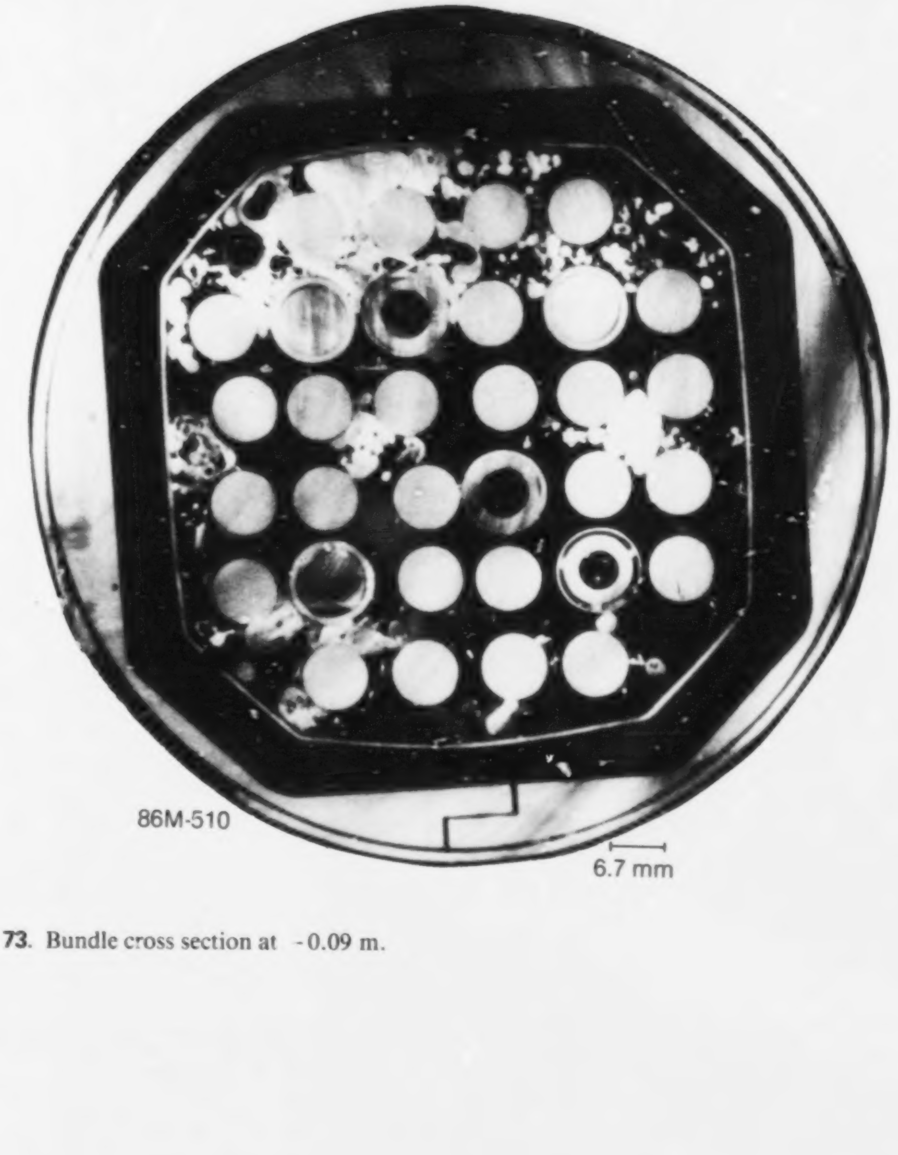
86M-510
6.7 mm

Figure 73. Bundle cross section at - 0.09 m.

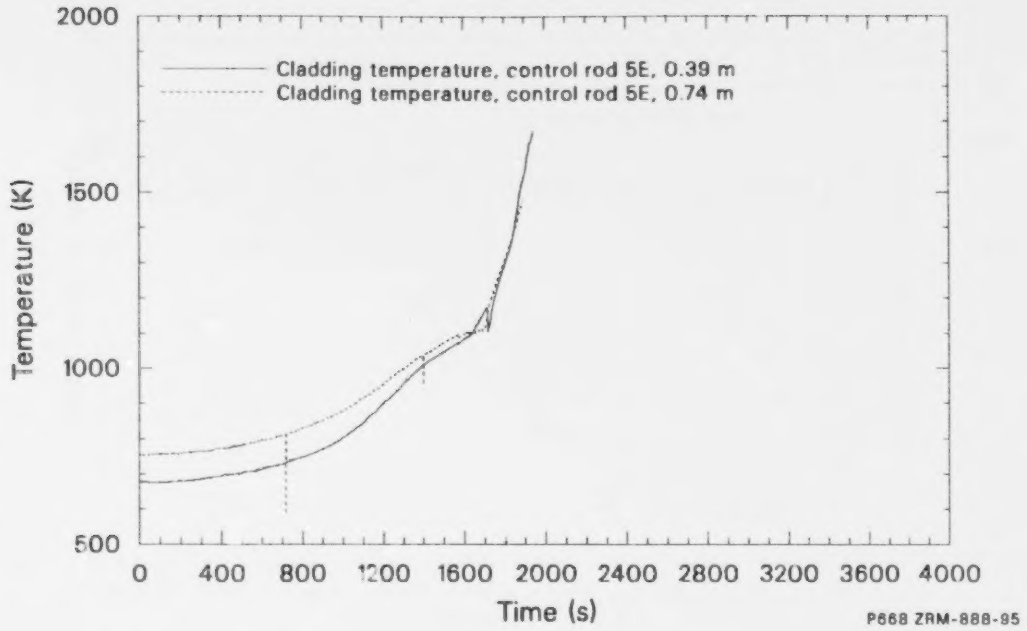

Figure 74. Cladding temperatures for control rod 5E at 0.39 and 0.74 m during Test SFD 1-4.

than the corresponding fuel rod cladding temperatures. Similarly, the control rod centerline temperature at 0.39 m was about 50 K less than the fuel rod centerline temperatures.

The instrumented control rod failed at ∼1708 s in Test SFD 1-4. As shown in Figure 75, failure was indicated by the rapid drop in the control rod internal pressure from 14 MPa to the bundle pressure of ∼6.9 MPa within 0.1 s and the subsequent 0.4-MPa coolant pressure spike at ∼1712 s (also shown in Figure 75) produced by the rapid generation of steam when the molten absorber material contacted the coolant plenum region. The inlet coolant thermocouples in the lower plenum at −0.36 m registered an increase of ∼8 K due to heating by the molten alloy (see Figure 76). At the time of rupture, the control rod cladding temperature was 1170 K at 0.39 m and 1130 K at 0.74 m, while the centerline temperature at 0.39 m was 1190 K.

The failure of the instrumented rod at ∼1170 K is not typical of PWR control rod behavior in severe accidents. To verify this, the expected control rod internal pressure was calculated as a function of temperature. The control rods were originally backfilled with helium to 1 atmosphere pressure. The partial pressures of silver, indium, and cadmium were calculated using Raoult's law, assuming isothermal conditions. As shown in Figure 77, the calculated internal rod pressure is well below the 6.9-MPa coolant pressure for temperatures up to 2400 K. Thus, the instrumented control rod failure was not due to vaporization of the alloy. Instead, the control rod is believed to have developed a small leak and become waterlogged prior to the transient. This is evidenced by the control rod pressure and temperature responses, shown in Figure 78, for the three coolant boildowns prior to the high-temperature transient. The internal pressure of the control rod during each boildown was significantly greater than the pressure that the backfill gas would have exerted at temperatures up to ∼700 K. The internal rod pressure also decreased slowly during the steady-state temperature hold after each boildown, indicating slow leakage of steam from the control rod. The rod evidently had a small defect in one of the 5 welded or 12 brazed joints on this assembly.

In addition to their primary role of measuring the coolant level in the bundle, the signals from an array of eight fission chambers mounted on the shroud outer wall were used to assess control rod and fuel material motion. Only qualitative information regarding material relocation was obtained

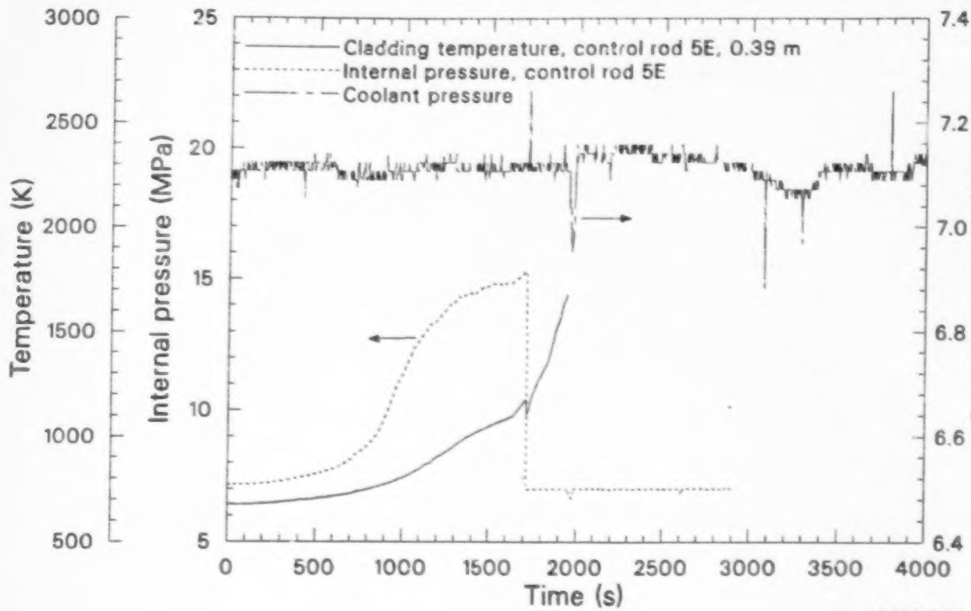

P668 ZRM-189-16A

Figure 75. Cladding temperature for control rod 5E at 0.39 m, internal rod pressure, and coolant pressure during Test SFD 1-4, indicating the time that the instrumented control rod failed.

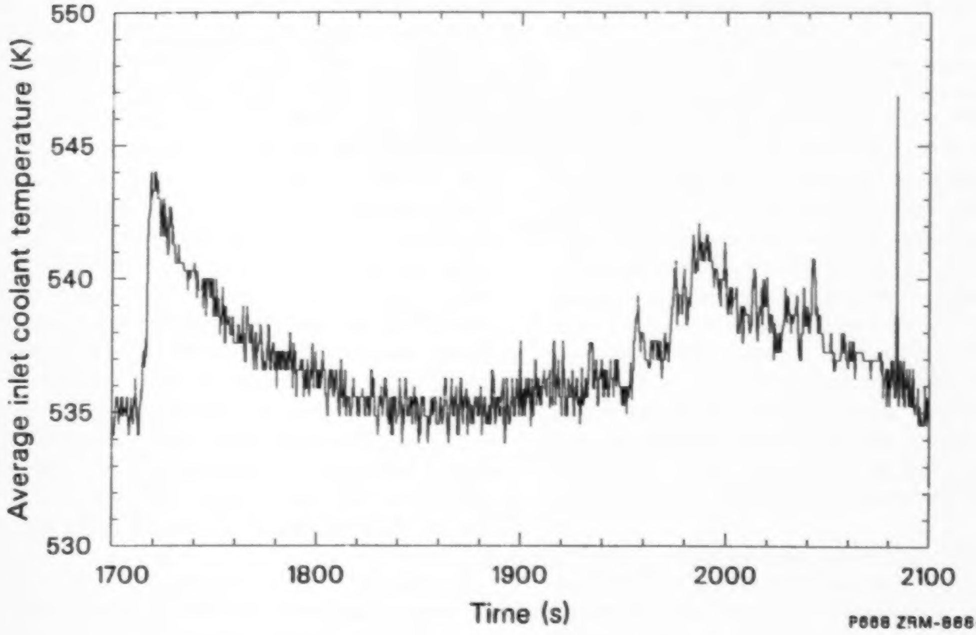

P668 ZRM-888-17

Figure 76. Average inlet coolant temperature during failure of the control rods in Test SFD 1-4.

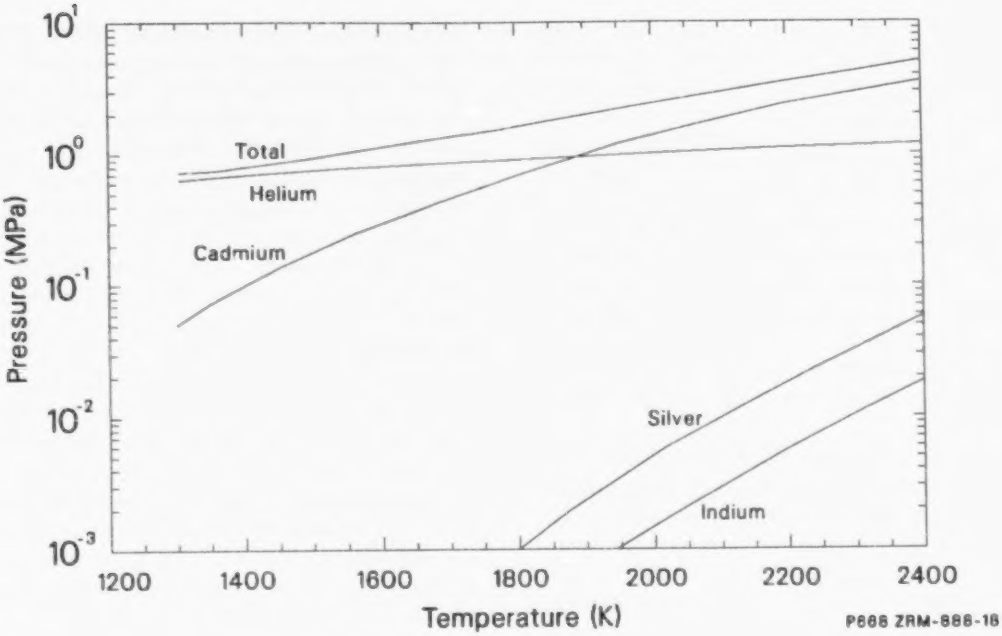

Figure 77. Calculated control rod internal pressure as a function of temperature.

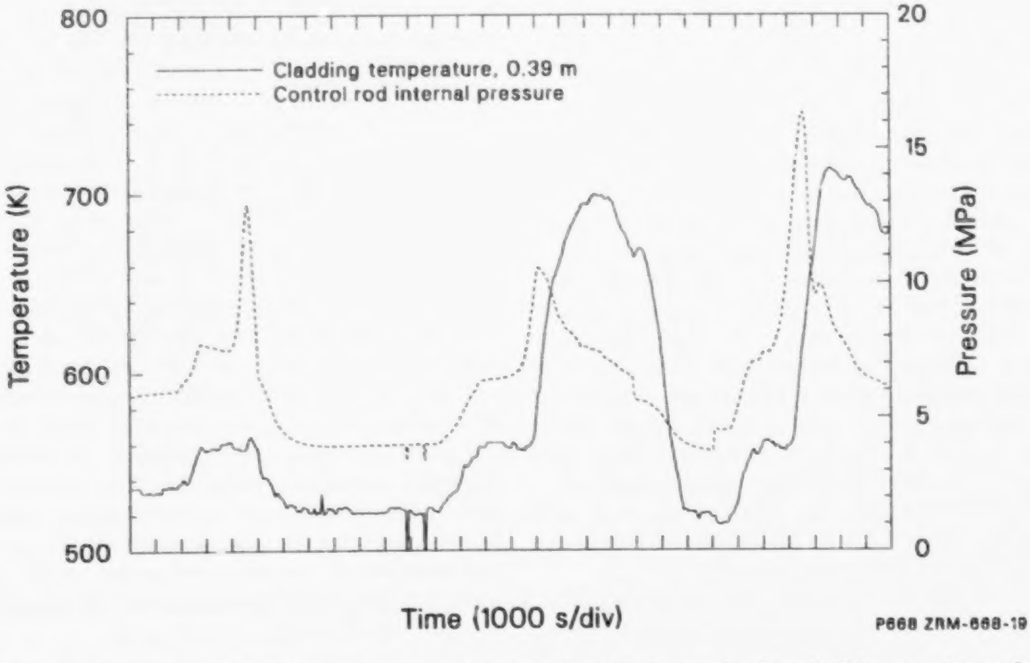

Figure 78. Pressure and cladding temperature of control rod 5E during the three boildowns prior to the Test SFD 1-4 high-temperature transient.

from the monitors because the sensitivity of individual fission chambers to fuel and/or control rod material was not calibrated. Reactor physics calculations, performed to aid the interpretation of fission chamber signals, indicated that the local fission rate should decrease slightly due to flux spectrum hardening for fuel material that relocated into a region. Conversely, loss of fuel material from a region should result in an increase in the thermal neutron flux due to reduced absorption. Control rod absorber material motion in the bundle can be detected because loss of poison material will increase the local thermal neutron flux, while additional poison material will decrease the thermal neutron flux.

Figure 61 shows the eight normalized fission chamber outputs during the high-temperature transient between 1500 and 3000 s. The fission chamber signals were normalized to the reactor power and are arranged in the figure according to their axial location. At ∿1500 s, the fission chamber output at 0.05 m steadily decreased, because of decreasing water level in the bundle near 0.05 m, while all the other normalized fission chamber outputs were relatively steady. The control rod internal pressure was considerably higher than the bundle steam pressure when the cladding ruptured at 1708 s, which resulted in the expulsion of molten absorber material out of the control rod. The molten alloy material, which has a low viscosity, probably flowed downwards very rapidly. As can be seen in Figure 61, the movement of the absorber material caused a sharp decrease starting at about 1712 s in the normalized signals at the −0.05-, 0.05-, 0.15- and 0.25-m elevations, while the signals from chambers at 0.35-m and above increased.

Time-expanded data plots after the first control rod failure from the normalized fission chambers were analyzed, and the results are summarized in Table 6. The delay time from the initial indication of material movement at the 0.51-m fission chambers to an indication at the −0.05 m fission chamber was 0.5 s. The actual velocity of the control rod alloy cannot be calculated because the original location of the material reaching the −0.05-m elevation is unknown. The delay time from control rod failure to the inlet coolant temperature increase was 7 s.

The normalized fission chamber outputs shown in Figure 79 indicate when the other three noninstrumented control rods probably failed. The fission chamber data concerning these other three control rod failures are also summarized in Table 6. The times of abrupt signal changes in the fission chambers are 1927, 1958, and 1978 s. It is believed that the three noninstrumented control rods failed between these times based on the large decreases observed in the output of the fission chambers. The centerline thermocouple at 0.39 m on the failed instrumented control rod indicates a value of 1690 K at 1927 s. A 6-K increase in the inlet coolant temperature (shown in Figure 76) from 1950 to 2100 s accompanied the failure of the remaining three control rods. Since the inlet coolant temperature remained below saturation, no coolant pressure spike was detected. After 2000 s, the normalized fission chamber outputs at −0.05, 0.05, 0.15, and 0.25 m continued to decrease, while the normalized signals for the 0.35- and 0.51-m chambers increased, perhaps due to control rod alloy or fuel material moving downward.

As the bundle continued to heat up, upper portions of the empty control rod guide tube melted and relocated downwards. The posttest bundle control material distribution shown in Figure 47 indicates that 83% of the control rod material relocated near the lower spacer grid location at the 0.08-m elevation in the bundle (see Figure 67). Much of the remaining control rod material had relocated to the lower plenum, but a small amount was held up in the high-temperature region of the bundle by means of physical mixing in melts. The relocated material at and below 0.08 m contained control rod alloy that was close to as-fabricated, whereas above 0.08 m some depletion of the alloy's constituents occurred. The control rod alloy and molten stainless steel interacted with zircaloy in the bundle during and following relocation but did not interact with fuel. As discussed in Section 7, relocated control rod material, low in the bundle, was reheated by relocating ceramic melts long after initial control rod failure, causing the vaporization of control materials, especially cadmium. The principal effects of the control rods were generation of cadmium aerosol and the formation of metallic melts that solidified at low elevations in the bundle to produce a lower crust that caused significant but not total flow blockage.

Table 6. Fission chamber response during control rod failure

Fission Chamber Elevation (m)	Indicated Relocation Time of Instrumented Control Rod (s)	Relative Change in Output	Suspected Failure Time of Other Control Rods (s)	Relative Change in Output
0.83	Not evident	—	Not evident	—
0.67	1711.7	Increase	1940 and 1970	Increase-increase
0.51	1711.5	Increase	1960 and 1975	Increase-decrease
0.35	1711.6	Slight increase	1927 and 1958 and 1975	Decrease
0.25	1711.6	Decrease	1927 and 1951	Decrease
0.15	1711.7	Decrease	1927 and 1977.5	Decrease
0.05	1711.8	Decrease	1970	Decrease
−0.05	1712.0	Decrease	1948 and 1978	Decrease

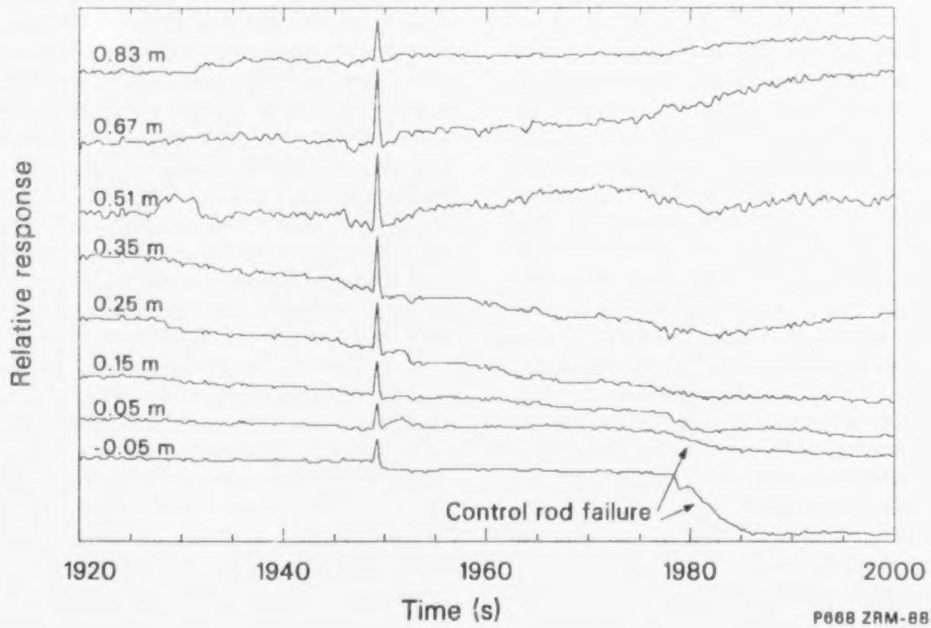

P668 ZRM-888-21

Figure 79. Normalized fission chamber output at the time of suspected control rod failure during Test SFD 1-4.

6. FISSION PRODUCT RELEASE AND RETENTION BEHAVIOR

A summary of the on-line, off-line, and posttest measurements and analyses that were performed to understand fission product release and retention in Test SFD 1-4 is presented in this section. The methodology used to obtain the ORIGEN2 inventories common to all of the fission product data analysis is described in Section 6.1. Section 6.2 presents a summary of the on-line and off-line fission product release and retention measurements and analysis. Fission gas release calculations using the FASTGRASS, CORSOR, and Booth models are compared to the measured data in Section 6.3. The major findings of these analyses are summarized in Section 6.4.

6.1 ORIGEN2 Inventory Calculations

Two separate calculations were performed using the ORIGEN2[12] code to calculate the fission product inventory of the SFD 1-4 bundle. The first calculation provided total bundle inventories for fission product and heavy metal isotopes needed to analyze the on-line and grab sample data. Each rod in the fuel bundle was modeled as a series of ten axial nodes. The irradiation of the 26 high-burnup fuel rods was modeled based on the BR-3 power histories. Rods with two different BR-3 irradiation histories (B500 and B300) were used in Test SFD 1-4. A single irradiation cycle was used for the 8 B500 rods, and two irradiation cycles were used for the 18 B300 rods in the SFD 1-4 bundle. For the B300 rods, the exposure split between the two cycles was based on the core-effective full-power split for the two cycles. The calculated bundle inventories were then decay-corrected to the start of the PBF irradiation. Both the fresh and irradiated rods were modeled for the PBF irradiation. The calculated bundle inventories of the selected radionuclides prior to and at the end of the SFD 1-4 transient are listed in Table 7.

In the second calculation, the individual fuel rod nodes were grouped into burnup bins, and the calculations were rerun to obtain fission product inventories as a function of fuel burnup for the B300 and B500 rods separately. These results were used to analyze the retained fission product measurements discussed in Section 6.2. Since only long-lived isotopic inventories were required, the PBF irradiation was not modeled. Additional information about the methodology used for both inventory calculations is found in Appendix G.

6.2 Measurements and Analysis

This section summarizes the on-line and off-line measurements that were performed to characterize fission product release and retention in Test SFD 1-4.

6.2.1 Gross Radiation Monitor Responses. Two ion chambers (gross gamma), three NaI(Tl) detectors (gross gamma), and a moderated BF_3 neutron counter (delayed neutron) were used to monitor the gross radiation at various locations in the effluent sampling system, as shown in Figure 80. Responses from these instruments provide timing information and insight into fission product release, transport, and deposition behavior. Unless otherwise stated, the detector responses were not corrected for effluent transit times.

Figure 81 shows the response of the two gamma-sensitive ion chambers located near the inlet of the filtered effluent sample cask on the reactor main floor (12.55 m from the bottom of the PBF core) and at the point in Cubicle 13 where the effluent line enters the radiation shield of the steamline gamma spectrometer (31.24 m). A spike in the response of the Cubicle 13 steamline ion chamber occurred at 1720 s and probably corresponds to gap release due to cladding rupture of several fuel rods. The mainfloor ion chamber did not respond to the gap release. The magnitude of the signal from the mainfloor ion chamber is lower than that of the steamline ion chamber signal because the mainfloor ion chamber viewed a smaller portion of the effluent line from a greater distance than the steamline ion chamber. The mainfloor and steamline ion chamber signals both increased rapidly between 1720 and 2000 s. The signals leveled off between 2600 and 2800 s and remained approximately constant up to and beyond 5000 s. The absence of any signal decrease with bundle cooldown indicates that some time after ~2000 s each detector was responding predominantly to activity deposited in the viewed section of the sample line.

Figure 82 shows the response of the three NaI(Tl) gross gamma detectors located near the steamline, liquidline, and gasline spectrometers at 31.2, 57.9 and 60.1 m from bottom of the PBF

Table 7. ORIGEN2 inventories of selected radionuclides

	Bundle Inventory[a] (μCi)	
Isotope	Prior to Test SFD 1-4[b]	End of Test SFD 1-4[c]
^{85}Kr	9.80 E + 07 ± 10	9.77 E + 07 ± 10
^{85m}Kr	0	1.01 E + 08 ± 10
^{88}Kr	0	1.69 E + 08 ± 10
^{88}Rb	0	1.76 E + 08 ± 10
^{90}Sr	9.75 E + 08 ± 10	9.75 E + 08 ± 10
^{95}Zr	6.51 E + 02 ± 10	4.24 E + 08 ± 10
^{95}Nb	1.45 E + 03 ± 10	1.41 E + 08 ± 10
^{103}Ru	1.31 E − 02 ± 10	4.72 E + 08 ± 10
^{106}Ru	1.69 E + 08 ± 10	1.86 E + 08 ± 10
^{125}Sb	3.94 E + 07 ± 10	3.88 E + 07 ± 10
^{127m}Te	4.95 E + 03 ± 10	1.85 E + 07 ± 10
^{129}Te	2.55 E − 06 ± 10	1.06 E + 07 ± 10
^{129m}Te	3.91 E − 06 ± 10	1.64 E + 07 ± 10
^{129}I	3.66 E + 02 ± 10	3.67 E + 02 ± 10
^{131}I	0	5.20 E + 08 ± 10
^{131m}Xe	0	6.82 E + 06 ± 10
^{131}Te	0	1.88 E + 08 ± 10
^{132}Te	0	4.88 E + 08 ± 10
^{133}I	0	4.99 E + 08 ± 10
^{133}Xe	0	1.08 E + 08 ± 10
^{134}Te	0	3.05 E + 08 ± 10
^{134}Cs	3.21 E + 08 ± 20	3.21 E + 08 ± 20
^{135}I	0	8.34 E + 08 ± 10
^{136}Cs	0	2.28 E + 07 ± 10
^{137}Cs	1.20 E + 09 ± 10	1.20 E + 09 ± 10
^{140}Ba	0	1.00 E + 09 ± 10
^{140}La	0	1.06 E + 09 ± 10
^{141}Ce	5.18 E − 05 ± 10	6.72 E + 08 ± 10
^{144}Ce	2.17 E + 08 ± 10	2.90 E + 08 ± 10
^{154}Eu	6.81 E + 07 ± 10	6.81 E + 07 ± 10
^{155}Eu	3.15 E + 07 ± 10	3.15 E + 07 ± 10
^{235}U	5.81 E + 02 ± 20	6.40 E + 02 ± 20
^{238}Pu	2.22 E + 07 ± 20	2.24 E + 07 ± 20
^{239}Pu	3.42 E + 06 ± 20	3.43 E + 06 ± 20
^{241}Am	7.65 E + 06 ± 20	7.73 E + 06 ± 20
^{242}Cm	4.50 E + 05 ± 20	3.08 E + 07 ± 20
^{244}Cm	6.06 E + 06 ± 20	6.10 E + 06 ± 20

---

a. The ± values are estimated uncertainties in percent.

b. Represents long-lived isotopes in BR-3 fuel as of February 7, 1985.

c. Activities as of 21:36:34 on 2/7/85.

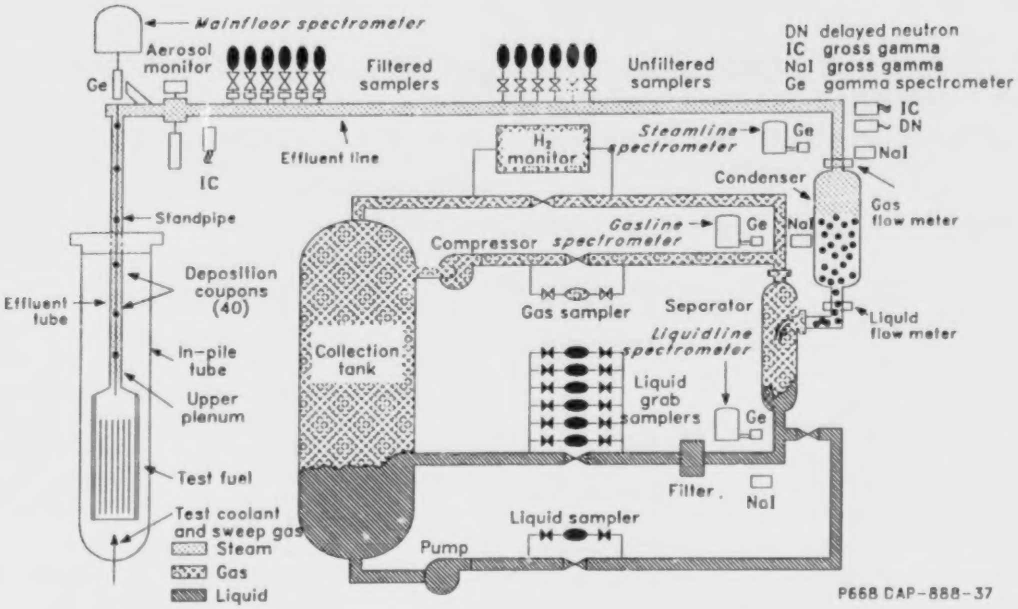
Mainfloor spectrometer
Aerosol monitor
Ge
Filtered samplers
Unfiltered samplers
DN delayed neutron
IC gross gamma
NaI gross gamma
Ge gamma spectrometer
IC
DN
NaI
Effluent line
IC
H_2 monitor
Steamline spectrometer
Ge
Condenser
Gas flow meter
Standpipe
Gasline spectrometer
Ge
NaI
Compressor
Deposition coupons (40)
Effluent tube
Gas sampler
Separator
Liquid flow meter
Liquidline spectrometer
In-pile tube
Collection tank
Liquid grab samplers
Ge
Upper plenum
Test fuel
Filter
NaI
Test coolant and sweep gas
Liquid sampler
Pump
Steam
Gas
Liquid
P668 DAP-888-37

Figure 80. Schematic of the SFD 1-4 sampling and monitoring system with locations of the four on-line gamma spectrometers noted.

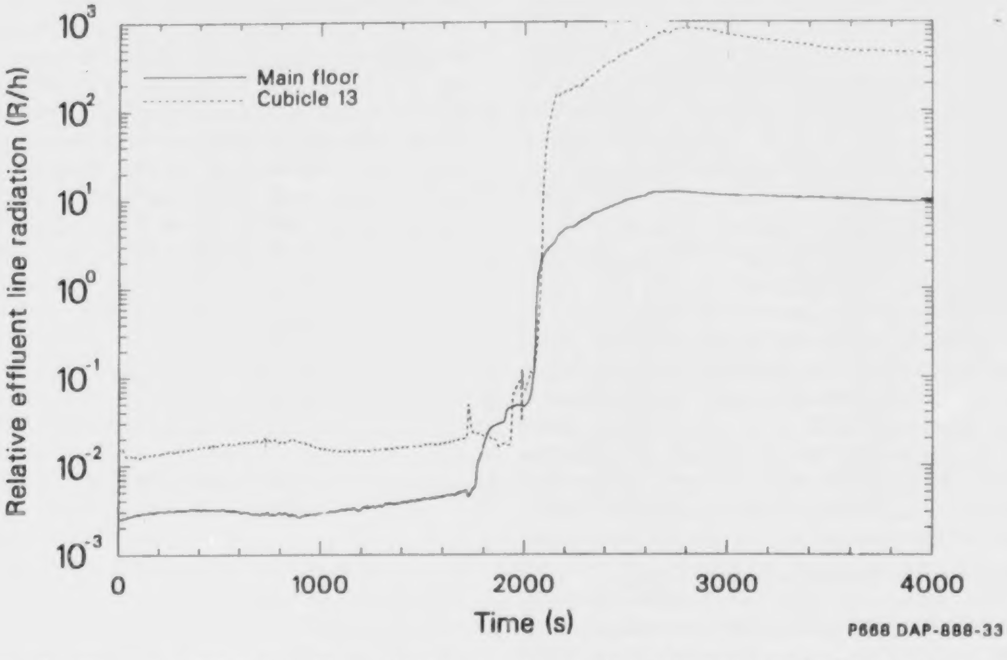

Figure 81. Response of SFD 1-4 effluent line ion chambers on the main floor and in Cubicle 13.

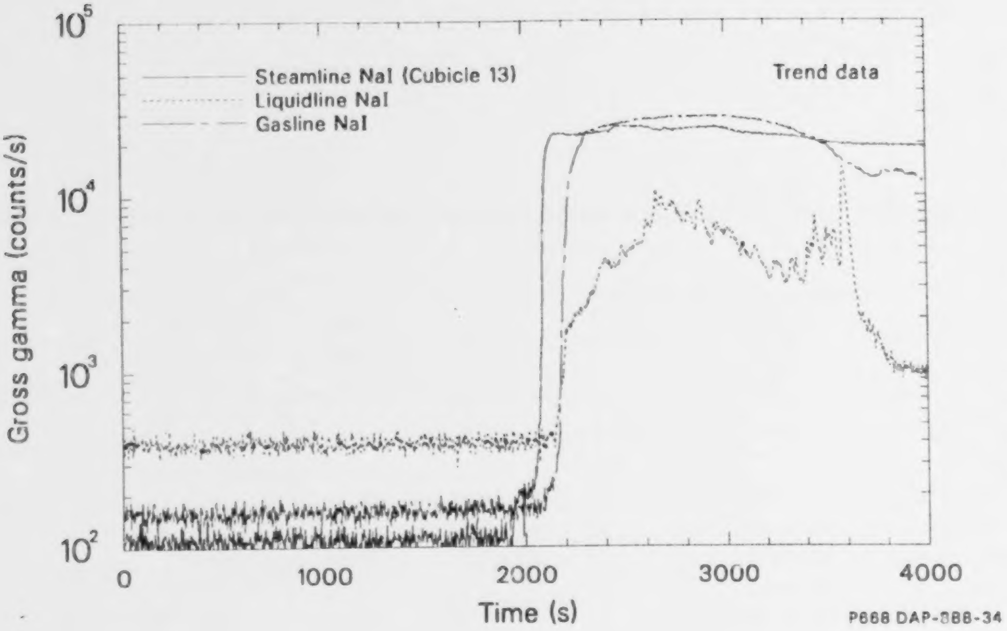

Figure 82. Gamma activities at the SFD 1-4 steamline (Cubicle 13), liquidline, and gasline NaI(Tl) gross gamma-ray detectors.

core, respectively. All three signals increased rapidly between 2000 and 2200 s. The differences in the timing of the responses are the result of different transit times to each detector. The steamline detector signal leveled off at 2050 s and remained at that level for the remainder of the experiment due to deposition in the viewed sample line. The gasline detector signal leveled off at 2200 s, but then began to decrease somewhat at 3300 s because of decreased release from the bundle and effluent dilution caused by the increased argon flow through the bundle.

Unlike the steamline and gasline detectors, the liquidline detector showed much more erratic behavior. The time-dependence of the liquidline detector response is similar to that of the hydrogen monitor (Figure 42) until the increase in argon flow late in the test. Because most of the radiation viewed by the liquidline detector is attributed to soluble fission products and the separator outlet flow rate is dominated by the dilution water flow (see Appendix B), the liquidline detector response is a relative indicator of the extent of soluble fission product transport to the separator. As the effluent flow rate increased during the test, more water was entrained or carried by the effluent flow to the separator, increasing the concentration of soluble fission products entering the separator. The soluble fission products included previously deposited species washed from the sample line walls. As a result, the liquidline detector responded more strongly to the changes in the total effluent flow in the sampling system than to changes in bundle release. The spiked increase in the response between 3300 and 3600 s is due to washout of the effluent line when the argon flow was increased late in the transient. In general, the responses of these instruments indicate that fission product deposition was greatest at upstream locations and decreased with increasing distance from the fuel bundle.

Figure 83 shows the response of the BF_3 delayed neutron counter located next to the Cubicle 13 ion chamber at 31.24 m. Delayed neutron activity was first detected at 2120 s, as evidenced by the 1000-fold increase in the detector signal. The response remained relatively steady until 2900 s and then decreased to the level prior to the rapid increase. The rapid increase is consistent with the three NaI(Tl) and two ion chamber responses. The decay rate of the delayed neutron counter signal, starting at about 3400 s, indicated that the associated radionuclides had a half-life of about 37 s, which is

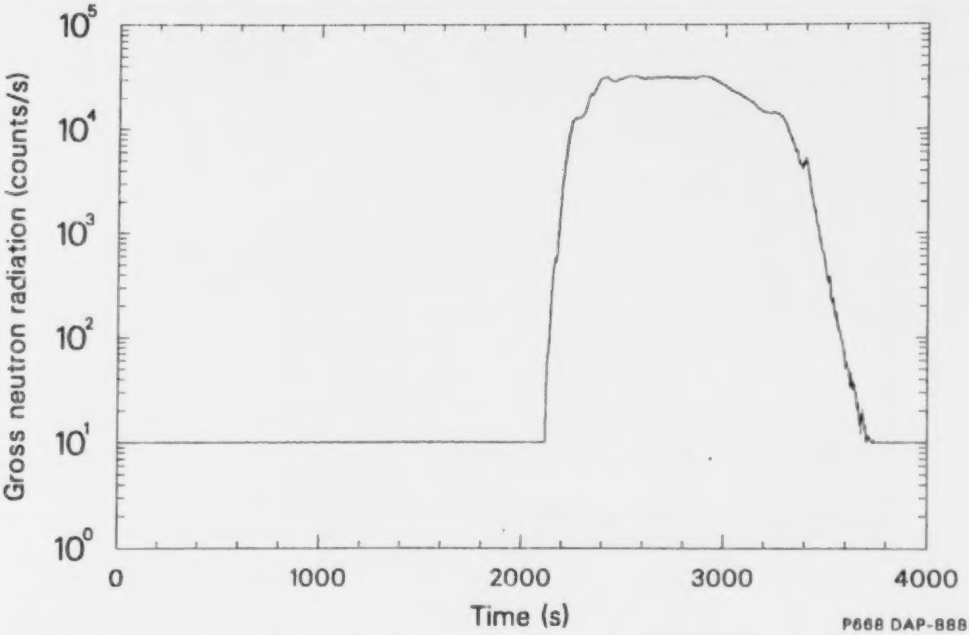

Figure 83. SFD 1-4 delayed neutron monitor (BF_3 type) response.

representative of the weighted decay from the three longest-lived delayed neutron emitters, ^{87}Br (55.5 s), ^{88}Br (16.4 s), and ^{137}I (24 s).

6.2.2 Fractional Release Rates Determined from the Effluent Grab Samplers. Six filtered and six unfiltered grab samplers were incorporated into the SFD 1-4 effluent sampling system. These effluent samplers were designed to provide discrete representative samples of the effluent at various times during the transient. The filtered effluent grab samplers were located immediately downstream of the aerosol monitor, while the unfiltered samplers were upstream of the steamline gamma spectrometer. The designs of the two sets of samplers were similar except that the filtered samplers were equipped with a sintered stainless steel particulate filter on the inlet side of a remotely operated actuating valve to capture entrained aerosol material. The samplers were designed to condense any sampled steam and thus provide both a liquid and a gaseous sample. The samples obtained during Test SFD 1-4 were analyzed posttest to provide information on fission product behavior during the experiment.

The calculated noble gas fractional release rates determined from the gas portion of the grab samples are presented in Table 8 and are plotted versus sample time in Figure 84. Details of the analysis are given in Appendix G. The noble gas release rates increased to a peak value of 4.8 E – 04 s^{-1} during the bundle heatup. A value of about 1.1 E – 05 s^{-1} was measured during cooldown. Transport and deposition effects bias the release rates calculated for the reactive fission products, yielding smaller release rates values at the downstream location of the grab samples; therefore, these release rates (from the condensed portion of the effluent sample) are not presented.[a]

6.2.3 Fission Product Release Rates from the On-line Spectrometer Data. Four on-line germanium gamma-ray spectrometers continuously monitored radionuclide concentrations in the effluent line during the SFD 1-4 transient. (The locations of the four spectrometers are illustrated in Figure 80.) The four units, designated the mainfloor spectrometer, the steamline spectrometer, the gasline spectrometer, and the liquidline

---

[a] Additional information about off-line fission product release and deposition measurements is found in the following EG&G limited distribution report: K. Vinjamuri et al., *Severe Fuel Damage Test 1-4 Data Report*, September 1987.

Table 8. Fractional release rates from the gas portion of the effluent line grab samplers

Sample	Transit Time-Corrected Sample Time (s)	Fill Time (s)	Gas Fractional Release Rates (s^{-1})[a] ^{85}Kr	 ^{131m}Xe	 ^{133m}Xe
Filtered					
FG – 1	1864	36.99	6.02 E – 07 ± 24	2.93 E – 07 ± 36	3.95 E – 08 ± 25
FG – 2	1950	42.29	1.61 E – 04 ± 24	1.08 E – 04 ± 24	9.15 E – 05 ± 25
FG – 3	2008	44.08	4.82 E – 04 ± 24	4.01 E – 04 ± 24	3.30 E – 04 ± 25
FG – 4	2287	34.78	3.13 E – 04 ± 24	3.86 E – 04 ± 24	3.40 E – 04 ± 25
FG – 5[b]	2770	38.08	7.67 E – 06 ± 24	3.29 E – 05 ± 46	1.11 E – 05 ± 30
FG – 6[b]	2990	41.37	6.49 E – 05 ± 24	4.71 E – 04 ± 24	3.83 E – 05 ± 25
Unfiltered					
UFG – 1	1697	45.96	—[c]	—[c]	—[c]
UFG – 2	1768	42.22	1.25 E – 05 ± 24	—[c]	6.29 E – 07 ± 26
UFG – 3	2150	46.69	1.71 E – 04 ± 24	1.52 E – 04 ± 25	1.57 E – 04 ± 24
UFG – 4	2460	45.69	8.68 E – 05 ± 24	1.14 E – 04 ± 24	1.24 E – 04 ± 24
UFG – 5	3310	47.63	1.61 E – 04 ± 24	2.16 E – 04 ± 26	2.46 E – 04 ± 26
UFG – 6	3780	58.11	5.64 E – 06 ± 24	1.04 E – 05 ± 24	8.68 E – 06 ± 24

---

a. The ± values are one estimated relative standard deviation in percent.

b. Release rates are biased because of large amount of water present in sample.

c. Not detected.

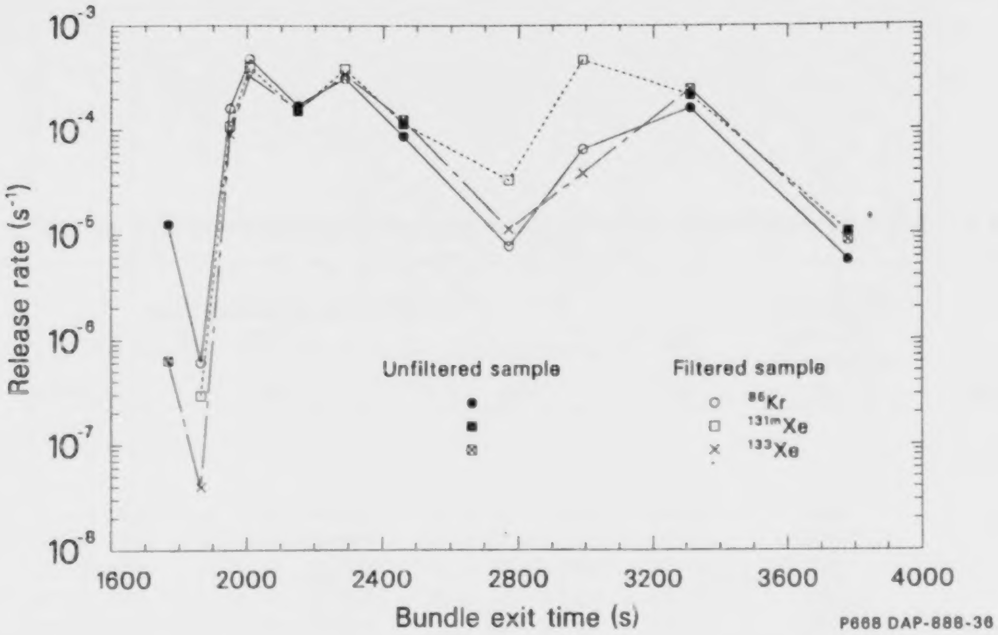

Figure 84. Fractional release rates of noble gases determined from the gaseous portion of the SFD 1-4 unfiltered and filtered effluent samples.

spectrometer, are located in the sampling system at 10.6, 31.2, 60.1, and 58.0 m, respectively, from the bottom of the PBF core.

Nearly 500 gamma-ray spectra were accumulated during the SFD 1-4 transient by these four spectrometers. These spectra were recorded on magnetic tape, transferred to the CYBER 176 computer system located at the INEL, and processed using a version of the quantitative gamma-ray spectroscopy program, GAUSS VIII[13] specially modified to support PBF on-line spectral data analyses. Radioisotopic concentrations derived from these four on-line spectrometers were plotted versus the time of acquisition (measurement time), and the plots are presented on microfiche attached to the inside back cover of this report (Appendix C). A few fission products were selected for presentation of their measured concentration histories in this section. These results are plotted versus measurement times.

The concentration profiles for selected nuclides calculated from the spectra collected by the mainfloor spectrometer and the steamline spectrometer are presented in Figures 85 and 86, respectively. The specific isotopes of xenon, iodine, cesium, and tellurium presented in the figures were selected because they are representative of the general behavior of these fission products. As seen in the figures, the concentrations of all nuclides dramatically increased between 1800 to 2000 s. This increase occurred during the period of rapid oxidation and heatup of the fuel to peak temperatures of ~2800 K. Between 2000 and 3000 s, the ^{135}Xe concentration at the detectors decreased somewhat, while the indicated iodine, cesium, and tellurium concentrations increased to their peak values. Beyond 3000 s, the concentrations of ^{131}I, ^{132}Te, and ^{137}Cs remained elevated due to plateout of reactive species on the viewed surfaces of the effluent line walls, whereas the ^{135}Xe concentration decreased. The large decrease in ^{135}Xe concentration between 3300 and 3450 s is probably the result of both decreased release from the bundle and effluent dilution caused by the argon flow rate increase through the bundle at 3280 s.

The on-line concentrations of noble gases (^{85m}Kr, ^{87}Kr, ^{88}Kr, ^{133}Xe, ^{135}Xe, ^{137}Xe, and ^{138}Xe) measured by the mainfloor, steamline, and gasline gamma spectrometers were converted to fractional release rates as part of the effluent transit analysis. Details of the methodology are presented in Appendix G. Fractional release rates for the reactive fission

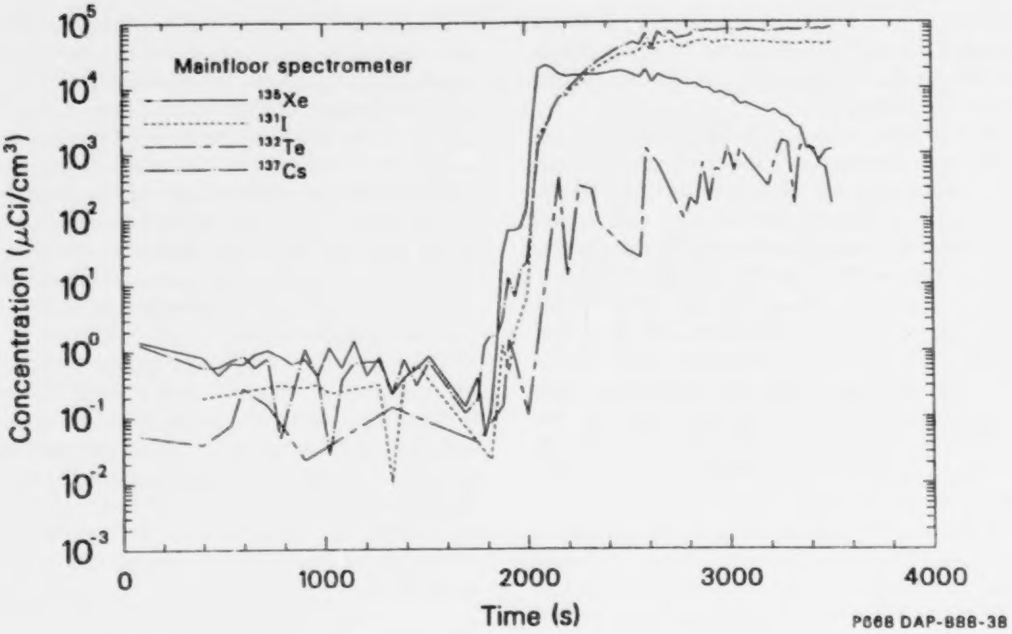

Figure 85. Selected isotopic concentrations at the SFD 1-4 mainfloor gamma-ray spectrometer.

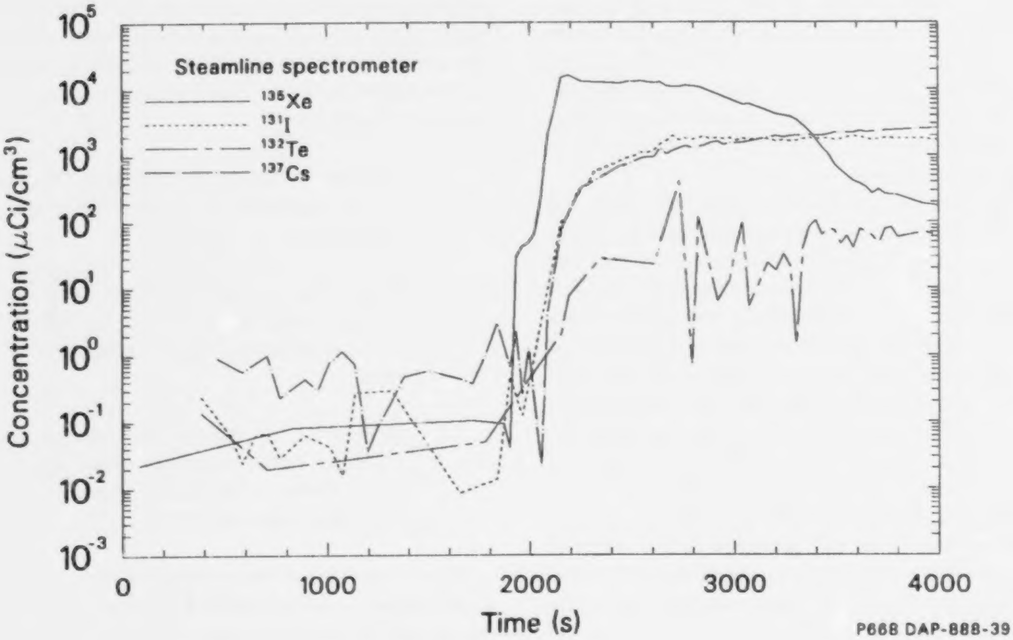

Figure 86. Selected isotopic concentrations at the SFD 1-4 steamline gamma-ray spectrometer.

products (cesium, iodine, tellurium, etc.) were not calculated because deposition and transport effects bias the concentrations measured by the on-line gamma spectrometers.

The fractional release rates for each noble gas isotope were averaged to obtain an average fractional release rate for each spectrometer. Deviations among the isotope-specific fractional release rates were small, indicating internal consistency in the data. The results of the three spectrometers are shown in Figure 87, along with the grab sample results. As can be seen in the figure, the fractional release rate based on the mainfloor spectrometer data is slightly higher than that determined from the steamline or gasline spectrometer data. In general, however, the fractional release rates from all three spectrometers agree, differing by approximately a factor of three, which is within the estimated factor of five uncertainty in the fractional release rate. The time-dependence of the fractional release rates is also very similar, indicating that the delay times to the various locations in the sampling system as calculated by the effluent transit analysis are reasonable. The fractional release rates calculated from grab sample data agree to within an order of magnitude with the on-line spectrometer data. The samples that do not agree with the online data were found to contain significant amounts of water (from condensed steam). The fill time for the grab samplers, which is used to calculate the fractional release rate, was found to be highly uncertain when large quantities of water were collected in the sampler.

The noble gas fractional release rates from the three gamma spectrometers were averaged to obtain the best-estimate fractional release rate for Test SFD 1-4. The result is shown in Figure 88. As with the gross radiation monitors, the fractional release rate curve did not provide any strong indication of the gap release of fission products following ballooning and rupture of the fuel rods because the fuel rods failed over a relatively long time interval, producing a reduced fission product concentration in the line compared with that expected from simultaneous rupture of all the rods. At 1850 s, the noble gas fractional release rate increased at a rapid rate, increasing four orders of magnitude by 2100 s. By this time, the fractional release rate for the noble gases leveled off at a value of $7 \times 10^{-4}\ s^{-1}$. The noble gas fractional release rate remained high during the remainder of the transient and into the cooldown phase of the experiment.

Similar elevated cooldown releases have been noted in previous SFD tests [3,4] with fresh fuel. These releases have been attributed to grain boundary separation and transgranular cracking that exposed new pathways for release from fresh fuel upon cooldown. For the high-burnup fuel in Test SFD 1-4, the cause of the elevated releases upon cooldown is not known. Extensive transgranular cracking was not observed during postirradiation examination. Although limited grain boundary shattering was observed during postirradiation examination, its effects on fission product release should be small, since extensive interconnected porosity already existed in the fuel prior to the SFD 1-4 transient. Cracking was also observed in the molten debris; however, it is believed that volatile fission products were released very quickly during the high-temperature portion of the experiment once the fuel matrix had been destroyed by the dissolution process. Therefore, the cause of the late releases in Test SFD 1-4 does not appear to be related to fuel morphology changes that occurred upon cooldown.

6.2.4 Integral Release Data. Measurements were taken before and after the SFD 1-4 bundle and sampling system were flushed with water to obtain data on fission product release and deposition in the experiment. Before the system was flushed with water, three separate measurements were taken to determine the fractional release of fission products to the collection tank. The fractional release estimates are based on:

1. Samples of the liquid and gaseous contents of the collection tank obtained after the experiment

2. Recirculation of the collection tank liquid and gas space contents past the respective gamma-ray spectrometers after the experiment

3. Integration of the on-line gamma spectrometer measurements from all four (mainfloor, steamline, gasline, and liquidline) spectrometers.

After removal of the deposition rod, effluent grab samples, and the aerosol monitor, temporary piping was installed in place to facilitate flushing of the effluent line and bundle. The effluent line was flushed with water approximately 3 months after the test, on May 15, 1985. Following the effluent line flushing, the bundle and the effluent line were flushed with water on both May 16 and

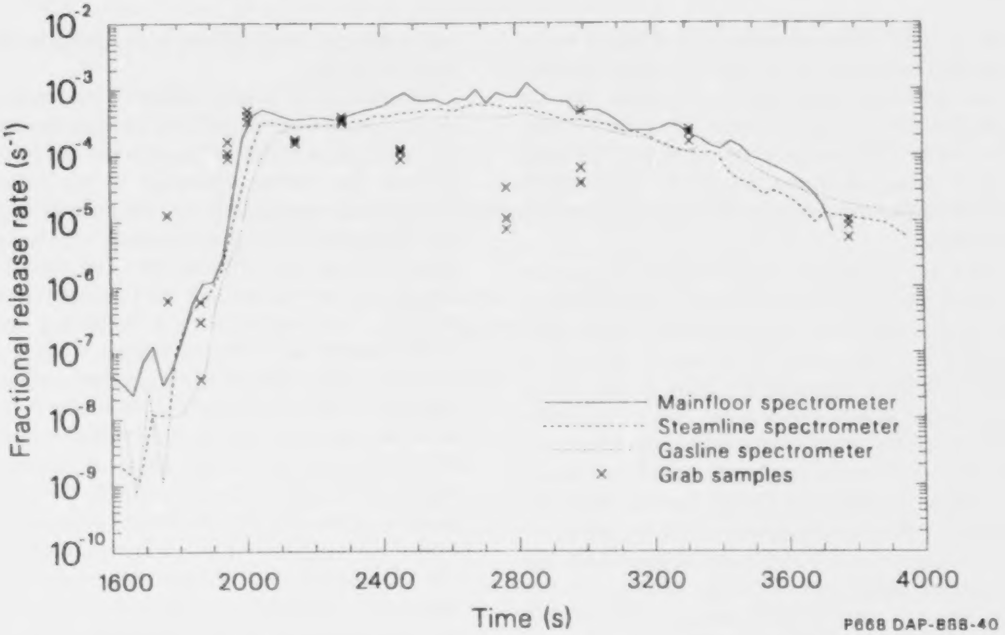

Figure 87. Comparison of fractional release rate from the on-line gamma spectrometers and the grab samples.

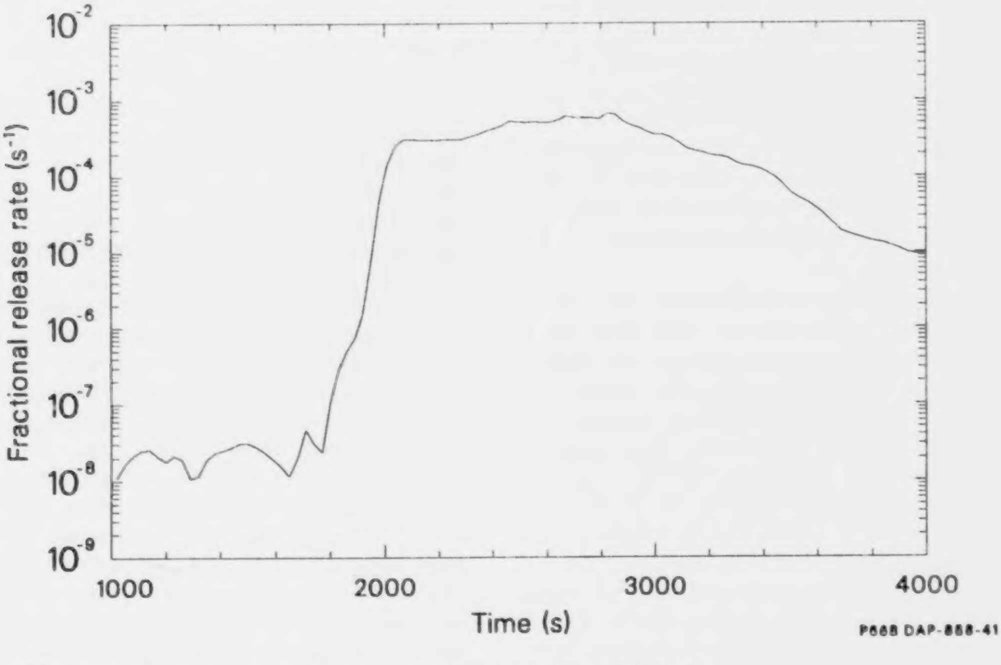

Figure 88. Best-estimate noble gas fractional release rate in Test SFD 1-4.

May 23, 1985. Grab samples of the liquid in the collection tank were taken, and the liquid contents of the collection tank were recirculated past the liquidline gamma spectrometer after each flush. This section will compare the results of all these integral release estimates. Details of the methods used to obtain the integral releases are found in Appendix G.

The noble gas release estimates from integration of the on-line gamma spectrometers, the collection tank grab sample, and recirculation of the gas contents of the collection tank are compared in Table 9. Release fractions for most of the noble gases from these measurements are in relatively good agreement. The uncertainties in these integral releases (~25%) are judged to be somewhat higher than the uncertainties in the gas recirculation and collection tank results because of the greater difficulty associated with the measurement and the uncertainty associated with the effluent transit times used to obtain these results. The integral release results from the mainfloor spectrometer appear to be biased high. The uncertainties in the concentrations of certain isotopes at the mainfloor spectrometer (^{85m}Kr, ^{87}Kr, and ^{88}Kr) were higher than expected because of the higher background on the main floor of the PBF and higher uncertainty associated with the detector calibration. With the exception of the mainfloor spectrometer results, the release fractions for all the noble gas isotopes range from 0.23 to 0.51. The results for ^{85}Kr from the gas recirculation (0.44 ± 20%) and the collection tank gas sample (0.39 ± 15%) are in excellent agreement. As a result, these two values were averaged to give a best-estimate release fraction for ^{85}Kr of 0.415 ± 13%.

Comparison of the integral fission gas release data in Table 9 implies that the releases of long-lived volatile fission product species were greater than those of short-lived species. The release fractions for ^{85}Kr and stable isotopes of krypton and xenon were ~0.50, yet the average release fraction of seven short-lived noble gases from the steamline and gasline spectrometer data was ~0.35. This difference in release is believed to be related to the morphology of the fuel and the location of the fission products in the fuel prior to release.[10] A larger portion of the long-lived species relative to the short-lived species reside at grain boundaries from which release is relatively fast during heatup because of the interconnected porosity in the high-burnup fuel. For the short-lived species, release is much slower because more of the inventory is in the fuel grain and must diffuse to the grain boundary prior to release.

Estimating the bundle release of the reactive fission products is more difficult because these materials can interact with surfaces in the test train and effluent line during transport to the collection tank. Measurements indicate that most of the reactive fission products were deposited in the test train, upper plenum, and effluent line. Less than 1% of the reactive fission products were transported to the collection tank during the test. Following flushing of the bundle and effluent line with water, large increases in the amount of cesium and iodine were measured in the collection tank; however, very little tellurium was measured in the collection tank following flushing. As a result, the total release of the reactive fission products in Test SFD 1-4 was estimated by summing the fraction of material measured in various parts of the effluent sample system (i.e., deposition rod, effluent line piping, collection tank). The results are shown in Table 10. Additional information on the deposition behavior of the reactive fission products before and after flushing is found in Section 7.

The release fractions for ^{131}I and ^{137}Cs are 0.243 ± 19% and 0.51 ± 15%, respectively. In light of the effect of half-life on release, the iodine release fraction in Test SFD 1-4 appears to be low, by about a factor of two. The release fraction for ^{131}I is based on the measured ^{129}I release and its ORIGEN2 inventory. Uncertainty in the ^{129}I measurement is high because the determination requires chemical separation and activation analysis which are complicated procedures especially given the low concentration in the sample. In addition, data[14] developed at the INEL comparing ORIGEN2-predicted fission product inventories with those measured from samples of TMI-2 fuel with known irradiation histories indicate that ORIGEN2-predicted ^{129}I inventory is biased high by about 30%. Based on the combination of these inventory and measurement uncertainties, confidence in the measured iodine release fraction is low.

Very little tellurium was released from the SFD 1-4 bundle. The release fractions for ^{127m}Te and ^{129m}Te are less than 4%. These results are similar in magnitude to those found in Test SFD 1-1.[4] These tellurium release results agree with out-of-pile experiments in which tellurium releases were small in the presence of unoxidized zircaloy due to sequestering and formation of tin and zirconium tellurides in the cladding.[15,16] Much smaller fractions of the lower-volatile fission products and actinides were released during the test.

Table 9. Comparison of noble gas release fractions based on various measurements

		Integration of On-line Gamma Spectrometers[a]				
Isotope	Half Life	Mainfloor	Steamline	Gasline	Collection Tank	Gas Recirculation
^{85}Kr	10.72 yr	—b	—b	—b	0.39 ± 15%	0.44 ± 20%
^{85m}Kr	4.48 h	0.484[c]	0.381	0.338	—b	—b
^{87}Kr	76 min	0.452[c]	0.445	0.365	—b	—b
^{88}Kr	2.84 h	0.655[c]	0.377	0.309	—b	—b
^{133}Xe	5.25 d	—b	0.325	0.285	—b	0.23 ± 18%
^{135}Xe	9.1 h	0.489	0.382	0.349	—b	—b
^{137}Xe	3.84 min	0.417[d]	0.288	0.233	—b	—b
^{138}Xe	14.1 min	0.598[c]	0.465	0.378	—b	--b
Krypton	Stable	—b	—b	—b	0.52 ± 100%	—b
Xenon	Stable	—b	—b	—b	0.51 ± 42%	—b

---

a. Uncertainty estimated to be ~25%.

b. Not detected.

c. Examination of individual data indicates high uncertainty in these spectral data.

d. Short-lived.

Table 10. Best-estimate release fractions for reactive fission products in Test SFD 1-4

Isotope	Release Fraction[a]
High Volatility	
^{129}I	2.42 E − 01 ± 19%
^{131}I[b]	2.43 E − 01 ± 19%
^{134}Cs	3.93 E − 01 ± 14%
^{137}Cs	5.11 E − 01 ± 15%
^{127m}Te	3.16 E − 02 ± 37%
^{129m}Te	3.16 E − 02 ± 37%
^{129}Te	1.10 E − 02 ± 50%
Medium and Low Volatility	
^{103}Ru	6.83 E − 05 ± 56%
^{125}Sb	1.32 E − 03 ± 35%
^{90}Sr	8.83 E − 03 ± 28%
^{154}Eu	7.60 E − 04 ± 40%
^{140}La	7.34 E − 03 ± 46%
^{144}Ce	1.28 E − 04 ± 70%
Actinides	
^{241}Am	4.21 E − 06 ± 47%
^{242}Cm	2.89 E − 07 ± 39%
^{244}Cm	9.22 E − 07 ± 49%
^{239}Pu	1.79 E − 06 ± 44%
^{235}U	3.14 E − 05 ± 42%

a. Represents total release from the bundle following flushing of the system with water.

b. Based partially on ^{129}I results.

6.2.5 Retained Fission Product Results. During postirradiation examination of the SFD 1-4 test bundle, 14 core drilled samples were extracted from areas of interest in the bundle cross sections and analyzed for their retained fission product content. The purpose of the analysis was to obtain information on fission product retention in specific materials or microstructures. The core drilled samples were analyzed by gamma-ray spectroscopy for the gamma-ray-emitting radionuclides; by radiochemical methods for ^{90}Sr; by radiochemical separation and neutron activation analysis for ^{129}I and ^{127m}Te; by neutron activation and delayed fission neutron counting for fissile material (^{235}U and ^{239}Pu); and by inductively coupled plasma (ICP) spectrometry for certain elements, including uranium.

As indicated by the sample morphologies in Table 11, the core drilled samples were obtained from a variety of different posttest bundle structures that had experienced a wide range of estimated peak temperatures. For the purpose of the following discussion, the structures are grouped into three general categories: fuel, control rods, and melts. Fuel samples are defined as samples containing greater than 75 wt% uranium and exhibiting the apparent structure of UO_2 fuel. (Sample M5B is included in this group based on its structure, although the uranium concentration of this sample is low because of a sampling error.) Control rod samples are previously molten metallic materials containing greater than 70 wt% silver. Melt samples are mixed-content previously molten materials.

As explained in Appendix G, adequate prediction of retention percentage required analysis results for ^{90}Sr, ^{235}U, and total uranium in order to estimate a sample burnup value. With an estimate of a sample's burnup, the original fission product inventory could be calculated; and, thus, a retention estimate could be made. The fission product retention estimates for these samples are presented in Table 12. Details of the measurements, the methodology, and the individual sample results are described in Appendix G.

6.2.5.1 Fuel. This group includes two fuel pellet samples, M5B and M10A, and two samples, M7C and M8C, that were identified as previously molten fuel. The retention results for the two pellet samples, M5B and M10A, generally showed complete retention for all fission products other than ^{144}Ce and ^{129}I, which exhibited anomalous results. Complete retention, however, was not noted for the two fuel samples that had melted. On the contrary, generally depleted inventories for all nuclides other than isolated results for $^{154/155}$Eu were measured. Both sample M7C and M8C showed sharply reduced ^{137}Cs retentions of 40% ± 8% and 11% ± 3%, respectively. (The quoted uncertainties are one estimated standard deviation of the retention percentage and are not relative values.) The behavior of the volatile cesium correlated well with expectations of high release from samples that experienced high temperatures. Moderate releases of the intermediate volatile antimony were expected and were noted.

Table 11. Composition and identification of core bore samples analyzed for retained fission product content

Sample Number	Sample Description	Estimated Peak Temperature (K)	Sample Composition[a] (wt.%)								
			U	Zr	Sn	Ag	In	Cd	Fe	Cr	Ni
M7C	Previously molten fuel at 0.39 m	2800	88.8	5.2	0	0.3	2.2	0.9	0.7	0	1.9
M10A	Fuel pellet fragment from 0.85 m	2200	87.9	6.7	0	0.2	0	0.9	2.3	0	2.1
M8C	Previously molten fuel at 0.54 m	2800	78.1	16.4	0	0.5	0	3.8	1.1	0	0
M8B	Previously molten ceramic at 0.54 m	2800	66.5	17.6	0	2.3	0.1	4.6	5.4	0	3.4
M6A	Previously molten ceramic at 0.25 m	2800	61.7	35.9	0	0.3	0	0.8	1.0	0.2	0
M5B	Fuel pellet from rod 4C at 0.17 m[b]	2200	35.9	32.3	0	8.8	0.9	9.3	3.4	0	9.3
M6B	Mixed metallic-ceramic melt at 0.25 m	2800	24	60.7	0.9	7.2	0.3	2.1	2.0	0.7	2.2
M4D	Mixed metallic-ceramic melt at 0.08 m	1700	1.2	56.2	2.7	19.8	4.0	1.1	7.3	2.7	5.1
M2B	Silvery previously molten metallic at −0.09 m	1700	1.1	11	0.4	24.3	4.7	4.4	32.4	10.2	11.5
M3B	Gray mixed phase previously molten metallic at 0.02 m	1700	0.7	54	1.9	28.7	5.3	2.1	4.5	0.9	1.9
M4B	Previously molten control rod material at 0.08 m	1700	0.2	5.6	0	75.4	12.7	5.1	0.6	0.2	0.2
M3C	Unmelted control rod material at 0.02 m	1073	0	0.9	0	75.2	18.4	5.5	0	0	0
M3D	Unmelted control rod material at 0.02 m	1073	0	1.1	0	74.6	18.8	5.5	0	0	0
M2D	Silvery previously molten metallic at −0.09 m	1700	0	98	1.3	0.3	0.1	0	0.2	0.1	0

---

a. Normalized wt.% values. Inductively coupled plasma (ICP) spectrometer results normalized so that the sum of reported sample composition percentages totals 100%.

b. Core bore failed to sample properly, and sample was dropped.

Table 12. Estimated fission product retention percentages[a]

Sample		Peak Temperature (K)	Estimated Burnup (GWd/MtU)	Retention (%)								
Number	Description			^{90}Sr[b]	^{106}Ru	^{125}Sb	^{129}I[c]	^{134}Cs	^{137}Cs	^{144}Ce	^{154}Eu	^{155}Eu
M7C	Previously molten fuel at 0.39 m	2800	37 ± 4	87 ± 15	33 ± 8 (85 ± 48)	± 26 (99 ± 27)	17 ± 4	38 ± 12 (59 ± 27)	40 ± 8	89 ± 24 (260 ± 70)	24 ± 9 (30 ± 17)	34 ± 23 (44 ± 19)
M10A	Fuel pellet fragment from 0.85 m	2200	25 ± 3	93 ± 20	40 ± 26 (81 ± 21)	70 ± 25 (83 ± 22)	6 ± 2	109 ± 51 (170 ± 75)	105 ± 17	221 ± 44 (652 ± 176)	79 ± 41 (96 ± 49)	87 ± 30 (104 ± 43)
M8C	Previously molten fuel at 0.54 m	2800	37 ± 4	97 ± 14	2 ± .6 (5 ± 6)	40 ± 11 (51 ± 14)	5 ± 1	10 ± 4 (18 ± 3)	11 ± 3	250 ± 58 (750 ± 228)	62 ± 23 (72 ± 27)	90 ± 41 (117 ± 51)
M8B	Previously molten ceramic at 0.54 m	2800	48 ± 4	98 ± 8	1 ± .3 (3 ± .7)	15 ± 4 (18 ± 4)	2 ± .4	1 ± .3 (1.6 ± .3)	1.6 ± .3	7 ± 2 (22 ± 4)	1.9 ± .5 (2.2 ± .6)	3 ± 1 (4 ± 1)
M6A	Previously molten ceramic at 0.25 m	2800	32 ± 4	88 ± 16	—[d]	13 ± 2 (16 ± 4)	—[d]	3 ± 1 (5 ± 2)	3 ± .8	9 ± 2 (26 ± 7)	4 ± 2 (5 ± 2)	6 ± 3 (8 ± 4)
M5B	Fuel pellet from rod 4D at 0.17 m[e]	2200	20 ± 2	97 ± 14	166 ± 58	119 ± 24	726 ± 175	140 ± 60	123 ± 19	214 ± 43	144 ± 97	93 ± 25
M6B	Mixed metallic-ceramic melt at 0.25 m	2800	27 ± 4	88 ± 19	152 ± 38 (420 ± 113)	123 ± 33 (146 ± 39)	4 ± 1	3 ± 2 (4 ± 2)	2.1 ± .7	218 ± 67 (671 ± 233)	93 ± 63 (100 ± 44)	107 ± 59 (132 ± 46)
M4D	Mixed metallic-ceramic melt at 0.08 m	1700	7 ± 4	69 ± 65	4042 ± 4063 (8085 ± 16190)	1915 ± 3357 (2198 ± 3758)	—[d]	197 ± 199 (—[f])	33 ± 21	314 ± 192 (1124 ± 1290)	—[e]	221 ± 222 (221 ± 222)
M2B	Silvery previously molten metallic at −0.09 m	1700	33 ± 6	105 ± 29	—[f]	140 ± 94 (166 ± 94)	2655 ± 1095	60 ± 62 (95 ± 96)	72 ± 33	138 ± 53 (403 ± 160)	15 ± 12 (17 ± 16)	31 ± 25 (39 ± 20)
M3B	Gray mixed phase previously molten metallic at 0.02 m	1700	7 ± 2	97 ± 38	—[f]	10938 ± 6923 (17500 ± 14108)	964 ± 528	330 ± 330 (—[f])	468 ± 352	—[f]	—[f]	—[f]

Table 12. (continued)

Sample		Peak Temperature (K)	Estimated Burnup (GWd/MtU)	Retention (%)								
Number	Description			^{90}Sr[b]	^{106}Ru	^{125}Sb	^{129}I[c]	^{134}Cs	^{137}Cs	^{144}Ce	^{154}Eu	^{155}Eu
M4B	Previously molten control rod material at 0.08 m	1700	11 ± 4	90 ± 46	—[f]	—[f]	—[f]	357 ± 359 (535 ± 538)	873 ± 584	—[f]	—[d]	—[d]
M3C	Unmelted control rod material at 0.02 m	1073	<5	—[f]	—[f]	—[f]	—[f]	—[f]	—[f]	—[f]	—[f]	—[f]
M3D	Unmelted control rod material at 0.02 m	1073	<5	—[f]	—[f]	—[f]	—[f]	—[f]	—[f]	—[f]	—[f]	—[f]
M2D	Silvery previously molten metallic at −0.09 m	1700	12 ± 38	100 ± 3	—[f]	201 ± 89 (256 ± 142)	107 ± 42	21 ± 21 (31 ± 32)	76 ± 38	18 ± 6 (55 ± 26)	—[f]	—[f]

a. Quoted uncertainties are one estimated standard deviation developed by propagating quantified errors. Listed retention values are based on a B-300 irradiation cycle. Parenthetical values are based on a B500 irradiation cycle.

b. Complete retention assumed.

c. Poor agreement with the expected inventory of samples M5B and M10A renders the results on these nuclides suspect.

d. Not detectable.

e. Core bore failed to sample properly, and the sample was dropped.

f. Not applicable.

g. Burnup was based on ^{90}Sr content only.

6.2.5.2 Control Rod Materials. Samples M3C, M3D, and M4B consisted mainly of silver, indium, and cadmium control materials. Their fission product content was generally low and in most cases nondetectable. Control rod material samples M3C and M3D showed no detectable concentration of ^{137}Cs or ^{144}Ce. Only sample M4B had entrained or dissolved enough fuel material to allow assignment of a burnup value. It contained more than eight times the ^{137}Cs and between two to seven times the ^{144}Ce that would be expected from its estimated burnup.

All three control material samples had measurable concentrations of ^{90}Sr, ^{127m}Te, and ^{110m}Ag. The ^{110m}Ag is a result of activation of the stable silver. The detection of ^{90}Sr and ^{127m}Te in samples M3C and M3D, and ^{129}I in M3C, while indicative of the presence of some activity, was primarily due to the enhanced detection limit of the radiochemical methods used for these measurements.

These results indicate that while limited mixing of fission product and fuel-bearing materials with relocating molten control materials occurred, the overall effect was slight. No gross retention of fission products by control materials was measured.

6.2.5.3 Melts. The melt materials studied included those classified as ceramic melts, metallic-ceramic melts, and metallic melts. Two of the three metallic melts were further classified as mixed melts, due both to their difference in appearance from a pure silvery metallic and due to their mixed composition.

The two ceramic melts (M6A and M8B) were among the highest temperature structures studied (see Table 11). The elevated peak temperature, coupled with the grain boundary destruction that occurred during melting and oxidation, resulted in very low retention of all the radionuclides measured. Less than 5% of the expected inventory of ^{137}Cs, ^{134}Cs, ^{129}I (in M8B), and ^{154}Eu was found in these samples. No detectable ^{106}Ru was measured in either specimen, and ^{129}I was not detected in M6A. Calculated retention percentages for the remaining nuclides were less than 26%. These results are consistent with the high peak temperature of the samples and the ease of release of fission product material from molten fuel-bearing materials.

The two melts identified as metallic-ceramic melts were very different in their composition and in their estimated peak temperatures. Melt M6B was a metallic-ceramic melt high in uranium and zirconium content. The sample was one of the highest temperature structures studied, having reached a peak temperature of about 2800 K. Melt M4D, on the other hand, was a metallic-ceramic melt low in uranium and high in zirconium and silver, with modest concentrations of stainless steel materials. It was one of the lower temperature melt structures studied, having reached an estimated peak temperature of ≤ 1700 K. These differences in composition and peak temperature were expected to result in significantly different fission product retention behavior; however, the uncertainties in the calculated retention values for the low uranium content sample M4D generally precluded quantitative comparisons on isotopes other than ^{137}Cs. The lower-temperature, lower-uranium-content melt M4D retained 33% ± 21% of its expected ^{137}Cs inventory, while only 2% ± 0.7% of the expected ^{137}Cs inventory of the higher-temperature, higher-uranium-content M6B melt was retained. Complete retention of all other nuclides in both of these melts was implied; however, statistical uncertainties precluded a definitive statement.

Samples M2B, M2D, and M3B were identified as metallic melts. These melts varied significantly in elemental content. All three had relocated from other bundle locations and were among the lowest temperature structures studied, with estimated peak temperatures of ≤ 1700 K. The retention estimates for these samples were difficult to interpret. The high uncertainties were a result of the low uranium content in the samples.

6.3 Model Comparisons

Integral in-pile experiments, like Test SFD 1-4, provide global information on fission product release in severe reactor accidents. However, such experiments have limitations when trying to assess the accuracy of specific models in fission product release codes because of uncertainties in the test thermal-hydraulic and fuel behavior boundary conditions required to perform the analysis. In addition, because deposition prevents accurate time-dependent release measurements for the reactive fission products, such as iodine, cesium, and tellurium, the analysis presented here is restricted solely to fission gas release behavior.

The fission product releases measured in Test SFD 1-4 are compared to calculations using the FASTGRASS,[17] CORSOR,[18] and the Booth diffusional release[19] models in this section. For the CORSOR and Booth calculations, best-estimate and sensitivity calculations have been performed to bound the fission product release estimates and to understand the effect that changes in input variables have on the calculated fractional release rate and the total release.

6.3.1 FASTGRASS Calculations. FASTGRASS[17] is a mechanistic computer code for predicting fission gas and volatile fission product behavior in UO_2 fuels. The version of FASTGRASS used in the SFD 1-4 analysis incorporated a model to account for the effects of liquefaction on fission product release. The model and assumptions used in the calculation and the results of the calculation are presented in this section.

6.3.1.1 Model Description. For the SFD 1-4 FASTGRASS calculation, both the steady-state BR-3 irradiation and the PBF irradiation were modeled. Details of the irradiation histories and the input model are presented in Appendix G.

As discussed in Section 6.2, the integral fission gas release fractions in the experiment (see Tables 9 and 10) suggest that the total release is dependent on the half-life of a given fission gas isotope and the changes in fuel morphology that occurred during the experiment. The location of fission products in the fuel pellet depends on their half-life. The high burnup fuel used in the experiment and the long decay time prior to the SFD 1-4 transient causes only long-lived and stable fission products (i.e. ^{85}Kr, ^{137}Cs, ^{90}Sr, etc) to be present in the fuel. Prior to the time of Test SFD 1-4, some of these long-lived and stable noble gases should have migrated to the grain boundaries via diffusion during the BR-3 irradiation. By contrast, the short- and moderate-lived fission gases produced during the PBF irradiation would primarily reside in the fuel grains. Very little diffusion of these fission gases to the grain boundaries would be expected, due to the low temperature of the irradiation. This mixed irradiation history of the fuel is thought to result in different release timings on heatup of the fuel. The longer-lived and stable fission gas inventory on the grain boundaries should be released quickly during the rapid heatup phase of Test SFD 1-4 because of the extensive interconnected porosity in the high burnup fuel. However, release of the short-lived fission gases would be delayed due to the additional time required to diffuse from the fuel grain to the grain boundary.[4,17] Upon liquefaction and gross dissolution of the fuel matrix, such half-life effects should be less noticeable because release is governed by bubble coalescence and rapid escape from the liquefied fuel. Calculations of fission gas and volatile fission product release from the TMI-2 accident[20] support this claim.

Although half-life differences were observed in the measured integral release fractions, a direct comparison of the differences in measured release timing between the BR-3-generated noble gases and the PBF-generated noble gases cannot be made to test this theory. The on-line gamma spectrometers can generally measure only short- and moderate-lived isotopes because of their large specific activities. However, the release differences were felt to be real, and model changes were made to FASTGRASS to accurately calculate fission product release for isotopes of different half-lives during the experiment. The tellurium release model in FASTGRASS was used to model the release of the PBF-generated noble gases by replacing the tellurium yield with the cumulative yield of the short- and moderate-lived noble gases. Since there are no chemistry calculations in the code for tellurium and tellurium release is based on noble gas diffusivity, this yield substitution allowed accurate modeling of the short- and moderate-lived noble gases as the surrogate tellurium. In this way, the BR-3-generated noble gases and the PBF-generated noble gases could be studied simultaneously.

The fuel was modeled as a series of ten equally spaced axial nodes. The temporal and axial fuel centerline temperature profiles provided to FASTGRASS were the SCDAP/RELAP5 best-estimate temperatures discussed in Section 8. A constant radial temperature gradient of 25 K was assumed throughout the calculation.

Changes in fuel morphology that occurred during Test SFD 1-4 were also modeled in the FASTGRASS calculation. The initial grain size of the fuel was 10 μm. Examination of sibling rods similar to those used in Test SFD 1-4 and cooler portions of the SFD 1-4 rods low in the bundle indicated limited grain growth to $\sim$14 μm following the BR-3 irradiation. Fuel pellets that had experienced the rapid heatup during Test SFD 1-4 showed evidence of grain growth up to $\sim$20 μm (see Appendix I). There was no explicit posttest evidence of fuel oxidation. All of these data dictated that the FASTGRASS empirical grain growth model that is driven only by temperature be used in the calculations. Postirradiation examination indicated that $\sim$18% of the fuel had been dissolved during the test. To account for this amount of fuel dissolution, the two hot test nodes in the FASTGRASS calculation (nodes 5 and 6 between 0.4 and 0.6 m) were assumed to begin to liquefy at 2170 K. At 2650 K, the monotectic temperature at which the solubility of UO_2 in molten zircaloy increases very drastically, the liquefied node was assumed to enter gross dissolution (the recommended default option in FASTGRASS). Release was expected to be very large for temperatures above 2650 K because of bubble coalescence and migration through the liquefied material.

Cooldown of the SFD 1-4 bundle began at ∿3200 s, yet noble gas release rates remained high during the remainder of the experiment. The reason for these elevated releases is not clear (see Section 6.2.3).

6.3.1.2 Steady-State BR-3 Irradiation Results. The calculated steady-state results from FASTGRASS have been compared to measurements from sibling rod I-830 from the B300 batch. FASTGRASS-calculated grain growth ranged from the as-fabricated value of 10 μm in the cooler portions of the rod up to 12.4 μm at the fuel hot spot. This result is in good agreement with the 13-μm grain size measured during postirradiation examination of rod I-830 after the BR-3 irradiation. The FASTGRASS-calculated gap release of fission gases was 2.2%, which is in reasonable agreement with the measured gap inventory of ∿2.5% from rod I-830 which experienced a similar irradiation history.

The distribution of long-lived and stable fission products within the fuel at the end of the BR-3 irradiation is very important to determining their release during the rapid heatup phase of Test SFD 1-4. FASTGRASS calculates that ∿11% of the retained noble gas inventory is on grain faces and edges and 89% is still in the fuel lattice.

6.3.1.3 Transient Noble Gas Release. The FASTGRASS-calculated noble gas release rates for long-lived and short-lived noble gases are plotted along with the on-line gamma spectral measurements in Figure 89. Also noted in the figure are key events that help explain the calculated releases.

The rapid increase in the calculated release for the long-lived noble gases that begins at ∿1500 s and continues until ∿2100 s is due to the rapid release of long-lived gas from the grain boundaries during the initial heatup of the fuel bundle. In contrast, the release rate of the short-lived noble gases is smaller in magnitude and delayed in time. This behavior is a result of the fact that the shorter-lived noble gases must diffuse through the fuel grain before being released via the grain boundary tunnel network that exists in the high-burnup fuel.[17] The short-lived noble gas release rate is in reasonable agreement with the SFD 1-4 fractional release rate data on heatup.

At 2100 s, both calculated release rates show slight changes due to the start of liquefaction at the two hottest nodes in the calculation. The long-lived noble gas release rate shows a decrease because FASTGRASS assumes that release is retarded upon liquefaction as molten material fills the open porosity in the high-burnup fuel. The effect of liquefaction on the release rate is less noticeable for the short-lived noble gases because the major resistance for release is diffusion from the grain to the grain boundary. As a result, the release rate only changes slope at the start of liquefaction. Both calculated release rates increase as temperatures increase and noble gases are released from the liquefied material. FASTGRASS underpredicts the measured short-lived noble gas release rate from the start of liquefaction to the time at which temperatures first exceed that assumed for gross dissolution (∿2250 s).

Rapid increases in release rate for both short-lived and long-lived noble gases are calculated to occur at 2250 and 2450 s. These times correspond to the times at which the two hottest nodes exceeded 2650 K, the assumed temperature at which gross dissolution occurs in FASTGRASS. The calculated rapid release of the gases is due to coalescence and release of grain boundary bubbles from the molten material. Two additional peaks in the calculated short-lived noble gas release rate are noted about 50 to 100 s later. These increases are the result of additional release of short-lived noble gas atoms that were in the solid fuel matrix in the form of small gas bubbles and atoms which require additional time to be released from the molten material. During gross dissolution, FASTGRASS overpredicts the release rate by a factor of two to four.

Differences exist between the calculated and measured short-lived noble gas release rates during the liquefaction and dissolution portions of the experiment. FASTGRASS underpredicts the release rate between the start of liquefaction (T = 2170 K) and the time at which gross dissolution is calculated to occur (T = 2650 K). Following gross dissolution, the calculated release rate exceeds the measured release rate by factors of two to four. These differences are thought to be the result of the discrete nodal representation of the SFD 1-4 fuel bundle and the simple serial

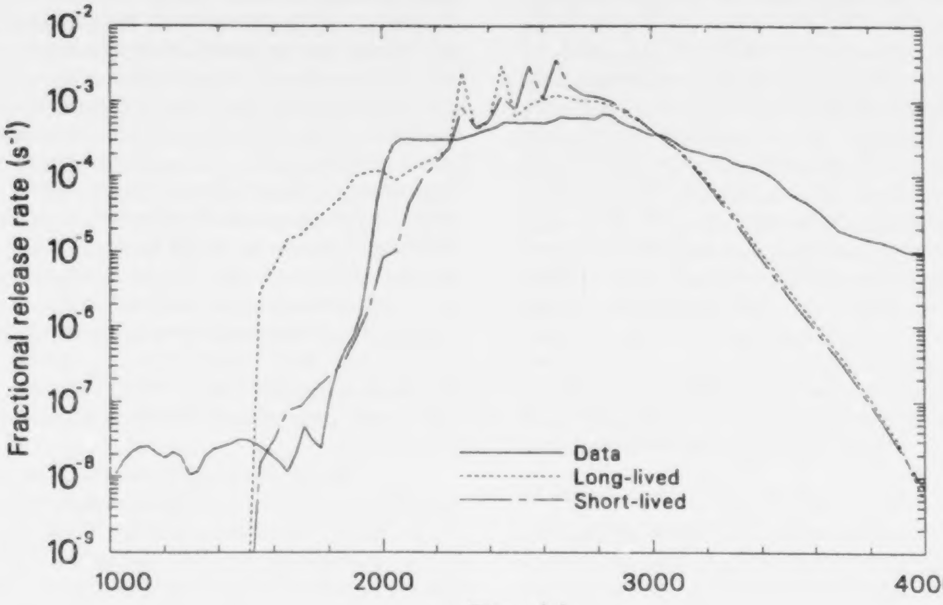

P688 DAP-888-42A

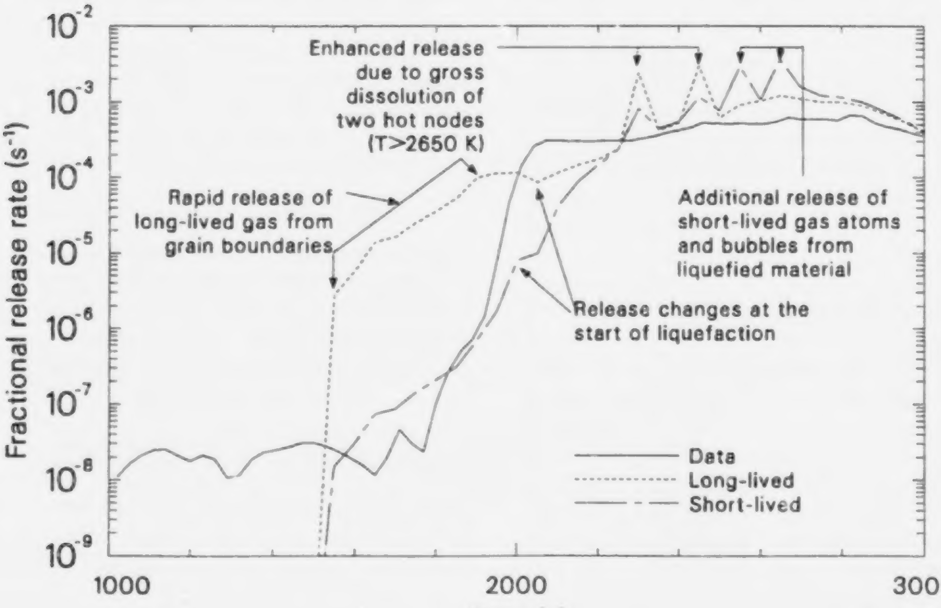

P688 DAP-888-42B

Figure 89. Comparison of FASTGRASS-calculated and measured noble gas release rates in Test SFD 1-4 with key events noted.

representation of the liquefaction and dissolution process used in FASTGRASS.

A schematic of the liquefaction and dissolution model in FASTGRASS is shown in Figure 90. In the model, once a node reaches 2170 K, all open porosity in the node is plugged instantaneously with molten material. In the absence of any temperature increase, this assumption would slow down the release because diffusion in the liquid material is slower than in the gas-filled porosity. The calculated release rates of both long- and short-lived species do not show sustained decreases in release following the onset of liquefaction. Instead, the release rates increase because of rising fuel temperatures which enhance the diffusivities of atoms and bubbles in the liquefied fuel. Upon gross dissolution at 2650 K, a sharp increase in the release is noted because of bubble coalescence and subsequent release. Such sharp discontinuities are not physical.

Examination of out-of-pile experiments[21,22] indicates that liquefaction is a two-stage process. The early stages of liquefaction occur on a very local scale. The liquefaction of UO_2 by molten zircaloy proceeds by the diffusion of oxygen from the UO_2 preferentially along grain boundaries into the zircaloy, leading to reduction of the UO_2 to liquid uranium in the grain boundaries. The boundaries are weakened by this process, allowing the second stage of liquefaction to begin. In the second stage, the grains of UO_2 are separated from the surface of the fuel and are surrounded by molten zircaloy. The high surface area of the individual grains contributes to their rapid dissolution by the zircaloy. As indicated in Figure 90, because a finite amount of time is required for an entire pellet to become liquefied, release from a pellet is determined by three distinct mechanisms which operate in parallel during a severe accident: (a) diffusion from the nonliquefied solid portion of the pellet which is large between 2100 and 2650 K; (b) liquefaction of grain boundaries at the liquefaction front, which would tend to slow down release from the grains; and (c) release from portions of the pellet that have been totally dissolved via bubble coalescence and rise.

Comparison of these two representations of the liquefaction process reveals some shortcomings in the FASTGRASS model. Examination of the out-of-pile experiments on UO_2 dissolution indicates that the liquefaction front associated with destruction of the grain boundaries is a microscopic phenomenon that does not involve a significant amount of the fuel. As a result, it is believed that

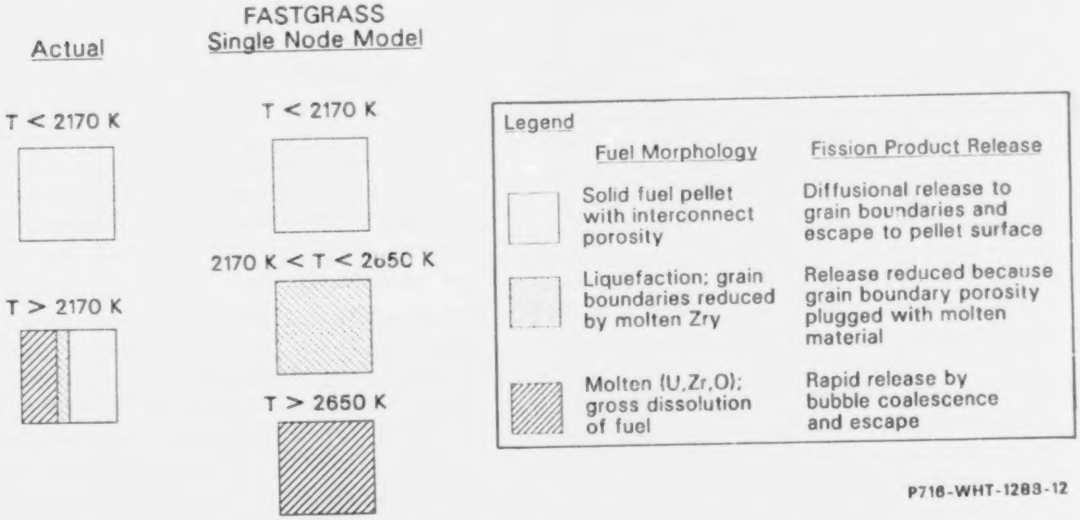
Actual
FASTGRASS Single Node Model
T < 2170 K
T > 2170 K
T < 2170 K
2170 K < T < 2650 K
T > 2650 K
Legend
Fuel Morphology
Fission Product Release
Solid fuel pellet with interconnect porosity
Diffusional release to grain boundaries and escape to pellet surface
Liquefaction; grain boundaries reduced by molten Zry
Release reduced because grain boundary porosity plugged with molten material
Molten (U,Zr,O); gross dissolution of fuel
Rapid release by bubble coalescence and escape
P716-WHT-1283-12

Figure 90. Schematic comparison of FASTGRASS-modeled and actual liquefaction process.

although releases might decrease locally in the region where the grain boundaries are being destroyed, such effects are exceedingly small (and do not need to be modeled) when compared to the releases associated with large-scale gross dissolution and diffusion from the intact regions of the fuel pellet. In addition, the assumption that gross dissolution occurs at temperatures in excess of 2650 K is not supported by the out-of-pile liquefaction data. The temperature at which gross dissolution begins can be as low as 2170 K, depending on the oxygen content of the zircaloy. As a result, rapid release from local dissolved regions of the fuel might be expected at temperatures much lower than 2650 K.

In Test SFD 1-4, the differences in the FASTGRASS-calculated and measured release rates are believed in large part to be due to the node-wide serial representation of the UO_2 liquefaction/dissolution process used in the model. With a finer radial and axial nodal mesh and a change in the input to the FASTGRASS model to allow gross dissolution to occur at a lower temperature, the discrete changes in the FASTGRASS-calculated release rates would be smoothed out over time. Releases during the early stages of liquefaction and dissolution would increase because diffusion would continue from the smaller intact portions of the liquefied nodes and gross dissolution would be allowed for nodes that exceeded 2170 K. Release rates later in time would decrease somewhat because earlier releases during the liquefaction process depleted much of the pellet inventory. This type of behavior would agree better with the SFD 1-4 noble gas release data.

The calculated short- and long-lived noble gas release rates decrease beyond 3000 s as temperatures begin to decrease in the bundle. However, the measured noble gas fractional release rate remained elevated until the experiment was terminated.

The integral release fraction for both long- and short-lived fission gases calculated by FASTGRASS is 0.63, which is higher than the range of 0.25 to 0.51 measured during Test SFD 1-4. The release calculated by FASTGRASS is predominantly from nodes 4 through 9, which experienced high temperatures between 2200 and 3000 s.

6.3.2 CORSOR Calculations. CORSOR[18] is a multinode computer code that estimates fission product release during a severe reactor accident. Release is modeled as the product of a fractional release rate coefficient that is assumed to be a function of local fuel temperature at the node and the nodal inventory of the selected fission product element at a given time.

Two separate CORSOR calculations were performed to bound the release observed in Test SFD 1-4. In the best-estimate calculation, fission product release was calculated using the best-estimate SCDAP/RELAP5 fuel temperatures (see Section 8) and the PBF axial power profile. (The PBF axial power profile was used to simulate the axial fission product distribution of the short- and moderate-lived fission products that were measured on-line during the transient.) In the second calculation, the fuel temperatures were systematically lowered by 15% from the best-estimate SCDAP/RELAP5 temperatures. The 15% decrease was felt to represent the lower bound of uncertainty in the SCDAP/RELAP5 temperature calculations.

6.3.2.1 Noble Gas Release Rate Comparison. The noble gas fractional release rates for the two CORSOR calculations are compared to the measured SFD 1-4 data in Figure 91. The best-estimate CORSOR calculation is in good agreement with the noble gas fractional release rate data on heatup between 1000 and 2000 s. The calculation predicts release slightly earlier (~50 s) than the data. However, the difference is within the 60-s uncertainty in the transit time estimates used to obtain the measured fractional release rate. During the peak of the transient, between 2000 and 3000 s, the CORSOR calculation exceeds the measured release data by almost an order of magnitude. Upon cooldown (>3000 s), CORSOR underpredicts the measured release rate by orders of magnitude.

For the CORSOR sensitivity calculation in which fuel temperatures were 15% lower than those calculated by SCDAP/RELAP5, the release rate on heatup agrees very well with the measured data. However, the time dependence of the release rate during the peak temperature portion of the transient is not well predicted. The peak release rate is delayed somewhat as compared to the best-estimate calculation due to the lower temperatures used in this calculation. As with the best-estimate calculation, the release rate on cooldown is underpredicted by orders of magnitude compared with the SFD 1-4 data.

The lack of measured release rate data for the reactive fission products due to deposition in the effluent sampling system prevents a release rate comparison from being made for these species.

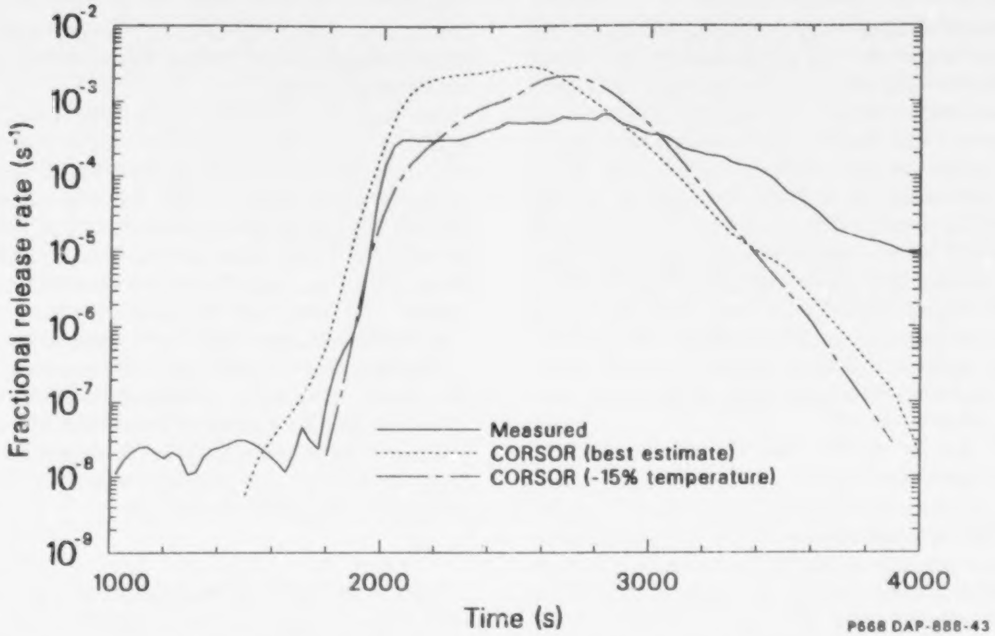

Figure 91. Comparison of CORSOR-predicted and measured noble gas release rates in Test SFD 1-4.

However, integral releases are compared in the next section.

6.3.2.2 Integral Release Comparisons. The integral release predictions for noble gases, cesium, iodine, and tellurium based on the two CORSOR calculations are compared with the integral releases from Test SFD 1-4 in Table 13. As can be seen, the CORSOR integral release fractions of 0.83 (and 0.66 in the sensitivity calculation) are higher than the noble gases, iodine, and cesium released during Test SFD 1-4. The tellurium release, using the zircaloy sequestering option in CORSOR, is overpredicted by about a factor of five in the best-estimate calculation; but in the 15%-lower-temperature case, the agreement is much better. The CORSOR-calculated integral releases are high because the calculated release rates were overpredicted during the peak of the transient.

6.3.3 Booth Diffusional Calculations. Many out-of-pile experiments[23-26] indicate that for temperatures between 1000 K and the start of liquefaction (2170 K), volatile fission product behavior is governed by diffusional release from the ruptured fuel rods. The Booth diffusional release model has been used successfully to describe the release results from experiments conducted in this temperature

Table 13. Comparison of CORSOR-calculated fission product release and Test SFD 1-4 data

Element	SFD 1-4	CORSOR Best Estimate	CORSOR – 15% Case
Noble gas	0.23-0.52	0.83	0.66
Cesium	0.51	0.83	0.66
Iodine	0.24	0.83	0.66
Tellurium	0.03	0.16	0.04

range. The Booth release model has not traditionally been applied to in-pile release experiments because of the effect of additional phenomena (i.e., knockout, recoil, trapping, and resolution) that contribute to fission product release during irradiation. However, for the high temperature and severe conditions that occurred during Test SFD 1-4, diffusion of volatile fission gases from the fuel should dominate the release process until fuel dissolution occurs. As a result, the Booth model has been used to calculate the releases in Test SFD 1-4. A description of the model as it has been applied to Test SFD 1-4 is found in Appendix G.

Many parametric calculations have been performed using the Booth release model in Test SFD 1-4. Four different Arrhenius correlations for the diffusion coefficient were used in the calculations and are listed in Table 14. The Lawrence correlation is based on an extensive survey of out-of-pile xenon release experiments.[27] The survey investigated the influence of several environmental conditions on the diffusional release of fission products, including stoichiometry, burnup, fuel density, power rating, and surface vaporization and sublimation. The data base used in determining this best-estimate diffusion coefficient for xenon included data from postirradiation annealing experiments with fuel densities ranging from 58% to 99% of theoretical, stoichiometry ranging from 1.9 to 2.22, temperatures ranging from 870 to 2470 K, and burnups up to 800 MWd/MtU. In general, this relationship is most applicable for trace-irradiated fuel. The Prussin correlation was also developed from postirradiation annealing of trace-irradiated fuel.[26] The Prussin correlation is expressed in terms of an effective diffusion coefficient, D', which is equal to D/a^2, where a is the equivalent sphere radius of the specimen.

The remaining two correlations are based on fission product release tests performed at Oak Ridge National Laboratory (ORNL) on moderate- to high-burnup fuel.[28] Most of the high-burnup fuel used in the experiments was from the same batch of BR-3 fuel that was used in Test SFD 1-4. It had an average burnup of ~40 GWd/MtU. The moderate-burnup fuel was irradiated in the H.B. Robinson, Oconee, Monticello, and Peach Bottom reactors. The burnup of this fuel varied, but was below 30 GWd/MtU.

In addition to fuel temperature and the diffusion coefficient, a value for the equivalent sphere radius, a, is required in the Booth release model. For the high-burnup fuel used in Test SFD 1-4, the fuel should exhibit significant interconnected porosity. Posttest examination of the fuel in the SFD 1-4 bundle indicates a grain size of about 20 μm. Most of this grain growth is believed to have occurred during the heatup phase of Test SFD 1-4. To account for this change in fuel morphology, the equivalent sphere radius was chosen to be 10 μm.

Base-case and sensitivity calculations have been performed to bound the Booth release predictions. A description of all of the Booth calculations is listed in Table 15. The set of base-case calculations used the diffusion coefficients discussed above, the best-estimate SCDAP/RELAP5 temperature calculations for the fuel bundle, and an equivalent sphere radius of 10 μm. Two sets of sensitivity studies were also performed to study the effects of changes in both temperature and equivalent sphere radius on the release. As with CORSOR, in the temperature sensitivity study, the temperatures were systematically lowered by 15%. In the last set of sensitivity calculations, the equivalent grain size was decreased to 5 μm to model release from fuel in lower-temperature portions of the bundle that may not have experienced the grain growth that was measured posttest. The results of the base-case calculations are compared to the measured noble gas fractional release rate data in Figure 92.

The release timing calculated for the heatup phase of the test (1800 to 2000 s) using the Lawrence correlation is delayed by about 100 s when compared to the data, as expected when applying a correlation developed from low-burnup fuel to the high-burnup fuel in Test SFD 1-4. Although the Lawrence correlation does a reasonably good job at predicting the releases between 2500 and 3000 s, the timing of the release is in general poorly predicted during the peak release period as compared to the other correlations. The Prussin correlation shows somewhat better agreement between 1000 and 2000 s; however, it severely overpredicts release during the peak release period. The releases predicted using the ORNL moderate burnup correlation are also delayed during the heatup as compared to the data. As with the other correlations, the release timing is not in agreement with the data.

The ORNL high-burnup correlation developed from the BR-3 fuel exhibits the best agreement with the measured data. During the heatup phase of the transient, the Booth release rate predictions are in excellent agreement with the SFD 1-4 data. During the peak release period, the release rate is reasonably well predicted, varying at most by a factor of three from the data. These results tend to indicate that the releases measured on heatup in the out-of-

Table 14. Arrhenius parameters for diffusion coefficients used in the Booth release model for Test SFD 1-4

Source	Preexponential Factor D_0 (cm^2/s)	Activation Energy Q (kcal/mole)
Lawrence	7.60 E − 06	70.0
Prussin	3.45 E + 07[a]	127.0
ORNL—high burnup (∼40 GWd/Mt)	7.63 E − 05	73.4
ORNL—moderate burnup	2.00 E − 03	95.7

---

a. Effective diffusion coefficient, $D' = D/a^2$.

pile ORNL tests with BR-3 fuel agree with those measured in the in-pile Test SFD 1-4.

The integral release fractions for all of the base-case calculations are shown in Table 16. As indicated in the table, the release fractions calculated using the various correlations vary within a factor of two. The ORNL high-burnup case agrees very well with the release measured during the test. The large release rates predicted by the Prussin correlation result in a total release fraction of 0.77 which is much larger than the measured data. Although the integral releases calculated with the Lawrence and ORNL moderate-burnup correlation are in good agreement with the data, the timing and magnitude of the calculated release rates do not agree as well with the data as does the ORNL high-burnup calculation. In all of the calculations, the release is dominated by release from the middle third of the

Table 15. Description of Booth release calculations

Case	Temperature	Equivalent Sphere Radius (μm)	Diffusion Coefficient
1	SCDAP/RELAP5[a]	10	ORNL high burnup
2	SCDAP/RELAP5[a]	10	ORNL moderate burnup
3	SCDAP/RELAP5[a]	10	Lawrence
4	SCDAP/RELAP5[a]	—[b]	Prussin
5	SCDAP/RELAP5—15%[c]	10	ORNL high burnup
6	SCDAP/RELAP5—15%[c]	10	ORNL moderate burnup
7	SCDAP/RELAP5—15%[c]	10	Lawrence
8	SCDAP/RELAP5[a]	5	ORNL high burnup
9	SCDAP/RELAP5[a]	5	ORNL moderate burnup
10	SCDAP/RELAP5[a]	5	Lawrence

---

a. Best-estimate SCDAP/RELAP5 fuel temperature.

b. The Prussin correlation is expressed in terms of $D' = D/a^2$. Thus, a is implicit in the formulation.

c. Temperatures were ∼15% lower than the SCDAP/RELAP5 best-estimate temperatures in this calculation.

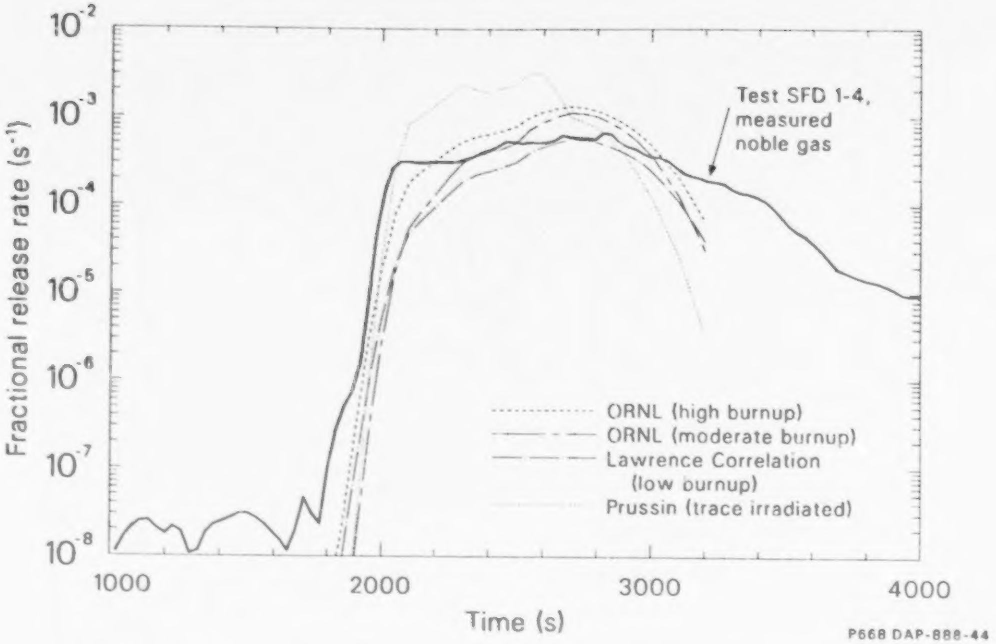

Figure 92. Comparison of Booth base-case-calculated and measured noble gas release rates in Test SFD 1-4.

SFD 1-4 bundle. Examination of the SCDAP/RELAP5 temperature calculations indicate that the peak temperatures are in the middle third of the bundle because of the shift in the axial power profile caused by control rod relocation.

The fractional release rate results from the temperature sensitivity calculations are shown in Figure 93. Lowering the temperatures systematically by 15% causes the predicted release to start much later in time, and the peak releases to fall well below the measured data. The effect of decreasing the effective sphere radius to 5 μm on the calculated fractional release rate is shown in Figure 94. The decrease produces larger release rates than the base-case calculations for the same temperature, resulting in better agreement with the measured fractional release rate data on heatup for all the diffusion correlations; however, they all overpredict the release rate during the peak of the transient by up to an order of magnitude.

Table 16. Calculated release fractions using the Booth model

Diffusion Coefficient[a] Correlation	Release Fraction
Lawrence	0.28
Prussin	0.77
ORNL moderate burnup	0.44
ORNL high burnup	0.54

[a] Using SCDAP/RELAP5 best-estimate temperatures and an equivalent sphere radius of 10 μm.

The results of these calculations indicate that the Booth model can be used to model volatile fission product release during severe reactor accidents. The excellent agreement between the results calculated using the ORNL high-burnup diffusion correlation and the SFD 1-4 data indicates that the release rates on heatup and during the peak release period for the BR-3 fuel are similar in both in-pile and out-of-pile tests. The other correlations tend to either predict a slightly delayed release on heatup, principally because they were developed for low-burnup fuel that does not have significant interconnected porosity, or else they fail to predict the release rate measured during the peak of the transient.

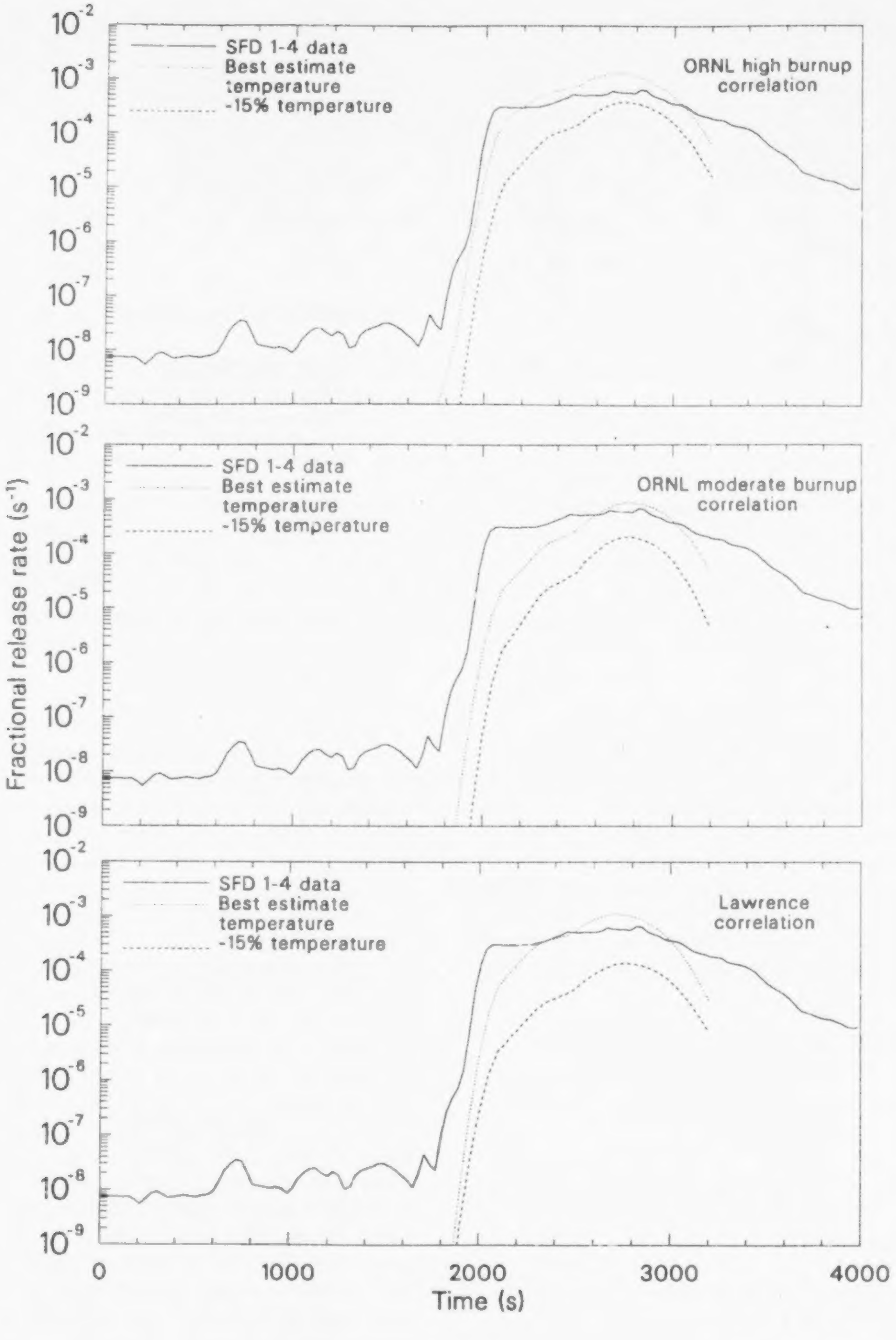

P688-WHT-888-47

Figure 93. Booth temperature sensitivity results, using a = 10 μm.

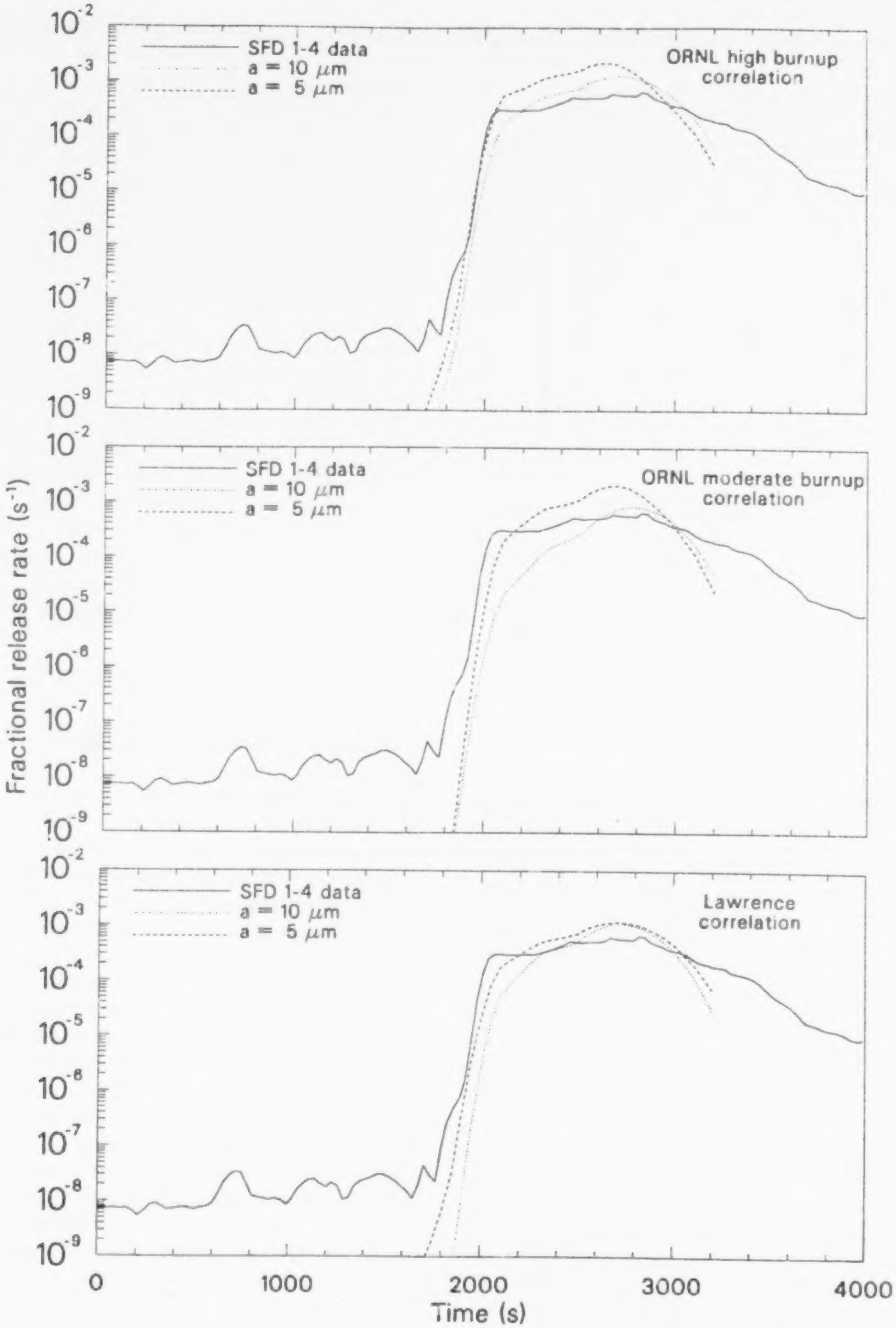

P668-WHT-888-50

Figure 94. Booth "a" sensitivity results, using the SCDAP/RELAP5 best-estimate temperature distribution.

Except for base-case calculation using the ORNL high-burnup correlation, the agreement between the peak release rates predicted by all the diffusion correlations and the measured data is generally poor. This result does not necessarily reflect any shortcoming in the Booth model but rather is probably the result of using the model outside of its range of validity. The Booth model is strictly valid for diffusion from solid UO_2. However, SCDAP/RELAP5 calculations and test data confirm that significant liquefaction and fuel dissolution occurred during the peak release period. The change of phase and the associated loss of geometry induced by the severe conditions in the fuel bundle are believed to change the release characteristics from the fuel during this portion of the transient. It is surprising that the ORNL high-burnup correlation does so well given these changes in fuel morphology that occurred during the high-temperature phase of Test SFD 1-4. No attempt was made to predict with the Booth model the elevated releases observed on cooldown in Test SFD 1-4.

6.4 Summary

A variety of measurements were made to characterize fission product release and retention in Test SFD 1-4. Measurements made by the on-line gamma spectrometers indicate that noble gas release began at ∿1700 s. The fractional release rate increased dramatically between 1800 and 2100 s as bundle temperatures were driven above 2100 K. Between 2100 and 3000 s, significant liquefaction and dissolution is thought to have occurred. During this portion of the transient, the fractional release rate was relatively constant. Beyond 3000 s, release rates decreased somewhat, but remained elevated during the remainder of the transient.

Integral releases of the noble gases ranged from 23 to 52%. Releases of iodine and cesium were 24 and 51%, respectively, whereas only 3% of the bundle inventory of tellurium was released. Most of the released iodine, cesium, and tellurium was deposited within the test train, upper plenum, and effluent line. Iodine and cesium were later washed from the system surfaces following flushing and measured in the collection tank. System flushing removed very little of the deposited tellurium. Lesser amounts of the low-volatility fission products (strontium, barium, lanthanum, europium, and cerium) were released during the experiment.

Comparison of the integral release data suggests that the releases of long-lived volatile fission product species are greater than those of short-lived species. The release fractions for ^{85}Kr and stable xenon and krypton isotopes were ∿0.5, yet the average release of seven short-lived noble gases was ∿0.35. This difference in release is believed to be related to the morphology of the fuel and the location of the fission products in the fuel prior to release. A larger proportion of the long-lived species relative to the short-lived species reside at grain boundaries from which release is relatively fast during heatup because of the interconnected porosity in the high-burnup fuel. For the short-lived species, release is much slower because more of the inventory is in the fuel grain and must diffuse to the grain boundary prior to release.

Calculations of fission gas release using CORSOR, FASTGRASS, and Booth-type release models have provided additional insight into the physical phenomena governing fission product release during Test SFD 1-4 and the accuracy of these models for source term calculations. All of the calculations did a reasonable job of calculating the release rates measured on heatup in Test SFD 1-4. The CORSOR calculation agreed much better with the heatup release in Test SFD 1-4 with high-burnup fuel than it did with the heatup release measured in Test SFD 1-1 with low burnup fuel.[4] The Booth model that used the diffusion coefficient derived from ORNL release tests using similar fuel provided the best agreement with the release measured during heatup. The FASTGRASS calculations indicated that release rates on heatup for short- and long-lived species should be different. Each of the three models overpredicted the measured releases during the high-temperature portion of the test, when significant fuel liquefaction and dissolution were occurring. All of the models failed to account for the sustained releases measured during the cooldown phase of the test.

7. FISSION PRODUCT AND AEROSOL TRANSPORT BEHAVIOR

An additional objective of Test SFD 1-4 was to study fission product and aerosol transport under severe accident conditions. This section presents fission product and aerosol test data, as well as engineering and computer code calculations performed to explain the fission product and aerosol behavior observed in the experiment. Section 7.1 describes the on-line aerosol monitor and grab sample measurements. The fission product and bundle material deposition measured in the upper plenum is reviewed in Section 7.2. Section 7.3 presents engineering calculations that describe the aerosol generation, transport, and deposition behavior of the principal aerosol material released from the bundle and the number concentration, mass concentration, and size of the aerosol as determined from the aerosol measurements. The fission product and aerosol behavior during Test SFD 1-4, as calculated by the fission product transport code PULSE, is discussed in Section 7.4. The aerosol data and the results of the calculations are integrated into an interpretation of aerosol behavior for Test SFD 1-4 in Section 7.5.

7.1 Aerosol Measurements

The on-line aerosol monitor, installed downstream of the mainfloor gamma spectrometer, was a fiber-optic, light-attenuation device that included a specially designed spool piece in the effluent line. The monitor was designed to measure the attenuation of a light beam resulting from aerosols in the effluent stream. The spool piece provided two different light beam path lengths (1 and 4 cm) to monitor a wide range of aerosol particle concentration. Details of the design are given in Reference 7. The responses of the 1-cm and 4-cm cells are shown in Figures 95 and 96. The scale on the y-axis is percent transmission; higher aerosol densities correspond to lower transmission percentages. The methodology used to obtain aerosol concentrations from the cell responses is discussed in Section 7.3.5 and Appendix H.

In addition to the on-line aerosol monitor, a series of six filtered effluent samplers, located immediately downstream of the aerosol monitor, were used to collect aerosol samples for posttest characterization of the time-dependent elemental composition and size distribution of the aerosol. These samplers were actuated remotely at different times during the experiment to collect a portion of the effluent. A filter was installed at the entrance of the sampler to trap aerosol material. The results of radioisotopic and elemental analysis of these filters and the time at which the samples were acquired are listed in Table 17. The sample times are plotted relative to the aerosol signal from the 1-cm cell in Figure 97. Because these samples may not represent the total quantity of material collected on the filters, the results were converted to mass percent of each element and/or isotope to obtain qualitative data on the relative composition of the aerosol and are shown in Table 18. The elemental data indicate that the aerosol collected on the first filter was predominantly tellurium and tin, with trace amounts of zirconium. During the remainder of the experiment, the aerosol that was collected was predominantly tin and cadmium. Smaller quantities of silver and zirconium were also found on the filters. Isotopic analysis of the filters revealed the presence of ^{137}Cs, ^{134}Cs, ^{110m}Ag, ^{114m}In, ^{131}I, and ^{129m}Te.

SEM photographs of portions of the six effluent filters are shown in Figures 98 through 100. Various magnifications of a photograph of material found on filter 6 is shown in Figure 101. Both needle-like crystals and spherical particles can be seen in the figures. The needle-like shape is similar to alkali halide "whiskers," a form commonly produced by vapor deposition at temperatures below the melting point. The spheres are most likely aerosol particles that formed upstream when the material was liquid and subsequently solidified during transport to the filter. The particles collected on the filters were generally spherical in shape and < 1 μm in diameter. Results of particle size analysis on all the filters are listed in Table 19. The diameter of average mass varied between 0.45 and 0.98 μm. The geometric mean diameter varied between 0.29 and 0.56 μm.

7.2 Deposition Measurements and Analysis

The SFD 1-4 upper plenum consisted of a volume immediately above the fuel termed the heat shield and an effluent tube that contained a 4.17-m-long deposition rod. The rod included 20 coupon holders, each of which housed two deposition coupons. The lower half of the deposition rod and effluent tube was heated to a temperature of between 700 and 800 K. The remainder of the rod

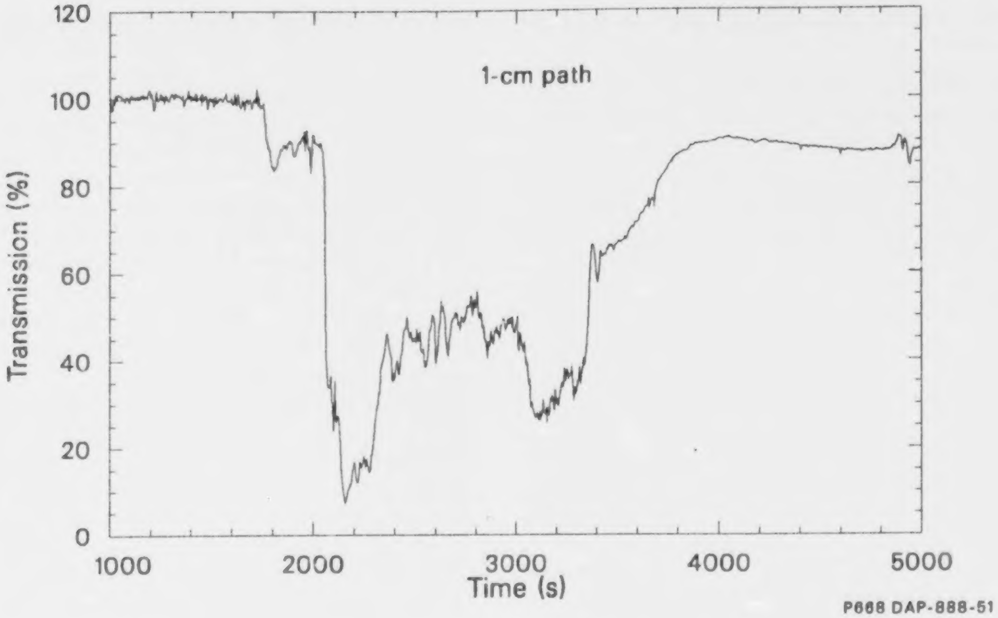

Figure 95. Aerosol monitor response in Test SFD 1-4 from the 1-cm path detector.

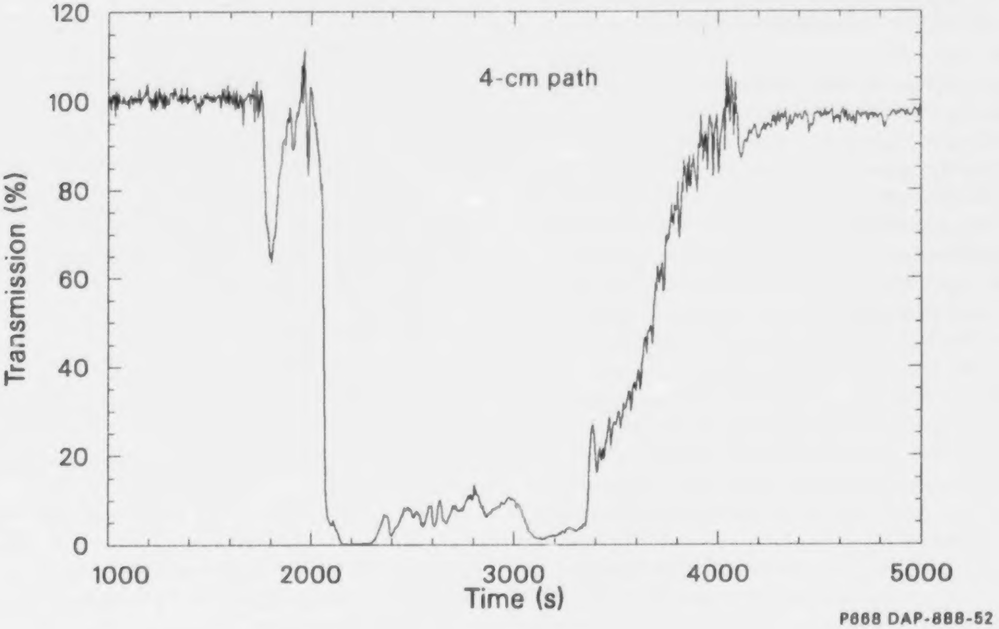

Figure 96. Aerosol monitor response in Test SFD 1-4 from the 4-cm path detector.

Table 17. **Radioisotopic and elemental analysis of effluent sample filters**

	Sample Number and Time					
Isotope (μCi/Sample)[a]	FEF-1 (1950 s)	FEF-2 (2040 s)	FEF-3 (2100 s)	FEF-4 (2385 s)	FEF-5 (2850 s)	FEF-6 (3060 s)
^{110m}Ag	9.7 E−01	1.5 E+00	2.0 E+00	2.6 E+00	5.8 E+00	1.6 E+01
^{114m}In	3.2 E+01	3.9 E+01	5.2 E+01	—	3.3 E+01	1.1 E+02
^{129m}Te	4.3 E+01	8.7 E+01	1.3 E+02	7.2 E+01	2.0 E+02	6.0 E+02
^{131}I	3.4 E+02	2.1 E+03	2.0 E+03	8.5 E+02	1.3 E+03	3.1 E+03
^{134}Cs	1.8 E+02	8.1 E+02	2.9 E+02	3.4 E+02	2.6 E+02	4.2 E+02
^{137}Cs	8.3 E+02	3.7 E+03	1.3 E+03	1.5 E+03	1.2 E+03	1.9 E+03
Element (μg/Sample)						
Ag	2.4 E+01	3.0 E+01	4.0 E+01	4.7 E+01	3.5 E+01	1.2 E+02
In	<2.4 E+02	<2.4 E+02	<2.4 E+02	<2.4 E+02	<2.4 E+02	<2.4 E+02
Cd	<1.8 E+01	9.6 E+01	7.8 E+02	7.0 E+02	3.8 E+02	3.8 E+02
Sn	9.1 E+02	1.2 E+03	1.1 E+03	1.0 E+03	1.2 E+03	9.0 E+02
Zr	7.1 E+01	6.0 E+01	7.2 E+01	<4.8 E+01	<4.8 E+01	7.2 E+01
Te	2.8 E+03	<9.7 E+02	<9.7 E+02	<9.7 E+02	<9.7 E+02	<9.7 E+02

---

[a] All samples were decay-corrected to February 7, 1985.

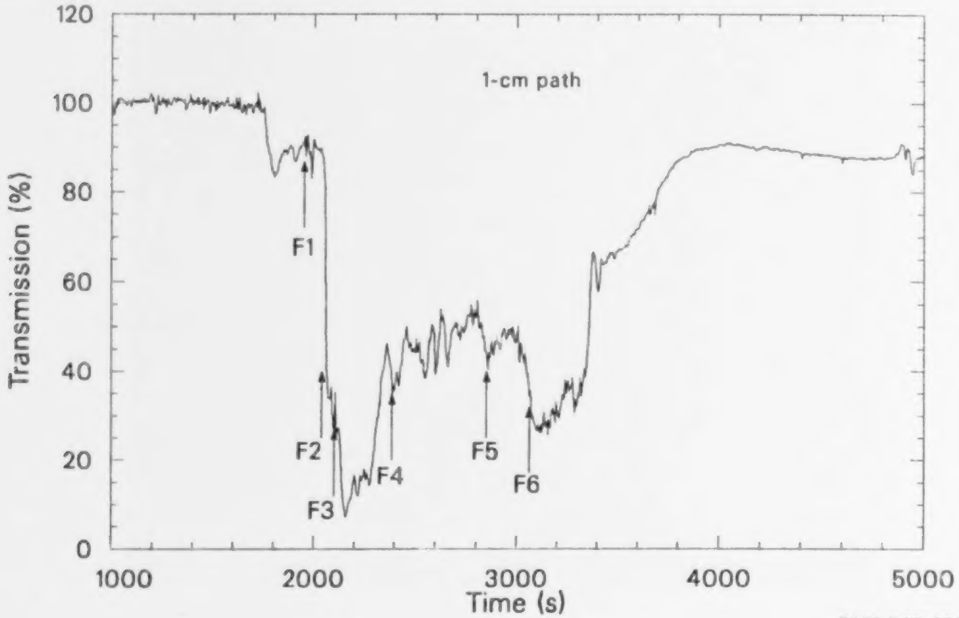

P668 DAP-888-53

Figure 97. Aerosol monitor response in Test SFD 1-4 from the 1-cm path detector with filtered effluent sampling times indicated.

Table 18. Aerosol composition based on the effluent sample filter results (wt.%)

Sample	Sampling Time (s)	Ag	In	Cd	Sn	Zr	Te	^{137}Cs
FEF-1	1950	0.6	—[a]	—[a]	24.7	1.9	73.1	0.3
FEF-2	2040	2.1	—[a]	6.8	83.7	4.3	—[a]	3.0
FEF-3	2100	2.0	—[a]	38.8	54.9	3.6	—[a]	0.8
FEF-4	2385	2.6	—[a]	38.6	57.8	—[a]	—[a]	1.0
FEF-5	2850	2.2	—[a]	24.2	72.7	—[a]	—[a]	0.8
FEF-6	3060	8.0	—[a]	25.6	60.0	4.8	—[a]	1.5

a. Below detection limits.

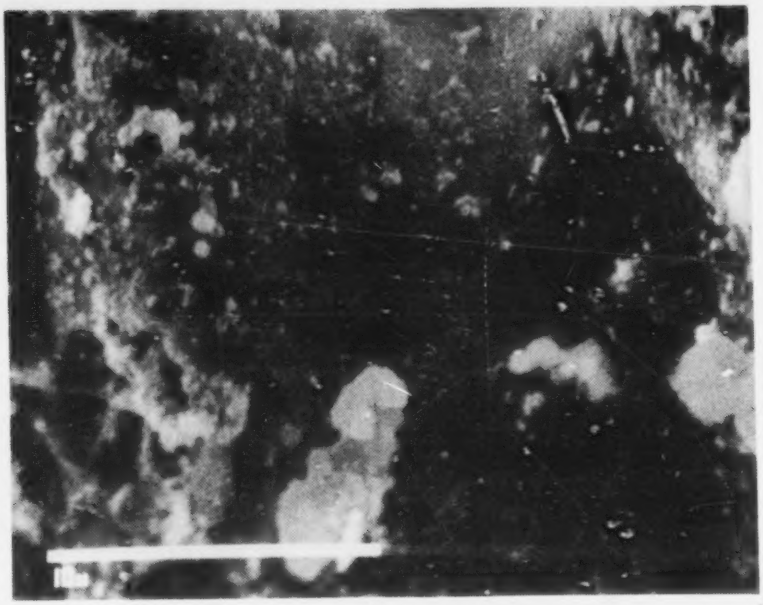

(a) Effluent filter FEF-1

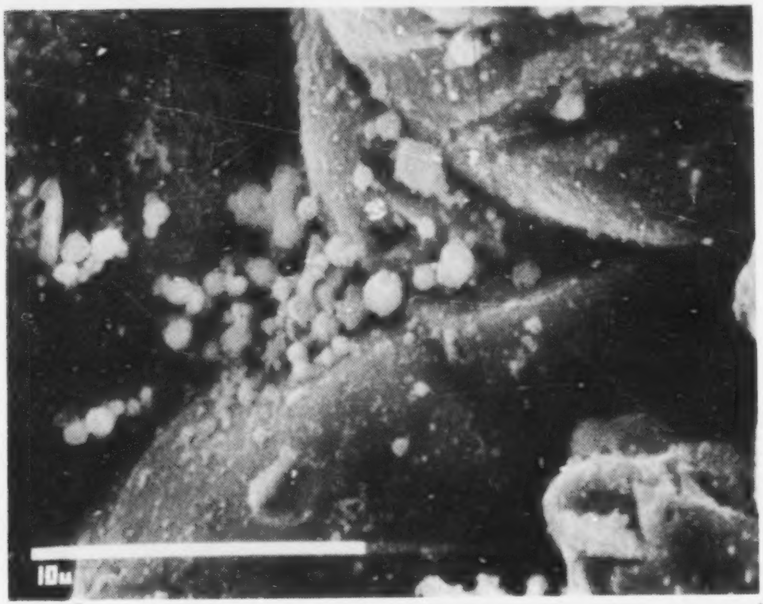

(b) Effluent filter FEF-2

Figure 98. SEM photomicrographs of SFD 1-4 effluent filters FEF-1 and FEF-2.

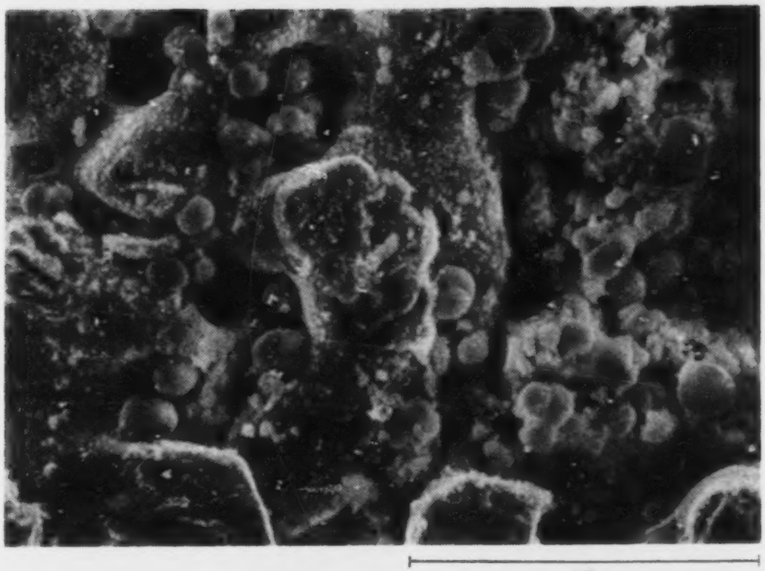

(a) Effluent filter FEF-3

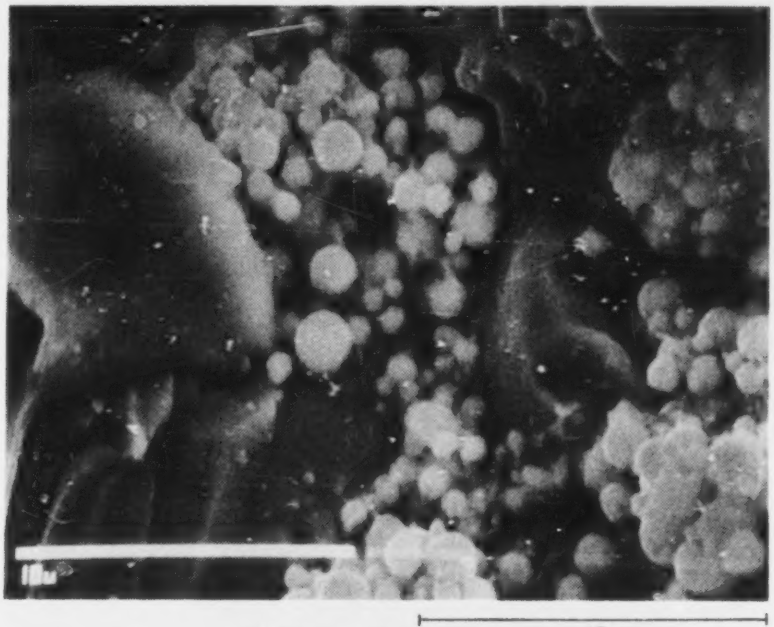

(b) Effluent filter FEF-4

Figure 99. SEM photomicrographs of SFD 1-4 effluent filters FEF-3 and FEF-4.

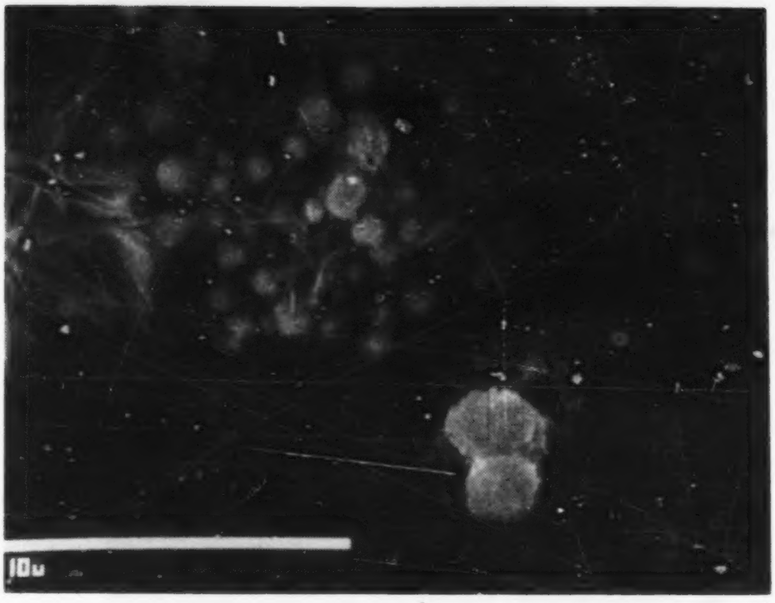

(a) Effluent filter FEF-5

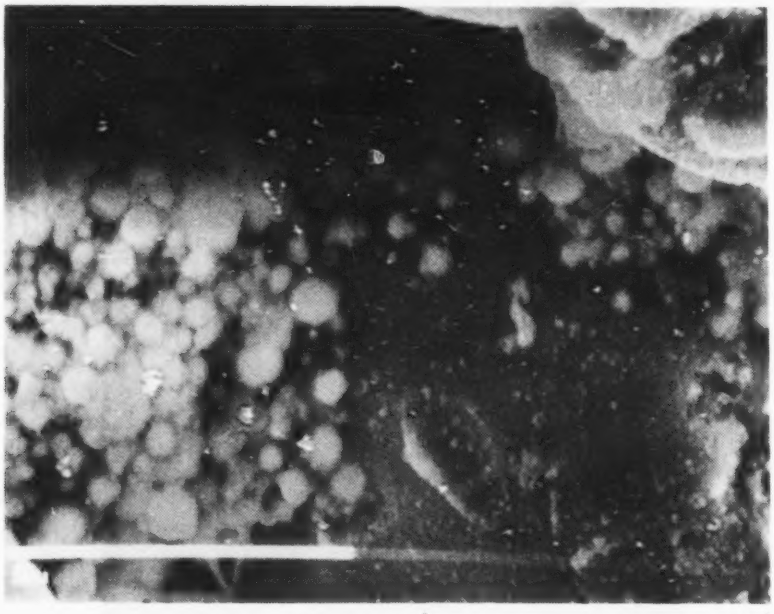

(b) Effluent filter FEF-6

Figure 100. SEM photomicrographs of SFD 1-4 effluent filters FEF-5 and FEF-6.

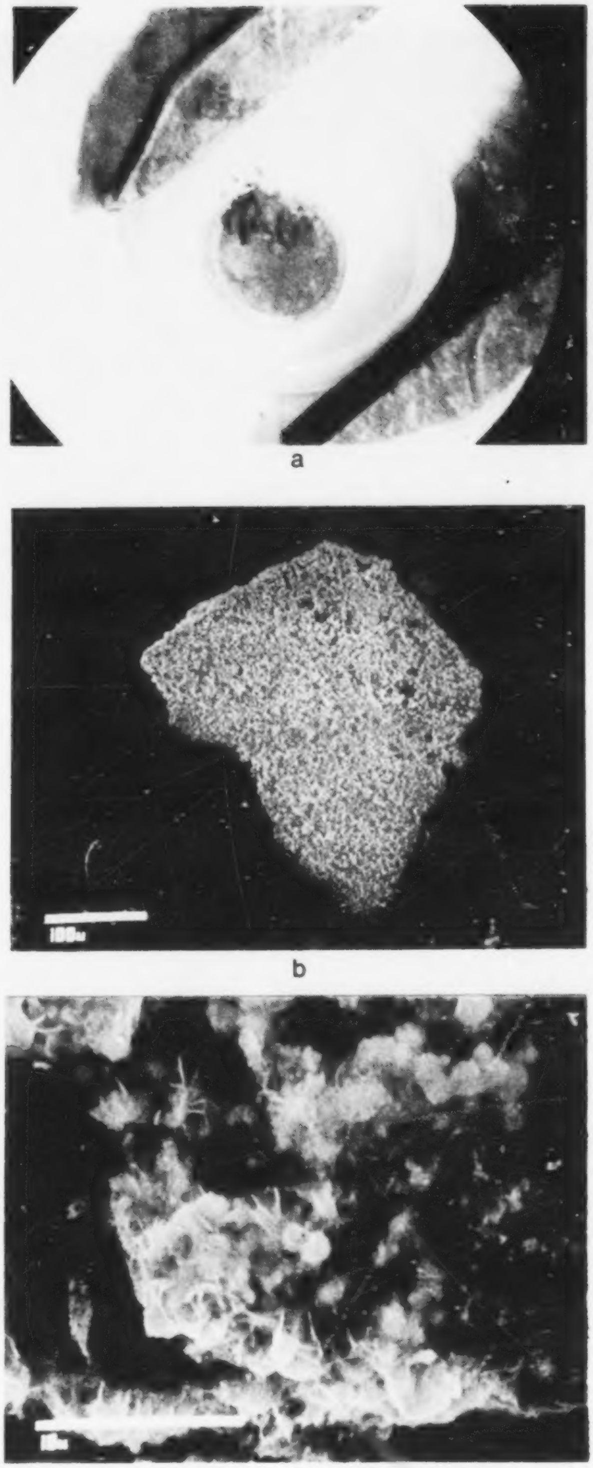
a
100µ
b
10µ
c

Figure 101. Photographs of materials removed from SFD 1-4 effluent filter FEF-6 (a) and examined by SEM (b and c).

Table 19. Results of particle size analysis of effluent filters

Sample	CMD[a] (μm)	AMD[b] (μm)	MMD[c] (μm)	GMD[d] (μm)	d_m[e] (μm)	σ_g[f]
FEF-1	0.34	1.34	2.24	0.29	0.64	1.60
FEF-2	0.39	1.11	1.48	0.32	0.65	1.73
FEF-3	0.70	1.34	1.52	0.56	0.98	1.98
FEF-4	0.44	0.99	1.14	0.33	0.64	1.79
FEF-5	0.58	1.53	1.92	0.44	0.94	2.06
FEF-6	0.37	0.56	0.67	0.33	0.45	1.52

a. Count-mean diameter (CMD) = $\frac{1}{N}\Sigma n_i d_i$,

where

n_i = number of particles of diameter d_i, and

N = total number of particles.

b. Area mean diameter (AMD) = $\frac{\Sigma n_i d_i^3}{\Sigma n_i d_i^2}$.

AMD is useful in calculating the cross-sectional area in light extinction studies.

c. Mass mean diameter (MMD) = $\frac{\Sigma n_i d_i^4}{\Sigma n_i d_i^3}$.

MMD is useful in aerosol sedimentation and transport analysis.

d. Geometric mean diameter (GMD) = $\bar{d}_g \left(d_1{}^{n_1} d_2{}^{n_2} \ldots d_i{}^{n_i} \right)^{1/N}$ or $\ln \bar{d}_g = \frac{\sum n_i \ln d_i}{N}$.

GMD represents the size occurring with the greater frequency.

e. Diameter of average mass (d_m = $\left(\frac{\Sigma n d^3}{N}\right)^{1/3}$.

f. The geometric standard deviation is given by $\ln(\sigma_g) = \left\{\frac{\Sigma n_i(\ln d_i - \ln \bar{d}_i)^2}{N}\right\}^{1/2}$,

where σ_g represents the spread in frequency distribution.

and the effluent tube up to the aerosol monitor was insulated but unheated (except for a heated section at the mainfloor spectrometer at the aerosol monitor inlet) and remained at about 600 K during the transient. (Schematics of the deposition rod and the effluent tube are shown in Figure 5.) The tops of the coupon holders and the surfaces of the 40 deposition coupons, the heat shield, and effluent tube were analyzed to characterize the fission product and aerosol deposition on horizontal and vertical surfaces. Some surfaces downstream of the aerosol monitor were also examined prior to flushing. This section will discuss the deposition measurements and the integral deposition in the SFD 1-4 sampling system.[a]

7.2.1 Deposition Measurements. Posttest photographs of the deposition rod indicate that a significant amount of material deposited on the rod. Specifically, large solid deposits of material were found on the upper horizontal surfaces of coupon holders CH-1 through CH-15. A photograph of the deposit at CH-12 is shown in Figure 102.

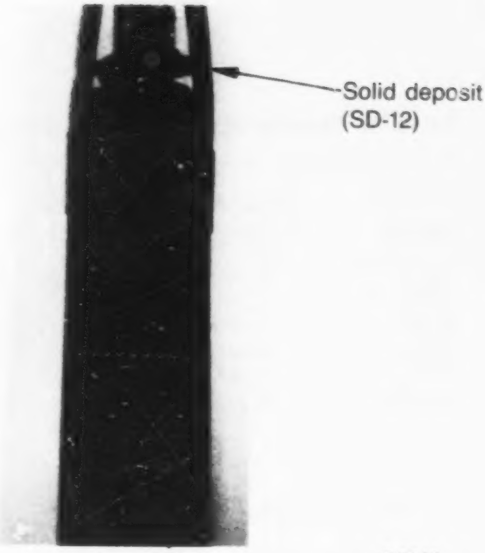

7-9013

Figure 102. Photograph of the cohesive deposit (SD-12) found at coupon holder 12. (The deposit has been raised off the surface for the photograph.)

Various analytic techniques were used to quantify and characterize the deposition on the surfaces of the SFD 1-4 sampling system. Gamma spectroscopy, radiochemical analysis, neutron activation, and alpha analysis were used to measure the radioactive species ^{137}Cs, ^{131}I, ^{129}I, ^{127m}Te, ^{90}Sr, ^{140}Ba (^{140}La), ^{154}Eu, and ^{244}Cm. Inductively coupled plasma spectrometry was used to determine the deposition of elemental species such as silver, cadmium, tin, and zirconium.

Plots of the radioactivity surface concentration for ^{137}Cs, ^{131}I, ^{129}I, ^{127m}Te, ^{90}Sr, ^{140}Ba (^{140}La), ^{154}Eu, and ^{244}Cm are shown in Figures 103 through 110. (Results for ^{131}I were estimated from measured ^{129}I data.) The data for ^{137}Cs have the highest confidence, since they were measured in-situ in the hot cell prior to disassembly and handling. The data for all the remaining radioactive species except ^{137}Cs have been corrected for losses due to remote handling and disassembly of the deposition rod posttest. As a result, the uncertainty in these data is estimated to be between a factor of 2 and 10. The measured mass surface concentrations for silver, cadmium, tin, and zirconium are plotted in Figures 111 through 114. Both the isotopic and elemental concentration data provide insight into aerosol transport and deposition behavior.

The ^{137}Cs deposition data in Figure 103 indicate a sharp increase in deposition at 1.33 m between the heat shield and the heated portion of the upper plenum. The deposition on the horizontal surfaces is lower than on the vertical surfaces between 1.33 and 1.57 m—the tip of the deposition rod and coupon holder 2. In the heated plenum region between 1.8 and 3.65 m, the vertical deposition is roughly uniform; and the deposition on the horizontal surfaces is a factor of 2 to 7 greater than the deposition on the vertical surfaces. Downstream of the heated upper plenum beyond 3.65 m, the horizontal and vertical deposition decreases by about an order of magnitude; and no differences between horizontal and vertical surface deposition are observed. The ^{137}Cs deposition measured on the horizontal surfaces of the deposition rod is associated with the cohesive solid deposits.

The deposition data for ^{131}I, ^{129}I, and ^{127m}Te in Figures 104 through 106 are more difficult to interpret. Remote disassembly of the deposition rod resulted in material being lost from the rod surfaces. Estimates have been made to correct for these losses; however the uncertainty is still large. Despite this fact, it is clear that the deposition for

---

[a] Additional information about off-line fission product release and deposition measurements is found in the following EG&G limited-distribution report: K. Vinjamuri et al., *Severe Fuel Damage Test 1-4 Data Report*, September 1987.

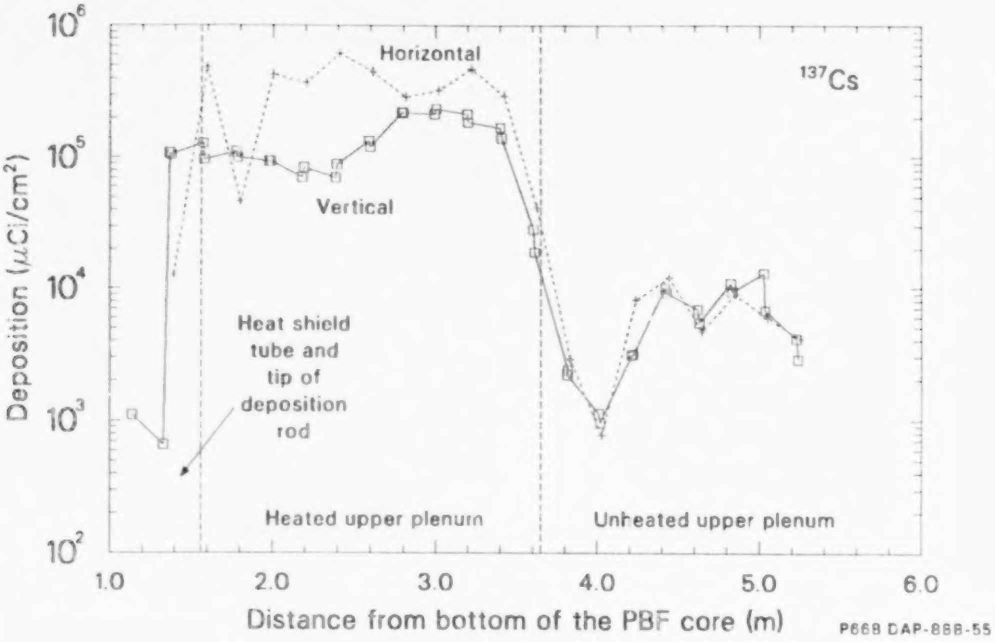

Figure 103. A comparison of ^{137}Cs deposition on vertical and horizontal surfaces of the SFD 1-4 deposition rod.

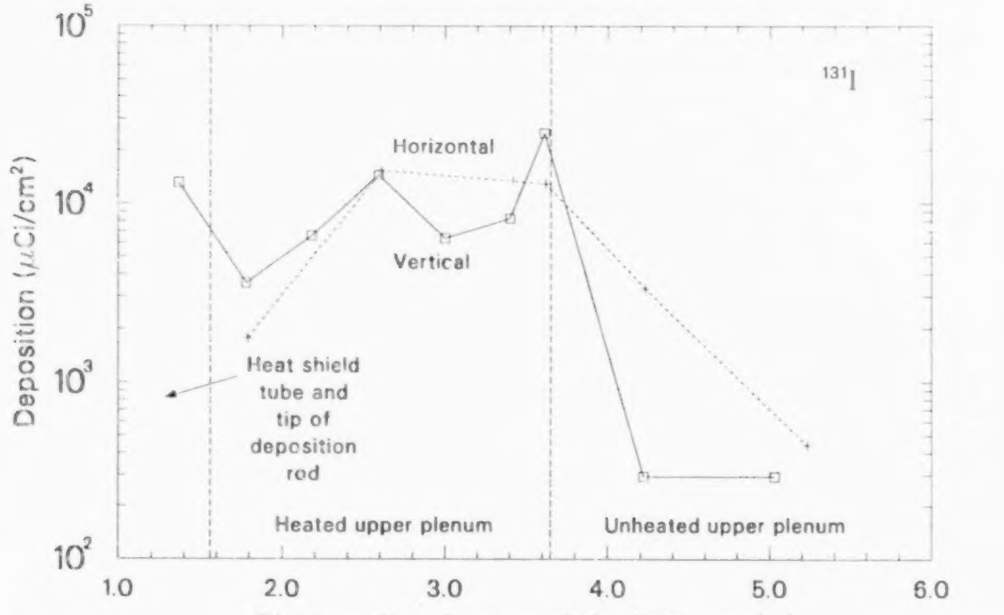

Figure 104. A comparison of ^{131}I deposition on vertical and horizontal surfaces of the SFD 1-4 deposition rod.

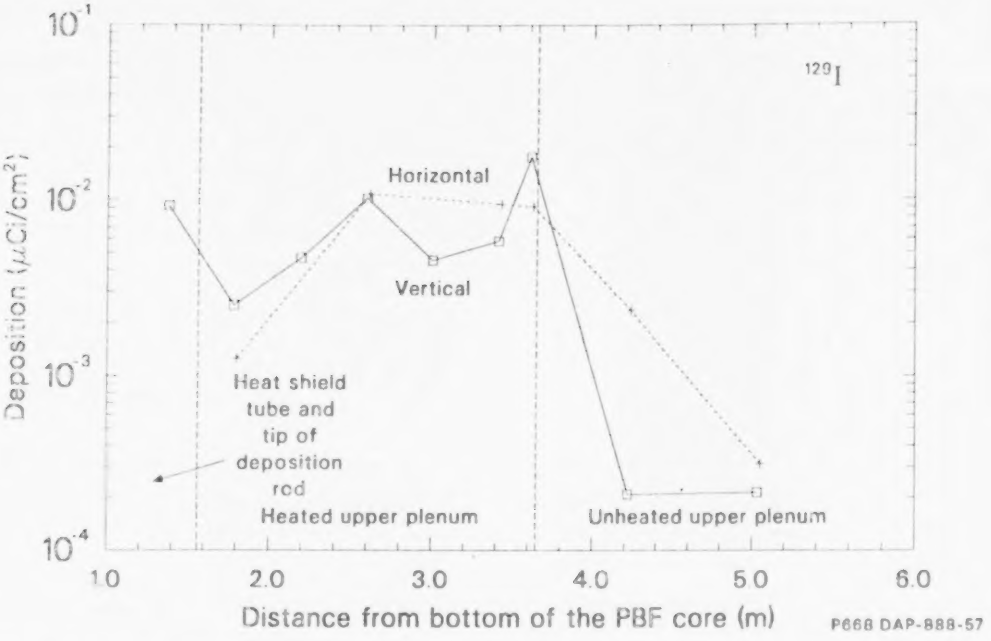

Figure 105. A comparison of ^{129}I deposition on vertical and horizontal surfaces of the SFD 1-4 deposition rod.

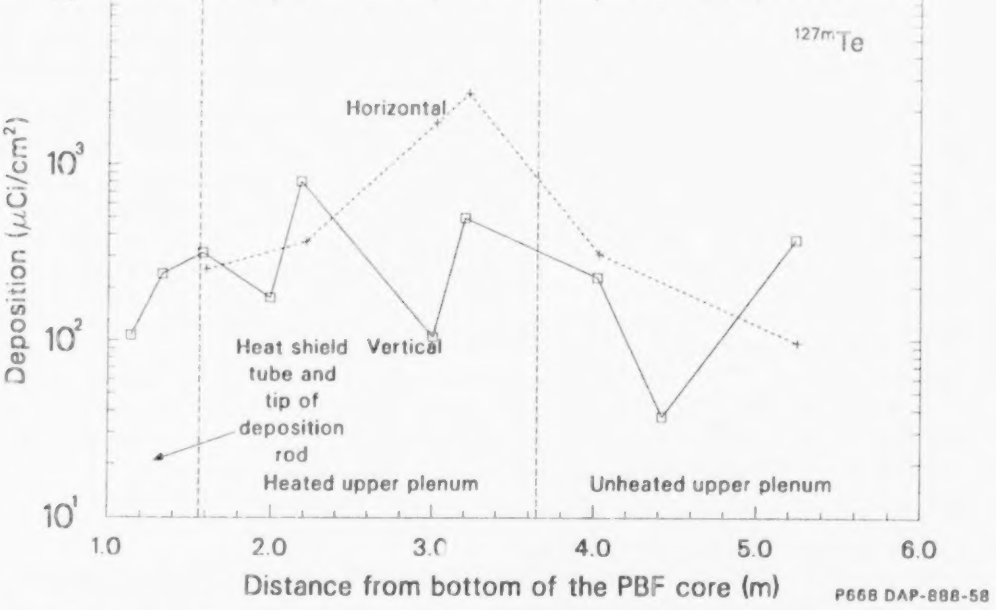

Figure 106. A comparison of ^{127m}Te deposition on vertical and horizontal surfaces of the SFD 1-4 deposition rod.

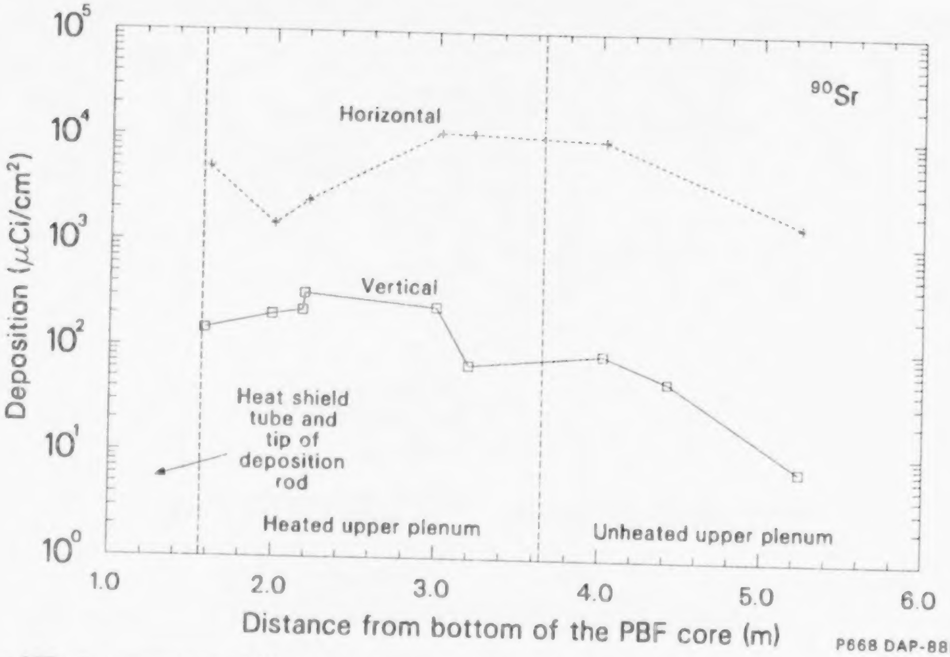

Figure 107. A comparison of ^{90}Sr deposition on vertical and horizontal surfaces of the SFD 1-4 deposition rod.

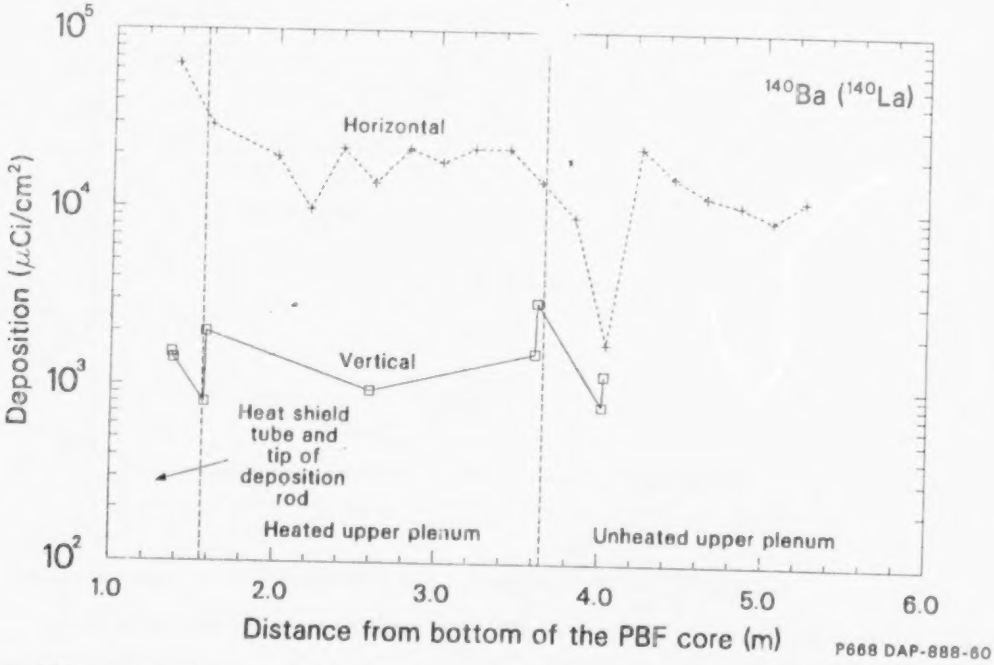

Figure 108. A comparison of ^{140}Ba (^{140}La) deposition on vertical and horizontal surfaces of the SFD 1-4 deposition rod.

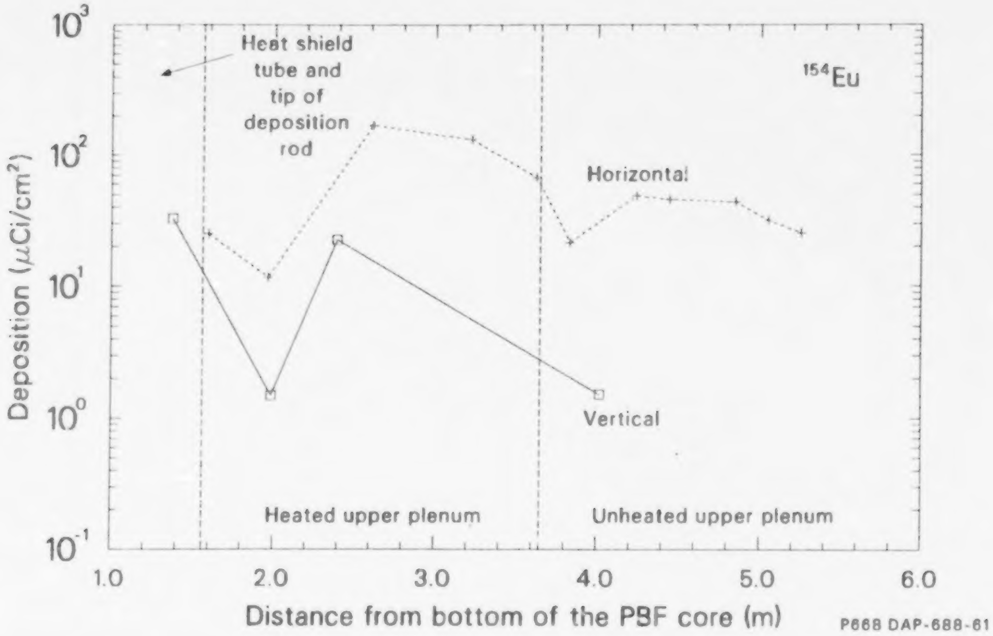

Figure 109. A comparison of ^{154}Eu deposition on vertical and horizontal surfaces of the SFD 1-4 deposition rod.

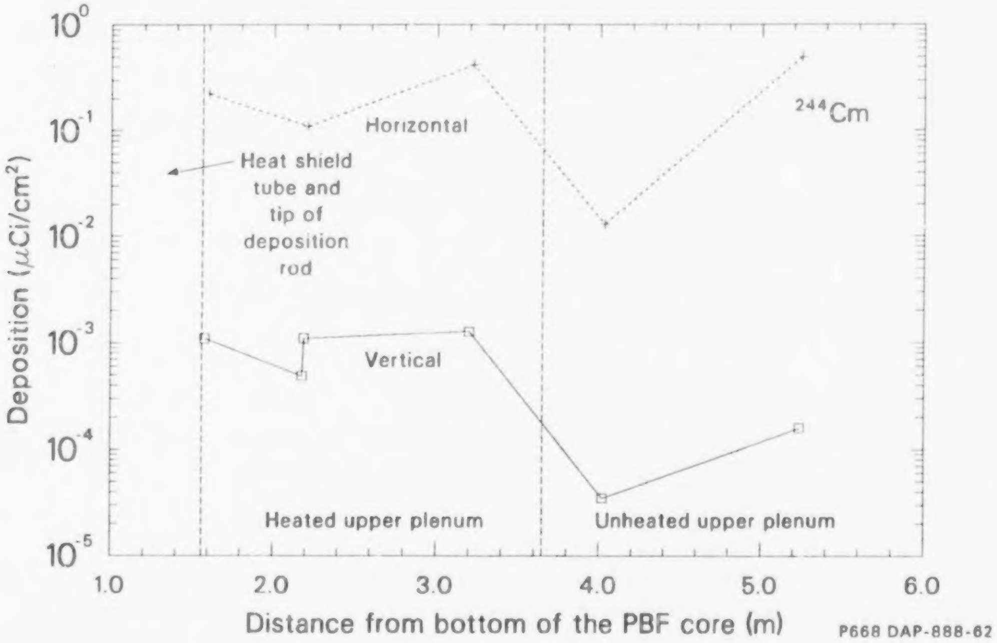

Figure 110. A comparison of ^{244}Cm deposition on vertical and horizontal surfaces of the SFD 1-4 deposition rod.

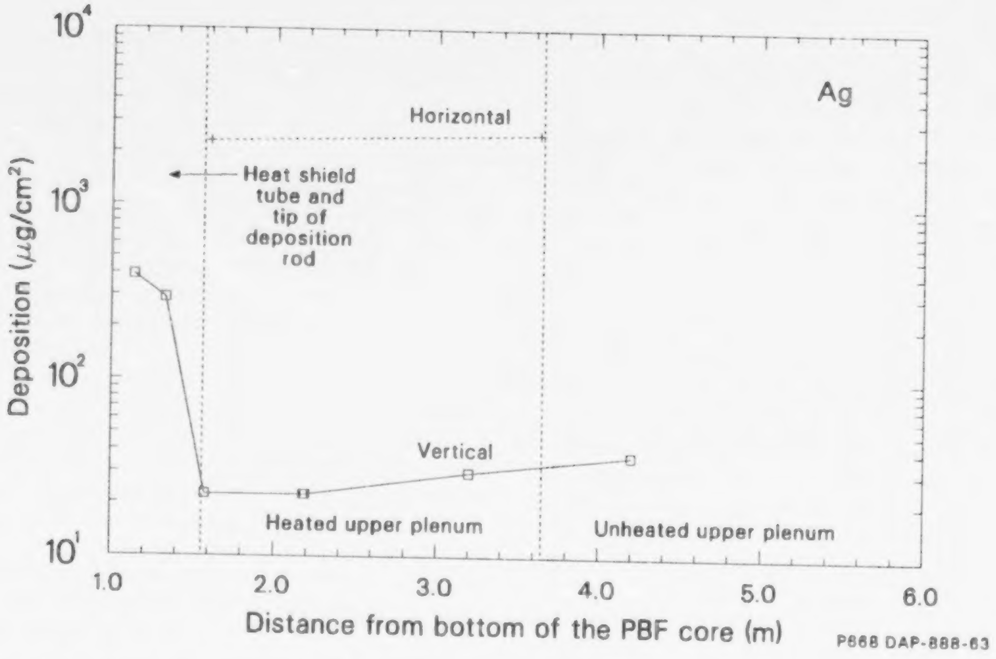

Figure 111. Silver deposition profile in the SFD 1-4 upper plenum.

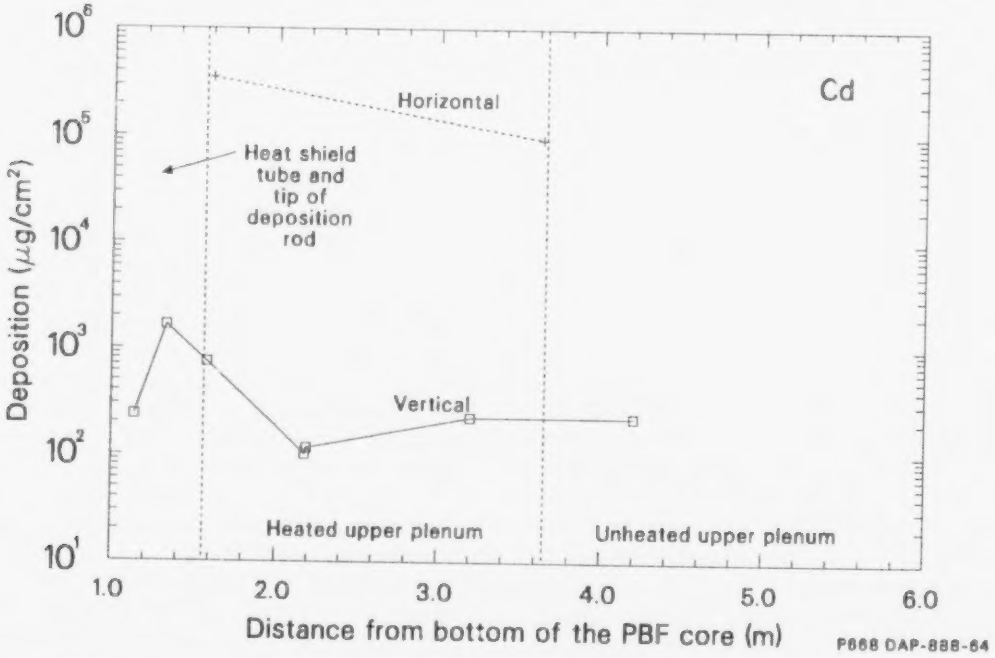

Figure 112. Cadmium deposition profile in the SFD 1-4 upper plenum.

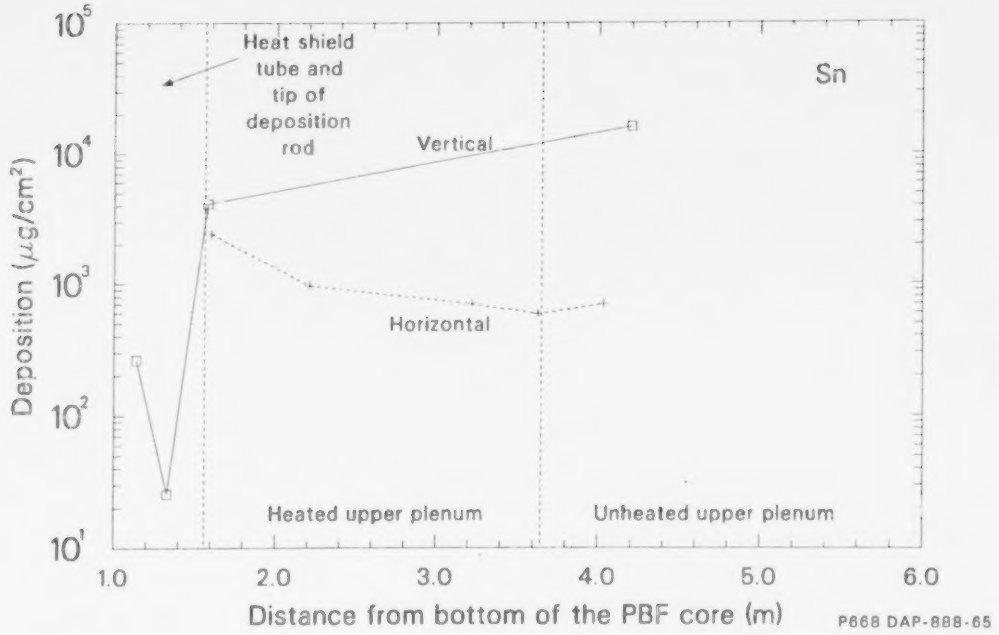

Figure 113. Tin deposition profile in the SFD 1-4 upper plenum.

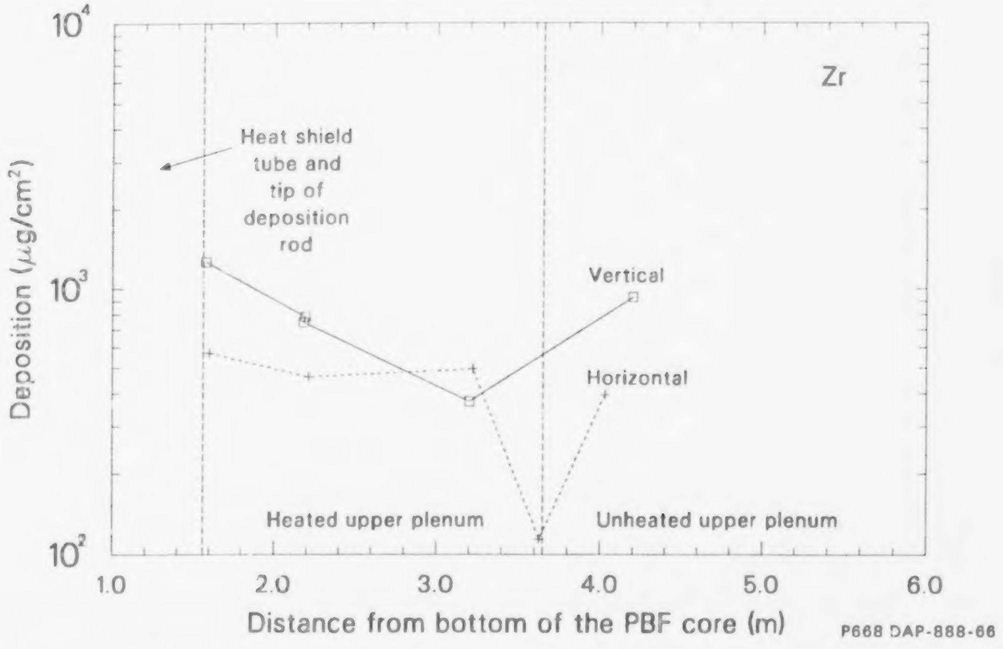

Figure 114. Zirconium deposition profile in the SFD 1-4 upper plenum.

both iodine isotopes and to a lesser extent ^{127m}Te decreased beyond 3.65 m as the effluent entered the unheated upper plenum.

The deposition profiles for the less volatile species ^{90}Sr, ^{140}Ba (^{140}La), ^{154}Eu, and ^{244}Cm, shown in Figures 107 through 110, all indicate generally greater deposition per unit surface area on the horizontal surfaces than on the vertical surfaces. Unlike the more volatile species, much less difference in the magnitude of the deposition is observed between the heated and unheated plenum surface concentrations.

The silver deposition pattern, shown in Figure 111, indicates that for vertical surfaces the deposition is greatest in the heat shield and decreases with increasing distance from the bundle. In the deposition rod area, the deposition was greatest on the horizontal surfaces where solid deposits of material collected. In general, the amount of deposition on the deposition rod (coupons and holders) was small; in many cases, it was below detection limits.

As indicated in Figure 112, the cadmium deposition in the heat shield area was within a factor of two of that for silver. On the deposition rod in the heated upper plenum, the cadmium surface concentration was an order of magnitude greater than the silver concentration. The greatest cadmium deposition was associated with the solid deposits on the horizontal surfaces. The data indicate that the deposition on the vertical surfaces of the deposition rod was relatively uniform at all elevations.

The deposition profiles for tin and zirconium in Figures 113 and 114 indicate a large amount of scatter. Tin was found primarily on the vertical and horizontal surfaces of the deposition rod, with lesser amounts on heat shield surfaces and the solid deposits. The low amount of tin associated with the solid deposits may be due to the difficulty in measuring tin in the presence of large amounts of cadmium. The zirconium deposition profile indicates no preferential deposition on the surfaces of the deposition rod. The zirconium is thought to be from loose particulates released from the shroud insulation (ZrO_2) cavity.

Some of the horizontal and vertical surfaces of the deposition rod were examined by EDS and WDX. The examination indicated the presence of cesium, cadmium, indium, silver, zirconium, tin, chlorine, iron, chromium and nickel. Chlorine is an impurity in the water. Iron, chromium, and nickel could be from the SEM substrate, the stainless steel or Inconel in the bundle, or impurities in the water. Comparison of the x-ray dot maps for each element suggests that cesium and chlorine were associated in many of the deposits. Cadmium, indium, and silver were associated in a few particles; and nickel and tin were associated on one particle that was analyzed. Spherical particles were observed on the vertical surfaces of the deposition rod, whereas agglomerates ranging in size between 25 and 250 μm were observed on the coupon holder horizontal surfaces.

7.2.2 Integral Deposition Estimates. The measured surface concentrations for the dominant nonradioactive bundle materials were integrated over the appropriate surface areas to estimate the total deposition in the upper plenum. In addition, an estimate was made of the material that was transported beyond the aerosol monitor, based on the aerosol mass flow in the experiment (see Section 7.3). The results, shown in Table 20, are best-estimate deposition values. However, they do not represent a total mass balance because (a) not all the surfaces in the system were analyzed, (b) minimum detection sensitivities for some elements were very high, and (c) the results of a limited number of samples were extrapolated to obtain the total deposition estimates.

Similar results for the distribution of fission products throughout the system are more difficult to obtain because many of the system surfaces were washed with water. However, the effects of water flushing on volatile fission product behavior were examined. Table 21 lists the pre- and postflush release fractions measured in the collection tank and effluent system for cesium, iodine, and tellurium. The preflush results indicate that except for cesium and iodine very little material was transported to the collection tank. The preflush release fractions measured in the collection tank for ^{131}I and ^{137}Cs were 2.14 E − 03 and 9.04 E − 03, respectively. Tellurium-129m was not detected in the collection tank prior to flushing. After flushing the bundle and the effluent line with water, the release fractions of ^{131}I and ^{137}Cs in the collection tank increased significantly to 0.23 and 0.46, respectively; the release fraction for ^{129m}Te following flushing was 2.2 E − 03. Comparison of pre- and postflush collection tank measurements indicates that 99% and 98% of iodine and cesium deposited on system surfaces during the test were easily transported into the collection tank during the flushing operation. However, tellurium was not easily washed out of the bundle and/or effluent line.

Table 20. Material deposition in the SFD 1-4 sampling system

Species	Upper Plenum Vertical[a]	 Horizontal	Downstream of Aerosol Monitor[b]	Total
Mass Deposition Estimates (g)[c]				
Silver	2.31 E − 01	2.66 E − 02	1.10 E − 01	3.68 E − 01
Indium	2.16 E − 01	1.03 E − 02	—[d]	2.26 E − 01
Cadmium	1.44 E + 00	2.36 E + 00	1.50 E + 00	5.30 E + 00
Tin	4.02 E − 02[d]	2.20 E − 02	3.90 E + 00	3.96 E + 00
Zirconium	3.25 E + 00	9.20 E − 03	1.90 E − 01	3.45 E + 00
Fraction of Bundle Inventory Deposited				
Silver	1.69 E − 04	1.94 E − 05	8.01 E − 05	2.69 E − 04
Indium	8.39 E − 04	4.00 E − 05	—[d]	8.79 E − 04
Cadmium	1.68 E − 02	2.75 E − 02	1.75 E − 02	6.18 E − 02
Tin	4.90 E − 04	2.68 E − 04	4.75 E − 02	4.83 E − 02
Zirconium	5.83 E − 04	1.65 E − 06	3.40 E − 05	6.19 E − 04

---

a. Vertical surfaces of the upper plenum include the heat shield, effluent tube, and vertical surfaces of the deposition rod.

b. Represents an estimate of the amount of material that flowed past the aerosol monitor.

c. Uncertainties are large because not all surfaces were sampled, some elements had very high detection sensitivities, and the results from a limited number of samples were extrapolated to obtain total deposition estimates.

d. Incomplete mass balance for these species due to high detection sensitivity

Table 21. Comparison of pre- and postflush collection tank and effluent system release fractions[a]

Isotope	Effluent System	Collection Tank
Preflush		
^{127m}Te	2.41 E − 02 ± 52	—[b]
^{129m}Te	3.72 E − 02 ± 35	—[b]
^{131}I	2.62 E − 01 ± 48	2.14 E − 03 ± 11
^{137}Cs	1.75 E − 01 ± 30	9.04 E − 03 ± 11
Postflush		
^{127m}Te	2.94 E − 02 ± 40	2.20 E − 03 ± 33
^{129m}Te	3.00 E − 02 ± 38	1.40 E − 03 ± 52
^{131}I	1.20 E − 02 ± 10	2.31 E − 01 ± 20
^{137}Cs	5.40 E − 02 ± 55	4.57 E − 01 ± 15

---

a. The ± values are uncertainties in percent.

b. Not detected.

7.3 Aerosol Generation, Deposition, and Transport Behavior

The deposition measurements and the on-line aerosol monitor data presented in Sections 7.1 and 7.2 have provided interesting information about fission product and aerosol behavior. The purpose of this section is to provide an understanding of the aerosol generation, deposition, and transport behavior that occurred during Test SFD 1-4. Specifically, this section will focus on the behavior of cadmium, silver, tin, and cesium iodide—four predominant aerosol sources—in the SFD 1-4 upper plenum. This section will try to answer the following questions:

1. What is the nucleation and condensation behavior of each of the major aerosol sources, as represented by cadmium, silver, tin, and cesium compounds, in Test SFD 1-4?
2. What is the mechanism responsible for the solid deposits observed on the horizontal surfaces of the deposition rod?
3. What mechanism(s) is responsible for all the deposition patterns observed on the deposition rod?
4. Why do the deposition measurements for cesium decrease in magnitude beyond 3.65 m (CH-12) whereas those for strontium, barium, europium, and curium do not?
5. Why is the aerosol composition, as measured by the filtered steam samples, predominantly tin and cadmium, whereas the composition of the solid deposits are >98% cadmium?
6. What fractions of fission product iodine, cesium, and tellurium were subject to vapor versus aerosol transport?

Basic aerosol models have been applied to the SFD 1-4 system to answer the first five questions. Results of the analysis indicate that distinct mechanisms governed aerosol behavior in different parts of the SFD 1-4 upper plenum. In the heat shield region, aerosol behavior was dominated by vapor condensation and aerosol formation. Aerosol agglomeration, settling, and deposition were important in the heated upper plenum. Downstream of the heated upper plenum, aerosol evaporation and fine aerosol transport processes governed the aerosol transport behavior. The results of this analysis will be discussed in the following sections. Information about the partitioning of fission products between vapor and aerosol states will be examined as part of the temporal fission product transport analysis in Section 7.4.

Section 7.3.1 describes the system geometry, the basic thermal-hydraulic boundary conditions, and the bundle material source rates that were used in the aerosol calculations. The aerosol nucleation and vapor condensation behavior of bundle materials in the heat shield is described and compared to the deposition data in Section 7.3.2. Aerosol deposition and settling calculations in the heated upper plenum are presented in Section 7.3.3. Section 7.3.4 describes the behavior of aerosols in the unheated upper plenum. Results of the on-line aerosol monitor analysis are presented in Section 7.3.5.

7.3.1 Boundary Conditions. Aerosol behavior in Test SFD 1-4 is a strong function of the system geometry and thermal-hydraulic conditions. A detailed description of the geometry of the SFD 1-4 upper plenum, including the deposition rod, is required for the aerosol calculations. Schematics of the upper plenum geometry from the top of the active fuel (1.06 m) to the top of coupon holder 2 (CH-2) and the deposition rod are presented in Figures 115 and 5. Details of the geometry are listed in Table 22.

The thermal-hydraulic conditions used for the aerosol analysis were obtained from the results of the effluent transit analysis (see Appendix E) and thermocouple measurements where appropriate. Although the conditions varied during the experiment, constant best-estimate values for the thermal-hydraulic conditions during the high-temperature transient were chosen to make the analysis more tractable. Bulk gas and wall temperatures in the upper plenum region were based on thermocouple measurements at the entrance of the heat shield at 1.14 m and at coupon holder 2 on the deposition rod at 1.57 m. The thermal-hydraulic conditions used in this analysis are listed in Table 23.

The source rate of vapors leaving the bundle is a key parameter that determines the vapor condensation and aerosol nucleation behavior. Four

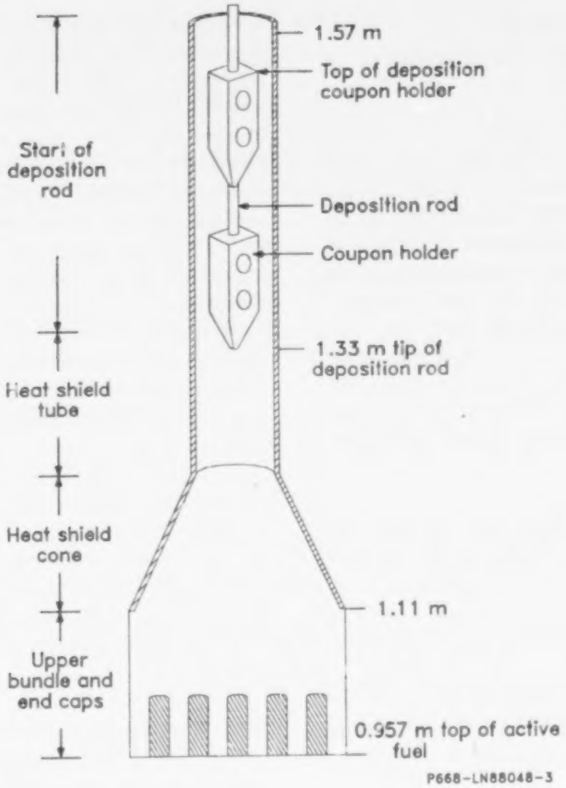
1.57 m
Top of deposition coupon holder
Start of deposition rod
Deposition rod
Coupon holder
1.33 m tip of deposition rod
Heat shield tube
Heat shield cone
1.11 m
Upper bundle and end caps
0.957 m top of active fuel
P668-LN88048-3

Figure 115. Schematic of the upper plenum geometry from the top of the active fuel to the top of coupon holder 2.

Table 22. System geometry for the SFD 1-4 upper plenum and deposition rod

	Upper Plenum Geometry		
Component	Volume (m^3)	Surface Area (m^2)	Hydraulic Diameter (m)
Upper bundle and end caps	3.82 E – 04	1.31 E – 01	1.07 E – 02
Heat shield cone	4.08 E – 04	2.18 E – 02	8.10 E – 02
Heat shield tube	7.33 E – 05	1.33 E – 02	2.22 E – 02
Tip of deposition rod	1.16 E – 04	3.35 E – 02	1.10 E – 02
		Deposition Rod Geometry	
Holder width		9.53 E – 03 m	
Rod diameter		4.78 E – 03 m	
Steam tube diameter		2.22 E – 02 m	
Flow area in holder region		2.96 E – 04 m^2	
Flow area in rod region		3.69 E – 04 m^2	

Table 23. Thermal-hydraulic conditions in the SFD 1-4 upper plenum

Parameter	Value	
Volumetric flow rate (at 800 K, 6.8 MPa)	5.42 E – 05 m^3/s	
Effluent composition	H_2 mole fraction = 0.75 Ar mole fraction = 0.25	
Average gas velocity along deposition rod	0.165 m/s	
Gas density (at 800 K, 6.8 MPa)[a]	11.75 kg/m^3	
Gas viscosity (at 800 K, 6.8 MPa)[a]	3.72 E – 05 kg/m-s	
Gas mean free path (at 800 K, 6.8 MPa)[a]	5.22 E – 09 m	
Temperatures:[b]	Bulk gas	Wall
Upper bundle and end caps	1800 K	1700 K
	1600 K	1500 K
	1500 K	1400 K
Heat shield cone	1400 K	1300 K
	1300 K	1200 K
	1200 K	1100 K
	1100 K	1000 K
Heat shield tube	1000 K	900 K
Deposition rod	900 K	800 K
	800 K	800 K

---

a. Average value based on effluent composition.

b. Estimated values based on thermocouple measurements at the entrance of the heat shield (at 1.14 m) and near coupon holder 2 on the deposition rod (1.57 m).

representative materials were considered for the analysis: cadmium, silver, tin, and cesium iodide. These materials were chosen because they were are all believed to have been released from the SFD 1-4 bundle and their physical properties (i.e., vapor pressure, surface tension, and release rate) were different enough that they would bracket the aerosol behavior expected in the experiment. Figure 116 is a plot of the vapor pressure of several potential aerosol sources. As seen in the figure, the behavior of tin and silver is representative of low volatile materials released from the bundle, whereas cadmium and cesium iodide represent the release behavior of volatile materials. Other materials (e.g. CsOH, SnTe) could have been used in the analysis. However, their behavior is not expected to be significantly different from the four species selected.

A range of source rates was used in the analysis to represent the uncertainty associated with the release of each material from the bundle. The range of source rates for each species is listed in Table 24. Cadmium and silver release rates, based on VAPOR code calculations, and the tin release rate from the oxidized zircaloy cladding, based on a simple mass transport model, are discussed in Appendix H. The cesium iodide release rate was calculated from the inventories of cesium and iodine in the SFD 1-4 bundle and the measured fractional release rate of noble gases.

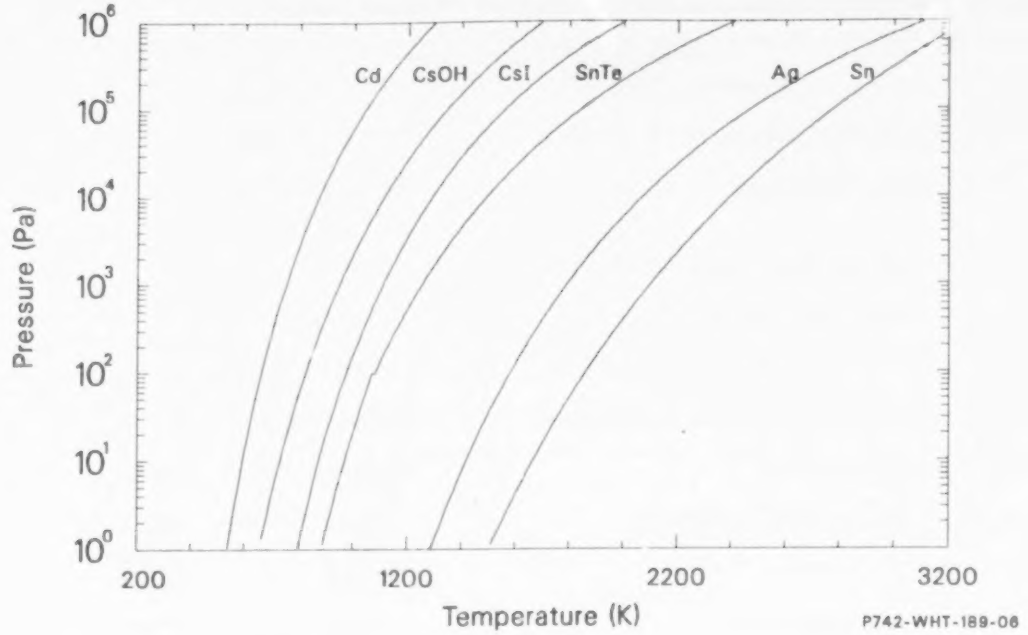

Figure 116. Vapor pressures of potential aerosol sources.

7.3.2 Aerosol Nucleation and Vapor Condensation Behavior. As the bundle heated up during Test SFD 1-4, hot vapors of cadmium and silver from the molten control rod material, tin from the oxidized cladding, and cesium iodide from the fuel exited the bundle and began to cool and supersaturate. The concentration of these materials, together with the effluent flow rate and the gas and wall temperatures, affected the location where these materials condensed and whether or not they formed an aerosol. This section presents the results of calculations that describe the condensation and nucleation behavior of cadmium, silver, tin, and cesium iodide in Test SFD 1-4. Details of the analytic model are found in Appendix H.

Aerosol formation or nucleation is a complex function of the supersaturation, the vapor pressure of the element, the gas temperature, and the surface tension of the material. Various aerosol formation models have been reviewed in Reference 29 and applied to cadmium, silver, and cesium iodide to explain their nucleation behavior in a severe reactor accident. The rate of aerosol formation by ion-induced nucleation was examined to determine the supersaturation required to form an aerosol in a

Table 24. Source rates and melting points of bundle materials used in the aerosol analysis

Species	Melting Point (K)	Source Rate (kg/s)
Cadmium	594	10^{-5} - 10^{-4}
Silver	1234	10^{-8} - 10^{-7}
Tin	505	10^{-7} - 10^{-5}
Cesium iodide	899	10^{-7} - 10^{-6}

clean system (with no preexisting aerosol). These results will be used here to explain the nucleation and condensation behavior of cadmium, silver, tin, and cesium iodide in Test SFD 1-4.

Figure 117 is a plot to describe the vapor condensation and aerosol formation behavior of tin in the SFD 1-4 upper plenum. The hatched region in the figure is the calculated range of tin supersaturations in the upper plenum if no aerosol were present. The supersaturation range in each section of the upper plenum accounts for condensation onto walls and the cooling of the effluent as it travels through the plenum. Also shown in the figure is the line S = 1, above which a vapor is supersaturated and will condense on aerosols if they are present in the system. Below S = 1, no condensation occurs. The line labeled "aerosol formation" represents the critical supersaturation range above which tin aerosols would form by ion-induced nucleation in a clean system without preexisting aerosols.

The results for tin shown in Figure 117 indicate that upon exiting the active fuel region, some of the tin vapor condensed on the surfaces of the upper bundle end caps. However, because of the low volatility of tin, the low surface-to-volume ratio, and cooler temperatures in the upper bundle end caps, the vapor became supersaturated very quickly as the effluent exited the fuel bundle. Thus, tin would have condensed onto aerosols if they were present in the system. If there were no aerosols or only a very low concentration of aerosol seeds or impurities in the system, then tin would have nucleated to form an aerosol between 1800 and 1600 K in the upper bundle end caps region during Test SFD 1-4.

Figure 118 is a composite plot of the nucleation and condensation behavior of tin, silver, cadmium, and cesium iodide. In general, the calculated behavior of the four species is somewhat different due to differences in the volatility and source rate of material exiting the bundle. The lines labeled "aerosol formation" represent a range for the four species considered.

The results for silver are similar to tin, primarily because of the similar volatility of silver and tin. Upon exiting the hot bundle region, the vapor remained subsaturated in the upper bundle end caps region. The source rate of silver vapor is too low to cause any condensation in the upper bundle end caps region. As the silver vapor entered the heat shield cone, it became supersaturated and passed the critical value required to form an aerosol. It is concluded that in addition to tin, silver could have also formed an aerosol between 1500 and 1200 K in the heat shield region, based on the relative release timing of the two materials during the experiment.

The behavior of cadmium in the upper plenum is much different than that of tin or silver. The results indicate that cadmium remained subsaturated until the vapor entered the heat shield tube and the area near the tip of the deposition rod. Although the release rate of cadmium was two to three orders of magnitude larger than silver or tin, the high vapor pressure of cadmium caused it to remain subsaturated until temperatures dropped below ~1000 K. As a result, it can be concluded that the cadmium exited the bundle and did not condense on walls in the heat shield cone. Upon entering the heat shield tube and deposition rod area, the vapor became supersaturated. For the range of source rates represented by the best-estimate saturation range, the cadmium vapor is predicted to have reached supersaturations of less than ~10. This supersaturated vapor then condensed on the walls, the deposition rod, and the tin and silver aerosols in the deposition rod area.

The behavior of cesium iodide is similar to cadmium in the upper bundle regions and heat shield cone. The source rate was too low and the temperatures were too high to cause any condensation. Upon entering the heat shield tube and deposition rod area, the cesium iodide vapor became supersaturated. There, the vapor condensed on the walls, the deposition rod, and any tin and silver aerosols that were present.

7.3.3 Aerosol Settling and Deposition. Following nucleation and aerosol growth by condensation, aerosol agglomeration caused the aerosol particle size to increase such that inertia played a role in the subsequent behavior of the aerosol. Solid deposits of materials found on the horizontal surfaces of the deposition rod can be interpreted as evidence that the aerosols must have had sufficient inertia to deposit on the rod. This section will examine the settling and deposition behavior of the aerosol to determine the mechanism(s) responsible for the observed deposition in Test SFD 1-4. Two mechanisms for the observed heavy deposition on

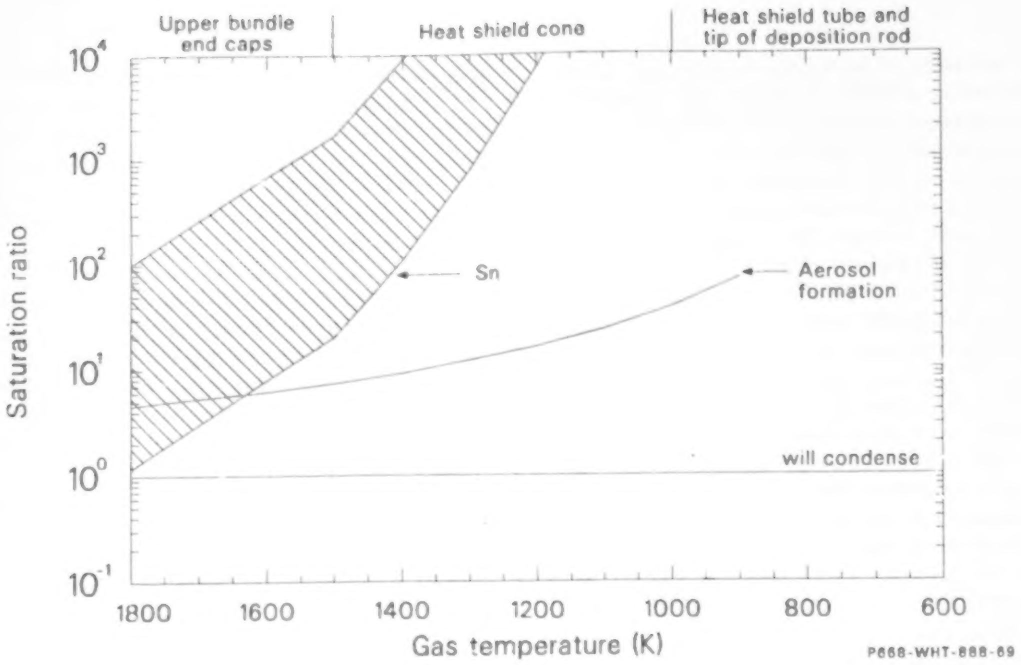

Figure 117. Vapor condensation and aerosol formation behavior of tin in the SFD 1-4 upper plenum.

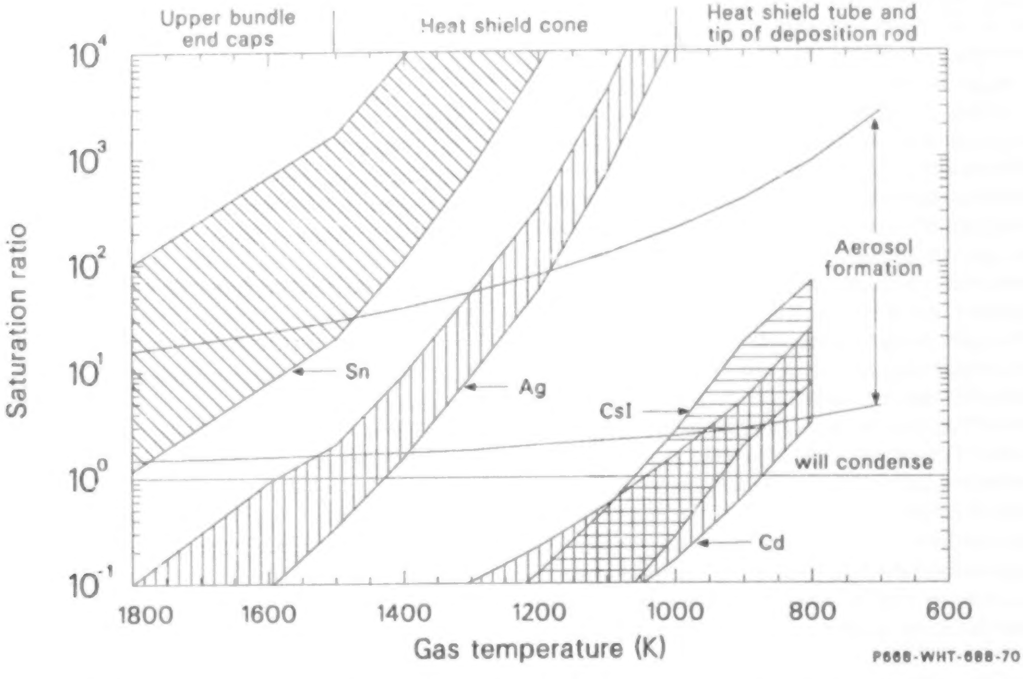

Figure 118. Vapor condensation and aerosol formation behavior of tin, silver, cadmium, and cesium iodide in the SFD 1-4 upper plenum.

the horizontal surfaces of the deposition rod are considered: gravitational settling and deposition due to trapping of aerosol particles in the wakes and recirculating eddies formed behind the horizontal surfaces of the deposition rod.

Once an aerosol particle has grown to sufficient size, it can settle out due to gravity. Stoke's law modified to account for the effects of particle slip has been used to calculate the particle settling velocity. Details of the calculation are described in Appendix H. The settling velocity is plotted in Figure 119 as a function of the particle size for the thermal-hydraulic conditions in the SFD 1-4 upper plenum. The settling velocity is the relative velocity between the flow and the aerosol particle. Thus, for a particle to settle against the flow, it must have a settling velocity greater than the flow velocity of 16.5 cm/s in the SFD 1-4 upper plenum. Examination of Figure 119 indicates that particles greater than ~50 μm would have settled against the flow, while particles less than 50 μm would have been swept out with the flow.

In addition to gravitational settling, other mechanisms could cause particle deposition. For the geometry of the SFD 1-4 upper plenum and particles greater than ~1 μm, the predominant deposition mechanism was inertial deposition of particles in the wake formed behind the upper horizontal surfaces of the deposition rod. Many researchers have studied deposition of aerosol particles around submerged bodies.[30] The magnitude of deposition is characterized by the Reynolds number of the flow and the Stokes number of the aerosol particle. The Stokes number is given by

$$St = \rho d^2 V/(18 \mu L) \qquad (1)$$

where

ρ = particle density (kg/m^3)

d = particle diameter (m)

V = settling velocity (m/s)

μ = viscosity (kg/m·s)

L = characteristic length (m).

The Stokes number is the ratio of the stopping distance of a particle to the characteristic dimension, L, of the obstacle. Inviscid flow calculations of the impaction efficiency for particles around a cylinder and a sphere are plotted in Figure 120a and 120b. For inviscid flow around obstacles, the critical Stokes number above which deposition is non-zero is given by:[30]

$$St_{crit} = 1/4b \qquad (2)$$

where b is equal to 3 for a cylinder and 2 for a sphere. Although data indicate that there is some effect of the Reynolds number on the impaction efficiency, significant impaction efficiencies (>50%) occur roughly at St >5. These inviscid flow results are in fairly good agreement with experiments over the entire range of Stokes numbers. However, the effects of flow separation and the formation of circulating eddies or wakes behind the obstacle are not accounted for in the inviscid theory and would tend to enhance the deposition. Standing eddies have been found behind cylinders at a Reynolds number of 40.[30] Kim et al.[31] have studied the deposition of aerosol particles in straight tubes with an abrupt obstruction. They found significant deposition due to turbulent wakes forming behind the obstacles at Stokes numbers between 0.1 and 1.0.

Although the SFD 1-4 deposition rod is not a sphere or a cylinder, the coupon holders do act as submerged bodies in the flow. As a result, it is believed that wakes and recirculating eddies formed behind the upper horizontal surfaces of the deposition rod in a manner similar to that depicted in Figure 121. Based on the work of Kim et al, it is expected that significant deposition would have occurred at Stokes numbers between 0.1 and 1.0. For an aerosol particle density of 7 g/cm^3 (that of cadmium) and a characteristic length of 0.95 cm (the width of the coupon holder), these Stokes numbers correspond to particles between 25 and 100 μm in diameter for the flow conditions in the SFD 1-4 upper plenum. Based on this analysis, it appears that the formation of large solid deposits of aerosol material found on the upper horizontal surfaces could be due to inertial impaction of particles larger than 25 μm in the wakes and recirculating eddies formed behind the coupon holders and gravitational settling of particles greater than 50 μm from the flow.

The 20 coupon holders that make up the deposition rod acted as a series of "filters" that captured the larger particles. For example, if the deposition efficiency was only 10% per coupon holder, then the overall transmission efficiency of aerosol particles past the rod would be

$$\text{Transmission efficiency} = [1 - 0.1]^{20} = 0.12.$$

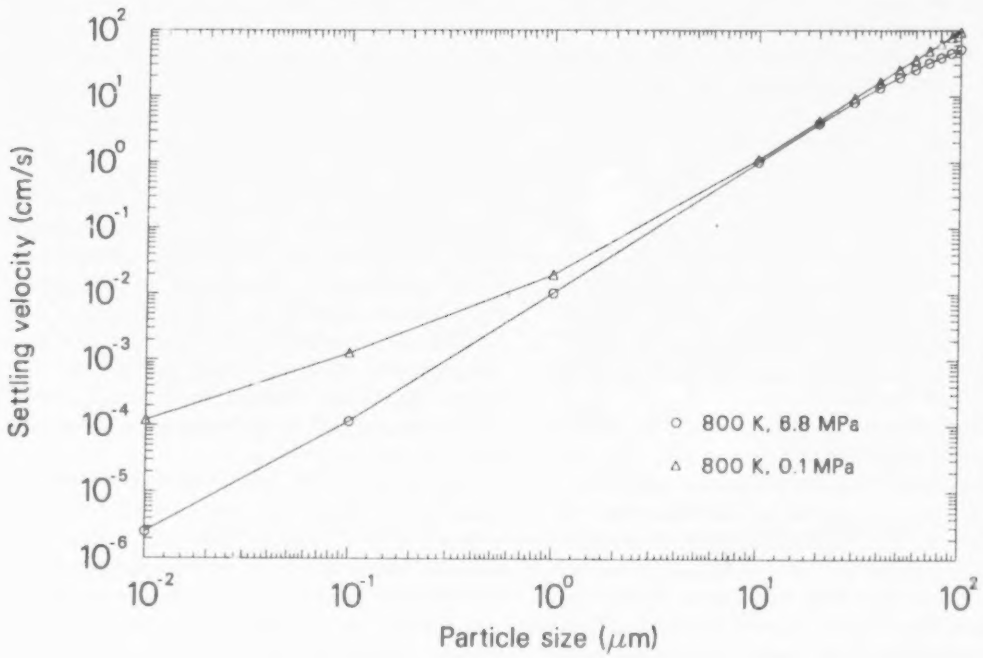

P668-WHT-888-71

Figure 119. Settling velocity versus particle size for aerosols in the SFD 1-4 upper plenum.

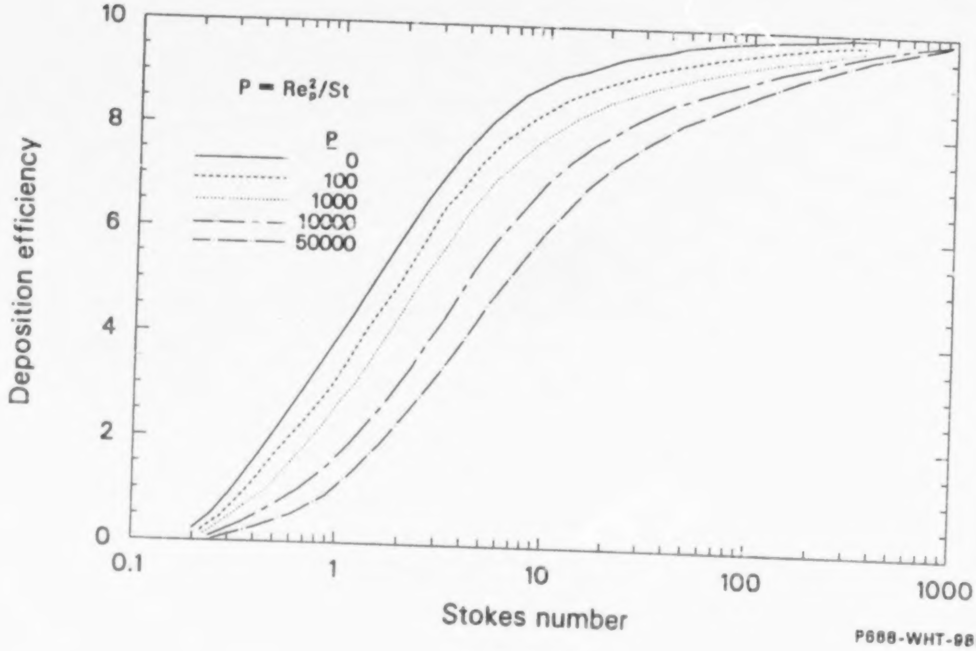

P668-WHT-988-74

a. Cylinder

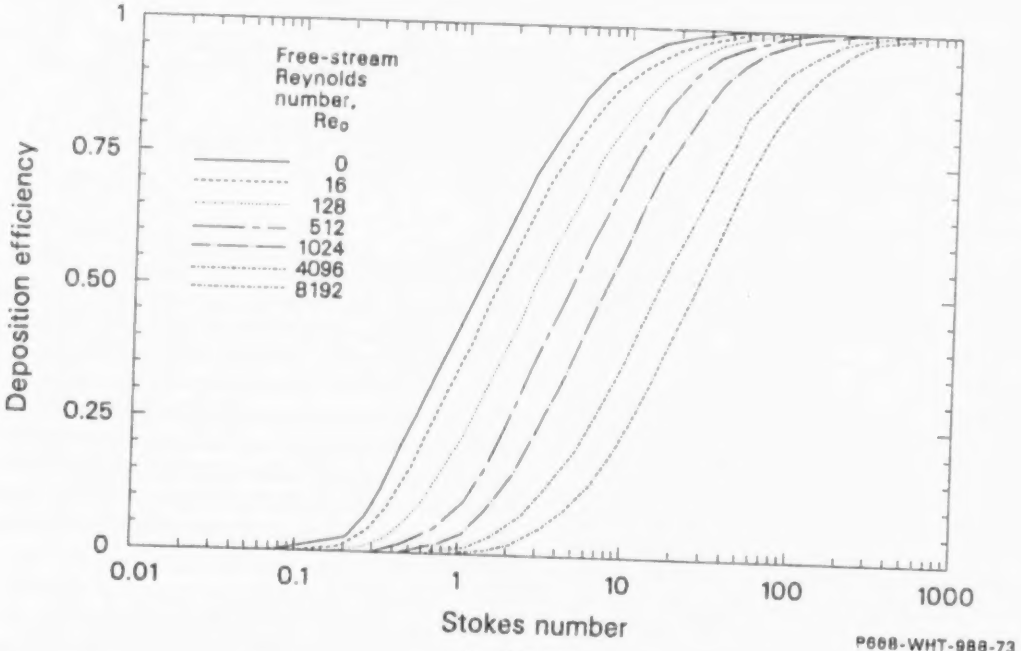

P668-WHT-988-73

b. Sphere

Figure 120. Inviscid flow calculations of the impaction efficiency for particles around a cylinder and a sphere.

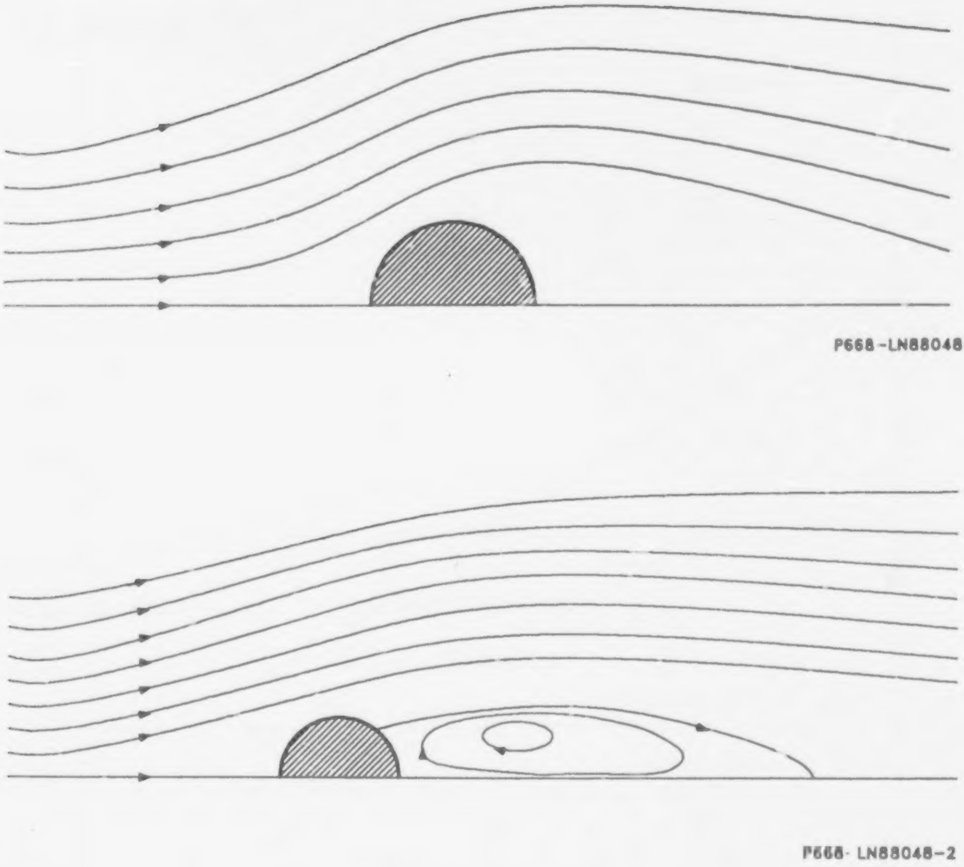

Figure 121. Streamlines for flow past a circular cylinder.

Thus, it appears that the design of the deposition rod made it a unique filter for trapping large particles.

7.3.4 Aerosol Evaporation and Fine Aerosol Transport. As the aerosol traveled through the unheated upper plenum, a change in the concentration of species occurred. The aerosol material found on horizontal surfaces was predominantly ($>98\%$) cadmium. However, elemental analysis of the effluent grab sample filters immediately downstream of the aerosol monitor indicate that the aerosol was composed mainly of tin ($\sim50\%$) and cadmium. This behavior, as shown in Figure 122, was the result of the relatively cold walls in the unheated upper plenum. The aerosol exiting the heated upper plenum was at ~800 K. However, thermocouple measurements in the unheated upper plenum indicate that the wall temperature was ~600 K during the transient. The temperature gradient would have caused condensation of the volatile aerosol components (i.e. cadmium, cesium iodide, cesium hydroxide) on the walls. In turn, these materials would have tended to evaporate from the aerosol to maintain equilibrium in the system. The vapor pressures of species like tin and silver are too low to result in any appreciable evaporation from the aerosol. Thus, the evaporation process resulted in a fine aerosol of tin, with some cadmium being transported to the aerosol monitor.

7.3.5 Analysis of Aerosol Monitor Results. As discussed in Section 7.1, the aerosol monitor consisted of two optical paths that measure the attenuation of a light beam due to the presence of aerosols. The responses of the 1-cm and 4-cm cells together with the results of the filtered effluent samplers have been used to determine the aerosol number concentration, the diameter of average

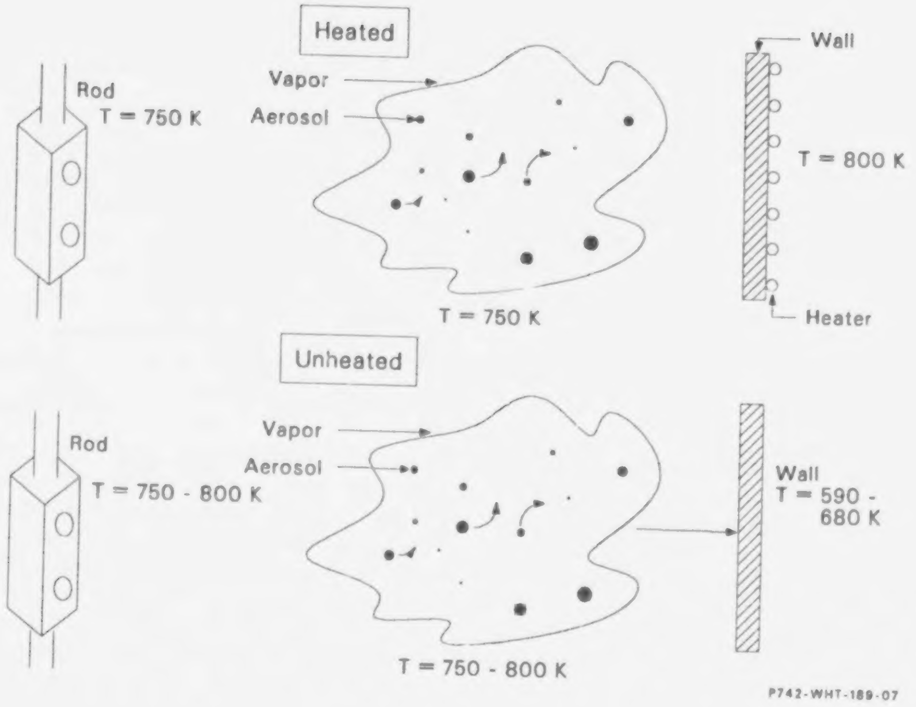

Figure 122. Aerosol behavior in the heated and unheated portions of the SFD 1-4 upper plenum.

mass, the aerosol mass concentration, and the aerosol mass flow rate as a function of time during Test SFD 1-4. Details and background about the analysis method are discussed in Reference 32, and a brief discussion of the analysis method is presented in Appendix H. The analysis in Reference 32 was based on preliminary estimates of the boundary conditions in the experiment. The results of the analysis using qualified boundary conditions are presented here.

The calculated particle number concentration is based on the ratio of the responses of the two optical cells, the transit time between the cells, and the agglomeration coefficient for a monodisperse aerosol. Uncertainties in the monitor signals and agglomeration coefficient were propagated to obtain uncertainty bounds on the particle number concentration. The aerosol number concentration at the aerosol monitor and its uncertainty bounds are plotted in Figure 123. (The data have been smoothed over 40-s intervals for the purposes of presentation.) The results indicate that following failure of the initial control rod, the number concentration was about 5 x 10^8 p/cm^3. Both signals (Figures 95 and 96) indicate a rapid decrease in transmission between 1950 and 2050 s. The overall uncertainty in number concentration became very large at this time because the signal responses were close together in absolute value. Between 2150 and 2300 s, the number concentration was highly

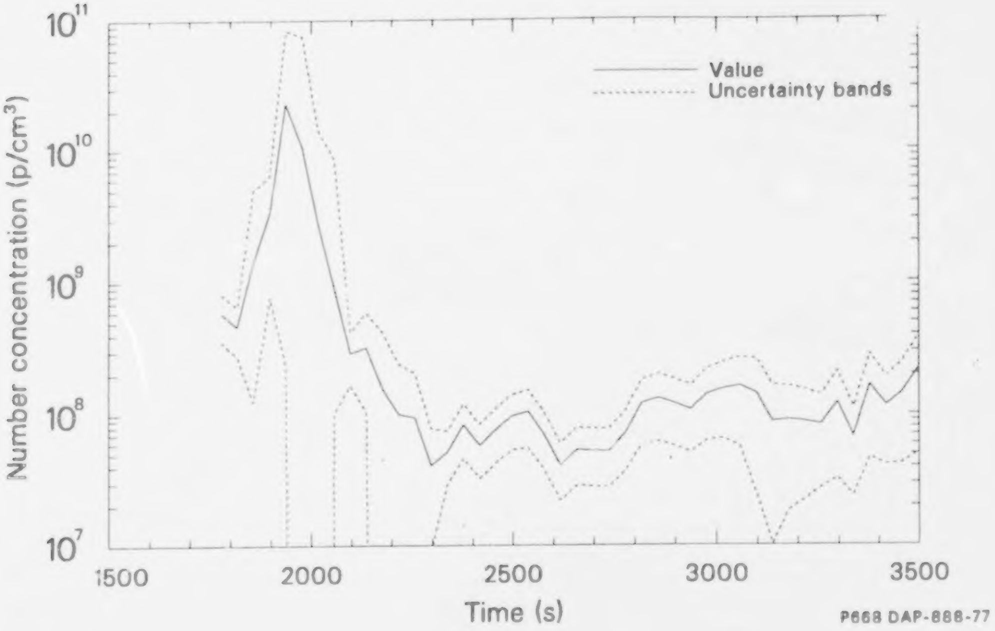

Figure 123. Aerosol number concentration at the SFD 1-4 aerosol monitor.

uncertain because cell 2 almost saturated. Despite these brief periods of high uncertainty, during most of the high-temperature transient the particle concentration remained high, between 10^7 and 5×10^8 p/cm³. Beyond 3500 s, the uncertainty increased because of particle deposition on the beam windows.

Size, mass, and elemental characteristics of the aerosol at 13.8 m were determined using the calculated number concentration and aerosol size and composition information obtained from the effluent filtered samplers discussed in Section 7.1. Particle size statistics from the analysis of the effluent filtered samples were used to determine the diameter of average mass at six times during the transient. Straight-line interpolations were used to construct the diameter of average mass of the aerosol as a function of time. The result is shown in Figure 124. Although the uncertainty in the particle size results is much less than 5%, an uncertainty of 20% was assigned to these data to represent the fact that the detailed time-dependent history of d_m is not known.

The aerosol mass concentration and the upper and lower uncertainty bounds are shown in Figure 125. As expected, the uncertainty in the aerosol mass concentration is very large early in the transient prior to 2300 s and very late in the transient beyond 3500 s because of the high uncertainty in the number concentration at these times. Between 2300 and 3500 s, the uncertainty is much smaller. During this time, the aerosol mass concentration at the aerosol monitor ranged between 5 E − 04 and 1 E − 05 g/cm³.

The total mass of aerosol that passed the aerosol monitor between 2300 and 3500 s (period of low uncertainty) was calculated using the mass concentration, the effluent flow rate in the experiment, and the elemental composition of the aerosol obtained from the filtered effluent samplers. Integration of the aerosol mass flow along with the upper and lower uncertainty curves indicates that 5.7 g of material passed the aerosol monitor between 2300 and 3500 s in Test SFD 1-4, with an upper bound of 9.1 g and a lower bound of 2.1 g. Based on the composition information from the filter samples, it appears that 3.9 g of tin and 1.5 g of cadmium flowed past the aerosol monitor.

7.4 Fission Product and Aerosol Transport Analysis

The preceding section addressed five important questions about aerosol behavior in Test SFD 1-4. This section supplements the analysis of Section 7.3 with detailed temporal calculations of the aerosol mass density, aerosol number density,

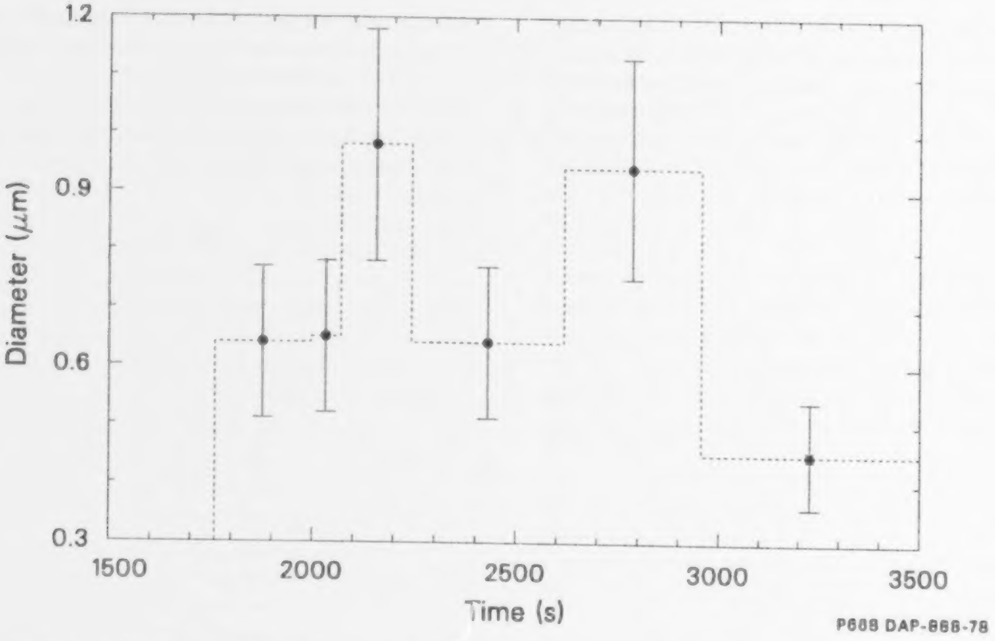

Figure 124. Diameter of average mass of the aerosol.

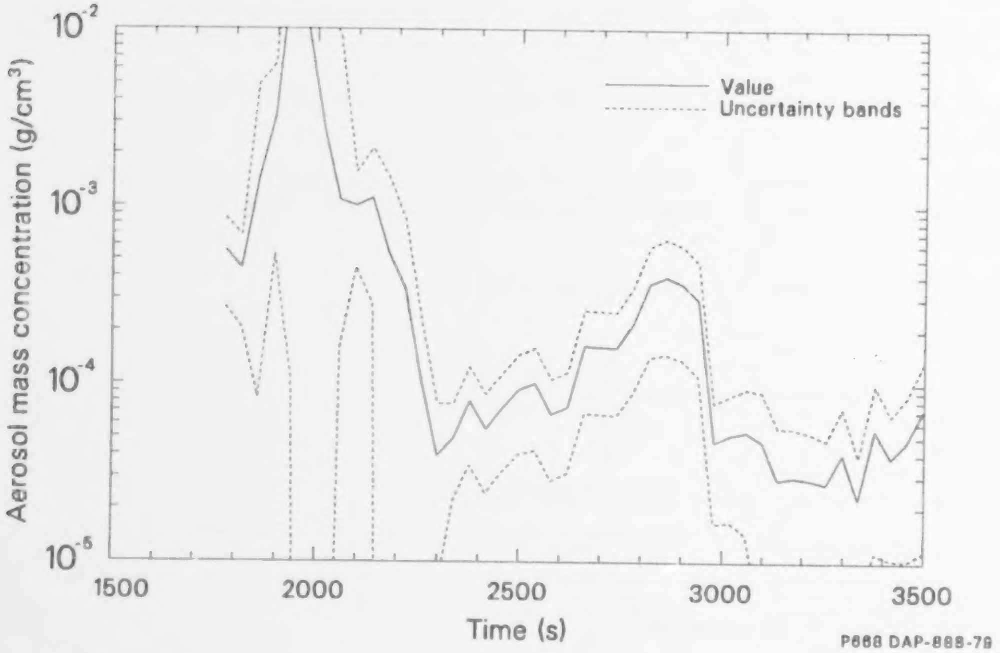

Figure 125. Aerosol mass concentration.

and aerosol size in the effluent line. It answers the question, "What is the distribution of fission product species between vapor, aerosol, and wall surfaces?" The analysis techniques are summarized in Section 7.4.1, and the results of the analysis are presented in Section 7.4.2. Section 7.4.3. discusses conclusions from the analysis.

7.4.1 Analysis Technique. Analysis of fission product and aerosol behavior in the SFD tests requires that a Lagrangian or slug-flow approach be used to model flow in the 10-m-long, 0.01-m-diameter effluent line. A Lagrangian analysis tool, whose mass transport models were originally based on the models in TRAP-MELT2,[33] was constructed and steadily improved to meet the increasing requirements for a complete analysis of the SFD test series. Table 25 is a summary of models included in the analysis. Changes made to the basic TRAP-MELT2 models include the omission of the zero-vapor-pressure aerosol seed and inclusion of tin as the chemical species with the lowest vapor pressure, the addition of cadmium as a chemical species, the addition of a model for the effect of wakes and eddies behind coupons on fission product deposition, the addition of a heat transfer model that includes radiation effects to calculate the gas temperature of the slug of gas (bulk gas temperature is an input quantity for TRAP-MELT2 analysis), and inclusion of a new correlation[34] for the vapor deposition velocity of cesium hydroxide reacting with stainless steel surfaces.

Basic model changes were supplemented by changes made to improve the numerical modeling of the mass transfer to and from the aerosol. The tolerance parameters that were originally concerned only with error control on the mass in each state were expanded to include error control on the aerosol particle number density as well. This new tolerance parameter placed an additional convergence requirement on the acceptable mass error variation of the smaller aerosol sizes to help ensure convergence of aerosol number density as well as mass. In addition, the model for aerosol particle size change due to evaporation and condensation of multiple species was revised to rigorously conserve both mass and particle number.

The chemical species considered were cesium iodide, cesium hydroxide, cadmium, and tin. Tin telluride (SnTe) was not considered because no satisfactory model for its release from the zircaloy cladding was available. The source rates of these species were calculated from noble gas release rates (cesium iodide and cesium hydroxide), analysis with the VAPOR[29] model (cadmium), and with a computer program written for this project (tin).

Thermochemical equilibrium calculations for the dominant chemical forms of cesium, iodine,

Table 25. Models included in the SFD 1-4 fission product transport analysis

1. Evaporation and condensation between aerosol particles, vapor, and walls. In contrast to TRAP-MELT2, no zero vapor pressure seed is used and an equilibrium distribution of chemical species among aerosol sizes is not assumed.

2. Chemisorbtion of vapors by stainless steel or zircaloy walls.

3. Aerosol deposition:

    a. Diffusion for turbulent or laminar flow;
    b. Gravitational settling;
    c. Thermophoresis;
    d. Lateral slip at pipe bends;
    e. Deposition due to wakes and eddies behind obstructions.

4. Aerosol agglomeration:

    a. Brownian motion;
    b. Differential gravitational settling;
    c. Turbulent eddies.

5. Heat transfer from the fluid phase to walls of specified temperature by convection and radiation.

and tellurium were used to determine the chemical species considered by the transport model. Details of the SOLGAS3[35] code calculations are given in Appendix H. The calculations indicate that cesium iodide was the dominant chemical form of iodine at all temperatures. Very little HI and no AgI are predicted to have formed. Figure 126 presents the calculated mole fraction of the dominant cesium species at thermochemical equilibrium for the conditions in Test SFD 1-4. The dominant chemical forms in this test are predicted be be cesium hydroxide, cesium iodide, and cesium. At 1500 K, 75% of the cesium is in the form of cesium hydroxide, 8% is cesium iodide, and 18% is elemental cesium. At temperatures above 1500 K, the cesium concentration increases, whereas at temperatures less than 1100 K very little cesium is predicted to be present. These results differ from the thermochemical equilibrium calculation results for Test SFD 1-1 because of the higher fission product concentrations and the presence of vapor released from damaged control rods in Test SFD 1-4.

Section H.5 of Appendix H provides additional information about the source rates and chemical speciation results and a complete description of the input boundary conditions used for the analysis.

7.4.2 Analysis Results. Excellent fission product and aerosol measurements were obtained during Test SFD 1-4. In this section, the calculated behavior is compared to the measured data; and some implications about aerosol behavior at locations where data were not available are discussed. The results of three calculations are considered: a best-estimate calculation; a calculation with a tenfold increase in the tin release; and a calculation with an 80% reduction in wall surface area in the deposition rod region. These sensitivity studies are presented because of their impact on the resulting fission product transport and deposition behavior.

7.4.2.1 Comparison of Results with Aerosol Monitor Data. One important key to understanding fission product behavior in Test SFD 1-4 is the nature of the aerosol that was formed as low-volatile vapors supersaturated above the fuel bundle in the heat shield region. The high number density and small size of the aerosol particles provided a large, mobile surface area that received other condensing species in downstream segments of the effluent line. If this time-and-location-dependent surface is not properly described, it is not likely that a correct description of the transport of the more volatile species will be produced.

Figures 127, 128, and 129 compare the calculated and measured aerosol mass concentration, number concentration, and geometric mean diameter (GMD) at the aerosol monitor. The

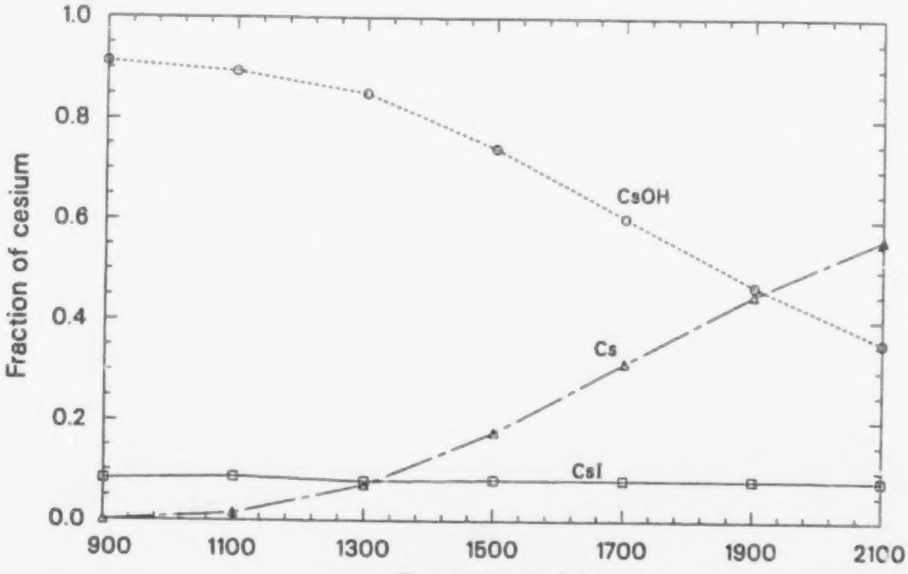

Figure 126. Calculated mole fraction of the dominant cesium chemical species at thermochemical equilibrium for the base-case conditions at temperatures between 900 and 2100 K.

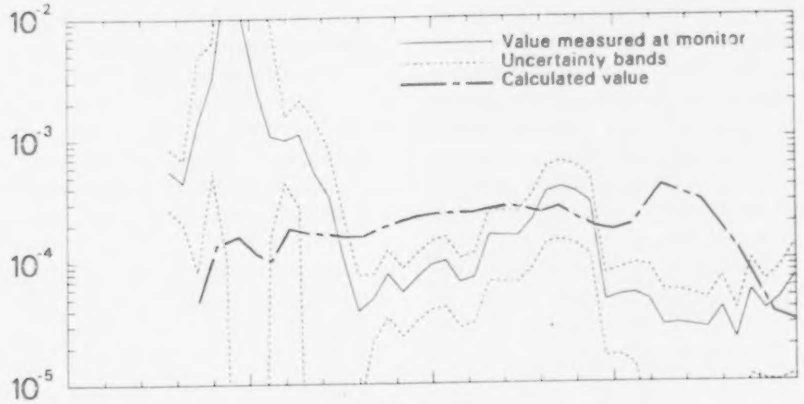

(a) Base case

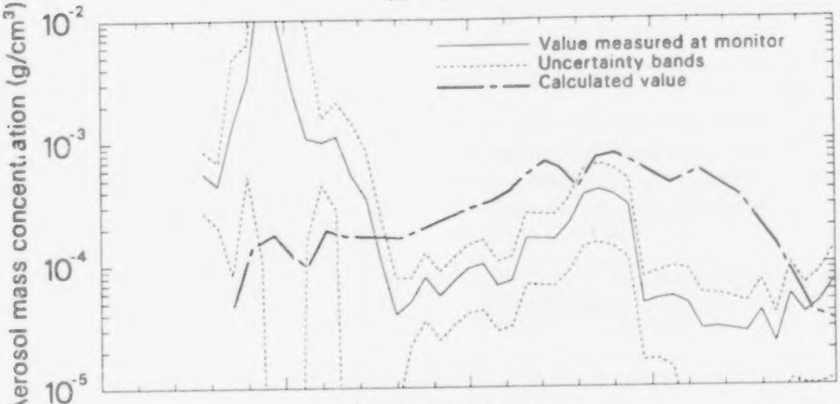

(b) Increased tin source

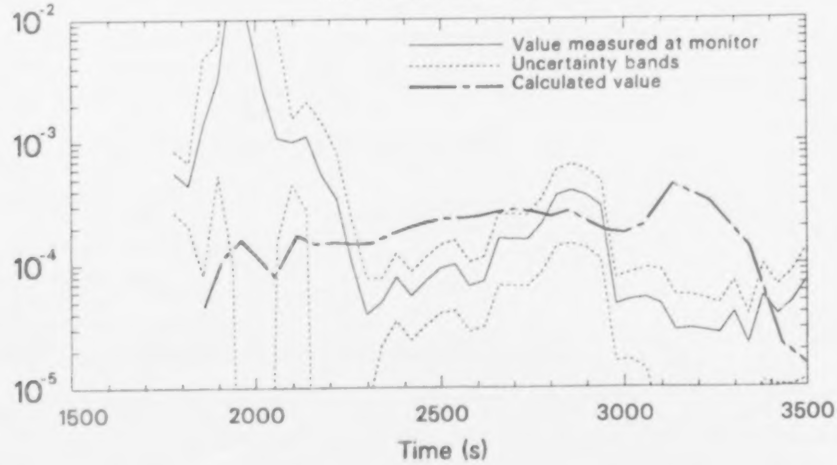

(c) Decreased wall surface area

P742 DAP-988-09C

Figure 127. Comparison of the calculated and measured aerosol mass density at the monitor for three calculations.

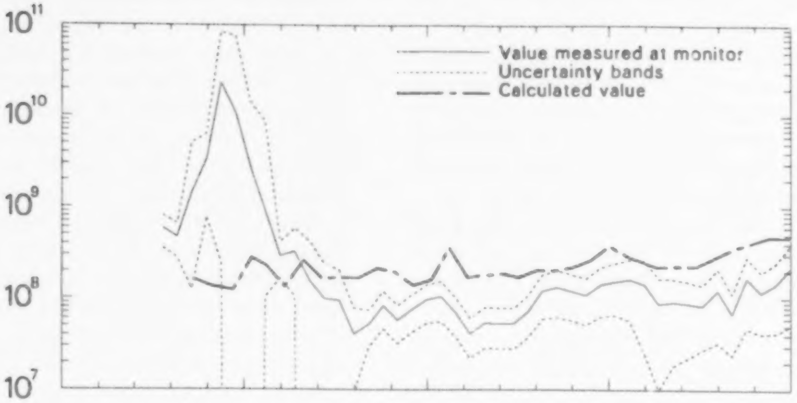

(a) Base case

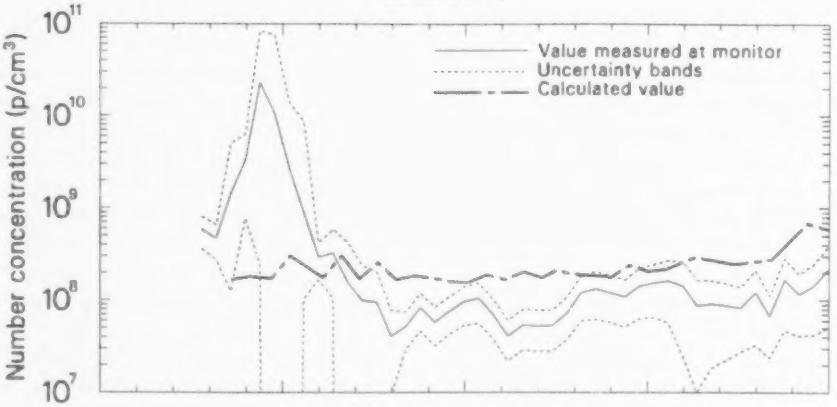

(b) Increased tin source

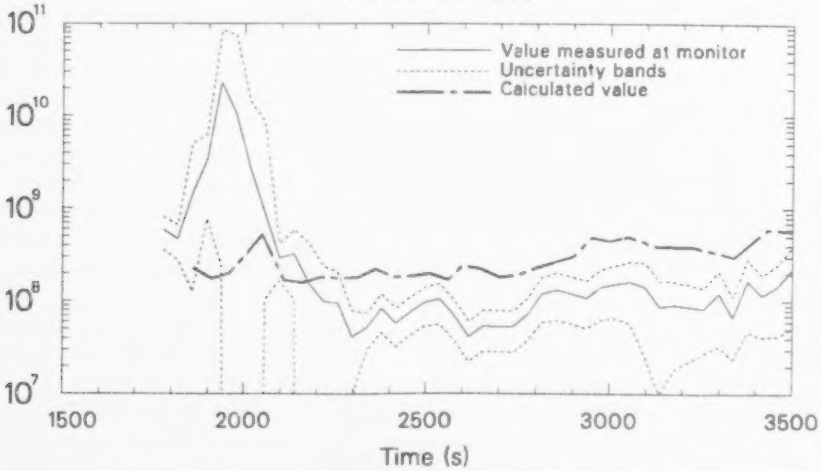

(c) Decreased wall surface area

P742 DAP-888-10C

Figure 128. Comparison of the calculated and measured aerosol number concentration at the monitor for three calculations.

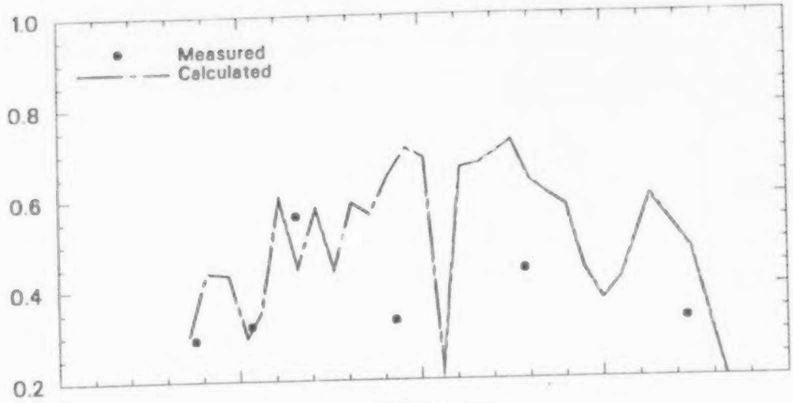

(a) Base case

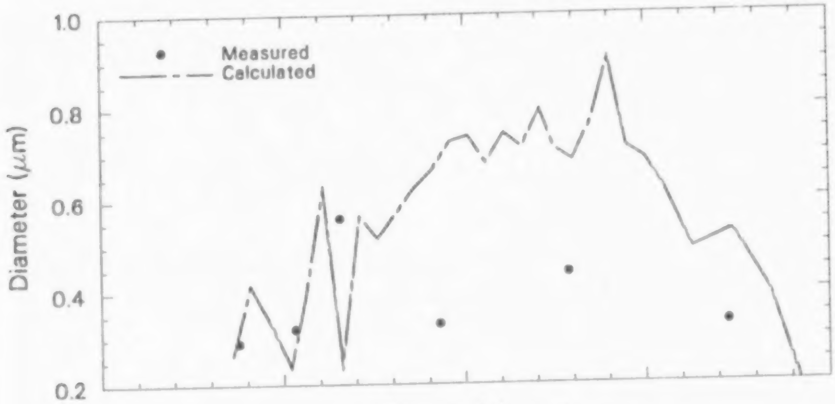

(b) Increased tin source

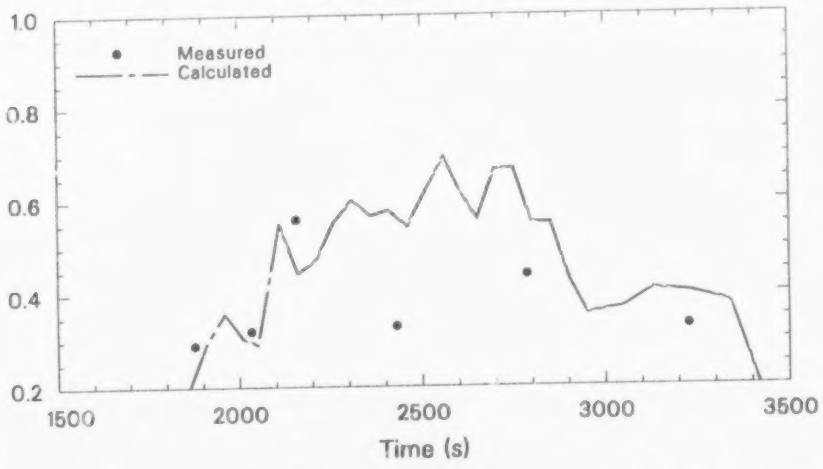

(c) Decreased wall surface area

P742 DAP-988-11C

Figure 129. Comparison of the calculated and measured geometric mean diameter (GMD) of the aerosol at the monitor for three calculations.

calculated mass densities shown in Figures 127a through 127c are consistent with the density obtained from the aerosol monitor data over the time domain where the monitor data have low uncertainty. The tenfold increase in the tin aerosol source rate produces only a threefold increase in the calculated mass density at the monitor near the time of maximum release (2800 to 3200 s). However, the reduction in the surface area of the deposition rod region produces a much smaller effect.

Figures 128a through 128c show that the calculated aerosol number density at the monitor is also consistent with the density determined at the monitor. Calculated changes in number density are even less sensitive than the mass density to the initial tin source rate and the surface area available for deposition and/or condensation in the deposition rod area. In all calculations, number concentrations were limited by agglomeration to approximately 10^8 per cubic centimeter at the monitor.

The calculated GMDs shown in Figures 129a through 129c agree well with the GMD data from the filtered samples taken just downstream from the aerosol monitor. Like the number and mass densities, the calculated particle size is not very sensitive to an order-of-magnitude increase in the tin source rate or a reduction in the deposition rod surface area. The lack of sensitivity of aerosol characteristics at the monitor is caused by particle agglomeration that limits the number density to a maximum and deposition of the larger particles that limits particle size and mass density.

Figures 130a and 130b compare the calculated aerosol mass density arriving at the monitor to the calculated aerosol density above the fuel bundle in the heat shield region. The aerosol mass density at the monitor is greater than the aerosol density at the heat shield because most of the volatile vapors (i.e. cadmium, cesium iodide, cesium hydroxide) condensed onto aerosols between the heat shield and the closure head at 3.65 m. Because the rate of condensation is considerably greater than the rate of aerosol deposition in the calculation, the aerosol mass density from the closure head at 3.65 m to the aerosol monitor is nearly constant. The calculated temporal behavior of the aerosol mass density at the monitor exhibited much less variation than the calculated three-order-of-magnitude change in the mass density at the radiation heat shield during the experiment. As vapor concentrations and aerosol particle densities increased above the fuel bundle, aerosol particles became more massive by both agglomeration and condensation, causing deposition in the upper plenum to increase. As a result, the increased mass density downstream was less sensitive to changes in bundle source rates.

Figure 131 shows the calculated aerosol number density at the heat shield and at the monitor in the best-estimate calculation. Prior to 2500 s when aerosol source rates were relatively low, the particle densities at the two locations were nearly the same. During the high-temperature portion of the experiment, the greater tin release caused an increase in the number density at the heat shield. Condensation of higher concentrations of more volatile species on the large number of tin particles caused them to become massive. Agglomeration and settling of the larger particles were sufficient to prevent an increase of the number density measured by the aerosol monitor between 2600 and 3200 s, in spite of the orders-of-magnitude increase in the number density at the source.

7.4.2.2 Calculated Aerosol Size and Fission Product Species Content. Figures 132a through 132c show the calculated aerosol size as a function of location of a slug of effluent at ∿2800 s, a time of high aerosol and fission product release but relatively low cadmium release. The assumed initial GMD in the heat shield region, 1.15 m above the bottom of the core, was small, 0.083 μm. Agglomeration and some tin vapor condensation as the gas cooled increased the GMD by factors of one to three in the different calculations as the slug approached the tip of the deposition rod. At this position, cesium iodide and cesium hydroxide supersaturated and began to condense on the tin-based aerosol.

As the slug approached the tip of the deposition rod at 1.4 m, agglomeration and some tin vapor condensation occurred as the gas cooled, increasing the GMD by 25% in the best-estimate and reduced-surface-area calculations (Figures 132a and 132c). In the calculation with an increased tin source rate, agglomeration increased the GMD by a factor of three but, at the same time, reduced the number of particles to only twice as many as the best-estimate calculation.

From 1.4 m downstream, the particle size was affected by condensation as well as agglomeration. The net mass condensed was controlled by the vapor supersaturation, not the number of particles. In the best-estimate calculation, condensation increased the GMD by a factor of two; however, the increase was not as large in the case with a tenfold increase in the amount of aerosol because each particle received only one-half as much mass. Condensation of cesium iodide and cesium hydroxide onto

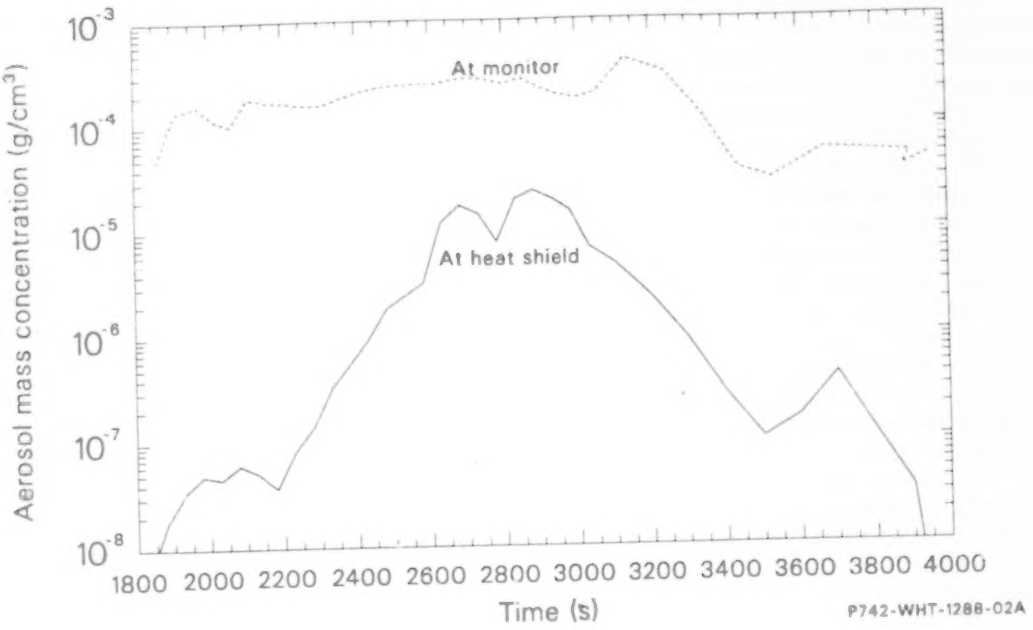

(a) Base case

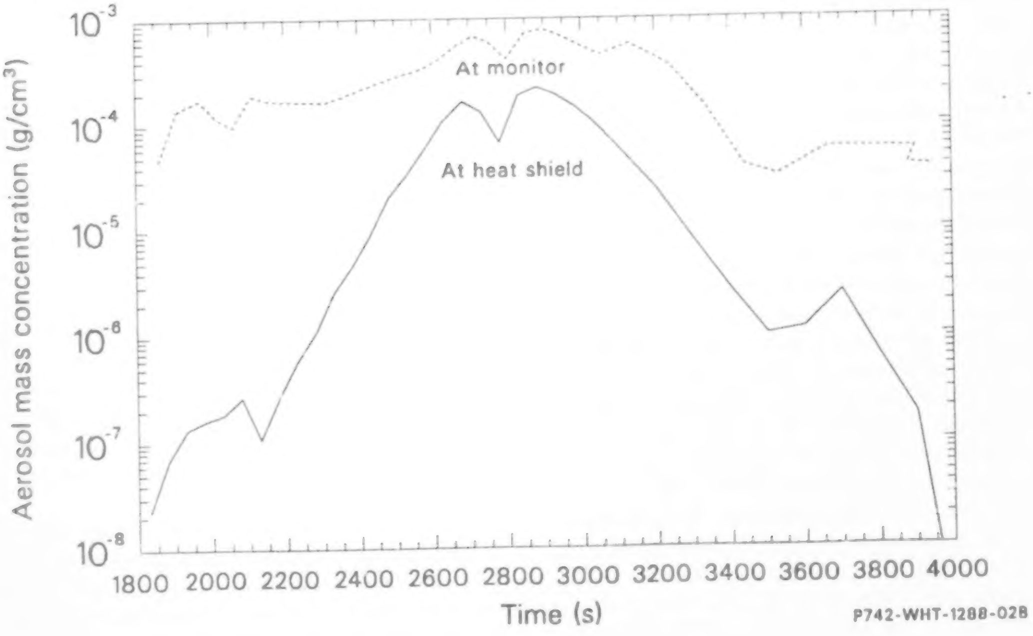

(b) Increased tin source

Figure 130. Calculated aerosol mass density at the heat shield and at the monitor.

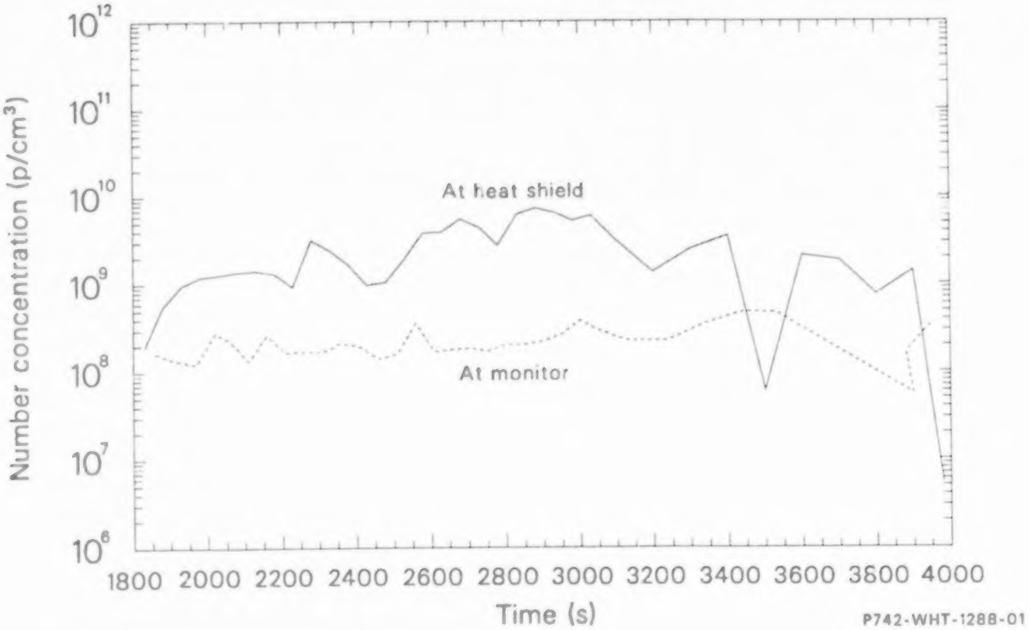

Figure 131. Calculated aerosol number density at the heat shield and at the monitor for the best-estimate calculation.

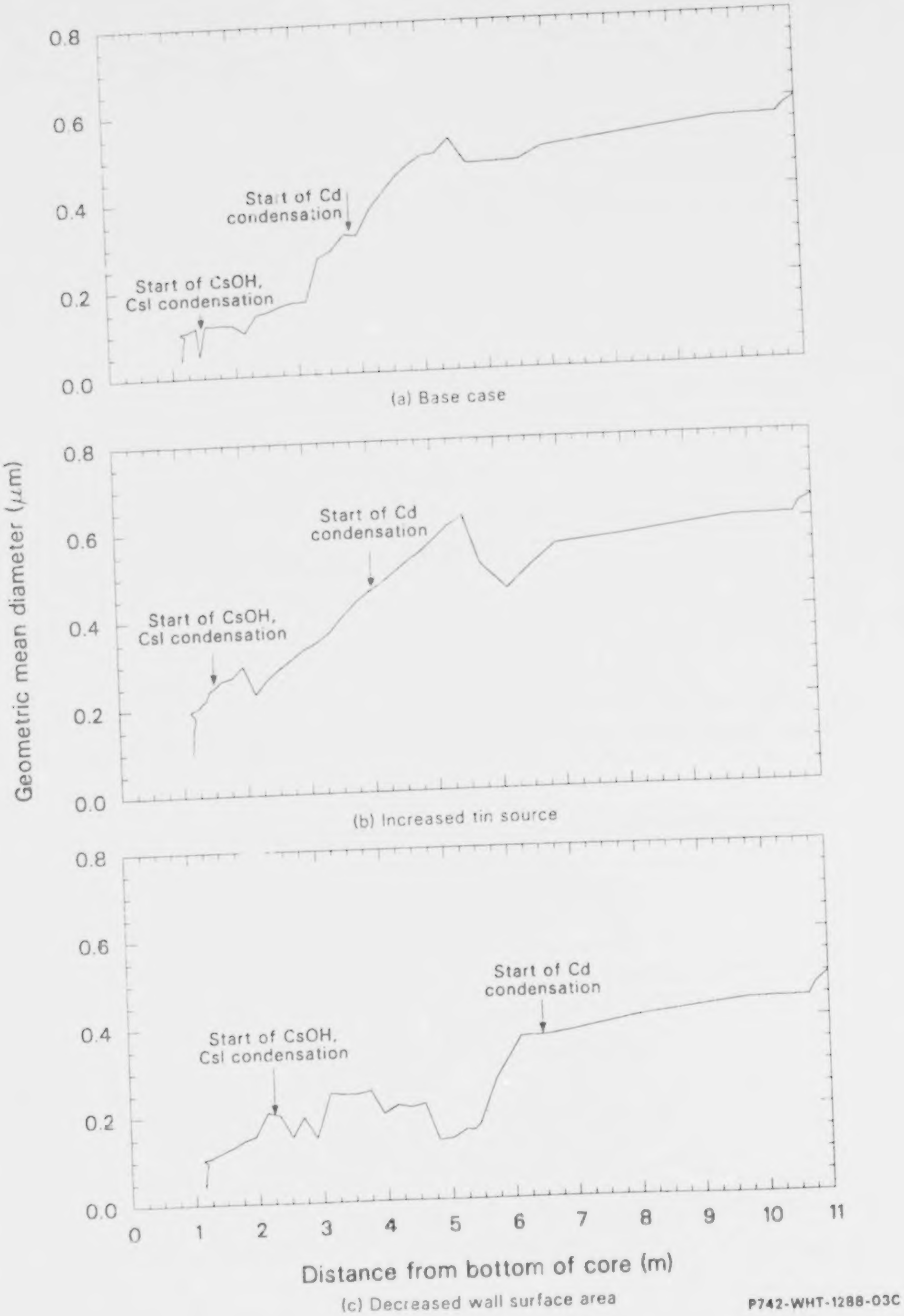

Figure 132. Calculated aerosol size of a slug of effluent at ~2800 s as a function of location for three calculations.

the aerosol occurred further downstream in the case with the reduced surface area, so the initial increase in GMD was delayed. The location at which these fission products became supersaturated was shifted due to slower gas cooling caused by the reduced surface area.

The condensation behavior of cadmium was similar to that of cesium iodide and cesium hydroxide. At 2800 s, the cadmium release rate was relatively low. As a result, the supersaturation and condensation of cadmium occurred at 2 to 5 m, somewhat farther downstream than the cesium iodide and cesium hydroxide. Cadmium condensation caused a larger increase of the GMD in the best-estimate calculation than in the other two calculations.

Figure 133 shows the calculated distribution of cesium hydroxide and cesium iodide in the vapor and as part of the aerosol particles. Very little condensation was present until 1.33 m, the tip of the deposition rod. At this point, condensation caused a rapid decrease in the amount of these species in the vapor and a corresponding increase in the amount on aerosol particles because of the large aerosol surface area. For the remainder of the transport of the slug to the aerosol monitor, the amount of cesium species on aerosol particles decreased slowly as the particles were deposited and mass evaporated from the aerosol through the vapor to the wall in the unheated portion of the upper plenum. A comparison of Figures 133a and 133b indicates that the amount of cesium species transported on aerosol particles was not a strong function of the initial tin source rate because there was ample aerosol surface area for vapor condensation in both cases. However, in Figure 133c, when the wall surface was reduced by 80%, the transition from vapor to aerosol for these cesium species occurred over a larger region because of slower gas cooling.

The calculated distribution of cadmium in the vapor and as part of an aerosol is shown in Figures 134a through 134c. Condensation from the vapor started a little farther downstream than the condensation of cesium hydroxide and cesium iodide. However, more cadmium than cesium hydroxide or cesium iodide remained in the vapor because of the higher vapor pressure of the cadmium.

7.4.2.3 Comparison of Results with Effluent Samples. Table 26 is a comparison of the calculated weight percent of several elements at the aerosol monitor with the concentrations found in the six effluent samples taken immediately downstream of the aerosol monitor. With the exception of the first samples, the calculated cesium aerosol fraction (mostly cesium hydroxide) is much greater than the fraction observed. The lack of cesium on the sampler filters could have been due to inefficient retention of the cesium hydroxide aerosol component by the sample filters, since 90% of the cesium is calculated to be cesium hydroxide, a compound that would be liquid at the temperature of the sample location (590 K). This hypothesis is supported by the fact that the ^{137}Cs activity in the condensed liquid effluent was ten times the activity on the filters of the high-temperature samples.

The cadmium fractions of the samples suggest that the first maximum of the cadmium release rate may have occurred from 2100 to 2900 s instead of 1900 to 2100 s, as shown in Figure H-11. Tin fractions for the first four samples provide similar indirect evidence that the calculated rate of release of tin from the cladding was too low during the heating time period, 1900 to 2500 s.

7.4.2.4 Comparison of Results with Deposition Coupon Data. Figures 135 through 137 compare the calculated surface concentrations of cesium, cadmium, and tin to data from selected locations on the deposition rod. In these three figures, the calculated curve is an average for all vertical and horizontal surfaces, while the data are from samples located on the deposition rod surfaces. The horizontal surface area is approximately 0.3% of the total area in the deposition rod region, but the higher concentrations of cesium and cadmium found on the horizontal surfaces from 2 to 4.5 m above the bottom of the core suggest that directional settling mechanisms were an important part of the mass deposition onto all but the downstream end of the deposition rod.

With the exception of the calculation with reduced surface area, the calculated deposition of the cesium compounds, cesium iodide and cesium hydroxide, was less than the measured surface concentrations on both vertical and horizontal surfaces. The results for the best-estimate calculation suggest that cesium hydroxide and cesium iodide condensation onto walls was the dominant deposition mechanism from the heat shield until just past the tip of the deposition rod at 1.5 m. Between 1.3 to 3.8 m, the calculated relative contributions of various mass-transfer mechanisms to the wall change. At 1.3 m, the cesium mass per surface area deposited by condensation to the wall was five orders of magnitude greater than that deposited by aerosol particles. By 3.8 m, the vapor concentration had approached

best copy available

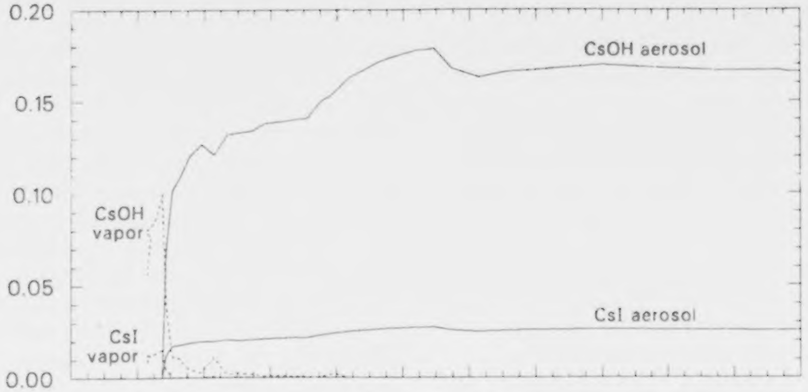

(a) Base case

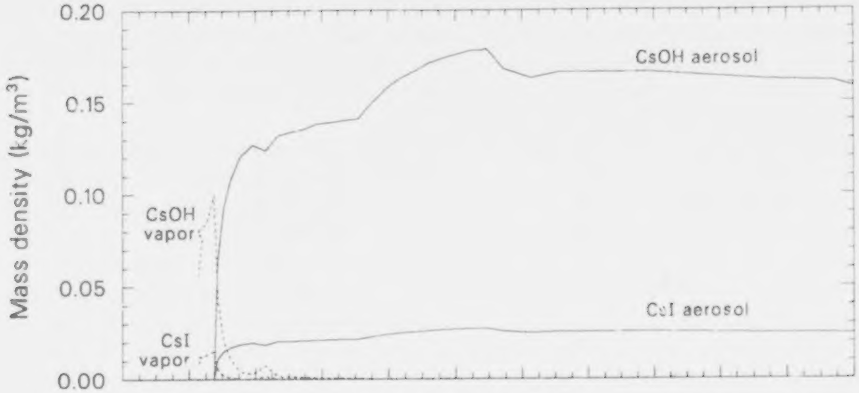

(b) Increased tin source

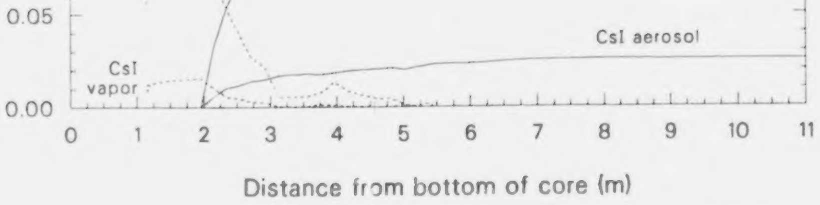

(c) Decreased wall surface area

P742-WHT-988-04C

Figure 133. Calculated distribution of cesium hydroxide and cesium iodide in the vapor and as an aerosol in a slug of effluent at ~2800 s for three calculations.

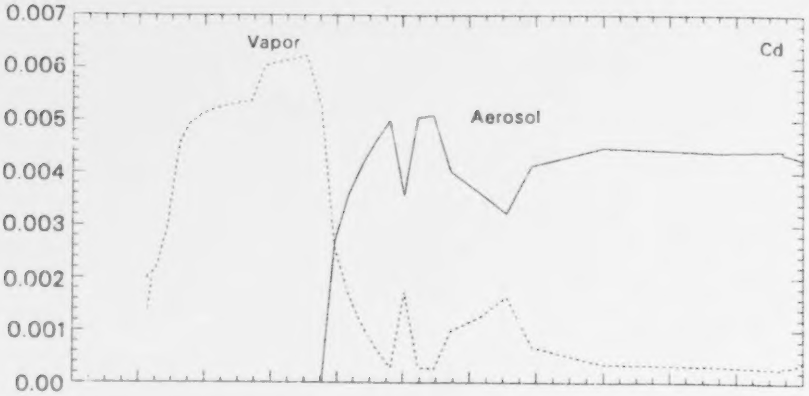

(a) Base case

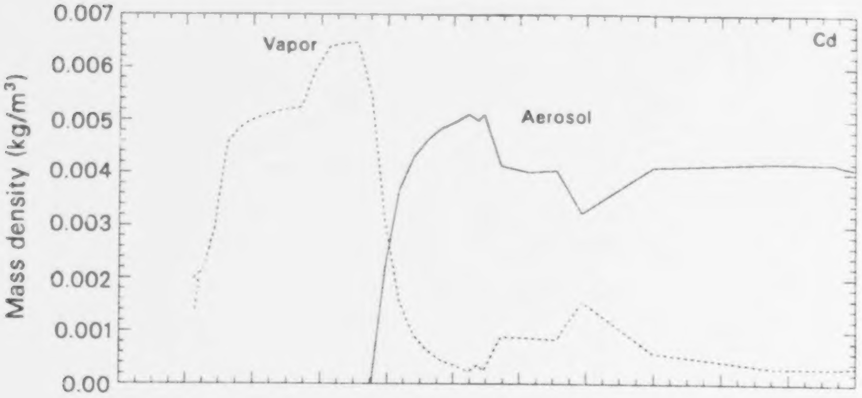

(b) Increased tin source

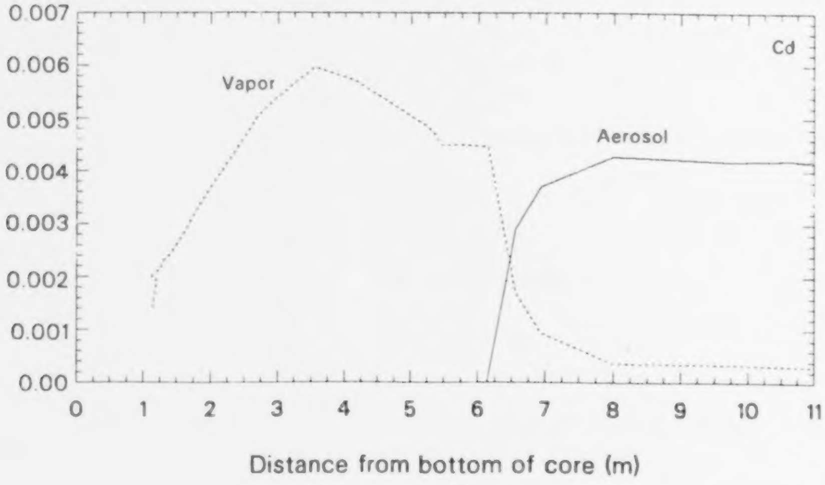

(c) Decreased wall surface area

P742-WHT-988-05C

Figure 134. Calculated distribution of cadmium in the vapor and as an aerosol in a slug of effluent at ∿2800 s for three calculations.

Table 26. Measured and calculated aerosol composition at 11.7 m

	Sampling Time (s)	Mass Percent of Sampled Aerosol					
		Ag	Cd	Sn	Zr	Te	^{137}Cs
Measured	1950	0.6	—[a]	24.7	1.9	73.1	0.3
Calculated[b]	1964	—[c]	99.5	0.4	—[d]	—[e]	0.5
Calculated[f]	1964	—[c]	99.4	0.16	—[d]	—[e]	0.4
Calculated[g]	1961	—[c]	99.6	0.05	—[d]	—[e]	0.4
Measured	2040	2.1	6.8	83.7	4.3	—[a]	3.0
Calculated[b]	2056	—[c]	64.1	0.2	—[d]	—[e]	35.7
Calculated[f]	2056	—[c]	62.0	0.8	—[d]	—[e]	37.3
Calculated[g]	2052	—[c]	50.5	0.3	—[d]	—[e]	49.2
Measured	2100	2.0	38.8	54.9	3.6	—[a]	0.8
Calculated[b]	2113	—[c]	24.9	0.2	—[d]	—[e]	74.8
Calculated[f]	2113	—[c]	25.0	0.8	—[d]	—[e]	74.2
Calculated[g]	2114	—[c]	8.9	0.2	—[d]	—[e]	90.9
Measured	2385	2.6	38.6	57.8	—[a]	—[a]	1.0
Calculated[b]	2360	—[c]	16.1	0.2	—[d]	—[e]	74.8
Calculated[f]	1964	—[c]	16.2	0.8	—[d]	—[e]	74.2
Calculated[g]	1961	—[c]	8.1	2.5	—[d]	—[e]	89.4
Measured	2850	2.2	24.2	72.7	—[a]	—[a]	0.8
Calculated[b]	2852	—[c]	2.2	58.5	—[d]	—[e]	39.3
Calculated[f]	2852	—[c]	0.6	90.6	—[d]	—[e]	8.8
Calculated[g]	2848	—[c]	3.8	58.7	—[d]	—[e]	37.5
Measured	3060	8.0	25.6	60.0	4.8	—[a]	1.5
Calculated[b]	3053	—[c]	57.4	29.0	—[d]	—[e]	13.6
Calculated[f]	3053	—[c]	19.1	76.4	—[d]	—[e]	4.6
Calculated[g]	3050	—[c]	58.7	28.0	—[d]	—[e]	13.4

---

a. Below detection limits. For tellurium, this was nearly equal to the mass of tin present.

b. Best-estimate calculation.

c. Silver was not considered in the analysis.

d. Zircaloy (probably the oxide) was not considered in the analysis.

e. Tellurium was not considered in the analysis.

f. Calculated with a tenfold increase in the tin release.

g. Calculated with an 80% reduction in wall surface area in the deposition rod region.

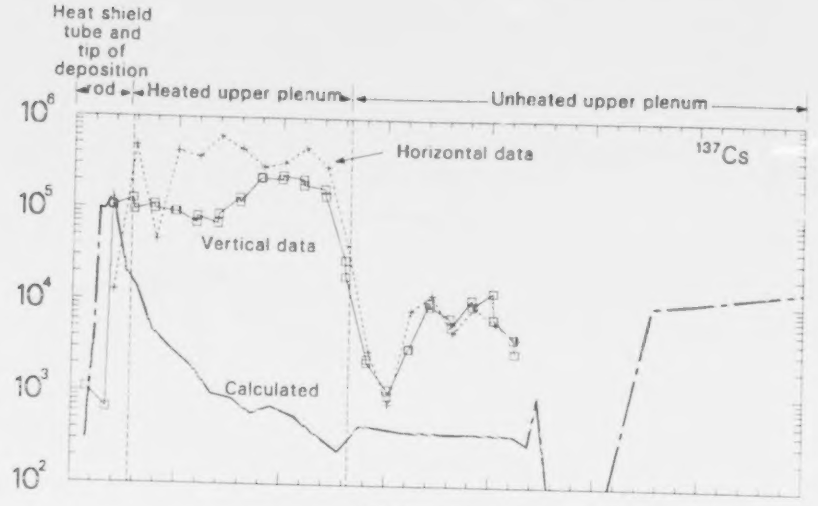

(a) Base case

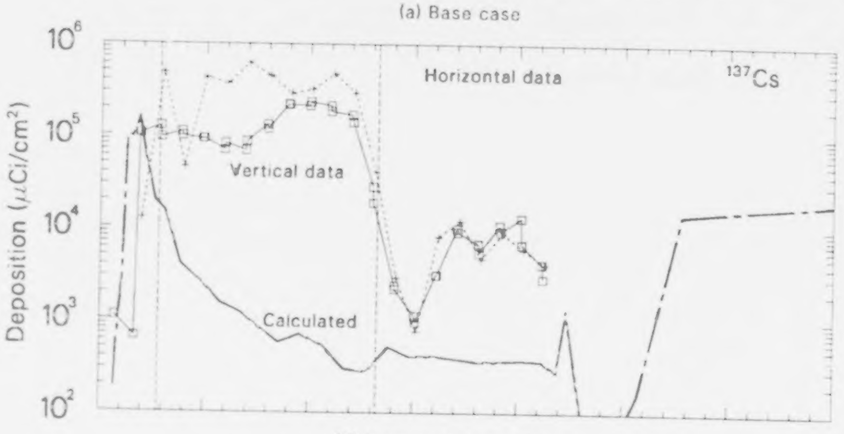

(b) Increased tin source

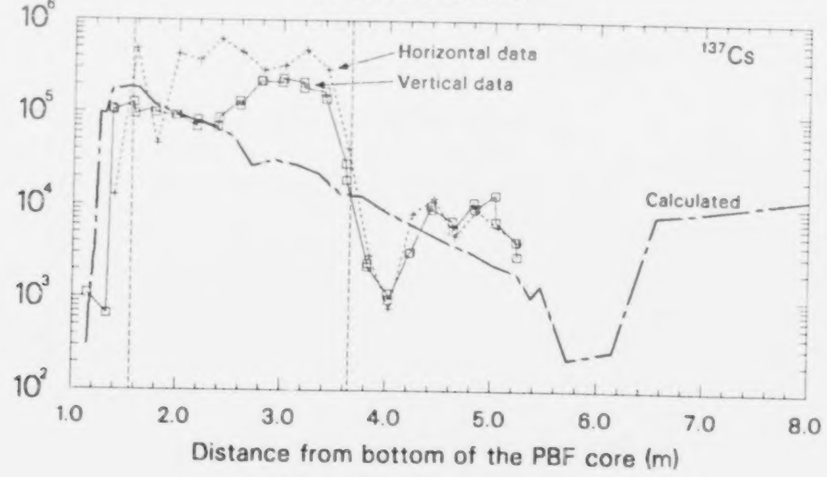

(c) Decreased wall surface area

P742 DAP-988-14C

Figure 135. Comparison of calculated and measured surface concentrations of cesium for three calculations.

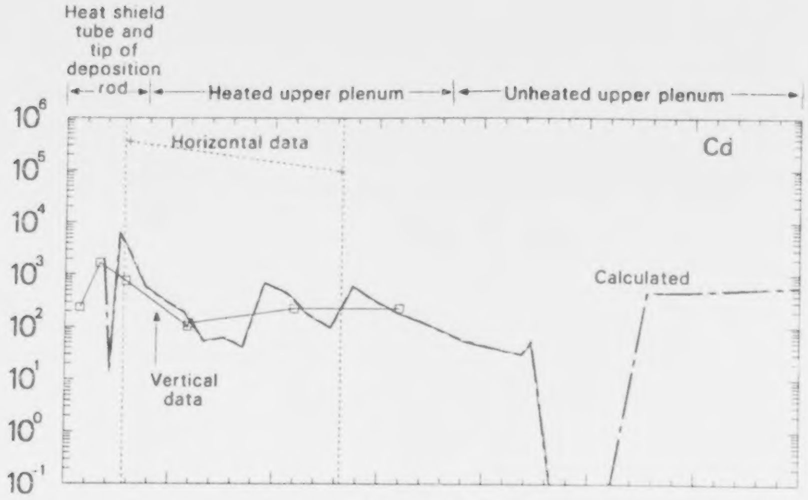

(a) Base case

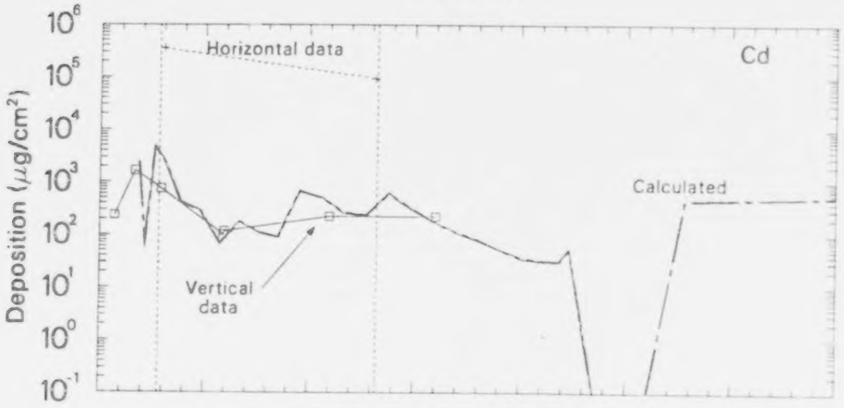

(b) Increased tin source

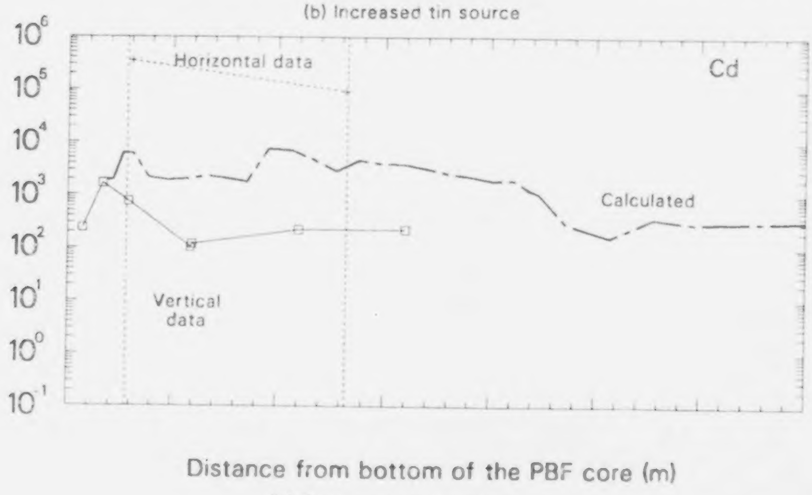

(c) Decreased wall surface area

P742 DAP-988-12C

Figure 136. Comparison of calculated and measured surface concentrations of cadmium for three calculations.

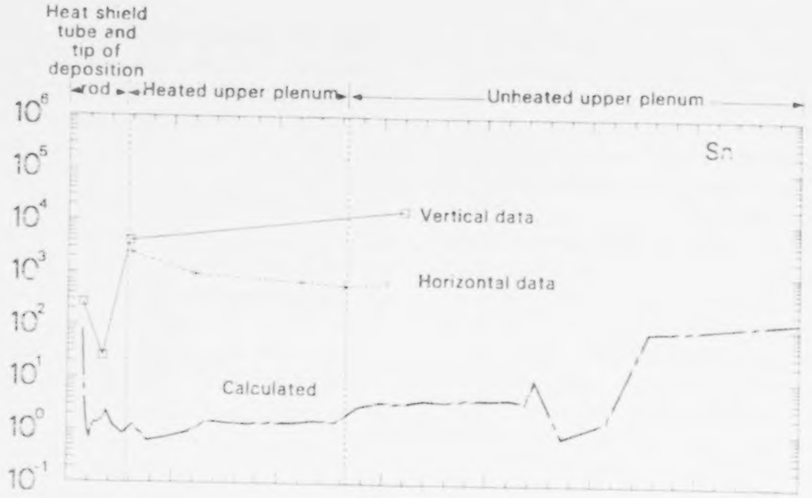

(a) Base case

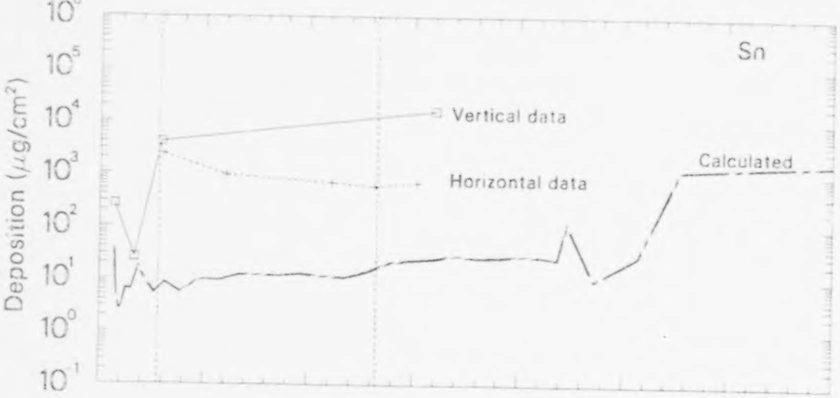

(b) Increased tin source

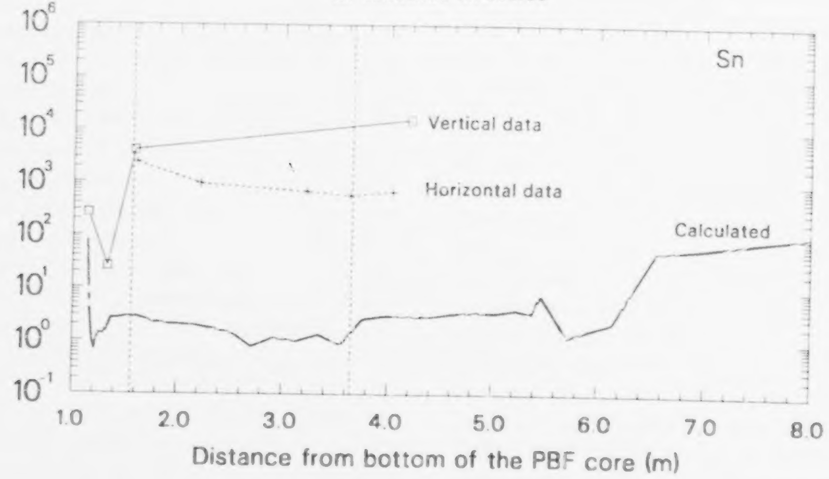

(c) Decreased wall surface area

P742 DAP-988-13C

Figure 137. Comparison of calculated and measured surface concentrations of tin for three calculations.

equilibrium and the particle size had increased to the point that particle deposition and condensation accounted for equal parts of the cesium deposition surface density.

As with the distribution of cesium hydroxide, cesium iodide, and cadmium between vapor and aerosol, the calculated surface densities of ^{137}Cs were not affected by assuming a tenfold increase in the tin aerosol because the best-estimate tin aerosol source rate provided ample aerosol surface area for condensation. When it was assumed that only 20% of the surface area in the deposition rod area was available for condensation and heat transfer, the calculated surface deposition (Figure 135c) was more consistent with the measured data. The change in deposition occurred because the rates of gas cooling and wall condensation decreased.

The calculated deposition of cadmium, shown with the data in Figure 136, is similar to that of the cesium compounds, cesium iodide and cesium hydroxide, but shifted to slightly cooler temperatures at downstream locations because the equilibrium vapor pressure of cadmium was higher relative to its concentration in the effluent.

In none of the calculations was there enough calculated cesium or cadmium deposition to explain the measured difference in deposition between the horizontal and vertical surfaces. This observation suggests that either (a) the calculation has greatly underestimated the large size portion of the aerosol size distribution in the deposition rod region (but recovered the correct result at the location of the aerosol monitor) or (b) flow of some of the liquid condensate on the vertical surface down to the lower horizontal surface was a major contributor to the cohesive debris found on the horizontal surface. The possibility of surface flow is supported by the observation that cesium hydroxide would have been a liquid and cadmium, which melts at 594 K, may have been liquid at the deposition rod temperatures in the heated region but solid in the unheated portion of the deposition rod.

The calculated deposition of tin is compared to measurements in Figure 137. The calculations severely underestimate the measured tin deposition. The reason for this discrepancy is difficult to explain. Some of the difference could be due to a low estimate of the tin source rate for the calculation, but the data shown may also be biased to high values by the fact that tin is difficult to measure. The only data shown in Figures 137a through 137c are those that yielded results above the detection threshold. Several measurements yielded results below detection limits and are not included.

7.4.3 Conclusions from the PULSE Analysis. Detailed analysis of fission product and aerosol transport with the PULSE analysis tool confirmed several results of the engineering calculations presented earlier. The formation of a fine aerosol by tin vapor (and perhaps silver) at the upper fuel bundle/radiation shield location is consistent with the deposition and time-dependent aerosol monitor data. Because Test SFD 1-4 is prototypical of reactor cores, it can be concluded that formation of a tin aerosol just above the hot part of the core is likely in many severe accidents.

The tin release model showed considerable tin condensation in the upper fuel rod regions. This condensate was a source of tin aerosol late in the experiment when the cladding that was the primary source had relocated to cooler regions. There is no reason to believe this sort of revaporization from tin condensed on remaining solid surfaces above relocated core is unique to Test SFD 1-4. It should be expected in all severe fuel damage accidents.

All calculations indicate that below 700 K more than 95% of the volatile fission products in the effluent were transported as an aerosol. This conclusion is a direct result of the temperature, the vapor pressure of the species, and the aerosol number density (which was consistent with measurements). The large surface area and 0.7- to 0.9-μm GMD of the aerosol resulted in 75% of the mass of the volatile species that left the fuel being transported 10 m to the aerosol monitor. Ninety percent of the less volatile tin aerosol from the fuel passed the aerosol monitor.

A strong negative feedback mechanism limits aerosol mass density to about 0.1 kg/m^3 and number density to about a few times 10^8 particles/cm^3 at the monitor. This sort of self-limiting would also be likely in severe accidents.

Test SFD 1-4 has considerable potential as a benchmark for fission product transport models. The analysis showed that some modification of the TRAP-MELT2 models, such as the addition of models to consider the wakes and eddies caused by structures and the addition of specific properties of tin aerosols, was required for an acceptable analysis. Considerable revision of the implementation of the TRAP-MELT2 models was also found to be necessary. The evaporation/condensation modeling techniques had to be revised to ensure conservation of both mass and particle number, and it was extremely helpful to replace the TRAP-MELT2 solution scheme that depends on assumptions about fast and slow mass transport mechanisms with a scheme that does not rely on a fixed ordering of rates.

Additional conclusions from the analysis are that there is need for development of a model for SnTe release from zircaloy cladding that is similar to the tin release model used with the analysis and that vertical and horizontal surfaces should be considered separately in future analytical work.

7.5 Aerosol Behavior Summary

The aerosol measurements and the engineering and PULSE code calculations of aerosol behavior can be integrated to determine the general aerosol behavior in Test SFD 1-4. The number concentration calculated from the on-line aerosol monitor data can be used with the elemental and size data from the effluent filtered samples to correlate aerosol generation with melt progression phenomena occurring in the SFD 1-4 bundle. The engineering type of aerosol calculations discussed in the previous sections can also provide details concerning the aerosol deposition and transport in the SFD 1-4 upper plenum. Together, these results form the aerosol formation, deposition, and transport scenario for Test SFD 1-4.

7.5.1 Aerosol Generation. Estimating the timing and duration of each aerosol source is difficult due to the integral nature of the experiment. Many phenomena occurred simultaneously during Test SFD 1-4, several of which could have caused aerosol formation. Data from the deposition coupons and the effluent filter samples indicate that vaporization of control rod material, the nucleation of volatile fission products like cesium iodide, the vaporization of tin from the oxidized zircaloy cladding, and the possible release of loose particulates from the shroud (ZrO_2) insulation cavity probably all contributed to the aerosol source exiting the bundle.

The following sections discuss aerosol generation during Test SFD 1-4 using the aerosol monitor response in Figures 95 and 96, the calculated number concentration in Figure 123, and the aerosol size information obtained from the filtered effluent samples in Figure 124.

7.5.1.1 Initial Aerosol Generation Period (1740 to 2300 s). The aerosol monitor first responded to the presence of aerosols in the effluent at 1742 s, 34 s after the waterlogged control rod failed. The number concentration was estimated to be $\sim 5 \times 10^8$ p/cm^3. The high internal pressure at the time of rod failure suggests that the molten alloy may have been ejected from the control rod breach. The small burst of aerosols measured by the aerosol monitor was due to the vaporization of the silver, indium, and cadmium from the molten alloy and the subsequent formation of aerosols. Since the vapor pressures of silver and indium are quite low at 1170 K, the failure temperature of the first control rod, the aerosol was most likely dominated by cadmium.

The signals from both test cells showed very large drops in transmission starting at 2050 s, indicating the presence of a dense aerosol in the effluent line. The 4-cm cell saturated 100 s later, while the 1-cm test cell reached a peak at 7% transmission. The aerosol number concentration at this time could not be determined with certainty because the 4-cm cell saturated. Results from effluent filtered samples 1 and 2 indicate that the aerosol measured prior to 2000 s was small, with a diameter of average mass of ~ 0.65 μm. However, by 2100 s, more aerosol was present in the line, as evidenced by a larger d_m of 0.98 μm and an increased mass concentration.

This large burst of aerosol activity that began at 2050 s can be correlated to events that occurred in the bundle. Between 1927 and 1978 s, the three remaining control rods failed. Given a delay time of ~ 70 s between the center of the bundle and the aerosol monitor, the presence of aerosol in the line can be in part attributed to the failure of the remaining control rods. The 1-cm test cell indicated that this burst of aerosol activity lasted roughly 250 s. This sustained aerosol signal when corrected for delay times coincided with the onset of high temperatures in the bundle. Fission chamber responses indicated that very rapid downward relocation of the control rod alloy to cooler portions of the bundle occurred at this time (see Figure 79). However, the control rod aerosol source is believed to have lasted longer than this initial relocation period due to continued vaporization of alloy material on the surfaces of the guide tube and spacer grids and the release and vaporization of control material beneath the initial failure locations in the control rods. Thus, it is reasonable to assume that the control rod aerosol source could have lasted a few hundred seconds.

Between 2000 and 2380 s, temperatures in the bundle were increasing rapidly to values in excess of 2400 K. The high temperatures in the bundle would have caused the tin to vaporize from the hot oxidized zircaloy cladding. During this portion of the experiment, significant fission product release occurred, as is evidenced by an increase in the fractional release rate of noble gases by three orders of magnitude. Also, at 1946 s, the shroud inner liner failed, which allowed loose particulate from the ZrO_2 insulation to enter the bundle region. Thus, the sustained aerosol signal that began at 2050 s and lasted for 250 s was probably a superposition of the four aerosol sources discussed above—cadmium, tin, ZrO_2, and fission products. As seen in Tables 17 and 18, results from radioisotopic and elemental analysis of the filtered effluent samples taken during the experiment support this scenario. Gamma spectroscopy of the first two effluent samples, acquired during this first aerosol burst, indicate the presence of ^{110m}Ag, ^{114m}In, ^{131}I, ^{134}Cs, ^{136}Cs, and ^{137}Cs. Elemental analysis indicates that the aerosol at this time consisted mainly of tin and cadmium, with some silver and zirconium.

7.5.1.2 Diminished Aerosol Generation Period (2300 to 2800 s). At 2300 s, the signals from the two aerosol monitor channels began to decrease. Based on the transmission data from the two channels, the aerosol number concentration was between $\sim$7 x 10^7 and 10^8 p/cm^3. The diameter of average mass, as measured by effluent filtered sample 4, decreased to 0.64 μm. The aerosol mass concentration also decreased, indicating that less aerosol was present in the line. This decrease coincided with the start of the 223-s hold at peak power and continued for $\sim$600 s. The exact reason for this decrease is not known. However, several explanations appear plausible:

- The decrease in aerosol signal may have been due to a reduction in the control rod aerosol source. Some of the additional alloy below the failure location in the rod may have interacted with the guide tube and flowed down to a cooler region of the bundle, where it refroze and hence ceased to be an aerosol source.

- The rate of zircaloy oxidation in the bundle may have begun to decrease due to the reduction in power and temperature in the bundle. A lower oxidation rate may have lowered the aerosol production rate.

- Molten zircaloy may have flowed away from its original location to cooler portions of the bundle, where it refroze, thus trapping the tin.

Any or all of these phenomena could explain the reduction in aerosol concentration.

7.5.1.3 Enhanced Aerosol Generation Period (2800 to 3100 s). Between 2800 and 2900 s, as the bundle power was being reduced, the aerosol concentration began to increase above 10^8 p/cm^3. The responses of both aerosol channels indicated that this decrease in transmission lasted $\sim$350 s. The diameter of average mass of material as measured by filter 5, increased to 0.94 μm; and the aerosol mass density also increased, indicating that more aerosol was present in the effluent line. Assuming a delay time of about 60 s to the aerosol monitor, it is believed that the additional aerosol generation late in Test SFD 1-4 was due to reactivation of prior aerosol sources resulting from the ceramic melt relocation that was occurring in the bundle beyond 2300 s (see Section 5.3). Fission chamber data indicate that there was significant relocation of molten material between 2300 and 2600 s. This hot material, which was estimated from posttest examination to be $\sim$2800 K, could have contacted control rod material that was frozen in the lower bundle region. Posttest examination indicates that at the 0.17- and 0.25-m elevations ceramic melt was in contact with the metallic melt containing control rod material, stainless steel, and zircaloy. The energy carried by this relocated ceramic material could have been enough to cause additional vaporization of the silver, indium, and cadmium to occur until the melt cooled. [The time lag between material relocation (2300 to 2600 s) and the change in aerosol monitor signal (2600 to 2900 s) is probably due to the time required to reheat the relocated melt debris and to transport the material to the monitor.] SEM analysis of melt samples indicates a depletion of cadmium at the 0.25-m elevation relative to silver (see Appendix I). In addition, the relocation of the ceramic melt could have exposed fresh surfaces of molten zircaloy from which tin could have vaporized. Analysis of effluent sample filters 5 and 6, taken at this time in the experiment, indicate that large quantities of tin, cadmium, and silver were present in the effluent line. Radioisotopic analysis of filter 6 indicates increased levels of ^{110m}Ag and ^{114m}In compared to those samples taken earlier in the experiment.

7.5.1.4 Cessation of Aerosol Generation (3100 to 4000 s). Both aerosol channels began to show an increase in transmission beyond 3200 s, indicating cessation of aerosol generation as the experiment was terminated. At ∿3100 s, data from filter 6 indicate that the diameter of average mass had decreased slightly to 0.45 μm. The uncertainty introduced by plateout on the cell windows prevents an accurate estimate of the aerosol number concentration beyond 3500 s.

7.5.2 Aerosol Formation, Deposition, and Transport Summary. Based on the aerosol calculations presented earlier, a scenario can be postulated concerning the aerosol deposition and transport behavior of the predominant aerosol species in Test SFD 1-4. During the high-temperature portion of Test SFD 1-4, hot vapors of tin, silver, cadmium, and cesium were released from the bundle. Data from the experiment indicate that, in general, all of these materials were being released at roughly the same time during the experiment. In addition, based on the presence of zirconium on the deposition rod, some ZrO_2 aerosol seed is thought to have been released. Other fission products (i.e., tellurium, strontium, barium, europium, and curium) and impurities in the water (i.e., chlorine) were also being released from the bundle.

Measurements indicate that at least 13 g of aerosol material were released from the bundle—∿5 g of cadmium, 0.4 g of silver, 0.2 g of indium, at least 4 g of tin, and 3.5 g of zirconium. Although these values represent a small fraction of the bundle inventory of these materials, the mass was sufficient to produce a very dense aerosol during the entire high-temperature portion of the transient.

Chemical equilibrium calculations indicate that the dominant forms of cesium and iodine in Test SFD 1-4 were cesium iodide and cesium hydroxide, with some elemental cesium at high temperatures. Because of the high concentrations of cesium and iodine released from the high-burnup fuel and the low release of silver, no hydrogen iodide and no silver iodide were predicted to form. The dominant form of tellurium released from the bundle was tin telluride. These results are consistent with posttest system flushing results that indicate most of the iodine and cesium deposition was easily removed by water, whereas very little of the deposited tellurium was removed. The heavily reducing environment resulted in silver, cadmium, and tin being released in their elemental form.

Upon exiting the bundle, silver and tin, because of their low volatility, condensed in the upper bundle end caps region. For cadmium, cesium hydroxide, and cesium iodide, the high temperatures above the bundle and the high vapor pressures of these materials prevented vapor condensation from occurring. As the silver and tin entered the heat shield cone, they became supersaturated and formed an aerosol. Because of the low release rate of these materials from the bundle, the aerosol would have been very fine. The low vapor pressures of tin and silver at 800 K (the temperature in the deposition rod area) would have prevented any substantial additional condensation and/or evaporation of these materials to or from the aerosol as it traveled downstream. As a result, the tin and silver probably acted as fine inert aerosol seeds. Because of their low vapor pressures, the low-volatile fission products (strontium, barium, europium, and curium) and possibly ZrO_2 particles also exited the bundle as aerosols.

As the vapors of cadmium, cesium hydroxide, and and cesium iodide entered the heat shield tube and deposition rod area, they supersaturated. These materials would have been expected to condense very rapidly on both wall surfaces and the tin and silver and other aerosol seeds to produce a relatively "mature" aerosol within a few centimeters downstream of the tip of the deposition rod. Data indicate that most of the silver and cadmium deposition on vertical surfaces was found in the heat shield region. The presence of significant quantities of ^{137}Cs with the solid deposits of cadmium in the upper plenum indicates that the aerosol generated in Test SFD 1-4 provided a large mobile surface on which volatile fission products could condense. Below 700 K, more than 95% of the volatile fission products in the effluent were transported as aerosols.

Once the aerosol moved further downstream, very little evaporation and/or condensation of the volatile species (i.e., cadmium, cesium hydroxide, and cesium iodide) would be expected because the upper plenum was heated to a uniform temperature of ∿800 K. However, the aerosol concentration was high enough that agglomeration was occurring during transport, causing the aerosol size to increase. Different deposition patterns on the vertical and horizontal surfaces in the heated upper plenum for almost all measured species suggest that directional depositional mechanisms were important. SEM photographs of aerosols on the horizontal surfaces indicate that the particles were agglomerates ranging in size between 25 and 250 μm, whereas those on the vertical surfaces were <20 μm. These differences in deposition can be explained by more than one mechanism. The solid deposits found on the horizontal surfaces of the deposition rod could have been the result of inertial impaction of particles larger than 25 μm in wakes and recirculating eddies formed behind the coupon holders, gravitational settling of particles greater than 50 μm from the flow, or flow of liquid condensate (e.g., cadmium, cesium hydroxide) from vertical surfaces down to horizontal surfaces. Because the aerosol stream encountered 20 deposition coupons in series, significant attenuation of large aerosol particles occurred during transit down the deposition rod. The size of the aerosol entering the unheated plenum was probably <25 μm.

The relatively cold wall (∼600 K) in the unheated upper plenum is thought to have affected fission product and aerosol transport and deposition. Elemental analysis of the solid deposits on the horizontal surfaces of the deposition rod indicates that the aerosol was predominantly cadmium. Yet, the aerosol that entered the aerosol monitor was >50% tin. In addition, the cesium deposition data indicate a significant decrease in deposition in the unheated upper plenum. The cold walls caused some of the volatile species, such as cadmium, cesium iodide, and cesium hydroxide, to condense on the walls. This behavior, in turn, caused these species to evaporate from the aerosol to produce a new equilibrium. Thus, most of the cesium deposition on the downstream surface of the deposition rod was due to vapor condensation of volatile species of cesium, like cesium iodide and cesium hydroxide, and/or deposition of fine aerosol particles. Evaporation of the lower-volatile species (e.g., tin, silver, zirconium, strontium, barium, europium, and curium) would have been insignificant. The deposition data indicate that these aerosols were not large enough to result in differential surface deposition. This aerosol evaporation behavior would suggest that the aerosol entering the aerosol monitor was small and composed mainly of a tin (and other low-volatile materials) seed and cadmium.

8. SCDAP/RELAP5 ANALYSES

The three primary objectives of the SCDAP/RELAP5-MOD1 analyses of Test SFD 1-4 were: (a) to define the probable damage progression history of the fuel bundle using a combination of calculations, on-line measurements, and postirradiation examination results; (b) to assess the influence of uncertainties in test conditions and modeling assumptions on the calculated behavior of the bundle; and (c) to define needed model improvements in the code.

In the following sections, the results of the calculations are presented and discussed. Section 8.1 briefly describes the version of SCDAP/RELAP5 and the modeling representation of the SFD 1-4 test train used for the calculations. The results of calculations that use modeling options and test boundary conditions to best represent the overall response of the bundle during the experiment are presented in Section 8.2. Section 8.3 presents results of sensitivity calculations that define the relative influence of important test conditions and modeling assumptions on the calculated bundle response. A discussion of the results and the probable damage progression scenario in the experiment, the influence of uncertainties in test conditions and code models on calculated results, and suggested model improvements are presented in Section 8.4.

8.1 Description of the SCDAP/RELAP5 Model

The first production version of SCDAP/RELAP5-MOD1^6 was used in the SFD 1-4 analysis. SCDAP/RELAP5-MOD1 offers a number of advantages over the SCDAP code used in the final analyses of the SFD-ST and SFD 1-1 experiments.^{3,4} First, the RELAP5 thermal-hydraulics models can represent more accurately the experiment thermal-hydraulic conditions, including the injection of argon into the lower test train and the generation of steam due to relocation of molten material. SCDAP/RELAP5-MOD1 also includes modeling improvements that have a significant influence upon the calculated heatup and meltdown of the SFD 1-4 bundle, including fuel rod liquefaction and relocation, shroud liner failure, and debris formation. These model improvements are discussed in more detail in Appendix J.

The SCDAP/RELAP5 model of the SFD 1-4 bundle is shown in Figure 138. The bundle was modeled with 10 axial zones, using two representative fuel rod components for the irradiated and fresh rods, respectively; one control rod component to represent the control rods and their zircaloy guide tubes; and a shroud component to represent the shroud inner liner, insulation, and saddles. The outer boundary for the shroud component corresponded to the inside surface of the bundle bypass region. The heat transfer from the outside of the shroud was modeled using a constant heat transfer coefficient of 10 kW/m^2-s-K and a constant coolant bypass temperature of 520 K.

The test conditions used in the best-estimate calculations are shown in Figures 139 through 141. The total bundle power and axial power profiles used in the calculations are shown in Figures 139 and 140. The "estimated" total bundle power curves shown in Figure 139 represent the upper and lower bounds of the uncertainty envelope on the bundle power obtained from reactor power measurements and reactor physics calculations. The axial power profiles shown in Figure 140 were calculated for three different bundle geometries: (a) an intact bundle partially filled with water; (b) an intact bundle filled with steam; and (c) a damaged bundle with relocated control rod material and filled with steam. The damaged bundle profile represented the posttest state of the bundle as determined from the postirradiation examination. Details of the bundle power calculations are discussed in Appendix D.

The axial power profile was represented in the calculations using three discrete curves. The calculation was started with the profile identified as the partially water-filled curve, then was shifted to the steam-filled curve at 1020 s, and then to the after-control-rod-failure curve at 2050 s. The timing for these changes was determined from a combination of liquid level measurements and estimates for the completion of control rod material relocation. Radial variations in the bundle power were neglected.

The steam and argon temperatures at the inlet to the lower plenum of the test train are shown in Figure 141. The two measured temperatures shown on the figure reflect the temperature of the water in the lower plenum rather than the inlet temperature, since the inlet temperature was not directly measured. The figure also shows the argon inlet flow rate. The constant water inlet flow rate of 0.6 g/s supplied by the positive displacement pump was

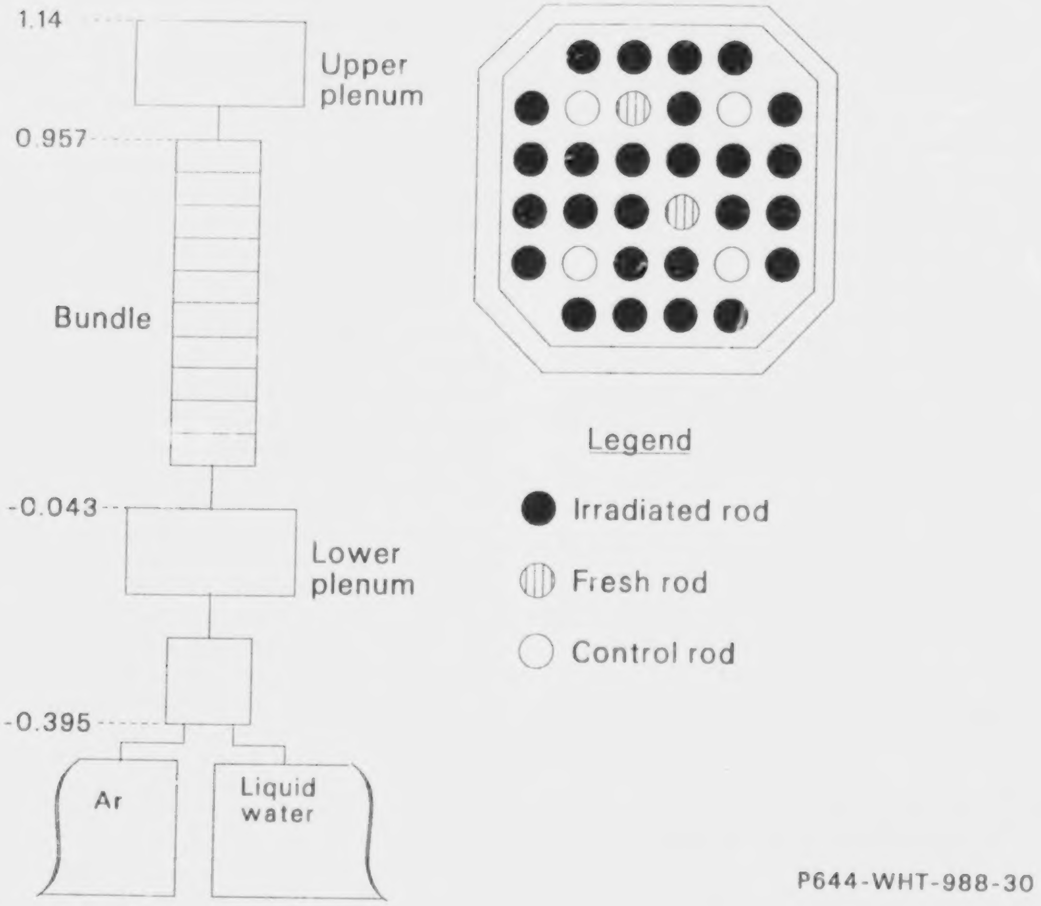
1.14
Upper plenum
0.957
Bundle
-0.043
Lower plenum
-0.395
Ar
Liquid water
Legend
● Irradiated rod
◍ Fresh rod
○ Control rod
P644-WHT-988-30

Figure 138. SCDAP/RELAP5 representation of the SFD 1-4 test train and bundle.

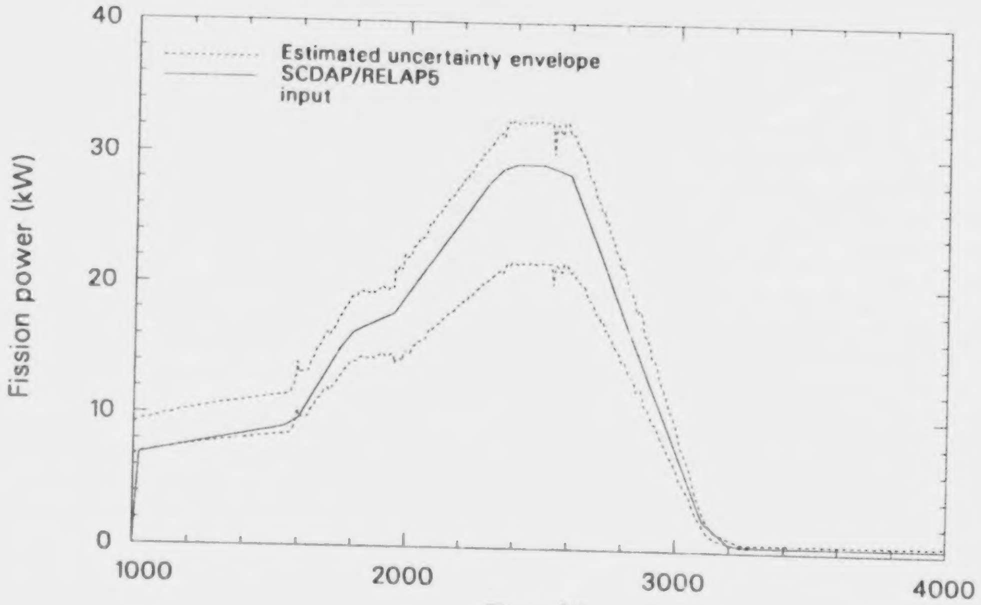

Figure 139. Bundle fission power used for the SCDAP/RELAP5 calculation.

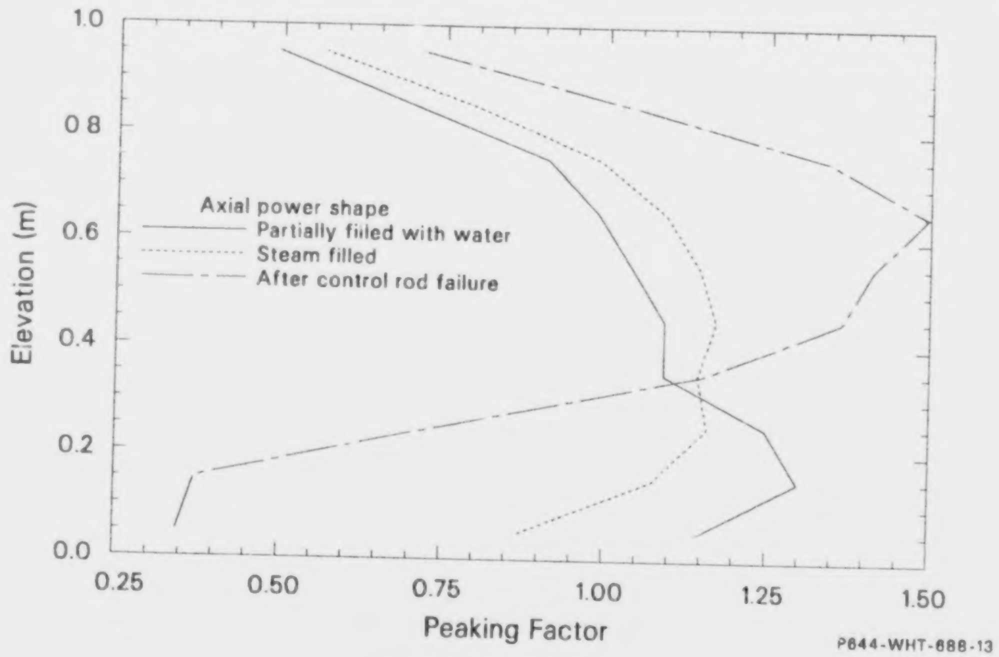

Figure 140. Axial power profile used for the SCDAP/RELAP5 calculation.

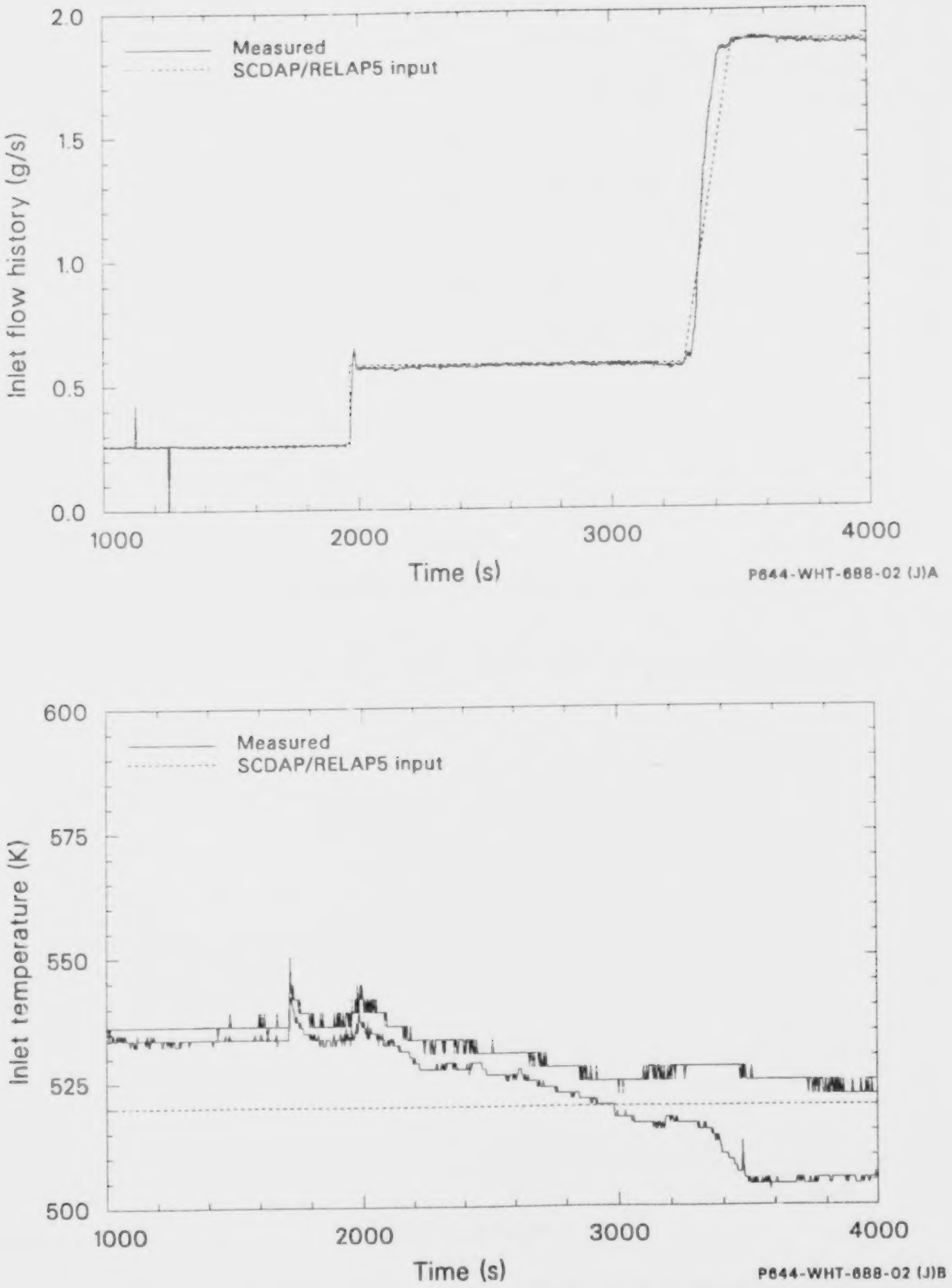

Figure 141. Steam and argon inlet temperature and flow rate histories used for the SCDAP/RELAP5 calculation.

also used as input to the SCDAP/RELAP5 calculations.

The calculated water level in the bundle and corresponding steam generation rate are compared to the measured values in Figures 142 and 143. The liquid level results in Figure 142 represent the approximate elevation of the top of the two-phase level. The measured level was determined by a combination of pressure drop and fission chamber measurements and could not be measured after 1946 s (see Section 4). The calculation is in good agreement with the data during boildown of the bundle coolant and indicates that the water remained below the bottom of the active fuel for the remainder of most of the transient, with changes in the liquid level following the changes in bundle power until 3200 s. Following 3200 s, the calculated liquid level increases because the steam generation rate is less than the inlet flow of 0.6 g/s. The bundle inlet water flow was turned off at 3456 s.

The estimated steam flow rate shown in Figure 143 was determined from the change in measured liquid level prior to 1946 s. Beyond 1946 s, a minimum steaming rate was determined from the measured hydrogen production rate, assuming complete steam consumption. These estimates are discussed in Section 4. The calculated steam generation rates respond to the changes in bundle power very closely, since most of the molten material was predicted to freeze above the water.

It should be noted that SCDAP/RELAP5 would normally predict that a significant amount of the steam would have been diverted from the bundle due to the predicted reduction in flow area and resultant increase in bundle pressure drop. However, since the bundle bypass and potential flow path in the porous insulation were not modeled, the calculated steam flow shown in the figure remained within the fuel rod bundle.

8.2 Results of SCDAP/RELAP5 Best-Estimate Calculations

The results of the best-estimate calculations of the bundle response, including the bundle and associated shroud temperatures, hydrogen production rates and integrals, release of fission gases, and changes in bundle geometry, are presented in this section. Where measurements or independent estimates are available, possible biases in either the calculations or the estimates are identified through code-to-data comparisons.

The overall calculations accurately represent the response of the bundle during the transient. Calculated temperatures are in good agreement with the measured bundle and shroud temperatures up to the point of thermocouple failure. Although the bundle thermocouples failed before peak bundle temperatures were reached, peak temperatures were estimated from the metallographic examination of the bundle. Comparisons of measured and calculated shroud temperature responses indicate that the calculated peak bundle temperatures are representative of the peak temperatures reached in the bundle. The calculated and estimated timing of key events, such as the failure of fuel rods and control rods, are consistent. The main discrepancies between measured and calculated results are those associated with hydrogen production and the amount of fuel liquefaction. The discrepancy in hydrogen production has been attributed to the analysis used to describe the initial mixing of hydrogen in the separator in the effluent system and/or temporary holdup of hydrogen in unoxidized zircaloy in the upper bundle, rather than errors in the calculated hydrogen production (see Section 5.2). On the other hand, the discrepancy in fuel liquefaction has been attributed to the fuel dissolution model. The results of sensitivity studies, discussed in Section 8.3, indicate that a new dissolution rate model significantly improved the agreement between the measured data and the calculations. Detailed comparisons between test data and measurements are presented in the following sections.

8.2.1 Temperatures. The calculated cladding temperatures at different elevations are shown in Figure 144. The elevations shown are relative to the bottom of the active fuel. The calculations predict that the middle third of the bundle heated up most rapidly as a result of the axial power peaking at the bundle midplane. The rapid heatup starting at 1800 s in the lower half of the bundle corresponds to the increasing oxidation rate of the bundle zircaloy. The oxidation heating increased exponentially until the steam in the bundle was completely consumed at a peak bundle temperature near 1700 K at 1900 s. Between 1900 and 2800 s, the upper portion of the bundle was calculated to be steam-starved. The calculated shroud inner liner temperatures also show the influence of steam starvation in the upper portion of the bundle, as illustrated in Figure 145. The distinct changes in the calculated temperature response of the bundle shown in these plots correspond to (a) the abrupt

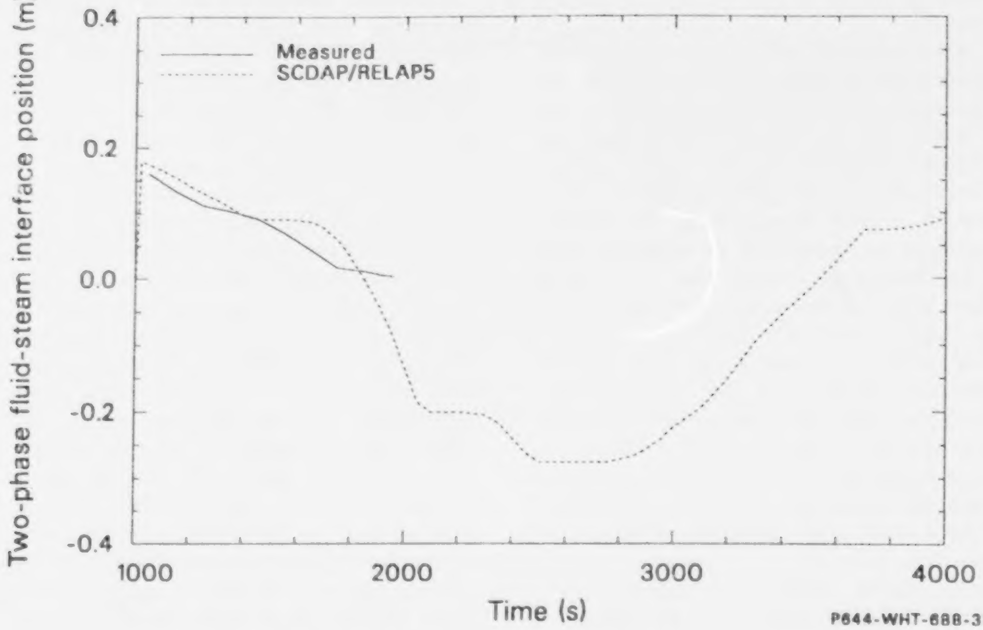

P644-WHT-688-31 (J)

Figure 142. Measured and calculated two phase fluid-steam interface.

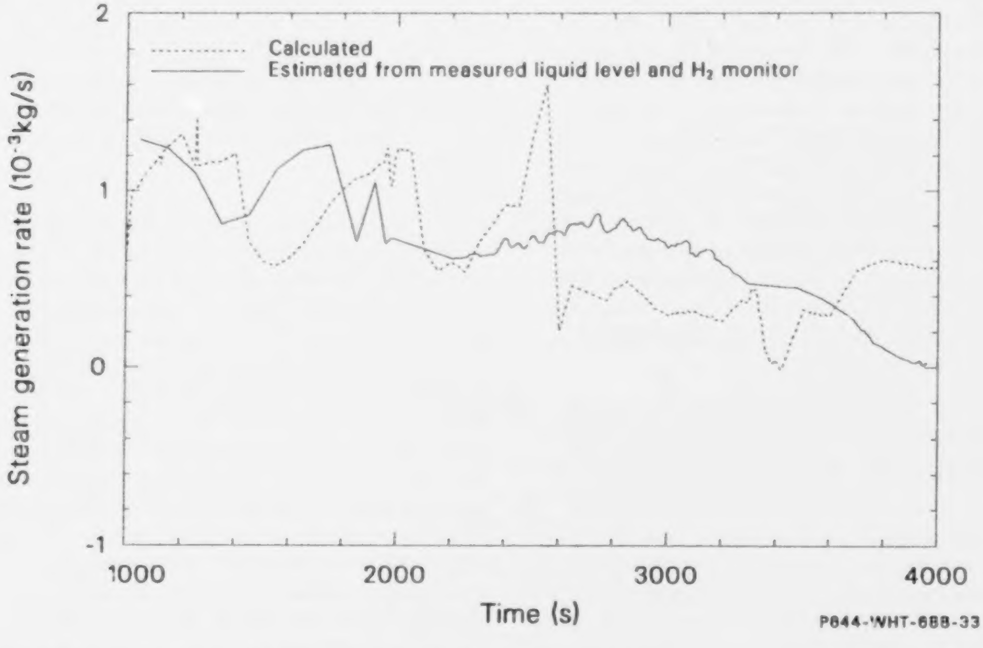

P644-WHT-688-33 (J)

Figure 143. Comparison of measured and calculated steaming rates.

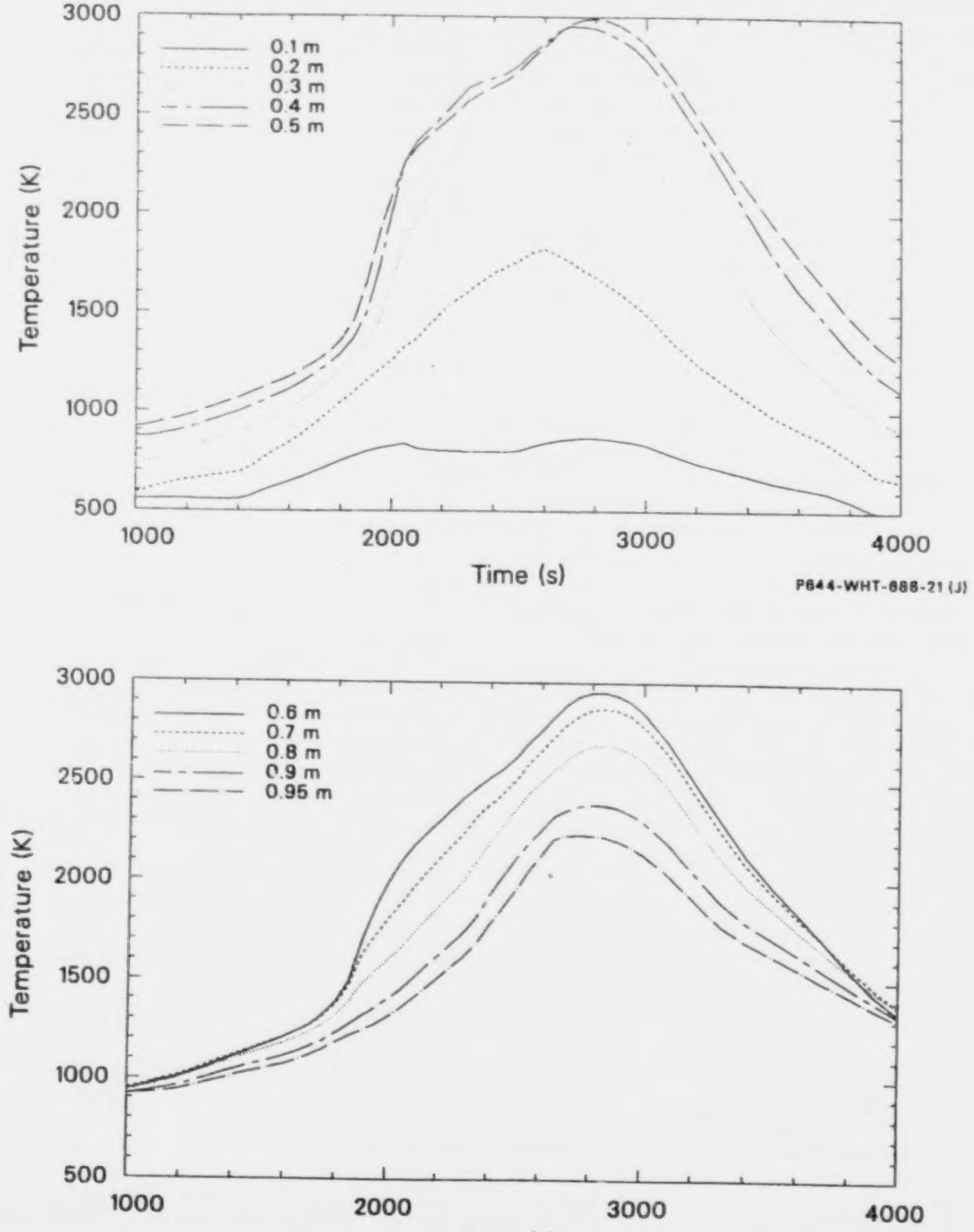

P644-WHT-688-21 (J)

P644-WHT-688-18 (J)

Figure 144. Calculated cladding temperatures for the SFD 1-4 bundle.

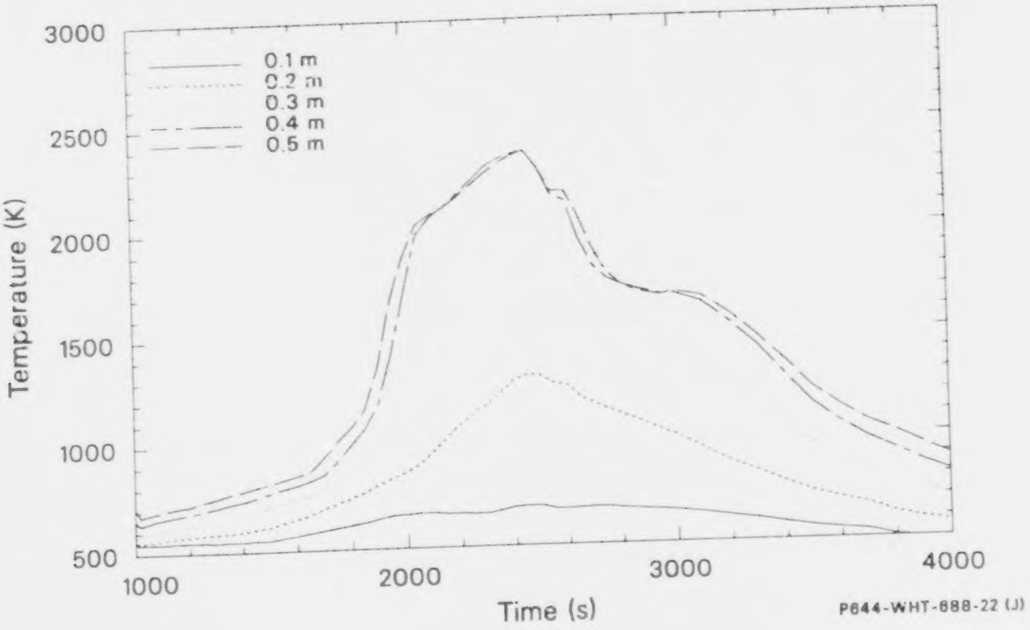

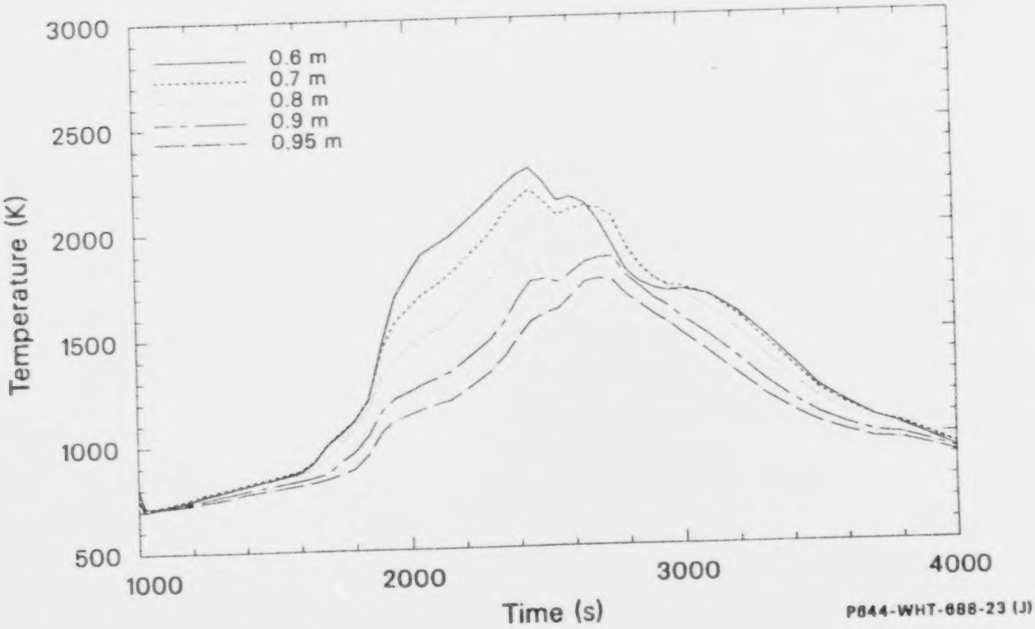

Figure 145. Calculated shroud inner liner temperatures for the SFD 1-4 bundle.

change in liner heating rate associated with the increase in argon flow at 1966 s; (b) initial relocation of the liquefied U-Zr-O at 2500 s; and (c) melting and relocation of UO_2 and ZrO_2 at 2800 s.

The calculated and measured fuel rod cladding temperatures at the 0.39-, 0.54-, and 0.74-m elevations, shown in Figure 146, agree relatively well until thermocouple failure. Similar comparisons of the coolant temperatures at 0.54 and 1.14 m (Figure 147) and the shroud inner liner temperatures at 0.39, 0.54, and 0.74 m (Figures 148) show the same trend.

Although there are no direct measurements of the bundle temperature response following the initial heatup due to thermocouple failure, comparisons of (a) calculated and measured shroud midwall and outer surface temperature histories (Figures 149 and 150) and (b) postirradiation examination estimated and calculated peak bundle temperatures (Figure 151) indicate that the bundle followed a temperature history comparable to that predicted by SCDAP/RELAP5. The calculated peak bundle temperatures are in reasonable agreement with the maximum temperatures estimated during postirradiation examination of the bundle. The measured peak temperatures represent the lower bound on peak material temperatures from different samples of either intact fuel (unrelocated fuel) or relocated material taken at each elevation. Near the bottom of the bundle, the calculated fuel temperatures are less than the metallurgically estimated values, whereas the calculated temperature exceeds the metallurgically estimated temperatures for the upper part of the bundle. This discrepancy is probably because more higher-temperature material relocated from the upper bundle and refroze in the lower bundle than was calculated.

8.2.2 Hydrogen Production. As shown on Figure 152, there is a considerable difference between the calculated and measured hydrogen production rates, although the total hydrogen produced agrees (calculated 87 g and measured 86 ± 12 g from the collection tank). Although the measured hydrogen production rate has been corrected for mixing in the bundle and separator and the transit time between the bundle and the hydrogen monitor, the measured hydrogen production rate is believed to be biased low at the start of zircaloy oxidation because of either incomplete mixing in the separator at the start of hydrogen production or temporary solution of hydrogen in zircaloy (see Section 5).

As shown in the figure, the calculated hydrogen production rate rapidly reaches the steam starvation limit. The calculated hydrogen production then follows the calculated steam starvation limit through most of the high-temperature transient. The notable exception where the hydrogen generation rate falls below the steam starvation limit occurs between 2300 and 2600 s when U-Zr-O is calculated to relocate and form a frozen crust on the rapidly oxidizing zircaloy cladding in the bottom third of the bundle.

8.2.3 Changes in Bundle Geometry. Four key events that changed the geometry of the SFD 1-4 bundle were calculated: (a) fuel rod cladding ballooning and rupture; (b) control rod failure and control rod material relocation; (c) fuel and cladding liquefaction and U-Zr-O relocation; and (d) fuel rod melting and ceramic $(U,Zr)O_2$ relocation. The calculated and measured timing, location, and temperature of these events are compared in Table 27. The initial change in bundle geometry is calculated to occur at 1050 s with the start of fuel rod cladding ballooning. Large, axially extended balloons were predicted, with the deformation extending over the upper half of the bundle. Although the calculated control rod response did not include the early failure of the instrumented control rod, there was close agreement between calculated and measured failure temperatures for the three uninstrumented control rods. The relocation of liquefied fuel and cladding material occurred over two distinct periods starting at the times indicated on the table. The initial relocation of molten zircaloy cladding and liquefied fuel was calculated to occur over the center third of the bundle at temperatures between 2250 and 2680 K. The later relocation of UO_2 and ZrO_2 was predicted to occur over the center portion of the bundle at a temperature of 2990 K. Although the exact timing of the actual fuel rod material relocation is not known, changes in fission chamber responses indicate the movement of fuel between 2300 and 2600s.

The comparison of calculated and measured fuel and melt cross-section area at the end of the test, shown in Figure 153, identified an important deficiency in the fuel liquefaction models. The amount of fuel that was either dissolved by molten zircaloy or melted was underpredicted in the calculations by nearly a factor of five. As a result, the melt cross-section was also underpredicted.

8.2.4 Fission Product Release. The calculated releases for the noble gases, cesium, and iodine

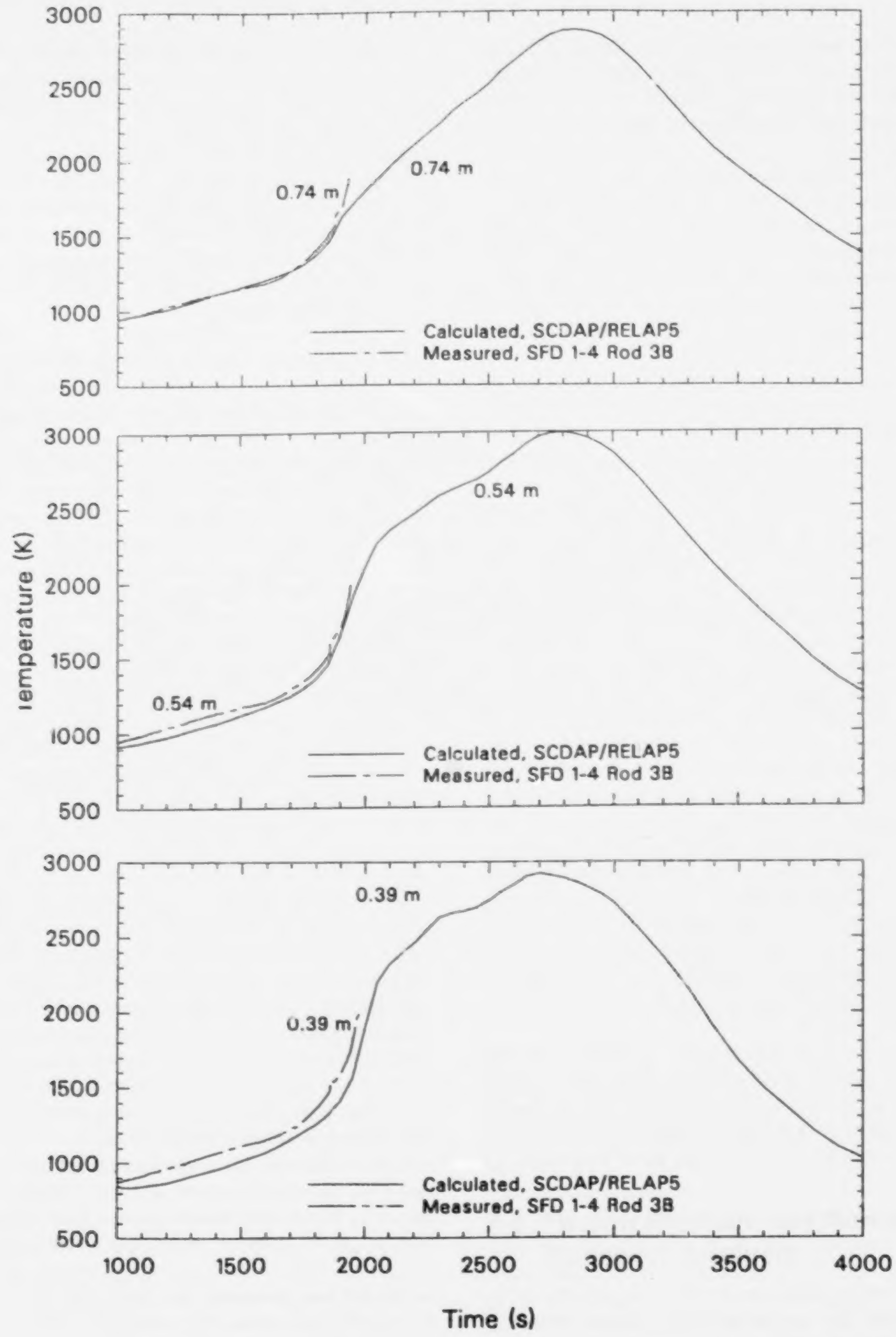

P844-WHT-688-09 (J)

Figure 146. Comparison of measured (rod 3B) and calculated cladding temperatures.

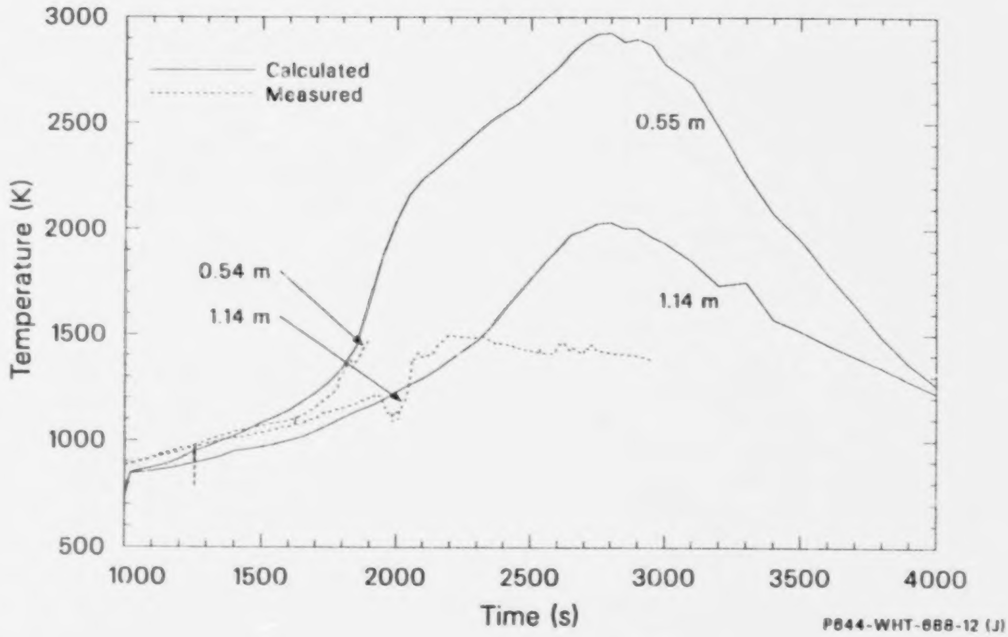

Figure 147. Comparison of measured and calculated coolant temperatures.

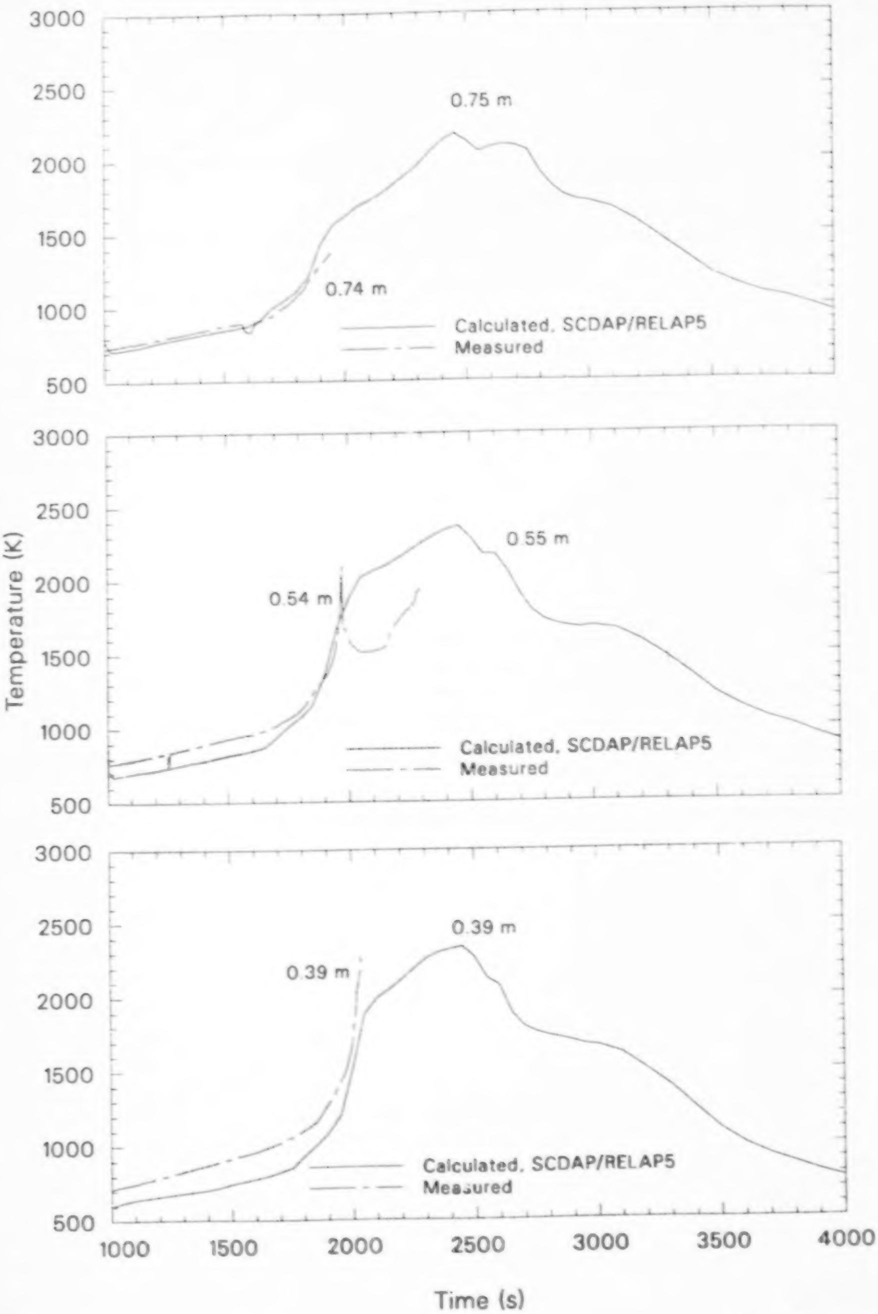

P644-WHT-688-05 (J)

Figure 148. Comparison of measured and calculated shroud inner liner temperatures.

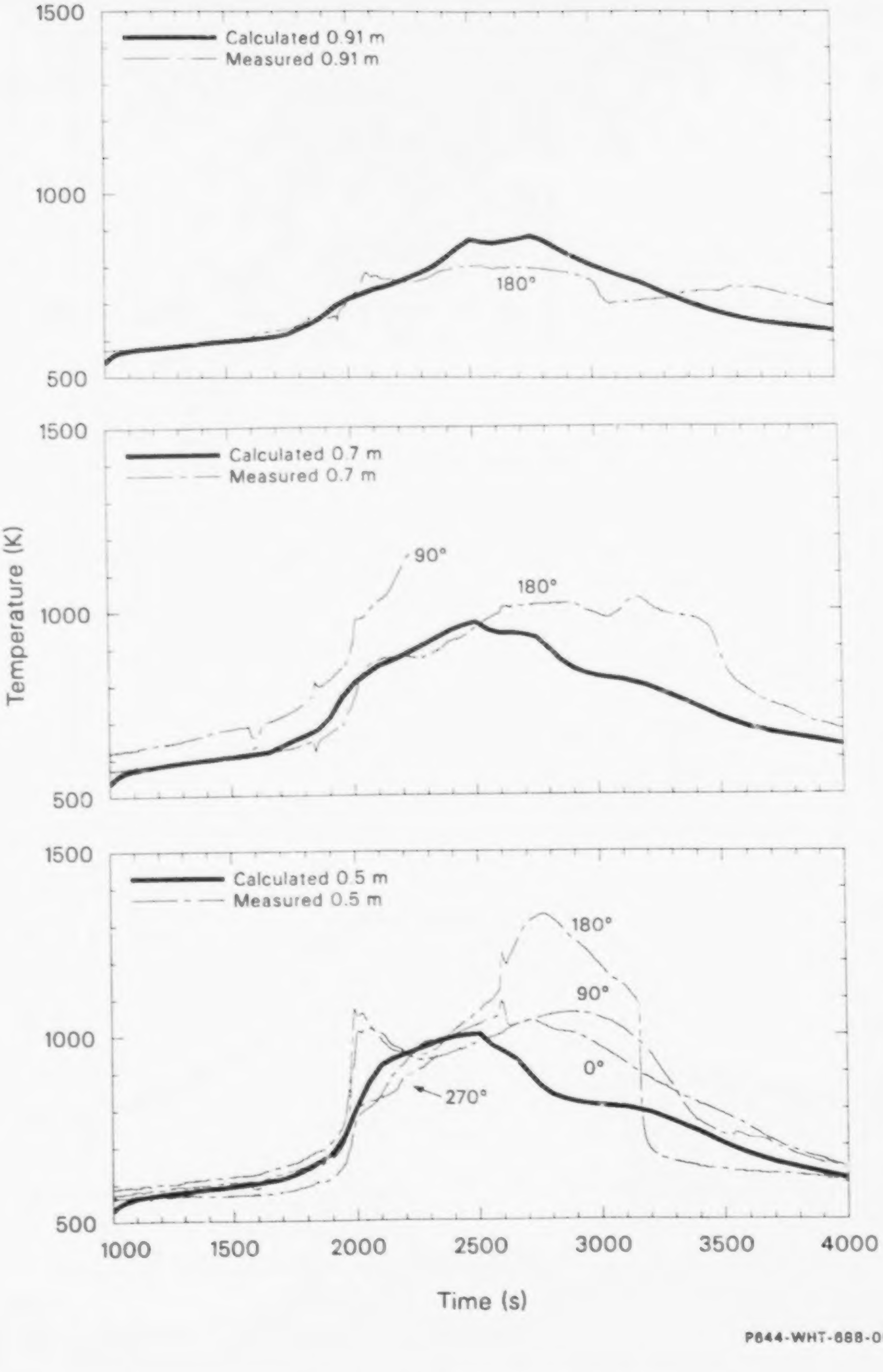

P844-WHT-688-06 (J)

Figure 149. Comparison of measured and calculated shroud midwall temperatures.

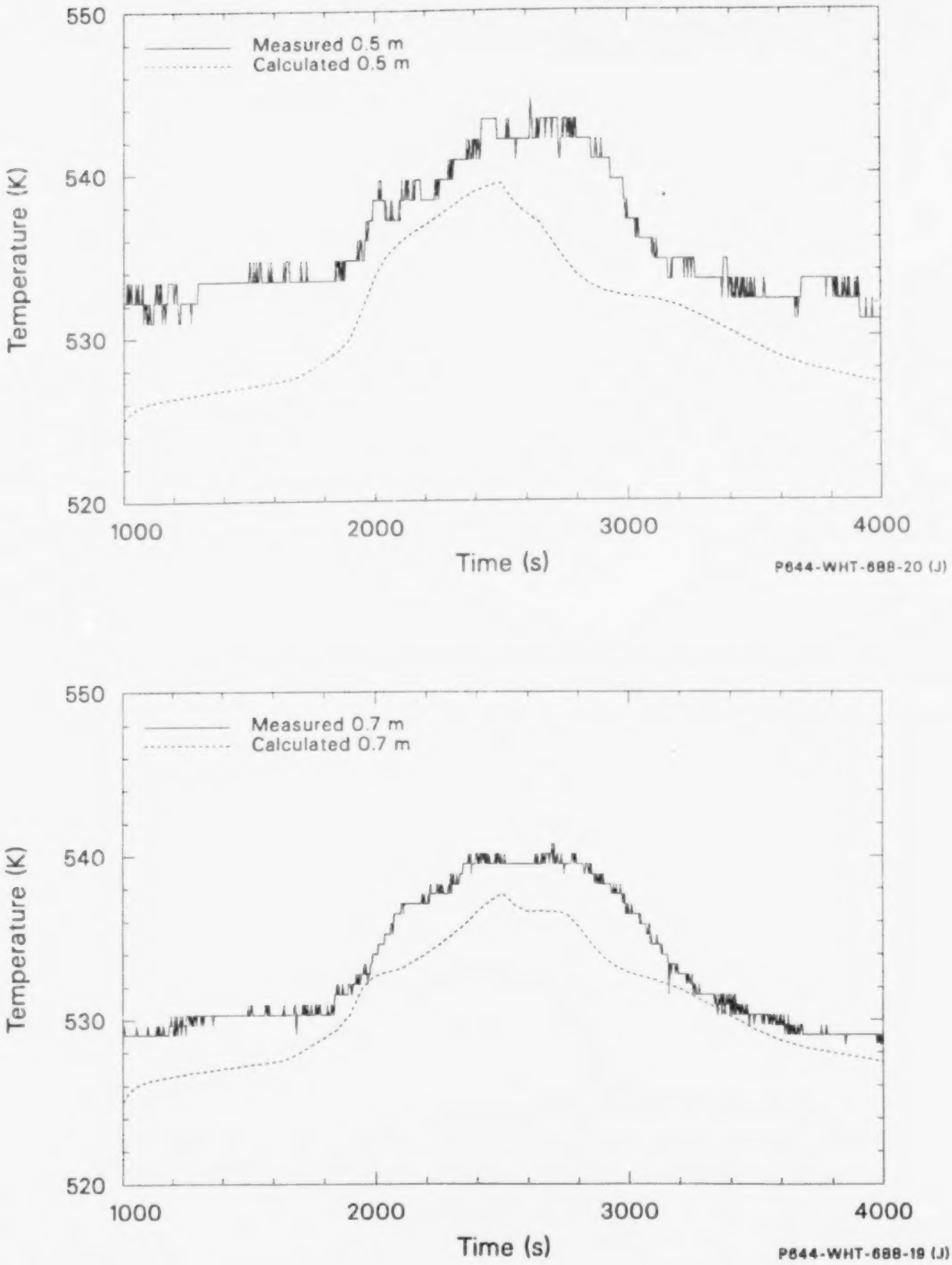

Figure 150. Comparison of measured and calculated shroud outer wall temperatures.

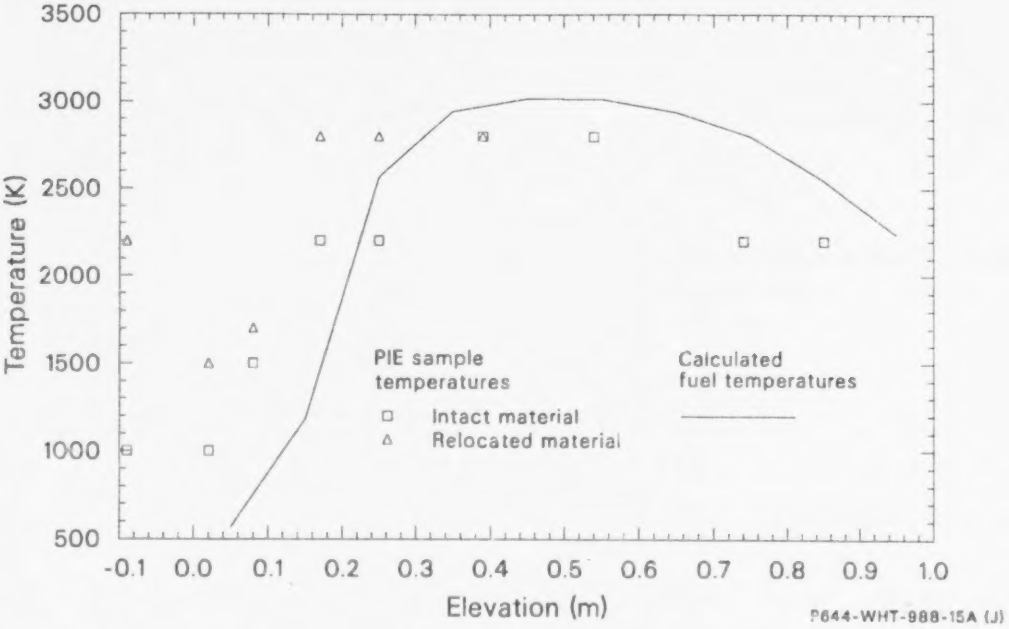

Figure 151. Comparison of metallurgically estimated and calculated peak fuel temperatures.

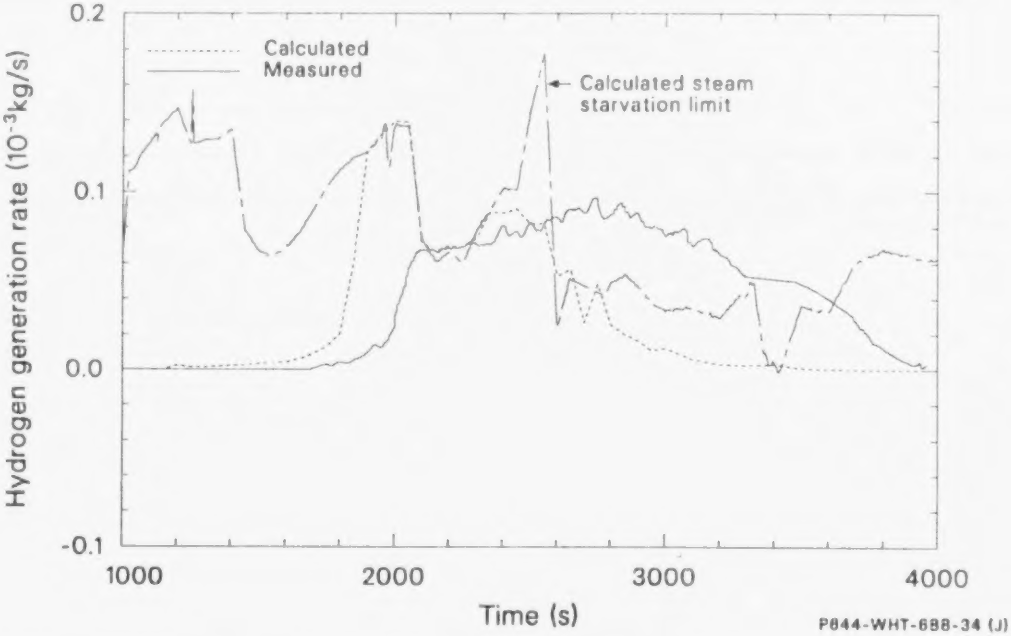

Figure 152. Comparison of the measured and calculated hydrogen generation rate with the calculated steam starvation limit.

Table 27. Calculated and measured key events

Event	Time (s)		Elevation (m)		Temperature (K)	
	Calculated	Measured	Calculated	Measured	Calculated	Measured
Start of ballooning	1050	—[a]	0.5 to 1.0	—[a]	910	—[a]
Initial fission product release	1750	1700 to 1800	0.6 to 0.7	—[a]	1265	1315
Initial control rod failure	1950	1928 to 1978	0.4	—[a]	1700	1700
Metallic U-Zr-O relocation	2325[b]	2300 to 2600	0.3 to 0.7	—[a]	2250 to 2680[c]	—[a]
Ceramic melt relocation	2680[b]	2300 to 2600	0.5 to 0.6	—[a]	2990	—[a]

---

a. Not measured.

b. The time and temperature given corresponds to the initial relocation of material. The relocation continued for some time.

c. The peak temperature was 2680 K at the time of relocation; the range of temperatures covers the range of elevations where the initial material relocated upon cladding failure.

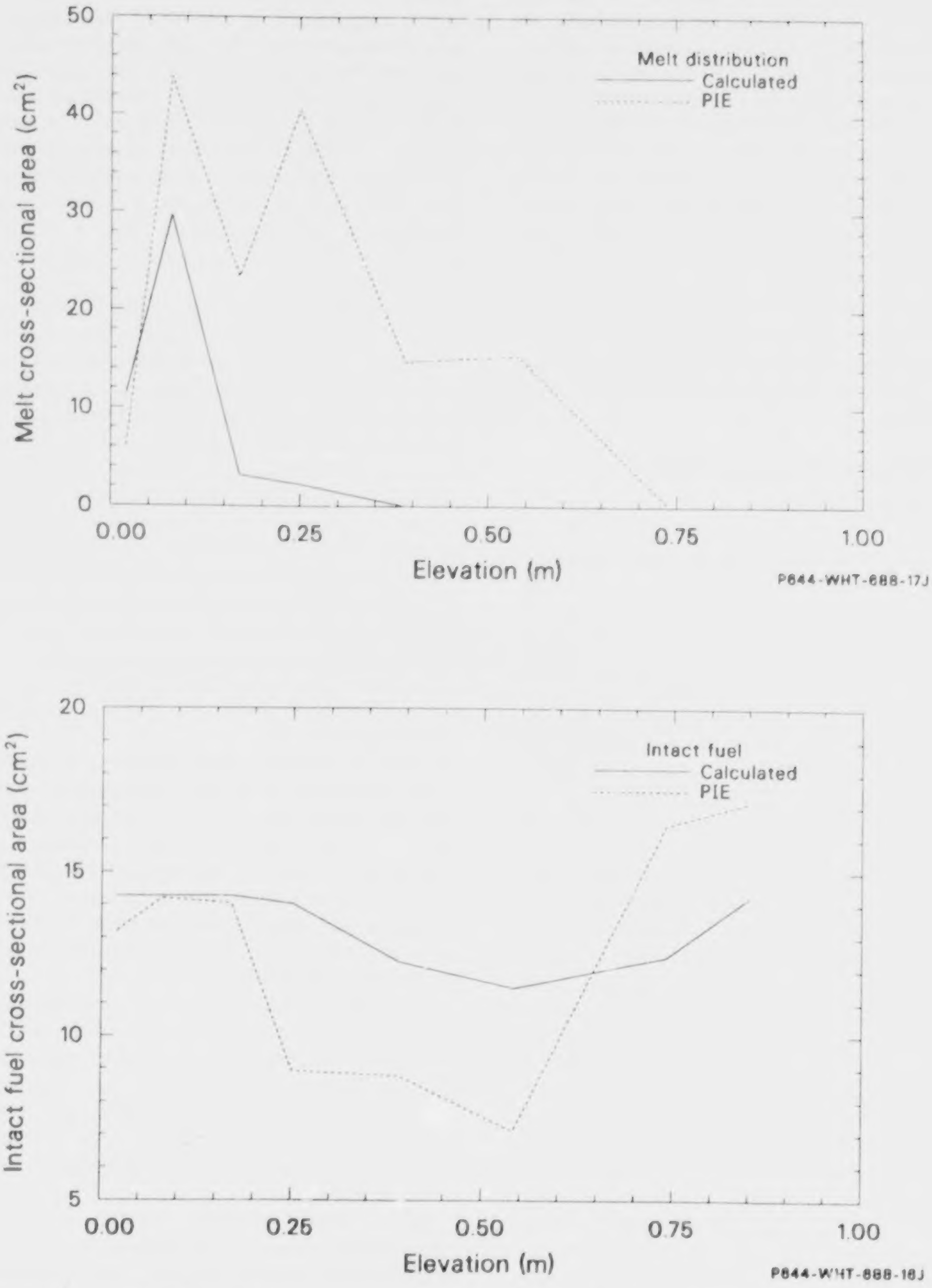

Figure 153. Comparison of the measured and calculated fuel and melt cross-sectional area.

were dominated by the dissolution of fuel. In the reference calculations, where the fuel dissolution was underpredicted by nearly a factor of five, the total predicted release, 11%, was also less than that measured by approximately the same amount. As discussed in the next section on sensitivity studies, introduction of the new fuel dissolution model also improved the prediction of fission product release, increasing the total release to 44% to 48%, as compared to the measured values of 23% to 51%. Figure 154 shows the calculated release for cesium using the improved fuel dissolution model; the calculated releases for the noble gases, iodine, and cesium were nearly identical. The first sharp increase in the calculated release between 2000 and 2500 s is caused by the rapid increase in fuel dissolution as temperatures exceed 2300 K. The second sharp increase at 3000 s is due to the heating of the lower portion of the bundle as a result of melt relocation.

8.3 Results of Sensitivity Calculations

Two sets of sensitivity studies were performed using SCDAP/RELAP5. The first set was used to determine the influence of uncertainties in important test boundary conditions, and the second set was used to evaluate the importance of modeling assumptions on the calculated bundle response.

The first set of calculations considered changes in fission power history, axial power profile, shroud liner failure, shroud bypass coolant temperature, and axial heat losses. The specific test conditions used for each calculation are listed in Table 28. The variation in power history of approximately 30% reflects the estimated uncertainty of ± 15% in average bundle power. The variation in axial power profile reflects the uncertainties introduced by the variation in liquid level and relocation of control material and, to a lesser extent, the variation in the predictions caused by the use of discrete changes in the profile as code input rather than a continuous change. The variation in shroud failure bounds the expected variation in shroud insulation thermal conductivity due to the local failure of the inner liner. In the case where shroud failure is not modeled, the as-manufactured thermal conductivity is used for the entire transient. The thermal conductivity as a function of temperature is included in the input described in Appendix J.

In the case of shroud failure, the as-manufactured thermal conductivity is increased by 50% over the full height of the bundle to represent the influence of steam penetration into the insulation. The variation in shroud bypass coolant temperature bounds the temporal and axial changes in bypass temperatures as determined from thermocouple measurements. This study was performed to determine the influence of using a constant bypass temperature in calculations even though there was a slight variation during the experiment. The axial heat loss variation represents an engineering estimate for the bounds in the axial heat conduction from the bottom of the bundle to the water and structures in the lower plenum, since a detailed multi-dimensional heat conduction analysis was not performed.

The second set of sensitivity studies to determine the influence of important modeling assumptions is listed in Table 29. These calculations included variations in minimum fuel relocation temperature, fuel dissolution modeling, Ag-In-Cd freezing temperatures, and fuel rod cladding oxidation. The variation in minimum fuel relocation temperature reflects the estimated uncertainty in the initial relocation of molten zircaloy and liquefied fuel. The lower relocation temperature of 2250 K results in molten zircaloy relocation near the melting temperature of zircaloy and represents the situation where the protective oxide shell on the exterior of the cladding is ineffective in holding the melt in place. At the opposite extreme, the higher relocation temperature of 2680 K represents [illegible] situation where the oxide shell is effective.

The old dissolution model represents the model used in the current production version of SCDAP/RELAP5-MOD1 while the new model represents a model developed from data from Hofmann[22] in more recent experimental versions of the code. The new dissolution model resulted in an increase in the amount of fuel dissolved by nearly a factor of five and is much more representative of the actual fuel dissolution estimated for the test.

The variation in Ag-In-Cd freezing temperature reflects not only the uncertainty in the freezing temperatures of mixtures of silver, zircaloy, and stainless steel but also reflects the uncertainties introduced by the discrete axial nodalization of the bundle, the prediction of liquid levels, and the prediction of the geometry of the relocating molten control material.

The variation in cladding oxidation represents the increased surface area available on the inside of ballooned and ruptured cladding. This increase in surface area includes only the upper half of the fuel

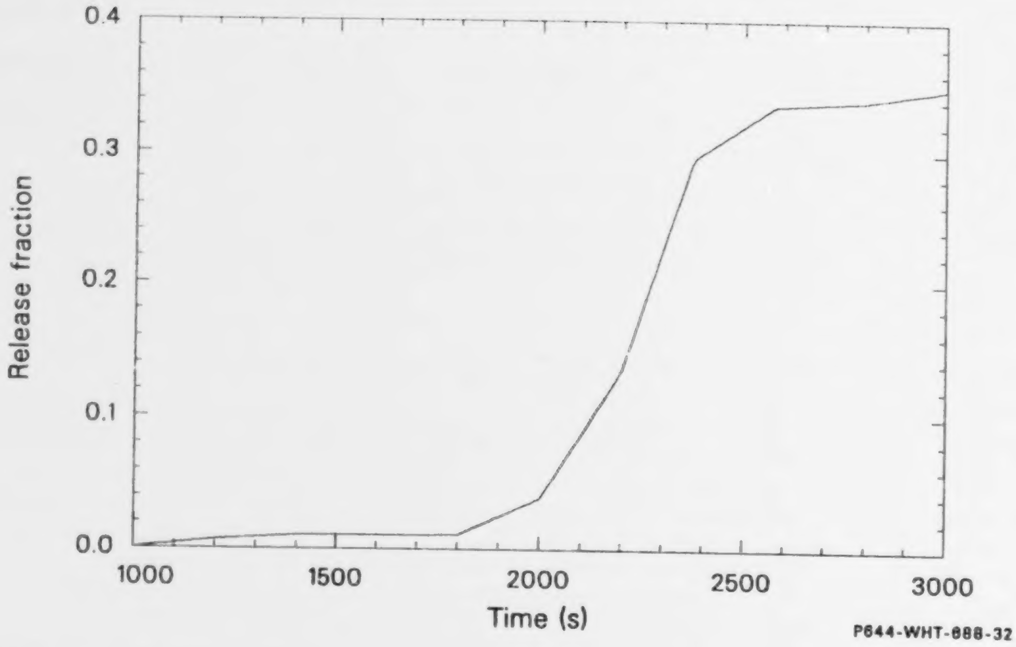

Figure 154. Calculated volatile fission product release.

Table 28. Sensitivity studies on test conditions

Case Identifier	Power History	Axial Power Profile	Shroud Failure	Bypass Temp. (K)	Axial Heat Loss[a]
Reference[b]	See Figure 139	10% water (1020 s)[c] CR failure (1900 s)	None	540	Modeled
Power	See Figure 139	Average[d] (0-1900 s) CR failure (1900 s)	None	540	Modeled
Power-1	85% of reference (t < 1590 s)	Average[d] (0-1900 s) CR failure (1900 s)	None	520	Modeled
Power-2[e]	85% of reference (t < 1590 s) 115% of reference (1930 s < t < 2360 s)	Average[d] (0-1900 s) CR failure (1900 s)	None	520	Modeled
Liner	Same as Power-1	Average[d] (0-1900 s) CR failure (1900 s)	Yes	520	Modeled
Axial[f]	Reference (t < 1590) 115% of reference (1990 s < t < 2360 s)	(same as reference)	Yes	540	Not modeled

---

a. The axial heat losses from the bottom of the water in the lower plenum was either modeled or not modeled. In the former case, the power in the lower 10% of the bundle was split equally between the bundle structures and the water in the lower plenum to simulate the effect of axial heat transfer. In the latter case, axial heat losses were neglected.

b. Inlet flow conditions corresponded to those specified as SCDAP/RELAP5 input on Figure 141. Modeling options were the same for all cases (with the exception of the axial study where the conditions are described under note f) with the minimum fuel relocation temperature set to 2680 K, the old fuel dissolution model, Ag-In-Cd freezing temperature set to the melting point of Ag minus 20 K, and double-sided cladding oxidation in ballooned regions.

c. The axial power profiles shown in Figure 140 with the shift from the completely water-filled profile to the 10%-water-filled profile occurring at 1020 s and the shift to the end-state profile associated with final position of the control material occurring at 1900 s.

d. Average represents the average of the completely water-filled and 10%-water-filled profiles.

e. The case identified as Power-2 corresponds to the best-estimate calculations and provides the best overall agreement to the experimental temperatures.

f. Modeling options were as follows: minimum fuel relocation temperature of 2500 K, the old fuel dissolution model, Ag-In-Cd freezing temperature set to the melting temperature of the alloy minus 100 K, and double-sided oxidation of the fuel rod cladding in ballooned elevations.

Table 29. Sensitivity studies on modeling assumptions

Case Identifier	Minimum Fuel Relocation Temperature (K)	Fuel Dissolution Model	Ag-In-Cd Freezing Oxidation (K)	Cladding Oxidation
Liner	2680	Old model	$T_m - 20$	Double-sided
Fuel relocation	2250	Old model	$T_m - 20$	Double-sided
Ag-In-Cd[a]	2680	New model	$T_m - 100$	Double-sided
Oxidation	2680	New model	$T_m - 100$	Single-sided

[a] This case also included the new fuel dissolution model, but this model did not have any influence on the results prior to 2400 s. The dominant influence with the change in the Ag-In-Cd freezing temperature was the generation of steam due to control rod material relocating into the water. In the first two cases presented in this table and the cases presented in Table 28, the control material froze above the liquid level and thus resulted in little additional steam generation. In the last two cases in the table, the control material froze below the liquid level.

rods, since that is the only portion with significant calculated deformation.

The results from both sets of sensitivity studies are summarized in Table 30. The relative variation in predicted test results for peak fuel temperature, hydrogen production, fission gas release, and fuel dissolution is listed in Table 31. The relative variation was computed by taking the maximum variation in time for each of the studies and dividing by the maximum variation over all the studies. The resulting variations in predicted fuel rod cladding temperatures at three representative elevations, 0.40, 0.55, and 0.74 m, are shown in Figures 155 through 160. Additional information for each sensitivity study is given in Table 28.

Although the influence of uncertainties in important test boundary conditions and modeling assumptions varies with time and individual output parameters, several important trends can be seen in the results. The uncertainties in test conditions and modeling assumptions have similar influences on the overall predicted results for bundle temperatures, as shown in the figures and Table 31. Power history and axial power variation are more influential during the heatup of the bundle when fission power is the dominant factor in the energy addition to the bundle. The minimum fuel relocation temperature becomes important as zircaloy melting temperatures are exceeded, reflecting the importance of the protective oxide in controlling the initial relocation of liquefied fuel rod material and zircaloy oxidation. The heat transfer to the shroud, as determined by the thermal conductivity of the shroud insulation, becomes the most influential during the bundle cooldown.

The variation in hydrogen production is also affected uniformly by test boundary conditions and modeling assumptions. The high influence of liner failure upon hydrogen production reflects both uncertainties in the shroud insulation thermal conductivity and the modeling of the oxidation of the outer surface of the zircaloy liner. Because the hydrogen production was a complex function of bundle temperature and changes in steam availability, it was not possible to separate the influence of each parameter shown on Table 31; but the total hydrogen production varied by nearly a factor of two for the range of conditions used. The comparable range for peak cladding temperatures shown in Figures 155 through 160 was approximately 30%. As clearly shown in Table 31, the largest change (a factor of five) in fission gas release and fuel dissolution was produced by varying the fuel dissolution modeling.

8.4 Discussion

The results of the SCDAP/RELAP5 analyses and comparisons with experimental data presented in the preceding three sections are discussed in order of the objectives presented in the introduction. First, the probable damage progression history of the fuel bundle is discussed. Second, the influence of uncertainties in test conditions and modeling assumptions

Table 30. Summary of results from sensitivity studies

Parameter	Result
Power history	The variations in bundle power during the initial heatup resulted in a corresponding change in the heatup rate, but had little impact on the predicted peak temperatures reached and damage progression.
Axial power	The variations in bundle axial power profile during the initial heatup had little effect on the overall temperatures but resulted in slight shifts in the axial temperature profile. The variation did have a significant impact on the calculated coolant liquid level prior to 1950 s due to variations in the steam production rate, the axial distribution of cladding oxidation, and the axial distribution of fuel dissolution.
Liner failure	Liner failure had no impact on the rate and timing of bundle heatup since the failure occurred late in the heatup. The failure had a strong influence on the predicted peak bundle temperatures, hydrogen production (due to oxidation of the outer surface of the shroud liner), and bundle cooldown.
Bypass temperature	The variation in bypass temperature had little effect on the predicted response of the bundle.
Minimum fuel relocation temperature	The variation in the minimum fuel relocation temperature had a strong impact on predicted peak temperatures, hydrogen production, and fuel and cladding relocation. A reduced fuel relocation temperature resulted in an earlier relocation of fuel and cladding and reduced hydrogen production, fission product release, peak temperatures, and material relocation.
Fuel dissolution model	Changing the fuel dissolution model had little impact on the predicted bundle heatup and peak temperatures but resulted in changes in the bundle temperatures during cooldown in the elevations where molten material had frozen. The "new" model had a strong impact on fuel dissolution, fuel and cladding relocation, and fission product release.
Ag-In-Cd freezing	The variation in Ag-In-Cd freezing temperatures had a significant impact in the steam generation rates and corresponding influences upon bundle oxidation and heatup, peak bundle temperatures, and material relocation because the freezing of control material either above or in the water results in a significant difference in heat transfer to the water.
Cladding oxidation	The variation in cladding oxidation had a corresponding effect on predicted hydrogen production rates and bundle heatup. The variation had little overall effect on predicted peak bundle temperatures, total hydrogen production, and total material relocation since the total oxidation was limited by the availability of steam.
Axial heat loss	The variation in axial heat loss had a strong impact on the initial heat and liquid level with increased axial heat losses resulting in lower bundle temperatures in the lower portion of the bundle but higher steam generation rates and coolant temperatures.

Table 31. **Relative variation in predicted test results for the variation in test conditions and modeling assumptions**

Parameters	Relative Variation in Results[a]			
	Peak Temperature	Hydrogen Production	Fission Gas Release	Fuel Dissolution
Power history	0.7	0.2	—[b]	—
Axial power history	0.1	—	—	—
Liner failure	1.0	1.0	—	—
Axial heat loss	0.5	—	—	—
Minimum fuel relocation temperature	0.8	0.3	—	—
Fuel dissolution and Ag-In-Cd freezing	0.4	0.2	1.0	1.0
Cladding oxidation	0.4	—	—	—

a. The relative variation in results was computed by taking the maximum variation between cases characterizing the influence of the noted parameter and then normalizing to the most influential parameter value.

b. The relative variation was less than 0.1.

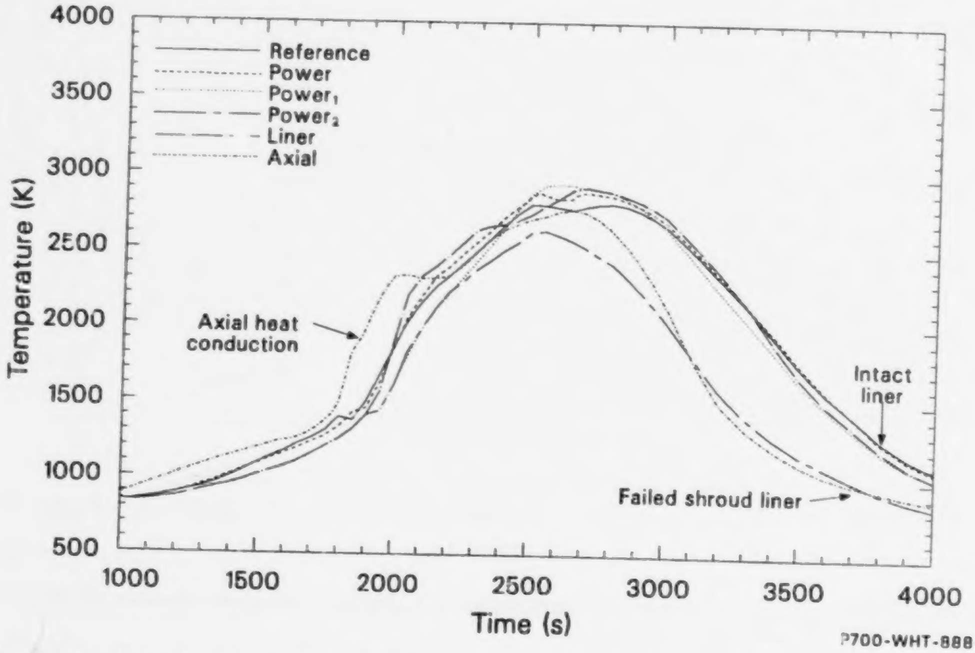

P700-WHT-888-01

Figure 155. Variation in calculated cladding temperature at 0.40 m with variations in test conditions.

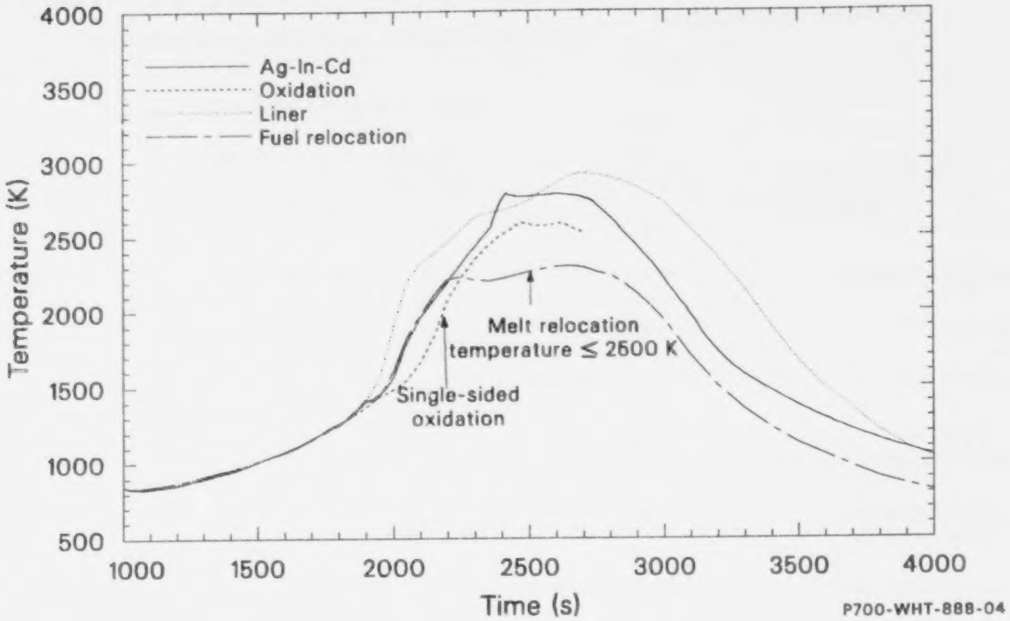

Figure 156. Variation in calculated cladding temperature at 0.40 m with variations in modeling assumptions.

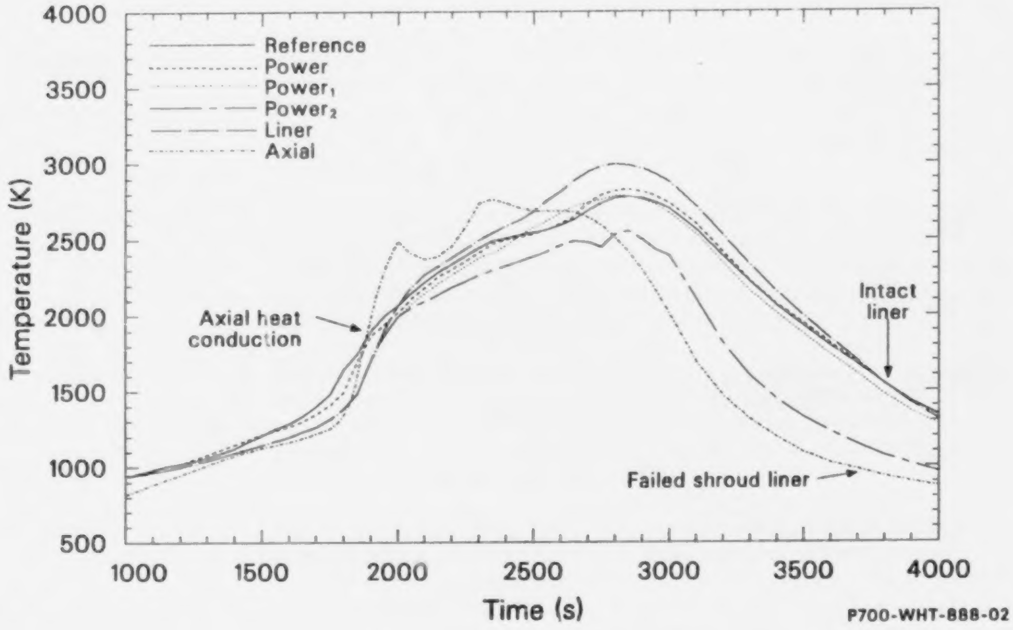

Figure 157. Variation in calculated cladding temperature at 0.55 m with variations in test conditions.

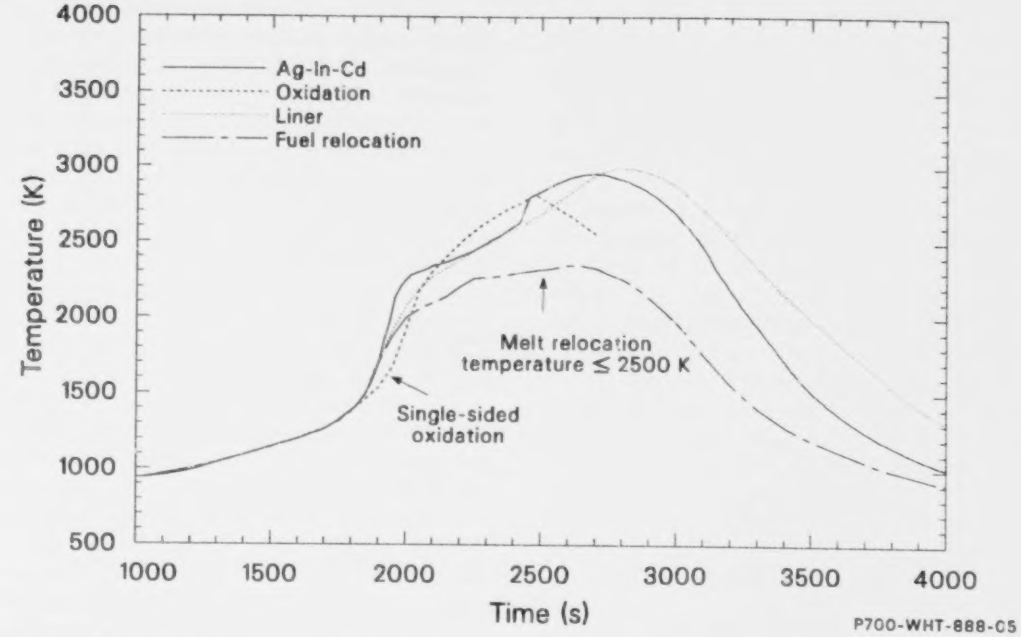

Figure 158. Variation in calculated cladding temperature at 0.55 m with variations in modeling assumptions.

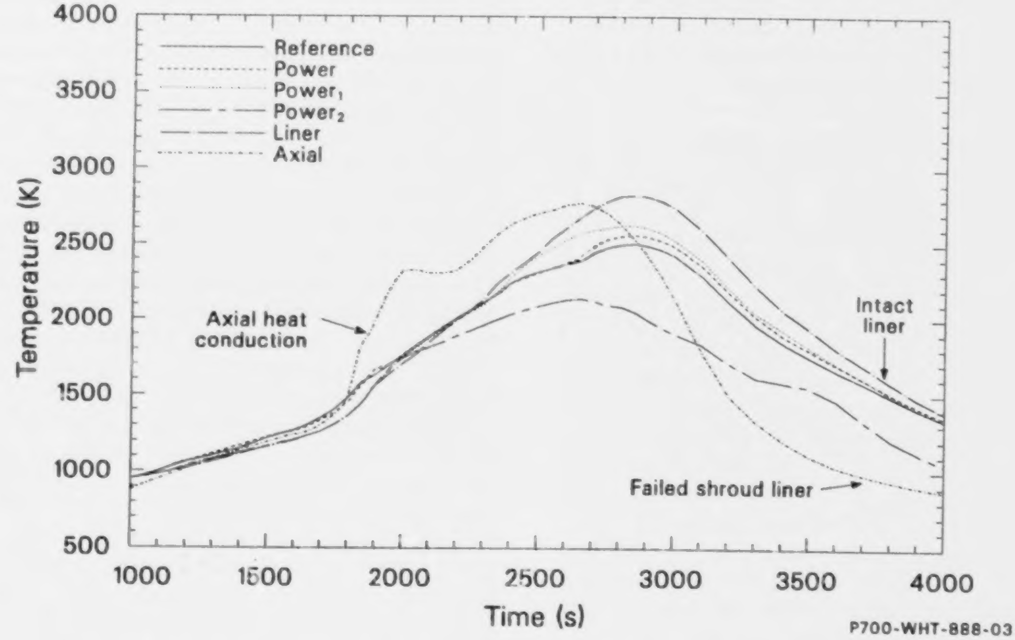

Figure 159. Variation in calculated cladding temperature at 0.74 m with variations in test conditions.

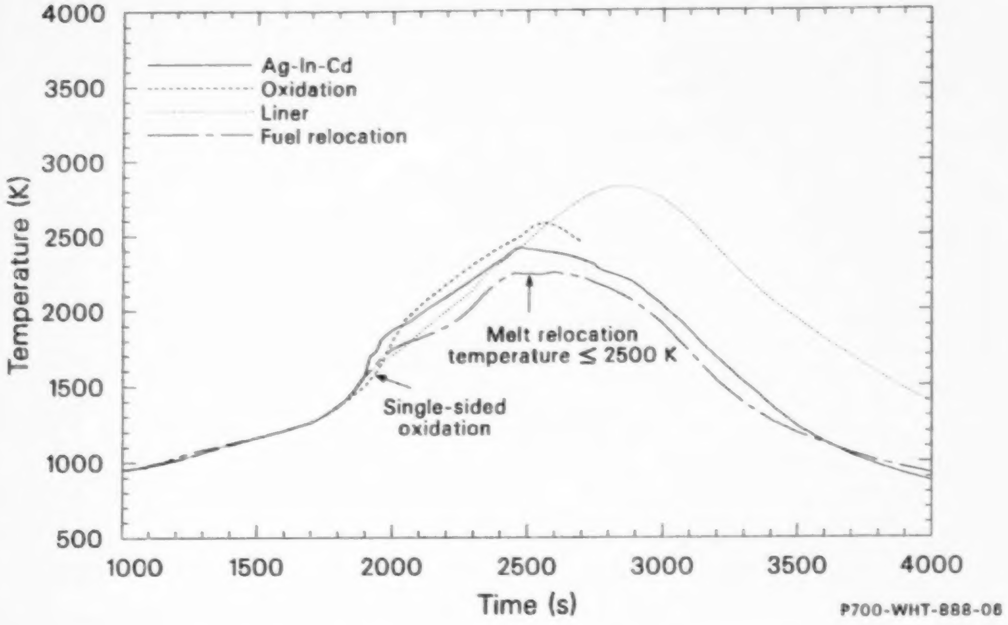

Figure 160. Variation in calculated cladding temperature at 0.74 m with variations in modeling assumptions.

upon the interpretation of the overall test results and validity of important code models is discussed. Finally, modeling improvements that have been identified in the analyses are presented.

8.4.1 Damage Progression History. The combination of the SCDAP/RELAP5 analyses, online measurements, and results from postirradiation examination provide a technically consistent picture of the overall response of the bundle. As shown in Figure 144, at a bundle temperature below 1500 K the bundle was heated initially at a rate of 0.5 K/s with a linear increase in fission power. The heatup rate accelerated during this period as oxidation heating became more influential. During this period, the fuel rods ballooned and ruptured over 50% of the length of the bundle and, as predicted by the code, oxidation of the inside surface of the ballooned cladding started.

As calculated bundle temperatures increased from 1500 to 2250 K, the heatup rate also accelerated because of the increasing fission and oxidation power. During this period, as shown in Figures 143 and 152, the liquid level had reached the bottom of the active fuel, with zircaloy oxidation consuming all of the steam that was being generated. Although the actual elevation and temperature at which the bundle oxidation reached the steam generation limit are not known, SCDAP/RELAP5 calculations indicated that the steam starvation limit was reached at the top of the bundle at a peak bundle temperature of 1900 K. The upper 70% of the bundle was steam-starved when the peak bundle temperatures had reached 2250 K. Also during this time, as described in Section 8.2.3, the melting and relocation of bundle materials started with (a) the failure of the control rods and the formation of a lower crust dominated by silver, stainless steel, and zircaloy and (b) the initial melting of zircaloy and liquefaction of fuel. Although beyond the scope of the SCDAP/RELAP5 models, it is likely that, at temperatures below 2250 K, small droplets or rivulets of liquefied U-Zr-O[36] were starting to drain from the hottest portions of the bundle, either inside the ballooned cladding or into the coolant channel through pin hole failures in the oxide shell on the fuel cladding.

As the temperatures exceeded 2250 K, the heating rate started to decrease as the heat losses to the damaged shroud increased and the oxidation heating continued to decrease. (The decrease in oxidation heating was driven by the reduction in the steam flow rate, as shown in Figure 143, resulting from reduced heat transfer from the fuel to the water in the lower plenum as the coolant level dropped.) As shown on

Figures 144 and 145, much of the bundle remained above 2250 K for 1000 to 1500 s. As a result, the bundle materials continued to melt and relocate into the lower portion of the bundle during this period. The calculations predicted that the melting and relocation of fuel rod materials occurred during two distinct events. First, the relocation of molten zircaloy and dissolved fuel occurred over the middle 40% of the bundle at temperatures between 2250 and 2680 K. Second, the relocation of molten ZrO_2 and UO_2 occurred at a temperature of 2990 K over the middle 10% of the bundle. The bulk of both melts froze well above the liquid level so that the steam generation rate was not significantly influenced by these relocation processes. The peak fission product release rate was calculated to have occurred during this time.

Bundle cooldown to temperatures below 2250 K was dominated by the stored heat in the bundle and the heat losses from the shroud. Although the fission power (see Figure 139) had been reduced to a low level prior to this period, the bundle cooled relatively slowly at a rate of between 1 to 2 K/s. No significant events were predicted to occur during this period, with the geometry remaining unchanged.

8.4.2 Influence of Uncertainties in Test Conditions and Modeling Assumptions. The sensitivity calculations indicated that the uncertainties in test boundary conditions and modeling assumptions were equal contributors to the overall uncertainties in SCDAP/RELAP5 calculations. As shown in Figures 155 through 160 and Tables 30 and 31, uncertainties in the fission power in the bundle had the most influence on the initial heatup of the bundle, while uncertainties in the shroud insulation thermal conductivity, following shroud liner failure, had the most influence on the cooldown. Fission power, shroud insulation thermal conductivity, and the assumed minimum melt relocation temperature had the most influence on the peak bundle temperatures. Hydrogen production was most influenced by the shroud liner failure that permitted the oxidation of the outer surface of the shroud liner. Fission product release and the relocation of fuel were dominated by the fuel dissolution and associated processes.

The relative importance of axial heat transfer from the bottom of the bundle to the lower plenum was an unexpected result. As shown on Figures 155 through 160, the uncertainties introduced by axial heat transfer had more influence on the temperature distribution during the initial heatup of the bundle than the uncertainties in power level. This surprising result indicates the importance of modeling the heat transfer from the bottom of the fuel to the water in the lower plenum. In the calculation identified as "Axial" in Table 28 and the associated figures, the heat transfer to the water in the lower plenum was ignored. Therefore, the water could not drop below the bottom of the active fuel since there would be no heating of the water in the lower plenum and thus no steam generation. Thus, in this calculation, after 2000 s water remained in the bottom of the bundle with a constant steam generation rate of 0.6 g/s. In the other calculations, the heat transferred to the water in the lower plenum due to axial heat conduction was simulated by partitioning the fission power in the lower axial node (lower 10% of the bundle) equally between the fuel and the water in the lower plenum. In these calculations, the water dropped below the active fuel zone, as shown in Figure 142. In addition, the steam generation rate (Figure 143) remained above 0.6 g/s as the fission power was increased (Figure 139) and the water level (Figure 142) continued to drop. Then as the power was decreased, the steam generation rate dropped below 0.6 g/s as the lower plenum refilled with water.

The relative influence of the Ag-In-Cd freezing temperature was also an unexpected result. The relatively small change in the freezing temperature, reflecting the influence of the mixing of molten control rod material, resulted in a small difference in the location of molten control rod material relocation. In the two calculations, identified as "Ag-In-Cd" and "Oxidation" in Table 29 and the associated figures, the molten mixture moved down the bundle and into the water. The resulting steam spike initially increased the zircaloy oxidation rate in the bundle, with a corresponding increase in bundle heating, but then resulted in reduced oxidation rates later in the test due to a reduced liquid level. In the other calculations, including the best-estimate calculations, the control rod material froze above the water level so that the steam generation rate and liquid level during the initial heatup were determined by the fission power and inlet water conditions alone.

One of the most important conclusions resulting from the sensitivity calculations was that the uncertainties in test conditions and modeling assumptions have little impact on the interpretation of the response of the bundle and upon validation of SCDAP/RELAP5 models, even though they result in uncertainties in specific calculated responses. The overall damage progression history presented in Section 8.4.1 is not impacted appreciably by these uncertainties. Modeling deficiencies, in both the input describing the bundle and lower plenum and process models, can clearly be defined.

8.4.3 Model Improvements. The code-to-data comparisons and sensitivity calculations have clearly quantified the benefits of additional improvements in the SCDAP/RELAP5-MOD1 fuel rod material relocation models. The new fuel dissolution model, developed from the work of Hofmann and others,[22] has made a significant improvement in the prediction of fuel liquefaction, relocation, and fission product release. Although the results presented in the sensitivity calculations are for an experimental version of SCDAP/RELAP5-MOD1, the factor of five increase in fuel dissolution with the new models eliminates a significant discrepancy between the best-estimate calculation and the data, as shown on Figure 153.

The enhanced fuel dissolution also improves the prediction of the final bundle geometry by increasing the fuel in the melt by a factor of five. However, postirradiation examination results indicate that the porosity of the melt is also a strong contributor to the total volume of the melt (Appendix I). Thus, flow area reduction models in SCDAP/RELAP5-MOD1 must also be modified to account for the increases in material porosity as it melts and relocates.

The final improvement in the fuel liquefaction and relocation models suggested by the SCDAP/RELAP5 analyses concerns the relocation of the ceramic melt. As shown in Figure 153, the ceramic melt downward movement was not restricted by the lower metallic melt, since a gap existed between the two melts. However, the calculations did not show a gap between the metallic and ceramic melts. This suggests that the ceramic melt may have relocated as a slurry with a relatively low latent heat of fusion, since the melt cooled quickly as it moved downward.

There was also a discrepancy between the predicted and measured hydrogen production rate, but it is believed that the discrepancy is related to biases in the data and not a modeling problem in the code. As shown in Figure 152, SCDAP/RELAP5 predicted a more rapid increase in the hydrogen production rate than was measured. There are two factors that indicate that the SCDAP/RELAP5 predicted rates may be correct. First, the initial heatup of the bundle is predicted accurately using the combination of fission and oxidation heating. The sensitivity studies comparing the influence of oxidation rate, as shown in Figure 157, indicate that a reduction in oxidation heating of the magnitude necessary to match the measured hydrogen production would also significantly delay the initial heatup of the bundle. Second, as noted in Section 5, the initial measured hydrogen production rate is low due either to incomplete mixing of hydrogen, nitrogen, and steam in the separator before a stable, well-mixed separator outlet flow is established or to temporary holdup of hydrogen in unoxidized zircaloy in the bundle.

The calculated and measured integral hydrogen productions were in good agreement, but there is evidence from the postirradiation examination that the oxidation of the relocated material may be more than predicted by the code. This implies that two related changes in the modeling should be evaluated further. First, molten zircaloy may have relocated at a slightly lower temperature than predicted, resulting in less oxidation of the zircaloy in the original rod-like geometry. Second, the molten or frozen zircaloy may have remained hotter for a longer period of time than predicted by the code, so that additional oxidation takes place after material relocation. The sensitivity studies, in particular the study which allowed the molten zircaloy to relocate at 2250 K, indicate that these two changes in the melt relocation and associated oxidation would not alter the overall predicted damage progression history and bundle temperatures.

Several other code and model improvements have been added to SCDAP/RELAP5-MOD1 as a result of the analyses of Test SFD 1-4, but they have had little impact on the overall results. However, it is important to note that this analysis has made a substantial impact on the validation of SCDAP/RELAP5 by confirming that many of the models developed from other experiments or basic physics are applicable to this test. RELAP5 thermal-hydraulic models that have had extensive validation for less severe conditions were able to describe the thermal-hydraulic response of the bundle accurately. The heat transfer models that describe the radial and axial heat conduction in the bundle and shroud and the radiation heat transfer between the bundle and shroud and to the coolant also described the temperature response accurately.

9. IMPACT OF TEST SFD 1-4 ON SEVERE ACCIDENT ISSUES

Numerous studies[37-40] have indicated that there are many outstanding severe accident and source term issues that must be addressed in order to ensure that the technical data base on severe accidents is complete and to reduce the uncertainty in current probabilistic risk assessments for nuclear power plants. The conclusions from Test SFD 1-4 can be used to address important severe accident and source term issues related to (a) melt progression, (b) Ag-In-Cd control rod behavior, (c) hydrogen generation and zircaloy oxidation, (d) fission product release, (e) fission product chemical form, and (f) fission product and aerosol transport. In this section, the impact of Test SFD 1-4 on various issues is addressed.

9.1 Melt Progression

What are the thresholds and mechanisms of molten zircaloy relocation, including flow blockage formation?

Melt relocation in Test SFD 1-4 occurred over a wide range of time and temperature. Postirradiation examination identified four basic relocation modes:

1. Eutectic formation between zircaloy and iron or nickel at 1700 K
2. Unoxidized metallic zircaloy melting at 2030 K
3. Eutectic formation between zircaloy and ZrO_2 and/or UO_2 at 2170 K
4. Ceramic melt $(U,Zr)O_2$ relocation at 2800 K.

The material relocation behavior in Test SFD 1-4 indicates that flow restrictions are likely to form at lower spacer grid locations.

What are the effects of a metallic-ceramic hard pan of relocated material forming at the fuel rod stub region?

A metallic melt of zircaloy, stainless steel, and control rod alloy solidified at the lower spacer grid and blocked ~87% of the flow area in Test SFD 1-4. The primary effect of this layer was to support later relocated material at an elevation where continued oxidation could take place.

What are the effects of collapsed, declad, cracked fuel pellets on top of the hard pan forming a debris bed, and what is the character of the bed?

A region of collapsed, unclad fuel pellets formed a rubble bed above 0.7 m in the SFD 1-4 bundle. The particle size in the bed was ~2 to 2.5 mm (one-fifth to one-fourth of a pellet). The apparent porosity of the bed was ~40% to 50%. The effects of the debris bed on the behavior of the bundle in Test SFD 1-4 were difficult to discern.

Are current models used in severe accident codes able to describe melt progression in a severe PWR accident?

Melt relocation models that are based on a single temperature criterion (i.e., coherency) are inadequate to describe melt progression in a severe accident. Test SFD 1-4 illustrates that melt progression is inherently an incoherent process. Multiple relocation events would occur over an extended period of time due to the spatial and temporal temperature gradients that develop during an accident, the variety of materials in a reactor core, their widely different melting points, and their potential for interaction. Such interactions must be modeled in severe accident codes to provide an accurate description of melt progression.

Is there a generic melt progression scenario that occurs during a severe accident in a PWR?

Maybe. The melt progression phenomena observed in Test SFD 1-4 are similar to those observed in the TMI-2 accident and other severe fuel damage tests. The debris bed of fuel fragments in the upper bundle is similar to the TMI-2 upper debris bed. The high-temperature U-Zr-O material in the lower bundle is a precursor to the molten pool in TMI-2. The accumulation of metallic melts (Ag-In-Cd, stainless steel, and zircaloy) near the bottom of the bundle is a precursor to the metallic crust found in TMI-2.

9.2 Zircaloy Oxidation and Hydrogen Generation

What is the extent of hydrogen generation after relocation of molten zircaloy and flow blockage formation?

Hydrogen was measured continuously during Test SFD 1-4, indicating that zircaloy oxidation continued unabated during the time when zircaloy melting, fuel dissolution, material relocation, and blockage formation were occurring. For the steam-starved conditions in Test SFD 1-4, at temperatures above 1700 K all of the available steam was converted to hydrogen, corresponding to oxidation of ~32% of the bundle zircaloy. The on-line hydrogen generation data indicate that greater than 90% of this oxidation occurred after the onset of zircaloy melting. Postirradiation examination also confirms that melts containing zircaloy continued to oxidize following relocation.

9.3 Ag-In-Cd Control Rod Behavior

What are the effects of Ag-In-Cd control rods upon melt progression, material relocation, flow blockage, and aerosol formation?

The principal effects of the control rods in Test SFD 1-4 were the generation of a cadmium aerosol and the formation of metallic melts that solidified at low elevations and partially blocked the flow. Most of the alloy relocated downwards. Very little was vaporized due to the high system pressure.[29] Molten control rod alloy and stainless steel interacted with bundle zircaloy during and following relocation; however, the control rod material did not interact significantly with the fuel pellets.

9.4 Fission Product Release

Are there significant differences between fission product releases measured during in-pile and out-of-pile severe fuel damage experiments?

No. Noble gas releases from high-burnup fuel on heatup in Test SFD 1-4 are similar to those measured during the ORNL out-of-pile release tests that used similar fuel.

Are current models capable of accurately describing fission gas release during a severe accident?

Based on Test SFD 1-4 results, CORSOR, FASTGRASS, and Booth-diffusion models all adequately predicted the release rates measured on heatup, overpredicted release rates by factors of two to five during the high-temperature portion of the transient when geometry changes were occurring, and underpredicted releases on cooldown by orders of magnitude.

9.5 Fission Product Chemical Form

What are the dominant chemical forms of fission products and aerosols released during a severe accident?

Fission product chemical form is a function of temperature, H_2/H_2O ratio, and fission product concentration. For Test SFD 1-4, with high-burnup fuel in a steam-starved environment, the dominant chemical forms of cesium and iodine were calculated to be cesium iodide and cesium hydroxide, with some elemental cesium at high temperature. Because of the high concentrations of cesium and iodine, no HI or AgI were predicted. The dominant form of tellurium released was probably tin telluride. Silver, cadmium, and tin aerosols were calculated to be released in their elemental form.

9.6 Fission Product and Aerosol Deposition and Transport

What are the dominant aerosol sources in a PWR severe accident?

Aerosols were generated in Test SFD 1-4 as a result of tin release from oxidized cladding, vaporization of control rod material, and volatile fission product release. The timing and magnitude of the different sources were affected by the details of core melt progression.

What role does the aerosol play in fission product transport?

Analysis of aerosol behavior in Test SFD 1-4 indicates that aerosols provide a mobile surface onto which fission products condense. Below 700 K, >95% of the volatile fission products in the effluent would be transported as an aerosol. Aerosols can transport this condensible material further distances than if the material were in a vapor state. If the aerosols grow to a large enough size, they can settle onto system surfaces, thus enhancing fission product deposition.

9.7 Summary

Test SFD 1-4 has provided data that have helped significantly to improve the understanding of early phase PWR melt progression, early phase Ag-In-Cd control rod behavior, zircaloy oxidation in an intact geometry, volatile fission product release, and fission product and aerosol transport. The data obtained from Test SFD 1-4 strengthen the in-vessel PWR severe accident data base, and the improved understanding of specific phenomena can be used to reduce uncertainty in the results of probabilistic risk assessments of nuclear power plants.

10. SUMMARY AND CONCLUSIONS

The overall objective of Test SFD 1-4 was to contribute to the understanding of in-vessel LWR severe accident behavior. Data were obtained from Test SFD 1-4 pertaining to (a) the thermal response of the fuel bundle; (b) zircaloy oxidation and hydrogen generation; (c) melt progression phenomena; (d) Ag-In-Cd control rod behavior; (e) fission product release; and (f) fission product and aerosol transport behavior. In addition, detailed analyses were performed to help understand the influence that boundary conditions and key phenomena have on the overall response of the bundle. In Sections 10.1 through 10.6, conclusions from Test SFD 1-4 pertaining to specific in-vessel severe accident phenomena are presented. Major conclusions from the SCDAP/RELAP5 analysis are presented in Section 10.7, and the impact of Test SFD 1-4 on the outstanding severe accident and source term issues is discussed in Section 10.8.

The SFD 1-4 high-temperature transient resulted in zircaloy oxidation and hydrogen generation, control rod melting and failure, zircaloy melting and UO_2 liquefaction, material relocation, and fission product and aerosol release. Posttest examination revealed four distinct damage regions in the bundle. The upper portion of the bundle consisted of a rubble bed of unclad fuel fragments. Partial fuel pellets and the remnants of fuel dissolution remained in the mid-bundle region. Molten zircaloy and liquefied fuel accumulated in the lower bundle, and metallic melts consisting of zircaloy, stainless steel, and control rod alloy material resided at the lower spacer grid, near the bottom of the bundle. A total of $\sim$18% of the fuel liquefied during the transient. Material relocation and refreezing reduced the available flow area between 70% and 87% in the lower portions of the bundle. The bundle was at temperatures in excess of 2200 K for $\sim$1200 s. Peak temperatures reached $\sim$2800 K over about 25% of the bundle. The best estimate of hydrogen generation during the experiment is 86 ± 12 g, equivalent to 32% oxidation of the bundle zircaloy.

Fission product release rate and integral releases were measured in Test SFD 1-4. Integral releases of the noble gases ranged from 23% to 52%. Integral releases for iodine and cesium were 24% and 51%, respectively, whereas only 3% of the bundle inventory of tellurium was released. Release rates were low prior to 1500 K, increased by four orders of magnitude as temperatures exceeded 2100 K, and peaked during the high-temperature portion of the transient. Release rates decreased by about a factor of fifty from the peak value and remained at that level well into the bundle cooldown phase of the experiment.

Aerosol generation and transport in Test SFD 1-4 were strongly coupled to bundle melt progression phenomena and the thermal-hydraulic conditions in the bundle and upper plenum. Tin release due to zircaloy oxidation, the vaporization of Ag-In-Cd control rod material, volatile fission product release, possible release of loose particulates from the shroud (ZrO_2) insulation cavity, and ceramic melt relocation and interaction with control rod material all contributed to the aerosol source exiting the SFD 1-4 bundle. A dense aerosol was generated continuously during the high-temperature portion of Test SFD 1-4. Measurements indicate that the aerosol was predominantly tin and cadmium, with lesser amounts of silver, zirconium, and fission products.

Significant attenuation of the aerosol occurred as it traveled through the upper plenum. Analysis indicates that aerosol nucleation, condensation and evaporation processes, aerosol agglomeration, and gravitational settling and deposition due to wakes and eddies were all important phenomena that influenced the observed behavior.

The important phenomena related to bundle thermal behavior, zircaloy oxidation and hydrogen generation, melt progression, Ag-In-Cd control rod behavior, fission product release, and aerosol transport are further discussed in the following sections.

10.1 Thermal Behavior

The thermal-hydraulic conditions of Test SFD 1-4 were very important in determining the course of the bundle behavior. The selected test boundary conditions produced heatup rates and peak temperatures consistent with those calculated for the TMI-2 accident and simulated PWR severe accidents. The measured heatup rates of 0.37 K/s from 800 to 1200 K, 1.6 K/s from 1200 to 1600 K, and up to 10 K/s at 1900 K are in good agreement with predicted values. The final bundle heatup rate was controlled primarily by the oxidation rate, which in turn was controlled by the steam availability.

The small amount of coolant flow limited the zircaloy oxidation to the lower two-thirds of the bundle and produced a hydrogen-rich environment in the upper third of the bundle during the high-temperature transient. Steam starvation conditions determined the magnitude and axial distribution of the temperature excursion, which influenced all aspects of the test bundle behavior. Peak temperatures were estimated to be at least 2800 K in the mid-bundle region, 2200 K in the upper bundle debris bed region, and below 1700 K in the lower bundle region where metallic melts accumulated.

10.2 Zircaloy Oxidation and Hydrogen Generation

The best estimate of hydrogen generation in Test SFD 1-4 is 86 ± 12 g, which corresponds to 32% oxidation of the zircaloy. For bundle temperatures above 1700 to 1800 K, all of the available steam was converted to hydrogen, independent of oxidation kinetics and changes in geometry. The oxidation front started at the bundle midplane, then propagated upward, downward, and later radially outward to the shroud liner. After nearly complete oxidation of the intact zircaloy in lower bundle regions (0.17 to 0.25 m), the oxidation front moved upward again to the higher power mid-bundle elevations (0.4 to 0.6 m), where nearly total oxidation produced temperatures of ~2800 K. The lower bundle region below 0.08 m was not hot enough to oxidize during the test.

Hydrogen generation continued unabated during the time when geometry changes occurred due to zircaloy melting, UO_2 dissolution, and material relocation. Postirradiation examination also indicated that zircaloy-containing melts continued to oxidize following relocation, with nearly complete oxidation of the zircaloy melts between 0.39 and 0.54 m and a decreasing fraction of oxidized zircaloy in the melts in the lower bundle region.

Some models assume that the steam/zircaloy reaction stops at the melting temperature of the oxygen-stabilized α-zirconium (2245 K). This concept is based upon the assumption that the flow channel will become completely blocked after the material melts and no further oxidation can take place. Other models assume that upon melting material relocates to a low-temperature region where no further oxidation will occur. The SFD 1-4 results are in direct contrast to these assumptions, since oxidation continued long after the cladding melted and relocated. Numerous examples of material that had oxidized following relocation were also found.

10.3 Melt Progression

The melt progression behavior that occurred in Test SFD 1-4 is believed to be typical of that expected during a severe accident in a PWR. Four distinct damage regions were observed. The upper portion of the bundle consisted of a rubble bed of unclad fuel fragments. Partial fuel pellets and the remnants of fuel dissolution remained in the mid-bundle region. Molten zircaloy and liquefied fuel collected in the lower bundle, and metallic melts consisting of zircaloy, stainless steel, and control rod alloy material resided at the lower spacer grid at the bottom of the bundle.

A total of 18% of the fuel liquefied during the transient, mostly over the central third of the bundle with little dissolution observed in the upper bundle region. Apparently, ballooning of the cladding prior to melting combined with poor wettability of unoxidized cladding essentially inhibited fuel dissolution in the upper bundle region.

Test SFD 1-4 illustrates that core melt progression during a severe accident is inherently an incoherent process. Multiple relocation events would be expected to occur over an extended period of time based on the spatial and temporal temperature gradients that develop during a severe accident, the variety of materials in a reactor core, their widely different melting points, and their potential for interaction. The SFD 1-4 bundle was at high temperatures, and melt relocation occurred for an extensive time period, as evidenced by the 1080- to 1440-s duration of hydrogen, aerosol, and fission product releases. The thickness of alternating metal and oxide layers in the lower bundle indicated multiple relocation events at 5- to 60-s intervals. Relocated material of different compositions and melting points was observed, which indicates that several discrete melt relocation events occurred. These melts include: ceramic $(U,Zr)O_2$ (melting point ~2800 K), zircaloy (melting point ~2200 K), stainless steel (melting point ~1700 K), and Ag-In-Cd (melting point ~1120 K).

The melt progression was influenced significantly by the presence of Inconel spacer grids and obstructions but not by the penetration of molten material into the lower coolant plenum, as might be expected. In spite of the shorter-than-typical active fuel length in Test SFD 1-4 which produced peak temperatures and oxidation low in the bundle, relocating material refroze at the lower spacer grid and did not reach the lower plenum. Similar behavior would be expected in a severe reactor accident. Material relocation significantly reduced the available flow area in Test SFD 1-4 by up to 87% at the bottom of the bundle. For similar diameter fuel rods and spacing, the blockage from a full-length fuel assembly could be even higher.

The melt progression phenomena observed in Test SFD 1-4 are similar to those more fully developed in the TMI-2 accident which was terminated at a later stage. The debris bed of fuel fragments in the upper bundle is similar to the TMI-2 debris bed. The high-temperature U-Zr-O melt in the lower bundle is a precursor of the molten pool in TMI-2. The accumulation of metallic melts (Ag-In-Cd, zirconium, stainless steel) near the bottom of the bundle is a precursor of the metallic crust found in TMI-2.

Some severe fuel damage models assume that the beginning of fuel relocation is dependent only on temperature. In some codes, only the eutectic formation between zircaloy and UO_2 is considered; and no attempt is made to model the melting and relocation of zircaloy or other structural materials. At the selected relocation temperature, the liquefied U-Zr-O material is assumed to instantly relocate to a lower-temperature region, thereby reducing fission product release and hydrogen production. Data from Test SFD 1-4 indicate that material relocation models based on a single temperature criterion are not correct. Material relocation in the test occurred over a wide range of temperatures and time.

Although a significant quantity of control rod material relocated to the lower plenum region during the transient, only a small pressure spike of 0.4 MPa magnitude was generated.

10.4 Control Rod Behavior

The instrumented control rod failed early in the test at 1170 K because of a weld defect that resulted in waterlogging and excessive internal pressure during the heatup. This non-typical control rod failure did not affect the test results appreciably, since the rod failed at a low temperature prior to oxidation or liquefaction. The other three non-instrumented control rods failed as expected at the melting temperature of the stainless steel cladding, ∿1700 K. Posttest examination indicates that ∿83% of the control rod material relocated near the lower spacer grid location, while most of the remaining control rod material relocated to the lower coolant plenum. A small fraction of the control rod alloy was retained in the mid-bundle, high-temperature zone by means of physical mixing in melts. The control rod alloy and molten stainless steel interacted with zircaloy in the bundle during and following relocation but did not interact with the fuel pellets or have significant global effects on all of the fuel rods.

Control rod material that relocated to the lower bundle regions was reheated by ceramic melts long after initial control rod failure, causing additional vaporization of control materials, especially cadmium. The principal effects of the control rods were generation of cadmium aerosol and the formation of metallic melts that solidified at low elevations in the bundle and produced a lower crust that partially blocked the open flow area.

10.5 Fission Product Release

Detailed analyses of the Test SFD 1-4 data indicate that fission product release is affected by changes in fuel morphology, isotopic half-life, and core melt progression.

Noble gas release was low prior to 1500 K. The noble gas fractional release rate increased four orders of magnitude as bundle temperatures were driven above 2100 K by oxidation of the zircaloy cladding. The effect of changes in fuel morphology, such as liquefaction and dissolution, on the rate of fission product release was difficult to detect, since the noble gas fractional release rate was generally constant during the high-temperature portion of the transient. Elevated releases were measured during the cooldown phase of the transient.

Integral releases of the noble gases ranged from 23% to 52%. Release of iodine and cesium were 24% and 51%, respectively, whereas only 3% of the bundle inventory of tellurium was released. Most of the released iodine, cesium, and tellurium was deposited on the test train, upper plenum, and effluent line surfaces. Iodine and cesium were later washed from these surfaces after flushing operations and measured in the collection tank. System flushing removed very little of the deposited tellurium. Lesser amounts of the low-volatility fission products (strontium, barium, lanthanum, europium, and cerium) were released during the experiment.

Comparison of the integral release data implies that the releases of long-lived volatile fission product species were greater than those of short-lived species. The release fractions for ^{85}Kr and stable krypton and xenon isotopes were ~0.5, yet the average release of seven short-lived noble gases was ~0.35. This difference in release is believed to be related to the morphology of the fuel and the location of the fission products in the fuel prior to release. More of the long-lived species, relative to short-lived species, reside at grain boundaries from which release is relatively fast during heatup because of the interconnected porosity in the high-burnup fuel. For the short-lived species, release is much slower because more of the inventory is in the fuel grain and must diffuse to the grain boundaries prior to release.

Calculations of fission gas release using CORSOR, FASTGRASS, and Booth-type release models provided additional insight into the physical phenomena governing fission product release during Test SFD 1-4. All of the results were in reasonable agreement with the release rates measured on heatup in Test SFD 1-4. For releases on heatup, CORSOR calculations were in much better agreement with the measurements from high-burnup fuel in Test SFD 1-4 than with those from low-burnup fuel in Test SFD 1-1.

The best agreement with the release measured during heatup was obtained with the Booth model that used the diffusion coefficient correlation derived from Oak Ridge National Laboratory fission product release tests with similar high-burnup fuel. The agreement suggests that for releases from high-burnup fuel on heatup very little difference should be expected between in-pile and out-of-pile experiments. FASTGRASS calculations indicated that release rates on heatup for short- and long-lived species should be different; however these differences should diminish once significant fuel dissolution occurs.

Each of the three models overpredicted the measured releases during the high-temperature portion of the test, when significant fuel liquefaction and dissolution occurred. All of the models failed to account for the sustained releases measured during the cooldown phase of the test.

10.6 Fission Product and Aerosol Transport Behavior

Aerosol generation in Test SFD 1-4 was continuous during the high-temperature portion of the experiment and was strongly coupled to melt progression phenomena in the bundle. The vaporization of Ag-In-Cd control rod material, tin release due to zircaloy oxidation, volatile fission product release, possible release of loose particulates from the shroud (ZrO_2) insulation cavity, and ceramic melt relocation and interaction with control rod material all contributed to the aerosol source exiting the SFD 1-4 bundle. Small fractions of control rod material, tin, and zircaloy were released from the bundle; however they were sufficient to produce a very dense aerosol.

Chemical equilibrium calculations indicate that the dominant forms of cesium and iodine in Test SFD 1-4 were cesium iodide and cesium hydroxide, with some elemental cesium at high temperatures. Because of the high concentrations of cesium and iodine released from the high-burnup fuel and the low release of silver, no HI and no AgI were predicted to form. The dominant form of tellurium released from the bundle was tin telluride. The reducing environment resulted in silver, cadmium, and tin being released in their elemental form.

Data and analysis indicate that the aerosol generated in Test SFD 1-4 provided a large mobile surface on which volatile fission products could condense. Upon exiting the bundle, silver and tin, because of their low volatility, condensed and formed aerosols near the top of the bundle. Upon cooling of the effluent, near the lower tip of the deposition rod (~800 K), cadmium and cesium iodide condensed very rapidly on the tin and silver aerosols and the downstream surfaces of the deposition rod. Below 700 K, >95% of the volatile fission products in the effluent were transported as an aerosol.

Significant attenuation of the aerosol occurred as it traveled through the upper plenum. Analysis indicates that aerosol agglomeration, gravitational settling, and deposition due to wakes and eddies were all important phenomena that influenced the observed behavior.

A fine-yet-dense aerosol was continuously measured 10 m downstream of the bundle at the aerosol monitor. The aerosol measured at the monitor was predominantly tin and cadmium, with small amounts of silver, zirconium, and fission products. The diameter of average mass of the aerosol at the aerosol monitor ranged from 0.4 to 1.0 μm, and the number concentration varied between 5×10^7 and 2×10^8 p/cm^3.

10.7 SCDAP/RELAP5 Analysis

SCDAP/RELAP5-MOD1 analyses of Test SFD 1-4 were made to help determine the probable damage progression history, to evaluate the importance of uncertainties in measured test boundary conditions and modeling assumptions on the calculated bundle behavior, and to define needed modeling improvements. In general, the code calculations accurately represented the bundle transient behavior. Calculated fuel, control rod, and shroud temperatures agreed well with the measurements until the thermocouples failed. The calculated peak bundle temperatures reached during the transient were representative of those determined from metallurgical estimates. The combination of the SCDAP/RELAP5 analyses, on-line measurements, and metallurgical examination provided a consistent scenario of the bundle behavior.

A series of sensitivity studies was performed to evaluate the relative influence of the bundle fission power, shroud thermal conductivity, shroud liner outer wall oxidation, melt relocation temperature, fuel dissolution modeling, and axial heat transfer on the calculated bundle response. The uncertainties in test boundary conditions and modeling assumptions contributed about equally to the uncertainties in the sensitivity calculations but had minor impact upon the interpretation of the bundle response and code validation. A discrepancy between the predicted and measured hydrogen production rate pointed out a bias in the hydrogen rate measurements. Comparisons of the calculations with test data and the sensitivity calculations have pointed out the need for additional improvements related to melt porosity, ceramic melt solidification, and fuel dissolution. A new fuel dissolution model, incorporated as a result of these analyses, made a significant improvement in the prediction of fuel liquefaction, relocation, and fission product release. These comparisons also made a substantial impact on the validation of SCDAP/RELAP5 by confirming that many of the models developed from other experiments or basic physics are applicable to severe accident conditions.

10.8 Impact

The results of Test SFD 1-4 have been applied to outstanding severe accident and source term issues related to (a) melt progression, (b) Ag-In-Cd control rod behavior, (c) hydrogen generation and zircaloy oxidation, (d) fission product release, (e) fission product chemical form, and (f) fission product and aerosol transport.

Test SFD 1-4 has provided data that have significantly improved the understanding of early-phase PWR melt progression related to the thresholds and mechanisms of material relocation, Ag-In-Cd control rod behavior, zircaloy oxidation in an intact geometry, and the extent of hydrogen generation after molten zircaloy relocation and blockage formation.

Information gained from Test SFD 1-4 has been used to address several source term issues. Fission product releases have been used to address questions related to differences between out-of-pile and in-pile release measurements and the adequacy of fission product release models. Fission product and aerosol transport behavior has helped define fission product chemical forms, dominant aerosol sources, and the impact of aerosols on fission product deposition and transport in a PWR severe accident.

The data obtained from Test SFD 1-4 strengthen the in-vessel PWR severe accident and source term behavior data base, and the improved understanding of specific phenomena can be used to reduce uncertainty in the results of probabilistic risk assessments of nuclear power plants.

11. REFERENCES

1. M. Rogovin, *Three Mile Island, A Report to the Commissioners and to the Public*, NUREG/CR-1250, January 1980.

2. J. T. Larkins and M. A. Cunningham, *Nuclear Power Plant Severe Accident Research Plan*, NUREG-0900, January 1983.

3. A. D. Knipe, S. A. Ploger, and D. J. Osetek, *PBF Severe Fuel Damage Scoping Test—Test Results Report*, NUREG/CR-4683, EGG-2413, August 1986.

4. Z. R. Martinson, D. A. Petti, and B. A. Cook, *PBF Severe Fuel Damage Test 1-1 Test Results Report*, NUREG/CR-4684, EGG-2463, October 1986.

5. D. J. Osetek, "Results of the Four PBF Severe Fuel Damage Tests," *Transactions of the Fifteenth Water Reactor Safety Information Meeting, Gaithersburg, MD, October 26-30, 1987*, NUREG/CP-0090.

6. T. C. Cheng, "RELAP5/SCDAP: An Integral Code for Severe Accident Analysis," *Transactions of the Thirteenth Water Reactor Safety Information Meeting, October 1985*, NUREG/CP-0072.

7. J. P Adams et al., "Development and Calibration of an Aerosol Monitor used for PBF Test SFD 1-4," *Fourth International Symposium on Multiphase Transport and Particulate Phenomena, Miami Beach, FL, December 14-17, 1986.*

8. V. H. Ransom et al., *RELAP5/MOD1 Code Manual, Volumes 1 and 2*, NUREG/CR-1826, EGG-2070, March 1982.

9. J. M. Broughton et al., "A Scenario of the TMI-2 Accident," *Topical Meeting on the TMI-2 Accident: Materials Behavior and Plant Recovery Technology, Washington, D. C., October 31-November 4, 1988.*

10. D. J. Osetek et al., "Fuel Morphology Effects on Fission Product Release," *Proceedings of the International ANS/ENS Topical Meeting on Thermal Reactor Safety, San Diego, CA, February 1-6, 1986*, pp. IX.2-1.

11. P. Hofmann, *Metallographic Examination of the Severe Fuel Damage Scoping Test (SFD-ST) Fuel Rod Bundle Cross Sections*, NUREG/CR-5119, EGG-2537, July 1988.

12. A. G. Croft, *ORIGEN2 - A Revised and Updated Version of the Oak Ridge Isotope Generation and Depletion Code*, ORNL-5621, July 1980.

13. R. G. Helmer, M. H. Putnam and C. M McCullagh, "Nuclide Activities Determined from Gamma-ray Spectra from Ge Detectors: A Review with GAUSS VIII as the Example," *Nuclear Instruments and Methods in Physics Research, Proceedings of the Sixth Symposium on X-ray and Gamma-ray Sources and Applications, Ann Arbor, MI, May 21-23, 1985*, A242 (1986), pp. 427-436.

14. D. W. Akers and B. G. Schnitzler, "Verification of the ORIGEN2 Code Analysis for the TMI-2 Reactor Core," *Nuclear Reactor Severe Accident Chemistry Symposium, Third North American Chemical Congress, Toronto, Canada, June 5-11, 1988.*

15. R. A. Lorenz, E. C. Beahm, and R. P. Wichner, "Review of Tellurium Release Rates from Fuel Elements Under Accident Conditions," *Proceedings of the International Meeting on Light Water Reactor Severe Accident Evaluation, Cambridge, MA, August 28-September 1, 1988.*

16. J. L. Collins, M. F. Osborne, and R. A. Lorenz, "Fission Product Tellurium Release Behavior Under Severe Light Water Reactor Accident Conditions," *Nuclear Technology, 77*, 1, April 1987.

17. J. Rest and A. W. Cronenberg, "Modeling the Behavior of Xe, I, Cs, Te, Ba and Sr in Solid and Liquefied Fuel During Severe Accidents," *Journal of Nuclear Materials, 150*, 1987, pp. 203-225.

18. M. R. Kuhlman, D. J. Lehmickle and R. O. Meyer, *CORSOR Users Manual*, NUREG/CR-4173, BMI-2122, March 1985.

19. A. H. Booth and G. T. Rymer, *Determination of the Diffusion Constant of Fission Xenon in UO_2 Crystals and Sintered Compacts*, CRDC-720, August 1958.

20. D. A. Petti et al., "Analysis of Fission Product Release Behavior During the TMI-2 Accident," *Fifteenth Water Reactor Safety Research Information Meeting, Gaithersburg, MD, October 26-30, 1987*, NUREG/CP-0090.

21. W. Dienst, P. Hofmann, and D. K. Kerwin-Peck, "Chemical Interactions between UO_2 and Zircaloy-4 from 1000 to 2000 C," *Nuclear Technology, 65*, April 1984, pp. 109-124.

22. P. Hofmann, et al., "Dissolution of Solid UO_2 by Molten Zircaloy and Its Modeling," *IAEA International Symposium on Severe Accidents in Nuclear Power Plants, Sorrento, Italy, March 21-25, 1988*, IAEA-SM-296/1.

23. R. H. Barnes et al., *Xenon Diffusion in Single Crystal and Sintered UO_2*, BMI-1533, August 1961.

24. J. B. Meleham, *Release of Fission Gases From UO_2 During and After Irradiation*, BMI-1623, March 1963.

25. D. R. Toner and J. L. Scott, "Study of Factors Controlling the Release of Xenon-133 from Bulk UO_2," *The 64th Annual Meeting of the American Society for Testing and Materials, Atlantic City, New Jersey, June 1961.*

26. S. G. Prussin et al., "Release of Volatile Fission Products from UO_2," *Proceedings of American Nuclear Society Meeting on Fission Product Behavior and Source Term Research, Snowbird, Utah, July 15-19, 1984.*

27. G. T. Lawrence, "A Review of the Diffusion Coefficient of Fission Product Rare Gases in Uranium Dioxide," *Journal of Nuclear Materials, 71*, 1978, pp. 195-218.

28. T. Nakamura and R. A. Lorenz, *Effective Diffusion Coefficient Calculations from ORNL Fission Product Release Test Results* (to be published).

29. D. A. Petti, *Silver-Indium-Cadmium Control Rod Behavior and Aerosol Formation in Severe Reactor Accidents*, NUREG/CR-4876, EGG-2501, April 1987.

30. S. K. Friedlander, *Smoke, Dust and Haze: Fundamentals of Aerosol Behavior*, New York: John Wiley and Sons, 1977

31. C. S. Kim et al., "Deposition of Aerosol Particles in a Straight Tube with an Abrupt Obstruction," *Journal of Aerosol Science, 15*, 2, 1984.

32. V. J.Novick, "Use of Series Light Extinction Cells to Determine Aerosol Number Concentration," *Aerosol Science and Technology, 9*, 3, 1988.

33. H. Jordan, J. A. Gieseke, and P. Baybutt, *TRAP-MELT User's Manual*, NUREG/CR-0632, 1979.

34. R. M. Elrick et al., "High-Temperature Fission-Product Chemistry and Transport," *Reactor Safety Research Semiannual Report, January-June 1986*, NUREG/CR-4805, SAND86-2752, May 1987.

35. T. M. Besmann, *SOLGASMIX-PV, A Computer Program to Calculate Equilibrium Relationships in Complex Chemical Systems*, ORNL/TM-5775, 1977.

36. S. Hagen, L. Sepold, P. Hofmann, and G. Schanz, "Out-of-pile Experiments on Severe Fuel Damage Behavior of LWR Fuel Elements (CORA Program)," *International Symposium on Severe Accidents in Nuclear Power Plants, Sorrento, Italy, March 21-25, 1988, IAEA-SM-296/26.*

37. M. L. Ernst et al., *Reactor Risk Reference Document*, NUREG-1150, Draft 1987.

38. *Uncertainty Papers on Severe Accident Source Terms*, NUREG-1265, 1987.

39. H. Kouts, *Review of Research on Uncertainties in Estimates of Source Terms from Severe Accidents in Nuclear Power Plants*, NUREG/CR-4883, April 1987.

40. R. Wilson, "Radionuclide Release from Severe Accidents at Nuclear Power Plants," *Reviews of Modern Physics, 57*, Part II, July 1985.

APPENDIX A

SYSTEM DESIGN FOR TEST SFD 1-4

APPENDIX A

SYSTEM DESIGN FOR TEST SFD 1-4

The design of the SFD 1-4 experiment is described in this appendix. Specifically, design details of the test train, fuel bundle, and insulating shroud are presented in Section A-1. The effluent sampling and monitoring system description is found in Section A-2.

A-1. Test Train, Fuel Bundle, and Insulating Shroud

The Test SFD 1-4 fuel bundle consisted of a 6 x 6 array without the four corner rods, containing 28 fuel rods and four simulated control rod assemblies in zircaloy guide tubes. This arrangement is shown in Figure A-1. Twenty-six of the fuel rods were previously irradiated, and two (in bundle locations 3B and 4D) were fresh. The as-fabricated enrichment of the irradiated rods was 5.76% ^{235}U (postirradiation effective enrichment of ∼3.6%), and the fresh rods were enriched to 2.9%. The active fuel length of the irradiated rods was 1.0 m, with the axial midplane centered at the Power Burst Facility (PBF) core midplane. The fresh fuel rods had an active length of 0.914 m, with the lower end of the fuel column located 0.0428 m above the bottom of the PBF core fuel region. This arrangement allowed the tops of the active, fresh rods and the preirradiated fuel rods to be at the same elevation (+0.9572 m above the bottom of the PBF core fuel). Details of the fresh and preirradiated fuel rod parameters are given in Tables A-1, A-2, and A-3.

Four simulated pressurized water reactor (PWR) control rod assemblies were located in bundle locations 2B, 5B, 2E, and 5E. The simulated control rods were fixed in position with no provision for withdrawal. The control rod located in bundle location 5E was instrumented (see Appendix B). The absorber material was an alloy composed of 80% silver-15% indium-5% cadmium by weight. The Ag-In-Cd alloy slugs were enclosed in a Type 304 stainless steel tube with a bullet-nosed, stainless steel plug located at the top end of the stainless steel tube. Zircaloy-4 guide tubes were fastened to the bottom support plate to position each control rod. The guide tubes provided an inlet coolant flow at

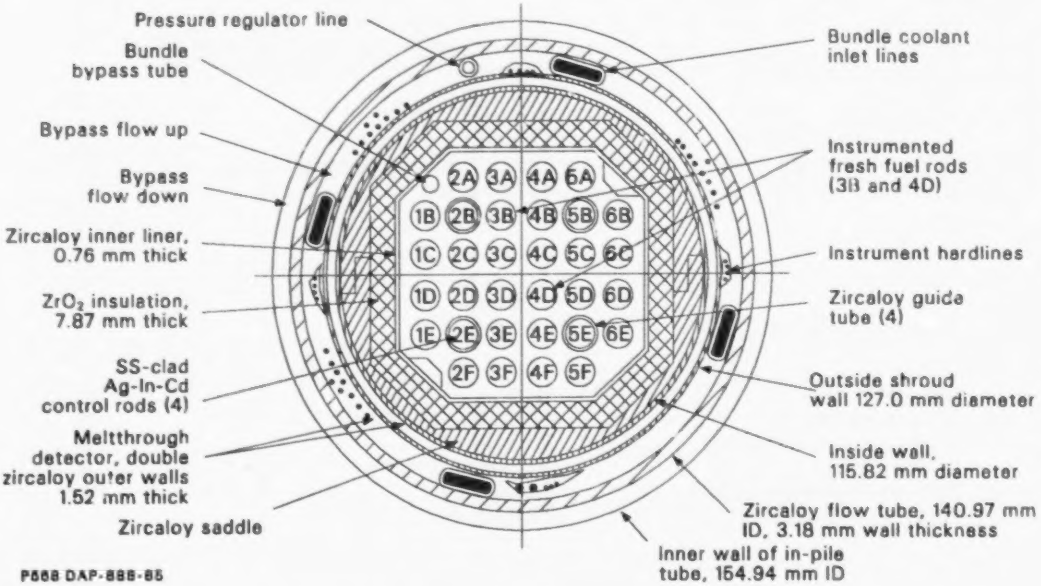
Pressure regulator line
Bundle bypass tube
Bypass flow up
Bypass flow down
Zircaloy inner liner, 0.76 mm thick
ZrO$_2$ insulation, 7.87 mm thick
SS-clad Ag-In-Cd control rods (4)
Meltthrough detector, double zircaloy outer walls 1.52 mm thick
Zircaloy saddle
Bundle coolant inlet lines
Instrumented fresh fuel rods (3B and 4D)
Instrument hardlines
Zircaloy guide tube (4)
Outside shroud wall 127.0 mm diameter
Inside wall, 115.82 mm diameter
Zircaloy flow tube, 140.97 mm ID, 3.18 mm wall thickness
Inner wall of in-pile tube, 154.94 mm ID
2A
3A
4A
5A
1B
2B
3B
4B
5B
6B
1C
2C
3C
4C
5C
6C
1D
2D
3D
4D
5D
6D
1E
2E
3E
4E
5E
6E
2F
3F
4F
5F
P888 DAP-888-85

Figure A-1. Cross-sectional diagram of the SFD 1-4 test train and fuel bundle region.

Table A-1. Nominal design characteristics for unirradiated fuel rods for Test SFD 1-4

Parameter	Value
Fuel	
Material	UO_2 sintered pellets
Density	95% theoretical density (TD - 10.98 g/cm^3)
Enrichment	2.9 wt.% ^{235}U in total uranium
Pellet OD	8.268 mm
Pellet length	9.525 mm
Fuel stack length	0.9144 m
Pellet end dish (2)	1.51% of pellet cylindrical volume
Pellet rims	0.57% of pellet cylindrical volume
UO_2 fuel mass	0.50625 kg/rod
Cladding	
Material	ASTM B353, Grade RA-2 (zircaloy-4 tubing)
Tube OD	9.627 mm
Tube ID	8.433 mm
Tube wall thickness	0.597 mm
Fuel Rod	
Spring material	Inconel X-750
Filler gas	Helium
Fill gas volume	14.16 cm^3
Initial gas pressure (STP)	Rod 3B to 2.0 MPa; rod 4D to 3.8 MPa
Diametral gap	0.165 mm
Plenum volume above fuel	2.79 cm^3
Insulator pellet material	Al_2O_3

Table A-2. Nominal design characteristics for irradiated fuel rods for Test SFD 1-4

Parameter	Value
Fuel	
Material	UO_2 sintered pellets
Density	95% theoretical density (TD - 10.98 g/cm^3)
Initial enrichment	5.76 wt.% ^{235}U in total uranium
Pellet OD	8.04 mm
Pellet length	12.0 mm
Fuel stack length	1.000 m
Pellet end dish (2)	1.5% of pellet cylindrical volume
UO_2 mass	0.529 kg/rod
Cladding	
Material	Zircaloy-4 tubing
Tube OD	9.50 mm
Tube ID	8.24 mm
Tube wall thickness	0.63 mm
Fuel Rod	
Fill gas	Helium
Fill gas volume	8.11 cm^3
Initial gas pressure (STP)	2.0 MPa
Diametral gap	0.2 mm
Plenum volume above fuel	4.44 cm^3
End plug material	Zircaloy-4

Table A-3. Summary of irradiated fuel rod characteristics for Test SFD 1-4

		Inspection Performed		Fuel Properties				Original Mass		Residual Mass				
Fuel Rod	Grid Location	Gamma Scan	Rod Diameter	Fuel Batch	Enrichment ^{235}U (%)	Average Burnup (GWd/MtU)	BR-3 Cycle(s)	^{235}U (g)	Total (g)	^{235}U (g)	Total U (g)	Fissile Pu (g)	Total Pu (g)	Total Fissile (g)
I-52	4B	—	—	B300	5.76	38.9	4A/B	26.469	459.526	9.74	439.11	2.19	2.88	11.93
I-61	1B	—	—	B300	5.76	37.1	4A/B	26.616	462.082	10.44	442.37	2.14	2.83	12.58
I-118	3C	X	X	B300	5.76	40.8	4A/B	56.428	458.821	8.67	437.45	1.99	2.70	10.66
I-159	4E	X	X	B300	5.76	39.2	4A/B	26.438	458.997	9.71	438.58	2.19	2.80	11.90
I-172	4A	X	X	B500	5.76	29.2	4A	26.519	460.407	13.61	443.72	2.64	3.29	16.25
I-221	6B	—	—	B300	5.76	38.7	4A/B	26.748	464.374	10.27	444.27	2.07	2.78	12.34
I-307	2F	—	—	B300	5.76	38.4	4A/B	26.398	458.292	10.22	438.58	2.14	2.83	12.36
I-411	5A	—	—	B300	5.76	36.6	4A/B	26.499	460.055	10.54	440.82	2.05	2.72	12.59
I-430	6E	X	X	B300	5.76	35.7	4A/B	26.514	460.319	10.55	441.08	2.05	2.72	12.60
I-455	5F	—	—	B300	5.76	39.9	4A/B	26.880	466.666	10.15	446.25	2.19	2.88	12.34
I-470	2D	—	—	B300	5.76	39.2	4A/B	26.484	459.790	9.75	439.37	2.19	2.88	11.94
I-561	3F	X	X	B500	5.76	30.2	4A	26.570	461.289	13.66	444.60	2.64	3.29	16.30
I-629	4F	—	—	B500	5.76	30.2	4A	26.469	459.526	12.94	442.25	2.56	3.21	15.50
I-640	4C	—	—	B300	5.76	41.7	4A/B	26.428	458.821	8.67	437.45	1.99	2.70	10.66
I-642	3E	—	—	B300	5.76	37.9	4A/B	26.540	460.760	10.06	440.66	2.07	2.78	12.13
I-659	1E	—	—	B300	5.76	39.1	4A/B	26.723	463.933	10.24	443.83	2.07	2.78	12.31
I-702	6D	—	—	B500	5.76	30.1	4A	26.453	459.261	12.92	441.98	2.56	3.21	15.48
I-726	5D	—	—	B300	5.76	39.9	4A/B	26.428	458.821	9.70	438.40	2.19	2.88	11.89
I-760	6C	—	—	B500	5.76	29.2	4A	26.651	462.699	13.74	446.01	2.64	3.29	16.38
I-788	3A	—	—	B500	5.76	30.2	4A	26.712	463.257	13.18	446.48	2.56	3.21	15.74
I-848	1D	X	X	B500	5.76	30.2	4A	26.489	459.879	13.58	443.19	2.64	3.29	16.22
I-881	2A	—	—	B300	5.76	38.9	4A/B	26.606	461.906	9.88	441.99	2.19	2.88	12.07
I-934	2C	—	—	B300	5.76	38.2	4A/B	26.398	458.292	9.67	437.87	2.19	2.88	11.86
I-978	5C	X	X	B300	5.76	38.2	4A/B	26.479	459.702	9.75	439.28	2.19	2.88	11.94
I-1004	1C	—	—	B500	5.76	30.1	4A	26.580	461.465	13.05	444.19	2.56	3.21	15.61
I-1050	3D	—	—	B300	5.76	38.0	4A/B	26.408	458.468	8.65	437.10	1.99	2.70	10.64

the lower end in the gap between the guide tube and the control rod cladding. Six 4.8-mm-diameter holes were drilled in the lower part of each guide tube to provide additional flow. Details of control rods and guide tubes are given in Table A-4.

The spacing between fuel rods and control rod guide tubes in the bundle assembly was maintained by three Inconel spacer grids. Each grid provided a square-pitch spacing pattern of 12.75 ± 0.25 mm (typical of a 17 x 17 PWR array). The spacer grids were 39.7 mm high, and the thickness was 0.43 mm. Total mass of the three spacer grids was 0.276 kg. The tops of the three grids were, respectively, 0.1129, 0.5109, and 0.9572 m above the bottom of the fuel in the PBF core. The elevations of various bundle features are shown in Figure A-2. Details of the bundle geometry are listed in Table A-5.

A zirconia bundle bypass tube located near the 1A grid position was intended to maintain a separate flow channel through the fuel region if the experiment produced extensive flow blockage. The outer and inner diameters of the tube were 6.35 and 4.75 mm, respectively.

The test bundle was contained in an insulating shroud consisting of zirconia insulation sandwiched between inner and outer zircaloy walls. The zirconia insulation, which had a higher density (1,440 kg/m^3) than that used in Tests SFD-ST and SFD 1-1 (960 kg/m^3), reduced both the radial heat loss through the shroud wall and, consequently, the power required to attain high bundle temperatures.

The test train was installed in the PBF in-pile tube (IPT), a thick-walled Inconel cylinder designed for a wide range of test coolant conditions. Figure A-1 shows a cross-sectional view of the test train in the IPT, and Figure A-3 presents a schematic view of the test train in the IPT. The bypass coolant (flow around the bundle) from the IPT inlet flowed downward to the test train inlet assembly, passed through a flow meter in the inlet region, and was directed up past the insulating flow shroud and the outlet assembly.

Bundle inlet flow was provided by a line entering through the closure head assembly. The flow from this line was divided into four small lines that lead down through the bypass region to the bottom of the test train where they penetrated the interior of the test train inlet assembly. Flow passed upward through the bundle and into the outlet effluent line. The outlet effluent line extended up through the IPT closure head to external piping, which split into two branches. One branch was connected to the sample collection piping, and the other was connected to the loop piping. The latter branch was used for preconditioning flow only and contained a check valve, an isolation valve, and a flow meter. During the transient, a low-flow injection pump provided a bundle flow of 0.6 g/s.

The shroud insulating region was pressurized using argon gas from a line that passed through the IPT closure head and into the bottom of the insulating shroud. Shroud pressure was measured through a similar line connected to the top of the shroud.

The region above the fuel was designated the upper plenum. It incorporated a heat shield and the effluent line. The heat shield reduced heat transfer through the noninsulating shroud area and provided a direct flow path to the effluent tube and the outlet effluent line. Three independent electrical heaters were used between the heat shield and the closure head to keep steam from condensing in the effluent tube during the transient.

A deposition rod, illustrated in Figure A-4, was mounted in the experiment effluent line. The rod was 4.17-m long and was positioned with its lower end 0.27 m above the top of the high burnup fuel rods (1.33 m from the bottom of the PBF core). Forty removable deposition coupons were mounted along the rod, and thermocouples were positioned on the rod to measure the effluent gas and coupon surface temperatures at three axial elevations. Details of the geometry of the upper plenum and the deposition rod are listed in Table A-5.

A-2. Effluent Sampling and Monitoring System

Effluent from the SFD 1-4 bundle was characterized by a remotely controlled sampling and monitoring system. Figure A-5 is a layout diagram showing the position of the major components in the system relative to the reactor. The label "Cubicle 13" in Figure A-5 refers to a shielded room in the reactor building which holds sampling equipment. Figure A-6 is a schematic diagram that illustrates the flow path through the various components. The effluent sampling and monitoring system consisted of a long, 6.35-mm-diameter pipe that directed the effluent flow past a series of on-line instruments and grab samples into a large collection tank.

The effluent line was shielded with lead, heat-traced, and insulated up to the condenser (with the exception of an uninsulated region at the steamline detector viewing position) to maintain effluent

Table A-4. Control rod design characteristics for Test SFD1-4

Parameter	Value
Neutron absorber	
Material	80% silver/15% indium/5% cadmium
OD	7.65 mm
Density	10.16 g/cm^3
Absorber slug length	25.4 mm
Absorber overall length	956.8 mm
Absorber total mass	1.715 kg
Cladding	
Material	Type 304 stainless steel
Tube OD	9.70 mm
Tube ID	8.89 mm
Tube wall thickness	0.405 mm
Control rod upper end plug	
Material	Type 304 stainless steel
OD	9.70 mm
Top end shape	Bullet-nosed
Control rod lower end plug	
Material	Type 304 stainless steel
OD	10.67 mm
Control rod assembly	
Initial gas pressure	0.101 MPa (absolute)
Fill gas	Helium
Spring material	Inconel
Spring load	36 N
Overall length	1.169 m
Guide tube	
Material	Zircaloy-4
OD	12.24 mm
ID	11.43 mm
Flow hole diameter	4.75 mm
Length	1.169 mm

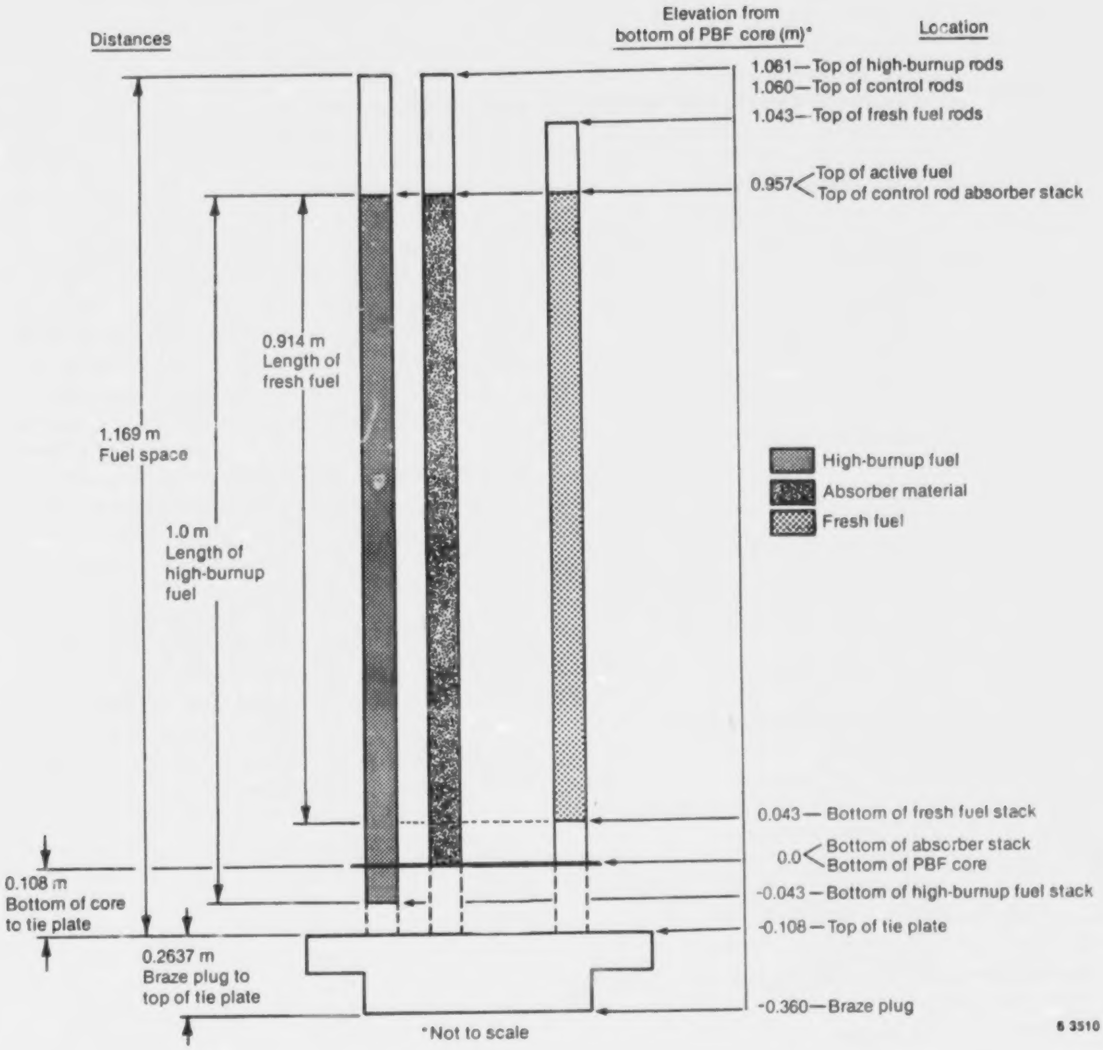
Distances
Elevation from bottom of PBF core (m)*
Location
1.061—Top of high-burnup rods
1.060—Top of control rods
1.043—Top of fresh fuel rods
0.957 Top of active fuel
Top of control rod absorber stack
0.914 m Length of fresh fuel
1.169 m Fuel space
1.0 m Length of high-burnup fuel
High-burnup fuel
Absorber material
Fresh fuel
0.043— Bottom of fresh fuel stack
0.0 Bottom of absorber stack
Bottom of PBF core
-0.043—Bottom of high-burnup fuel stack
-0.108—Top of tie plate
-0.360—Braze plug
0.108 m Bottom of core to tie plate
0.2637 m Braze plug to top of tie plate
*Not to scale
6 3510

Figure A-2. Axial schematic of the SFD 1-4 fuel bundle.

Table A-5. Sample system component dimensions for Test SFD 1-4

Component Number	Component Description	Inside Diameter (m)	Length (m)	Cumulative Length (m)	Volume (m^3)	Cumulative Volume (m^3)	Surface Area (m^2)	Cumulative Surface Area (m^2)
1	Fuel space	8.13 E − 02	1.17	1.06	6.50 E − 03	6.50 E − 03	3.01 E − 01	3.01 E − 01
1A	High-burnup fuel rods (26)	9.50 E − 03	1.13	—	1.96 E − 03	—	8.23 E − 01	1.12 E + 00
1B	Fresh fuel rods (2)	9.50 E − 03	1.00	—	1.48 E − 04	—	6.23 E − 02	1.19 E + 00
1C	Instrumented control rod (1)	1.22 E − 02	1.06	—	1.19 E − 04	—	3.88 E − 02	1.23 E + 00[a]
1D	Noninstrumented control rods (3)	1.22 E − 02	1.06	—	3.74 E − 04	3.90 E − 03[b]	1.22 E − 01	1.35 E + 00[a]
2	Space above fuel	8.13 E − 02	0.05	1.11	3.25 E − 04	4.23 E − 03	6.13 E − 04	1.35 E + 00
3	Heat shield cone	9.09 E − 02	0.03	1.14	8.36 E − 05	4.31 E − 03	7.13 E − 03	1.36 E + 00
4	Heat shield cone to tip of deposition rod	2.22 E − 02	0.19	1.33	7.35 E − 05	4.38 E − 03	1.32 E − 02	1.37 E + 00
5	Tip of deposition rod to closure head	2.22 E − 02	2.32	3.65	7.88 E − 04	5.17 E − 03	2.28 E − 01	1.60 E + 00
6	Deposition rod	4.78 E − 03	4.17	—	2.00 E − 04	4.97 E − 03	1.17 E − 01	1.71 E + 00
7	Closure head to end of standpipe	2.22 E − 02	1.85	5.50	6.84 E − 04	5.66 E − 03	1.39 E − 01	1.85 E + 00
8	Standpipe to 90° bend	2.22 E − 02	0.11	5.61	4.26 E − 05	5.70 E − 03	7.67 E − 03	1.86 E + 00
9	90° bend to top of deck plates	2.22 E − 02	0.75	6.36	2.90 E − 04	5.99 E − 03	5.23 E − 02	1.91 E + 00
10	Top of deck to transition #1	2.22 E − 02	0.76	7.12	2.94 E − 04	6.28 E − 03	5.30 E − 02	1.97 E + 00
11	Transition #1 to main floor gamma spectrometer	8.48 E − 03	3.49	10.61	1.97 E − 04	6.48 E − 03	9.30 E − 02	2.06 E + 00
12	Aerosol spool	Variable (0.01 − 0.04)	0.72	11.33	4.38 E − 04	6.92 E − 03	6.00 E − 02	2.12 E + 00

Table A-5. (continued)

Component Number	Component Description	Inside Diameter (m)	Length (m)	Cumulative Length (m)	Volume (m^3)	Cumulative Volume (m^3)	Surface Area (m^2)	Cumulative Surface Area (m^2)
13	Aerosol spool to filtered effluent samples	8.48 E − 03	1.22	12.55	6.89 E − 05	6.99 E − 03	3.25 E − 02	2.15 E + 00
14	Filtered effluent samples to unfiltered samples	8.48 E − 03	4.05	16.60	2.29 E − 04	7.22 E − 03	1.08 E − 01	2.26 E + 00
15	Unfiltered effluent sample outlet to 90° bend	8.48 E − 03	4.88	21.48	2.75 E − 04	7.49 E − 03	1.30 E − 01	2.39 E + 00
16	90° bend to Cubicle 13 penetration	8.48 E − 03	0.51	21.99	2.92 E − 05	7.52 E − 03	1.38 E − 02	2.40 E + 00
17	Cubicle 13 penetration to transition #2	8.48 E − 03	1.10	23.09	6.20 E − 05	7.58 E − 03	2.92 E − 02	2.43 E + 00
18	Transition #2 to steamline spectrometer	6.20 E − 03	8.15	31.24	4.60 E − 04	8.04 E − 03	1.59 E − 01	2.59 E + 00
19	Steamline spectrometer to condenser	6.20 E − 03	0.41	31.65	1.24 E − 05	8.05 E − 03	7.99 E − 03	2.60 E + 00
20	Condenser	3.86 E − 03	2.44	34.09	2.86 E − 05	8.08 E − 03	3.00 E − 02	2.63 E + 00
21	Condenser to separator	6.22 E − 03	1.83	35.92	5.56 E − 05	8.14 E − 03	3.60 E − 02	2.66 E + 00
Gasline								
22	Separator	9.20 E − 02	0.35	36.27	2.39 E − 03	1.05 E − 02	3.10 E − 01	2.97 E + 00
23	Separator exit to delay coil	6.22 E − 03	1.10	37.37	3.34 E − 05	1.06 E − 02	2.98 E − 02	3.00 E + 00
24	Delay coil	1.02 E − 02	18.30	55.67	1.50 E − 03	1.21 E − 02	5.87 E − 01	3.59 E + 00
25	Delay coil to gasline spectrometer	6.22 E − 03	4.43	60.10	1.35 E − 04	1.22 E − 02	1.07 E − 01	3.70 E + 00

Table A-5. (continued)

Component Number	Component Description	Inside Diameter (m)	Length (m)	Cumulative Length (m)	Volume (m³)	Cumulative Volume (m³)	Surface Area (m²)	Cumulative Surface Area (m²)
Gasline (continued)								
26	Gasline spectrometer to hydrogen monitor	6.22 E − 03	4.96	65.06	1.51 E − 04	1.23 E − 02	1.29 E − 01	3.83 E + 00
27	Hydrogen monitor to collection tank	6.22 E − 03	9.35	74.41	2.84 E − 04	1.26 E − 02	2.98 E − 01	4.13 E + 00
Liquidline								
22	Separator	9.20 E − 02	0.35	36.27	2.39 E − 03	1.11 E − 02	3.10 E − 01	3.02 E + 00
28	Line to delay coil	6.22 E − 03	0.34	36.61	1.02 E − 05	1.11 E − 02	6.56 E − 03	3.03 E + 00
24	Delay coil	1.02 E − 03	18.30	54.91	1.50 E − 03	1.26 E − 02	5.87 E − 01	3.61 E + 00
29	Line to liquidline spectrometer	6.22 E − 03	3.05	57.96	9.26 E − 05	1.27 E − 02	5.60 E − 02	3.67 E + 00
30	Line to filters	6.22 E − 03	3.35	61.31	1.02 E − 04	1.28 E − 02	6.56 E − 02	3.74 E + 00
31	Filters (3)	1.27 E − 01	0.64	61.95	1.22 E − 02	2.50 E − 02	1.24 E + 00	4.98 E + 00
32	Line to liquid samples	6.22 E − 03	1.83	63.78	5.56 E − 05	2.51 E − 02	1.14 E − 01	5.09 E + 00
33	Line to collection tank	6.22 E − 03	18.3	82.08	5.56 E − 04	2.56 E − 02	3.57 E − 01	5.45 E + 00

---

a. Includes the surface area of the zircaloy guide tubes.

b. Void volume = 1 − 1A − 1B − 1C − 1D.

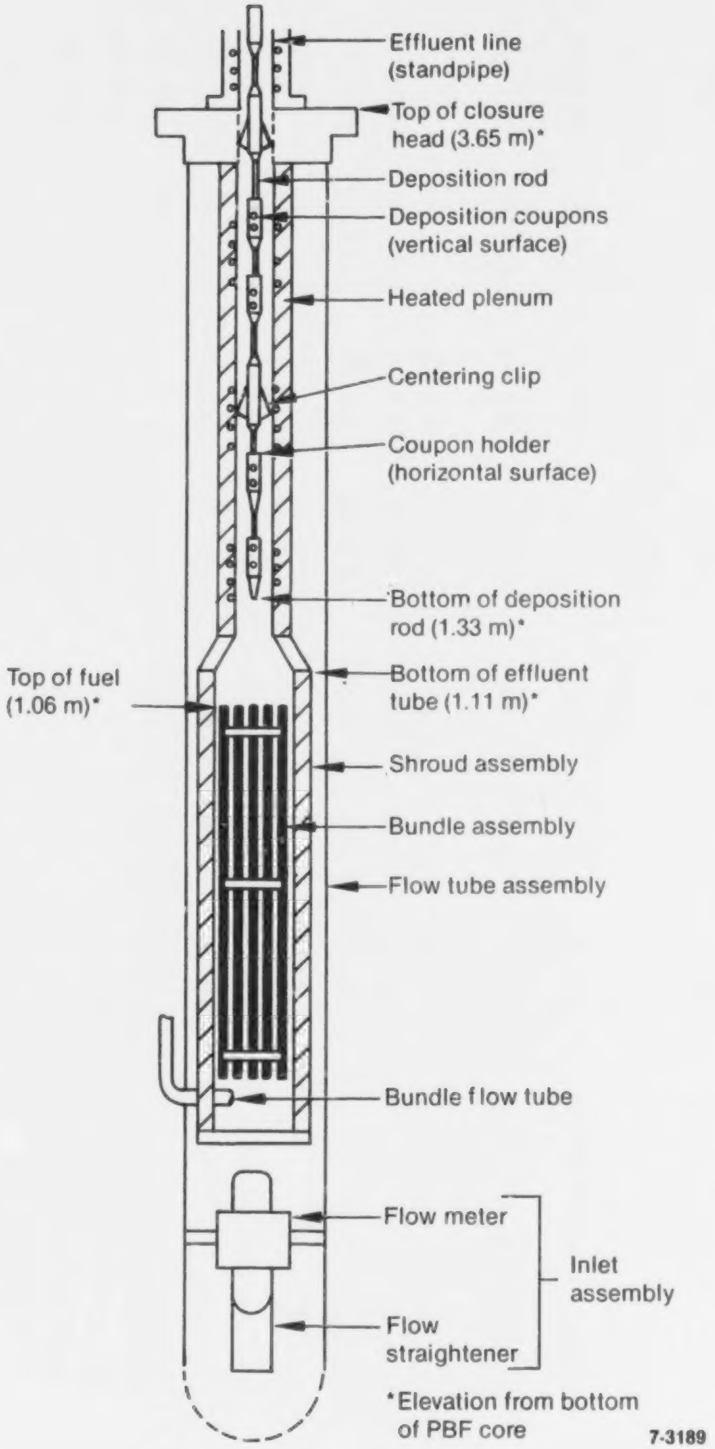
Effluent line (standpipe)
Top of closure head (3.65 m)*
Deposition rod
Deposition coupons (vertical surface)
Heated plenum
Centering clip
Coupon holder (horizontal surface)
Bottom of deposition rod (1.33 m)*
Top of fuel (1.06 m)*
Bottom of effluent tube (1.11 m)*
Shroud assembly
Bundle assembly
Flow tube assembly
Bundle flow tube
Flow meter
Inlet assembly
Flow straightener
*Elevation from bottom of PBF core
7-3189

Figure A-3. Axial diagram of the SFD 1-4 test train and effluent line with deposition rod.

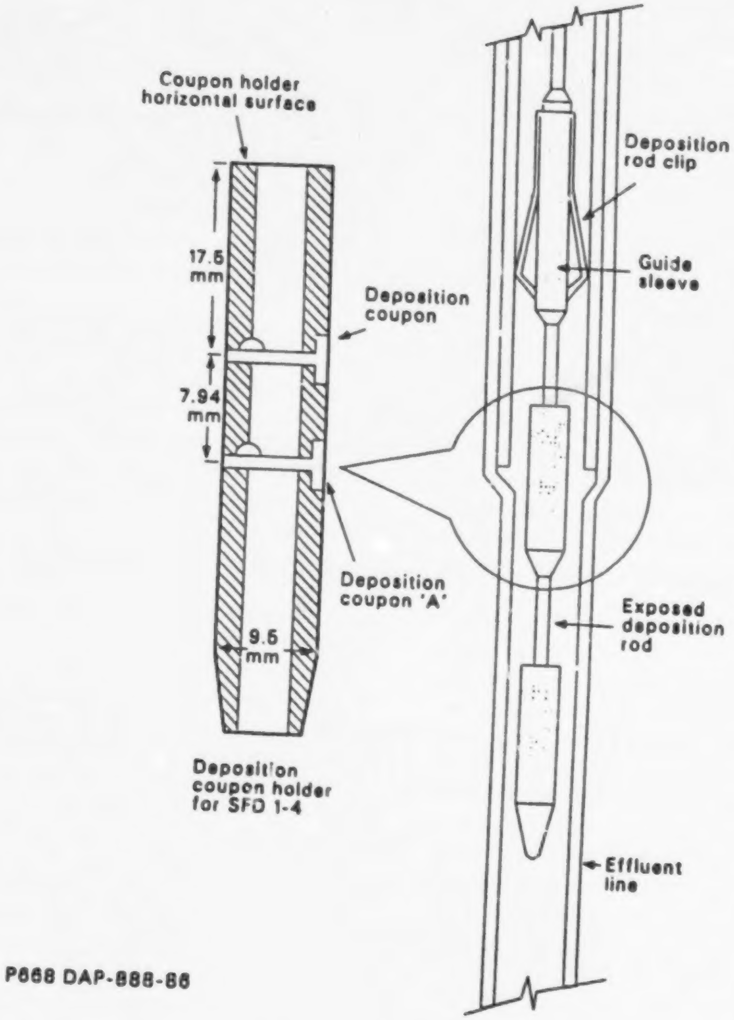
Coupon holder horizontal surface
17.5 mm
7.94 mm
Deposition coupon
Deposition coupon 'A'
9.5 mm
Deposition coupon holder for SFD 1-4
Deposition rod clip
Guide sleeve
Exposed deposition rod
Effluent line
P668 DAP-888-86

Figure A-4. Schematic of fission product deposition rod.

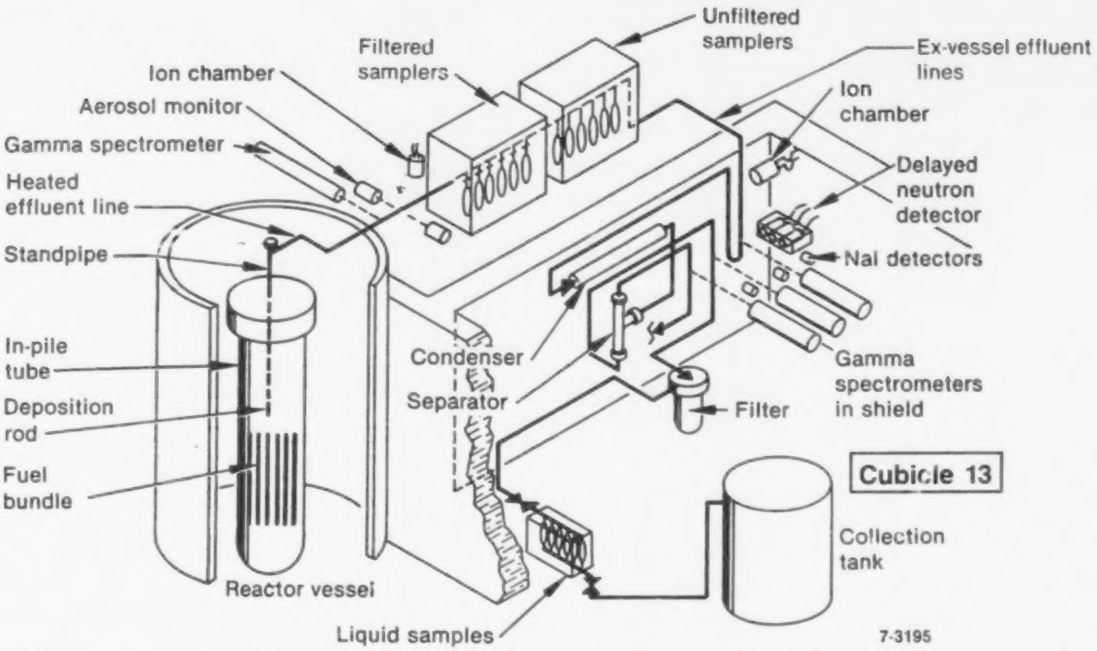
Unfiltered samplers
Filtered samplers
Ex-vessel effluent lines
Ion chamber
Aerosol monitor
Ion chamber
Gamma spectrometer
Delayed neutron detector
Heated effluent line
NaI detectors
Standpipe
In-pile tube
Condenser
Gamma spectrometers in shield
Deposition rod
Separator
Filter
Fuel bundle
Cubicle 13
Collection tank
Reactor vessel
Liquid samples
7-3195

Figure A-5. Layout diagram of the SFD 1-4 fission product sampling and monitoring system.

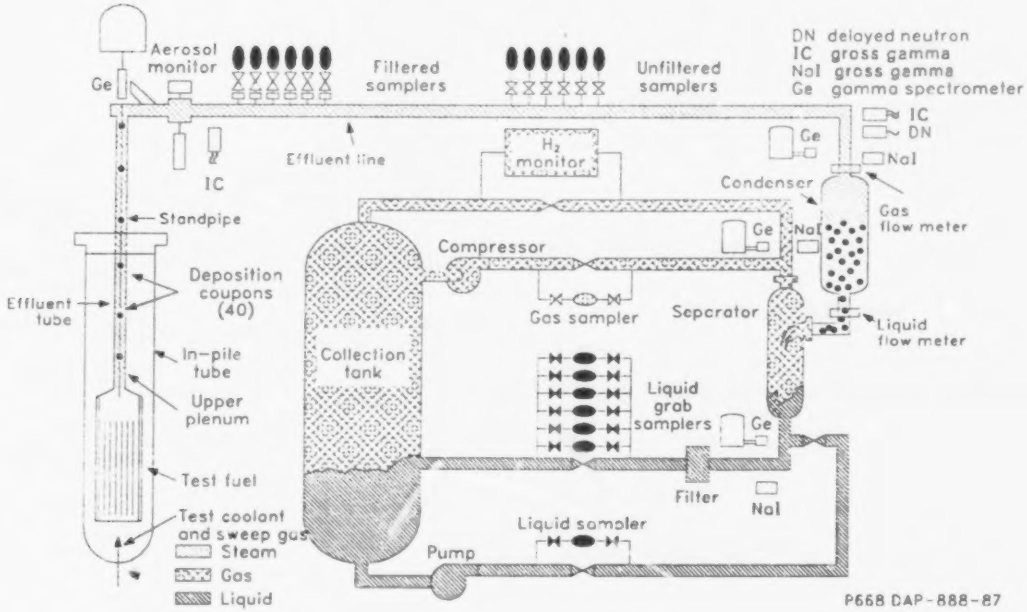
DN delayed neutron
IC gross gamma
NaI gross gamma
Ge gamma spectrometer
Aerosol monitor
Filtered samplers
Unfiltered samplers
Ge
IC
DN
NaI
Effluent line
H₂ monitor
Ge
IC
Condenser
Gas flow meter
Standpipe
Ge
NaI
Compressor
Deposition coupons (40)
Effluent tube
Gas sampler
Separator
Liquid flow meter
In-pile tube
Collection tank
Upper plenum
Liquid grab samplers
Ge
Test fuel
Filter
NaI
Test coolant and sweep gas
Liquid sampler
Steam
Gas
Liquid
Pump
P668 DAP-888-87

Figure A-6. Schematic of the SFD 1-4 sampling and monitoring system.

temperatures above saturation. Thermocouples were positioned at various locations along the line to measure effluent line temperatures.

Upon exiting the upper plenum region, the effluent flow passed the first of four gamma spectrometers, termed the mainfloor, steamline, gasline and liquidline spectrometers for their respective positions in the system. Each spectrometer used a shielded intrinsic germanium detector and a variable aperture collimator between the sample line and the detector to allow for remote adjustment of the gamma flux incident on the detector crystal during the experiment. The electronics package used to operate each spectrometer was specially designed and built at the INEL to perform in the severe accident environments produced during the SFD tests.[A-1]

A specially designed aerosol monitor was fabricated and installed in the effluent line immediately downstream of the mainfloor spectrometer for monitoring aerosol concentrations during Test SFD 1-4. Aerosol concentrations were measured by projecting a light beam across the effluent stream and recording the beam attenuation as aerosol passed through the light path. Fiber optics were used to transmit and receive the light beam. A special aerosol monitor spool piece (shown in Figure A-7) was designed and tested under high-temperature and high-pressure conditions for this application. The spool piece provided for two differing light beam path lengths (1 and 4 cm), to monitor different ranges of particle concentrations, and incorporated four fiber-optic probe assemblies with spinel windows to provide the pressure boundary. A diagram of the fiber-optic probe assembly is shown in Figure A-8. Details of the aerosol monitor design are discussed in Reference A-2. Nitrogen gas was purged through pinholes between the windows and the effluent stream to prevent steam and aerosols from attacking the spinel windows.

Downstream of the aerosol monitor, the effluent line was routed to the first of two ion chambers and a series of six filtered and six unfiltered effluent samplers. These effluent samplers were designed to operate remotely at different times during the test and to obtain data on fission product and aerosol behavior in the effluent line throughout the experiment.

The sample line was then routed past the second ion chamber, a delayed neutron monitor (moderated BF_3 tube-type), a NaI gross gamma detector, and the steamline spectrometer before entering the condenser. Two flow meters were used to measure flow into and out of the condenser. A paddle wheel flow meter was mounted in the effluent line just upstream of the condenser to measure the flow rate during the transient and the liquid flow rate during the posttransient operations. A heated-wall-type flow meter was mounted in the sample line immediately after the condenser to measure the liquid flow rate during pretest fuel bundle leakage measurements.

Upon leaving the condenser, the flow entered the separator where the entrained gas was separated from the liquid. To reduce the transit time and to ensure transport of fission products in the liquid line downstream of the separator, a dilution water flow of 30 g/s was added at the separator inlet. The liquid that drained from the separation vessel was measured using an orifice differential pressure-type flow meter. The condensed liquid then flowed past the liquidline spectrometer, a NaI gross gamma detector, and through a particulate filter. A pressure transducer was located across the particulate filter bypass to indicate if the filter was being bypassed. Downstream of the on-line fission product monitors there was a manifold with six flow-through liquid sample containers to take samples of condensed coolant. The coolant finally passed through a level control valve into the collection tank.

Nitrogen gas was bled into the separator at a constant flow rate (1.13 g/s) to ensure fission product and hydrogen transport out of the separator gas space, to provide control of the back pressure in the system, and to dilute the hydrogen concentration below 70%. The gaseous effluent, consisting of both the gases separated from the bundle effluent and the nitrogen carrier gas, was routed through a pressure control valve. The pressure control system regulated the gas flow through the pressure control valve to maintain a fixed differential pressure between the bypass and the separator. The effluent gas then traveled past a NaI gross gamma detector and the gasline gamma spectrometer. A continuous fraction of the gas (3.3 cm^3/s) was diverted through a parallel-path pipe to a Beckman Model 7C thermal conductivity gas analyzer. This analyzer determined the concentration of hydrogen in the effluent by measuring the conductivity of the gas passing through the detector cell and comparing it to a reference gas of known conductivity. All of the gaseous effluent then entered the collection tank. The pressure of the tank was monitored with a pressure transducer.

An argon sweep gas system introduced gas at the bottom of the bundle during the transient to stabilize the bundle pressure, to transport fission

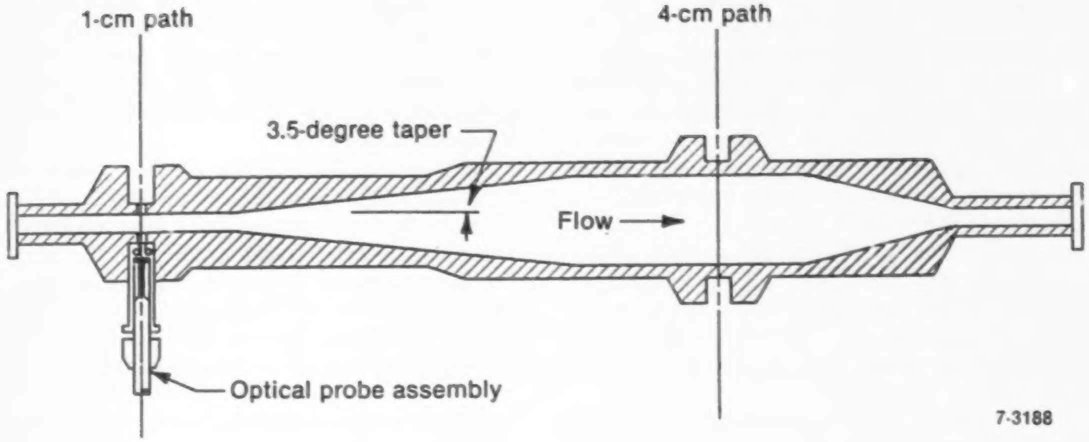
1-cm path
4-cm path
3.5-degree taper
Flow
Optical probe assembly
7-3188

Figure A-7. Schematic of the SFD 1-4 aerosol monitor spool piece.

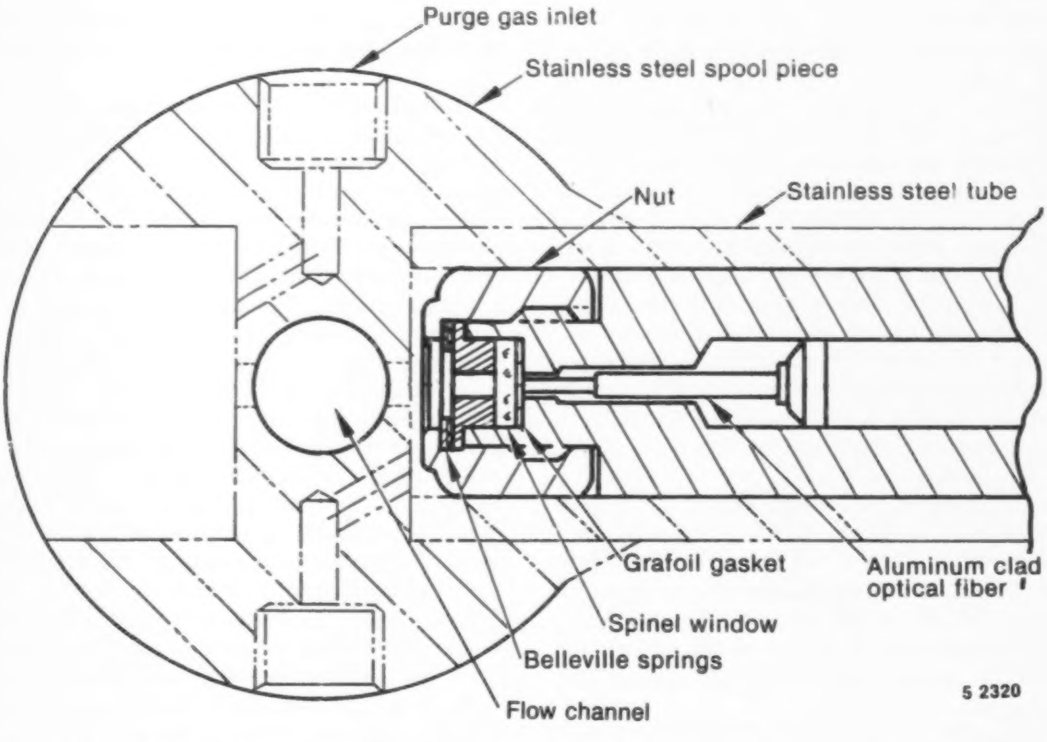
Purge gas inlet
Stainless steel spool piece
Nut
Stainless steel tube
Grafoil gasket
Aluminum clad optical fiber
Spinel window
Belleville springs
Flow channel
5 2320

Figure A-8. Diagram of the SFD 1-4 aerosol monitor fiber-optic probe.

products through the sample system, and to cool the bundle following the transient while keeping the fission product deposition rod dry. Nitrogen gas was used after the test to pressurize the bundle and keep the deposition rod dry until the IPT was pumped dry. Remote sampling and monitoring of the collection tank gas and liquid contents were facilitated after the test by recirculation systems that pumped the tank contents through in-line sample containers and past the gamma spectrometers. Quantitative details of the sample system geometry are given in Table A-5 and in Figure A-9.

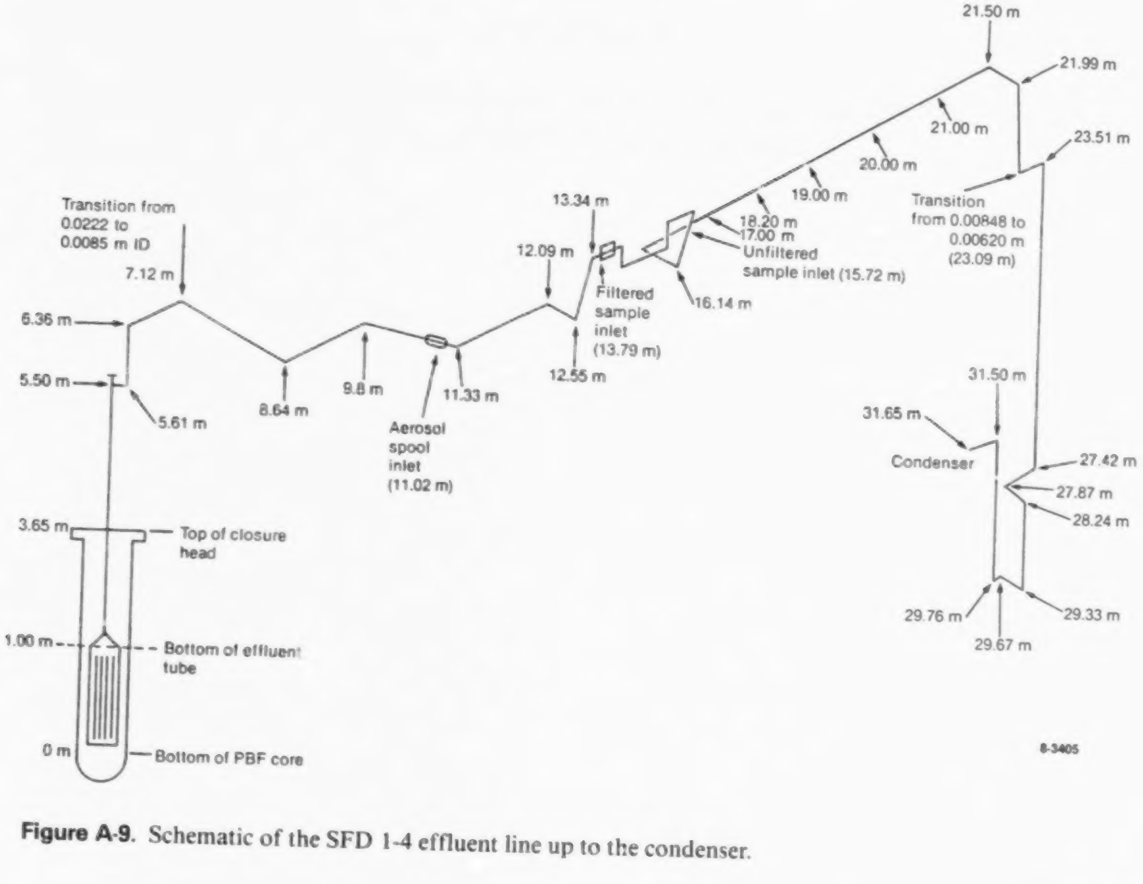

21.50 m
21.99 m
21.00 m
23.51 m
20.00 m
19.00 m
Transition from 0.00848 to 0.00620 m (23.09 m)
13.34 m
18.20 m
17.00 m
Unfiltered sample inlet (15.72 m)
Transition from 0.0222 to 0.0085 m ID
12.09 m
7.12 m
Filtered sample inlet (13.79 m)
16.14 m
6.36 m
12.55 m
31.50 m
5.50 m
9.8 m
11.33 m
31.65 m
8.64 m
5.61 m
Aerosol spool inlet (11.02 m)
Condenser
27.42 m
27.87 m
28.24 m
3.65 m
Top of closure head
29.76 m
29.33 m
29.67 m
1.00 m
Bottom of effluent tube
0 m
Bottom of PBF core
8-3405

Figure A-9. Schematic of the SFD 1-4 effluent line up to the condenser.

A-3. References

A-1. J. K. Hartwell and E. W. Killian, "On-Line Gamma-Ray Acquisition at the Power Burst Facility," *Nucl. Instr. and Meth. in Physics Research, A242*, 1986, pp. 487-492.

A-2. J. P. Adams, J. K. Partin, D. A. Petti, and T. R. Reed, "Development and Calibration of an Aerosol Monitor used for PBF Test SFD 1-4," *Fourth International Symposium on Multiphase Transport and Particulate Phenomena, Miami Beach, FL, December 14-17, 1986.*

APPENDIX B

INSTRUMENTATION AND SAMPLER DESCRIPTION, LOCATION, AND PERFORMANCE

APPENDIX B

INSTRUMENTATION AND SAMPLER DESCRIPTION, LOCATION, AND PERFORMANCE

Brief descriptions of all the Test SFD 1-4 instrumentation and effluent samplers, together with tables and diagrams to identify each instrument and its location, are given in Section B-1 of this appendix. The thermal hydraulic instrumentation measured the fuel rod and control rod cladding inside surface temperatures, fuel and control rod centerline temperatures, various coolant temperatures, flows, and pressures. Fission product and aerosol instrumentation measured the isotopic fission product concentrations and aerosol concentration in the effluent sampling system. The hydrogen instrumentation measured the hydrogen concentration in the effluent line. In addition, numerous plant instruments were recorded. A summary of instrument performance is provided in Section B-2.

B-1. Instrumentation and Samplers

Two major systems were used to process instrumentation signals during Test SFD 1-4. The PBF Data Acquisition and Reduction System (DARS) recorded signals from all of the test train instrumentation, the on-line aerosol monitor, the hydrogen (thermal conductivity) monitor, and the gross gamma radiation and neutron detectors in the effluent sampling and monitoring system. The Fission Product Detection System (FPDS) collected spectral data obtained from the four on-line gamma ray spectrometers.

The DARS instrumentation associated with Test SFD 1-4 is listed in Table B-1. The table summarizes the instrument number, type, location, and identifier for each measurement. The DARS parameter number for each measurement is also listed. The DARS parameter number is also used to identify instruments on cross-section schematics shown in Figures B-1 and B-2. Figure B-3 is a view of the test train showing instrument locations by elevation, and Figure B-4 is a schematic of the test train and pressure control system. The FPDS instrumentation that was part of the DARS is also listed in Table B-1.

B-1.1 Fuel Rod Instrumentation. Instrumentation for the measurement of fuel rod parameters on fresh fuel rods 3B and 4D only consisted of the following:

- Three interior cladding surface thermocouples, with W/Re thermal elements, BeO insulation, and zircaloy sheaths lined with tantalum, were installed in each fuel rod. The thermocouple leads entered the bottom of the fuel rods, and junctions were located at 0.39, 0.54, and 0.74 m. (All elevations are referenced with respect to the bottom of the PBF core.)

- One centerline thermocouple was installed in each fuel rod, with the measurement junctions at 0.39 m. The thermocouples consisted of W/Re elements in BeO insulation sheathed in Mo50/Re50.

- One pressure switch was mounted on the bottom of each of the two rods to signal fuel rod rupture.

B-1.2 Control Rod Instrumentation. Instrumentation for the measurement of control rod parameters on rod 5E consisted of the following:

- Three interior cladding surface thermocouples, with W/Re thermal elements, alumina insulation, and stainless steel sheaths, entered the bottom of the control rod. The measurement junctions were located at 0.39, 0.54, and 0.74 m.

- A centerline thermocouple was mounted from the bottom of the control rod with its measurement junction at 0.39 m. This device used a W/Re thermal element, BeO insulation, and a tantalum sheath.

- A pressure transducer was connected to the bottom of the control rod through a tube. The pressure transducer, located below the lower braze plug, was a Kaman

Table B-1. Test SFD 1-4 instrument identification and data channel recording

Measurement	Instrument	Location[a]	Rod Number	Identifier	Recording Range	DARS Parameter Number
Fuel rod cladding temperature	Thermocouple Type C	Interior cladding wall	—	—	290 to 2915 K	
		0.39 m, 135 degrees	3B	CLADTEMPbb135b393B	—	67
		0.39 m, 135 degrees	4D	CLADTEMPbb135b394D	—	68
		0.54 m, 000 degrees	3B	CLADTEMPbb000b543B	—	69
		0.54 m, 000 degrees	4D	CLADTEMPbb000b544D	—	70
		0.74 m, 225 degrees	3B	CLADTEMPbb225b743B	—	57
		0.74 m, 225 degrees	4D	CLADTEMPbb225b744D	—	58
Fuel centerline temperature	Thermocouple Type C	0.39 m	3B	FUELTEMPbbCLb393B	290 to 2915 K	41
		0.39 m	4D	FUELTEMPbbCLb394D	—	42
Shroud outer wall temperature	Thermocouple Type K	0.35 m, 000 degrees	—	SHRDTEMPbbOUT00035	290 to 2915 K	241
		0.35 m, 090 degrees	—	SHRDTEMPbbOUT09035	—	242
		0.35 m, 180 degrees	—	SHRDTEMPbbOUT18035	—	243
		0.35 m, 270 degrees	—	SHRDTEMPbbOUT27035	—	245
		0.50 m, 000 degrees	—	SHRDTEMPbbOUT00050	—	246
		0.50 m, 180 degrees	—	SHRDTEMPbbOUT18050	—	77
		0.70 m, 090 degrees	—	SHRDTEMPbbOUT09070	—	78
		0.70 m, 270 degrees	—	SHRDTEMPbbOUT27070	—	85
Bundle steam temperature[b]	Thermocouple Type C	0.54 m, 5A-315 degrees	—	STEAMTMPbb5A315b54	290 to 820 K power calib, 338 to 2915 K, transient	79
		0.99 m, 1B-225 degrees	—	STEAMTMPbb1B225b99		80
		0.99 m, 4D-135 degrees	—	STEAMTMPbb4D135b99		81
		1.14 m, 120 degrees	—	STEAMTMPbbb120b114		65
		1.14 m, 300 degrees	—	STEAMTMPbbb300b114	—	83
		1.14 m, 150 degrees	—	STEAMTMPbbb150b114	—	82
		1.14 m, 330 degrees	—	STEAMTMPbbb330b114	—	66
Effluent tube wall temperature	Thermocouple Type K	90 degrees, 1.84 m outer wall	—	STTUBTMPbbWL090184	190 to 1581 K	156
		270 degrees, 1.84 m outer wall	—	STTUBTMPbbWL270184	—	167
		90 degrees, 2.29 m outer wall	—	STTUBTMPbbWL090229	190 to 1581 K	169

Table B-1. (continued)

Measurement	Instrument	Location[a]	Rod Number	Identifier	Recording Range	DARS Parameter Number
Effluent tube wall temperature (continued)	Thermocouple Type K (continued)	270 degrees, 2.29 m outer wall	—	STTUBTMPbbWL270229	—	170
		90 degrees, 2.83 m outer wall	—	STTUBTMPbbWL090283	—	171
		270 degrees, 2.83 m outer wall	—	STTUBTMPbbWL270283	—	173
		90 degrees, 3.40 m outer wall	—	STTUBTMPbbWL090340	—	174
		270 degrees, 3.40 m outer wall	—	STTUBTMPbbWL270340	—	175
Effluent temperature in steam tube	Steam probe thermocouple Type K	1.54 m, 225 degrees	—	STEAMTMPbb225154	290 to 1581 K	117
		2.35 m, 225 degrees	—	STEAMTMPbb225235	—	118
		3.36 m, 225 degrees	—	STEAMTMPbb225336	—	71
Control rod clad temperature	Thermocouple Type C	Interior cladding wall	5E	—		
		0.39 m, 135 degrees	—	CRCLADTPbb135b395E	290 to 2915 K	61
		0.54 m, 000 degrees	—	CRCLADTPbb000b545E	—	63
		0.74 m, 225 degrees	—	CRCLADTPbb2255745E	—	64
Control rod centerline temperature	Thermocouple Type C	0.39 m	5E	CRCENTERbbTEMP395E	290 to 2915 K	15
Control rod pressure	Pressure transducer	Lower plenum	5E	CRbPRESSbb5E	0 to 9 MPa	18
Shroud inner liner wall temperature	Thermocouple Type C	0.35 m, 090 degrees	—	SHRDTEMPbbIN09035	290 to 2915 K	73
		0.35 m, 270 degrees	—	SHRDTEMPbbIN27035	—	75
		0.50 m, 090 degrees	—	SHRDTEMPbbIN090b50	—	76
		0.50 m, 270 degrees	—	SHRDTEMPbbIN270b50	—	87
		0.70 m, 270 degrees	—	SHRDTEMPbbIN270b70	—	88
Pressure switch position	Pressure switch	Lower plenum at −0.227 m	3B	RODPRESSbbSWTCHb3B	As required	89
			4D	RODPRESSbbSWTCHb4D	—	90

Table B-1. (continued)

Measurement	Instrument	Location[a]	Rod Number	Identifier	Recording Range	DARS Parameter Number
Shroud midwall temperature (middle of insulation)	Thermocouple Type C	0.50 m, 000 degrees	—	SHRDTEMPbbMID00050	290 to 2915 K	91
		0.50 m, 090 degrees	—	SHRDTEMPbbMID09050	—	92
		0.50 m, 180 degrees	—	SHRDTEMPbbMID18050	—	93
		0.50 m, 270 degrees	—	SHRDTEMPbbMID27050	—	94
		0.70 m, 090 degrees	—	SHRDTEMPbbMID09070	—	95
		0.70 m, 180 degrees	—	SHRDTEMPbbMID18070	—	96
		0.70 m, 270 degrees	—	SHRDTEMPbbMID27070	—	107
		0.91 m, 000 degrees	—	SHRDTEMPbbMID00091	—	108
		0.91 m, 180 degrees	—	SHRDTEMPbbMID18091	—	109
Bundle coolant flow	Flow meter (low)	Plant FT1014PT	—	FLOWRATEbbBNDLOWIN	0 to 0.32 L/s 0 to 3 gpm	221 220
Bundle coolant flow	Flow meter (high)	Plant FT1013PT	—	FLOWRATEbbBNDHIbIN	0 to 2.5 L/s	219
Bundle pressure	Pressure transducer	Lower test train, −0.36 m	—	SYSbPRESbb69EGbLTT SYSbPRESbb17EGbLTT	0 to 69 MPa 0 to 17 MPa	37 38
Bundle coolant pressure	Pressure transducer	Outside reactor (PISF-5)	—	SYSbPRESbbBUNDLETT	0 to 10.3 MPa	39
Bypass-bundle differential pressure	Differential pressure transducer	0.5 m bypass to 1.43 m bundle (DPT 13-2)	—	DIFFPRESbbBYBUNDLE	±0.69 MPa	14
Bundle coolant pressure drop	Differential pressure transducer	−0.36 to 1.43 m	—	DIFFPRESbbBUNDLE	±0.21 MPa −0.02 to ±0.02 MPa	40 23 17
Molten metal detection cavity	Pressure transducer	Outside reactor	—	MELTTHRUbbPRESSURE	0 to 10.3 MPa	11
Bypass-separator differential pressure	Differential pressure transducer	0.5 m bypass to separator (DPT 13-4)	—	DIFFPRESbbBYPbbSEP	±0.69	13
Neutron flux	SPND	0.31 m at 0 degrees	—	SPNDbb31bbNEUTb000	Log scale	123
		0.31 m at 180 degrees	—	SPNDbb31bbNEUTb180	—	110
FPDS coupon holder temperature	Thermocouple Type K	1.57 m at 45 degrees	—	COUPTEMPbbFPDSb157	290 to 1581 K	195
		2.38 m at 45 degrees	—	COUPTEMPbbFPDSb238	—	196
		3.40 m at 45 degrees	—	COUPTEMPbbFPDSb340	—	207

Table B-1. (continued)

Measurement	Instrument	Location[a]	Rod Number	Identifier	Recording Range	DARS Parameter Number
Bundle inlet coolant temperature[b]	Thermocouple Type C	−0.36 m, 15 degrees	—	INLTTEMPbb015bb-36	290 to 820 K	43
		−0.36 m, 105 degrees	—	INLTTEMPbb105bb-36	(power calib)	225
		−0.36 m, 232 degrees	—	INLTTEMPbb232bb-36	290 to 2915 K	226
		−0.36 m, 322 degrees	—	INLTTEMPbb322bb-36	(transient)	237
	Thermocouple Type K	−0.36 m, 135 degrees	—	INLTTEMPbb135bb-36	290 to 1581 K	59
Bundle temperature rise[b]	Thermocouple Type C	Lower legs at −0.36 and 15 degrees, 105 degrees, 232 degrees, 332 degrees, Upper legs at 1.14 m and 30 degrees, 210 degrees, 300 degrees, 330 degrees	—	DELbTEMPbbBNDLE030	0 to 50 K	47
			—	DELbTEMbbbBNDLE210	—	48
			—	DELbTEMPbbBNDLE300	—	49
			—	DELbTEMPbbBNDLE330	—	60
Bypass inlet temperature	Thermocouple Type K	−0.31 m, 0 degrees	—	BYPbTEMPbb000bb-31	190 to 820 K	209
		−0.31 m, 090 degrees	—	BYPbTEMPbb090bb-31	—	210
		−0.31 m, 180 degrees	—	BYPbTEMPbb180bb-31	—	211
		−0.31 m, 270 degrees	—	BYPbTEMPbb270bb-31	—	228
Bypass outlet temperature	Thermocouple Type K	+1.14 m, 000 degrees	—	BYPbTEMPbb000bb114	290 to 820 K	229
		+1.14 m, 090 degrees	—	BYPbTEMPbb090bb114	—	231
		+1.14 m, 180 degrees	—	BYPbTEMPbb180bb114	—	232
		+1.14 m, 270 degrees	—	BYPbTEMPbb270bb114	—	233
Bypass coolant temperature rise	Thermocouples Type K	Lower legs at −0.31 m Upper legs +1.14 m				
		0 degrees	—	DELbTEMPbbBYPbb000	0 to 24 K	50
		90 degrees	—	DELbTEMPbbBYPbb090	—	52
		180 degrees	—	DELbTEMPbbBYPbb180	—	44
		270 degrees	—	DELbTEMPbbBYPbb270	—	45
Bypass coolant volumetric flow rate	Flow meter	Lower test train −0.483 m	—	FLOWRATEbbBYPASSbb	0.25 to 2.52 L/s	129
Bundle coolant volumetric flow rate	Flow meter	Out of reactor FE10-16	—	FLOWRATEbbBNDHIOUT	0.20 to 2.0 L/s	187

Table B-1. (continued)

Measurement	Instrument	Location[a]	Rod Number	Identifier	Recording Range	DARS Parameter Number
Neutron flux, dc signal	Fission chambers	0.827 m, 090 degrees	—	FISSCHAMbb090bDC83	0 to 1 MA	1
		0.507 m, 090 degrees	—	FISSCHAMbb090bDC51	—	2
		0.247 m, 090 degrees	—	FISSCHAMbb090bDC25	—	3
		0.047 m, 090 degrees	—	FISSCHAMbb090bDC05	—	5
		0.667 m, 270 degrees	—	FISSCHAMbb270bDC67	—	6
		0.347 m, 270 degrees	—	FISSCHAMbb270bDC35	—	7
		0.147 m, 270 degrees	—	FISSCHAMbb270bDC15	—	9
		−0.053 m, 270 degrees	—	FISSCHAMbb270bD-05	—	10
Neutron flux, ac signal	Fission chamber	0.827 m, 090 degrees	—	FISSCHAMbb090bAC83	−5 V to +5 V	29
		0.507 m, 090 degrees	—	FISSCHAMbb090bAC51	—	19
		0.247 m, 090 degrees	—	FISSCHAMbb090bAC25	—	31
		0.047 m, 090 degrees	—	FISSCHAMbb090bAC05	—	32
		0.667 m, 270 degrees	—	FISSCHAMbb270bAC67	—	33
		0.347 m, 270 degrees	—	FISSCHAMbb270bAC35	—	34
		0.147 m, 270 degrees	—	FISSCHAMbb270bAC15	—	35
		−0.053 m, 270 degrees	—	FISSCHAMbb270bA-05	—	36
Reactor power NMS-3	Ion chamber	Plant	—	REACbPOWbbNMS-03PT	0 to 30 MW	21
Reactor power NMS-4	Ion chamber	Plant	—	REACbPOWbbNMS-04PT	0 to 30 MW	22
Reactor power PPS-1	Ion chamber	Plant	—	REACbPOWbbPPS-01PT	0 to 30 MW	53
Reactor power PPS-2	Ion chamber	Plant	—	REACbPOWbbPPS-02PT	0 to 30 MW	255
System pressure	PXD	Plant	—	SYSbPRESbbHEISEbPT	0 to 17.3 MPa	72
Loop flow	Orifice	Plant	—	LOOPbFLOWbbFRE-10PT	0 to 63.1 L/s	74
Gross gamma rate steam line	NaI detector	FPDS	—	FPbGAMMAbbSTEAMbb	10 to 10^6 counts/s	213
Gross gamma rate liquid line	NaI detector	FPDS	—	FPbGAMMAbbLIQUIDbb	10 to 10^6 counts/s	214
Gross gamma rate gas line	NaI detector	FPDS	—	FPbGAMMAbbGASbbbbb	10 to 10^6 counts/s	215
Gross gamma rate steam line	Ion chamber detector	FPDS	—	FPGAMIONbbSTEAMLIN	10 mR/h to 10,000 R/h	141
Gross gamma rate steam sample	Ion chamber detector	FPDS	—	FPGAMIONbbSTEAMSPL	10 mR/h to 10,000 R/h	142

Table B-1. (continued)

Measurement	Instrument	Location[a]	Rod Number	Identifier	Recording Range	DARS Parameter Number
Delayed neutron rate	Neutron detector	FPDS	—	FPbNEUTbbbDETECTOR	10 to 10^6 counts/s	227
Hydrogen concentration	H_2 detector(XT 1354)	FPDS	—	FPbHYDRbbbCONCENTb	0 to 100%	143
inlet line temperature	thermocouple TE13-8 Type K	FPDS	—	FPbTEMPbbbINLETbbb	290 to 1090 K	133
Condenser outlet fluid temperature	Thermocouple TE13-29 Type K	FPDS	—	FPbTEMPbbbCONDENSR	290 to 480 K	134
Separation vessel pressure	PXD	FPDS	—	FPbPRESSbbPT13-42	0 to 10.3 MPa	135
Filter bypass flow	Switch	FPDS	—	FPSWITCHbbDP13-66	go/no go	147
Separation vessel liquid flow	Flow meter	FPDS	—	FPbFLOWbbbFT13-69	3.8 to 35 g/s	148
Collection vessel liquid flow	Diff PXD	FPDS	—	BLOWbLEVbbLTT17bPT	0 to 100%	149
Collection vessel pressure	PXD	FPDS	—	BLOWPRESbbPT12bbPT	0 to 2.76 MPa	151
Aerosol monitor	820 nm—Unit A	FPDS	—	FPbb820AbbAEROSIG	0 to 100%	127
	820 nm—Unit A	FPDS	—	FPbb820AbbAEROREF	—	253
	820 nm—Unit B	FPDS	—	FPbb820BbbAEROSIG	—	130
	820 nm—Unit B	FPDS	—	FPbb820RbbAEROREF	—	238
Gas sampler actuation	Limit switch	FPDS	—	FPbGASbbbSAMPLE01	Start/stop	—
			—	FPbGASbbbSAMPLE02	—	—
			—	FPbGASbbbSAMPLE03	—	—
			—	FPbGASbbbSAMPLE04	—	—
			—	FPbGASbbbSAMPLE05	—	—
			—	FPbGASbbbSAMPLE06	—	—
Filtered gas sampler actuation	Limit switch	FPDS	—	FPFILTERbbGASbNo.1	Start/stop	—
			—	FPFILTERbbGASbNo.2	—	—
			—	FPFILTERbbGASbNo.3	—	—
			—	FPFILTERbbGASbNo.4	—	—
			—	FPFILTERbbGASbNo.5	—	—
			—	FPFILTERbbGASbNo.6	—	—

Table B-1. (continued)

Measurement	Instrument	Location[a]	Rod Number	Identifier	Recording Range	DARS Parameter Number
Liquid sample actuation	Limit switch	FPDS	—	FBbLIQDbbbSAMPLE01	Start/stop	—
			—	FBbLIQDbbbSAMPLE02	—	—
			—	FBbLIQDbbbSAMPLE03	—	—
			—	FBbLIQDbbbSAMPLE04	—	—
			—	FBbLIQDbbbSAMPLE05	—	—
			—	FBbLIQDbbbSAMPLE06		—
Sample line flow into condenser	Paddle wheel flow meter (FE-SF-19)	FPDS	—	FBPSFLOWbbCONDbbIN	1-71 cm^3/s (referred to hydrogen)	152
Sample line flow out of condenser	Heated wall flow meter (FE-SF-20)	FPDS	—	FPDSFLOWbbCONDbOUT	0-3.0 cm^3/s	153
Inert sweep gas flow rate	Paddle wheel flow meter (FE-SF-18)	FPDS	—	FPDSFLOWbbSWEEPGAS	0-30 mL/s	86
Shroud meltthrough	Melt detector	Outer shroud wall	—	SHRDMELTbbTHRUWW01	0 to 5 V	97
			—	SHRDMELTbbTHRUWS01		98
			—	SHRDMELTbbTHRUWW02		97
			—	SHRDMELTbbTHRUWS02		100
			—	SHRDMELTbbTHRUWW03		105
			—	SHRDMELTbbTHRUWS03		114
			—	SHRDMELTbbTHRUWW04		115
			—	SHRDMELTbbTHRUWS04		116
Instrumented spool piece flow	Flow meter	Spool piece	—	ICSVFLOWbbFE055PIC	0 to 5 L/s	122
Instrumented spool piece temperature	RTD	Spool piece	—	ICSSTEMPbbTE20SPIC	290 to 600 K	112
Instrumented spool piece pressure	Pressure	Spool piece	—	ICPRESSWbbPE09SPIC	0 to 10 MPa	113
Reactor heat exchanger differential temperature	Differential thermocouple	Plant	—	PFHXRDTbbbHXFTPT	0 to 25°F	125

Table B-1. (continued)

Measurement	Instrument	Location[a]	Rod Number	Identifier	Recording Range	DARS Parameter Number
Reactor coolant flow rate	Flow meter	Plant (FR 1-1)	—	REARFLOWbbPRIMEFLOW	0 to 18 Kgpm	126
Steam tube heater temperature	Thermocouple Type K	Upper test train				
		1.71 m, 000 degrees	—	HEATTEMPbb171ST000	290 to 1360 K	235
		1.71 m, 180 degrees	—	HEATTEMPbb171ST180	—	236
		2.04 m, 000 degrees	—	HEATTEMPbb204ST000	—	247
		2.04 m, 180 degrees	—	HEATTEMPbb204ST180	—	249
		2.57 m, 000 degrees	—	HEATTEMPbb257ST000	—	250
		2.57 m, 180 degrees	—	HEATTEMPbb257ST180	—	251
		3.64 m, 000 degrees	—	HEATTEMPbb364ST000	—	128
Bundle water level elevation	Fission chamber data	—	—	BUNDLEbbbWTRbLVL	– 20 to 100 cm	119
Shroud insulator pressure	Pressure transducer	Outside IPT	—	SHROUDbbbPRESSbTT	0 to 10.3 MPa	120
Bundle-shroud differential pressure	Differential pressure transducer	Outside IPT	—	DIFFPRESbbBDLESHRD	± 3.5 MPa	121
Bundle-separator differential pressure	Arithmetic difference between (bypass-separator) ΔP and (bypass-bundle) ΔP	Outside IPT	—	DIFFPRESbbBDLEbSEP	± 0.69 MPa	188

---

a. Elevations are with respect to the bottom of the PBF core, and the azimuths are relative to fuel bundle "north."

b. The steam temperature thermocouples at 1.14 m and the inlet coolant thermocouples at 15 and 232 degrees were also used to make bundle differential thermocouples, i.e., they were dual-purpose thermocouples.

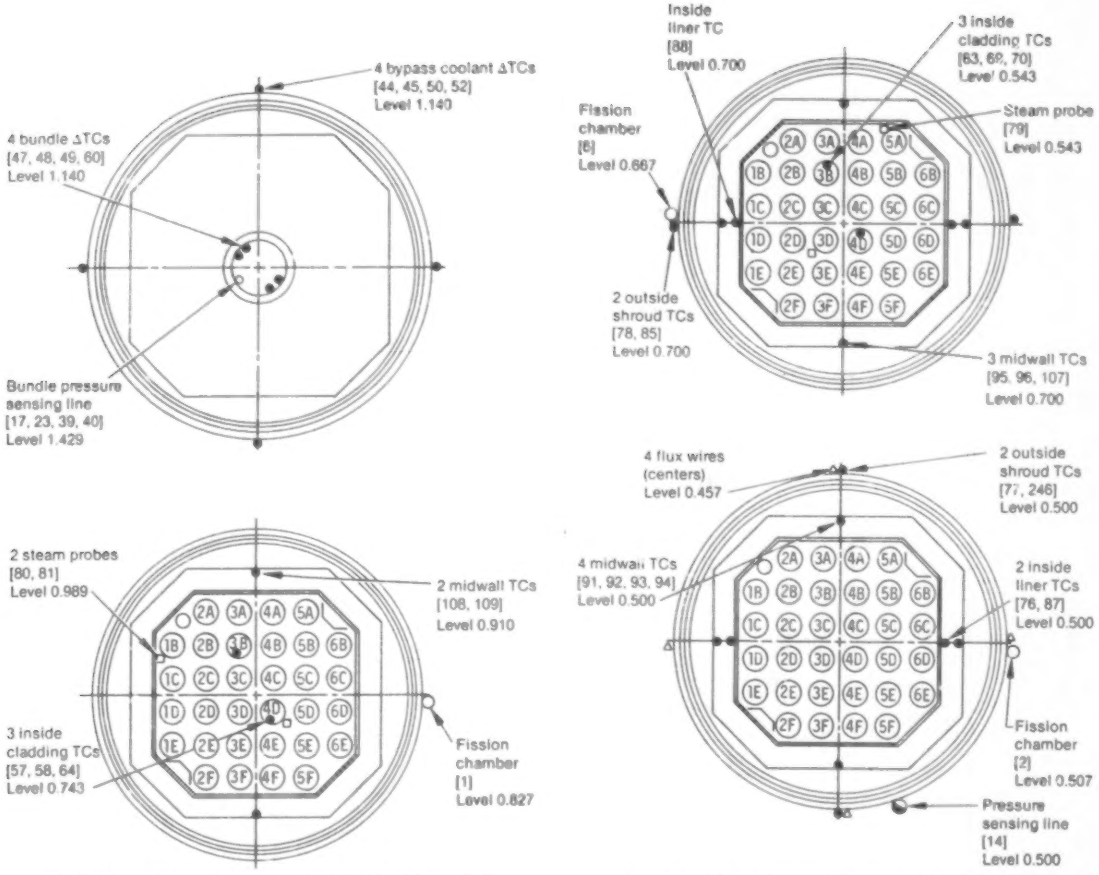
4 bypass coolant ΔTCs
[44, 45, 50, 52]
Level 1.140
4 bundle ΔTCs
[47, 48, 49, 60]
Level 1.140
Bundle pressure
sensing line
[17, 23, 39, 40]
Level 1.429
2 steam probes
[80, 81]
Level 0.989
2 midwall TCs
[108, 109]
Level 0.910
3 inside
cladding TCs
[57, 58, 64]
Level 0.743
Fission
chamber
[1]
Level 0.827
2A 3A 4A 5A
1B 2B 3B 4B 5B 6B
1C 2C 3C 4C 5C 6C
1D 2D 3D 4D 5D 6D
1E 2E 3E 4E 5E 6E
2F 3F 4F 5F
Inside
liner TC
[88]
Level 0.700
3 inside
cladding TCs
[63, 69, 70]
Level 0.543
Fission
chamber
[6]
Level 0.667
Steam probe
[79]
Level 0.543
2 outside
shroud TCs
[78, 85]
Level 0.700
3 midwall TCs
[95, 96, 107]
Level 0.700
4 flux wires
(centers)
Level 0.457
2 outside
shroud TCs
[77, 246]
Level 0.500
4 midwall TCs
[91, 92, 93, 94]
Level 0.500
2 inside
liner TCs
[76, 87]
Level 0.500
Fission
chamber
[2]
Level 0.507
Pressure
sensing line
[14]
Level 0.500

All levels in meters (referenced to bottom of PBF core fuel rods)

8-3339

All levels in meters (referenced to bottom of PBF core fuel rods)

8-3338

Figure B-1. Cross sections of the Test SFD 1-4 shroud and test bundle, indicating instrumentation between the 1.429- and 0.457-m elevations, with DARS parameter numbers in square brackets.

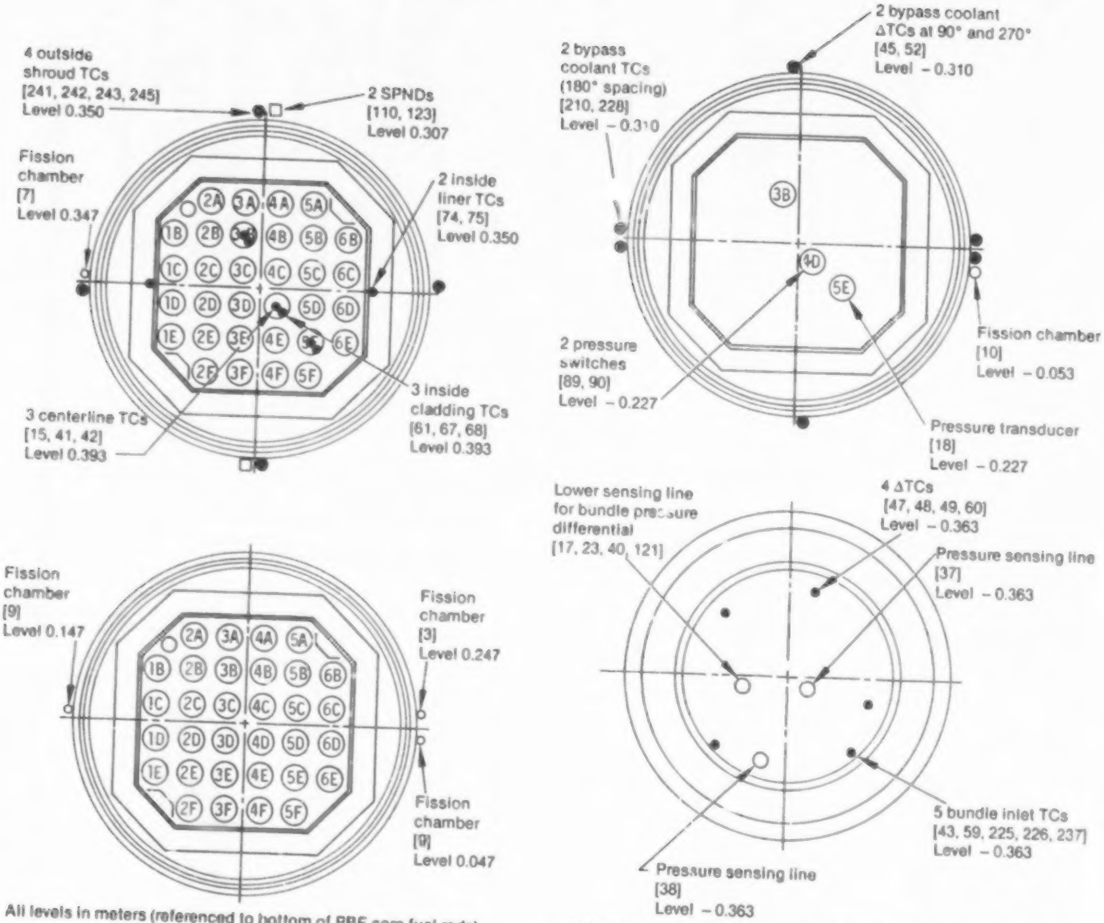
4 outside shroud TCs [241, 242, 243, 245] Level 0.350
2 SPNDs [110, 123] Level 0.307
Fission chamber [7] Level 0.347
2 inside liner TCs [74, 75] Level 0.350
2A 3A 4A 5A
1B 2B 3B 4B 5B 6B
1C 2C 3C 4C 5C 6C
1D 2D 3D 5D 6D
1E 2E 3E 4E 5E 6E
2F 3F 4F 5F
3 centerline TCs [15, 41, 42] Level 0.393
3 inside cladding TCs [61, 67, 68] Level 0.393
Fission chamber [9] Level 0.147
Fission chamber [3] Level 0.247
Fission chamber [9] Level 0.047
2 bypass coolant TCs (180° spacing) [210, 228] Level – 0.310
2 bypass coolant ΔTCs at 90° and 270° [45, 52] Level – 0.310
3B
4D
5E
Fission chamber [10] Level – 0.053
2 pressure switches [89, 90] Level – 0.227
Pressure transducer [18] Level – 0.227
Lower sensing line for bundle pressure differential [17, 23, 40, 121]
4 ΔTCs [47, 48, 49, 60] Level – 0.363
Pressure sensing line [37] Level – 0.363
5 bundle inlet TCs [43, 59, 225, 226, 237] Level – 0.363
Pressure sensing line [38] Level – 0.363

All levels in meters (referenced to bottom of PBF core fuel rods)

8-3336

All levels in meters (referenced to bottom of PBF core fuel rods)

8-3337

Figure B-2. Cross sections of the Test SFD 1-4 shroud and test bundle, indicating instrumentation between the 0.393- and 0.363-m elevations, with DARS parameter numbers in square brackets.

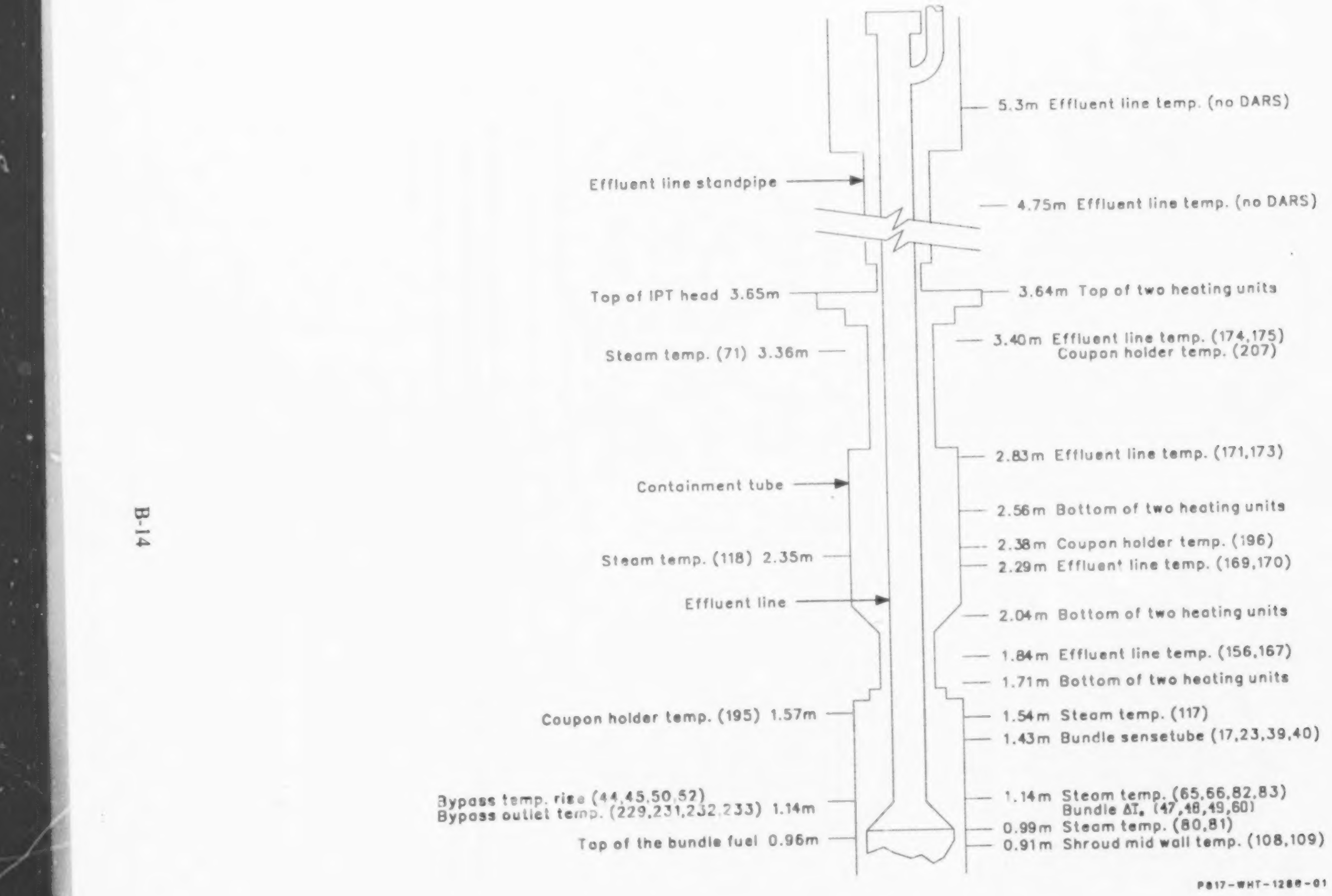

5.3m Effluent line temp. (no DARS)
Effluent line standpipe
4.75m Effluent line temp. (no DARS)
Top of IPT head 3.65m
3.64m Top of two heating units
3.40m Effluent line temp. (174,175)
Coupon holder temp. (207)
Steam temp. (71) 3.36m
2.83m Effluent line temp. (171,173)
Containment tube
2.56m Bottom of two heating units
2.38m Coupon holder temp. (196)
Steam temp. (118) 2.35m
2.29m Effluent line temp. (169,170)
Effluent line
2.04m Bottom of two heating units
1.84m Effluent line temp. (156,167)
1.71m Bottom of two heating units
Coupon holder temp. (195) 1.57m
1.54m Steam temp. (117)
1.43m Bundle sensetube (17,23,39,40)
Bypass temp. rise (44,45,50,52)
Bypass outlet temp. (229,231,232,233) 1.14m
1.14m Steam temp. (65,66,82,83)
Bundle ΔT, (47,48,49,60)
0.99m Steam temp. (80,81)
Top of the bundle fuel 0.96m
0.91m Shroud mid wall temp. (108,109)
P817-WHT-1288-01

Figure B-3. Schematic of axial locations of SFD 1-4 test train instrumentation, with DARS parameter numbers in parentheses.

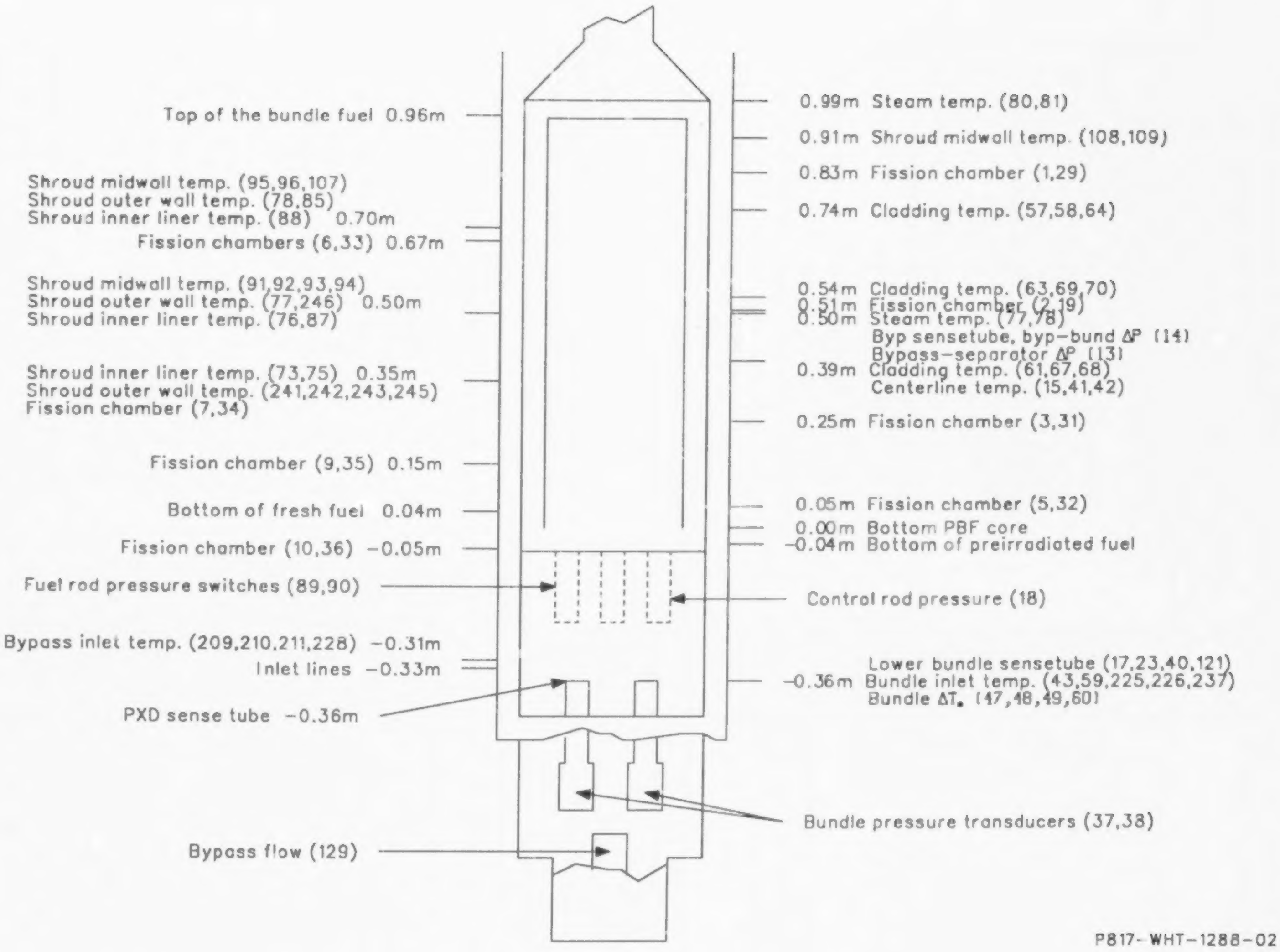
Top of the bundle fuel 0.96m
Shroud midwall temp. (95,96,107)
Shroud outer wall temp. (78,85)
Shroud inner liner temp. (88) 0.70m
Fission chambers (6,33) 0.67m
Shroud midwall temp. (91,92,93,94)
Shroud outer wall temp. (77,246) 0.50m
Shroud inner liner temp. (76,87)
Shroud inner liner temp. (73,75) 0.35m
Shroud outer wall temp. (241,242,243,245)
Fission chamber (7,34)
Fission chamber (9,35) 0.15m
Bottom of fresh fuel 0.04m
Fission chamber (10,36) −0.05m
Fuel rod pressure switches (89,90)
Bypass inlet temp. (209,210,211,228) −0.31m
Inlet lines −0.33m
PXD sense tube −0.36m
Bypass flow (129)
0.99m Steam temp. (80,81)
0.91m Shroud midwall temp. (108,109)
0.83m Fission chamber (1,29)
0.74m Cladding temp. (57,58,64)
0.54m Cladding temp. (63,69,70)
0.51m Fission chamber (2,19)
0.50m Steam temp. (77,78)
Byp sensetube, byp−bund ΔP (14)
Bypass−separator ΔP (13)
0.39m Cladding temp. (61,67,68)
Centerline temp. (15,41,42)
0.25m Fission chamber (3,31)
0.05m Fission chamber (5,32)
0.00m Bottom PBF core
−0.04m Bottom of preirradiated fuel
Control rod pressure (18)
Lower bundle sensetube (17,23,40,121)
−0.36m Bundle inlet temp. (43,59,225,226,237)
Bundle ΔT. (47,48,49,60)
Bundle pressure transducers (37,38)
P817-WHT-1288-02

Figure B-3. (continued).

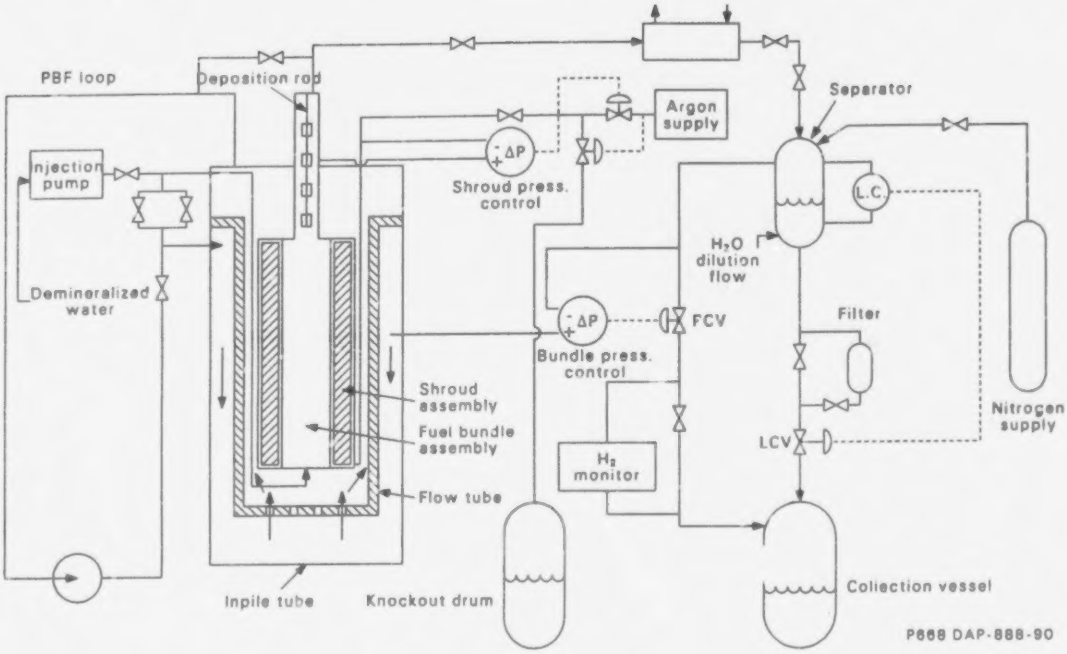
PBF loop
Deposition rod
Injection pump
Demineralized water
Argon supply
Separator
$\bar{+}\Delta P$
Shroud press. control
L.C.
H_2O dilution flow
Filter
FCV
Bundle press. control
Shroud assembly
Fuel bundle assembly
Flow tube
H_2 monitor
LCV
Nitrogen supply
Inpile tube
Knockout drum
Collection vessel
P868 DAP-888-90

Figure B-4. Schematic of the SFD 1-4 test train coolant system, pressure control system, and effluent sampling and measuring system.

eddy-current-type transducer with a 13.8-MPa maximum range.

B-1.3 Shroud Instrumentation. The instrumentation used to measure shroud temperatures was as follows:

- Five W/Re thermocouples were mounted on the outside of the shroud inner liner (the dry side), with two junctions each at elevations of 0.35 and 0.5 m and one at 0.7 m. The paired thermocouples at each elevation were on opposite sides of the shroud, i.e., at 90- and 270-degree orientations. The construction of the thermocouples was the same as the fuel rod cladding thermocouples.

- Nine Type C thermocouples were mounted immediately outside the ZrO_2 shroud insulation, four at an elevation of 0.5 m, three at 0.7 m, and two at 0.91 m. These thermocouples were constructed in the same manner as the fuel rod cladding thermocouples.

- Eight Type K thermocouples were attached to the outer surface of the test train (in the bypass water) to monitor heat loss. Four were mounted at 90-degree intervals around the shroud at the 0.35-m elevation; two were mounted at the 0.5-m elevation; and two were mounted at the 0.7-m elevation.

- A detector to determine excessive heating or meltthrough of the shroud outer wall was contained in a cylindrical cavity just inside the shroud outer wall. In addition, the cavity was pressurized; and a 10.3-MPa pressure transducer was included to monitor pressure changes.

All the Type C thermocouples used a 1.0-mm-OD zircaloy sheath with a tantalum liner. The insulation was BeO, and the thermal elements were W/5%Re and W/26%Re. The Type K thermocouples had Inconel-600 sheaths, MgO insulation, and a chromel-alumel thermal element.

B-1.4 Neutron Flux Instrumentation. The instrumentation used to measure neutron flux and fluence in the in-pile tube (IPT) was as follows:

- Eight fission chambers at elevations of approximately −0.05, 0.05, 0.15, 0.25, 0.35, 0.51, 0.67, and 0.83 m. The chambers were mounted in two strings of four at 90 and 270 degrees, alternating with elevation.

- Two self-powered neutron detectors (SPNDs) at 0.31 m, one each at 0 and 180 degrees.

- Four aluminum-cobalt alloy flux wires extended over the entire fuel region on the outside shroud wall, one each at 0, 90, 180, and 270 degrees.

B-1.5 Water and Steam Instrumentation. Instrumentation to measure the water and steam parameters within the IPT included the following:

- Four W/Re thermocouples and one Type K thermocouple, all located at −0.36 m, were used to measure the bundle water inlet temperature. The four W/Re thermocouples had stainless steel sheaths and Al_2O_3 insulation and were also used as the lower junction of differential thermocouples to measure the coolant temperature rise across the bundle.

- Four Type K thermocouples were used to measure the bypass inlet water temperature at the −0.31-m elevation, and four Type K thermocouples were used to measure the bypass outlet water temperature at the 1.14-m elevation.

- Four differential thermocouples were used to measure the temperature rise of the water flowing upward through the bypass region on the outside of the shroud. The lower junctions were located at 90-degree intervals around the shroud at −0.31 m; the upper junctions were located at the 1.14-m level of the corresponding azimuths.

- Seven thermocouples were used to measure steam temperatures within and above the fuel bundle. One thermocouple was located at 0.54 m, two at 0.99 m, and four at 1.14 m. The steam thermocouples at 1.14 m were also used as the upper junction of differential thermocouples measuring the coolant temperature rise across the bundle. The four thermocouples at 1.14 m used zircaloy sheaths with tantalum liners. The four remaining thermocouples used all-zircaloy sheaths. Insulation in all cases was BeO.

- Four differential thermocouples were used to measure the coolant temperature rise across the bundle. As noted above, the bottom four junctions, at −0.36 m, were also used to measure bundle water inlet temperature and the four top junctions, at 1.14 m, were also used to measure steam temperatures.

- Three Type K thermocouples were used to measure steam temperatures in the effluent tube at elevations of 1.54, 2.35, and 3.36 m.

- One turbine flow meter was used to measure the volumetric flow rate through the bypass region. This device was located at the −0.48-m level of the test train.

- Three differential pressure transducers were located outside the IPT and sensed the pressure through tubes. The bypass-to-bundle transducer was connected to the bypass at 0.5 m and to the bundle at 1.43 m. The bundle differential pressure sensing lines were at −0.36 and 1.43 m, and the bypass-to-separator pressure sensing line was located in the bypass region at an elevation of 0.5 m.

- A flow meter was located outside the reactor in the bundle outlet flow tube to measure the bundle volumetric flow during subcooled operation (preconditioning). Two flow meters (FE 10-13 and FE 10-14) were located outside the reactor and were mounted in parallel to measure the bundle inlet flow rate during subcooled operation.

- The bundle coolant pressure was measured by three pressure transducers, two located in the lower test train and the third located outside the reactor. One of the two transducers located below the test train had a range of 69 MPa to record major system overpressures, and the other had a range of 17 MPa for more precise measurement of system pressure. Both of these transducers monitored pressure through short sensing tubes entering the shroud at an elevation of −0.31 m. A third pressure transducer (10.3 MPa) was mounted outside the reactor to monitor bundle pressure through a long sensing tube entering the test train at an elevation of 1.43 m.

B-1.6 Upper Test Train Instrumentation. The array of thermocouples used to provide upper test train temperature measurement included the following:

- Eight Type K thermocouples were mounted on the outer wall of the effluent tube, two each at elevations of 1.84, 2.29, 2.83, and 3.4 m. Each pair of thermocouples was located at 90 and 270 degrees at each elevation.

- Another eight Type K thermocouples were mounted on the effluent tube heater sheaths at locations of 1.71, 2.04, 2.57, and 3.64 m. These thermocouples, installed by the heater manufacturer, indicated the heater temperature.

- Three thermocouples mounted on the deposition rod measured fission product coupon holder temperatures at 1.57, 2.38, and 3.4 m.

B-1.7 Fission Chamber Liquid Level System Instrumentation. Eight neutron fission chambers were installed external to the fuel bundle assembly in the bypass flow region during Test SFD 1-4. The primary objectives of using these detectors were to (a) measure the axial power distribution within the test bundle and (b) nonintrusively determine the temporal position of the boiling liquid boundary (two-phase/steam). Other objectives included two-phase coolant velocity measurements and investigation of the potential for cladding and fuel motion detection and analysis.

The fission chamber signal conditioning and control system consisted of eight ac (noise) data channels, eight dc data channels, a microcomputer controller, and a remote terminal. Each ac data channel consisted of a battery power supply, an amplifier, and a current suppression card. Current suppression altered the dynamic range of the analysis by removing most of the dc component and allowing higher amplifier gains to be utilized. The dc data channel for each fission chamber was derived from the sum of the suppression current level and the average of the fluctuating ac component for that channel. Each pair of data channels (ac and dc) for an individual fission chamber could be operated in two modes—manual or automatic—through the remote control capability supplied by the microcomputer. The terminal was the only part of the system accessible during the test and provided system gain and current suppression monitoring and control. The 16 data channels from the fission chambers were recorded on the PBF DARS. The ac signals were sampled 500 times/s, and the dc signals were sampled 50 times/s.

B-1.8 Fission Product Detection System Instrumentation. The FPDS consisted of a series of gross gamma and neutron detectors and isotopic gamma ray spectrometers designed to characterize fission product concentrations in the SFD 1-4 effluent. The specific instrumentation is as follows:

- Five gamma detectors measured gross gamma activity in the sampling system, and four germanium detectors were used to measure the gamma spectral activity. A germanium detector was used to monitor the effluent line activity on the main floor. The first gross gamma detector was an ion chamber located near the effluent line inlet to the mainfloor gamma spectrometer enclosure. The second gross gamma detector was an ion chamber located at the inlet to the filtered effluent samplers on the main floor. Three NaI gross gamma detectors and the remaining three germanium gamma spectrometers were used (one each) on the steam line in Cubicle 13, on the gas line leaving the separator, and on the liquid line leaving the separator. The five gross gamma detector responses were recorded by the DARS. The germanium detector responses were recorded and analyzed by a separate computer system associated with the FPDS.

- A delayed neutron monitor (moderated BF_3 tube type) measured the delayed neutron flux in the effluent line near the inlet to the spectrometer enclosure in Cubicle 13. The delayed neutron monitor response was recorded by the DARS.

B-1.9 Aerosol Monitor. An aerosol monitor was used on the main floor effluent line to measure the aerosol density during the experiment. The instrument consisted of a light attenuation turbidity meter with two channels (4 and 1 cm) to provide a wide dynamic range of aerosol concentration. (Details of the monitor are found in Appendix A.) The signals from both channels and two reference channels were records by the DARS.

B-1.10 Hydrogen Measurement. A thermal-conductivity-type hydrogen analyzer (Beckman Model 7C) sampled and measured the hydrogen concentration of the gaseous effluent leaving the separator.

B-1.11 Effluent Samplers and Filters. Four sets of effluent samplers were used to characterize the SFD 1-4 effluent at different times during the experiment. They include:

- Six filtered effluent samplers located immediately downstream of the aerosol monitor.
- Six unfiltered effluent samplers located downstream of the steamline gamma spectrometer.
- Six gas samplers, which sampled the gas exiting the separator.
- Six liquidline flowthrough samplers, which provided samples of the condensed liquid effluent exiting the separator.

In addition to the samplers, an in-line filter was located in the liquid line to collect any particulates in the liquid effluent.

B-1.12 Additional Effluent Sampling and Monitoring System Instrumentation. Additional instruments used in the effluent sampling and monitoring system are as follows:

- Temperature measurements were made with thermocouples located on the heated effluent line, on the standpipe, and downstream on the effluent line up to the condenser inlet.
- A paddle wheel flow meter (FE-SF-19) was mounted in the effluent line just before the condenser. This device measured the gas flow rate during the transient and the liquid flow rate during the posttransient flushes, up to a maximum of 71 cm^3/s.
- A heated-wall-type flow meter (FE-SF-20) was mounted in the effluent line immediately after the condenser. This device measured the liquid flow rate during the bundle leakage measurements, with a maximum capacity of 3.3 cm^3/s.
- A flow meter was used to measure the liquid flow out of the separator. The flow meter was of the orifice-differential-pressure type, with a maximum capacity of 35 g/s.
- A pressure transducer was located across the filter bypass on the liquid outlet of the separator. The purpose of this measurement was to indicate when the filter was being bypassed.
- A pressure transducer measured the collection tank (blowdown tank) pressure.
- A level indicator monitored the liquid level in the collection tank.
- A flow meter (FE-SF-18) in the argon/nitrogen sweep gas system was used to measure the flow rate into the fuel bundle. This instrument was a paddle-wheel-type transducer, with a maximum capacity of 30 cm^3/s.
- A transducer was mounted on the separator vessel to monitor the contained gas/liquid interface.

B-1.13 Plant Instrumentation. The plant instrumentation used in this test is listed below.

- Four ion chambers were used to measure reactor power: PPSO1, PPSO2, NMSO3, and NMSO4.
- The loop pressure was measured by the Model 7780 Ashcroft pressure gage, commonly referred to as the "Heise" gage.
- The loop flow rate was measured with a Venturi flow meter.

- A radiation area monitor was used to indicate radiation levels in sample system Cubicle 13.

- There were three instruments on the inlet spool piece: a pressure transducer, a temperature transducer, and a turbine flow meter.

- The reactor primary coolant flow rate was measured.

- The reactor primary coolant heat exchanger differential temperature was measured.

B-2. Instrument Performance

This section of Appendix B discusses the performance of the more important instruments in the test train and effluent sampling and monitoring system used during Test SFD 1-4.

B-2.1 High-Temperature Thermocouples. The SFD 1-4 test train was instrumented with about 80 thermocouples. The low-temperature thermocouples were Type K with Inconel or stainless steel sheaths. The high-temperature thermocouples used W/Re thermal elements and zircaloy, MoRe, tantalum, or stainless steel sheaths. The fuel rod cladding thermocouples had tantalum-lined zircaloy sheaths, BeO insulation, and W/Re thermal elements.

The typical cladding thermocouple response to experimental transient temperature was manifested by a slow temperature rise, a rapid indicated temperature rise, a period of erratic signal breakup, and a very smooth and consistent cooldown. The location of the thermocouple junction after erratic signal breakup was unknown. Virtual thermocouple junctions probably formed at a higher temperature region at a lower elevation in the bundle. Electrically heated furnace tests of Ta-sheathed, BeO-insulated, fuel centerline thermocouples (1.60 mm OD) have shown that new permanent measurement junctions are formed because of tantalum contamination of the BeO at temperatures above ∼2300 K. It would be expected that this phenomenon would be even more pronounced in the smaller diameter (1 mm OD) cladding thermocouples used in Test SFD 1-4.

Table B-2 summarizes the performance of the high-temperature thermocouples in Test SFD 1-4. The maximum qualified temperatures that were attained by the cladding or centerline thermocouples varied from 1370 to 1580 K. Generally speaking, the performance of the cladding thermocouples was fair. No sheathed thermocouple can be expected to perform perfectly when the thermocouple sheath passes through a region that is at higher temperature than the junction.

Two of the control rod thermocouples were cladding inner surface thermocouples (stainless steel sheath, BeO insulation, W/Re thermal elements) qualified to ∼1500 K and ∼1100 K. The expected maximum temperature was ∼1670 K, the melting point of the stainless steel thermocouple sheath material. The tantalum-sheathed control rod centerline thermocouple was qualified up to ∼1580 K before becoming erratic and failing completely at 2255 K.

The two Mo-Re-sheathed fuel centerline thermocouples operated up to ∼1475 K before exhibiting signs of insulation breakdown or junction relocation. The thermocouples failed at ∼2200 K, but the location of the effective thermocouple junction was unknown prior to failure.

The four steam thermocouples within the fuel bundle had zircaloy sheaths without a tantalum liner. One of the thermocouples failed prior to the test, and two others failed at low temperatures early in the transient. The remaining thermocouple was qualified to 1375 K and failed at 1470 K.

The four steam thermocouples above the bundle at 1.14 m had zircaloy sheaths with tantalum liners. These four thermocouples were qualified to temperatures of 1150 K and failed at 1255 K. The solid zircaloy sheaths (used in the lower elevation bundle steam thermocouples) appear to be slightly inferior to those with a tantalum liner in an oxidizing environment.

Of the six thermocouples on the shroud inner liner, one failed prior to the test and the others failed at temperatures ranging from 1370 to 1850 K. Of the ten thermocouples measuring the shroud insulation midwall temperature, three failed prior to the test; the others failed at temperatures ranging from 710 to 1070 K.

B-2.2 Low-Temperature Thermocouples. There were 44 low-temperature thermocouples on the test train to measure water, steam, and metal temperatures. Eleven of the 12 bypass coolant absolute and differential temperature thermocouples operated satisfactorily, while one differential thermocouple

Table B-2. Test SFD 1-4 instrumentation performance

Thermocouple Location	Average Peak Qualified Temperature (K)	Average Peak Failure Temperature (K)
Fuel rod cladding (6)	1500 ± 40[a]	1800 ± 190[a]
Control rod cladding (3)	1370 ± 225	1420 ± 285
Fuel rod centerline (2)	1475 ± 10	2250 ± 60
Control rod centerline (1)	1580	2255
Steam probe (Zr sheath) (3)	1130 ± 345	1175 ± 295
Steam probe (Zr + Ta) (4)	1150 ± 120	1255 ± 178
Shroud inner wall (5)	1575 ± 195	1680 ± 205
Shroud midwall (7)	915 ± 130	1045 ± 95

a. One standard deviation.

was sometimes erratic. Four of the five bundle inlet thermocouples operated properly, and the other thermocouple failed late in the transient. All eight of the shroud outer wall thermocouples operated properly. The eight effluent tube wall thermocouples operated properly, as did the three upper steam thermocouples. One of the eight heater thermocouples failed prior to the transient, but the remaining seven thermocouples functioned properly.

B-2.3 Pressure Switches. Two pressure switches were mounted in the two fresh rods (3B and 4D) to provide an indication of cladding failure. The switch on rod 3B (which was prepressurized to 2.0 MPa) reached the pressure switch set point of 6.3 MPa shortly before it indicated that the rod had ruptured. The switch was alternately cocking and uncocking for about 100 s before the rod failed. The switch on rod 4D (which was prepressurized to 3.8 MPa) never did evidently cock because the internal rod pressure did not reach the switch set point pressure of 8.1 MPa.

B-2.4 Pressure Transducers. The pressure transducer on control rod 5E indicated the time of rod rupture very clearly, although the absolute pressure value was inaccurate. The three coolant pressure transducers (69, 17, and 10.3 MPa) operated properly.

B-2.5 Neutron Detectors. The eight fission chambers and two self-powered neutron detectors operated properly.

B-2.6 Flow Meters. The three turbine flow meters used to measure the bundle and bypass inlet coolant flow rates operated satisfactorily.

The flow meter measuring the condenser outlet flow gave erroneous readings due to calibration problems and argon flow through the transducer.

B-2.7 Shroud Meltthrough Detector. The shroud meltthrough detector consisted of four sheathed and insulated wires wrapped around the inner portion of the shroud double outer wall. Indications of the shroud outer wall temperature were derived from the change in insulation resistance between the wires and sheaths. The meltthrough detector cavity was pressurized with helium to about 0.49 MPa, and the pressure was monitored.

Three of four shroud meltthrough detector wires operated properly throughout the test. Although insulation resistance of the outer wire was about a decade lower than the other three, it exhibited the same general response curve.

B-2.8 Aerosol Monitor. The aerosol monitor worked very well during Test SFD 1-4. Both the 1- and 4-cm signal paths exhibited the same qualitative behavior during the experiment. The posttest signal ($t > 4000$ s) indicates some degree of aerosol plateout on the windows. This plateout indicates uncertainties of about +4% in the 4-cm cell signal and +12% in the 1-cm cell signal. The transmission loss versus time may be decreased by this amount.

The 4-cm channel showed a drift characteristic of less than 0.1% during the test, indicating that the light source was extremely stable and introduced no error into the turbidity measurement. Several hours before the test, the 1-cm channel reference signal was lost due to a lock-in amplifier malfunction. However, recordings of this signal in the days preceding the transient indicate that it also exhibited a high degree of stability. It is reasonable to assume that it also introduced no significant error into the measurement.

B-2.9 Fission Product Detection System. The FPDS operated as designed during Test SFD 1-4. The four gamma ray spectrometers collected spectra continuously during the experiment. The entire test was monitored using automatic collimator control. This method of monitoring resulted in no spectral data loss due to excessive count rate. The addition of a gamma spectrometer on the main floor provided data on fission product concentrations just upstream of the aerosol monitor. The FPDS gross detectors also operated properly during the SFD 1-4 transient.

The FPDS was also used in a recirculation mode to monitor the content of the collection tank posttest. The liquid recirculation system worked properly, but the gas space recirculation system failed. The gas recirculation system was made operational following maintenance about five weeks posttest. Both the gasline and liquidline spectrometers collected data during the recirculation phase.

B-2.10 Hydrogen Monitor. The on-line hydrogen monitor worked relatively well during the experiment. With the exception of data collected following the argon purge late in the experiment, the data did represent the hydrogen concentration in the gas line during the test. However, posttest experimentation with an identical monitor indicated that the increase in concentration late in the experiment was due to the water entering the monitor following the pressure surge generated by the argon purge. Additional information about the hydrogen monitor response is found in Appendix E.

APPENDIX C

TEST SFD 1-4 DATA QUALIFICATION, UNCERTAINTIES, AND DATA PLOTS

APPENDIX C

TEST SFD 1-4 DATA QUALIFICATION, UNCERTAINTIES, AND DATA PLOTS

The data qualification procedures, methods for evaluating uncertainties, and detailed plots of the qualified DARS and FPDS data for Test SFD 1-4 are presented in this appendix.

C-1. DARS Data Qualification Procedures

The following section describes the procedures used before, during, and after Test SFD 1-4 in order to assure proper categorization of the DARS data as qualified, trend, or failed. These procedures were performed sequentially.

C-1.1 Data Acquisition Specification (DAS). Transducer calibration coefficients were developed and checked for use in the Data Acquisition and Reduction System (DARS) directory. For those instruments that were not calibrated, coefficients were determined on the basis of laboratory calibration data. Some of the coefficients were adjusted as a result of in-place calibration or special experiment requirements. All such adjustments were either directed or approved by the Data Integrity Review Committee (DIRC).

C-1.2 System Checkout. After the installation of the test train and interconnections to the PBF/DARS were completed, the following data were taken on each channel where applicable:

1. Millivolt readings were taken from the sensor.
2. The sensor was connected to the input patch panel with the same millivolt output as determined in (1), and readings were taken on:

   Low-level amplifier output in millivolts;
   Counts as indicated on the DARS input;
   Engineering unit value indicated on DARS terminal or printout.
3. The various readings were compared against calculated outputs for the same input values. If discrepancies were found, appropriate corrective action was taken.

C-1.3 DARS Pretest Calibration. Each DARS channel was calibrated prior to the start of the test by voltage insertion at the electronic input. The magnitude, frequency, sign, or wave form of the test signal was representative of the transducer output for that channel. The calibration performed immediately prior to the test is termed the DARS precalibration. The experiment test data were evaluated during the data qualification process for zero offset or gain error introduced by the electronics based on this pretest calibration.

C-1.4 Cold Hydro Pressure Verification. With the loop piping at approximately ambient temperature, the pressure was varied in 20% steps from 0.62 to 8.3 to 0.62 MPa. Millivolt readings of the pressure transducers were taken at each step at the bridge, as were system point summaries at the control room. These were compared to verify proper operation.

C-1.5 Calibration. A system automatic calibration of selected channels was performed prior to initiation of each major phase of the test. By remote control from the control room, the front end of the PBF/DARS was instructed (channel by channel) to disconnect itself from the transducer, read five voltage steps provided by a highly accurate programmable dc source, then calculate second-order regression coefficients to correct all future readings to what they would be were the PBF/DARS totally free of gain and zero drift errors. The narrow band parameters which provided DARS output signals greater than the 1-mV range were calibrated in this manner. Those parameters which provided DARS output signals in the 1-mV range or less were removed from the calibration list.

C-1.6 Heatup. This phase of the test raised the system from ambient temperature and pressure to system operating conditions of 520 K and 6.9 MPa. The loop pressure transducers were corrected at the end of heatup to agree with the SYSPRES Ashcroft gauge. At the end of heatup, under assumed isothermal conditions, all test train thermocouples reading outside of one standard deviation from the mean of all thermocouples and RTD were adjusted to read the mean, after wild points were discarded. All differential thermocouples were set to zero under no-power, normal-flow conditions. All corrections made were applied by adjusting autocalibration coefficients, which are time-dependent and automatically applied by the reduction process.

C-1.7 Power Calibration and Preconditioning. Nuclear operation was begun, and the system was ramped to and held at various power levels to provide verification of nuclear instrumentation operation. This verification included correct fission chamber operation and correct differential thermocouple connection, and also provided a fission product buildup and rod power history.

C-1.8 Transient. Each parameter was examined for thermal and other transient effects. The data were classified in accordance with DIRC classifications for engineering unit data during both steady-state operation prior to the transient and the transient itself.

C-1.9 PBF/DARS Posttest Calibration. Each PBF/DARS channel was calibrated at the completion of the test in the same manner as the precalibration. Pre- and postcalibrations were compared to determine correctable electronic drift or offsets. Due largely to the use of auto calibration and checking during the test, no corrections based on the pre- and/or postcalibrations were made.

C-1.10 Data Qualification. Data qualification was performed by a trained group of engineers who were knowledgable about the reactor, the experiment, the instrumentation, and the data acquisition system.

C-1.11 Uncertainty Bands. Uncertainty bands for the qualified data from Test SFD 1-4 represent the overall estimate with 95% confidence level. Uncertainty bands are presented in an up-to-third-order equation format. These uncertainty equations are derived from first-, second-, or third-order regression results of the calculated uncertainty values; the order is chosen according to that which best fits the curves generated. Data were qualified only for the times of interest. Error band information is supplied only on qualified data. Trend data are supplied with no uncertainty values or error bands.

C-2. DARS Qualification Categories and Process

The classification of engineering unit data is made by assignment of data to defined categories during particular test intervals. The assignment is made first by determining which data are not to be reviewed and which will be left unqualified. These data are retained in raw form on computer tapes and are not presented in this report. The remaining data are assigned categories during particular time intervals using documented methods, procedures, and guidelines. The assignment of data to defined categories during particular time intervals is made through measurement-by-measurement examination of single-channel test data in engineering units. The examination process determines whether the measurement channel output represents the expected, predicted, or required response. As a result of examination, one or more of the categories defined below is assigned to each measurement, as a function of time.

- Qualified engineering unit data (Q)
- Trend data (T)
- Failed data (F)

C-2.1 Qualified Data. Data are qualified with DIRC approval and must meet all the following criteria:

- Engineering unit conversion equations have been applied.
- Data acquisition system calibrations have been applied.
- All identifiable and verifiable systematic errors have been removed.
- Uncertainty limits have been established for the 95% confidence level, including:
  - — All calibration uncertainties;
  - — Systematic and random uncertainties due to effects on perturbations of the phenomena;

- Uncertainties due to the application of any models;
- Uncertainties in the measurement channels and DARS.

- Some useful information is contained in the data.

C-2.2 Trend Data. Trend data have been verified (by DIRC with input from appropriate analysts and data integrity specialists) to represent the relative changes in the phenomenon measured but do not necessarily represent the absolute level in the phenomenon measured because of one or more of the following:

- Instrument calibrations do not adequately represent the environment which the transducer measures.
- The calibration and performance of the data acquisition system are suspect, but known errors have been eliminated.
- Uncertainty limits cannot be adequately quantified.
- Transducer performance is suspect but is thought to be relatively correct.
- Environmental effects cannot be adequately compensated.

These data have met the following criteria:

- Instrument and data acquisition calibrations have been applied.
- Wild points have been removed.
- Data have been filtered by appropriate anti-aliasing filters.

C-2.3 Failed Data. Data are failed with DIRC approval for one or more of the following reasons:

- Data do not meet the requirements of any other data classification categories.
- Useful information is irretrievable from data.
- There was a component failure in the measurement channel or in the data acquisition system.
- Inadequate rejection of extraneous noise, transients, or frequencies.
- Loss of synchronization, data channel continuity, etc.
- Enigmas in the data.

C-3. Test SFD 1-4 DARS Data Qualification

This section describes the categories of qualification for each measurement considered important for experimental analysis and presentation. Instrument data is classified as qualified with error band (Q), trend (T), or failed (F). Table C-1 lists the DARS parameter numbers, instrument identifiers, data qualification category, and start and stop time for each qualification. Table C-2 shows the date and time when various phases of the test were occurring.

C-3.1 Notes on Data Qualification. The following information should be noted when using Table C-1.

1. Though Parameter Nos. 219 and 187 are shown in Table C-2 as qualified, the level of confidence in these data is reduced because of erratic signals.
2. The SPND output data (Nos. 110 and 111) are in logarithmic form. It should be noted that the data near the times the reactor is shut down will go negative. Since the log amplifiers only have positive output, the log trace shows positive after the abrupt reversal. The SPND signal has a negative output for a predominately gamma radiation field and positive output for neutrons.
3. Several cladding temperature thermocouples were classified as trend during the time when the thermocouples began to form new junctions (high-temperature range). This choice was because the trace may show useful trends when compared with other thermocouples.
4. Parameter No. 188 is the electrical difference between parameter No. 13 and parameter No. 14. These instruments agreed with each other and plant strip charts very closely, but an offset is present due to water pressure head in the instrument lines that is not accounted for in the

Table C-1. DARS data qualifications

DARS PARAMETER NUMBER	INSTRUMENT IDENTIFIER	QUALIFICATION	START TIME	STOP TIME
1	FISSCHAM090 DC83	QUALIFIED	01/13 13:30: 0.0	01/14 11:00: 0.0
		QUALIFIED	01/14 18:30: 0.0	01/17 10:00: 0.0
		QUALIFIED	01/17 15:00: 0.0	01/19 14:30: 0.0
		QUALIFIED	01/19 15:45: 0.0	01/22 21:00: 0.0
		QUALIFIED	02/05 15:00: 0.0	02/06 10:00: 0.0
		QUALIFIED	02/07 00:00: 0.0	02/07 22:00: 0.0
2	FISSCHAM090 DC51	QUALIFIED	01/13 13:30: 0.0	01/14 11:00: 0.0
		QUALIFIED	01/14 18:30: 0.0	01/17 10:00: 0.0
		QUALIFIED	01/17 15:00: 0.0	01/19 14:30: 0.0
		QUALIFIED	01/19 15:45: 0.0	01/22 21:00: 0.0
		QUALIFIED	02/05 15:00: 0.0	02/06 10:00: 0.0
		QUALIFIED	02/07 00:00: 0.0	02/07 22:00: 0.0
3	FISSCHAM090 DC25	QUALIFIED	01/13 13:30: 0.0	01/14 11:00: 0.0
		QUALIFIED	01/14 18:30: 0.0	01/17 10:00: 0.0
		QUALIFIED	01/17 15:00: 0.0	01/19 14:30: 0.0
		QUALIFIED	01/19 15:45: 0.0	01/22 21:00: 0.0
		QUALIFIED	02/05 15:00: 0.0	02/06 10:00: 0.0
		QUALIFIED	02/07 00:00: 0.0	02/07 22:00: 0.0
5	FISSCHAM090 DC05	QUALIFIED	01/13 13:30: 0.0	01/14 11:00: 0.0
		QUALIFIED	01/14 18:30: 0.0	01/17 10:00: 0.0
		QUALIFIED	01/17 15:00: 0.0	01/19 14:30: 0.0
		QUALIFIED	01/19 15:45: 0.0	01/22 21:00: 0.0
		QUALIFIED	02/05 15:00: 0.0	02/06 10:00: 0.0
		QUALIFIED	02/07 00:00: 0.0	02/07 22:00: 0.0
6	FISSCHAM270 DC67	QUALIFIED	01/13 13:30: 0.0	01/14 11:00: 0.0
		QUALIFIED	01/14 18:30: 0.0	01/17 10:00: 0.0
		QUALIFIED	01/17 15:00: 0.0	01/19 14:30: 0.0
		QUALIFIED	01/19 15:45: 0.0	01/22 21:00: 0.0
		QUALIFIED	02/05 15:00: 0.0	02/06 10:00: 0.0
		QUALIFIED	02/07 00:00: 0.0	02/07 22:00: 0.0
7	FISSCHAM270 DC35	QUALIFIED	01/13 13:30: 0.0	01/14 11:00: 0.0
		QUALIFIED	01/14 18:30: 0.0	01/17 10:00: 0.0
		QUALIFIED	01/17 15:00: 0.0	01/19 14:30: 0.0
		QUALIFIED	01/19 15:45: 0.0	01/22 21:00: 0.0
		QUALIFIED	02/05 15:00: 0.0	02/06 10:00: 0.0
		QUALIFIED	02/07 00:00: 0.0	02/07 22:00: 0.0
9	FISSCHAM270 DC15	FAILED	01/13 13:30: 0.0	01/14 11:00: 0.0
		QUALIFIED	01/14 18:30: 0.0	01/17 10:00: 0.0
		QUALIFIED	01/17 15:00: 0.0	01/19 14:30: 0.0
		QUALIFIED	01/19 15:45: 0.0	01/22 21:00: 0.0
		QUALIFIED	02/05 15:00: 0.0	02/06 10:00: 0.0
		QUALIFIED	02/07 00:00: 0.0	02/07 22:00: 0.0
10	FISSCHAM270 D-05	FAILED	01/13 13:30: 0.0	01/14 11:00: 0.0
		QUALIFIED	01/14 18:30: 0.0	01/17 10:00: 0.0
		QUALIFIED	01/17 15:00: 0.0	01/19 14:30: 0.0
		QUALIFIED	01/19 15:45: 0.0	01/22 21:00: 0.0
		QUALIFIED	02/05 15:00: 0.0	02/06 10:00: 0.0
		QUALIFIED	02/07 00:00: 0.0	02/07 22:00: 0.0
13	DIFFPRESBYP SEP	FAILED	02/07 20:30: 0.0	02/07 21:04:15.0
		QUALIFIED	02/07 21:04:15.0	02/07 23:40: 0.0
		FAILED	02/07 23:40: 0.0	02/08 03:00: 0.0
14	DIFFPRESBYBUNDLE	QUALIFIED	02/06 02:00: 0.0	02/06 10:00: 0.0
		QUALIFIED	02/07 14:00: 0.0	02/08 03:00: 0.0

Table C-1. (continued)

DARS PARAMETER NUMBER	INSTRUMENT IDENTIFIER	QUALIFICATION	START TIME	STOP TIME
15	CRCENTERTEMP395E	QUALIFIED	02/07 20:30: 0.0	02/07 21:01:27.0
		TREND	02/07 21:01:27.0	02/07 21:03:40.0
		FAILED	02/07 21:03:40.0	02/07 22:00: 0.0
17	DIFFPRESBUNDLE7R	FAILED	02/07 20:30: 0.0	02/08 03:00: 0.0
18	CR PRESS 5E	QUALIFIED	02/07 20:30: 0.0	02/07 21:18:20.0
		FAILED	02/07 21:18:20.0	02/07 22:00: 0.0
19	FISSCHAM090 AC51	TREND	02/06 02:00: 0.0	02/06 10:00: 0.0
		TREND	02/07 14:00: 0.0	02/07 22:00: 0.0
21	REAC POWNMS-03PT	QUALIFIED	01/13 13:30: 0.0	01/14 11:00: 0.0
		QUALIFIED	01/14 18:30: 0.0	01/17 10:00: 0.0
		QUALIFIED	01/17 15:00: 0.0	01/19 14:30: 0.0
		QUALIFIED	01/19 15:45: 0.0	01/22 21:00: 0.0
		QUALIFIED	02/05 15:00: 0.0	02/06 10:00: 0.0
		QUALIFIED	02/07 00:00: 0.0	02/07 22:00: 0.0
22	REAC POWNMS-04PT	QUALIFIED	01/13 13:30: 0.0	01/14 11:00: 0.0
		QUALIFIED	01/14 18:30: 0.0	01/17 10:00: 0.0
		QUALIFIED	01/17 15:00: 0.0	01/19 14:30: 0.0
		QUALIFIED	01/19 15:45: 0.0	01/22 21:00: 0.0
		QUALIFIED	02/05 15:00: 0.0	02/06 10:00: 0.0
		QUALIFIED	02/07 00:00: 0.0	02/07 22:00: 0.0
23	DIFFPRESBUNDLE7R	FAILED	02/07 20:30: 0.0	02/08 03:00: 0.0
29	FISSCHAM090 AC83	TREND	02/06 02:00: 0.0	02/06 10:00: 0.0
		TREND	02/07 14:00: 0.0	02/07 22:00: 0.0
31	FISSCHAM090 AC25	TREND	02/06 02:00: 0.0	02/06 10:00: 0.0
		TREND	02/07 14:00: 0.0	02/07 22:00: 0.0
32	FISSCHAM090 AC05	TREND	02/06 02:00: 0.0	02/06 10:00: 0.0
		TREND	02/07 14:00: 0.0	02/07 22:00: 0.0
33	FISSCHAM270 AC67	TREND	02/06 02:00: 0.0	02/06 10:00: 0.0
		TREND	02/07 14:00: 0.0	02/07 22:00: 0.0
34	FISSCHAM270 AC35	TREND	02/06 02:00: 0.0	02/06 10:00: 0.0
		TREND	02/07 14:00: 0.0	02/07 22:00: 0.0
35	FISSCHAM270 AC15	TREND	02/06 02:00: 0.0	02/06 10:00: 0.0
		TREND	02/07 14:00: 0.0	02/07 22:00: 0.0
36	FISSCHAM270 A-05	TREND	02/06 02:00: 0.0	02/06 10:00: 0.0
		TREND	02/07 14:00: 0.0	02/07 22:00: 0.0
37	SYS PRES69EG LTT	QUALIFIED	01/13 13:30: 0.0	01/14 11:00: 0.0
		FAILED	01/14 18:30: 0.0	01/17 19:30: 0.0
		QUALIFIED	01/17 19:30: 0.0	01/19 14:30: 0.0
		FAILED	01/19 15:45: 0.0	01/22 21:00: 0.0
		QUALIFIED	02/05 15:00: 0.0	02/06 10:00: 0.0
		QUALIFIED	02/07 00:00: 0.0	02/07 22:00: 0.0
		QUALIFIED	02/07 22:00: 0.0	02/08 03:00: 0.0

best copy available

Table C-1. (continued)

DARS PARAMETER NUMBER	INSTRUMENT IDENTIFIER	QUALIFICATION	START TIME	STOP TIME
38	SYS PRES17EG LTT	QUALIFIED	01/13 13:30: 0.0	01/14 11:00: 0.0
		QUALIFIED	01/14 18:30: 0.0	01/17 10:00: 0.0
		QUALIFIED	01/17 15:00: 0.0	01/19 14:30: 0.0
		QUALIFIED	01/19 15:45: 0.0	01/22 21:00: 0.0
		QUALIFIED	02/05 15:00: 0.0	02/06 10:00: 0.0
		QUALIFIED	02/07 00:00: 0.0	02/07 22:00: 0.0
		QUALIFIED	02/07 22:00: 0.0	02/07 23:40: 0.0
		TREND	02/07 23:40: 0.0	02/08 03:00: 0.0
39	SYS PRESBUNDLETT	QUALIFIED	01/13 13:30: 0.0	01/14 11:00: 0.0
		QUALIFIED	01/14 18:30: 0.0	01/17 10:00: 0.0
		QUALIFIED	01/17 15:00: 0.0	01/19 14:30: 0.0
		QUALIFIED	01/19 15:45: 0.0	01/22 21:00: 0.0
		QUALIFIED	02/05 15:00: 0.0	02/06 10:00: 0.0
		QUALIFIED	02/07 00:00: 0.0	02/07 22:00: 0.0
		QUALIFIED	02/07 22:00: 0.0	02/08 03:00: 0.0
40	DIFFPRESBUNDLE7R	QUALIFIED	02/07 20:30: 0.0	02/08 03:00: 0.0
41	FUELTEMPCL 393B	QUALIFIED	02/07 20:30: 0.0	02/07 21:01: 0.0
		TREND	02/07 21:01: 0.0	02/07 21:04:14.0
		FAILED	02/07 21:04:14.0	02/07 22:00: 0.0
42	FUELTEMPCL 394D	QUALIFIED	02/07 20:30: 0.0	02/07 21:00:43.0
		TREND	02/07 21:00:43.0	02/07 21:03: 0.0
		FAILED	02/07 21:03: 0.0	02/07 22:00: 0.0
43	INLTTEMP015 -36	QUALIFIED	01/13 13:30: 0.0	01/14 11:00: 0.0
		QUALIFIED	01/14 18:30: 0.0	01/17 10:00: 0.0
		QUALIFIED	01/17 15:00: 0.0	01/19 14:30: 0.0
		QUALIFIED	01/19 15:45: 0.0	01/22 21:00: 0.0
		QUALIFIED	02/05 15:00: 0.0	02/06 10:00: 0.0
		QUALIFIED	02/07 00:00: 0.0	02/07 22:00: 0.0
44	DEL TEMPBYP 180	QUALIFIED	02/07 20:30: 0.0	02/07 22:00: 0.0
45	DEL TEMPBYP 270	QUALIFIED	02/07 20:30: 0.0	02/07 22:00: 0.0
47	DEL TEMPBNDLE030	QUALIFIED	01/13 13:30: 0.0	01/14 11:00: 0.0
		QUALIFIED	01/14 18:30: 0.0	01/17 10:00: 0.0
		QUALIFIED	01/17 15:00: 0.0	01/19 14:30: 0.0
		QUALIFIED	01/19 15:45: 0.0	01/22 21:00: 0.0
		QUALIFIED	02/05 15:00: 0.0	02/06 02:00: 0.0
		QUALIFIED	02/07 00:00: 0.0	02/07 11:00: 0.0
48	DEL TEMPBNDLE210	QUALIFIED	01/13 13:30: 0.0	01/14 11:00: 0.0
		QUALIFIED	01/14 18:30: 0.0	01/17 10:00: 0.0
		QUALIFIED	01/17 15:00: 0.0	01/19 14:30: 0.0
		QUALIFIED	01/19 15:45: 0.0	01/22 21:00: 0.0
		QUALIFIED	02/05 15:00: 0.0	02/06 02:00: 0.0
		QUALIFIED	02/07 00:00: 0.0	02/07 11:00: 0.0
49	DEL TEMPBNDLE300	QUALIFIED	01/13 13:30: 0.0	01/14 11:00: 0.0
		FAILED	01/14 18:30: 0.0	01/17 10:00: 0.0
		QUALIFIED	01/17 15:00: 0.0	01/19 14:30: 0.0
		QUALIFIED	01/19 15:45: 0.0	01/21 09:25: 0.0
		FAILED	01/21 09:25: 0.0	01/22 21:00: 0.0
		FAILED	02/05 15:00: 0.0	02/06 02:00: 0.0
		FAILED	02/07 00:00: 0.0	02/07 11:00: 0.0
50	DEL TEMPBYP 000	QUALIFIED	02/07 20:30: 0.0	02/07 22:00: 0.0

Table C-1. (continued)

DARS PARAMETER NUMBER	INSTRUMENT IDENTIFIER	QUALIFICATION	START TIME	STOP TIME
52	DEL TEMPBYP 090	QUALIFIED	02/07 20:30: 0.0	02/07 21:03:20.0
		FAILED	02/07 21:03:20.0	02/07 21:05: 0.0
		QUALIFIED	02/07 21:05: 0.0	02/07 22:00: 0.0
53	REAC POWPPS-01PT	QUALIFIED	01/13 13:30: 0.0	01/14 11:00: 0.0
		QUALIFIED	01/14 18:30: 0.0	01/17 10:00: 0.0
		QUALIFIED	01/17 15:00: 0.0	01/19 14:30: 0.0
		QUALIFIED	01/19 15:45: 0.0	01/22 21:00: 0.0
		QUALIFIED	02/05 15:00: 0.0	02/06 10:00: 0.0
		QUALIFIED	02/07 00:00: 0.0	02/07 22:00: 0.0
54	REAC POWPPS-02PT	QUALIFIED	01/13 13:30: 0.0	01/14 11:00: 0.0
		QUALIFIED	01/14 18:30: 0.0	01/17 10:00: 0.0
		QUALIFIED	01/17 15:00: 0.0	01/19 14:30: 0.0
		QUALIFIED	01/19 15:45: 0.0	01/22 21:00: 0.0
		QUALIFIED	02/05 15:00: 0.0	02/06 10:00: 0.0
		QUALIFIED	02/07 00:00: 0.0	02/07 22:00: 0.0
57	CLADTEMP225 743B	QUALIFIED	02/06 02:00: 0.0	02/06 10:00: 0.0
		QUALIFIED	02/07 14:00: 0.0	02/07 21:01: 8.0
		TREND	02/07 21:01: 8.0	02/07 21:02:13.0
		FAILED	02/07 21:02:13.0	02/07 22:00: 0.0
58	CLADTEMP225 744D	QUALIFIED	02/06 02:00: 0.0	02/06 10:00: 0.0
		QUALIFIED	02/07 14:00: 0.0	02/07 21:00:40.0
		TREND	02/07 21:00:40.0	02/07 21:02:13.0
		FAILED	02/07 21:02:13.0	02/07 22:00: 0.0
59	INLTTEMP135 -36	QUALIFIED	01/13 13:30: 0.0	01/14 11:00: 0.0
		QUALIFIED	01/14 18:30: 0.0	01/17 10:00: 0.0
		QUALIFIED	01/17 15:00: 0.0	01/19 14:30: 0.0
		QUALIFIED	01/19 15:45: 0.0	01/22 21:00: 0.0
		QUALIFIED	02/05 15:00: 0.0	02/06 10:00: 0.0
		QUALIFIED	02/07 00:00: 0.0	02/07 22:00: 0.0
60	DEL TEMPBNDLE330	QUALIFIED	01/13 13:30: 0.0	01/14 11:00: 0.0
		QUALIFIED	01/14 18:30: 0.0	01/17 10:00: 0.0
		QUALIFIED	01/17 15:00: 0.0	01/19 14:30: 0.0
		QUALIFIED	01/19 15:45: 0.0	01/22 21:00: 0.0
		QUALIFIED	02/05 15:00: 0.0	02/06 02:00: 0.0
		QUALIFIED	02/07 00:00: 0.0	02/07 11:00: 0.0
61	CRCLADTP135 395E	QUALIFIED	02/07 20:30: 0.0	02/07 21:01:22.0
		TREND	02/07 21:01:22.0	02/07 21:02:23.0
		FAILED	02/07 21:02:23.0	02/07 22:00: 0.0
63	CRCLADTP000 545E	QUALIFIED	02/07 20:30: 0.0	02/07 20:56:37.0
		FAILED	02/07 20:56:37.0	02/07 22:00: 0.0
64	CRCLADTP225 745E	QUALIFIED	02/07 20:30: 0.0	02/07 21:01:31.0
		FAILED	02/07 21:01:31.0	02/07 22:00: 0.0
65	STEAMTMP210 114	QUALIFIED	01/13 13:30: 0.0	01/14 11:00: 0.0
		QUALIFIED	01/14 18:30: 0.0	01/17 10:00: 0.0
		QUALIFIED	01/17 15:00: 0.0	01/19 14:30: 0.0
		QUALIFIED	01/19 15:45: 0.0	01/22 21:00: 0.0
		QUALIFIED	02/05 15:00: 0.0	02/06 10:00: 0.0
		QUALIFIED	02/07 00:00: 0.0	02/07 21:02: 0.0
		TREND	02/07 21:02: 0.0	02/07 21:15: 0.0
		FAILED	02/07 21:15: 0.0	02/08 03:00: 0.0

Table C-1. (continued)

DARS PARAMETER NUMBER	INSTRUMENT IDENTIFIER	QUALIFICATION	START TIME	STOP TIME
66	STEAMTMP330 114	FAILED	01/13 13:30: 0.0	01/15 19:30: 0.0
		QUALIFIED	01/15 19:30: 0.0	01/17 10:00: 0.0
		QUALIFIED	01/17 15:00: 0.0	01/19 14:30: 0.0
		QUALIFIED	01/19 15:45: 0.0	01/20 21:45: 0.0
		FAILED	01/20 21:45: 0.0	01/20 23:30: 0.0
		QUALIFIED	01/20 23:30: 0.0	01/22 21:00: 0.0
		QUALIFIED	02/05 15:00: 0.0	02/06 10:00: 0.0
		QUALIFIED	02/07 00:00: 0.0	02/07 21:02:15.0
		TREND	02/07 21:02:15.0	02/07 21:19:10.0
		FAILED	02/07 21:19:10.0	02/08 03:00: 0.0
67	CLADTEMP135 393B	QUALIFIED	02/06 02:00: 0.0	02/06 10:00: 0.0
		QUALIFIED	02/07 14:00: 0.0	02/07 21:01: 0.0
		TREND	02/07 21:01: 0.0	02/07 21:02:56.0
		FAILED	02/07 21:02:56.0	02/07 22:00: 0.0
68	CLADTEMP135 394D	QUALIFIED	02/06 02:00: 0.0	02/06 10:00: 0.0
		QUALIFIED	02/07 14:00: 0.0	02/07 21:00:43.0
		TREND	02/07 21:00:43.0	02/07 21:02:24.0
		FAILED	02/07 21:02:24.0	02/07 22:00: 0.0
69	CLADTEMP000 543B	QUALIFIED	02/06 02:00: 0.0	02/06 10:00: 0.0
		QUALIFIED	02/07 14:00: 0.0	02/07 21:00:58.0
		TREND	02/07 21:00:58.0	02/07 21:02:26.0
		FAILED	02/07 21:02:26.0	02/07 22:00: 0.0
70	CLADTEMP000 544D	QUALIFIED	02/06 02:00: 0.0	02/06 10:00: 0.0
		QUALIFIED	02/07 14:00: 0.0	02/07 21:00:38.0
		TREND	02/07 21:00:38.0	02/07 21:02: 6.0
		FAILED	02/07 21:02: 6.0	02/07 22:00: 0.0
71	STEAMTMP225 336	QUALIFIED	02/07 20:30: 0.0	02/07 22:00: 0.0
72	SYS PRESHEISE PT	QUALIFIED	01/13 13:30: 0.0	01/22 21:00: 0.0
		QUALIFIED	02/05 15:00: 0.0	02/07 22:50:59.0
		FAILED	02/07 22:50:59.0	02/07 23:00: 0.0
		QUALIFIED	02/07 23:00: 0.0	02/08 03:00: 0.0
73	SHRDTEMPIN090 35	QUALIFIED	02/07 20:30: 0.0	02/07 21:02:32.0
		TREND	02/07 21:02:32.0	02/07 21:04: 0.0
		FAILED	02/07 21:04: 0.0	02/07 22:00: 0.0
75	SHRDTEMPIN270 35	QUALIFIED	02/07 20:30: 0.0	02/07 21:03:27.0
		FAILED	02/07 21:03:27.0	02/07 22:00: 0.0
76	SHRDTEMPIN090 50	QUALIFIED	02/07 20:30: 0.0	02/07 21:02:30.0
		TREND	02/07 21:02:30.0	02/07 21:02:54.0
		FAILED	02/07 21:02:54.0	02/07 22:00: 0.0
77	SHRDTEMPOUT18050	QUALIFIED	02/07 20:30: 0.0	02/07 22:00: 0.0
78	SHRDTEMPOUT09070	QUALIFIED	02/07 20:30: 0.0	02/07 22:00: 0.0
79	STEAMTMP5A315 54	QUALIFIED	02/07 20:30: 0.0	02/07 21:00:30.0
		TREND	02/07 21:00:30.0	02/07 21:01:40.0
		FAILED	02/07 21:01:40.0	02/07 22:00: 0.0
80	STEAMTMP1B225 99	TREND	02/07 20:30: 0.0	02/07 21:02: 0.0
		FAILED	02/07 21:02: 0.0	02/07 22:00: 0.0
81	STEAMTMP4D135 99	QUALIFIED	02/07 20:30: 0.0	02/07 20:51:28.0
		TREND	02/07 20:51:28.0	02/07 21:01:20.0
		FAILED	02/07 21:01:20.0	02/07 22:00: 0.0

Table C-1. (continued)

DARS PARAMETER NUMBER	INSTRUMENT IDENTIFIER	QUALIFICATION	START TIME	STOP TIME
82	STEAMTMP030 114	QUALIFIED	01/13 13:30: 0.0	01/14 11:00: 0.0
		QUALIFIED	01/14 18:30: 0.0	01/17 10:00: 0.0
		QUALIFIED	01/17 15:00: 0.0	01/19 14:30: 0.0
		QUALIFIED	01/19 15:45: 0.0	01/22 21:00: 0.0
		QUALIFIED	02/05 15:00: 0.0	02/06 10:00: 0.0
		QUALIFIED	02/07 00:00: 0.0	02/07 20:30: 0.0
		TREND	02/07 20:30: 0.0	02/07 21:13:20.0
		FAILED	02/07 21:13:20.0	02/08 03:00: 0.0
83	STEAMTMP300 114	QUALIFIED	01/13 13:30: 0.0	01/14 11:00: 0.0
		QUALIFIED	01/14 18:30: 0.0	01/17 10:00: 0.0
		QUALIFIED	01/17 15:00: 0.0	01/19 14:30: 0.0
		QUALIFIED	01/19 15:45: 0.0	01/22 21:00: 0.0
		QUALIFIED	02/05 15:00: 0.0	02/06 10:00: 0.0
		QUALIFIED	02/07 00:00: 0.0	02/07 20:53:26.0
		FAILED	02/07 20:53:26.0	02/08 03:00: 0.0
85	SHRDTEMPOUT27070	QUALIFIED	02/07 20:30: 0.0	02/07 22:00: 0.0
86	FPDSFLOWSWEEPGAS	QUALIFIED	02/07 20:30: 0.0	02/08 03:00: 0.0
87	SHRDTEMPIN270 50	QUALIFIED	02/07 20:30: 0.0	02/07 21:02:55.0
		TREND	02/07 21:02:55.0	02/07 21:08:20.0
		FAILED	02/07 21:08:20.0	02/07 22:00: 0.0
88	SHRDTEMPIN270 70	QUALIFIED	02/07 20:30: 0.0	02/07 21:02:25.0
		FAILED	02/07 21:02:25.0	02/07 22:00: 0.0
91	SHRDTEMPMID00050	QUALIFIED	02/07 20:30: 0.0	02/07 21:12:55.0
		TREND	02/07 21:12:55.0	02/07 22:00: 0.0
92	SHRDTEMPMID09050	QUALIFIED	02/07 20:30: 0.0	02/07 21:03:10.0
		TREND	02/07 21:03:10.0	02/07 22:00: 0.0
93	SHRDTEMPMID18050	QUALIFIED	02/07 20:30: 0.0	02/07 21:03:20.0
		TREND	02/07 21:03:20.0	02/07 22:00: 0.0
94	SHRDTEMPMID27050	QUALIFIED	02/07 20:30: 0.0	02/07 21:03:20.0
		TREND	02/07 21:03:20.0	02/07 21:08:48.0
		FAILED	02/07 21:08:48.0	02/07 22:00: 0.0
95	SHRDTEMPMID09070	QUALIFIED	02/07 20:30: 0.0	02/07 21:07:25.0
		FAILED	02/07 21:07:25.0	02/07 22:00: 0.0
96	SHRDTEMPMID18070	QUALIFIED	02/07 20:30: 0.0	02/07 21:03:20.0
		TREND	02/07 21:03:20.0	02/07 22:00: 0.0
107	SHRDTEMPMID27070	FAILED	02/07 20:30: 0.0	02/07 22:00: 0.0
108	SHRDTEMPMID00091	FAILED	02/07 20:30: 0.0	02/07 22:00: 0.0
109	SHRDTEMPMID18091	QUALIFIED	02/07 20:30: 0.0	02/07 21:04:30.0
		TREND	02/07 21:04:30.0	02/07 22:00: 0.0
110	SPND 31GAMA 180	QUALIFIED	01/13 13:30: 0.0	01/14 11:00: 0.0
		QUALIFIED	01/14 18:30: 0.0	01/17 10:00: 0.0
		QUALIFIED	01/17 15:00: 0.0	01/19 14:30: 0.0
		QUALIFIED	01/19 15:45: 0.0	01/22 21:00: 0.0
		QUALIFIED	02/05 15:00: 0.0	02/06 10:00: 0.0
		QUALIFIED	02/07 00:00: 0.0	02/07 22:00: 0.0

Table C-1. (continued)

DARS PARAMETER NUMBER	INSTRUMENT IDENTIFIER	QUALIFICATION	START TIME	STOP TIME
111	SPND 31NEUT 180	QUALIFIED	01/13 13:30: 0.0	01/14 11:00: 0.0
		QUALIFIED	01/14 18:30: 0.0	01/17 10:00: 0.0
		QUALIFIED	01/17 15:00: 0.0	01/19 14:30: 0.0
		QUALIFIED	01/19 15:45: 0.0	01/22 21:00: 0.0
		QUALIFIED	02/05 15:00: 0.0	02/06 10:00: 0.0
		QUALIFIED	02/07 00:00: 0.0	02/07 22:00: 0.0
117	STEAMTMP225 154	QUALIFIED	02/07 20:30: 0.0	02/07 22:00: 0.0
118	STEAMTMP225 235	QUALIFIED	02/07 20:30: 0.0	02/07 22:00: 0.0
119	BUNDLE WTR LVL	FAILED	02/06 02:00: 0.0	02/06 06:50: 0.0
		QUALIFIED	02/06 06:50: 0.0	02/06 09:12: 0.0
		FAILED	02/06 09:12: 0.0	02/06 10:00: 0.0
		QUALIFIED	02/07 14:00: 0.0	02/07 20:58:40.0
		FAILED	02/07 20:58:40.0	02/07 22:00: 0.0
120	SHROUD PRESS TT	QUALIFIED	02/07 20:30: 0.0	02/07 22:00: 0.0
121	DIFFPRESBDLESHRD	QUALIFIED	02/07 20:30: 0.0	02/07 21:25: 0.0
		FAILED	02/07 21:25: 0.0	02/07 22:00: 0.0
123	SPND 31GAMA 000	QUALIFIED	01/13 13:30: 0.0	01/14 11:00: 0.0
		QUALIFIED	01/14 18:30: 0.0	01/17 10:00: 0.0
		QUALIFIED	01/17 15:00: 0.0	01/19 14:30: 0.0
		QUALIFIED	01/19 15:45: 0.0	01/22 21:00: 0.0
		QUALIFIED	02/05 15:00: 0.0	02/06 10:00: 0.0
		QUALIFIED	02/07 00:00: 0.0	02/07 22:00: 0.0
124	SPND 31NEUT 000	QUALIFIED	01/13 13:30: 0.0	01/14 11:00: 0.0
		QUALIFIED	01/14 18:30: 0.0	01/17 10:00: 0.0
		QUALIFIED	01/17 15:00: 0.0	01/19 14:30: 0.0
		QUALIFIED	01/19 15:45: 0.0	01/22 21:00: 0.0
		QUALIFIED	02/05 15:00: 0.0	02/06 10:00: 0.0
		QUALIFIED	02/07 00:00: 0.0	02/07 22:00: 0.0
127	FP 820AAEROSIG	QUALIFIED	02/07 20:30: 0.0	02/07 21:04:35.0
		TREND	02/07 21:04:35.0	02/07 21:26: 5.0
		QUALIFIED	02/07 21:26: 5.0	02/08 03:00: 0.0
129	FLOWRATEBY PASS	QUALIFIED	02/07 20:30: 0.0	02/07 22:00: 0.0
130	FP 820B AEROSIG	QUALIFIED	02/07 20:30: 0.0	02/07 21:05: 0.0
		QUALIFIED	02/07 21:05: 0.0	02/07 21:28:20.0
		QUALIFIED	02/07 21:28:20.0	02/08 03:00: 0.0
133	FP TEMPINLET	QUALIFIED	02/07 20:30: 0.0	02/08 03:00: 0.0
134	FP TEMPCONDENSR	QUALIFIED	02/07 20:30: 0.0	02/08 03:00: 0.0
135	FP PRESSPT13-42	QUALIFIED	02/06 02:00: 0.0	02/06 10:00: 0.0
		QUALIFIED	02/07 14:00: 0.0	02/08 03:00: 0.0
141	FPGAMIONSTEAMLIN	TREND	02/07 20:30: 0.0	02/08 03:00: 0.0
142	FPGAMIONSTEAMSPL	TREND	02/07 20:30: 0.0	02/08 03:00: 0.0
143	FP HYDR CONCENT	QUALIFIED	02/07 20:30: 0.0	02/08 03:00: 0.0
148	FP FLOWFT13-69	QUALIFIED	02/07 20:30: 0.0	02/08 03:00: 0.0
149	BLOW LEVLIT17 PT	QUALIFIED	02/07 20:30: 0.0	02/08 03:00: 0.0

Table C-1. (continued)

DARS PARAMETER NUMBER	INSTRUMENT IDENTIFIER	QUALIFICATION	START TIME	STOP TIME
151	BLOWPRESPT12 PT	QUALIFIED	02/07 20:30: 0.0	02/08 03:00: 0.0
152	FPDSFLOWCOND IN	TREND TREND	02/06 02:00: 0.0 02/07 14:00: 0.0	02/06 10:00: 0.0 02/08 03:00: 0.0
153	FPDSFLOWCOND OUT	TREND TREND	02/06 02:00: 0.0 02/07 14:00: 0.0	02/06 10:00: 0.0 02/08 03:00: 0.0
156	STTUBTMPWL090184	QUALIFIED	02/07 20:30: 0.0	02/07 22:00: 0.0
167	STTUBTMPWL270184	TREND	02/07 20:30: 0.0	02/07 22:00: 0.0
169	STTUBTMPWL090229	QUALIFIED	02/07 20:30: 0.0	02/07 22:00: 0.0
170	STTUBTMPWL270229	FAILED	02/07 20:30: 0.0	02/07 22:00: 0.0
171	STTUBTMPWL090283	FAILED	02/07 20:30: 0.0	02/07 22:00: 0.0
173	STTUBTMPWL270283	QUALIFIED	02/07 20:30: 0.0	02/07 22:00: 0.0
174	STTUBTMPWL090340	QUALIFIED	02/07 20:30: 0.0	02/07 22:00: 0.0
175	STTUBTMPWL270340	QUALIFIED	02/07 20:30: 0.0	02/07 22:00: 0.0
187	FLOWRATEBNDHIOUT	FAILED FAILED QUALIFIED QUALIFIED FAILED QUALIFIED QUALIFIED QUALIFIED	01/13 13:30: 0.0 01/14 18:30: 0.0 01/17 15:00: 0.0 01/19 15:45: 0.0 01/19 22:41:40.0 01/20 02:51:40.0 02/05 15:00: 0.0 02/07 00:00: 0.0	01/14 11:00: 0.0 01/17 10:00: 0.0 01/19 14:30: 0.0 01/19 22:41:40.0 01/20 02:51:40.0 01/22 21:00: 0.0 02/06 10:00: 0.0 02/07 20:30: 0.0
188	DIFFPRESBDLE SEP	QUALIFIED QUALIFIED	02/06 02:00: 0.0 02/07 14:00: 0.0	02/06 10:00: 0.0 02/08 03:00: 0.0
195	COUPTEMPFPDS 157	QUALIFIED	02/07 20:30: 0.0	02/08 03:00: 0.0
196	COUPTEMPFPDS 238	QUALIFIED	02/07 20:30: 0.0	02/08 03:00: 0.0
207	COUPTEMPFPDS 340	QUALIFIED	02/07 20:30: 0.0	02/08 03:00: 0.0
209	BYP TEMP000 -31	QUALIFIED	02/07 20:30: 0.0	02/07 22:00: 0.0
210	BYP TEMP090 -31	QUALIFIED	02/07 20:30: 0.0	02/07 22:00: 0.0
211	BYP TEMP180 -31	QUALIFIED	02/07 20:30: 0.0	02/07 22:00: 0.0
213	FP GAMMASTEAM	TREND	02/07 20:30: 0.0	02/08 03:00: 0.0
214	FP GAMMALIQUID	TREND	02/07 20:30: 0.0	02/08 03:00: 0.0
215	FP GAMMAGAS	TREND	02/07 20:30: 0.0	02/08 03:00: 0.0

Table C-1. (continued)

DARS PARAMETER NUMBER	INSTRUMENT IDENTIFIER	QUALIFICATION	START TIME	STOP TIME
219	FLOWRATEBNDHI IN	QUALIFIED	01/13 13:30: 0.0	01/14 11:00: 0.0
		QUALIFIED	01/14 18:30: 0.0	01/17 10:00: 0.0
		QUALIFIED	01/17 15:00: 0.0	01/19 14:30: 0.0
		QUALIFIED	01/19 15:45: 0.0	01/22 21:00: 0.0
		QUALIFIED	02/05 15:00: 0.0	02/06 02:31:40.0
		FAILED	02/06 02:31:40.0	02/06 10:00: 0.0
		QUALIFIED	02/07 00:00: 0.0	02/07 13:13:20.0
		FAILED	02/07 13:13:20.0	02/07 13:32: 0.0
		QUALIFIED	02/07 13:32: 0.0	02/07 17:43: 0.0
		FAILED	02/07 17:43: 0.0	02/08 03:00: 0.0
225	INLTTEMP105 -36	QUALIFIED	01/13 13:30: 0.0	01/14 11:00: 0.0
		QUALIFIED	01/14 18:30: 0.0	01/17 10:00: 0.0
		QUALIFIED	01/17 15:00: 0.0	01/19 14:30: 0.0
		QUALIFIED	01/19 15:45: 0.0	01/22 21:00: 0.0
		QUALIFIED	02/05 15:00: 0.0	02/06 10:00: 0.0
		QUALIFIED	02/07 00:00: 0.0	02/07 22:00: 0.0
226	INLTTEMP232 -36	QUALIFIED	01/13 13:30: 0.0	01/14 11:00: 0.0
		QUALIFIED	01/14 18:30: 0.0	01/17 10:00: 0.0
		QUALIFIED	01/17 15:00: 0.0	01/19 14:30: 0.0
		QUALIFIED	01/19 15:45: 0.0	01/22 21:00: 0.0
		QUALIFIED	02/05 15:00: 0.0	02/06 10:00: 0.0
		QUALIFIED	02/07 00:00: 0.0	02/07 21.15:15.0
		FAILED	02/07 21:15:15.0	02/07 21:15:55.0
		QUALIFIED	02/07 21:15:55.0	02/07 22:00: 0.0
227	FP NEUT DETECTOR	TREND	02/07 20:30: 0.0	02/08 03:00: 0.0
228	BYP TEMP270 -31	QUALIFIED	02/07 20:30: 0.0	02/07 22:00: 0.0
229	BYP TEMP000 114	QUALIFIED	02/07 20:30: 0.0	02/07 22:00: 0.0
231	BYP TEMP090 114	QUALIFIED	02/07 20:30: 0.0	02/07 22:00: 0.0
232	BYP TEMP180 114	QUALIFIED	02/07 20:30: 0.0	02/07 22:00: 0.0
233	BYP TEMP270 114	QUALIFIED	02/07 20:30: 0.0	02/07 22:00: 0.0
237	INLTTEMP322 -36	QUALIFIED	01/13 13:30: 0.0	01/14 11:00: 0.0
		QUALIFIED	01/14 18:30: 0.0	01/17 10:00: 0.0
		QUALIFIED	01/17 15:00: 0.0	01/19 14:30: 0.0
		QUALIFIED	01/19 15:45: 0.0	01/22 21:00: 0.0
		QUALIFIED	02/05 15:00: 0.0	02/06 10:00: 0.0
		QUALIFIED	02/07 00:00: 0.0	02/07 21:19:40.0
		FAILED	02/07 21:19:40.0	02/07 22:00: 0.0
238	FP 820BAERO REF	FAILED	02/07 20:30: 0.0	02/08 03:00: 0.0
253	FP 800AAEROREF	FAILED	02/07 20:30: 0.0	02/08 03:00: 0.0

Table C-2. Time spans for various phases of Test SFD 1-4

Phase	Time From	Time To
Power calibration	1/13/85:13:30:00.0	1/14/85:11:00:00.0
Preconditioning No. 1	1/14/85:18:30:00.0	1/17/85:10:00:00.0
Preconditioning No. 2	1/17/85:15:00:00.0	1/19/85:14:30:00.0
Preconditioning No. 3	1/19/15:45:00:00.0	1/22/85:21:00:00.0
Fission buildup No. 1	2/05/15:00:00:00.0	2/06/85:02:00:00.0
Boildown No. 1	2/06/85:02:00:00.0	2/06/05:30:00:00.0
Boildown No. 2	2/06/85:05:30:00.0	2/06/85:10:00:00.0
Fission buildup No. 2	2/07/85:00:00:00.0	2/07/85:11:00:00.0
Boildown No. 3	2/07/85:14:00:00.0	2/07/85:20:30:00.0
Transient	2/07/85:20:30:00.0	2/07/85:22:00:00.0
Cooldown	2/07/85:22:00:00.0	2/07/85:03:00:00.0

calibration. Parameter No. 13 and parameter No. 188 have been corrected for an estimated 0.055-MPa pressure head difference in the separator sense line.

5. Parameter Nos. 127 and 130 are the aerosol monitor signals. These signals have a larger uncertainty as the transient progresses, due to plating out on the windows of the aerosol monitor. Parameter No. 127 is considered trend during portions of the transient because the signal has reached its lower limit (i.e. the light beam is nearly completely blocked). During this time, Parameter No. 130 should be used.

C-4. Methods of Evaluating DARS Data Uncertainties

Test parameters within the PBF in-pile tube and pressurized water loop are monitored by many types of instruments and measurement channels. A transducer and associated signal-conditioning electronics introduce uncertainty into the measurement of a specific parameter. Measurement uncertainties propagate through the experimental data to the evaluation of the analytical models and overall program results. The test measurement uncertainty analysis results are presented in this section for each measurement channel.

A measurement channel includes the transducer, signal conditioning, and DARS. The form of uncertainty presented may be either tabular, presenting the uncertainty values for a particular operating condition, or graphical, with uncertainty versus input signal from which the user can determine the uncertainty for any value within the useful range of the transducer. The uncertainty values, in either engineering units or percent of reading, are determined from the equation

$$U = [B^2 + t_{95} S^2]^{1/2} \quad \text{(C-1)}$$

where

U = total uncertainty

B = total channel systematic error (bias)

S = total channel random error (precision index)

t_{95} = two-tailed Student "t" factor for 95% confidence level.

The t_{95} factor is determined from a Student "t" table and the degrees of freedom associated with random error measurement. The bias, B, is the root-sum-square (RSS) of all the elemental biases in the measurement channel. Likewise, the precision index is the RSS of all the elemental precision indexes in the measurement channel on the data plots. The uncertainty, U, is shown for each measurement channel. The values for bias, precision index, and degrees of freedom are given as backup and for use in propagating errors for any calculated parameters based on these measurements.

Test-independent uncertainty analyses of PBF measurement systems have been performed. The methodology used in the analysis of the uncertainties is based on standard statistical practices, which are applied in evaluating the constant and variable portions of both the bias and random error components of each measurement channel. The individual error components are then combined to produce a total measurement channel uncertainty.

When a measurement channel is analyzed for test-independent measurement uncertainty, that uncertainty applies to a representative assembly of specific types of channel components rather than a specific component. If an individual component is replaced by a component of the same type, the uncertainty of the measurement channel remains unchanged.

The data qualification procedure, performed by the PBF DIRC, served to identify some of the significant test-dependent uncertainties introduced in specific tests, such as instrument mounting effects, two-phase flow regimes, and transient measurements. In some cases, additional or special calibrations, multiple instrumentation, and additional engineering calculations can result in significantly lower uncertainty estimates than those found in the uncertainty analyses. These test-dependent considerations have been factored into the total uncertainty values presented for each measurement.

C-5. DARS Data Plots

Plots of the qualified DARS data from Test SFD 1-4 are presented on microfiche cards mounted on the back cover of this report. Plot numbers and parameters are given in Table C-3. Only data categorized as "qualified" and "trend" are presented in this report. Qualified data are presented as a solid line, and trend data appear as a dashed line on the microfiche plots. In cases where part of the data on a plot is considered failed, there will be no plot lines.

The total uncertainty values presented on the data plots are error bars presenting the 95% confidence level. It should be noted that on some plots the size of the error bars is not constant. This is because uncertainties vary as a function of instrument readings or as a function of time. On some plots, there are both steady-state and transient portions of the data which have different uncertainties. Trend data have no uncertainty established for it and therefore have no error bars.

C-6. FPDS Data Qualification Procedure

C-6.1 Acquisition System Operation. The FPDS is a remotely operated system that uses injected pulser data for real-time system operational checking and for spectral data validation. Dual amplitude electronic pulser pulses are injected into each FPDS detector preamplifier at a rate of 800 pulses per second. The injected pulser events are processed through the same electronics as are the gamma-ray events, but during storage the pulser events are separated from the gamma-ray events and are stored in special pulser storage buffers. During data acquisition, the control computer interrogates these pulser buffers each 15 s and relays the result to the operator's screen, allowing the operator to determine immediately if any system component has failed. The pulser data are stored with the gamma-ray spectrum and provide for spectrum-specific gain and zero calibration and precise corrections for count-rate effects.[C-1]

C-6.2 FPDS Data Analysis. Gamma-ray spectra acquired by the FPDS were analyzed using the gamma-ray spectral analysis program GAUSS VIII.[C-2] GAUSS VIII is a fully featured

Table C-3. List of microfiche DARS data plots

PRETRANSIENT DATA

FIGURE PARAMETERS

C-1. System pressure heise during Test SFD 1-4 power calibration (SYS PRESHEISE PT - Parameter 72).

C-2. Lower test train system pressure 69 MPa during Test SFD 1-4 power calibration (SYS PRES69EG LTT - Parameter 37).

C-3. Lower test train system pressure 17 MPa during Test SFD 1-4 power calibration (SYS PRES17EG LTT - Parameter 38).

C-4. System pressure in the bundle during Test SFD 1-4 power calibration (SYS PRESBUNDLETT - Parameter 39).

C-5. Bundle inlet flow rate high flow transducer during Test SFD 1-4 power calibration (FLOWRATEBNDHI IN - Parameter 219).

C-6. Bundle coolant inlet temperature at -0.36m and 15 degrees during Test SFD 1-4 power calibration (INLTTEMP015 -36 - Parameter 43).

C-7. Bundle coolant inlet temperature at -0.36m and 135 degrees during Test SFD 1-4 power calibration (INLTTEMP135 -36 - Parameter 59).

C-8. Bundle coolant inlet temperature at -0.36m and 105 degrees during Test SFD 1-4 power calibration (INLTTEMP105 -36 - Parameter 225).

C-9. Bundle coolant inlet temperature at -0.36m and 232 degrees during Test SFD 1-4 power calibration (INLTTEMP232 -36 - Parameter 226).

C-10. Bundle coolant inlet temperature at -0.36m and 322 degrees during Test SFD 1-4 power calibration (INLTTEMP322 -36 - Parameter 237).

C-11. Bundle coolant differential temperature at 30 degrees during Test SFD 1-4 power calibration (DEL TEMPBNDLE030 - Parameter 47).

C-12. Bundle coolant differential temperature at 210 degrees during Test SFD 1-4 power calibration (DEL TEMPBNDLE210 - Parameter 48).

C-13. Bundle coolant differential temperature at 300 degrees during Test SFD 1-4 power calibration (DEL TEMPBNDLE300 - Parameter 49).

C-14. Bundle coolant differential temperature at 330 degrees during Test SFD 1-4 power calibration (DEL TEMPBNDLE330 - Parameter 60).

Table C-3. (continued)

C-15. Reactor power Ion chamber PPS-01 during Test SFD 1-4 power calibration (REAC POWPPS-01PT - Parameter 53). .....

C-16. Reactor power Ion chamber PPS-02 during Test SFD 1-4 power calibration (REAC POWPPS-02PT - Parameter 54). .....

C-17. Reactor power Ion chamber NMS-03 during Test SFD 1-4 power calibration (REAC POWNMS-03PT - Parameter 21). .....

C-18. Reactor power Ion chamber NMS-04 during Test SFD 1-4 power calibration (REAC POWNMS-04PT - Parameter 22). .....

C-19. Fission chamber at 0.83m and 90 degrees DC signal during Test SFD 1-4 power calibration (FISSCHAM090 DC83 - Parameter 1). ....

C-20. Fission chamber at 0.51m and 90 degrees DC signal during Test SFD 1-4 power calibration (FISSCHAM090 DC51 - Parameter 2). ....

C-21. Fission chamber at 0.25m and 90 degrees DC signal during Test SFD 1-4 power calibration (FISSCHAM090 DC25 - Parameter 3). ....

C-22. Fission chamber at 0.05m and 90 degrees DC signal during Test SFD 1-4 power calibration (FISSCHAM090 DC05 - Parameter 5). ....

C-23. Fission chamber at 0.67m and 270 degrees DC signal during Test SFD 1-4 power calibration (FISSCHAM270 DC67 - Parameter 6). ....

C-24. Fission chamber at 0.35m and 270 degrees DC signal during Test SFD 1-4 power calibration (FISSCHAM270 DC35 - Parameter 7). ....

C-25. Steam temperature at 1.14m and 210 degrees during Test SFD 1-4 power calibration (STEAMTMP210 114 - Parameter 65). ....

C-26. Steam temperature at 1.14m and 30 degrees during Test SFD 1-4 power calibration (STEAMTMP030 114 - Parameter 82). ....

C-27. Steam temperature at 1.14m and 300 degrees during Test SFD 1-4 power calibration (STEAMTMP300 114 - Parameter 83). ....

C-28. Self-powered neutron detector at 0.31m and 180o gamma signal during Test SFD 1-4 power calibration (SPND 31GAMA 180 - Parameter 110). ....

C-29. Self-powered neutron detector at 0.31m and 180o neutron signal during Test SFD 1-4 power calibration (SPND 31NEUT 180 - Parameter 111). ....

C-30. Self-powered neutron detector at 0.31m and 0o gamma signal during Test SFD 1-4 power calibration (SPND 31GAMA 000 - Parameter 123). ....

C-31. Self-powered neutron detector at 0.31m and 0o neutron signal during Test SFD 1-4 power calibration (SPND 31NEUT 000 - Parameter 124). ....

Table C-3. (continued)

C-32. System pressure heise during Test SFD 1-4 first power history (SYS PRESHEISE PT - Parameter 72). ....

C-33. Lower test train system pressure 17 MPa during Test SFD 1-4 first power history (SYS PRES17EG LTT - Parameter 38). ....

C-34. System pressure in the bundle during Test SFD 1-4 first power history (SYS PRESBUNDLETT - Parameter 39). ....

C-35. Bundle inlet flow rate high flow transducer during Test SFD 1-4 first power history (FLOWRATEBNDHI IN - Parameter 219). ....

C-36. Bundle coolant inlet temperature at -0.36m and 15 degrees during Test SFD 1-4 first power history (INLTTEMP015 -36 - Parameter 43). ....

C-37. Bundle coolant inlet temperature at -0.36m and 135 degrees during Test SFD 1-4 first power history (INLTTEMP135 -36 - Parameter 59). ....

C-38. Bundle coolant inlet temperature at -0.36m and 105 degrees during Test SFD 1-4 first power history (INLTTEMP105 -36 - Parameter 225). ....

C-39. Bundle coolant inlet temperature at -0.36m and 232 degrees during Test SFD 1-4 first power history (INLTTEMP232 -36 - Parameter 226). ....

C-40. Bundle coolant inlet temperature at -0.36m and 322 degrees during Test SFD 1-4 first power history (INLTTEMP322 -36 - Parameter 237). ....

C-41. Bundle coolant differential temperature at 30 degrees during Test SFD 1-4 first power history (DEL TEMPBNDLE030 - Parameter 47). ....

C-42. Bundle coolant differential temperature at 210 degrees during Test SFD 1-4 first power history (DEL TEMPBNDLE210 - Parameter 48). ....

C-43. Bundle coolant differential temperature at 330 degrees during Test SFD 1-4 first power history (DEL TEMPBNDLE330 - Parameter 60). ....

C-44. Reactor power Ion chamber PPS-01 during Test SFD 1-4 first power history (REAC POWPPS-01PT - Parameter 53). ...

C-45. Reactor power Ion chamber PPS-02 during Test SFD 1-4 first power history (REAC POWPPS-02PT - Parameter 54). ...

C-46. Reactor power Ion chamber NMS-03 during Test SFD 1-4 first power history (REAC POWNMS-03PT - Parameter 21). ...

C-47. Reactor power Ion chamber NMS-04 during Test SFD 1-4 first power history (REAC POWNMS-04PT - Parameter 22). ...

C-48. Fission chamber at 0.83m and 90 degrees DC signal during Test SFD 1-4 first power history (FISSCHAM090 DC83 - Parameter 1). ....

Table C-3. (continued)

C-49. Fission chamber at 0.51m and 90 degrees DC signal during Test SFD 1-4 first power history (FISSCHAM090 DC51 - Parameter 2). ....

C-50. Fission chamber at 0.25m and 90 degrees DC signal during Test SFD 1-4 first power history (FISSCHAM090 DC25 - Parameter 3). ....

C-51. Fission chamber at 0.05m and 90 degrees DC signal during Test SFD 1-4 first power history (FISSCHAM090 DC05 - Parameter 5). ....

C-52. Fission chamber at 0.67m and 270 degrees DC signal during Test SFD 1-4 first power history (FISSCHAM270 DC67 - Parameter 6). ....

C-53. Fission chamber at 0.35m and 270 degrees DC signal during Test SFD 1-4 first power history (FISSCHAM270 DC35 - Parameter 7). ....

C-54. Fission chamber at 0.15m and 270 degrees DC signal during Test SFD 1-4 first power history (FISSCHAM090 DC15 - Parameter 9). ....

C-55. Fission chamber at -0.05m and 270 degrees DC signal during Test SFD 1-4 first power history (FISSCHAM270 D-05 - Parameter 10). ....

C-56. Steam temperature at 1.14m and 210 degrees during Test SFD 1-4 first power history (STEAMTMP210 114 - Parameter 65). ....

C-57. Steam temperature at 1.14m and 330 degrees during Test SFD 1-4 first power history (STEAMTMP330 114 - Parameter 6 6). ....

C-58. Steam temperature at 1.14m and 30 degrees during Test SFD 1-4 first power history (STEAMTMP030 114 - Parameter 82). ....

C-59. Steam temperature at 1.14m and 300 degrees during Test SFD 1-4 first power history (STEAMTMP300 114 - Parameter 83). ....

C-60. Self-powered neutron detector at 0.31m and 180o gamma signal during Test SFD 1-4 first power history (SPND 31GAMA 180 - Parameter 110). ....

C-61. Self-powered neutron detector at 0.31m and 180o neutron signal during Test SFD 1-4 first power history (SPND 31NEUT 180 - Parameter 111). ....

C-62. Self-powered neutron detector at 0.31m and 0o gamma signal during Test SFD 1-4 first power history (SPND 31GAMA 000 - Parameter 123). ....

C-63. Self-powered neutron detector at 0.31m and 0o neutron signal during Test SFD 1-4 first power history (SPND 31NEUT 000 - Parameter 124). ....

C-64. System pressure heise during Test SFD 1-4 second power history (SYS PRESHEISE PT - Parameter 72). ....

Table C-3. (continued)

C-65. Lower test train system pressure 69 MPa during Test SFD 1-4 second power history (SYS PRES69EG LTT - Parameter 37). ....

C-66. Lower test train system pressure 17 MPa during Test SFD 1-4 second power history (SYS PRES17EG LTT - Parameter 38). ....

C-67. System pressure in the bundle during Test SFD 1-4 second power history (SYS PRESBUNDLETT - Parameter 39). ....

C-68. Bundle inlet flow rate high flow transducer during Test SFD 1-4 second power history (FLOWRATEBNDHI IN - Parameter 219). ....

C-69. Bundle coolant outlet flow rate during Test SFD 1-4 second power history (FLOWRATEBNDHIOUT - Parameter 187). ....

C-70. Bundle coolant inlet temperature at -0.36m and 15 degrees during Test SFD 1-4 second power history (INLTTEMP015 -36 - Parameter 43). ....

C-71. Bundle coolant inlet temperature at -0.36m and 135 degrees during Test SFD 1-4 second power history (INLTTEMP135 -36 - Parameter 59). ....

C-72. Bundle coolant inlet temperature at -0.36m and 105 degrees during Test SFD 1-4 second power history (INLTTEMP105 -36 - Parameter 225). ....

C-73. Bundle coolant inlet temperature at -0.36m and 232 degrees during Test SFD 1-4 second power history (INLTTEMP232 -36 - Parameter 226). ....

C-74. Bundle coolant inlet temperature at -0.36m and 322 degrees during Test SFD 1-4 second power history (INLTTEMP322 -36 - Parameter 237). ....

C-75. Bundle coolant differential temperature at 30 degrees during Test SFD 1-4 second power history (DEL TEMPBNDLE030 - Parameter 47). ....

C-76. Bundle coolant differential temperature at 210 degrees during Test SFD 1-4 second power history (DEL TEMPBNDLE210 - Parameter 48). ....

C-77. Bundle coolant differential temperature at 300 degrees during Test SFD 1-4 second power history (DEL TEMPBNDLE300 - Parameter 49). ....

C-78. Bundle coolant differential temperature at 330 degrees during Test SFD 1-4 second power history (DEL TEMPBNDLE330 - Parameter 60). ....

C-79. Reactor power Ion chamber PPS-01 during Test SFD 1-4 second power history (REAC POWPPS-01PT - Parameter 53). ....

C-80. Reactor power Ion chamber PPS-02 during Test SFD 1-4 second power history (REAC POWPPS-02PT - Parameter 54). ....

Table C-3. (continued)

C-81. Reactor power Ion chamber NMS-03 during Test SFD 1-4 second power history (REAC POWNMS-03PT - Parameter 21). ....

C-82. Reactor power Ion chamber NMS-04 during Test SFD 1-4 second power history (REAC POWNMS-04PT - Parameter 22). ....

C-83. Fission chamber at 0.83m and 90 degrees DC signal during Test SFD 1-4 second power history (FISSCHAM090 DC83 - Parameter 1). ....

C-84. Fission chamber at 0.51m and 90 degrees DC signal during Test SFD 1-4 second power history (FISSCHAM090 DC51 - Parameter 2). ....

C-85. Fission chamber at 0.25m and 90 degrees DC signal during Test SFD 1-4 second power history (FISSCHAM090 DC25 - Parameter 3). ....

C-86. Fission chamber at 0.05m and 90 degrees DC signal during Test SFD 1-4 second power history (FISSCHAM090 DC05 - Parameter 5). ....

C-87. Fission chamber at 0.67m and 270 degrees DC signal during Test SFD 1-4 second power history (FISSCHAM270 DC67 - Parameter 6). ....

C-88. Fission chamber at 0.35m and 270 degrees DC signal during Test SFD 1-4 second power history (FISSCHAM270 DC35 - Parameter 7). ....

C-89. Fission chamber at 0.15m and 270 degrees DC signal during Test SFD 1-4 second power history (FISSCHAM090 DC15 - Parameter 9). ....

C-90. Fission chamber at -0.05m and 270 degrees DC signal during Test SFD 1-4 second power history (FISSCHAM270 D-05 - Parameter 10). ....

C-91. Steam temperature at 1.14m and 210 degrees during Test SFD 1-4 second power history (STEAMTMP210 114 - Parameter 65). ....

C-92. Steam temperature at 1.14m and 330 degrees during Test SFD 1-4 second power history (STEAMTMP330 114 - Parameter 66). ....

C-93. Steam temperature at 1.14m and 30 degrees during Test SFD 1-4 second power history (STEAMTMP030 114 - Parameter 82). ....

C-94. Steam temperature at 1.14m and 300 degrees during Test SFD 1-4 second power history (STEAMTMP300 114 - Parameter 83). ....

C-95. Self-powered neutron detector at 0.31m and 180o gamma signal during Test SFD 1-4 second power history (SPND 31GAMA 180 - Parameter 110). ....

C-96. Self-powered neutron detector at 0.31m and 180o neutron signal during Test SFD 1-4 second power history (SPND 31NEUT 180 - Parameter 111). ....

Table C-3. (continued)

C-97. Self-powered neutron detector at 0.31m and 0o gamma signal during Test SFD 1-4 second power history (SPND 31GAMA 000 - Parameter 123). ....

C-98. Self-powered neutron detector at 0.31m and 0o neutron signal during Test SFD 1-4 second power history (SPND 31NEUT 000 - Parameter 124). ....

C-99. System pressure heise during Test SFD 1-4 third power history (SYS PRESHEISE PT - Parameter 72). ....

C-100. Lower test train system pressure 17 MPa during Test SFD 1-4 third power history (SYS PRES17EG LTT - Parameter 38). ....

C-101. System pressure in the bundle during Test SFD 1-4 third power history (SYS PRESBUNDLETT - Parameter 39). ....

C-102. Bundle inlet flow rate high flow transducer during Test SFD 1-4 third power history (FLOWRATEBNDHI IN - Parameter 219). ....

C-103. Bundle coolant outlet flow rate during Test SFD 1-4 third power history (FLOWRATEBNDHIOUT - Parameter 187). ....

C-104. Bundle coolant inlet temperature at -0.36m and 15 degrees during Test SFD 1-4 third power history (INLTTEMP015 -36 - Parameter 43). ....

C-105. Bundle coolant inlet temperature at -0.36m and 135 degrees during Test SFD 1-4 third power history (INLTTEMP135 -36 - Parameter 59). ....

C-106. Bundle coolant inlet temperature at -0.36m and 105 degrees during Test SFD 1-4 third power history (INLTTEMP105 -36 - Parameter 225). ....

C-107. Bundle coolant inlet temperature at -0.36m and 232 degrees during Test SFD 1-4 third power history (INLTTEMP232 -36 - Parameter 226). ....

C-108. Bundle coolant inlet temperature at -0.36m and 322 degrees during Test SFD 1-4 third power history (INLTTEMP322 -36 - Parameter 237). ....

C-109. Bundle coolant differential temperature at 30 degrees during Test SFD 1-4 third power history (DEL TEMPBNDLE030 - Parameter 47). ....

C-110. Bundle coolant differential temperature at 210 degrees during Test SFD 1-4 third power history (DEL TEMPBNDLE210 - Parameter 48). ....

C-111. Bundle coolant differential temperature at 300 degrees during Test SFD 1-4 third power history (DEL TEMPBNDLE300 - Parameter 49). ....

C-112. Bundle coolant differential temperature at 330 degrees during Test SFD 1-4 third power history (DEL TEMPBNDLE330 - Parameter 60). ....

Table C-3. (continued)

C-113. Reactor power Ion chamber PPS-01 during Test SFD 1-4 third power history (REAC POWPPS-01PT - Parameter 53). ...

C-114. Reactor power Ion chamber PPS-02 during Test SFD 1-4 third power history (REAC POWPPS-02PT - Parameter 54). ...

C-115. Reactor power Ion chamber NMS-03 during Test SFD 1-4 third power history (REAC POWNMS-03PT - Parameter 21). ...

C-116. Reactor power Ion chamber NMS-04 during Test SFD 1-4 third power history (REAC POWNMS-04PT - Parameter 22). ...

C-117. Fission chamber at 0.83m and 90 degrees DC signal during Test SFD 1-4 third power history (FISSCHAM090 DC83 - Parameter 1). ....

C-118. Fission chamber at 0.51m and 90 degrees DC signal during Test SFD 1-4 third power history (FISSCHAM090 DC51 - Parameter 2). ....

C-119. Fission chamber at 0.25m and 90 degrees DC signal during Test SFD 1-4 third power history (FISSCHAM090 DC25 - Parameter 3). ....

C-120. Fission chamber at 0.05m and 90 degrees DC signal during Test SFD 1-4 third power history (FISSCHAM090 DC05 - Parameter 5). ....

C-121. Fission chamber at 0.67m and 270 degrees DC signal during Test SFD 1-4 third power history (FISSCHAM270 DC67 - Parameter 6). ....

C-122. Fission chamber at 0.35m and 270 degrees DC signal during Test SFD 1-4 third power history (FISSCHAM270 DC35 - Parameter 7). ....

C-123. Fission chamber at 0.15m and 270 degrees DC signal during Test SFD 1-4 third power history (FISSCHAM090 DC15 - Parameter 9). ....

C-124. Fission chamber at -0.05m and 270 degrees DC signal during Test SFD 1-4 third power history (FISSCHAM270 D-05 - Parameter 10). ....

C-125. Steam temperature at 1.14m and 210 degrees during Test SFD 1-4 third power history (STEAMTMP210 114 - Parameter 65). ....

C-126. Steam temperature at 1.14m and 330 degrees during Test SFD 1-4 third power history (STEAMTMP330 114 - Parameter 6 6). ....

C-127. Steam temperature at 1.14m and 30 degrees during Test SFD 1-4 third power history (STEAMTMP030 114 - Parameter 82). ....

C-128. Steam temperature at 1.14m and 300 degrees during Test SFD 1-4 third power history (STEAMTMP300 114 - Parameter 83). ....

C-129. Self-powered neutron detector at 0.31m and 180o gamma signal during Test SFD 1-4 third power history (SPND 31GAMA 180 - Parameter 110). ....

Table C-3. (continued)

C-130. Self-powered neutron detector at 0.31m and 180o neutron signal during Test SFD 1-4 third power history (SPND 31NEUT 180 - Parameter 111). ....

C-131. Self-powered neutron detector at 0.31m and 0o gamma signal during Test SFD 1-4 third power history (SPND 31GAMA 000 - Parameter 123). ....

C-132. Self-powered neutron detector at 0.31m and 0o neutron signal during Test SFD 1-4 third power history (SPND 31NEUT 000 - Parameter 124). ....

C-133. System pressure heise during Test SFD 1-4 first boil down (SYS PRESHEISE PT - Parameter 72). ....

C-134. Lower test train system pressure 69 MPa during Test SFD 1-4 first boil down (SYS PRES69EG LTT - Parameter 37). ....

C-135. Lower test train system pressure 17 MPa during Test SFD 1-4 first boil down (SYS PRES17EG LTT - Parameter 38). ....

C-136. System pressure in the bundle during Test SFD 1-4 first boil down (SYS PRESBUNDLETT - Parameter 39). ....

C-137. Bundle inlet flow rate high flow transducer during Test SFD 1-4 first boil down (FLOWRATEBNDHI IN - Parameter 219). ....

C-138. Bundle coolant outlet flow rate during Test SFD 1-4 first boil down (FLOWRATEBNDHIOUT - Parameter 187). ......

C-139. Bundle coolant inlet temperature at -0.36m and 15 degrees during Test SFD 1-4 first boil down (INLTTEMP015 -36 - Parameter 43). ....

C-140. Bundle coolant inlet temperature at -0.36m and 135 degrees during Test SFD 1-4 first boil down (INLTTEMP135 -36 - Parameter 59). ....

C-141. Bundle coolant inlet temperature at -0.36m and 105 degrees during Test SFD 1-4 first boil down (INLTTEMP105 -36 - Parameter 225) . ...

C-142. Bundle coolant inlet temperature at -0.36m and 232 degrees during Test SFD 1-4 first boil down (INLTTEMP232 -36 - Parameter 226) . ...

C-143. Bundle coolant inlet temperature at -0.36m and 322 degrees during Test SFD 1-4 first boil down (INLTTEMP322 -36 - Parameter 237) . ...

C-144. Bundle coolant differential temperature at 30 degrees during Test SFD 1-4 first boil down (DEL TEMPBNDLE030 - Parameter 47). ....

C-145. Bundle coolant differential temperature at 210 degrees during Test SFD 1-4 first boil down (DEL TEMPBNDLE210 - Parameter 48). ....

Table C-3. (continued)

C-146. Bundle coolant differential temperature at 330 degrees during Test SFD 1-4 first boil down (DEL TEMPBNDLE330 - Parameter 60). ....

C-147. Reactor power Ion chamber PPS-01 during Test SFD 1-4 first boil down (REAC POWPPS-01PT - Parameter 53). ....

C-148. Reactor power Ion chamber PPS-02 during Test SFD 1-4 first boil down (REAC POWPPS-02PT - Parameter 54). ....

C-149. Reactor power Ion chamber NMS-03 during Test SFD 1-4 first boil down (REAC POWNMS-03PT - Parameter 21). ....

C-150. Reactor power Ion chamber NMS-04 during Test SFD 1-4 first boil down (REAC POWNMS-04PT - Parameter 22). ....

C-151. Fission chamber at 0.83m and 90 degrees DC signal during Test SFD 1-4 first boil down (FISSCHAM090 DC83 - Parameter 1). ....

C-152. Fission chamber at 0.51m and 90 degrees DC signal during Test SFD 1-4 first boil down (FISSCHAM090 DC51 - Parameter 2). ....

C-153. Fission chamber at 0.25m and 90 degrees DC signal during Test SFD 1-4 first boil down (FISSCHAM090 DC25 - Parameter 3). ....

C-154. Fission chamber at 0.05m and 90 degrees DC signal during Test SFD 1-4 first boil down (FISSCHAM090 DC05 - Parameter 5). ....

C-155. Fission chamber at 0.67m and 270 degrees DC signal during Test SFD 1-4 first boil down (FISSCHAM270 DC67 - Parameter 6). ....

C-156. Fission chamber at 0.35m and 270 degrees DC signal during Test SFD 1-4 first boil down (FISSCHAM270 DC35 - Parameter 7). ....

C-157. Fission chamber at 0.15m and 270 degrees DC signal during Test SFD 1-4 first boil down (FISSCHAM090 DC15 - Parameter 9). ....

C-158. Fission chamber at -0.05m and 270 degrees DC signal during Test SFD 1-4 first boil down (FISSCHAM270 D-05 - Parameter 10). ....

C-159. Fission chamber at 0.83m and 90 degrees AC signal during Test SFD 1-4 first boil down (FISSCHAM090 AC83 - Parameter 29). ....

C-160. Fission chamber at 0.51m and 90 degrees AC signal during Test SFD 1-4 first boil down (FISSCHAM090 AC51 - Parameter 19). ....

C-161. Fission chamber at 0.25m and 90 degrees AC signal during Test SFD 1-4 first boil down (FISSCHAM090 AC25 - Parameter 31). ....

C-162. Fission chamber at 0.05m and 90 degrees AC signal during Test SFD 1-4 first boil down (FISSCHAM090 AC05 - Parameter 32). ....

Table C-3. (continued)

C-163. Fission chamber at 0.67m and 270 degrees AC signal during Test SFD 1-4 first boil down (FISSCHAM270 AC67 - Parameter 33).

C-164. Fission chamber at 0.35m and 270 degrees AC signal during Test SFD 1-4 first boil down (FISSCHAM270 AC35 - Parameter 34).

C-165. Fission chamber at 0.15m and 270 degrees AC signal during Test SFD 1-4 first boil down (FISSCHAM270 AC15 - Parameter 35).

C-166. Fission chamber at -0.05m and 270 degrees AC signal during Test SFD 1-4 first boil down (FISSCHAM270 A-05 - Parameter 36).

C-167. Steam temperature at 1.14m and 210 degrees during Test SFD 1-4 first boil down (STEAMTMP210 114 - Parameter 65).

C-168. Steam temperature at 1.14m and 330 degrees during Test SFD 1-4 first boil down (STEAMTMP330 114 - Parameter 66).

C-169. Steam temperature at 1.14m and 30 degrees during Test SFD 1-4 first boil down (STEAMTMP030 114 - Parameter 82).

C-170. Steam temperature at 1.14m and 300 degrees during Test SFD 1-4 first boil down (STEAMTMP300 114 - Parameter 83).

C-171. Fuel rod 3B cladding inner surface temperature at 0.39m and 135 degrees during Test SFD 1-4 first boil down (CLADTEMP135 393B - Parameter 67).

C-172. Fuel rod 4D cladding inner surface temperature at 0.39m and 135 degrees during Test SFD 1-4 first boil down (CLADTEMP135 394D - Parameter 68).

C-173. Fuel rod 3B cladding inner surface temperature at 0.54m and 0 degrees during Test SFD 1-4 first boil down (CLADTEMP000 543B - Parameter 69).

C-174. Fuel rod 4D cladding inner surface temperature at 0.54m and 0 degrees during Test SFD 1-4 first boil down (CLADTEMP000 544D - Parameter 70).

C-175. Fuel rod 3B cladding inner surface temperature at 0.74m and 270 degrees during Test SFD 1-4 first boil down (CLADTEMP225 743B - Parameter 57).

C-176. Fuel rod 4D cladding inner surface temperature at 0.74m and 225 degrees during Test SFD 1-4 first boil down (CLADTEMP225 744D - Parameter 58).

C-177. Self-powered neutron detector at 0.31m and 180o gamma signal during Test SFD 1-4 first boil down (SPND 31GAMA 180 - Parameter 110).

C-178. Self-powered neutron detector at 0.31m and 180o neutron signal during Test SFD 1-4 first boil down (SPND 31NEUT 180 - Parameter 111).

Table C-3. (continued)

C-179. Self-powered neutron detector at 0.31m and 0o gamma signal during Test SFD 1-4 first boil down (SPND 31GAMA 000 - Parameter 123). ....

C-180. Self-powered neutron detector at 0.31m and 0o neutron signal during Test SFD 1-4 first boil down (SPND 31NEUT 000 - Parameter 124). ....

C-181. Bypass to bundle pressure differential during Test SFD 1-4 first boil down (DIFFPRESBYBUNDLE - Parameter 14). ....

C-182. Bundle to separator pressure differential during Test SFD 1-4 first boil down (DIFFPRESBDLE SEP - Parameter 188). ....

C-183. Water level in reactor bundle during Test SFD 1-4 first boil down (BUNDLE WTR LVL - Parameter 119) ....

C-184. Sample line flow rate into condenser during Test SFD 1-4 first boil down (FPDSFLOWCOND IN - Parameter 152) ....

C-185. Sample line flow rate out of condenser during Test SFD 1-4 first boil down (FPDSFLOWCOND OUT - Parameter 153) ....

C-186. FPDS separator vessel pressure PT13-42 during Test SFD 1-4 first boil down (FP PRESSPT13-42 - Parameter 135). ....

C-187. System pressure heise during Test SFD 1-4 second boil down (SYS PRESHEISE PT - Parameter 72). ....

C-188. Lower test train system pressure 69 MPa during Test SFD 1-4 second boil down (SYS PRES69EG LTT - Parameter 37). ....

C-189. Lower test train system pressure 17 MPa during Test SFD 1-4 second boil down (SYS PRES17EG LTT - Parameter 38). ....

C-190. System pressure in the bundle during Test SFD 1-4 second boil down (SYS PRESBUNDLETT - Parameter 39). ....

C-191. Bundle inlet flow rate high flow transducer during Test SFD 1-4 second boil down (FLOWRATEBNDHI IN - Parameter 219). ....

C-192. Bundle coolant outlet flow rate during Test SFD 1-4 second boil down (FLOWRATEBNDHIOUT - Parameter 187). .....

C-193. Bundle coolant inlet temperature at -0.36m and 15 degrees during Test SFD 1-4 second boil down (INLTTEMP015 -36 - Parameter 43) . ...

C-194. Bundle coolant inlet temperature at -0.36m and 135 degrees during Test SFD 1-4 second boil down (INLTTEMP135 -36 - Parameter 59) . ...

C-195. Bundle coolant inlet temperature at -0.36m and 105 degrees during Test SFD 1-4 second boil down (INLTTEMP105 -36 - Parameter 225). ....

Table C-3. (continued)

C-196. Bundle coolant inlet temperature at -0.36m and 232 degrees during Test SFD 1-4 second boil down (INLTTEMP232 -36 - Parameter 226). ....

C-197. Bundle coolant inlet temperature at -0.36m and 322 degrees during Test SFD 1-4 second boil down (INLTTEMP322 -36 - Parameter 237). ....

C-198. Bundle coolant differential temperature at 30 degrees during Test SFD 1-4 second boil down (DEL TEMPBNDLE030 - Parameter 47). ....

C-199. Bundle coolant differential temperature at 210 degrees during Test SFD 1-4 second boil down (DEL TEMPBNDLE210 - Parameter 48). ....

C-200. Bundle coolant differential temperature at 330 degrees during Test SFD 1-4 second boil down (DEL TEMPBNDLE330 - Parameter 60). ....

C-201. Reactor power Ion chamber PPS-01 during Test SFD 1-4 second boil down (REAC POWPPS-01PT - Parameter 53). ......

C-202. Reactor power Ion chamber PPS-02 during Test SFD 1-4 second boil down (REAC POWPPS-02PT - Parameter 54). ......

C-203. Reactor power Ion chamber NMS-03 during Test SFD 1-4 second boil down (REAC POWNMS-03PT - Parameter 21). ......

C-204. Reactor power Ion chamber NMS-04 during Test SFD 1-4 second boil down (REAC POWNMS-04PT - Parameter 22). ......

C-205. Fission chamber at 0.83m and 90 degrees DC signal during Test SFD 1-4 second boil down (FISSCHAM090 DC83 - Parameter 1). ....

C-206. Fission chamber at 0.51m and 90 degrees DC signal during Test SFD 1-4 second boil down (FISSCHAM090 DC51 - Parameter 2). ....

C-207. Fission chamber at 0.25m and 90 degrees DC signal during Test SFD 1-4 second boil down (FISSCHAM090 DC25 - Parameter 3). ....

C-208. Fission chamber at 0.05m and 90 degrees DC signal during Test SFD 1-4 second boil down (FISSCHAM090 DC05 - Parameter 5). ....

C-209. Fission chamber at 0.67m and 270 degrees DC signal during Test SFD 1-4 second boil down (FISSCHAM270 DC67 - Parameter 6). ....

C-210. Fission chamber at 0.35m and 270 degrees DC signal during Test SFD 1-4 second boil down (FISSCHAM270 DC35 - Parameter 7). ....

C-211. Fission chamber at 0.15m and 270 degrees DC signal during Test SFD 1-4 second boil down (FISSCHAM090 DC15 - Parameter 9). ....

C-212. Fission chamber at -0.05m and 270 degrees DC signal during Test SFD 1-4 second boil down (FISSCHAM270 D-05 - Parameter 10). ....

Table C-3. (continued)

C-213. Fission chamber at 0.83m and 90 degrees AC signal during Test SFD 1-4 second boil down (FISSCHAM090 AC83 - Parameter 29). ....

C-214. Fission chamber at 0.51m and 90 degrees AC signal during Test SFD 1-4 second boil down (FISSCHAM090 AC51 - Parameter 19). ....

C-215. Fission chamber at 0.25m and 90 degrees AC signal during Test SFD 1-4 second boil down (FISSCHAM090 AC25 - Parameter 31). ....

C-216. Fission chamber at 0.05m and 90 degrees AC signal during Test SFD 1-4 second boil down (FISSCHAM090 AC05 - Parameter 32). ....

C-217. Fission chamber at 0.67m and 270 degrees AC signal during Test SFD 1-4 second boil down (FISSCHAM270 AC67 - Parameter 33). ....

C-218. Fission chamber at 0.35m and 270 degrees AC signal during Test SFD 1-4 second boil down (FISSCHAM270 AC35 - Parameter 34). ....

C-219. Fission chamber at 0.15m and 270 degrees AC signal during Test SFD 1-4 second boil down (FISSCHAM270 AC15 - Parameter 35). ....

C-220. Fission chamber at -0.05m and 270 degrees AC signal during Test SFD 1-4 second boil down (FISSCHAM270 A-05 - Parameter 36). ....

C-221. Steam temperature at 1.14m and 210 degrees during Test SFD 1-4 second boil down (STEAMTMP210 114 - Parameter 65). ....

C-222. Steam temperature at 1.14m and 330 degrees during Test SFD 1-4 second boil down (STEAMTMP330 114 - Parameter 66). ....

C-223. Steam temperature at 1.14m and 30 degrees during Test SFD 1-4 second boil down (STEAMTMP030 114 - Parameter 82) ....

C-224. Steam temperature at 1.14m and 300 degrees during Test SFD 1-4 second boil down (STEAMTMP300 114 - Parameter 83). ....

C-225. Fuel rod 3B cladding inner surface temperature at 0.39m and 135 degrees during Test SFD 1-4 second boil down (CLADTEMP135 393B - Parameter 67). ....

C-226. Fuel rod 4D cladding inner surface temperature at 0.39m and 135 degrees during Test SFD 1-4 second boil down (CLADTEMP135 394D - Parameter 68). ....

C-227. Fuel rod 3B cladding inner surface temperature at 0.54m and 0 degrees during Test SFD 1-4 second boil down (CLADTEMP000 543B - Parameter 69). ....

C-228. Fuel rod 4D cladding inner surface temperature at 0.54m and 0 degrees during Test SFD 1-4 second boil down (CLADTEMP000 544D - Parameter 70). ....

Table C-3. (continued)

C-229.	Fuel rod 3B cladding inner surface temperature at 0.74m and 270 degrees during Test SFD 1-4 second boil down (CLADTEMP225 743B - Parameter 57).
C-230.	Fuel rod 4D cladding inner surface temperature at 0.74m and 225 degrees during Test SFD 1-4 second boil down (CLADTEMP225 744D - Parameter 58).
C-231.	Self-powered neutron detector at 0.31m and 180o gamma signal during Test SFD 1-4 second boil down (SPND 31GAMA 180 - Parameter 110).
C-232.	Self-powered neutron detector at 0.31m and 180o neutron signal during Test SFD 1-4 second boil down (SPND 31NEUT 180 - Parameter 111).
C-233.	Self-powered neutron detector at 0.31m and 0o gamma signal during Test SFD 1-4 second boil down (SPND 31GAMA 000 - Parameter 123).
C-234.	Self-powered neutron detector at 0.31m and 0o neutron signal during Test SFD 1-4 second boil down (SPND 31NEUT 000 - Parameter 124).
C-235.	Bypass to bundle pressure differential during Test SFD 1-4 second boil down (DIFFPRESBYBUNDLE - Parameter 14).
C-236.	Bundle to separator pressure differential during Test SFD 1-4 second boil down (DIFFPRESBDLE SEP - Parameter 188).
C-237.	Water level in reactor bundle during Test SFD 1-4 second boil down (BUNDLE WTR LVL - Parameter 119)
C-238.	Sample line flow rate into condenser during Test SFD 1-4 second boil down (FPDSFLOWCOND IN - Parameter 152)
C-239.	Sample line flow rate out of condenser during Test SFD 1-4 second boil down (FPDSFLOWCOND OUT - Parameter 153)
C-240.	FPDS separator vessel pressure PT13-42 during Test SFD 1-4 second boil down (FP PRESSPT13-42 - Parameter 135).

TRANSIENT AND COOL DOWN

FIGURE	PARAMETERS
C-241.	System pressure heise during Test SFD 1-4 transient (SYS PRESHEISE PT - Parameter 72).
C-242.	Lower test train system pressure 69 MPa during Test SFD 1-4 transient (SYS PRES69EG LTT - Parameter 37).
C-243.	Lower test train system pressure 17 MPa during Test SFD 1-4 transient (SYS PRES17EG LTT - Parameter 38).

Table C-3. (continued)

C-244. System pressure in the bundle during Test SFD 1-4 transient (SYS PRESBUNDLETT - Parameter 39). ....

C-245. Shroud insulation region pressure during Test SFD 1-4 transient (SHROUD PRESS TT - Parameter 120) ....

C-246. Control rod 5E internal pressure during Test SFD 1-4 transient (CR PRESS 5E - Parameter 18) ....

C-247. Bypass coolant flow rate during Test SFD 1-4 transient (FLOWRATEBY PASS - Parameter 129). ....

C-248. Bundle coolant inlet temperature at -0.36m and 15 degrees during Test SFD 1-4 transient (INLTTEMP015 -36 - Parameter 43). ....

C-249. Bundle coolant inlet temperature at -0.36m and 135 degrees during Test SFD 1-4 transient (INLTTEMP135 -36 - Parameter 59). ....

C-250. Bundle coolant inlet temperature at -0.36m and 232 degrees during Test SFD 1-4 transient (INLTTEMP232 -36 - Parameter 226). ....

C-251. Bundle coolant inlet temperature at -0.36m and 322 degrees during Test SFD 1-4 transient (INLTTEMP322 -36 - Parameter 237). ....

C-252. Bypass coolant temperature at -0.31m and 0 degrees during Test SFD 1-4 transient (BYP TEMP000 -31 - Parameter 209). ....

C-253. Bypass coolant temperature at -0.31m and 90 degrees during Test SFD 1-4 transient (BYP TEMP090 -31 - Parameter 210). ....

C-254. Bypass coolant temperature at -0.31m and 180 degrees during Test SFD 1-4 transient (BYP TEMP180 -31 - Parameter 211). ....

C-255. Bypass coolant temperature at -0.31m and 270 degrees during Test SFD 1-4 transient (BYP TEMP270 -31 - Parameter 228). ....

C-256. Bypass coolant temperature at 1.14m and 0 degrees during Test SFD 1-4 transient (BYP TEMP000 114 - Parameter 229). ....

C-257. Bypass coolant temperature at 1.14m and 90 degrees during Test SFD 1-4 transient (BYP TEMP090 114 - Parameter 231). ....

C-258. Bypass coolant temperature at 1.14m and 180 degrees during Test SFD 1-4 transient (BYP TEMP180 114 - Parameter 232). ....

C-259. Bypass coolant temperature at 1.14m and 180 degrees during Test SFD 1-4 transient (BYP TEMP270 114 - Parameter 233). ....

C-260. Bypass flow differential temperature at 180 degrees during Test SFD 1-4 transient (DEL TEMPBYP 180 - Parameter 44). ....

Table C-3. (continued)

C-261. Bypass flow differential temperature at 270 degrees during Test SFD 1-4 transient (DEL TEMPBYP 270 - Parameter 45). ....

C-262. Reactor power Ion chamber PPS-01 during Test SFD 1-4 transient (REAC POWPPS-01PT - Parameter 53). ....

C-263. Reactor power Ion chamber PPS-02 during Test SFD 1-4 transient (REAC POWPPS-02PT - Parameter 54). ....

C-264. Reactor power Ion chamber NMS-03 during Test SFD 1-4 transient (REAC POWNMS-03PT - Parameter 21). ....

C-265. Reactor power Ion chamber NMS-04 during Test SFD 1-4 transient (REAC POWNMS-04PT - Parameter 22). ....

C-266. Fission chamber at 0.83m and 90 degrees DC signal during Test SFD 1-4 transient (FISSCHAM090 DC83 - Parameter 1). ....

C-267. Fission chamber at 0.51m and 90 degrees DC signal during Test SFD 1-4 transient (FISSCHAM090 DC51 - Parameter 2). ....

C-268. Fission chamber at 0.25m and 90 degrees DC signal during Test SFD 1-4 transient (FISSCHAM090 DC25 - Parameter 3). ....

C-269. Fission chamber at 0.05m and 90 degrees DC signal during Test SFD 1-4 transient (FISSCHAM090 DC05 - Parameter 5). ....

C-270. Fission chamber at 0.67m and 270 degrees DC signal during Test SFD 1-4 transient (FISSCHAM270 DC67 - Parameter 6). ....

C-271. Fission chamber at 0.35m and 270 degrees DC signal during Test SFD 1-4 transient (FISSCHAM270 DC35 - Parameter 7). ....

C-272. Fission chamber at 0.15m and 270 degrees DC signal during Test SFD 1-4 transient (FISSCHAM090 DC15 - Parameter 9). ....

C-273. Fission chamber at -0.05m and 270 degrees DC signal during Test SFD 1-4 transient (FISSCHAM270 D-05 - Parameter 10). ....

C-274. Fission chamber at 0.83m and 90 degrees AC signal during Test SFD 1-4 transient (FISSCHAM090 AC83 - Parameter 29). ....

C-275. Fission chamber at 0.51m and 90 degrees AC signal during Test SFD 1-4 transient (FISSCHAM090 AC51 - Parameter 19). ....

C-276. Fission chamber at 0.25m and 90 degrees AC signal during Test SFD 1-4 transient (FISSCHAM090 AC25 - Parameter 31). ....

C-277. Fission chamber at 0.05m and 90 degrees AC signal during Test SFD 1-4 transient (FISSCHAM090 AC05 - Parameter 32). ....

Table C-3. (continued)

C-278. Fission chamber at 0.67m and 270 degrees AC signal during Test SFD 1-4 transient (FISSCHAM270 AC67 - Parameter 33). ....

C-279. Fission chamber at 0.35m and 270 degrees AC signal during Test SFD 1-4 transient (FISSCHAM270 AC35 - Parameter 34). ....

C-280. Fission chamber at 0.15m and 270 degrees AC signal during Test SFD 1-4 transient (FISSCHAM270 AC15 - Parameter 35). ....

C-281. Fission chamber at -0.05m and 270 degrees AC signal during Test SFD 1-4 transient (FISSCHAM270 A-05 - Parameter 36). ....

C-282. Steam temperature at 1.14m and 210 degrees during Test SFD 1-4 transient (STEAMTMP210 114 - Parameter 65). .....

C-283. Steam temperature at 1.14m and 330 degrees during Test SFD 1-4 transient (STEAMTMP330 114 - Parameter 66). .....

C-284. Steam temperature at 1.14m and 30 degrees during Test SFD 1-4 transient (STEAMTMP030 114 - Parameter 82). .....

C-285. Steam temperature at 1.14m and 300 degrees during Test SFD 1-4 transient (STEAMTMP300 114 - Parameter 83). .....

C-286. Steam temperature at 0.54m and 315 degrees near rod 5A during Test SFD 1-4 transient (STEAMTMP5A315 54 - Parameter 79). ....

C-287. Steam temperature at 0.99m and 225 degrees near rod 1B during Test SFD 1-4 transient (STEAMTMP1B225 99 - Parameter 80). ....

C-288. Steam temperature at 0.99m and 135 degrees near rod 4D during Test SFD 1-4 transient (STEAMTMP4D135 99 - Parameter 81). ....

C-289. Steam temperature at 3.36m and 225 degrees during Test SFD 1-4 transient (STEAMTMP225 336 - Parameter 71). .....

C-290. Steam temperature at 1.54m and 225 degrees in steam tube during Test SFD 1-4 transient (STEAMTMP225 154 - Parameter 117). ....

C-291. Steam temperature at 2.35m and 225 degrees in steam tube during Test SFD 1-4 transient (STEAMTMP225 235 - Parameter 118). ....

C-292. Fuel rod 3B cladding inner surface temperature at 0.39m and 135 degrees during Test SFD 1-4 transient (CLADTEMP135 393B - Parameter 67). ....

C-293. Fuel rod 4D cladding inner surface temperature at 0.39m and 135 degrees during Test SFD 1-4 transient (CLADTEMP135 394D - Parameter 68). ....

C-294. Fuel rod 3B cladding inner surface temperature at 0.54m and 0 degrees during Test SFD 1-4 transient (CLADTEMP000 543B - Parameter 69). ....

Table C-3. (continued)

C-295. Fuel rod 4D cladding inner surface temperature at 0.54m and 0 degrees during Test SFD 1-4 transient (CLADTEMP000 544D - Parameter 70). ....

C-296. Fuel rod 3B cladding inner surface temperature at 0.74m and 270 degrees during Test SFD 1-4 transient (CLADTEMP225 743B - Parameter 57). ....

C-297. Fuel rod 4D cladding inner surface temperature at 0.74m and 225 degrees during Test SFD 1-4 transient (CLADTEMP225 744D - Parameter 58). ....

C-298. Shroud inner wall temperature at 0.35m and 90 degrees during Test SFD 1-4 transient (SHRDTEMPIN090 35 - Parameter 73). ....

C-299. Shroud inner wall temperature at 0.35m and 270 degrees during Test SFD 1-4 transient (SHRDTEMPIN270 35 - Parameter 75). ....

C-300. Shroud inner wall temperature at 0.5m and 90 degrees during Test SFD 1-4 transient (SHRDTEMPIN090 50 - Parameter 76). ....

C-301. Shroud inner wall temperature at 0.5m and 270 degrees during Test SFD 1-4 transient (SHRDTEMPIN270 50 - Parameter 85). ....

C-302. Shroud inner wall temperature at 0.7m and 270 degrees during Test SFD 1-4 transient (SHRDTEMPIN270 70 - Parameter 88). ....

C-303. Shroud insulation temperature at 0.5m and 0 degrees during Test SFD 1-4 transient (SHRDTEMPMID00050 - Parameter 91). ....

C-304. Shroud insulation temperature at 0.5m and 90 degrees during Test SFD 1-4 transient (SHRDTEMPMID09050 - Parameter 92). ....

C-305. Shroud insulation temperature at 0.5m and 180 degrees during Test SFD 1-4 transient (SHRDTEMPMID18050 - Parameter 93). ....

C-306. Shroud insulation temperature at 0.5m and 270 degrees during Test SFD 1-4 transient (SHRDTEMPMID27050 - Parameter 94). ....

C-307. Shroud insulation temperature at 0.7m and 90 degrees during Test SFD 1-4 transient (SHRDTEMPMID09070 - Parameter 95). ....

C-308. Shroud insulation temperature at 0.7m and 180 degrees during Test SFD 1-4 transient (SHRDTEMPMID18070 - Parameter 96). ....

C-309. Shroud insulation temperature at 0.91m and 180 degrees during Test SFD 1-4 transient (SHRDTEMPMID18091 - Parameter 109). ....

C-310. Shroud outer wall temperature at 0.5m and 180 degrees during Test SFD 1-4 transient (SHRDTEMPOUT18050 - Parameter 77). ....

Table C-3. (continued)

C-311. Shroud outer wall temperature at 0.7m and 90 degrees during Test SFD 1-4 transient (SHRDTEMPOUT09070 - Parameter 78). ....

C-312. Shroud outer wall temperature at 0.7m and 270 degrees during Test SFD 1-4 transient (SHRDTEMPOUT27070 - Parameter 85). ....

C-313. Fuel rod 3B centerline temperature at 0.39m during Test SFD 1-4 transient (FUELTEMPCL 393B - Parameter 41). .....

C-314. Fuel rod 4D centerline temperature at 0.39m during Test SFD 1-4 transient (FUELTEMPCL 394D - Parameter 42). .....

C-315. Control rod 5E centerline temperature at 0.39m during Test SFD 1-4 transient (CRCENTERTEMP395E - Parameter 15) ....

C-316. Control rod 5E cladding inner surface temperature at 0.39m and 135 degrees during Test SFD 1-4 transient (CRCLADTP135 395E - Parameter 61) ....

C-317. Control rod 5E cladding inner surface temperature at 0.54m and 0 degrees during Test SFD 1-4 transient (CRCLADTP000 545E - Parameter 63) ....

C-318. Control rod 5E cladding inner surface temperature at 0.74m and 225 degrees during Test SFD 1-4 transient (CRCLADTP225 545E - Parameter 64) ....

C-319. Steam tube wall temperature at 1.84m and 90 degrees during Test SFD 1-4 transient (STTUBTMPWL090184 - Parameter 156) ....

C-320. Steam tube wall temperature at 1.84m and 270 degrees during Test SFD 1-4 transient (STTUBTMPWL270184 - Parameter 167) ....

C-321. Steam tube wall temperature at 2.29m and 90 degrees during Test SFD 1-4 transient (STTUBTMPWL090229 - Parameter 169) ....

C-322. Steam tube wall temperature at 2.83m and 270 degrees during Test SFD 1-4 transient (STTUBTMPWL270283 - Parameter 173) ....

C-323. Steam tube wall temperature at 3.4m and 90 degrees during Test SFD 1-4 transient (STTUBTMPWL090340 - Parameter 174) ....

C-324. Steam tube wall temperature at 3.4m and 270 degrees during Test SFD 1-4 transient (STTUBTMPWL270340 - Parameter 175) ....

C-325. FPDS coupon holder temperature at 1.57m in steam line during Test SFD 1-4 transient (COUPTEMPFPDS 157 - Parameter 195) ....

C-326. FPDS coupon holder temperature at 2.38m in steam line during Test SFD 1-4 transient (COUPTEMPFPDS 238 - Parameter 196) ....

Table C-3. (continued)

C-327. FPDS coupon holder temperature at 3.4m in steam line during Test SFD 1-4 transient (COUPTEMPFPDS 340 - Parameter 209) ....

C-328. Self-powered neutron detector at 0.31m and 180 degrees gamma signal during Test SFD 1-4 transient (SPND 31GAMA 180 - Parameter 110). ....

C-329. Self-powered neutron detector at 0.31m and 180 degrees neutron signal during Test SFD 1-4 transient (SPND 31NEUT 180 - Parameter 111). ....

C-330. Self-powered neutron detector at 0.31m and 0 degrees gamma signal during Test SFD 1-4 transient (SPND 31GAMA 000 - Parameter 123). ....

C-331. Self-powered neutron detector at 0.31m and 0 degrees neutron signal during Test SFD 1-4 transient (SPND 31NEUT 000 - Parameter 124). ....

C-332. Bypass to separator pressure differential during Test SFD 1-4 transient (DIFFPRESBYP SEP - Parameter 13). .....

C-333. Bypass to bundle pressure differential during Test SFD 1-4 transient (DIFFPRESBYBUNDLE - Parameter 14). .....

C-334. Bundle coolant pressure drop during Test SFD 1-4 transient (DIFFPRESBUNDLE7R - Parameter 40). ....

C-335. Differential pressure between bundle region and shroud insulation region during Test SFD 1-4 transient (DIFFPRESBDLESHRD - Parameter 121) ....

C-336. Bundle to separator pressure differential during Test SFD 1-4 transient (DIFFPRESBDLE SEP - Parameter 188). ....

C-337. Water level in reactor bundle during Test SFD 1-4 transient (BUNDLE WTR LVL - Parameter 119) ....

C-338. Sample line flow rate into condenser during Test SFD 1-4 transient (FPDSFLOWCOND IN - Parameter 152) ....

C-339. Sample line flow rate out of condenser during Test SFD 1-4 transient (FPDSFLOWCOND OUT - Parameter 153) ......

C-340. Inert sweep gas flow rate during Test SFD 1-4 transient (FPDSFLOWSWEEPGAS - Parameter 86) ....

C-341. FPDS sample line inlet temperature during Test SFD 1-4 transient (FP TEMPINLET - Parameter 133). ....

C-342. FPDS condenser outlet fluid temperature during Test SFD 1-4 transient (FP TEMPCONDENSR - Parameter 134). ....

C-343. FPDS separation vessel liquid flow rate FT13-69 during Test SFD 1-4 transient (FP FLOWFT13-69 - Parameter 148). ....

C-344. FPDS separator vessel pressure PT13-42 during Test SFD 1-4 transient (FP PRESSPT13-42 - Parameter 135). ....

Table C-3. (continued)

C-345. FPDS gross gamma rate detector in steam line during Test SFD 1-4 transient (FP GAMMASTEAM - Parameter 213). ....

C-346. FPDS gross gamma rate detector in liquid line during Test SFD 1-4 transient (FP GAMMLIQUID - Parameter 214). ....

C-347. FPDS gross gamma rate detector in gas line during Test SFD 1-4 transient (FP GAMMAGAS - Parameter 215). ....

C-348. FPDS gross gamma rate ion detector in steam line during Test SFD 1-4 transient (FPGAMIONSTEAMLIN - Parameter 141). ....

C-349. FPDS gross gamma rate ion detector in steam sample line during Test SFD 1-4 transient (FPGAMIONSTEAMSPL - Parameter 142). ....

C-350. FPDS delayed neutron detector during Test SFD 1-4 transient (FP NEUT DETECTOR - Parameter 227). ....

C-351. FPDS hydrogen concentration during Test SFD 1-4 transient (FP HYDR CONCENT - Parameter 143). ....

C-352. Aerosol monitor unit A - 820nm output signal during Test SFD 1-4 transient (FP 820AAEROSIG - Parameter 127) ....

C-353. Aerosol monitor unit B - 820nm output signal during Test SFD 1-4 transient (FP 820B AEROSIG - Parameter 130) ....

C-354. Blowdown tank liquid level during Test SFD 1-4 transient (BLOW LEVLIT17 PT - Parameter 149). ....

C-355. Blowdown tank gas pressure during Test SFD 1-4 transient (BLOWPRESPT12 PT - Parameter 151). ....

C-356. System pressure heise during Test SFD 1-4 cool down (SYS PRESHEISE PT - Parameter 72). ....

C-357. Lower test train system pressure 69 MPa during Test SFD 1-4 cool down (SYS PRES69EG LTT - Parameter 37). ....

C-358. FPDS coupon holder temperature at 1.57m in steam line during Test SFD 1-4 cool down (COUPTEMPFPDS 157 - Parameter 195) ....

C-359. FPDS coupon holder temperature at 2.38m in steam line during Test SFD 1-4 cool down (COUPTEMPFPDS 238 - Parameter 196) ....

C-360. FPDS coupon holder temperature at 3.4m in steam line during Test SFD 1-4 cool down (COUPTEMPFPDS 340 - Parameter 209) ....

C-361. Bypass to separator pressure differential during Test SFD 1-4 cool down (DIFFPRESBYP SEP - Parameter 13). ....

C-362. Bypass to bundle pressure differential during Test SFD 1-4 cool down (DIFFPRESBYBUNDLE - Parameter 14). ....

C-363. Bundle coolant pressure drop during Test SFD 1-4 cool down (DIFFPRESBUNDLE7R - Parameter 40). ....

Table C-3. (continued)

C-364. Bundle to separator pressure differential during Test SFD 1-4 cool down (DIFFPRESBDLE SEP - Parameter 188). ....

C-365. Sample line flow rate into condenser during Test SFD 1-4 cool down (FPDSFLOWCOND IN - Parameter 152) ....

C-366. Sample line flow rate out of condenser during Test SFD 1-4 cool down (FPDSFLOWCOND OUT - Parameter 153) ......

C-367. Inert sweep gas flow rate during Test SFD 1-4 cool down (FPDSFLOWSWEEPGAS - Parameter 86) ....

C-368. Bypass to separator pressure differential during Test SFD 1-4 cool down (DIFFPRESBYP SEP - Parameter 13). .....

C-369. FPDS condenser outlet fluid temperature during Test SFD 1-4 cool down (FP TEMPCONDENSR - Parameter 134). ....

C-370. FPDS separation vessel liquid flow rate FT13-69 during Test SFD 1-4 cool down (FP FLOWFT13-69 - Parameter 148). ....

C-371. FPDS separator vessel pressure PT13-42 during Test SFD 1-4 cool down (FP PRESSPT13-42 - Parameter 135). ....

C-372. FPDS gross gamma rate detector in steam line during Test SFD 1-4 cool down (FP GAMMASTEAM - Parameter 213). ....

C-373. FPDS gross gamma rate detector in liquid line during Test SFD 1-4 cool down (FP GAMMLIQUID - Parameter 214). ....

C-374. FPDS gross gamma rate detector in gas line during Test SFD 1-4 cool down (FP GAMMAGAS - Parameter 215). ....

C-375. FPDS gross gamma rate ion detector in steam line during Test SFD 1-4 cool down (FPGAMIONSTEAMLIN - Parameter 141). ....

C-376. FPDS gross gamma rate ion detector in steam sample line during Test SFD 1-4 cool down (FPGAMIONSTEAMSPL - Parameter 142). ....

C-377. FPDS delayed neutron detector during Test SFD 1-4 cool down (FP NEUT DETECTOR - Parameter 227). ....

C-378. FPDS hydrogen concentration during Test SFD 1-4 cool down (FP HYDR CONCENT - Parameter 143). ....

C-379. Aerosol monitor unit A - 820nm output signal during Test SFD 1-4 cool down (FP 820AAEROSIG - Parameter 127) ......

C-380. Aerosol monitor unit B - 820nm output signal during Test SFD 1-4 cool down (FP 820B AEROSIG - Parameter 130) ......

C-381. Blowdown tank liquid level during Test SFD 1-4 cool down (BLOW LEVLIT17 PT - Parameter 149). ....

C-382. Blowdown tank gas pressure during Test SFD 1-4 cool down (BLOWPRESPT12 PT - Parameter 151). ....

mainframe-type of code specifically developed at the INEL to provide researchers with a state-of-the-art analysis program that was compatible with batch analysis requirements.

GAUSS VIII uses both a search method and an operator-specified required nuclide list to locate gamma-ray photopeaks for analysis. Although GAUSS VIII allows the use of multiple-tailed Gaussians for the non-linear least-squares fitting of the located photopeaks, a simple untailed Gaussian function was used for these analyses since the spectral count times had been short and, consequently, very few large photopeaks with significant tails were acquired.

GAUSS VIII fits full regions of a gamma-ray spectrum rather than operating on single photopeaks. The results from a fitted region must pass operator-selected goodness-of-fit tests or an additional photopeak is inserted at the point of highest residuals. This recycle fit capability significantly improves the code fit performance on complex spectra. Final nuclide concentration values are derived by solution of a matrix of nuclide tags and photopeak areas. Through this matrix solution method, all photopeak energy interferences are resolved. Stated uncertainties in the final concentration values are estimated one-sigma errors determined from the individual photopeak areas, the crossproduct term of the fit matrix, the photopeak goodness of fit, and error components from the final matrix solution. Although corrections can be applied for daughter and/or granddaughter growth from parent nuclides, this option was not used in the Test SFD 1-4 analysis.

GAUSS VIII was tested extensively on on-line spectra acquired during the SFD Scoping Test and Test SFD 1-1. These tests included verification of the pulser-based count-rate-effects corrections and energy calibrations. The results of these and other tests performed to verify the accuracy of GAUSS VIII analyses are reported in Reference C-2.

The concentration results (with their estimated one-sigma errors) generated by GAUSS VIII were operated on by several mainframe- and PC-based formatting and calculational programs to develop the final isotopic release results. All of these operations used electronic file transfers, and selected calculations were checked by hand to ensure accuracy. Plots of isotopic concentrations from the mainfloor, steamline, gasline, and liquidline detectors are reproduced as microfiche located on the back cover of this report.

C-7. References

C-1. L. O. Johnson, E. W. Killiam, R. G. Helmer, and R. A. Coates, "Use of Concurrently Gathered Pulser Data for Real-Time Validation of Gamma Ray Spectra," *Transactions-Nuclear Science, NS-28,* 1981, p. 310.

C-2. M. H. Putnam, R. G. Helmer, and C. M. McCullagh, *GAUSS VIII, A Computer Program for the Nuclide Activity Analysis of γ-Ray Spectra from Ge Semiconductor Detectors*, EGG-PBS-6768, December 1985.

APPENDIX D

BUNDLE POWER RESULTS

APPENDIX D

BUNDLE POWER RESULTS

This appendix identifies the major individual contributions to the energy deposition within the SFD 1-4 test train and outlines the power balance resulting from the overall heat transfer process. The axial power profiles obtained from reactor physics calculations are also provided. Although the energy sources within the test bundle are primarily the fission power of the fuel rods and the energy released by the zircaloy-steam oxidation reaction, the gamma and fast neutron fluxes have a slight influence on the total bundle power produced.

D-1. Major Energy Sources

The major energy sources contributing to the bundle power were the nuclear energy (that was deposited in the test bundle, the bundle coolant, the bypass coolant, and the shroud materials) and the steam-zircaloy chemical reaction. These energy sources are described in this section.

The nuclear energy deposition within the test bundle excluding the coolant contribution, E_b, is given by

$$E_b = f_b + \beta_b + \gamma_b \tag{D-1}$$

where

f_b = the fission fragment contribution from fissions within the fuel bundle that can be considered to deposit their energy at the point of fission. This source provides 169.58 MeV/fission.[D-1]

β_b = the energy generated in the form of beta particles from the decay of fission fragments that can be considered to deposit their energy at the point of fission. This source provides 6.43 MeV/fission, and

γ_b = the energy deposition from gamma-rays produced both in the test train and reactor core. This energy is deposited in the fuel, cladding, and structural materials.

The nuclear energy deposition within the bundle coolant, E_{bc}, is given by

$$E_{bc} = n_{bc} + \gamma_{bc} \tag{D-2}$$

where

n_{bc} = the fast neutron contribution from fissions within both the test fuel and the core, and

γ_{bc} = the energy deposition from gamma-rays produced both in the test train and reactor core.

The nuclear energy deposition within the shroud, E_s, is equal to γ_s, the energy deposition from gamma rays produced both in the test train and reactor core.

The nuclear energy deposition within the bypass coolant, E_{by}, is given by

$$E_{by} = n_{by} + \gamma_{by}, \tag{D-3}$$

where

n_{by} = the fast neutron contribution within the bypass coolant from fissions within both the test fuel and reactor core, and

γ_{by} = the energy deposition within the bypass coolant from gamma rays produced both in the test train and reactor core.

The gamma-ray source contributions referred to above are generated during fission (prompt gamma-rays), the decay of fission fragments (delayed gamma-rays), neutron capture, and neutron inelastic scattering.

At a temperature above ∿1100 K, there is an exothermic reaction between the steam and zircaloy that provides a chemical energy source:

$$Zr + 2H_2O \rightarrow ZrO_2 + 2H_2 + E_o \tag{D-4}$$

where

E_o = 6.5 MJ per kilogram of zirconium reacted.

D-2. Power Balance

The energy sources identified in Section D-1 and the heat transfer process result in the following overall energy balance:

$$\frac{d}{dt}\left(E_b + E_{bc} + E_s + E_{by} + E_o\right) =$$

$$\left(Q_b + Q_{bc} + Q_s + Q_{by}\right) \qquad \text{(D-5)}$$

where

Q_b = the rate of internal heat gain by the fuel bundle,

Q_{bc} = the rate of internal heat gain by the bundle coolant,

Q_s = the rate of internal heat gain by the shroud, and

Q_{by} = the rate of internal heat gain by the bypass coolant.

The bundle nuclear power, P_{bn}, is given by:

$$P_{bn} = \frac{dE_b}{dt} + \frac{dE_{bc}}{dt} \; . \qquad \text{(D-6)}$$

At temperatures below the onset of oxidation and under steady-state conditions, dE_o/dt, Q_b, and Q_s are zero; the bundle nuclear power can be defined by:

$$P_{bn} = Q_{bc} + Q_{by} - \frac{dE_s}{dt} - \frac{dE_{by}}{dt} \; . \qquad \text{(D-7)}$$

Thermocouples mounted above and below the test bundle and in the bypass coolant region, together with coolant flow rate and pressure measurements, were used to determine the rate of heat gain by the bundle coolant, Q_{bc}, and bypass coolant, Q_{by}. The rate of heat transfer to the bypass coolant was calculated with the use of the Dittus-Boelter correlation[D-2] for subcooled water at the bundle outlet. Both the gamma-ray energy deposition rate in the shroud, dE_s/dt, and the direct nuclear energy deposition rate in the bypass coolant, dE_{by}/dt, were obtained from reactor physics calculations described below.

D-3. Reactor Physics Analysis

Reactor physics calculations were performed primarily to establish a pretest relationship between the bundle nuclear power and the overall reactor thermal power. The relationship is a function of the reactor control rod position, the coolant conditions, and the bundle coolant level.

The ratio of the bundle power to the reactor thermal power, defined as the figure of merit (FOM), was calculated as:

$$\text{FOM} = \frac{kjSE_b}{\nu P_{rt}} \qquad \text{(D-8)}$$

where

k = the number of neutrons produced per neutron entering the in-pile tube,

j = the neutron current entering the in-pile tube (n/m^{2}s),

S = the inside surface area of the in-pile tube (m^2),

E_b = the nuclear energy deposited in the test bundle per fission in the test fuel (kW/fission),

ν = the number of neutrons produced per fission in the test fuel, and

P_{rt} = the reactor thermal power which yields the current j (MW).

The major contributions to the total nuclear energy deposited in the bundle were identified in Equations (D-1) and (D-2). The fission fragments and beta particles deposit their kinetic energy effectively at the point of interaction and total 175.3 MeV/fission. A further 10.9 MeV/fission is produced from the prompt and delayed gamma rays originating in the bundle. The average heating from gammas originating in the core was assumed to follow a chopped cosine shape having a peak-to-average ratio of 1.35. End peaking effects in the bundle were estimated from a previous calculation.

The calculations also assumed the reactor had been operational long enough to attain saturation of fission-product activity.

Monte Carlo calculations using the RAFFLE[D-3] code were performed for the three test coolant conditions shown in Table D-1—a water-filled bundle, a partially water-filled bundle, and a steam-filled bundle. These calculations modeled the previously irradiated BR-3 rods using the axial distribution of uranium and plutonium isotopes determined from ORIGEN2 calculations. The model accurately simulated the axial lengths and positions of the fresh and irradiated fuel rods and the control rods in the bundle. The ratio of bundle power to reactor power (FOM) for each configuration is given in Table D-1, while the axial power distributions are given in Figures D-1 through D-3. The local values presented in the figures represent the power in kilowatts for 0.1-m-long sections of the bundle per megawatt of core power. The uncertainty ranges represent the $\pm 2\sigma$ values of the Monte Carlo code results only. These results apply to the core configuration in which the transient rods are fully withdrawn and the PBF control rods are withdrawn 0.591 m. Fully inserting the transient rods decreases the ratio by 10 to 12%, while fully inserting the control rods from the full-out position increases the ratio by 35%. For the center one-third of control rod travel, the rate of change is 0.055% per millimeter of control rod insertion.

The Test SFD 1-4 bundle power and PBF core power were measured during the power calibration phase when single-phase water conditions were maintained at both the bundle inlet and outlet. A computer program with curve-fits of steam table values was used to calculate the coolant enthalpy rise along the bundle, based on the temperature rise measured by thermocouples located at the inlet and outlet and the flow rate measured by the bundle inlet flow meter. A correction was made for the small heat loss through the insulated shroud walls for subcooled water at the bundle outlet. The bundle power and reactor power were measured at three different reactor powers (i.e., three different control rod positions) during the first power ramp. A comparison of the three measured and calculated FOMs and corresponding control rod positions is given in Table D-2. The calculated ratio of bundle power to reactor power was 11% to 17% higher than measured for the three measurements. Previous reactor physics calculations for tests with similar or different geometries than Test SFD 1-4 in PBF have also tended to overestimate the measured fuel rod power. As a result, the calculated FOM for the high-temperature transient was decreased by 16.6% to account for the average difference observed between the measured and calculated bundle power at 10.2 and 17.7 MW. This correction was selected because the control rod position during the power hold in the high-temperature transient was approximately the same as the average control rod position during the 10.2- and 17.7-MW power calibration measurement.

D-4. Effect of Control Rod Material Relocation on Bundle Power

A posttest reactor physics calculation was made to estimate the effect of control rod material relocation that occurred between 1927 and 1987 s on the FOM. Data from posttest examination of the bundle were used to model the control rod material axial and radial distribution in a RAFFLE code calculation. Table D-3 lists the axial pointwise control rod material distribution estimated from the metallurgical cross-section samples, as well as the original as-built configuration. Based on the pointwise distribution, a posttest axial histogram of control rod material was developed for the RAFFLE calculation and is given in Table D-4.

The radial distribution of the control rod material used in the calculation was based on radial control rod material distribution at each elevation observed during posttest examination. Figure D-4 depicts the geometrical form and dimensions that were used to best approximate the actual distributions. The simulated distributions varied from homogeneous mixtures of control material and steam between fuel rods to reduced-diameter control rods at the four original locations to a thin annulus of control material around selected fuel rods. The coolant conditions used in the bundle were the same as those used for a steam-filled intact bundle, i.e., steam at 13.9 kg/m^3 in the fuel bundle and water at 787 kg/m^3 in the bypass and downcomer regions.

The calculated FOM decreased slightly from 3.16 kW/MW for an intact, steam-filled bundle to 3.06 kW/MW for a steam-filled bundle after relocation of the control rods. The small decrease of 3% in the bundle power following control rod relocation is caused by the fact that a relatively small amount of homogenized control rod material is more effective as a neutron absorber than a larger amount of lumped control rod material in the original rod-like configuration. The axial power

Table D-1. Test SFD 1-4 ratio of bundle power to reactor power as a function of coolant density

Test Condition	Water Density (kg/m³)		FOM
	Bundle	Bypass & Downcomer	Ratio of Bundle Power to Reactor Power (kW/MW of Core Power)
Water-filled	774.4	811.3	6.54
24.3 cm of water and remainder steam-filled	747 (water) 17.1 (steam)	787	3.83
Steam-filled	13.9	787	3.16

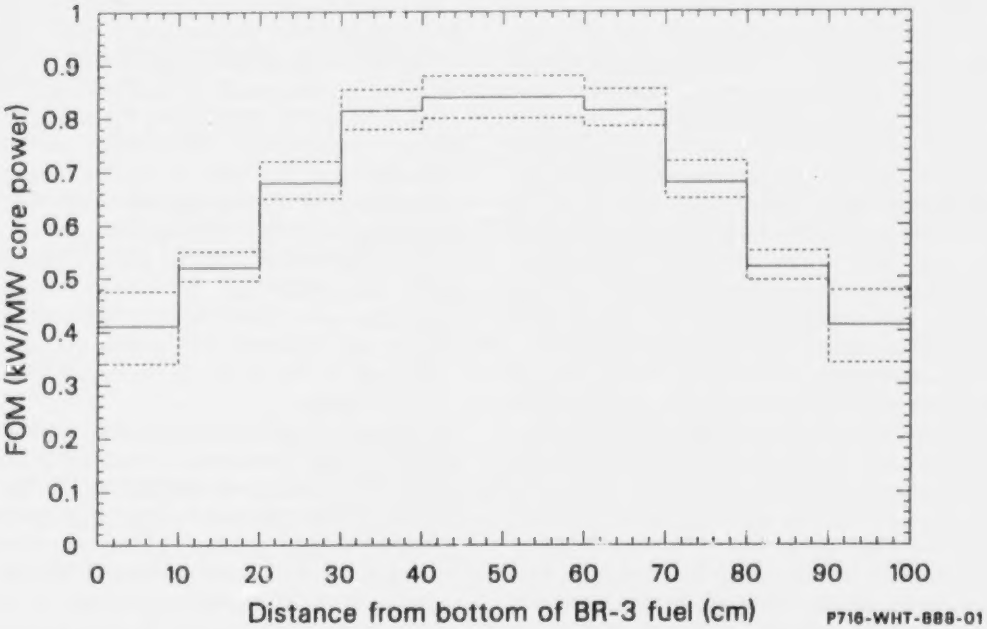

Figure D-1. Axial power distribution for an intact, water-filled SFD 1-4 bundle.

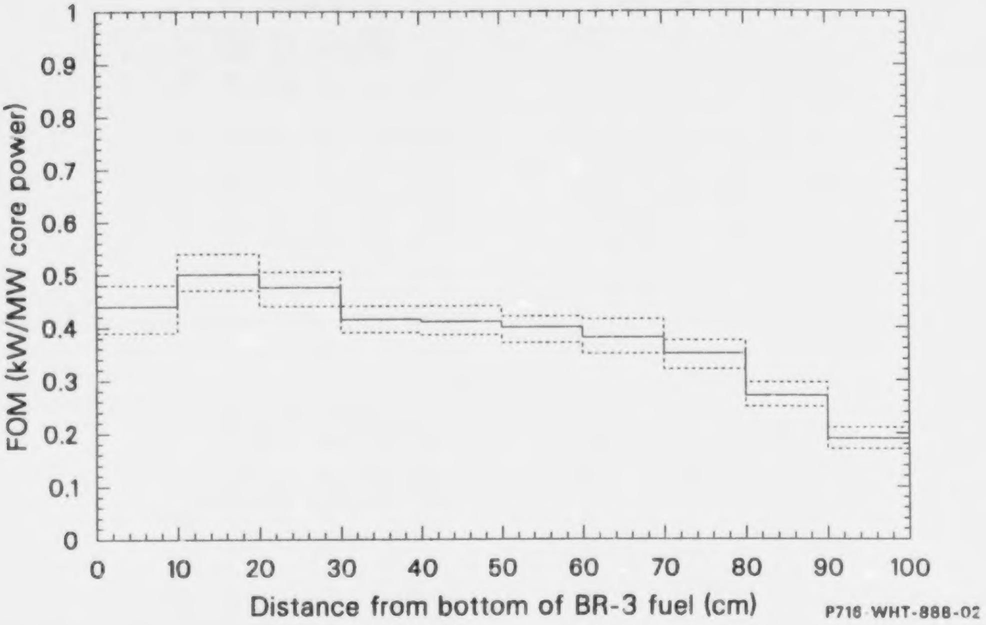

Figure D-2. Axial power distribution for an intact, partially steam-filled SFD 1-4 bundle.

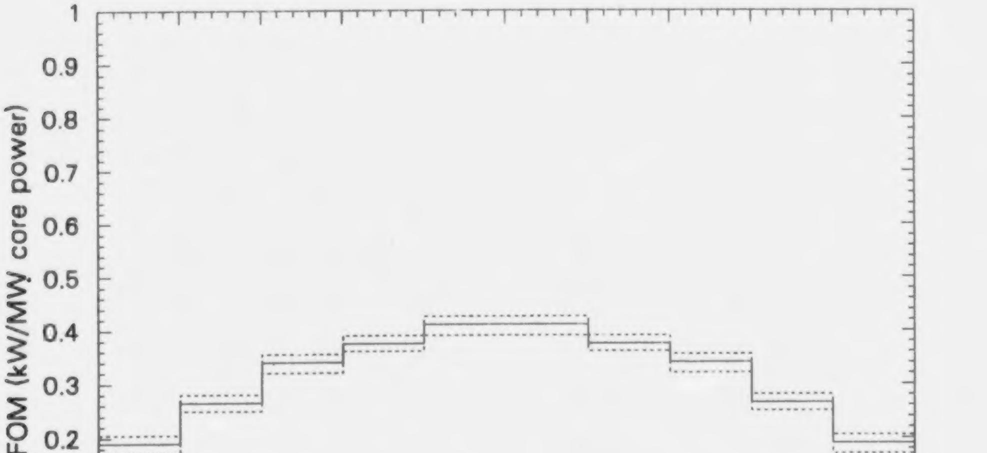

Figure D-3. Axial power distribution for an intact, steam-filled SFD 1-4 bundle.

Table D-2. Test SFD 1-4 measured and calculated ratio of bundle to reactor power

Measured Bundle Power (kW)	Measured Reactor Power (MW)	Measured Control Rod Position (m)	FOM Ratio of Bundle to Reactor Power (kW/MW)		
			Measured	Calculated	% Difference
58.3	10.2	0.4973	5.7	6.90	17.4
99.3	17.7	0.5616	5.6	6.65	15.8
145.8	25.7	0.6238	5.7	6.42	11.2

distributions of the steam-filled bundle before and after control rod material relocation are shown in Figure D-5. As expected, the power in the upper half of the bundle increased appreciably relative to the power in the intact bundle, while the power in the lower half of the bundle decreased a greater amount because of the increased worth of the redistributed control material.

Table D-3. Test SFD 1-4 axial pointwise control rod material distribution

Elevation[a] (m)	Control Material Distribution (kg/m)	
	Pretest	Posttest
0	0.0	1.593
0.0428	0.0	1.593
0.0432	1.793	3.914
0.0598	1.793	3.914
0.0857	1.793	4.881
0.0858	1.793	4.881
0.1198	1.793	13.589
0.2098	1.793	1.115
0.2898	1.793	1.392
0.4328	1.793	0.136
0.5828	1.793	0.138
0.7828	1.793	0.0
0.8898	1.793	0.0
0.9998	1.793	0.0

a. Relative to bottom of active fuel of BR-3 fuel rod.

D-5. Bundle Power Determination

Since the bundle power could not be measured during the high-temperature transient because of non-equilibrium thermal conditions, the bundle power was determined from the calculated FOM and the measured indicated reactor power. The FOM is dependent on the average PBF control rod position (which was not recorded except for the start of the transient and during the power hold). In order to estimate the control rod position during

Table D-4. Test SFD 1-4 axial histogram of control rod material used in RAFFLE calculation

Elevation[a] (m)	Control Material Distribution (kg/m)
0.0 - 0.10	3.428
0.10 - 0.16	10.887
0.16 - 0.25	3.071
0.25 - 0.35	1.206
0.35 - 0.60	0.258
0.60 - 1.00	0.00

a. Relative to bottom of active fuel of BR-3 fuel rod

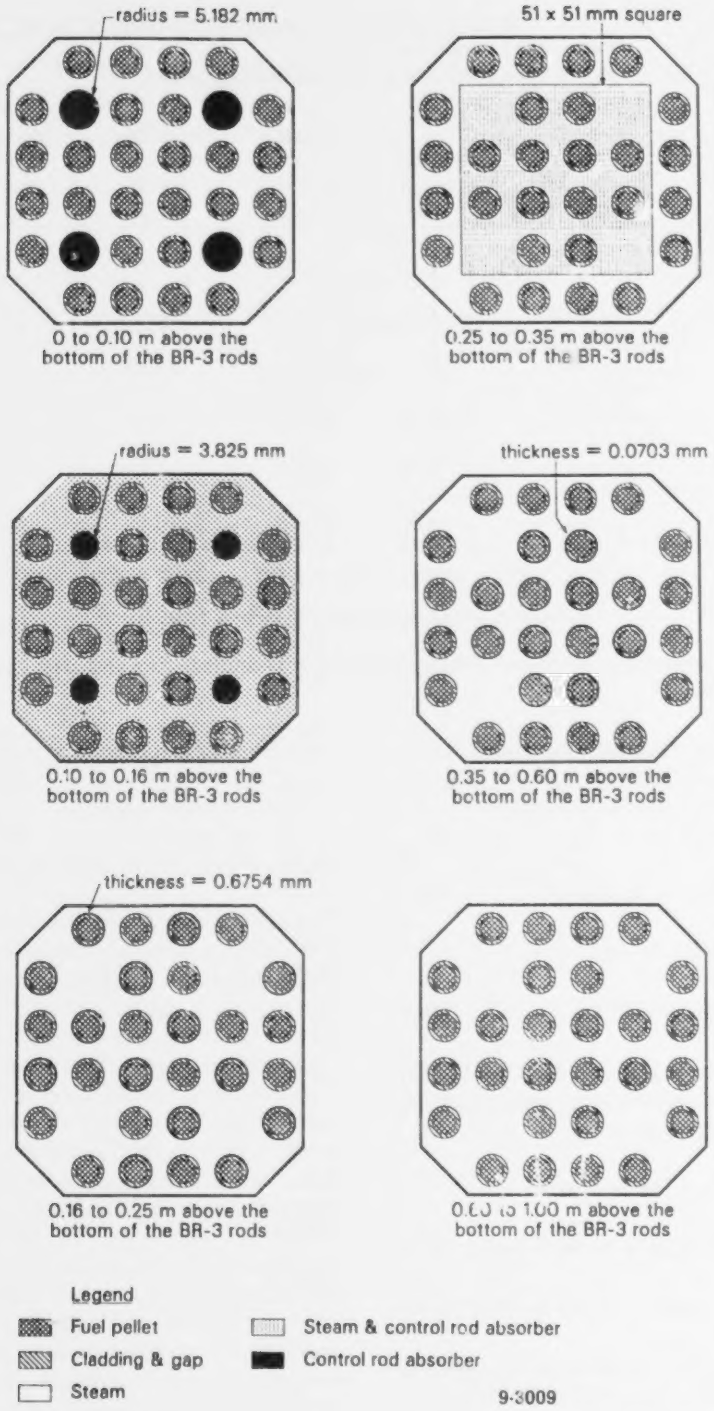
radius = 5.182 mm
51 x 51 mm square
0 to 0.10 m above the bottom of the BR-3 rods
0.25 to 0.35 m above the bottom of the BR-3 rods
radius = 3.825 mm
thickness = 0.0703 mm
0.10 to 0.16 m above the bottom of the BR-3 rods
0.35 to 0.60 m above the bottom of the BR-3 rods
thickness = 0.6754 mm
0.16 to 0.25 m above the bottom of the BR-3 rods
0.60 to 1.00 m above the bottom of the BR-3 rods
Legend
▩ Fuel pellet
▨ Cladding & gap
☐ Steam
▤ Steam & control rod absorber
■ Control rod absorber
9-3009

Figure D-4. SFD 1-4 bundle material distribution used for the reactor physics calculations.

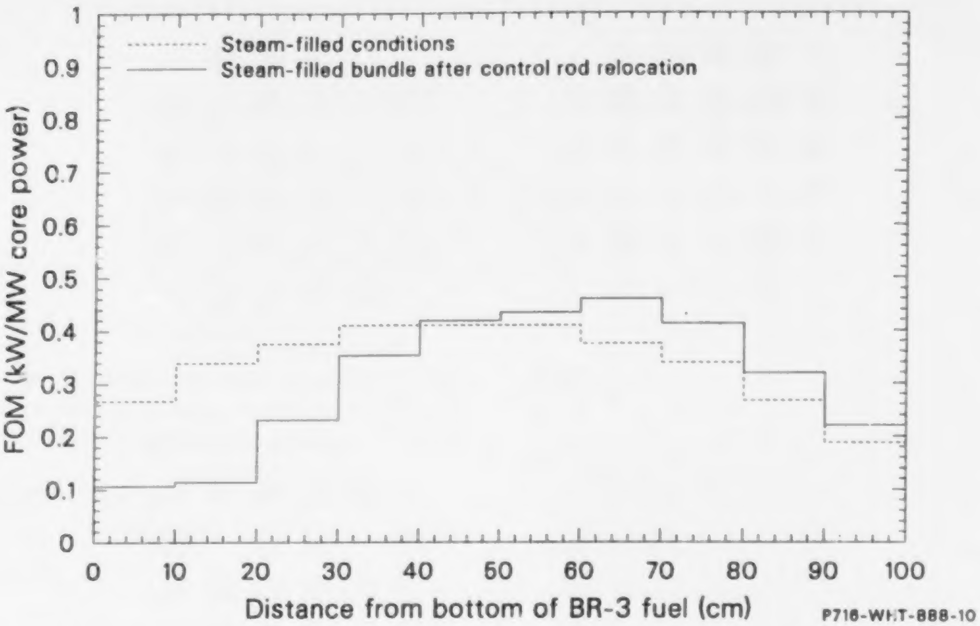

Figure D-5. Axial power distribution of steam-filled SFD 1-4 bundle before and after control rod material relocation.

the remainder of the transient, equations for the Doppler and thermal reactivity feedback and control rod worth curves had to be used. Doppler reactivity, RD, is given by

$$RD = 8.739\ E\text{-}04 + 0.246P_T - 6.307\ E-03\ P_T^2 + 8.65\ E-05\ P_T^3 \qquad (D\text{-}9)$$

where P_T is the thermal reactor power (MW). The PBF reactor control rod worth to compensate for the Doppler reactivity is given by:

$$R_{cr} = -3.08516 + 1.666\ E-02Z + 7.4362\ E-03Z^2 + 1.488\ E-03Z^3 - 7.0671\ E-05Z^4 + 8.263\ E-07Z^5 \quad (D\text{-}10)$$

where Z is the control rod position (in.), which was 16.77 in. at zero power and 20.52 to 20.58 in. during the power hold.

From reactor power calibration measurements, the indicated reactor power from the NMS-3 neutron chamber is related to actual thermal power by

$$\text{Indicated Reactor Power} = (0.796 + 0.0533\ RD)\ \text{actual thermal power} \qquad (D\text{-}11)$$

The FOM is also dependent on the steam interface level in the bundle. Interpolation of the calculated FOM values as a function of steam interface level that is given in Table D-1 was used to derive a correction factor for the bundle power prior to achieving completely steam-filled conditions.

The resulting bundle power calculations are summarized in Table D-5, and the transient bundle power history is shown in Figure D-6. The maximum fission bundle power was 27.1 kW, with an associated estimated uncertainty of ± 15% prior to control rod relocation and ± 20% afterwards. It should be noted that the high-temperature transient power calculation assumed fixed fuel geometry. The observed fuel rod liquefaction and relocation would tend to decrease the overall bundle power by a small amount, but would increase the linear power density somewhat in the lower regions. Fuel relocation was not included in the calculation because of the small quantity of relocated material and uncertainty in the actual time of relocation.

Table D-5. Calculated Test SFD 1-4 transient bundle power

Reactor Thermal Power (MW)	Reactivity Relative to Zero Power ($)	Indicated Reactor Power (MW)	Control Rod Position (m)	Steam Level (m)	Bundle Power Ratio (kW/MW)	Corrected Bundle Power (kW)	Test Time (s)
0	0	0	0.425	1.0	—	—	—
0.8	0.19	0.64	0.435	0.24	3.56	2.85	132
1.0	0.24	0.81	0.437	0.25	3.57	3.6	292
2.0	0.47	1.64	0.449	0.20	3.42	6.8	854
3.0	0.68	2.50	0.459	0.10	3.14	9.4	1339
4.0	0.89	3.37	0.469	0.04	3.00	12.0	1642
5.0	1.08	4.27	0.479	0.016	2.92	14.6	1738
6.0	1.27	5.18	0.488	0.007	2.89	17.3	1903
6.2	1.30	5.36	0.490	0.005	2.79	17.0	1927[a]
7.0	1.44	6.11	0.497	<0	2.68	18.8	2017
8.0	1.61	7.05	0.506	<0	2.67	21.4	2125
9.0	1.79	8.01	0.513	<0	2.66	24.0	2239
10.0	1.92	8.98	0.521	<0	2.65	26.5	2356
10.22	1.95	9.20	0.523	<0	2.64	27.1	2369-2592[b]
8.0	1.61	7.05	0.506	<0	2.67	21.4	2725[c]
6.0	1.27	5.18	0.488	<0	2.69	16.2	2832
5.0	1.08	4.27	0.479	<0	2.71	13.5	2876
4.0	0.89	3.37	0.469	<0	2.72	10.9	2933
3.0	0.68	2.50	0.459	<0	2.73	8.2	2989
2.0	0.47	1.64	0.449	<0	2.75	5.5	3040

---

[a] Time of control rod failure.

[b] Time of power hold.

[c] After power hold, during power decrease.

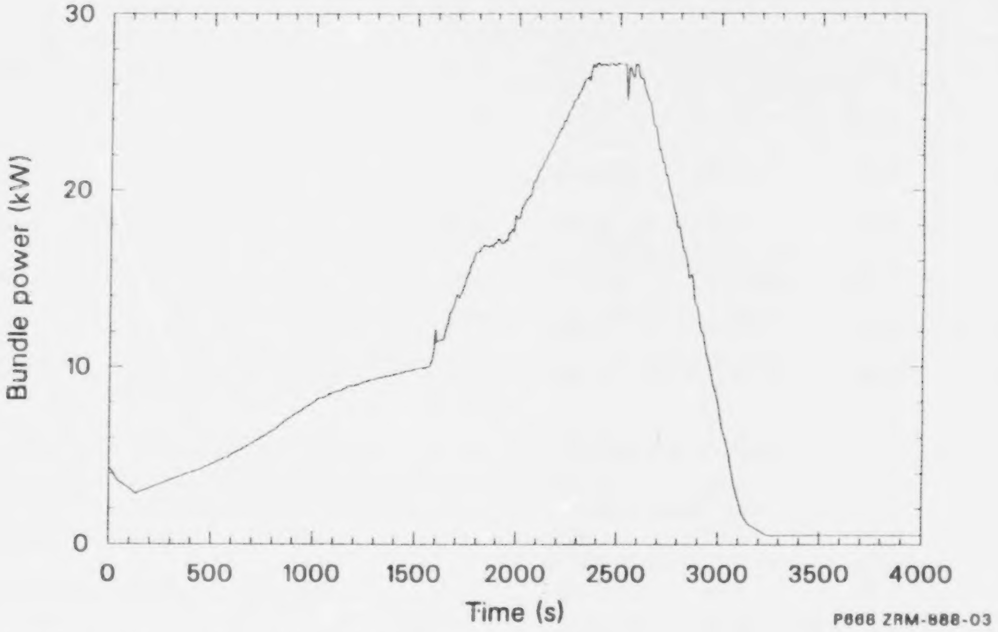

Figure D-6. Transient SFD 1-4 bundle power history.

D-6. References

D-1. American National Standard for Decay Heat Power in Light Water Reactors, ANSI/ANS-5.1-1979.

D-2. F. W. Dittus and L. M. K. Boelter, *Heat Transfer in Automobile Radiators of the Tubular Type*, University of California Publication, 2 (1930), pp. 443-461.

D-3. F. J. Wheeler et al., *The RAFFLE V General Purpose Monte Carlo Code for Neutron and Gamma Transport*, EGG-PHYS-6003, Rev. 1, October 1983.

APPENDIX E

HYDROGEN MEASUREMENTS

APPENDIX E

HYDROGEN MEASUREMENTS

Two different measurements were made to determine the hydrogen generation in Test SFD 1-4. The gaseous contents of the collection tank were analyzed posttest to determine the integral hydrogen production. In addition, time-dependent measurements of the hydrogen concentration in the gaseous portion of the effluent line were made using a Beckman Model 7C thermal conductivity analyzer. This measurement was used with the results of the effluent transit analysis to yield the time-dependent hydrogen generation rate in the bundle and an additional estimate of the total hydrogen produced in Test SFD 1-4.

This appendix provides a detailed description of the methods used to obtain the hydrogen generation rate and its integral from the measurements. In Section E-1, the results of the collection tank measurement are discussed and benchmarked against other results to provide confidence in the results. Section E-2 presents a description of the SFD 1-4 on-line hydrogen monitor data. In Section E-3, the results of the effluent transit analysis, which determines the delay time through the SFD 1-4 sampling and monitoring system and the hydrogen generation rate in the bundle, are discussed. Conclusions relative to the best estimate of hydrogen generation in Test SFD 1-4 are presented in Section E-4.

E-1. Collection Tank Results and Benchmarking

A sample of the collection tank gas was analyzed posttest to determine the quantities of the various gases found in the collection tank following Test SFD 1-4. This section will discuss the results of the analysis of the data and will benchmark these results against the quantities of gases expected in the tank following the test.

E-1.1 Spectroscopy Results and Analysis. Mass and gamma spectroscopy were performed to determine the contents of the collection tank posttest. The results are presented in Table E-1. The initial conditions of the collection tank were:

Total volume	8706 L
Liquid volume	1306 L
Pressure	15 psig

Table E-1. Test SFD 1-4 collection tank mass and gamma spectroscopy results

Gas	Quantity
N_2	77 vol%
Ar	14 vol%
O_2	6.9 vol%
H_2	2.0 vol%
CO_2	0.06 vol%
He	<0.01 vol%
^{85}Kr	326 μCi/sample

Temperature	295 K
Atmospheric pressure at PBF	12.7 psia

The collection tank pressure was changed to 56.2 psig to account for leakage that occurred between the end of the test and the time the sample was taken.

Based on the data in Table E-1 and the initial conditions of the tank, total quantities of each gas in the tank were calculated. The results are presented in Table E-2. By combining the assumed 10% error in the liquid level in the tank, the 2% error in the mass spectroscopy results, and the 10%

Table E-2. Test SFD 1-4 collection tank contents based on results from mass and gamma spectroscopy

Gas	Mass
N_2	30.8 ± 4.4 kg
Ar	8.06 ± 1.15 kg
O_2	3.15 ± 0.45 kg
H_2	57.8 ± 8.26 g
CO_2	37.8 ± 5.40 g
^{85}Kr	3.42 ± 0.52 μCi/cm^3

error in the pressure measurement in quadrature, the overall uncertainty is found to be 14.3%.

The ^{85}Kr concentration in Table E-1 was determined by dividing the results of gamma spectroscopy by the volume the gas sample would occupy at the collection tank conditions. The gas sample volume is nominally 2.8 L. Following expansion in the hot cell, the sample was at a pressure of 121.1 mm Hg (2.342 psia). Correcting this volume to the volume the gas would occupy at collection tank conditions at the end of the test (56.2 psig) yields

$$V = V_N \frac{P_e}{P_T + P_A} = 95.3 \text{ cm}^3 \qquad \text{(E-1)}$$

where

V_N = volume of the gas sample (cm^3),

P_e = sample pressure following expansion in the hot cell (psia),

P_T = tank pressure (psig), and

P_A = atmospheric pressure at PBF (psia).

Combining a 10% error in the gas sample volume, a 2% error in the hot cell pressure measurement, a 10% error in the collection tank pressure, and the 5% error in the concentration measurement in quadrature results in an overall uncertainty of 15.1%. As a result, the ^{85}Kr concentration is estimated to be 3.42 ± 0.52 μCi/cm^3.

The results in Table E-2 suggest that ~3 kg of oxygen were present in the collection tank. This large quantity of oxygen is difficult to explain as being related to the experiment because there were not any sources of oxygen introduced into the test train and sampling system that could produce such a large quantity of oxygen. (In the previous SFD tests, low levels of oxygen were observed, indicative of a small quantity of air in the tank.) As a result, it was assumed that air in-leakage occurred in the hot cell during sample preparation.

The mass spectroscopy results in Table E-1 were corrected to account for air in-leakage using the formula

$$V' = V_{coll} - \frac{6.9}{20.9} V_{air} \qquad \text{(E-2)}$$

where

V_{air} = volume percent of the gas in air (N_2 = 78.08%, O_2 = 20.95%, Ar = 0.93%, and CO_2 = 0.04%)

V_{coll} = volume percent of gas found in the collection tank based on mass spectroscopy in Table E-1

V' = volume percent of gas corrected for air in-leakage.

These results were then normalized to 100%. The results of this correction and the corrected quantities of gas in the collection tank are found in Table E-3.

The ^{85}Kr collection tank concentration was also corrected for air in-leakage. Since the 6.9 vol% O_2 measured by mass spectroscopy corresponds to (6.9/0.209) 32.95 vol% air, the actual volume that should be used in the calculation is

$$V = 2.8 * (1 - 0.3295) = 1.88 \text{ L}.$$

Thus, the ^{85}Kr concentration when corrected for air in-leakage by the factor (2.8/1.88) 1.49 is 5.10 ± 0.77 μCi/cm^3.

E-1.2 Benchmarking the Collection Tank Results. Benchmarking calculations were performed to determine the amount of each gas (nitrogen, argon, ^{85}Kr) expected in the collection tank following the experiment.

There were three different sources of nitrogen in Test SFD 1-4. Initially (at t = 0), the collection tank was filled with nitrogen to a pressure of 25.9 psia and the liquid level was at 11%. Given the

Table E-3. Test SFD 1-4 collection tank contents corrected for air in-leakage

Gas	Vol %	Mass
N_2	76.5	30.7 ± 4.39 kg
Ar	20.43	11.7 ± 1.67 kg
CO_2	0.0733	46.2 ± 6.61 g
H_2	2.98	86.1 ± 12.3 g
^{85}Kr	—	5.10 ± 0.77 μCi/cm^3

collection tank volume, this corresponds to 15.8 kg of nitrogen. Nitrogen was also introduced into the separator as a sweep gas at a rate of 1.13 g/s. The separator nitrogen flow operated until the sampling system was isolated at t = 11,400 s, resulting in 12.9 kg of nitrogen entering the collection tank. In addition, nitrogen was used prior to argon in the bundle to stabilize the system pressure and late in the experiment once the argon supply was depleted. The amount of nitrogen that flowed through the bundle was estimated to be 4.3 kg. Thus, the total nitrogen estimated to be in the collection tank is 33 kg.

Argon was used to stabilize pressure in the bundle during most of the transient and to cool the bundle posttest. The argon volumetric flow rate was:

5.72 mL/s at 6.9 MPa and 534 K	for $0 < t < 1966$ s (argon was shut off momentarily between 700 and 725 s)
9.05 mL/s at 6.9 MPa and 526 K	for $1966 < t < 3280$
28.92 mL/s at 6.9 MPa and 516.6 K	for $3280 < t < 7800$

Integrating this flow and converting to kg yields 9.8 kg of argon.

The ^{85}Kr from the collection tank can be compared to the ^{85}Kr measured during the on-line gas recirculation following the experiment. (The on-line measurement was not subject to the air in-leakage or tank depressurization.) The concentration of ^{85}Kr measured during recirculation of the collection tank gas was 2.32 ± 0.22 μCi/cm^3. Correcting this value for the pressure loss in the collection tank following the test yields 5.77 ± 0.55 μCi/cm^3.

E-1.3 Summary. A comparison of the expected quantities of gases in the collection tank with and without the assumption of air in-leakage and the benchmarked results are shown in Table E-4. The results indicate that the benchmarked data do not lie within the uncertainty of the collection tank data that are not corrected for air in-leakage. However, the benchmarked data do lie within the uncertainty of the collection tank data corrected for air in-leakage, indicating that the assumption of air in-leakage into the gas sample during expansion in the hot cell is reasonable. Thus, the results from collection tank samples corrected for air in-leakage indicate that the best estimate of total hydrogen generated during Test SFD 1-4 is 86 ± 12 g.

E-2. Hydrogen Monitor Measurements

The on-line hydrogen monitor used in Test SFD 1-4 is a thermal conductivity device that measures the conductivity of the gas passing through the detector cell. Nitrogen carrier gas at a constant flow rate of 1.13 g/s was used to sweep hydrogen from the separator and past the analyzer. The instrument was set to read 0% for pure nitrogen and 100% for pure hydrogen. A nonlinear calibration was used to convert the measured hydrogen percentage to the actual hydrogen percentage.

Because thermal conductivity of a gas changes with temperature, it was necessary to keep the temperature of gases passing through the analyzer constant. This was accomplished by using a thermostatically controlled heater to maintain a temperature of 322 K for incoming gases over a wide range of temperature and flow rates. The gas flowing from the separator was sampled by a metering valve so that a flow of 200 cm^3/min was maintained through the analyzer, essentially independent of flow fluctuation through the separator during the experiment.

The on-line hydrogen concentration measured during Test SFD 1-4 is shown in Figure E-1. In general, the data indicate that hydrogen generation increased during the experiment, peaked at about 2900 s, then started to decrease. However, at about 3500 s, the monitor registered an increase in concentration, corresponding to the argon flow increase in the bundle at 3280 s. This increase in the monitor response was questioned. All other thermal-hydraulic measurements in the bundle (heat loss to the bypass, shroud thermocouples) indicated that the bundle was cooling down, yet the hydrogen monitor showed an increase.

As a result of this discrepancy, a series of experiments was performed to determine what phenomena other than an increase in hydrogen concentration could cause the hydrogen monitor signal to increase. The laboratory experiments examined the effects of flow rate, argon, moisture, water aerosols, and water injected under pressure on the signal of the conductivity meter. A detailed description of the experiments is provided on microfiche at the back of this report.

Table E-4. **Comparison of Test SFD 1-4 collection tank and benchmarking results**

Gas	Collection Tank	Collection Tank Corrected for Air In-leakage	Benchmark
N_2 (kg)	30.8 ± 4.40	30.7 ± 4.39	33.0
Ar (kg)	8.06 ± 1.15	11.7 ± 1.67	9.8
^{85}Kr (μCi/cm^3)	3.43 ± 0.52	5.10 ± 0.77	5.77 ± 0.55

The results of the tests indicate that only water injected under pressure could cause an increase in the magnitude of the monitor signal similar to that observed in Test SFD 1-4. Thus, it appears that the brief pressure pulse generated by the increase in argon flow at the end of the test pushed some condensed water through the separator and into the hydrogen monitor. The presence of water in the monitor cooled the filaments, which caused its signal to increase. As discussed in the next section, the monitor data were modified to account for this effect.

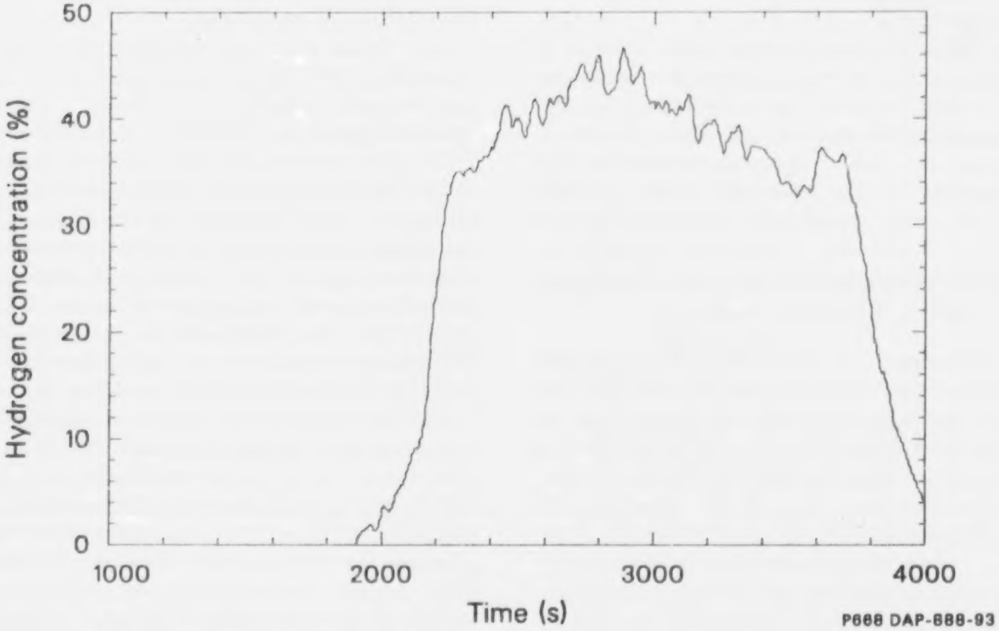

Figure E-1. Measured H_2 monitor response in Test SFD 1-4.

E-3. Effluent Transit Analysis

The purpose of the effluent transit analysis is to calculate transit times through the effluent sampling system and hydrogen generation and fission gas release rates in the bundle. With the calculated transit times, measurements from the fission product detection system (FPDS) and the hydrogen monitor can be correlated to events occurring in the bundle during the experiment. (The fission gas release rates calculated from transit times and FPDS measurements are discussed in Appendix G.)

Section E-3.1 provides a brief description of the model and the input used in the analysis. The hydrogen generation rate in the bundle is discussed in Section E-3.2. Section E-3.3 presents the calculated transit times associated with various portions of the effluent sampling and monitoring system. The results of the effluent transit analysis are assessed and uncertainties are assigned in Section E-3.4.

E-3.1 Model Description and Input. The effluent transit analysis was developed to determine the transit time through the sampling system and the hydrogen generation rate and fission gas release rates in the bundle based on the concentrations measured by the hydrogen monitor and the FPDS. Figure E-2 is a simplified schematic of the effluent sampling and monitoring system, highlighting details important to the transit analysis. The model assumes that the bundle and separator act as well-mixed volumes, whereas plug flow is assumed to exist in the upper plenum and the remaining piping in the system. The model considers potential steam condensation during transit through the effluent line, the mixing of hydrogen and nitrogen in the separator, the introduction of argon into the bundle in the experiment, and the effect of hydrogen generation on transit times and effluent flow rates. The effect of noble gases on transit times through the sample line is neglected because of their low concentration.

The well-mixed volume and plug flow assumptions have different effects on the calculated transport of fission products and hydrogen through the sample system. In a well-mixed volume, the concentration of material exiting the volume is assumed to change from that entering as a result of the mixing process. The rate that material enters the volume can be reconstructed if the flow rate and mole fraction of each material in the volume are known and instantaneous mixing is assumed, i.e.

$$V \frac{dX}{dt} = R_{in} - XQ_{out} \qquad \text{(E-3)}$$

where

R_{in} = source rate of material entering the volume (m^3/s),

Q_{out} = total effluent flow exiting the mixing volume (m^3/s),

X = mole fraction of material in the volume,

V = mixing volume (m^3).

Hence, this equation allows the details of hydrogen generation that were smeared out by the mixing process to be recovered.

In the long effluent line, plug flow appears to be a better assumption because it implies that concentrations of material entering the pipe are not altered in transit (except for thermal and radioactive decay corrections). Transport through the pipe does, however, introduce a delay between the time material first enters the pipe and the time at which it passes by the monitoring stations, i.e.

$$X_1 (t) = X_2 (t - \Delta t) \qquad \text{(E-4)}$$

where

$X_1(t)$ = mole fraction of material at the downstream location at time t,

$X_2(t - \Delta t)$ = mole fraction of material at the upstream location at an earlier time, $t - \Delta t$,

Δt = transit time between upstream and downstream locations.

Thus, both the shape and timing of the hydrogen concentration profile are changed during transit to the various detector locations in the system. Additional details of the models used in the effluent transit analysis are found in Reference E-1.

The effluent transit model requires the following input: (a) the system geometry, (b) volumetric flow

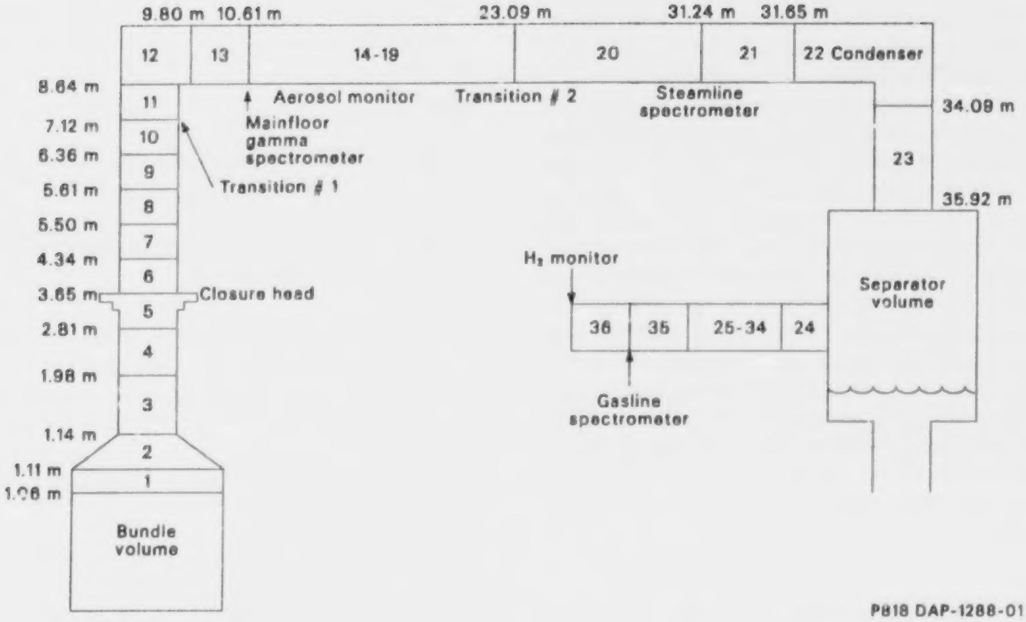
9.80 m
10.61 m
23.09 m
31.24 m
31.65 m
12
13
14-19
20
21
22 Condenser
8.64 m
11
Aerosol monitor
Transition # 2
Steamline spectrometer
34.09 m
7.12 m
10
Mainfloor gamma spectrometer
6.36 m
9
23
5.61 m
Transition # 1
8
35.92 m
5.50 m
7
4.34 m
H₂ monitor
6
Separator volume
3.65 m
Closure head
5
2.81 m
36
35
25-34
24
4
1.98 m
Gasline spectrometer
3
1.14 m
2
1.11 m
1
1.06 m
Bundle volume
P818 DAP-1288-01

Figure E-2. Schematic of the geometry used in the effluent transit analysis for Test SFD 1-4.

rates of steam and argon into the bundle and nitrogen into the separator, (c) temperatures of the effluent sampling and monitor system, and (d) the measured hydrogen concentration at the hydrogen monitor.

A schematic of the geometry of the effluent sampling and monitor system used for the transit analysis is shown in Figure E-2. The physical volume of each portion of the effluent line is presented in Table E-5. The volumetric flows of argon and nitrogen were taken from data recorded by the DARS, and the steaming rate was calculated from the change in water level in the experiment (see Appendix F). These flow rates are plotted in Figure E-3. The temperatures of the piping were taken from thermocouple readings recorded during the experiment and are listed in Table E-6. The measured hydrogen concentration is shown in Figure E-4.

E-3.2 Hydrogen Generation Rate. As discussed in Section E-3, the reliability of the hydrogen monitor data beyond ~3500 s was questioned. Specifically, laboratory experiments using the monitor indicate that the increase in the hydrogen monitor response at ~3500 s was caused by water entering the monitor and did not represent true hydrogen. As a result, the data were modified beyond 3500 s, as shown in Figure E-4. The best-estimate curve takes into account the dilution of hydrogen in the bundle following the argon flow increase and then decreases gradually until the end of the transient. The actual concentration profile beyond 3500 s is not known, which results in a large uncertainty in the integral hydrogen production from the monitor. Two separate calculations have been performed. Preliminary calculations were made using the raw data, and final calculations were made using the best-estimate data. This section discusses both calculations and explains why the final calculation is considered to represent the best estimate of the hydrogen generation rate in the experiment.

The hydrogen generation rate in the bundle calculated using both sets of data is shown in Figure E-5. As indicated in the figure, prior to the final increase in argon flow at ~3280 s the generation rates are identical in both calculations. The mole fractions of steam, hydrogen, and argon exiting the bundle for the final calculation are shown in Figure E-6.

Hydrogen generation began at approximately 1800 s. As shown in Figure E-6, the mole fraction

Table E-5. Volumes of the effluent sampling and monitoring system for Test SFD 1-4

Volume Number	Distance from Bottom of PBF Core (m)	Description	Volume (m^3)
1	1.06 - 1.11	Space above fuel	3.25 E – 04
2	1.11 - 1.14	Heat shield cone	8.36 E – 05
3	1.14 - 1.98	Effluent tube to closure head	2.84 E – 04
4	1.98 - 2.81		2.84 E – 04
5	2.81 - 3.65		2.93 E – 04
6	3.65 - 4.34	Closure head to end of standpipe	2.35 E – 04
7	4.34 - 5.50		4.49 E – 04
8	5.50 - 5.61	Standpipe to 90° bend	4.26 E – 05
9	5.61 - 6.36	90° bend to top of deck plates	2.90 E – 04
10	6.36 - 7.12	Top of deck to transition 1	2.94 E – 04
11	7.12 - 8.64	Transition 1 to main-floor gamma spectrometer	8.58 E – 05
12	8.64 - 9.80		6.55 E – 05
13	9.80 - 10.61		4.57 E – 05
14	10.61 - 11.33	Aerosol spool	4.38 E – 04
15	11.33 - 12.55	Aerosol spool to filtered steam samplers	6.89 E – 05
16	12.55 - 16.60	Filtered steam samplers to unfiltered samplers	2.29 E – 04
17	16.60 - 21.48	Unfiltered steam sampler outlet to 90° bend	2.75 E – 04
18	21.48 - 21.99	90° bend to Cubicle 13 penetration	2.92 E – 05
19	21.99 - 23.09	Cubicle 13 penetration to Transition 2	6.20 E – 05
20	23.09 - 31.24	Transition 2 to steamline gamma spectrometer	4.60 E – 04
21	31.24 - 31.65	Steamline gamma spectrometer to condenser	1.24 E – 05
22	31.65 - 34.09	Condenser	2.86 E – 05
23	34.09 - 35.92	Condenser to separator	5.56 E – 05
—	—[a]	Separator	2.39 E – 03
24	0.00 - 1.10	Separator exit to delay coil	3.34 E – 05

Table E-5. (continued)

Volume Number	Distance from Separator Exit (cm)	Description	Volume (m^3)
25	1.10 - 2.93	Delay coil	1.50 E – 04
26	2.93 - 4.76		1.50 E – 04
27	4.76 - 6.59		1.50 E – 04
28	6.59 - 8.42		1.50 E – 04
29	8.42 - 10.25		1.50 E – 04
30	10.25 - 12.08		1.50 E – 04
31	12.08 - 13.91		1.50 E – 04
32	13.91 - 15.74		1.50 E – 04
33	15.74 - 17.57		1.50 E – 04
34	17.57 - 19.40		1.50 E – 04
35	19.40 - 23.83	Delay coil to gasline spectrometer	1.35 E – 04
36	23.83 - 28.79	Gasline spectrometer to H_2 monitor	1.51 E – 04

---

a. Because separator is a mixing volume, no linear distance is provided.

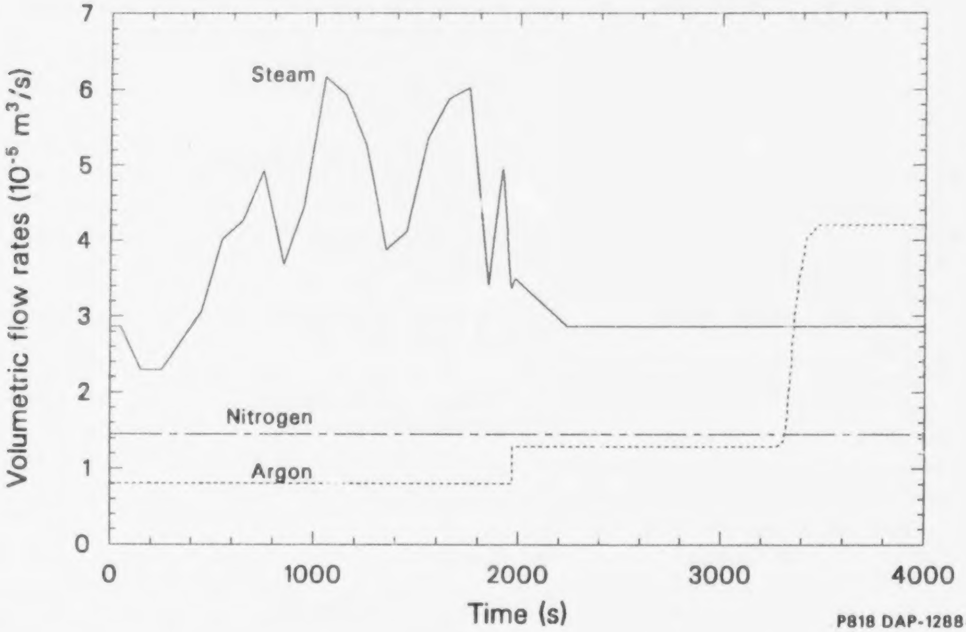

Figure E-3. Flow rates of steam, argon, and nitrogen input to the effluent transit analysis for Test SFD 1-4.

Table E-6. Temperatures of the effluent line in Test SFD 1-4 (K)

Time (s)	Heat Shield Cone (Vol 1,2)[a]	Steam Tube to Closure Head (Vol 3)[b]	Steam Tube to Closure Head (Vol 4)[c]	Steam Tube to Closure Head (Vol 5)[d]	Above Closure Head (Vol 6,7)	Top of Standpipe (Vol 8,9)	Inlet to Aerosol Monitor (Vol 10-13)	Middle of Aerosol Monitor (Vol 14)	Outlet of Filtered Samplers (Vol 15,16)	Outlet of Unfiltered Samplers (Vol 17)	Bend Before Cubicle 13 (Vol 18)	Before FPDS in Cubicle 13 (Vol 19-21)	Condenser Inlet (Vol 22,23)
0	723	679	681	730	595	673	578	582	589	410	509	511	511
300	729	682	683	725	606	678	580	585	589	442	512	512	512
600	757	703	686	728	607	678	580	585	589	442	512	512	512
900	808	733	696	726	628	668	578	581	538	517	515	515	515
1200	888	760	704	725	636	668	589	589	589	533	528	524	525
1500	960	771	706	725	629	678	589	589	517	528	524	522	522
1800	1071	817	717	726	623	679	580	589	589	522	528	522	517
2100	1393	730	705	720	578	688	595	595	595	505	546	558	505
2400	1455	778	699	725	566	687	595	595	589	494	567	589	497
2700	1437	788	700	730	580	685	602	603	592	480	588	612	494
3000	1390	748	696	727	573	683	601	601	589	455	600	633	500
3300	1050	721	693	725	622	673	606	606	651	400	623	650	505
3600	900	817	711	732	640	673	606	606	600	400	606	645	522
3900	850	793	713	728	640	673	606	606	600	400	606	645	522
4200	800	772	711	724	640	673	606	606	600	400	606	645	522

---

[a] Average of two steam TCs at 0.99 m and three steam TCs at 1.14 m; values beyond 3000 s are estimated.

[b] Average of steam TC at 1.54 m, two steam tube TCs at 1.84 m, and a coupon TC at 1.57 m.

[c] Average of steam TC at 2.35 m, two steam tube TCs at 2.29 m, and a coupon TC at 2.38 m.

[d] Average of steam TC at 3.36 m, three steam tube TCs at 3.4 m, and a coupon TC at 3.4 m.

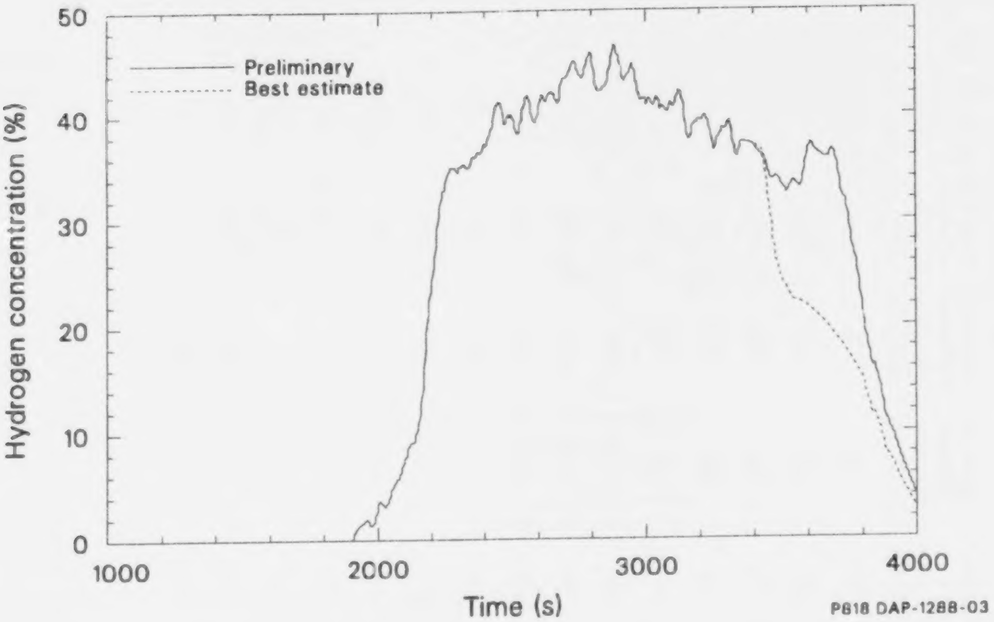

Figure E-4. Preliminary and best-estimate hydrogen monitor data for Test SFD 1-4.

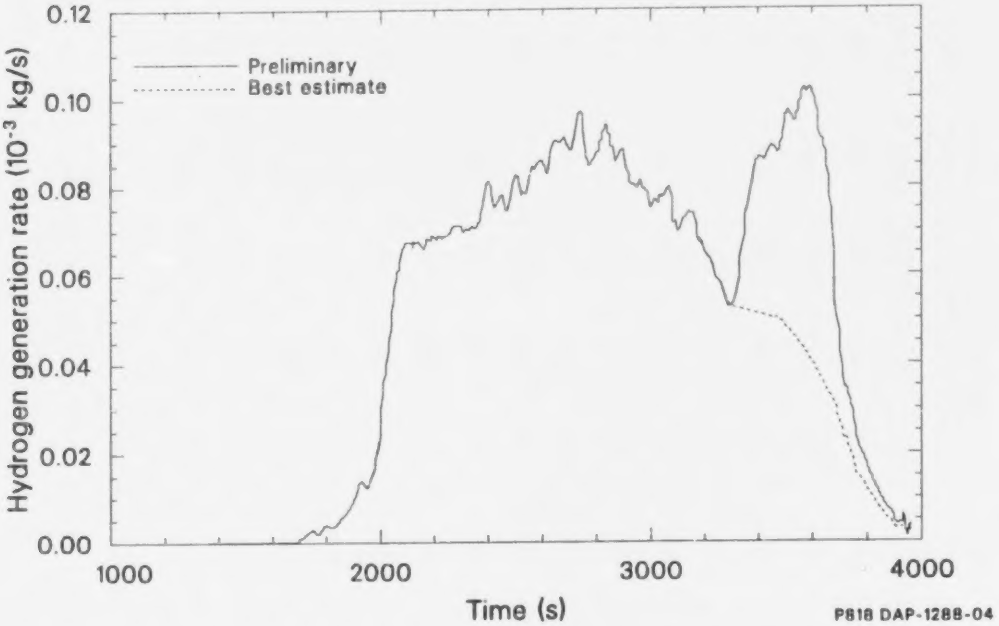

Figure E-5. Preliminary and best-estimate hydrogen generation rates in the bundle for Test SFD 1-4.

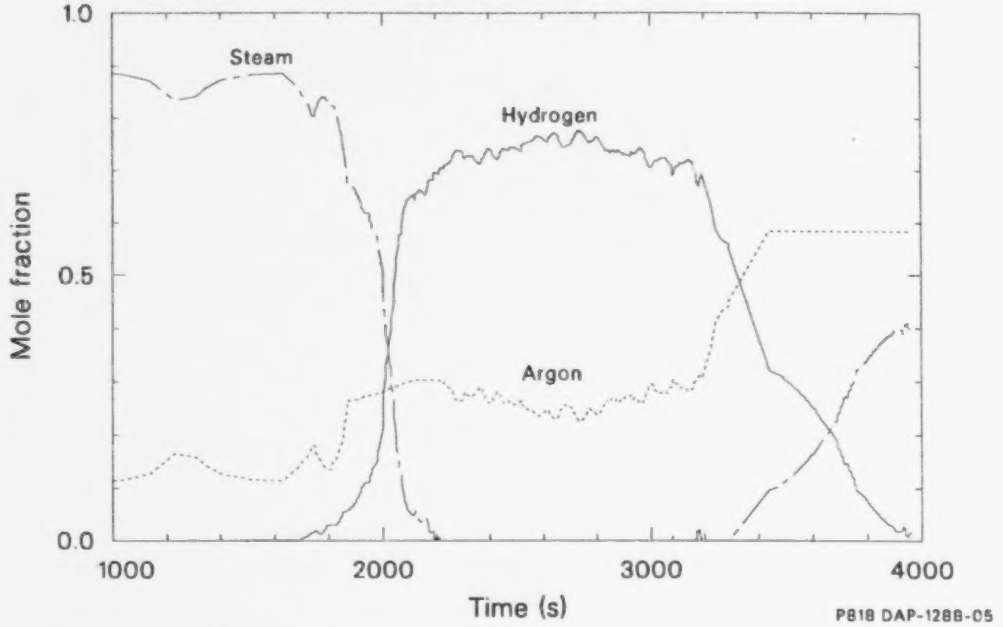

Figure E-6. Mole fraction of steam, hydrogen, and argon exiting the bundle in Test SFD 1-4.

of steam exiting the bundle was about 0.05, indicating that most of the input steam was being converted to hydrogen. The generation rate increased quickly thereafter and leveled off at 0.7 g/s by 2100 s.

The rapid increase in hydrogen generation lags behind the rapid increase in cladding thermocouple temperature measured in the bundle beyond 1700 s. This delay in the increase of the H_2 generation rate is associated with the perfect mixing assumption used in the effluent transit analysis and not the estimate of the transit time through the sampling system. Results in Section E-3.4.1 indicate that the calculated transit times agree with those determined from measurements of short- and long-lived isotopes made by the on-line gamma spectrometers. Equation (E-3) assumes that the concentrations exiting the bundle and separator are representative of the average concentration in those volumes. The model does not account for the effects of transient or imperfect mixing that might occur prior to attaining a well-mixed state. When hydrogen is first generated, the volume is probably not perfectly well-mixed. As a result, the measured concentration of hydrogen exiting the volume is lower than the actual average concentration in the volume. This behavior would suggest that the hydrogen generation rate is biased low during the early part of the transient until the separator and volume become well mixed. The rapid increase between 2000 and 2100 s suggests that the bundle and separator became well mixed during this time.

Between 2300 and 3100 s, the hydrogen generation rate exceeded that predicted by total consumption of the inlet steam flow shown in Figure E-3. As a result, the steaming rate was increased to match the volumetric hydrogen generation rate. (This procedure was used to assure a proper estimate of the transit time through the system.) The modified steaming rate based on the hydrogen data is shown in Figure E-7. Figure E-6 illustrates that during most of the high-temperature phase of the transient, the effluent consisted of hydrogen and argon. The hydrogen generation rate continued to increase during and following the 223-s power hold (2369 to 2592 s). The hydrogen generation rate began to decrease at about 2700 s.

At 3280 s (the time that the argon flow was increased), the preliminary and best-estimate calculations differ. In the preliminary analysis with the raw monitor data, the hydrogen generation rate increased greatly, coincident with the increased

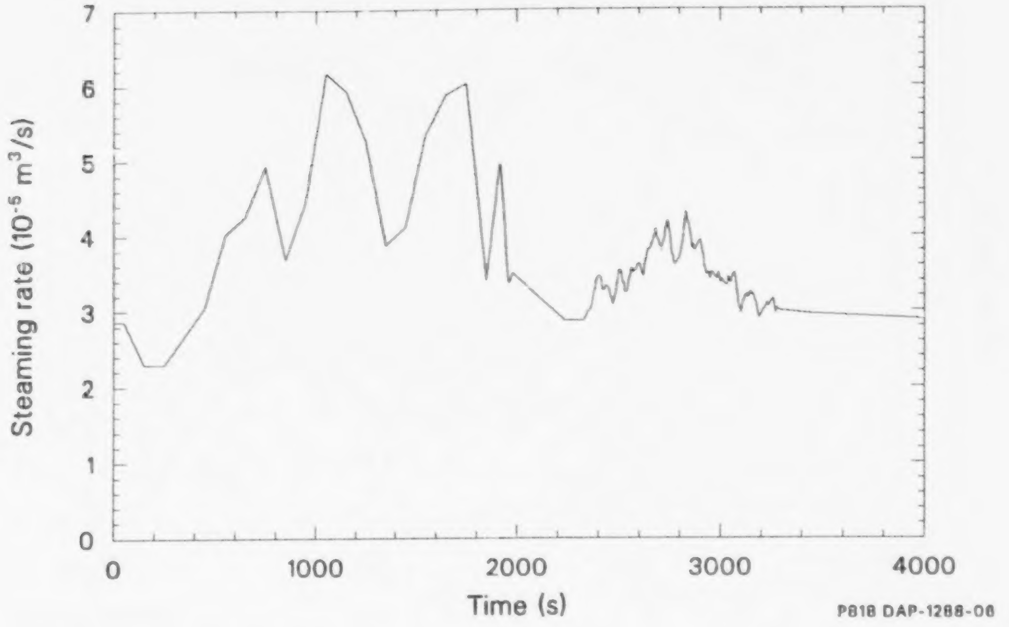

Figure E-7. Modified steaming rate for Test SFD 1-4.

argon flow used to cool the bundle. The calculated hydrogen generation rate exceeded that for total consumption of the nominal input steam. This apparent late increase in the hydrogen generation rate is not in agreement with other observations from Test SFD 1-4. First, if this late apparent hydrogen is ignored, then for Test SFD 1-4 the on-line monitor would suggest that ∿98 g of hydrogen were generated, in good agreement with the collection tank value of 86 ± 12 g. Second, this late increase in hydrogen generation rate would correspond to heatup rates as large as the heatup rates generated during rapid oxidation early in the experiment. Finally, because the heat loss to the bypass decreased during this time, temperatures were probably also decreasing in the bundle. Based on these observations, the large increase in the hydrogen generation rate is not consistent with other test data and is clearly not in agreement with our understanding of the behavior of the bundle at this time. As discussed in Section E-2, laboratory experiments on the monitor indicate that the monitor signal beyond 3500 s is believed to be due to water entering the analyzer due to the pressure pulse generated by the argon flow increase.

As can be seen in Figure E-6, the calculated hydrogen generation rate in the best-estimate calculation decreased following the argon flow increase as the bundle cooled and the experiment was terminated. This result agrees with other cooldown data in the experiment. In the following section, the results and sensitivity studies are based on the best-estimate calculation.

The integral of the hydrogen generation rate is plotted in Figure E-8. The total hydrogen generated in Test SFD 1-4 up to the time of the argon flow increase at 3280 s is 98 g. As discussed in Section E-5, assuming a 5% error in the on-line data, an engineering estimate of 5 g is assigned to the uncertainty in the integral hydrogen predicted from the on-line monitor up to 3280 s. Beyond 3280 s, the integral is highly uncertain because the actual concentration following the argon flow increase is not known. Integration of the best-estimate hydrogen generation rate from 3280 s to the end of the transient yields an additional 23 g. This 23 g is considered to be an upper estimate of the hydrogen generated late in Test SFD 1-4. As a result, the hydrogen generation from integration of the on-line monitor is 98 (+ 28/ − 5) g. This value is in

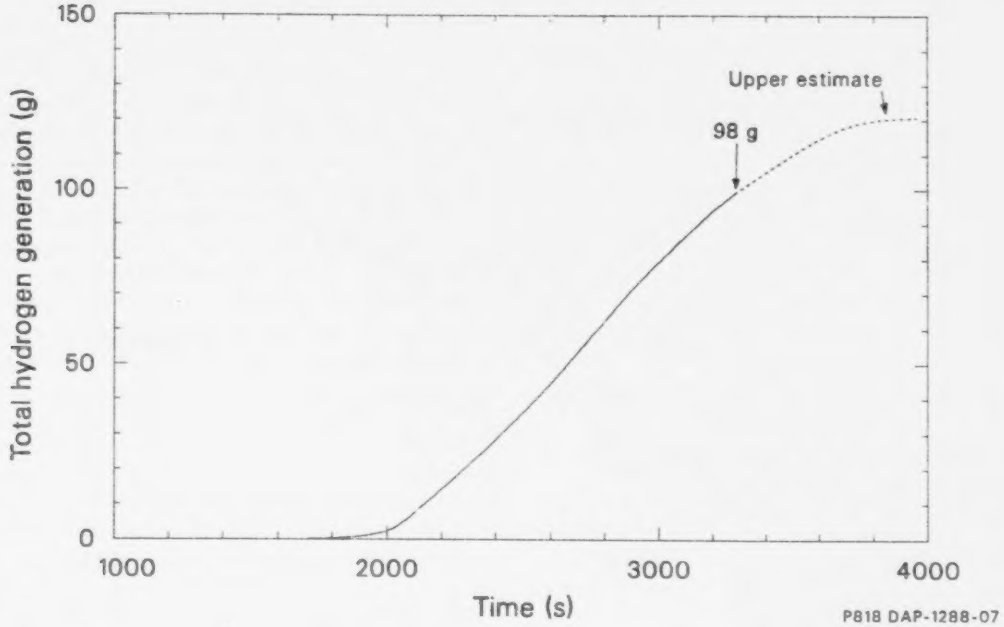

Figure E-8. Integral hydrogen production in Test SFD 1-4.

good agreement with the collection tank value of 86 ± 12 g.

E-3.3 Transit Times. The effluent transit analysis calculates the transit time from the bundle to various detector locations in the sample system. Transit times can only be calculated for the plug flow volumes because instantaneous mixing is assumed in the well-mixed regions.

Figure E-9 presents the calculated transit time from the bundle exit to the separator inlet. Initially, the transit time in the line is about 120 s. The transit time increases to a peak of 150 s at approximately 1500 s due to both a decrease in the steaming rate (as shown in Figure E-7) and steam condensation in the line. Between 1500 and 2000 s, the transit time through the effluent line generally decreases, with the exception of the sudden increase at 1780 s. This sudden increase corresponds to a decrease in the steaming rate at that time, as indicated in Figure E-7. The transit time between 2000 and 3000 s decreases slowly from 120 to 90 s due to the increase in steaming (and hydrogen generation) rate. At 3280 s, the transit time begins to decrease as a result of the increase in argon flow through the bundle. At 3700 s, the transit time levels off at 70 s.

Figure E-10 is a plot of the transit times through various sections of the line in the effluent sampling and monitoring system, specifically from the bundle exit to the mainfloor gamma spectrometer, between the mainfloor and steamline spectrometers, and from the steamline spectrometer to the separator inlet. Prior to 1800 s, the transit time from the mainfloor to the steamline spectrometer exceeds the transit time from the bundle exit to the mainfloor spectrometer. Examination of wall temperatures and effluent composition at this time indicates that temperatures were cool enough to cause steam condensation in the line between the spectrometers. As a result, the transit time increased in that section of line. After 1900 s, the noncondensible gas fraction increased due to increases in hydrogen and argon, resulting in a reduction in the partial pressure of steam thus limiting steam condensation. As a result, the transit time in the line between the spectrometers decreased to between 35 and 40 s.

As can be seen in the figure, beyond 1900 s the transit times behave in the same manner as the overall transit time in Figure E-9. The transit time from

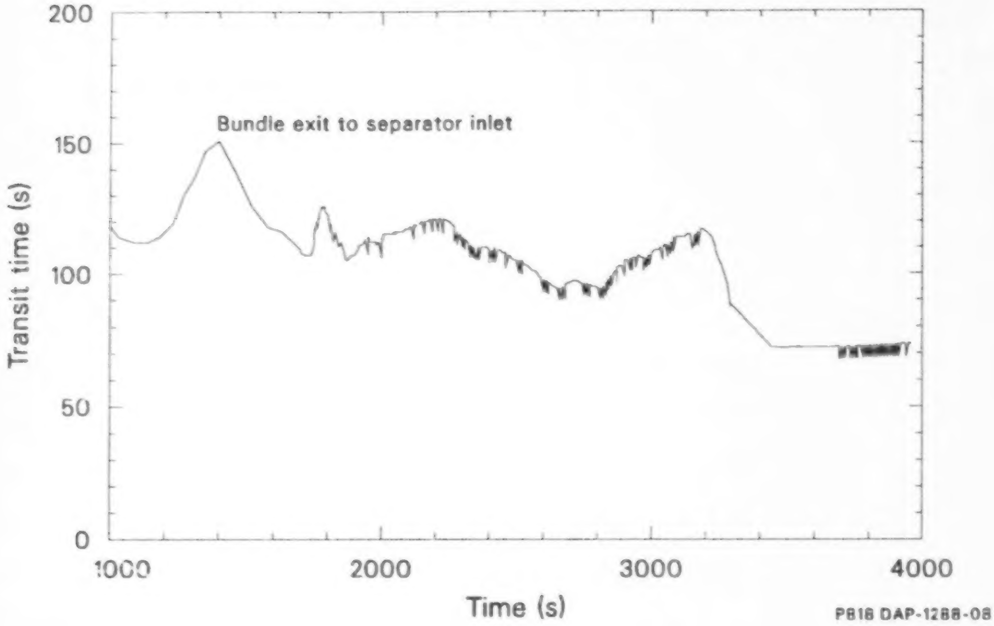

Figure E-9. Transit time from bundle exit to separator inlet for Test SFD 1-4.

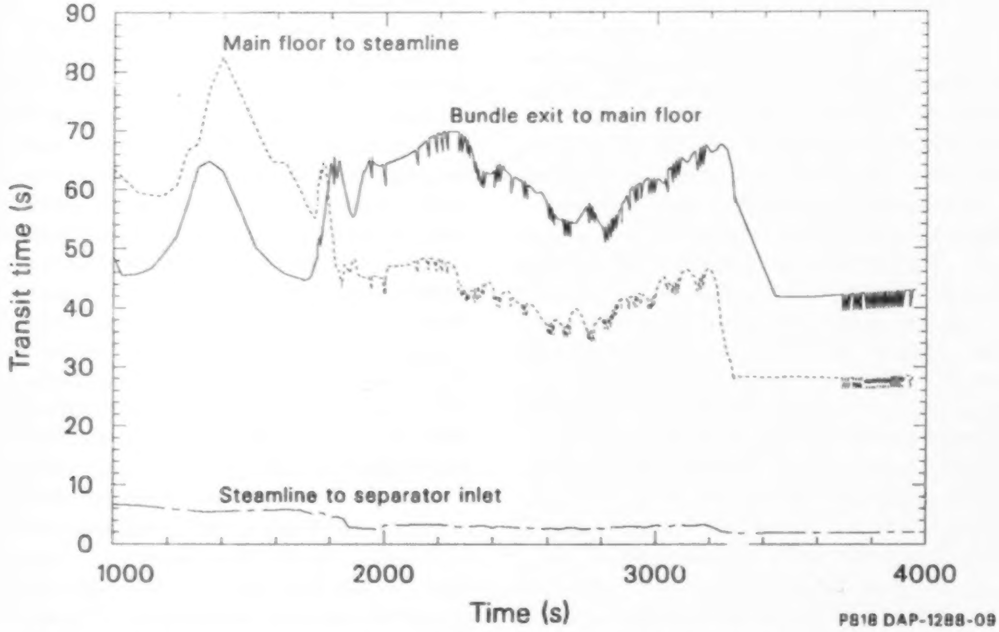

Figure E-10. Transit time to various locations in the effluent sampling and monitoring system for Test SFD 1-4.

the bundle exit to the mainfloor spectrometer represents about 58% of the total transit time in the effluent line. The transit time from the mainfloor spectrometer to the steamline detector accounts for about 40% of the total delay, and the remaining 2% of the transit time is associated with the line from the steamline spectrometer to the separator inlet.

Figure E-11 is a plot of the transit time from the separator outlet to the hydrogen monitor as a function of the time at the separator. The overall transit time is partitioned into the transit time from the separator outlet to the gasline spectrometer and from the gasline spectrometer to the hydrogen monitor. The transit times in the gas line are inversely proportional to the rate of hydrogen, argon, and nitrogen flow out of the separator. Prior to any significant hydrogen generation ($t < 1700$ s), the transit time is approximately 100 s. As hydrogen is produced in the test, more gas flows out of the separator, causing the transit time in the gas line to decrease and level off at about 50 s. Late in the experiment, the additional argon that was injected to cool the bundle reaches the separator, causing the transit time to decrease to about 35 s. A large portion of the transit time in the gas line was due to a delay line that was installed between the separator outlet and the gasline spectrometer.

E-3.4 Benchmarking and Assessment of the Effluent Transit Analysis. Both the assumptions used in modeling the sampling system and the uncertainties associated with the input parameters used in the analysis require an assessment of the effluent transit analysis to be performed. The assessment not only increases confidence that both the modeling assumptions and transit time calculations are valid, but also establishes that the timing of the calculated hydrogen generation rate and fission gas release rates is reasonable. The assessment will be divided into three parts. First, the calculated transit time will be compared to the transit time based on isotopic ratios measured by the gamma spectrometers. Second, the results of sensitivity analyses using the model will be presented. Finally, these results will be combined to determine an engineering estimate of the uncertainty in both the timing and magnitude of the hydrogen generation rate.

E-3.4.1 Transit Time Comparison. On-line temporal data from the mainfloor and steamline gamma spectrometers can be used to determine the transit time between the two spectrometers. Each spectrum recorded by a given spectrometer contains information on the relative concentration of a variety of noble gas isotopes. For example, both the mainfloor and steamline spectrometers recorded concentrations of some very short-lived krypton and xenon isotopes (i.e ^{89}Kr, ^{90}Kr, and ^{139}Xe) and some relatively long-lived krypton and xenon isotopes (i.e., ^{85m}Kr, ^{88}Kr, and ^{135}Xe). By comparing a ratio of short- to long-lived isotopes at the mainfloor spectrometer to the same ratio at the steamline spectrometer, the transit time can be calculated, i.e.

$$\frac{A_{mf,s}(t_1)}{A_{mf,\ell}(t_1)} = \frac{A_{st,s}(t_2)}{A_{st,\ell}(t_2)} \exp(\lambda_s t_d) \qquad \text{(E-5)}$$

where

$A_{mf,s}(t_1)$ = activity concentration of short-lived nuclide at the mainfloor detector at time t_1 (μCi/cm^3),

$A_{mf,\ell}(t_1)$ = activity concentration of long-lived nuclide at the mainfloor detector at time t_1 (μCi/cm^3),

$A_{st,s}(t_2)$ = activity concentration of short-lived nuclide at the steamline detector at time t_2 (μCi/cm^3),

$A_{st,\ell}(t_2)$ = activity concentration of long-lived nuclide at the steamline detector at time t_2 (μCi/cm^3),

λ_s = decay constant of short-lived isotope,

t_d = transit time ($= t_2 - t_1$).

Equation (E-3) can be readily solved by iteration to determine t_d, the desired transit time between detectors.

A Taylor expansion was used to propagate the estimated concentration uncertainties to uncertainties in transit time. The uncertainty in the transit time, t_d, is estimated as

$$^{\sigma}t_d(t_1) = \frac{1}{\lambda_s} \left\{ \left[\frac{^{\sigma}A_{mf,s}(t_1)}{A_{mf,s}(t_1)} \right]^2 + \left[\frac{^{\sigma}A_{mf,\ell}(t_1)}{A_{mf,\ell}(t_1)} \right]^2 + \left[\frac{^{\sigma}A_{st,s}(t_2)}{A_{st,s}(t_2)} \right]^2 + \left[\frac{^{\sigma}A_{st,\ell}(t_2)}{A_{st,\ell}(t_2)} \right]^2 \right\} \qquad \text{(E-6)}$$

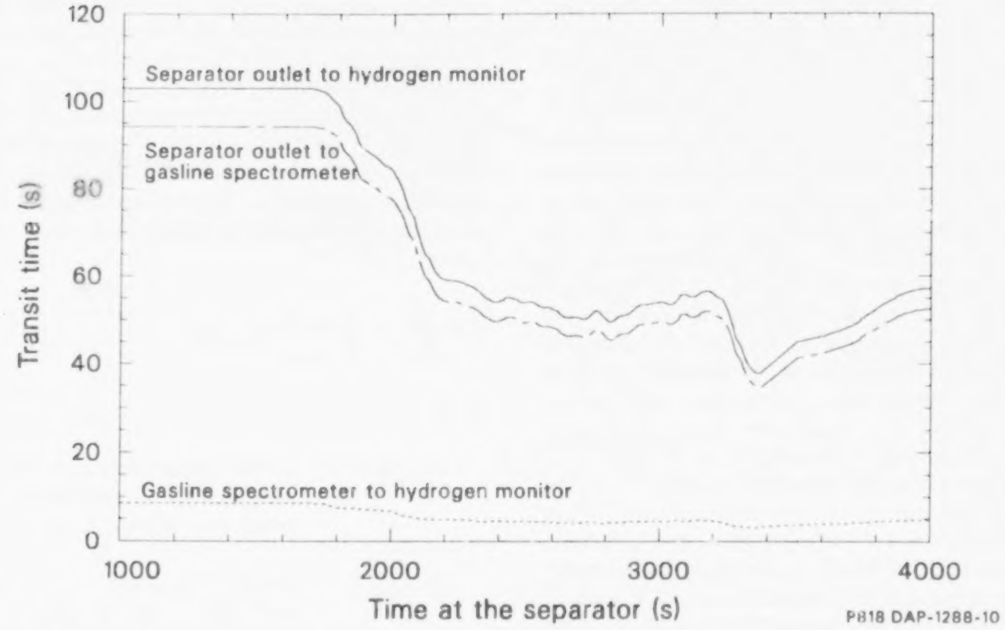

Figure E-11. Transit time through the gas line versus time at the separator for Test SFD 1-4.

The activity ratios in Equation (E-3) were calculated for ^{89}Kr/^{85m}Kr, ^{89}Kr/^{88}Kr, ^{90}Kr/^{88}Kr, ^{90}Kr/^{85m}Kr, and ^{139}Xe/^{135}Xe. The calculated activity ratios and their estimated relative errors were smoothed (three point smooth) and interpolated (modified spline interpolation). Before 2000 s, very little fission product release occurred in the experiment; after 3000 s, the reactor power was so low that very few short-lived fission gases were being generated. As a result, the interpolated curve was used to develop a set of ratios and uncertainties at 10-s intervals from about 2000 to 3000 s.

To determine the t_d values that satisfied Equation (E-3), a technique was used that allowed multiple solutions for a given t_1. An activity ratio was read from the interpolated mainfloor detector file. The next entry in the steamline detector file was inspected to determine if t_d calculated from Equation (E-3) was within 10 s of the value $(t_2 - t_1)$ from the time entries in the interpolated files. If this criterion was satisfied, then the mainfloor detector time (t_1), the calculated transit time (t_d), and the steamline detector time (t_2) were recorded. Then the next entry in the steamline detector file was read and inspected in the same manner. If the criterion on transit time was met, this result was also recorded. Note that this method allows multiple results for a given t_1. However, detailed inspection of the results indicate that there were fewer than five solutions for a given t_1 and that multiple solutions yielded transit times that were not significantly different.

The results for all five isotopic ratios investigated are shown in Figure E-12. The transit times show wide fluctuation depending on the isotopic ratio. In general, because the uncertainty is inversely proportional to the short-lived decay constant, λ_s, the ^{89}Kr results are more uncertain. To determine a best estimate of t_d as a function of t_1, a weighted average of the transit times was calculated. To determine an arithmetic average of the transit times that results in the minimum error, the transit time for each isotopic ratio was weighted inversely by the square of its own error,$^{E\text{-}3}$ i.e.,

$$\bar{t}_d = \frac{\sum_{i=1}^{N} a_i t_{d_i}}{\sum_{i=1}^{N} a_i} \qquad \text{(E-7)}$$

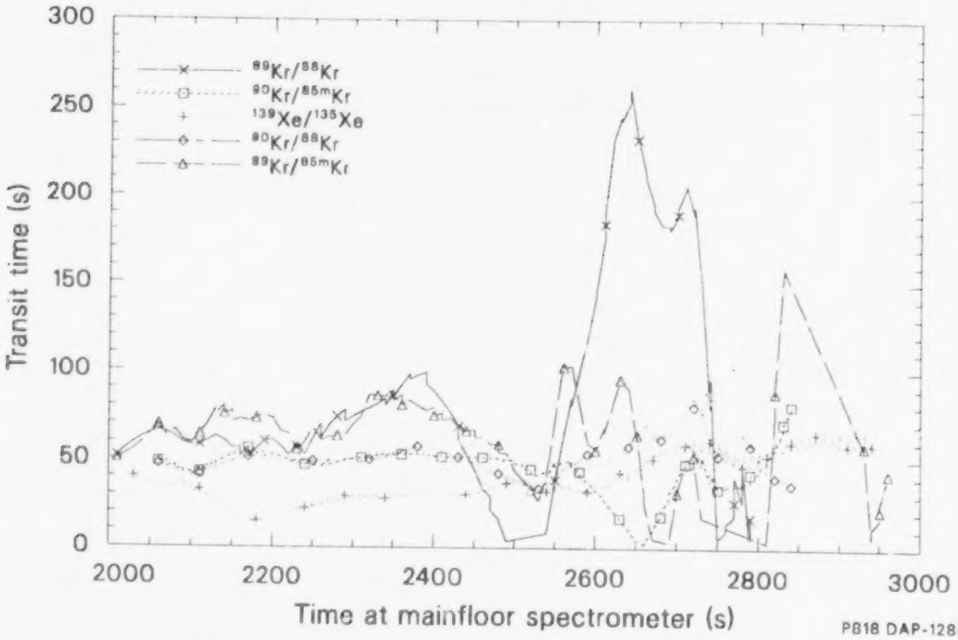

PB18 DAP-1288-11

Figure E-12. Transit times calculated from spectrometer isotopic ratios from Test SFD 1-4.

where

$$a_i = \frac{\dfrac{1}{\sigma^2_{t_{d_i}}}}{\displaystyle\sum_{i=1}^{N} \frac{1}{\sigma^2_{t_{d_i}}}} \tag{E-8}$$

t_d is the weighted transit time, t_{d_i} is the transit time determined from ratio i, and $\sigma_{t_{d_i}}$ is the associated error. The standard deviation was then calculated using

$$\frac{1}{\sigma^2_{t_{di}}} = \left(\sum_{i=1}^{N} \frac{1}{\sigma^2_{t_{d_i}}}\right)^{1/2} . \tag{E-9}$$

Because five individual transit times were calculated, a student t distribution with four degrees of freedom (t = 2.776) was used to determine the 95% confidence interval on the weighted average transit time, t_d. For simplicity, the weighted average transit time based on the spectrometer data will be termed the measured transit time.

The results are compared in Figure E-13 to the transit time from the mainfloor to steamline spectrometer as calculated by the effluent transit analysis. As seen in the figure, the agreement is almost always within the 95% confidence interval. Between 2300 and 2700 s main floor time, the agreement is excellent. The difference between the measured transit time and the transit time from the effluent transit analysis is about 5 s. Based on this comparison, the steaming rate and hence the transit time calculated by the effluent transit analysis are considered to be reasonable.

E-3.4.2 Sensitivity Results. Statistical uncertainties are difficult to assign to the calculated hydrogen generation rate because of the difficulty in trying to describe the level of confidence associated with the various assumptions in the effluent transit model. Uncertainties in the assumptions of the well-mixed character of the bundle and separator, as well as in the physical volumes, the steaming rate, and the effluent line temperatures, contribute to the overall uncertainty in the calculated hydrogen generation rate. Because a rigorous statistical

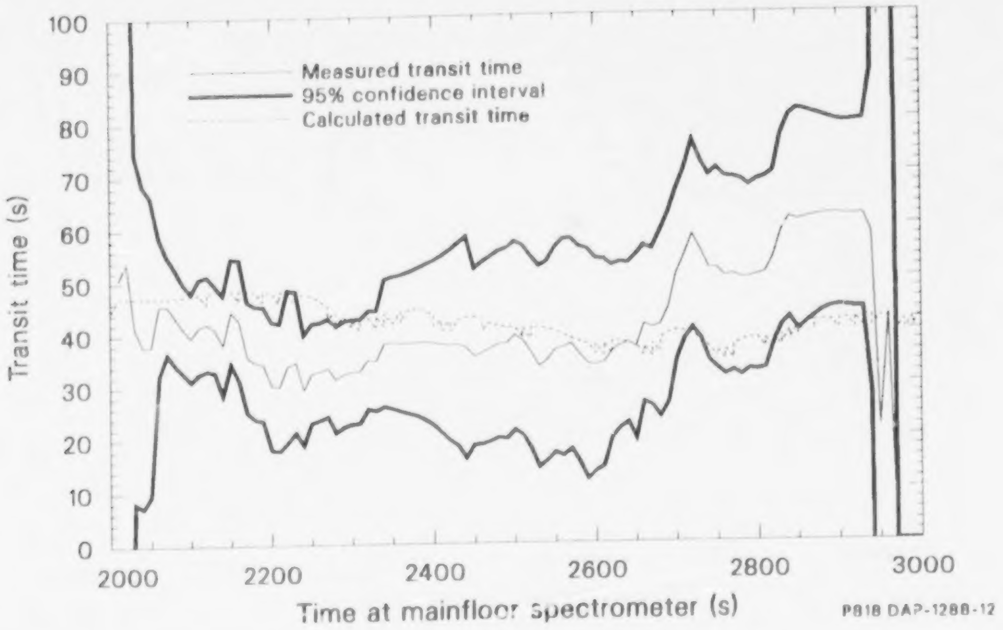

Figure E-13. A comparison of the measured and calculated transit times for Test SFD 1-4.

uncertainty analysis cannot be performed, sensitivity studies have been performed to determine the effect changes in both the steaming rate and the measured hydrogen data have on the predicted timing and magnitude of the hydrogen generation rate in the bundle.

Sensitivity calculations were performed to determine the effect of a ± 5% change in the measured hydrogen data on the predicted hydrogen generation rate in the bundle. Only data prior to the argon cooldown were used in the sensitivity study. The hydrogen generation rates for the ± 5% change and the original base case are shown in Figure E-14. As expected, the 5% change in the concentration data affects the magnitude but not the timing of the hydrogen generation rate up to 3280 s. Examination of the tabular data suggests that a 5% change in the concentration data results in an average 7% change in the magnitude of the hydrogen generation rate.

The integrals of the three curves in Figure E-14 are shown in Figure E-15. The total hydrogen generated up to 3280 s is estimated to be 98 g for the base case, 103 g for the + 5% change and 93 g for the – 5% change.

A sensitivity calculation was also performed to examine the effect of doubling the nominal input steaming rate (shown in Figure E-3) on the predicted hydrogen generation rate. It was expected that, given the hydrogen concentration measured at the monitor, the change in the steaming rate would not affect the magnitude of the predicted rate but rather would affect the timing of the hydrogen generation rate through the transit time calculation. The results shown in Figure E-16 confirm these expectations. With a higher steaming rate, there is a general shift in the predicted hydrogen generation rate. Because the steaming rate is greater, the transit time decreases and events recorded at the hydrogen monitor are correlated to later bundle times relative to the base case. Examination of the tabulated data indicates that a change in steaming rate by a factor of two results in an average change of 1.8% in the magnitude of the hydrogen generation rate and less than 2.5% change in the integral hydrogen production.

The factor of two change in the steaming rate was intended merely to illustrate the effect that such a large change would have on the timing of the predicted hydrogen generation rate. The transit time comparison of Section E-3.4.1 indicates that the

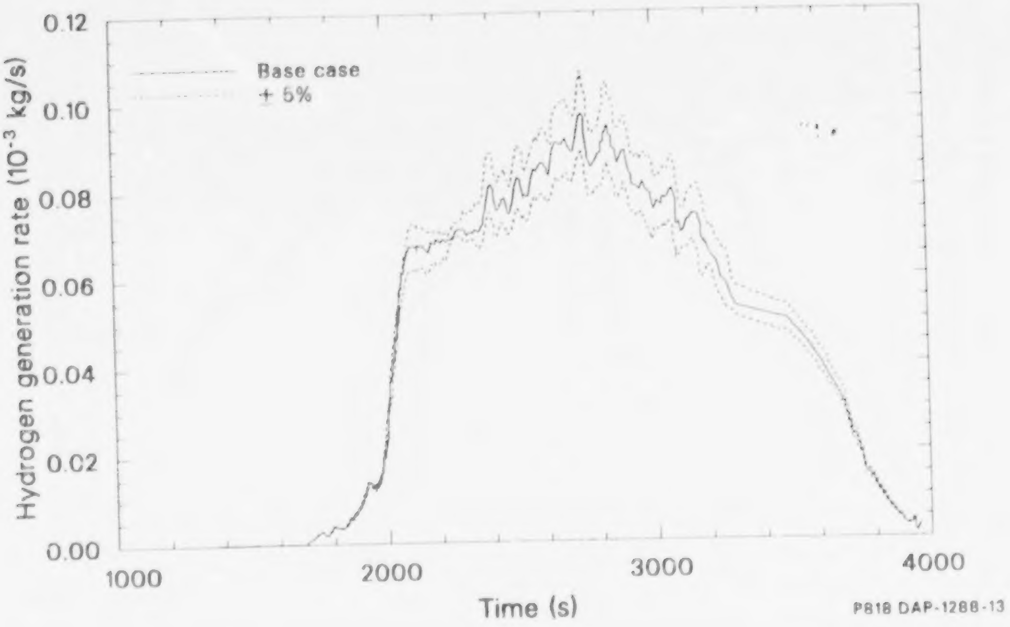

Figure E-14. The effect of a ± 5% change in the measured hydrogen concentration on the hydrogen generation rate for Test SFD 1-4.

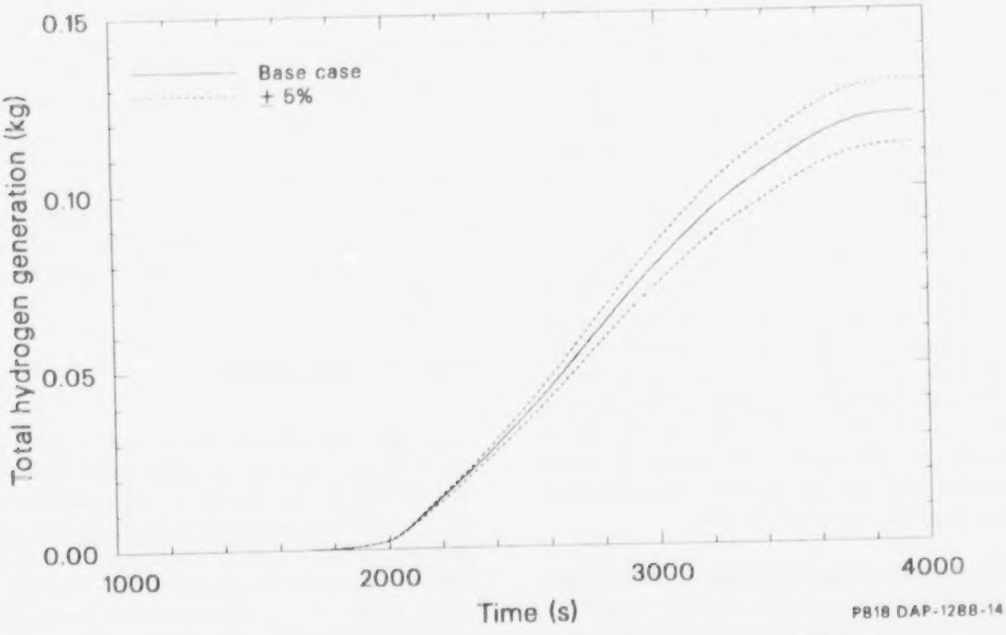

Figure E-15. The effect of a ± 5% change in the measured hydrogen concentration on the integral hydrogen generation rate for Test SFD 1-4.

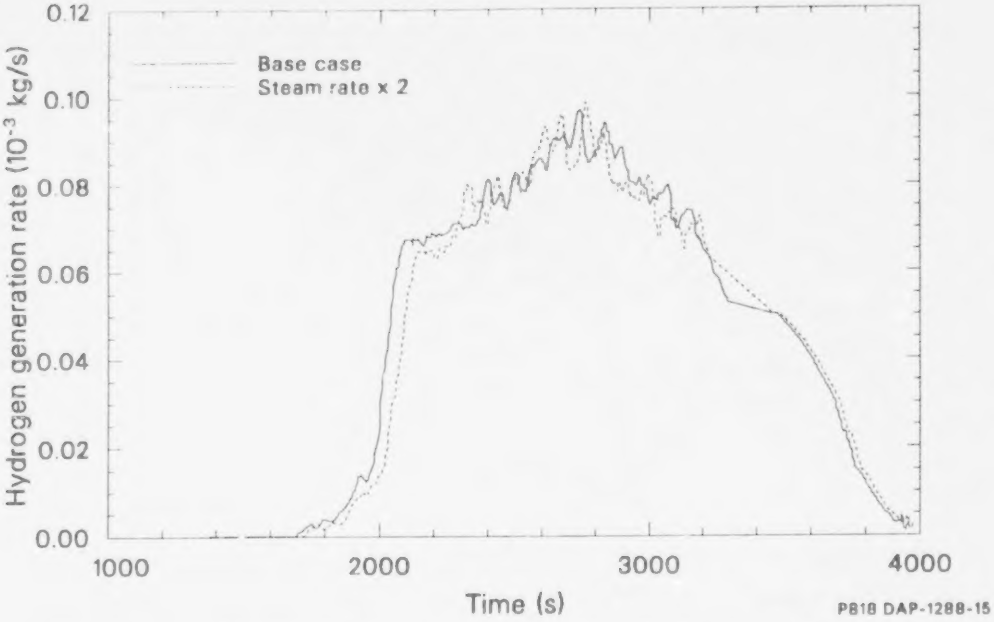

Figure E-16. The effect of doubling the input steaming rate on the predicted hydrogen generation rate for Test SFD 1-4.

uncertainty in the steaming rate and transit time is much less than a factor of two. As seen in Figure E-13, the difference between the calculated transit time from the mainfloor to the steamline spectrometer and the measured transit time ranges from + 15 to − 20 s but is usually within 5 to 10 s of the average time. In terms of percentages, the calculated transit times range from +43% to −33% of the measured transit time. However, most of the calculated transit times are within 15% of the measured transit time data. Hence, given the uncertainties associated with the on-line isotopic data, for simplicity a constant of 15% will be used as an engineering estimate of the uncertainty in the predicted transit time. The effect of a 15% change in the overall transit time on the hydrogen generation rate is shown in Figure E-17. The effect is difficult to see on the plot because the 15% change in transit time results in a small change in the predicted bundle time at which events are plotted.

E-3.4.3 Engineering Uncertainty Estimates. The transit time comparison and the sensitivity study of Sections E-3.4.1 and E-3.4.2 provide a means of obtaining an engineering estimate of the uncertainty associated with the timing and magnitude of the predicted hydrogen generation rate. By overlaying the plots in Figures E-14 and E-17, an envelope can be developed that would represent an engineering estimate of the uncertainty in both the magnitude and timing of the hydrogen generation rate in the bundle. This result, shown in Figure E-18, indicates that the envelope is relatively narrow, reflecting high confidence in the estimated hydrogen generation rate and its integral prior to 3280 s. Beyond 3280 s, the hydrogen generation rate represents a best estimate and is more uncertain.

E-4. Conclusions

On-line and off-line measurements have been made to determine the hydrogen generated during Test SFD 1-4. The results of the collection tank have been corrected for air in-leakage and benchmarked against values of other gases expected in the tank. Based on this analysis, the collection tank result of 86 ± 12 g represents the best-estimate value for hydrogen generation in the experiment.

The response of the hydrogen monitor following the argon flow increase is not consistent with the

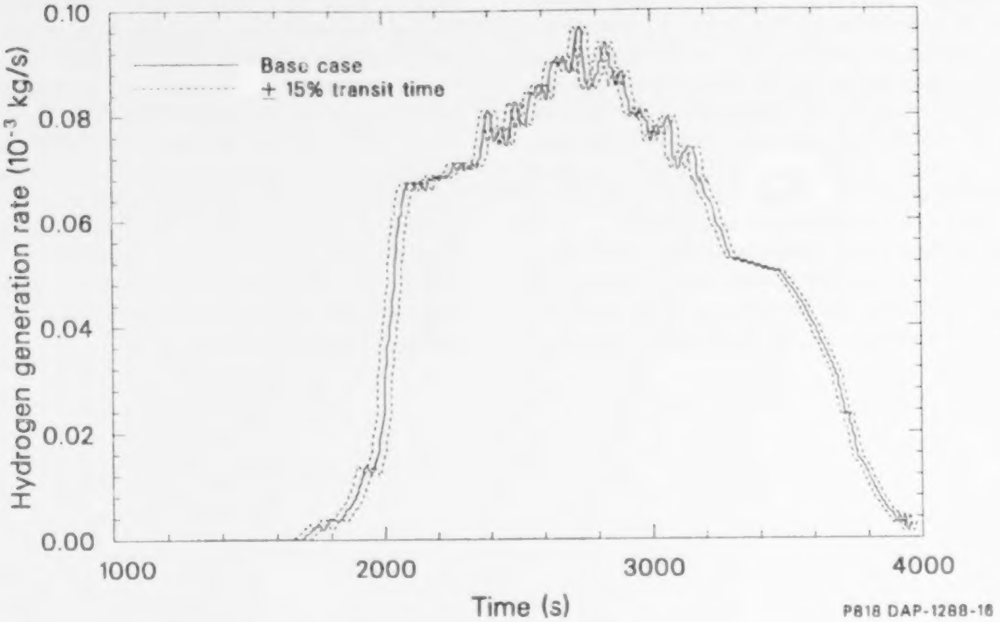

Figure E-17. The effect of a 15% change in total transient time on the hydrogen generation rate for Test SFD 1-4.

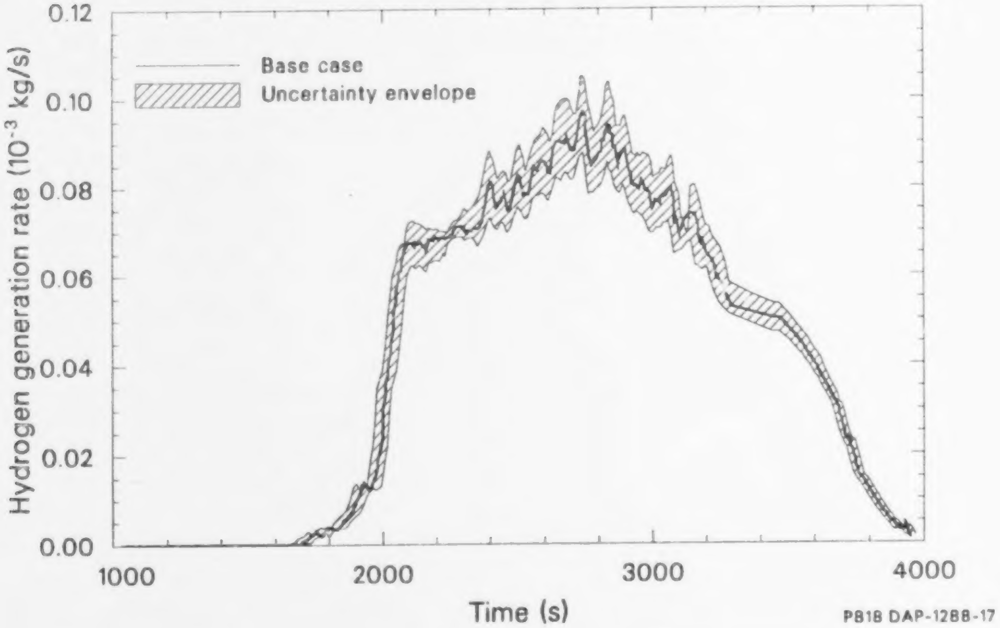

Figure E-18. The hydrogen generation rate for Test SFD 1-4 and its uncertainty envelope.

thermal-hydraulic conditions in the bundle late in the experiment. As a result, laboratory experiments were performed on an identical monitor to better understand its behavior during Test SFD 1-4. The laboratory experiments indicate that the increase in the monitor signal beyond ~3500 s was the result of water entering the monitor coincident due to the pressure pulse generated by the argon flow increase in the bundle. As a result, a best-estimate curve was developed to describe the monitor response beyond 3500 s; and this was used in the effluent transit analysis.

The effluent transit analysis has been performed for Test SFD 1-4 to determine transit times in the effluent sampling and monitoring system and the hydrogen generation rate in the bundle. The effluent transit analysis was assessed by comparing the calculated transit times to transit times based on short-to-long-lived isotopic ratios measured by the gamma spectrometers. The calculated transit time was in good agreement with the data, indicating that the assumptions and input used in the analysis were reasonable. In addition, based on the transit time comparison and the uncertainty in the on-line response of the monitor, an engineering estimate of the uncertainty in the hydrogen generation rate and its integral was developed. The integral hydrogen production in Test SFD 1-4 is calculated to be 98 (+28/−5 g). This value is in reasonable agreement with the best-estimate value of 86 ± 12 g from the collection tank gas sample.

E-5. References

E-1. J. K. Hartwell et al., *Fission Product Behavior During the PBF Severe Fuel Damage Test 1-1*, NUREG/CR-4925, EGG-2462, May 1987.

E-2. Z. R. Martinson, D. A. Petti, B. A. Cook, *Severe Fuel Damage Test 1-1 Test Results Report*, NUREG/CR-4684, EGG-2463, October 1986.

E-3. G. F. Knoll, *Radiation Detection and Measurement*, New York: John Wiley and Sons, 1979.

APPENDIX F

COOLANT LEVEL MEASUREMENTS

APPENDIX F

COOLANT LEVEL MEASUREMENTS

Accurate determination of the steam interface level as a function of time was a requirement of the design of Test SFD 1-4. This appendix provides a brief description of the method and measurements used to determine the steam interface level during the transient.

A system was developed by R. W. Albrecht and R. D. Crowe for the SFD test series to provide on-line measurement of the steam interface level. Eight fission chambers, located on the shroud outer wall, measured the influence of the two-phase steam/single-phase steam interface on the neutron flux as the level decreased. Because these chambers are sensitive to thermal neutrons, their electrical output changed dramatically when the moderator between them and the test fuel changed from a two-phase steam and water mixture to steam. The movement of the two phase/steam transition point past a particular fission chamber was detected by a sudden change in its output signal.

The fission chambers, with an active length of 0.025 m, were centered at elevations of approximately −0.05, 0.05, 0.15, 0.25, 0.35, 0.51, 0.67, and 0.83 m relative to the bottom of the PBF core. The chambers were mounted in two strings of four on opposite sides of the outer shroud wall at 90 and 270 degrees, alternating with elevation. The output of each of the fission chambers was normalized to the reactor power to remove the effects of changing reactor power level from the fission chamber currents.

The following expression was used to make on-line estimates of the liquid level from the fission chambers

$$I(z) = \frac{I_a e^{\lambda(z - z_d)} + \frac{I_b}{I_a}}{1 + e^{\lambda(z - z_d)}} \qquad \text{(F-1)}$$

where

$I(z)$ = power-normalized detector output for detector d with the level at level z

z_d = elevation of detector d

I_a = power-normalized output for detector d when the level is far above z_d

I_b = power-normalized output for detector d when the level is far below z_d

λ = detector sensitivity parameter (cm^{-1}).

In addition

$$I_{z_d} = \frac{I_a + I_b}{2} \quad . \qquad \text{(F-2)}$$

If $z \simeq z_d$, then the approximation can be made that $\lambda/2(z - z_d) << 1$, with the result that

$$I(z) = \frac{I_a + I_b}{2} + \frac{\lambda(z - z_d)I_a}{2} \quad . \qquad \text{(F-3)}$$

Using this formulation, the steam interface level could be measured until 1712 s (about the time that the instrumented control rod failed and relocated). From 1712 to 1935 s, the steam interface level during the transient was deduced from the measurement of the differential pressure across the bundle. A differential pressure transducer measured the pressure drop from -0.36 to 1.43 m, which was proportional to the liquid level in the bundle below 1.43 m. The differential pressure measurement could not be used after about 1946 s, because the argon sweep gas flow rate was increased at this time, perturbing the bundle pressure drop measurement which used the same sensing line. The differential pressure data were converted to bundle height by dividing by the density of water in the sensing lines and the acceleration due to gravity. The level data derived from the differential pressure were then smoothed and normalized to the fission chamber steam interface level data. The normalization procedure consisted of subtracting an offset equal to the difference in indicated levels from the two measurement methods over the time interval from 0 to 70 s. A plot of the steam interface level during the boildown and high-temperature transient, derived from the fission chamber and differential pressure, is shown in Figure F-1.

The estimated uncertainty in the steam interface level obtained from the fission chambers is ±0.02 m. This estimate was verified by comparing the average cladding thermocouple dryout times at

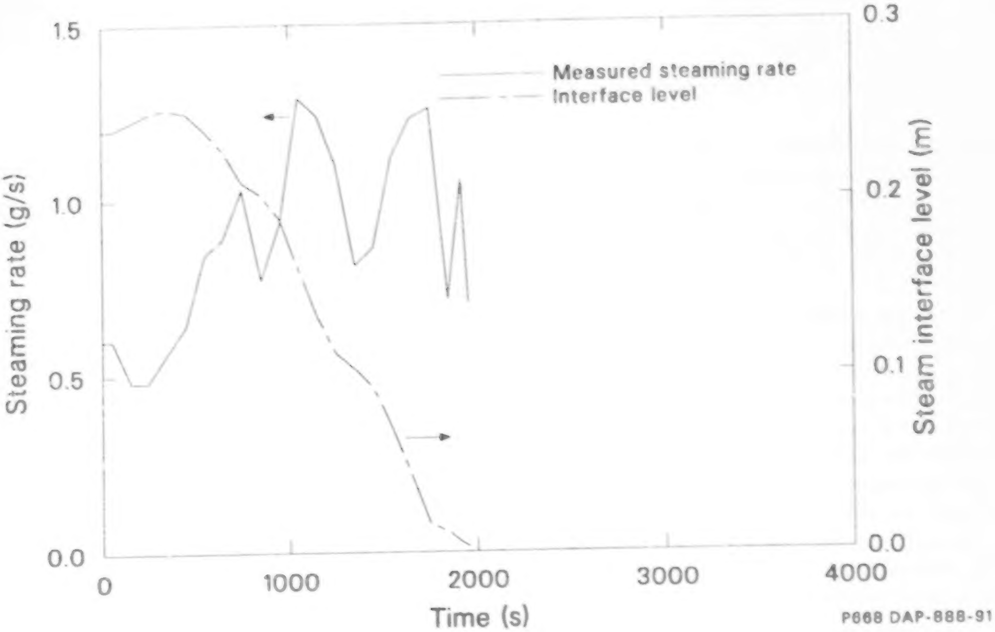

Figure F-1. Steam interface level and steaming rate during Test SFD 1-4.

0.39-, 0.54-, and 0.74-m elevations with the fission chamber level data during the boildown phase.

The bundle inlet flow was provided by a positive displacement injection pump that was calibrated to deliver at 0.6 g/s, with an estimated uncertainty of ±5%. The steaming rate (also shown in Figure F-1) was calculated from the known inlet flow rate, the steam-interface level history data, and the lower plenum flow area (32.08 cm^2). A coolant density of 742 kg/m^3 (corresponding to saturated water at 6.95 MPa) was used to calculate the steaming mass flow rate into the bottom of the bundle. Beyond 1946 s, the steaming rate could not be determined from these measurements.

APPENDIX G

FISSION PRODUCT RELEASE AND RETENTION MEASUREMENTS AND ANALYSIS

APPENDIX G

FISSION PRODUCT RELEASE AND RETENTION MEASUREMENTS AND ANALYSIS

Many fission product release and retention measurements were made for Test SFD 1-4. Details about the methods used to reduce the data and to predict the measured release are presented in this appendix.

G-1. ORIGEN2 Inventory Calculations

The fission product inventory of the SFD 1-4 bundle was calculated using the ORIGEN2 code.[G-1] The two separate calculations that were performed for the SFD 1-4 analysis are discussed in this section.

G-1.1 Total Fuel Bundle Fission Product Inventory. Whole bundle inventories for fission product and heavy metal isotopes were calculated using ORIGEN2 and a generic PWR cross-section library. These bundle inventory values were needed to analyze the on-line and grab sample data. Each rod in the fuel bundle was modeled as a series of ten axial nodes. The burnup of each node was determined using the rod average burnup and an assumed axial burnup distribution. The assumed axial distribution was a smooth, chopped cosine based on the beginning-of-cycle, middle-of-cycle, and end-of-cycle peak-to-average linear power values for the BR-3 power history.[G-2]

The BR-3 irradiations for the high-burnup fuel rods were modeled either in a single cycle (B500 batch) or two cycles (B300 batch), depending on the specific rod. Eighteen rods in the SFD 1-4 bundle were from the B300 batch, and eight rods were from the B500 batch. For the B300 fuel, the exposure split between the two cycles was based on the core effective full-power hours for each cycle. The resulting bundle inventories were then decayed to the start of the PBF irradiation. Both the fresh and irradiated rods were modeled for the PBF irradiation. The inventories of selected radionuclides at the end of the BR-3 irradiation and the end of the SFD 1-4 transient are listed in Table G-1.

The adequacy of the methodology and the cross-section library used by ORIGEN2 can be assessed by comparing the calculated and measured fuel inventories for the high-burnup BR-3 fuel rods. Isotopic analyses have been performed on two BR-3 fuel rods, rods I-830 and I-887. Rod I-830 had undergone irradiation in two cycles to a reported burnup of 34.7 GWd/MtU, whereas rod I-887 had been irradiated in cycle BR3/4A to a burnup of 34.9 GWd/MtU.

Uranium and plutonium isotopic ratios have been determined by mass spectrometry for three fuel samples from rod I-830 and five fuel samples from rod I-887. ORIGEN2 calculations were performed for each sample location. The burnup of each sample was calculated using the assumed chopped cosine distribution and the rod average burnup. A comparison of the measured and calculated uranium and plutonium isotopic inventory ratios is shown in Table G-2.

Consistently closer agreement is observed for the samples obtained from rod I-830. For the two nuclides that dominate the fission rate (^{235}U and ^{239}Pu), the differences between the calculations and measurements are very small, indicating that the calculated fission rate is quite accurate.

The poorer agreement for the samples from rod I-887 is due to the assumed axial burnup distribution. The gross gamma scan data of rod I-887[G-2] indicate that the axial burnup distribution for this rod is not well represented by a simple analytic function. Isotopic fission product analysis was performed for sample 4-B from rod I-887. A comparison of the measured and calculated activities for five nuclides is listed in Table G-3. The error in burnup for this rod is reflected in the calculated fission product activities. The calculated ^{154}Eu and ^{155}Eu inventories are 60% to 80% higher than the measured values, and the calculated ^{134}Cs inventories are about 15% to 20% too high. Much better agreement is observed for ^{144}Ce and ^{137}Cs.

In general, the uncertainty in the ORIGEN2 inventories for most of the radiologically significant nuclides is estimated to be about 10%. This uncertainty is used to represent the overall uncertainty associated with the fission product yields and the fission rates of the various contributing fissionable nuclides. However, the limited results from rod I-887 and recent analysis of undamaged fuel pellets from the TMI-2 reactor core[G-3]

Table G-1. ORIGEN2 inventories of selected radionuclides

	Bundle Inventory[a] (μCi)	
Isotope	Prior to Test SFD 1-4[b]	End of Test SFD 1-4[c]
^{85}Kr	9.80 E+07 ± 10	9.77 E+07 ± 10
^{85m}Kr	0	1.01 E+08 ± 10
^{88}Kr	0	1.69 E+08 ± 10
^{88}Rb	0	1.76 E+08 ± 10
^{90}Sr	9.75 E+08 ± 10	9.75 E+08 ± 10
^{95}Zr	6.51 E+02 ± 10	4.24 E+08 ± 10
^{95}Nb	1.45 E+03 ± 10	1.41 E+08 ± 10
^{103}Ru	1.31 E−02 ± 10	4.72 E+08 ± 10
^{106}Ru	1.69 E+08 ± 10	1.86 E+08 ± 10
^{125}Sb	3.94 E+07 ± 10	3.88 E+07 ± 10
^{127m}Te	4.95 E+03 ± 10	1.85 E+07 ± 10
^{129}Te	2.55 E−06 ± 10	1.06 E+07 ± 10
^{129m}Te	3.91 E−06 ± 10	1.64 E+07 ± 10
^{129}I	3.66 E+02 ± 10	3.67 E+02 ± 10
^{131}I	0	5.20 E+08 ± 10
^{131m}Xe	0	6.82 E+06 ± 10
^{131}Te	0	1.88 E+08 ± 10
^{132}Te	0	4.88 E+08 ± 10
^{133}I	0	4.99 E+08 ± 10
^{133}Xe	0	1.08 E+08 ± 10
^{134}Te	0	3.05 E+08 ± 10
^{134}Cs	3.21 E+08 ± 20	3.21 E+08 ± 20
^{135}I	0	8.34 E+08 ± 10
^{136}Cs	0	2.28 E+07 ± 10
^{137}Cs	1.20 E+09 ± 10	1.20 E+09 ± 10
^{140}Ba	0	1.00 E+09 ± 10
^{140}La	0	1.06 E+09 ± 10
^{141}Ce	5.18 E−05 ± 10	6.72 E+08 ± 10
^{144}Ce	2.17 E+08 ± 10	2.90 E+08 ± 10
^{154}Eu	6.81 E+07 ± 10	6.81 E+07 ± 10
^{155}Eu	3.15 E+07 ± 10	3.15 E+07 ± 10
^{235}U	5.81 E+02 ± 20	6.40 E+02 ± 20
^{238}Pu	2.22 E+07 ± 20	2.24 E+07 ± 20
^{239}Pu	3.42 E+06 ± 20	3.43 E+06 ± 20
^{241}Am	7.65 E+06 ± 20	7.73 E+06 ± 20
^{242}Cm	4.50 E+05 ± 20	3.08 E+07 ± 20
^{244}Cm	6.06 E+06 ± 20	6.10 E+06 ± 20

---

a. The ± values are uncertainties in percent.

b. Represents long-lived isotopes in BR-3 fuel.

c. Activities as of 21:36:34 on 2/7/85.

Table G-2. Comparison of measured and calculated BR-3 isotopic ratios

	Percent Difference in Measured and Calculated Isotopic Ratios[a]							
	Rod I-830 Samples[b]			Rod I-887 Samples				
Isotope	12-A	4-B	20-B	30-A	12-A	4-B	20-B	38-B
^{235}U	−0.83	+0.79	+0.88	−7.4	−6.2	−8.6	+0.73	+16.0
^{236}U	−7.2	−8.2	−8.6	−0.71	−4.0	−2.1	−10.0	−27.0
^{238}U	+0.16	+0.10	+0.11	+0.45	+0.36	−0.42	+0.11	+0.50
^{239}Pu	+2.0	+2.2	+2.8	−4.0	−3.2	−4.4	−0.23	−6.2
^{240}Pu	−0.04	−0.81	−0.14	+25.0	+18.0	+19.0	+13.0	−3.0
^{241}Pu	−15.0	−14.0	−22.0	−23.0	−21.0	−17.0	−28.0	−49.0
^{242}Pu	—[c]	—[c]	—[c]	−22.0	−30.0	−26.0	−42.0	−68.0

---

a. (Measured—calculated) X 100/(measured).

b. Sample designation also indicates location; 12-A is 12 cm above the fuel centerline, 4-B is 4 cm below the fuel centerline.

c. No measured values reported.

Table G-3. Comparison of measured and calculated isotopic activities from BR-3 rod I-887

	Disintegrations/Second-Gram U		
Isotope	Measured	Calculated	Difference (%)
^{134}Cs	6.56×10^8	7.71×10^8	+18
^{137}Cs	4.28×10^9	4.81×10^9	+12
^{144}Ce	3.56×10^8	3.65×10^8	+3
^{154}Eu	1.14×10^8	2.06×10^8	+81
^{155}Eu	5.20×10^7	8.59×10^7	+65

indicate that the ORIGEN2-calculated inventories for some nuclides, specifically ^{125}Sb, ^{154}Eu, ^{155}Eu and ^{129}I, may be greater than the values listed in Table G-1.

G-1.2 Burnup-Specific Fission Product Inventory. In the second ORIGEN2 calculation, the individual fuel rod nodes were grouped into burnup bins; and the calculations were rerun to obtain fission product inventories as a function of fuel burnup during the BR-3 irradiation. The PBF irradiation was not modeled. These results were used to analyze the retained fission product measurements discussed in Section G-4.

Inventories were calculated at twelve different BR-3 exposures for both the B300 and B500 rods. The modeled exposures range from 5 GWd/MtU to 50 GWd/MtU in increments of 5 GWd/MtU. Each inventory was then decay-corrected to 1/7/86, the sample analysis date. The results are plotted in Figures G-1 through G-14. On the ordinate, the fission product concentration is expressed as Curies per gram equivalent ^{235}U. The term of gram equivalent ^{235}U is the effective fissile content and is used in this analysis to facilitate direct comparison with the retained fission product measurements. The effective fissile content is defined as

$$EFC = M(^{235}U) + K\,M(^{239}Pu) \qquad (G\text{-}1)$$

where

EFC = effective fissile content (grams U^{235} equivalent)

$M(^{235}U)$ = mass of ^{235}U (g)

$M(^{239}Pu)$ = mass of ^{239}Pu (g)

K = constant calculated from decay systematics and confirmed by measurements ($K = 0.66 \pm 0.03$).

The effective fissile content divided by the total uranium content is plotted as a function of exposure in Figure G-15.

G-2. Fractional Release Rate Methodology

The fractional release rate results were obtained from two sets of data—the effluent grab sample results and the on-line gamma spectrometers. The

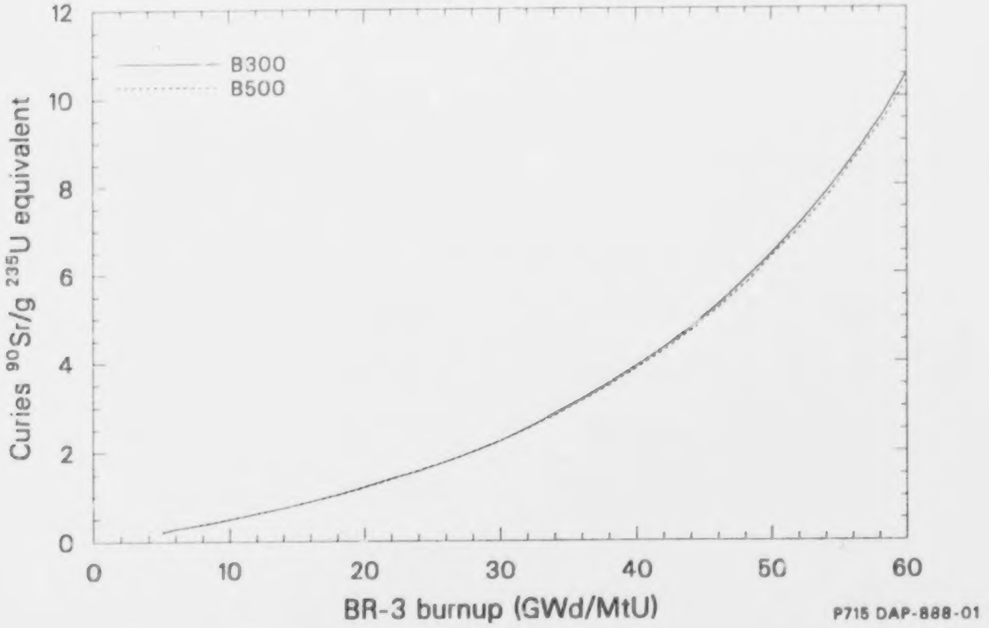

Figure G-1. Activity of ^{90}Sr as a function of exposure for BR-3 B300 and B500 series irradiations.

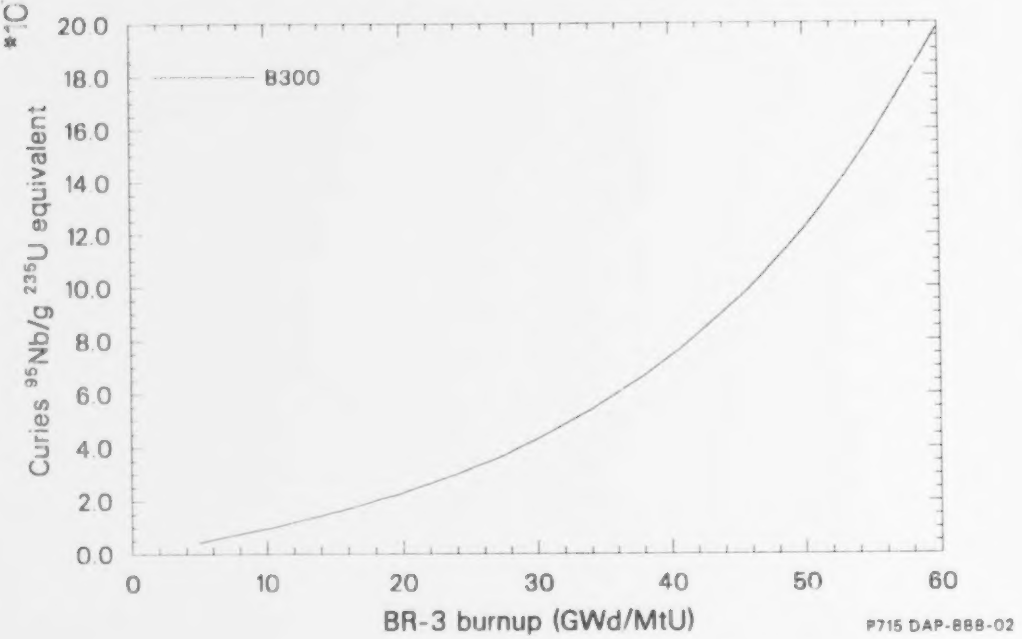

Figure G-2. Activity of ^{95}Nb as a function of exposure for BR-3 B300 series irradiation.

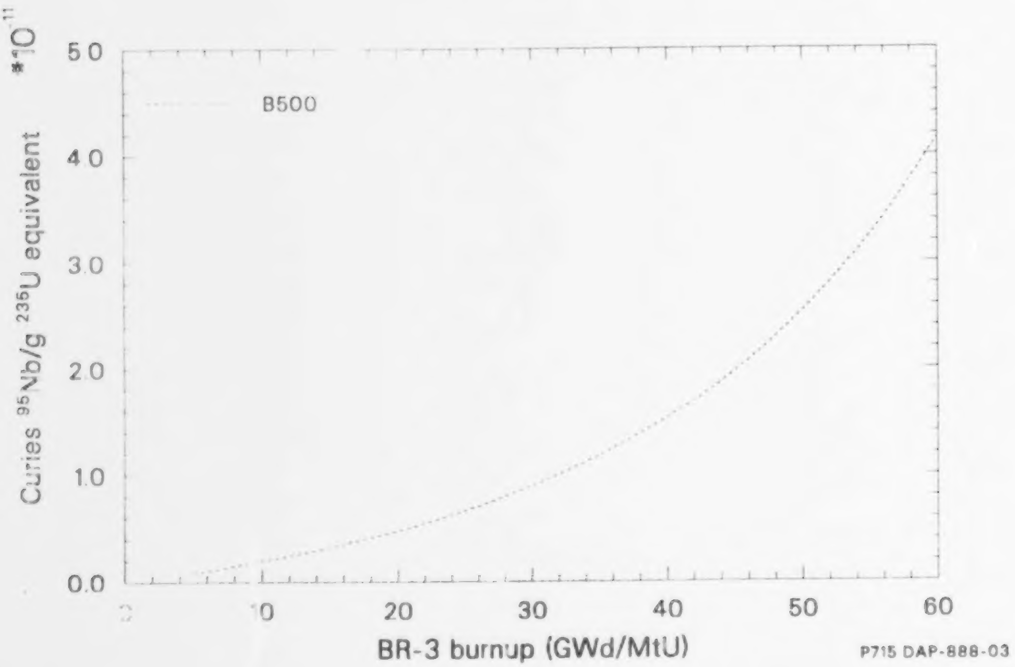

Figure G-3. Activity of ^{95}Nb as a function of exposure for BR-3 B500 series irradiation.

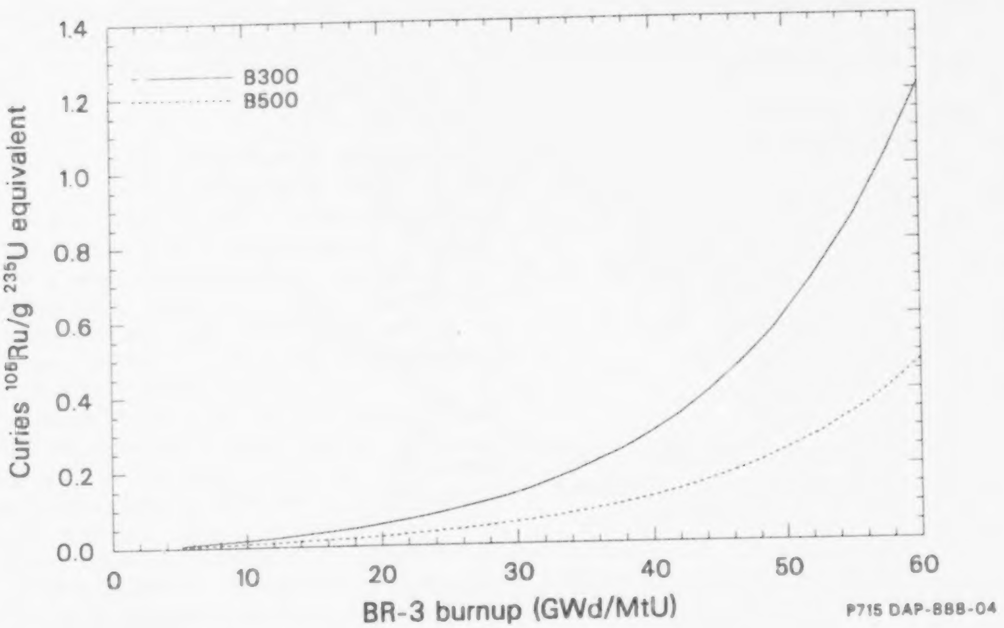

Figure G-4. Activity of ^{106}Ru as a function of exposure for BR-3 B300 and B500 series irradiations.

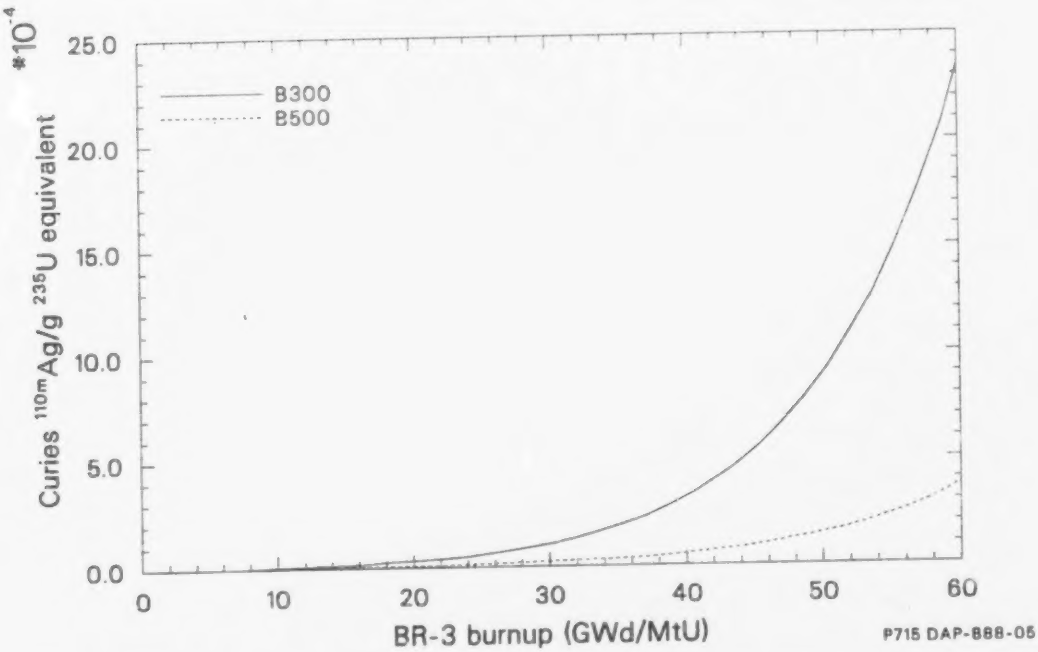

igure G-5. Activity of ^{110m}Ag as a function of exposure for BR-3 B300 and B500 series irradiations.

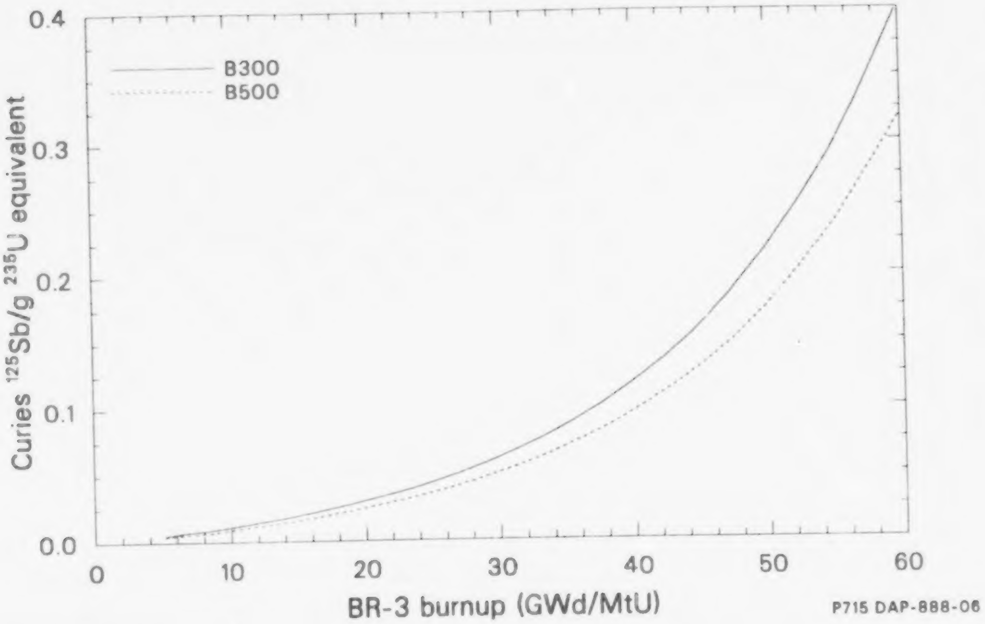

Figure G-6. Activity of ^{125}Sb as a function of exposure for BR-3 B300 and B500 series irradiations.

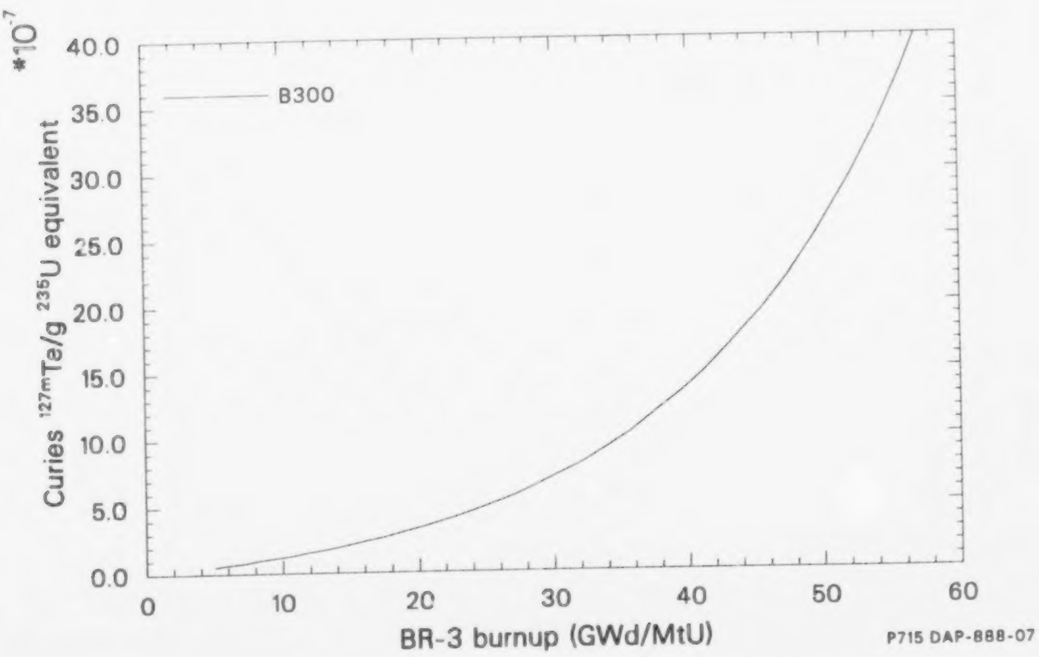

Figure G-7. Activity of ^{127m}Te as a function of exposure for BR-3 B300 series irradiation.

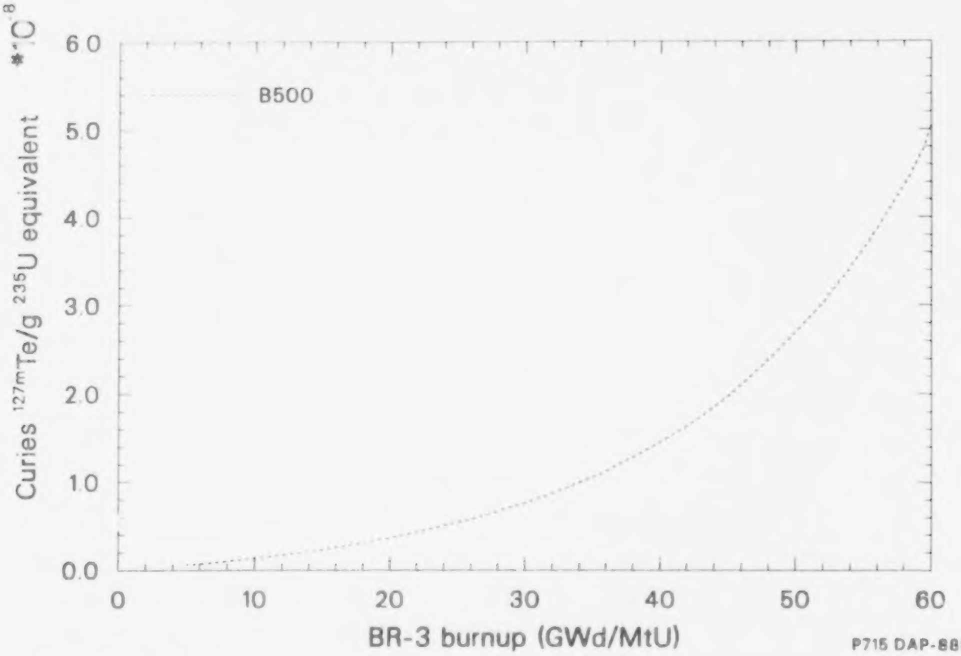

P715 DAP-888-08

Figure G-8. Activity of ^{127m}Te as a function of exposure for BR-3 B500 series irradiation.

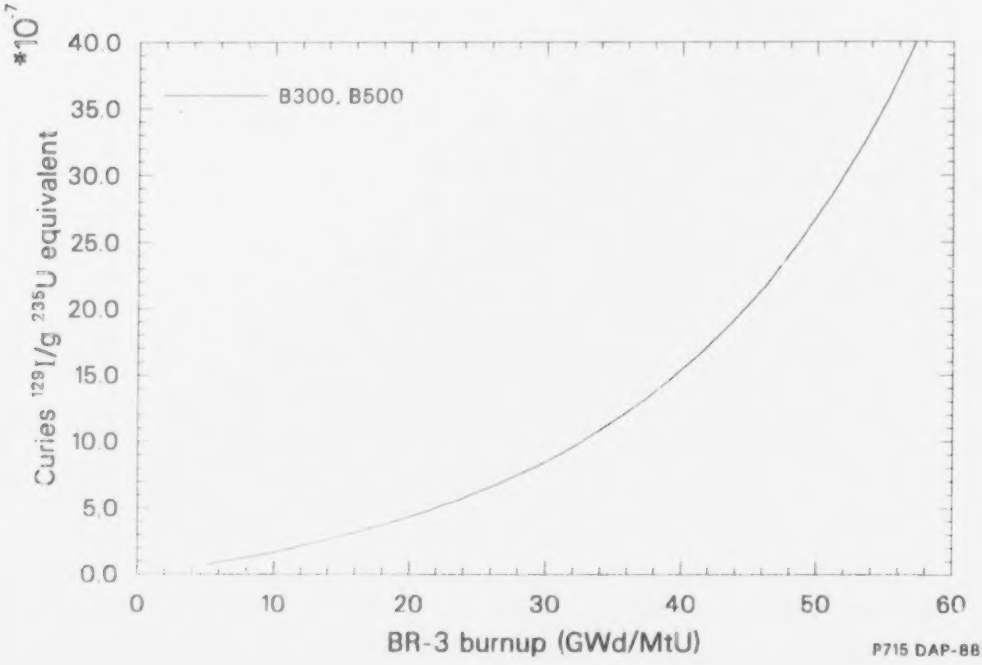

P715 DAP-888-09

Figure G-9. Activity of ^{129}I as a function of exposure for BR-3 B300 and B500 series irradiations.

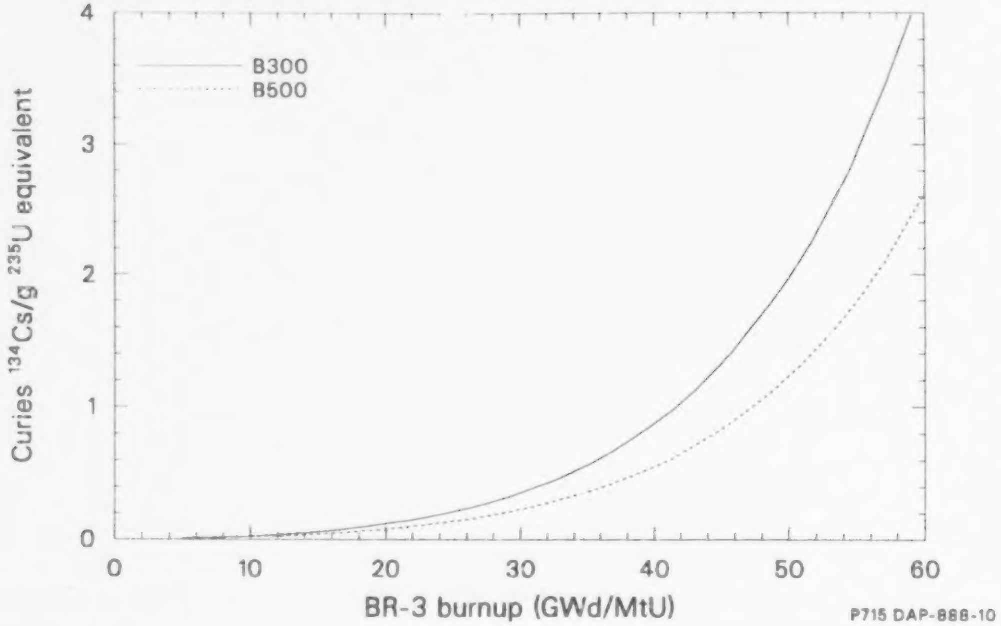

Figure G-10. Activity of ^{134}Cs as a function of exposure for BR-3 B300 and B500 series irradiations.

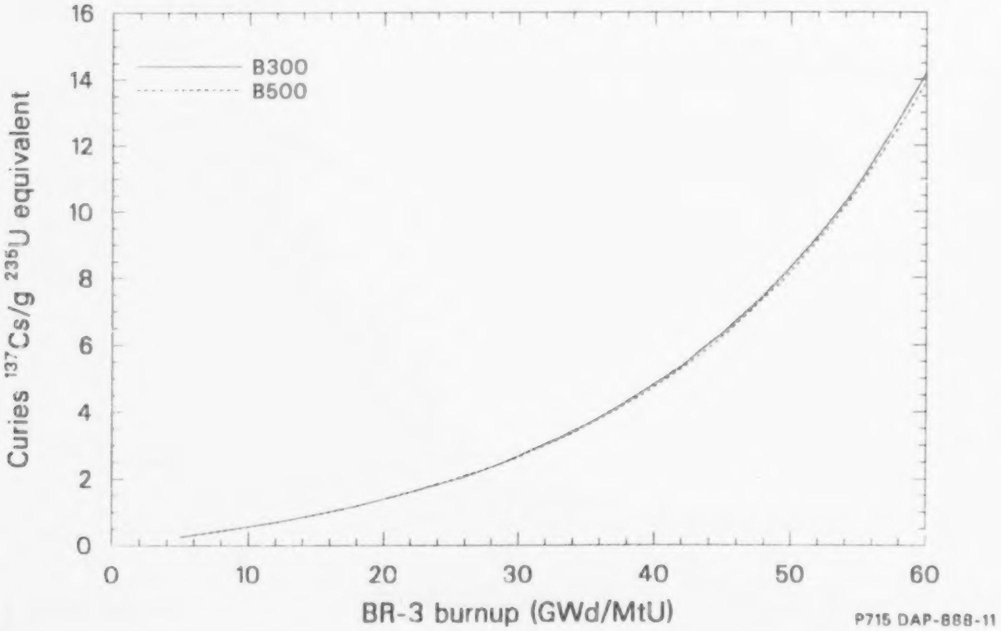

Figure G-11. Activity of ^{137}Cs as a function of exposure for BR-3 B300 and B500 series irradiations.

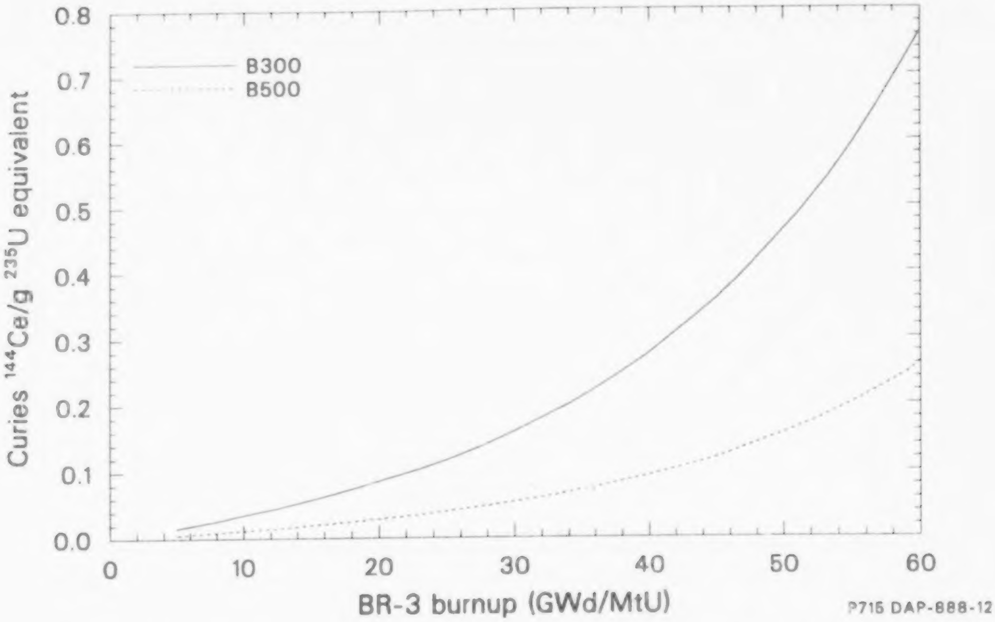

Figure G-12. Activity of ^{144}Ce as a function of exposure for BR-3 B300 and B500 series irradiations.

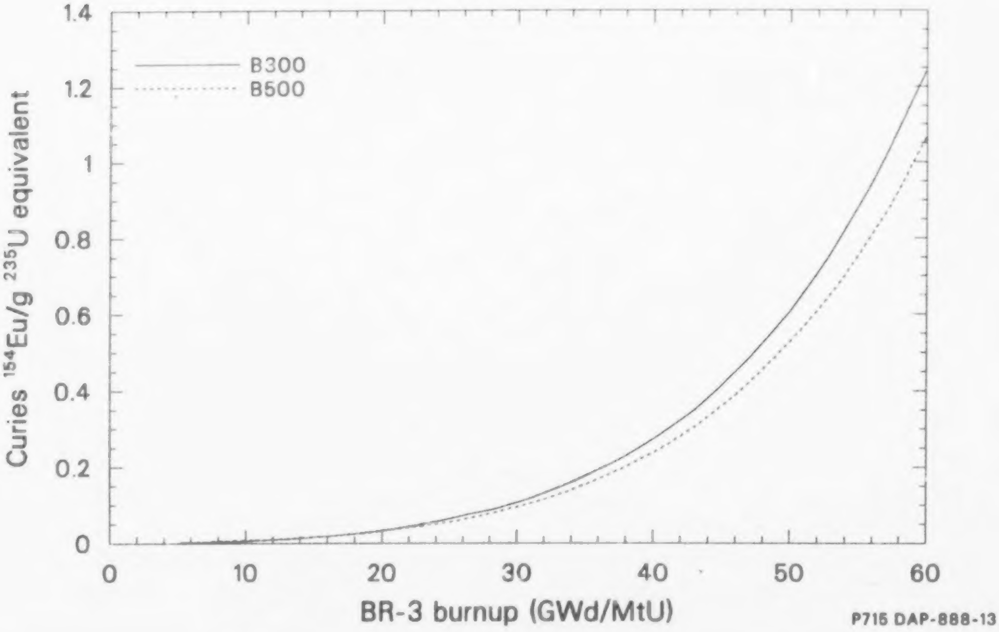

Figure G-13. Activity of ^{154}Eu as a function of exposure for BR-3 B300 and B500 series irradiations.

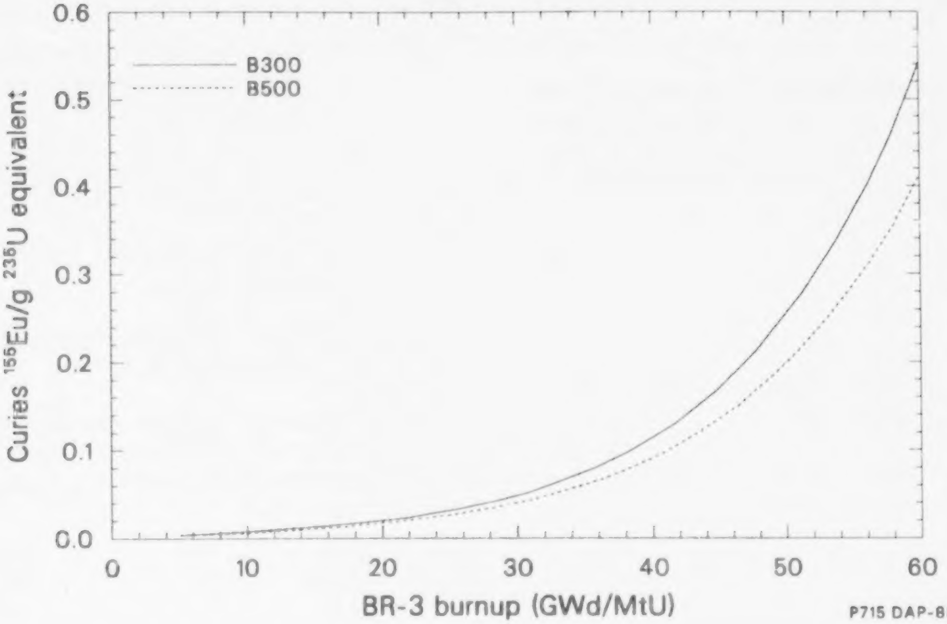

Figure G-14. Activity of ^{155}Eu as a function of exposure for BR-3 B300 and B500 series irradiations.

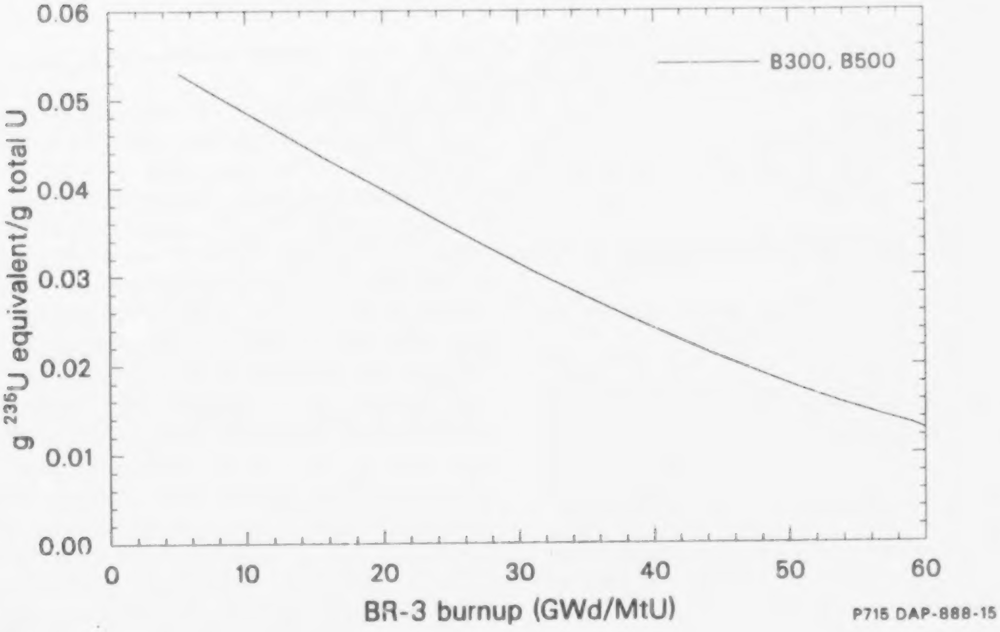

Figure G-15. Ratio of gram ^{235}U equivalent to total grams uranium.

methodologies used to calculate the release rates are discussed in this section.

G-2.1 Fractional Release Rates from Effluent Grab Samples. The fractional release rate (fraction of bundle inventory per second), $\dot{F}$, determined from the effluent grab samples during Test SFD 1-4 is given by

$$\dot{F} = \frac{A_g + A_s}{ISt} \tag{G-2}$$

where

A_g = activity in gas portion of the effluent sample (Ci)

A_s = activity in the condensed portion of the effluent sample (Ci)

I = bundle inventory (Ci)

S = sampling fraction

t = effluent sampler fill time (s).

The sampling fraction S is used to account for the fact that not all the effluent was sampled by the sampler. It is given by

$$S = \frac{M_{Ar}}{\dot{M}_{Ar}t} \tag{G-3}$$

where

M_{Ar} = mass of argon in the effluent sample (g)

$\dot{M}_{Ar}$ = mass flow rate of argon (g/s).

Equations (G-2) and (G-3) are used to calculate the fractional release rates in Table G-4.

G-2.2 Fractional Release Rate from the On-line Gamma Spectrometers. The results of the effluent transit analysis in Appendix E can be used to convert the on-line gamma spectrometer concentration measurements into fractional release rates. The isotopic concentration at a given measurement location is related to the concentration exiting the fuel bundle by

$$C_b = C_d \exp(\lambda \Delta t_p) \tag{G-4}$$

where

C_d = concentration of a given isotope at a given measurement location (Ci/m^3)

C_b = concentration of a given isotope at the bundle exit (Ci/m^3)

λ = decay constant for isotope of interest (s^{-1})

Δt_p = transit time from bundle exit to measurement location (s).

In the effluent transit analysis, the bundle is considered to be a well-mixed volume. As a result, the concentration exiting the bundle, C_b, is related to the release rate, R, by

$$\frac{dC_b}{dt} = \frac{R}{V_b} - \frac{Q}{V_b} C_b - \lambda C \tag{G-5}$$

where

Q = volumetric flow rate of effluent exiting the bundle (m^3/s)

V_b = void volume of bundle (m^3)

R = release rate of isotope (Ci/s).

Equations (G-4) and (G-5) were used to convert concentrations of ^{85m}Kr, ^{87}Kr, ^{88}Kr, ^{133}Xe, ^{135}Xe, ^{137}Xe, and ^{138}Xe measured at the three spectrometer locations to isotopic release rates in the bundle. The effect of plateout on the pipe viewed by each spectrometer was so large that release rates could not be calculated for reactive fission products (i.e., iodine, cesium, tellurium, etc.). Similar behavior for the reactive fission products was noted in Test SFD 1-1.[G-3]

The release rates for the noble gas isotopes were converted to fractional release rates using

$$\dot{F}R = \frac{R(t)}{I - \int_0^t R \, dt'} \tag{G-6}$$

where

$\dot{F}R$ = fractional release rate of species (s^{-1})

Table G-4. Fractional release rates from the gas portion of the effluent line grab samplers

Sample	Transit Time-Corrected Sample Time (s)	Fill Time (s)	Gas Fractional Release Rates (s^{-1})[a]		
			^{85}Kr	^{131m}Xe	^{133}Xe
Filtered					
FG – 1	1864	36.99	6.02 E – 07 ± 24	2.93 E – 07 ± 36	3.95 E - 08 ± 25
FG – 2	1950	42.29	1.61 E – 04 ± 24	1.08 E – 04 ± 24	9.15 E – 05 ± 25
FG – 3	2008	44.08	4.82 E – 04 ± 24	4.01 E – 04 ± 24	3.30 E – 04 ± 25
FG – 4	2287	34.78	3.13 E – 04 ± 24	3.86 E – 04 ± 24	3.40 E – 04 ± 25
FG – 5[b]	2770	38.08	7.67 E – 06 ± 24	3.29 E – 05 ± 46	1.11 E – 05 ± 30
FG – 6[b]	2990	41.37	6.49 E – 05 ± 24	4.71 E – 04 ± 24	3.83 E – 05 ± 25
Unfiltered					
UFG – 1	1697	45.96	—[c]	—[c]	—[c]
UFG – 2	1768	42.22	1.25 E – 05 ± 24	—[c]	6.29 E – 07 ± 26
UFG – 3	2150	46.69	1.71 E – 04 ± 24	1.52 E – 04 ± 25	1.57 E – 04 ± 24
UFG – 4	2460	45.69	8.68 E – 05 ± 24	1.14 E – 04 ± 24	1.24 E – 04 ± 24
UFG – 5	3310	47.63	1.61 E – 04 ± 24	2.16 E – 04 ± 26	2.46 E – 04 ± 26
UFG – 6	3780	58.11	5.64 E – 06 ± 24	1.04 E – 05 ± 24	8.68 E – 06 ± 24

---

a. The ± values are one estimated relative standard deviation in percent.

b. Release rates are biased because of large amount of water present in sample.

c. Not detected.

R = isotopic release rate (Ci/s)

I = initial inventory at isotope at scram (Ci).

The denominator in Equation (G-6) accounts for release of material up to time t when calculating the fractional release rate. However, it neglects changes in the inventory during the transient because of irradiation. This effect is small for the majority of isotopes chosen because they have half-lives greater than one hour and consequently their inventory changes slowly during irradiation. This effect is important for ^{137}Xe ($t_{1/2}$ = 3.8 min) and ^{138}Xe ($t_{1/2}$ = 14 min), since these nuclides reach saturation during the PBF irradiation. Thus, the depletion term in the denominator of Equation (G-6) will result in an underestimate of the actual inventory at time t. The results of this analysis are discussed in Section 6.

G-3. Integral Release Estimates

Numerous measurements were taken to obtain data on fission product release in Test SFD 1-4. Data were collected both before and after the system was flushed with water to obtain information on fission product release and transport. Before the system was flushed with water, three separate measurements were taken to determine the fraction of fission product inventory in the bundle that was transported to the collection tank:

1. Samples of the liquid and gaseous contents of the collection tank were obtained after the experiment.

2. The on-line gamma spectrometers recorded time-dependent data on the isotopic fission product concentrations in the effluent which could then be integrated to determine the total release.

3. The contents of the collection tank liquid and gas spaces were recirculated past the respective gamma-ray spectrometers after the experiment.

After the experiment, the deposition rod, effluent grab samples, and the aerosol monitor were removed; temporary piping was installed; and the bundle and effluent line were flushed. The effluent line was flushed with water on May 15, 1985. Following the effluent line flushing, the bundle and the effluent line were flushed with water on both May 16 and May 23, 1985. Samples were taken after the flushing operations to determine the fraction of fission product inventory that was transported via the water flush to the collection tank. Specifically, (a) a grab sample of the liquid in the collection tank was taken; and (b) the liquid contents of the collection tank were recirculated past the liquidline gamma spectrometer after each flush. This section will present the results of all these integral release estimates.

G-3.1 Preflush Collection Tank Samples. The results of the preflush collection tank gas and liquid samples are presented in Tables G-5 and G-6. The collection tank gas results have been corrected for leakage from the collection tank posttest and oxygen in-leakage during sample processing. (These effects are discussed in Appendix E.) The results from the gas sample indicate that the release fraction for ^{85}Kr is 0.39 ± 15%. Release fractions for stable krypton and xenon based on mass spectrometer results are 0.52 ± 100% and 0.51 ± 100%, respectively. The liquid sample results indicate that very little of the reactive fission products reached the collection tank during the experiment. The fraction of material reaching the collection tank was 2.14 E – 03 for ^{131}I and 9.04 E – 03 for ^{137}Cs.

G-3.2 Preflush Recirculation Results. Recirculation of the gaseous contents of the collection tank was performed on March 19, 1985. At the time of the gas recirculation, the collection tank pressure had dropped to 0.191 MPa (absolute). Since the tank pressure immediately following the test was 0.475 MPa, the measured concentrations were corrected by the factor 0.475/0.191 = 2.487 to compensate for the pressure loss in the collection tank following the test. The results of the collection tank gas recirculation measurements and release fractions prior to bundle flush are presented in Table G-7. Noble gas release fractions for ^{85}Kr and ^{133}Xe were 0.44 ± 20% and 0.23 ± 18%, respectively. The results for iodine, cesium, and lanthanum isotopes are biased due to plate-out in the section of the sample line viewed by the detector.

The results of the recirculation of the liquid line prior to flushing are shown in Table G-8. As with the results from the preflush collection tank sample, very little of any reactive fission product was released to the collection tank prior to flushing. The release fractions for ^{131}I and ^{137}Cs were 2.37 E – 03 and 7.71 E – 03, respectively. As noted in the table, in a few cases the liquid recirculation results were biased by deposition on the view segment of the sample line.

G-3.3 Integration of the On-Line Spectrometer Results. The release rates, R, of moderate-lived noble gas isotopes measured by the mainfloor, steamline, and gasline spectrometers [see Equation (G-5)] were integrated to estimate the integral releases during the experiment. The results are shown in Table G-9. The steamline and gasline spectrometer release fractions for most of the noble gases are in relatively good agreement. The uncertainty in these integral release results are judged to be somewhat higher than the gas recirculation and collection tank results (–25%) because of the greater difficulty associated with the measurement and the uncertainty associated with the effluent transit analysis used to obtain these results. The integral release results from the mainfloor spectrometer appear to be biased high. The uncertainties in the concentrations of certain isotopes at the mainfloor spectrometer (^{85m}Kr, ^{87}Kr, and ^{88}Kr) were higher than expected, due to the higher background on the main floor of the PBF and higher uncertainty associated with the detector calibration.

Selected isotopic concentrations measured by the liquidline spectrometer were multiplied by the dilution flow rate (33.1 g/s) in the liquid line and then integrated to obtain an estimate of the amount of material that passed the detector and entered the collection tank during the experiment. The results are shown in Table G-10. In some cases, the results are biased due to deposition in the line and parent-daughter effects for certain isotopes.

Table G-5. Preflush collection tank gas sample results

Isotope	Activity (μCi/sample)	Total Release[a] (μCi)	Release Fraction
^{85}Kr	3.26 E+02 ± 5%	37.8	0.387
^{134}Cs	3.90 E−03 ± 9%	451.97	1.41 E−06
^{137}Cs	3.60 E−02 ± 6%	4172.1	3.48 E−06

---

a. Total release is calculated using

$$\text{Release} = \frac{\text{Activity in tank sample} \cdot \text{volume of collection tank at end test}}{\text{Volume of sample at collection tank conditions corrected for air in-leakage}}$$

Volume of sample at collection tank corrected for air in-leakage (237/1.49) = 158.77 cm^3

Volume of collection tank gas at end of Test SFD 1-4 accounting for pressure loss (7.4 E+06 x 2.487) = 1.84 E+07 cm^3

See Appendix E for additional details.

Table G-6. Preflush collection tank liquid sample results

Isotope	Concentration[a] (μCi/mL)	Release Fraction
^{131}I	9.43 E−01 ± 10%	2.14 E−03 ± 11%
^{134}Cs	1.94 E+00 ± 10%	7.15 E−03 ± 11%
^{136}Cs	4.98 E−02 ± 10%	2.58 E−03 ± 11%
^{137}Cs	9.19 E−02 ± 10%	9.04 E−03 ± 11%
^{140}La	1.25 E−01 ± 10%	2.39 E−04 ± 11%

---

a. Collection tank liquid volume = 1.18 E+06 mL (±10%).

best copy available

Table G-7. Collection tank gas recirculation measurements and release fractions prior to bundle flushing

Isotope	Concentration[a] (μCi/cm^3)	Total Activity[b] (μCi)	Inventory[c] (μCi)	Release Fraction
^{85}Kr	2.32 E + 0 ± 10	4.27 E + 7	9.70 E + 7	4.40 E − 1 ± 20
^{131}I[d]	5.40 E − 2 ± 7	9.95 E + 5	1.69 E + 7	5.89 E − 2 ± 19
^{133}Xe	7.05 E − 2 ± 4	1.30 E + 6	5.62 E + 6	2.31 E − 1 ± 18
^{134}Cs[d]	4.70 E − 1 ± 4	8.65 E + 6	3.09 E + 8	2.80 E − 2 ± 18
^{136}Cs[d]	6.50 E − 3 ± 8	1.20 E + 5	2.75 E + 6	4.36 E − 2 ± 19
^{137}Cs[d]	2.27 E + 0 ± 9	4.18 E + 7	1.20 E + 9	3.48 E − 2 ± 20
^{140}La[d]	9.00 E − 3 ± 9	1.66 E + 5	2.05 E + 8	8.10 E − 4 ± 20

---

a. Collection tank gas concentrations at 1200 h on March 19, 1985. The ± values are uncertainties in percent.

b. Collection tank gas volume was 7.40 E + 6 cm^3. The measured concentrations were adjusted by the factor 2.487 (0.475 MPa/0.191 MPa) to compensate for the pressure loss in the collection tank prior to measurement.

c. Calculated using ORIGEN2. A ± 10% error was estimated.

d. The results for these isotopes are biased high due to plate-out in the section of the sample line viewed by the detector.

Table G-8. Collection tank liquid recirculation measurements and release fractions prior to bundle flushing

Isotope	Concentration[a] (μCi/cm^3)	Total Activity[b] (μCi)	Inventory[c] (μCi)	Release Fraction
^{56}Mn[d]	3.60 E − 2 ± 72	4.65 E + 4 ± 74	—[d]	—[d]
^{85m}Kr	6.50 E − 2 ± 63	8.52 E + 4 ± 64	3.22 E + 7	2.65 E − 3 ± 65[e]
^{88}Kr	8.20 E − 2 ± 32	1.07 E + 5 ± 34	2.78 E + 7	3.86 E − 3 ± 35[e]
^{88}Rb[f]	4.89 E + 0 ± 7	6.39 E + 6 ± 12	3.33 E + 7	1.92 E − 1 ± 16[g]
^{125}Sb	6.80 E − 2 ± 93	8.85 E + 4 ± 94	3.88 E + 7	2.28 E − 3 ± 95[h]
^{131}Te	1.60 E − 1 ± 29	2.09 E + 5 ± 31	1.58 E + 8	1.32 E − 3 ± 33
^{132}Te	3.09 E + 0 ± 3	4.04 E + 6 ± 10	4.57 E + 8	8.84 E − 3 ± 14
^{134}Te	1.62 E − 1 ± 37	2.11 E + 5 ± 38	2.02 E + 5	1.00 E + 0 ± 39[g]
^{131}I	5.00 E − 1 ± 10	6.53 E + 5 ± 11	2.75 E + 8	2.37 E − 3 ± 12
^{132}I[f]	3.25 E + 0 ± 4	4.24 E + 6 ± 10	5.33 E + 7	7.95 E − 2 ± 14
^{133}I	4.06 E + 1 ± 2	5.30 E + 7 ± 11	8.43 E + 8	6.29 E − 2 ± 15
^{135}I	1.88 E + 1 ± 2	2.46 E + 7 ± 10	3.83 E + 8	6.42 E − 2 ± 14
^{133}Xe	2.75 E + 0 ± 7	3.59 E + 6 ± 12	8.43 E + 8	4.25 E − 3 ± 16[e]
^{135}Xe	3.39 E + 0 ± 4	6.51 E + 6 ± 11	3.21 E + 8	2.03 E − 2 ± 15[e]
^{134}Cs	1.53 E + 0 ± 7	2.00 E + 6 ± 12	3.21 E + 8	6.22 E − 3 ± 16
^{137}Cs	7.08 E + 0 ± 11	9.25 E + 6 ± 12	1.20 E + 9	7.71 E − 3 ± 14

---

a. Results are net μCi/cm^3 at 0500 h on February 8, 1985. The ± values are uncertainties in percent.

b. At the time of measurement, the collection tank was 20% full. Liquid volume was 1.306 E + 6 cm^3. A ± 10% error in the volume was assumed.

c. Calculated using ORIGEN2 and a qualified power history. Inventory errors were estimated to be ± 10%.

d. Activation product.

e. Dissolved gas activity only.

f. Behavior may be strongly linked to parent nuclide.

g. Isotope is too short-lived for accurate inventory assessment. Estimated errors are ± 50%.

h. This value is an example of a high bias due to deposition on the viewed segment of the sample line.

Table G-9. Noble gas release fractions based on integration of the on-line gamma spectrometer results[a]

Isotope	Mainfloor	Steamline	Gasline
^{85m}Kr	0.484[b]	0.381	0.338
^{87}Kr	0.452[b]	0.445	0.365
^{88}Kr	0.655[b]	0.377	0.309
^{133}Xe	—[c]	0.325	0.285
^{135}Xe	0.489	0.382	0.349
^{137}Xe	0.417[d]	0.288	0.233
^{138}Xe	0.598[b]	0.465	0.378

a. Uncertainty estimated to be ∼25%.

b. Examination indicates high uncertainty in certain spectral data.

c. Not measured.

d. Short-lived.

Table G-10. Results of integrating the liquidline spectrometer data

Isotope	Integral Release[a] (Ci)	ORIGEN2 Inventory[b] (Ci)	Release Fraction
^{85m}Kr	0.752	74.15	0.010
^{87}Kr	1.136	30.70	0.037
^{88}Kr	0.899	103.74	0.0087
^{133}Xe	7.445	869.2	0.0086
^{135}Xe	13.53	1089.0	0.012
^{131}I	6.59	516.38	0.013
^{132}I	5.58	271.56	0.021
^{133}I	12.07	1008.5	0.012
^{134}I[c]	3.14	67.47	0.047
^{135}I	10.22	675.7	0.015
^{132}Te	0.298	479.5	0.0006
^{133}Te[c]	0.139	0.185	0.75
^{134}Te[c]	0.396	42.04	0.0094
^{134}Cs	1.936	321.0	0.006
^{137}Cs	13.49	1196.0	0.011
^{138}Cs[c]	5.032	30.65	0.16
^{139}Ba	1.651	109.6	0.015
^{141}Ba[c]	0.342	1.44	0.24

---

[a] Liquidline spectrometer results integrated to 210.6 min after the initiation of the transient.

[b] ORIGEN2 inventories at 210.6 min after initiation of the transient.

[c] Short-lived fission product. Half-life is much less than duration of the transient, and resultant biasing of calculated release fractions.

G-3.4 Postflush Collection Tank Samples. A collection tank liquid sample was taken after all of the flushing operations. The results, shown in Table G-11, indicate significant increases in all of the isotopes measured following flushing. The fraction of bundle inventory found in the collection tank was 0.23 ± 22% for ^{129}I and 0.46 ± 11% for ^{137}Cs. Lesser quantities of tellurium, strontium, and actinides were also found.

G-3.5 Postflush Recirculation Results. The collection tank liquid contents were recirculated three times during flushing operations. The first measurement was taken after the effluent line was flushed. Two additional recirculation measurements were taken following both the first and second bundle flush. The results are shown in Table G-12. Flushing the bundle and effluent line significantly increased the amount of all the reactive fission products that were measured.

G-4. Retained Fission Product Analysis

This section discusses the methodology used to estimate the fission product retention for the core drilled samples and the results of the analysis.

G-4.1 Sample Description and Analysis. During postirradiation examination of the SFD 1-4 test bundle, 14 core drilled samples were extracted from areas of interest in the bundle cross sections. Requisite schedule considerations delayed extraction and analysis of these core drilled samples until early in 1987, about two years following Test SFD 1-4. Because of this long decay period, the short- and moderate-lived nuclides produced predominately in the PBF (^{131}I, ^{103}Ru, ^{129m}Te, etc.) had already decayed, thus limiting the retention investigation to those long-lived nuclides produced in the BR-3 reactor. Additionally, this delay required that the behavior of some radiologically important fission product elements, such as iodine and tellurium, would have to be gleaned from difficult analyses for species such as ^{129}I and ^{127m}Te. These constraints further complicated an already challenging investigation.

The core drilled samples were analyzed by gamma-ray spectroscopy for the gamma-ray-emitting radionuclides; by radiochemical methods for ^{90}Sr; by radiochemical separation and neutron activation analysis for ^{129}I and ^{127m}Te; by neutron activation and delayed fission neutron counting for fissile material (^{235}U and ^{239}Pu); and by inductively coupled plasma (ICP) spectrometry for certain elements, including uranium. Gamma-ray spectroscopy and radiochemical results are presented along with the ICP uranium results in Table G-13.

Table G-11. Results of postflush collection tank liquid grab samples

Isotope	Concentration[a] (μCi/mL)	Release Fraction
^{129}I	2.17 E − 01 ± 21%	2.30 E − 01 ± 22%
^{134}Cs	5.20 E + 01 ± 10%	3.56 E − 01 ± 11%
^{137}Cs	2.49 E + 02 ± 10%	4.57 E − 01 ± 11%
^{127m}Te	1.85 E − 02 ± 29%	2.20 E − 03 ± 33%
^{129}Te	7.82 E − 03 ± 50%	1.62 E − 03 ± 52%
^{129m}Te	1.04 E − 02 ± 19%	1.62 E − 04 ± 22%
^{90}Sr	3.10 E + 00 ± 9%	7.00 E − 03 ± 33%
^{238}Pu	4.04 E − 07 ± 21%	3.97 E − 08 ± 38%
^{239}Pu	2.00 E − 07 ± 33%	7.49 E − 08 ± 53%
^{241}Am	4.04 E − 07 ± 21%	1.15 E − 07 ± 38%
^{242}Cm	2.00 E − 07 ± 33%	1.43 E − 08 ± 46%
^{244}Cm	8.40 E − 08 ± 60%	3.03 E − 08 ± 68%

---

[a] Collection tank liquid volume following flushing = 2.20 E + 06 mL ± 10%

Table G-12. Collection tank liquid recirculation measurements and release fractions after flushing operations

Isotope	Concentration[a] (μCi/cm^3)	Total Activity (μCi)	Inventory (μCi)	Release Fraction[a]
Following Effluent Line Flushing[b]				
^{134}Cs	5.50 E+0 ± 2	6.88 E+6	3.02 E+8	2.28 E−2 ± 14
^{137}Cs	2.74 E+1 ± 4	3.43 E+7	1.19 E+9	2.88 E−2 ± 14
^{140}La	5.00 E−3 ± 60	6.25 E+3	2.81 E+7	2.22 E−4 ± 62
Following the First Bundle Flush[c]				
^{125}Sb	4.50 E−2 ± 100	7.16 E+4	3.70 E+7	1.94 E−3 ± 102
^{129m}Te	6.80 E−2 ± 68	1.08 E+5	4.00 E+6	2.70 E−2 ± 70
^{131}I	1.70 E−2 ± 59	2.70 E+4	1.48 E+6	1.82 E−2 ± 61
^{134}Cs	1.14 E+1 ± 3	1.81 E+7	3.02 E+8	5.99 E−2 ± 15
^{137}Cs	5.65 E+1 ± 4	8.98 E+7	1.19 E+9	7.55 E−2 ± 15
^{140}Ba	1.40 E−1 ± 36	2.23 E+5	2.51 E+7	8.88 E−3 ± 39
^{140}La	3.00 E−2 ± 70	4.77 E+4	2.81 E+7	1.70 E−3 ± 71
Following the Second Bundle Flush[d]				
^{131}I	2.00 E−3 ± 1150	4.40 E+3	8.09 E+5	5.44 E−3 ± 1150
^{134}Cs	2.12 E+1 ± 2	4.60 E+7	3.00 E+8	1.55 E−1 ± 15
^{137}Cs	1.40 E+2 ± 7	3.08 E+8	1.20 E+9	2.57 E−1 ± 16
^{140}Ba	9.00 E−2 ± 67	1.98 E+5	1.72 E+7	1.15 E−2 ± 69
^{140}La	1.79 E−1 ± 9	3.94 E+5	1.82 E+7	2.17 E−2 ± 17

---

a. The ± values are uncertainties in percent.

b. The effluent line flush was performed on May 15, 1985. All reported values were determined from on-line measurements and are subject to biases due to deposition. All activity values were measured on May 15, 1985. The collection tank liquid volume following the effluent line flush was 1.25 E+6 cm^3 (± 10%). Bundle inventory values were calculated as of May 15, 1985, using ORIGEN2.

c. The first bundle flush was performed on May 16, 1985. All reported values were determined from on-line measurements and are subject to biases due to deposition. All activity values were measured on May 16, 1985. The collection tank liquid volume = 1.59 E+6 (± 10%). Bundle inventory values were calculated as of May 16, 1985, using ORIGEN2.

d. The second bundle flush was performed on May 23, 1985. All activity values are as measured on May 23, 1985. Collection tank liquid volume following the second bundle flush was 2.20 E+6 cm^3 (± 10%).

Table G-13. Radioanalytical results for the SFD 1-4 core bore samples

Sample Number	Sample Type	Weight (g)	^{235}U Equivalent (μg)	Estimated Error	Total U (mg/g)	^{134}Cs (μCi/g)	^{137}Cs (μCi/g)	^{60}Co (μCi/g)	^{144}Ce (μCi/g)	^{90}Sr (μCi/g)	^{154}Eu (μCi/g)
M7C	Molten fuel	2.367	1.2 E+04	10%	747	3.2 E+03	1.9 E+04	5.2 E+00	2.5 E+03	2.6 E+04	6.4 E+02
M10A	Fuel	2.255	2.3 E+04	10%	721	5.5 E+03	4.6 E+04	7.1 E+00	6.0 E+03	3.5 E+04	1.1 E+03
M8C	Molten fuel	0.79	1.1 E+04	10%	490	8.7 E+02	4.9 E+03	4.6 E+00	6.6 E+03	3.0 E+04	1.5 E+03
MBB	Ceramic melt	1.431	6.9 E+03	10%	446	1.3 E+02	8.3 E+02	6.1 E+00	2.1 E+02	3.9 E+04	7.1 E+01
M6A	Ceramic melt	3.125	9.5 E+03	10%	512	1.3 E+02	8.5 E+02	2.3 E+00	1.5 E+02	1.9 E+04	5.2 E+01
M5B	Fuel	0.197	2.2 E+04	10%	634	3.7 E+03	3.8 E+04	3.5 E+01	4.0 E+03	2.5 E+04	9.5 E+02
M6B	Met-ceramic melt	2.456	5.3 E+03	10%	229	4.2 E+01	2.6 E+02	3.9 E+01	1.6 E+03	8.4 E+03	3.7 E+02
M4D	Met-ceramic melt	2.008	4.7 E+02	25%	12.4	9.3 E+00	6.2 E+01	9.0 E+01	3.7 E+01	1.0 E+02	9.0 E+00
M2B	Metallic melt	1.666	4.2 E+02	20%	11.7	1.2 E+02	1.0 E+03	1.3 E+02	1.1 E+02	1.2 E+03	9.5 E+00
M3B	Metallic melt	1.19	2.4 E+02	20%	6.3	7.9 E+00	4.5 E+01	4.9 E+01	—[a]	7.4 E+01	—[a]
M4B	Control material	14.19	8.4 E+01	20%	2.1	9.0 E+00	4.4 E+01	6.8 E+00	5.8 E+01	4.5 E+01	—[a]
M3C	Control material	1.186	9.0 E+01	50%	<0.6	—[a]	—[a]	—[a]	—[a]	1.3 E+02	—[a]
M3D	Control material	0.692	8.0 E+01	50%	<2.1	—[a]	—[a]	—[a]	—[a]	8.8 E+00	—[a]
M2D	Metallic melt	1.428	1.1 E+02	25%	<0.5	6.9 E−01	5.0 E+00	2.3 E−01	0.1 E−01	6.9 E+00	—[a]
				Estimated Uncertainty =		10%	5%	10%	10%	10%	10%

Sample Number	^{155}Eu (μCi/g)	^{125}Sb (μCi/g)	^{110}Ag (μCi/g)	^{241}Am (μCi/g)	^{182}Ta (μCi/g)	^{54}Mn (μCi/g)	^{106}Ru (μCi/g)	^{95}Nb (μCi/g)	^{127m}Te (μCi/g)	^{129}I (μg/g)
M7C	3.7 E+02	9.5 E+02	—[a]	1.9 E+02	—[a]	—[a]	9.2 E+02	1.8 E+03	—[b]	1.5 E+01
M10A	6.0 E+02	7.1 E+02	—[a]	3.3 E+02	—[a]	—[a]	7.5 E+02	1.2 E+03	—[a]	5.1 E+00
M8C	9.0 E+02	4.5 E+02	3.4 E+00	4.1 E+02	—[a]	—[a]	5.8 E+01	1.5 E+03	—[a]	4.3 E+00
MBB	4.6 E+01	2.0 E+02	4.0 E+00	2.8 E+01	8.9 E+00	1.2 E+00	4.4 E+01	1.0 E+03	—[a]	1.7 E+00
M6A	3.3 E+01	8.9 E+01	4.9 E+00	7.5 E+01	6.1 E+01	1.0 E+00	—[a]	1.2 E+03	—[b]	—[b]
M5B	4.1 E+02	7.6 E+02	9.0 E+01	4.7 E+02	4.0 E+02	—[a]	2.2 E+03	2.7 E+03	—[a]	3.7 E+02
M6B	2.1 E+02	3.4 E+02	1.0 E+02	1.6 E+02	5.9 E+02	3.4 E+02	8.9 E+02	—[a]	—[b]	9.3 E−01
M4D	5.2 E+00	3.6 E+02	1.7 E+03	1.0 E+02	2.4 E+03	9.8 E+00	3.6 E+02	—[a]	—[b]	—[b]
M2B	8.1 E+00	4.4 E+01	2.3 E+03	1.2 E+01	—[a]	7.4 E+00	—[a]	—[a]	1.5 E+03	6.3 E+01
M3B	—[a]	2.1 E+02	2.4 E+03	6.4 E+01	1.0 E+03	7.1 E+00	—[a]	—[a]	1.5 E+03	1.7 E+00
M4B	—[a]	—[a]	4.8 E+03	—[a]	—[a]	—[a]	—[a]	—[a]	2.2 E+03	—[b]
M3C	—[a]	—[a]	5.2 E+03	—[a]	—[a]	—[a]	—[a]	—[a]	1.3 E+03	5.1 E−02
M3D	—[a]	—[a]	5.0 E+03	—[a]	—[a]	—[a]	—[a]	—[a]	1.3 E+03	—[a]
M2D	—[a]	3.1 E+00	2.6 E+01	—[a]	—[a]	—[a]	—[a]	—[a]	—[a]	1.4 E−01
	10%	10%	10%	15%	10%	20%	10%	10%	50%	10%

---

a. Not detected.

b. Analysis was not performed.

G-4.2 Fission Product Retention Methodology. An estimate of the original fission product inventory was required to calculate the sample retention. Sample-specific inventory estimates were required because of the wide variation in fuel burnup within the SFD 1-4 test bundle. Local BR-3 exposures, considering the axial profile, for the SFD 1-4 rods varied from somewhat less than 8 GWd/MtU to nearly 60 GWd/MtU.[G-3] Ideally, this estimate would be determined from knowledge of the exact local exposure history and the location of the sample. However, the degree of material relocation and rearrangement in the SFD 1-4 bundle and the varying pretest rod burnups required that an alternate method be used.

This alternate method of inventory estimation relied upon the ORIGEN2-generated correlations between fission product concentrations and fuel burnup discussed in Section G-1 and the measured concentrations of ^{90}Sr, ^{235}U, and total uranium in the samples. Sample-specific burnup estimates were derived by comparing the ORIGEN2-generated plots of the burnup-dependent values for $^{235}U_{eq}$/total uranium and $^{90}Sr/^{235}U_{eq}$ with the same measured radionuclide ratios for each sample. The ORIGEN2-generated inventories are presented in Curies of the fission product per gram ^{235}U equivalent. As discussed in Section G-1, the unit of grams ^{235}U equivalent ($^{235}U_{eq}$) was dictated by the neutron activation/delayed neutron counting measurement method that measured the total fissile content of the sample. The technique measured both ^{235}U and ^{239}Pu and reported the result as $^{235}U_{eq}$. If the SFD 1-4 core samples contained no ^{239}Pu, then the total fissile result ($^{235}U_{eq}$) would equal the ^{235}U content; however, since a gram of ^{239}Pu provides a total fissile response that is two-thirds of the ^{235}U response, a gram ^{235}U equivalent is the total grams of ^{235}U plus 0.66 times the ^{239}Pu content in grams.[G-5]. Since the ORIGEN2 calculations estimate a ^{239}Pu and a ^{235}U content at each burnup, calculation of the $^{235}U_{eq}$ values was straightforward.

The rationale for using the ^{90}Sr-to-total-fissile ratio as a burnup indicator, rather than the somewhat more common choice of ^{144}Ce content, is readily apparent through reference to Figures G-1 and G-10. Although both elements are relatively nonvolatile and would not be expected to migrate away from the fuel, the shorter half-life of the ^{144}Ce would cause the ORIGEN2-predicted concentration to be very sensitive to irradiation cycle (B300 versus B500). As a result, for a given sample in the SFD 1-4 bundle, since the actual irradiation cycle was unknown, the sample burnup would be highly uncertain.

Uncertainties in the measured concentration ratios were propagated from the estimated relative standard deviation in each measurement. Uncertainties in the sample-specific burnup were then derived from these ratios by determining the burnup that would result from an indicator ratio at its maximum (measured ratio plus one estimated standard deviation). The difference between the burnup at the measured ratio and at its maximum was taken as the burnup uncertainty estimate. Using this technique for uncertainty estimation results in smaller uncertainty estimates for burnups determined using the $^{90}Sr/^{235}U_{eq}$ indicator ratio than for $^{235}U_{eq}$/total uranium, since the ^{90}Sr ratio is more strongly burnup-dependent.

Sample-specific burnup estimates were derived in this manner for 11 of the 14 core drilled samples. Sample M3C and M3D were control material containing silver, indium, cadmium and a small amount of zirconium, but with no detectable total uranium and marginally detectable $^{235}U_{eq}$. Thus, burnups were not estimated for these two samples. Additionally, Sample M2D, drilled from a previously molten metallic material that was overwhelmingly zirconium (98 wt%), had no detectable uranium during ICP analysis. However, both ^{90}Sr and $^{235}U_{eq}$ results were obtained on Sample M2D; consequently, an M2D sample-specific burnup was estimated from the $^{90}Sr/^{235}U_{eq}$ ratio alone.

Table G-14 details the result of the sample-specific burnup estimates. The general agreement between the ^{90}Sr-based and the total uranium-based estimates is encouraging. Of the 11 samples with two burnup estimates, 8 of these samples exhibit agreement between the two estimates at about the one standard deviation level (one sigma). None of the samples have dual estimates that differ by more than three estimated standard deviations. Albeit the relatively large uncertainty values assigned to the total uranium-based burnup estimates somewhat obviate this agreement, nonetheless the general agreement is encouraging.

To derive an unbiased estimate of the sample-specific burnup from the dual estimate samples, an error-weighted average was computed and accepted as the best estimated burnup. The assigned weights were the inverse of the square of the estimated standard deviation. This procedure gives greater weight to the more precise ^{90}Sr-based burnup estimates. The accepted values in Table G-14 were developed from this averaging procedure.

Table G-14. Sample specific burnup estimates derived from indicator ratios

Sample		Burnup Estimates[a] (GWd/MtU)			
Number	Description	^{90}Sr	^{235}U Equivalent	Average[b]	Peak Temperature (K)
M7C	Previously molten fuel at 0.39 m	31.9 ± 4.5	52 ± 8	36.7 ± 3.9	2800
M10A	Fuel pellet fragment from 0.85 m	23 ± 4	28.5 ± 6	24.7 ± 3.3	2200
M8C	Previously molten fuel at 0.54 m	36 ± 4	42 ± 8	37.2 ± 3.6	2800
M8B	Previously molten ceramic at 0.54 m	47.2 ± 3	54 ± 8	48.0 ± 2.8	2800
M6A	Previously molten ceramic at 0.25 m	28 ± 4	47 ± 8	31.8 ± 3.6	2800
M5B	Fuel pellet from rod 4D at 0.17 m	19 ± 2	25 ± 6	19.6 ± 1.9	2200
M6B	Mixed metallic-ceramic melt at 0.25 m	24 ± 4	41 ± 8	27.4 ± 3.6	2800
M4D	Mixed metallic-ceramic melt at 0.08 m	5 ± 4	21.5 ± 10	7.3 ± 3.7	1700
M2B	Silvery previously molten metallic at −0.09 m	35 ± 7	24 ± 16	33.2 ± 6.4	1700
M3B	Gray mixed phase previously molten metallic at 0.02 m	7 ± 2	22 ± 16	7.2 ± 2.0	1700
M4B	Previously molten control rod material at 0.08 m	10 ± 4	17 ± 9	11.2 ± 3.7	1700
M3C	Unmelted control rod material at 0.02 m	—[c]	—[c]	[c]	1073
M3D	Unmelted control rod material at 0.02 m	—[c]	—[c]	—[c]	1073
M2D	Silvery previously molten metallic at −0.09 m	12 ± 3	—[c]	12.0 ± 3	1700

---

a. Quoted uncertainties are one estimated standard deviation developed from propagated errors.

b. Error-weighted average.

c. Not applicable.

The estimated sample-specific inventory of each isotope of interest was then determined using the ORIGEN2-generated plots of burnup-dependent fission product concentrations and the estimated sample-specific burnup. The lack of detailed knowledge concerning the BR-3 irradiation cycle caused an ambiguity in the inventory estimates for certain of the shorter-lived nuclides (^{144}Ce, ^{125}Sb, and ^{106}Ru), while inventory estimates for the longer-lived nuclides (^{137}Cs and ^{129}I) are not ambiguous. Estimated inventories were not developed for those nuclides that are sufficiently short lived that their inventories at the time of analysis were dominated by the non-modeled irradiation in the PBF (^{95}Nb and ^{127m}Te); nor were estimated inventories developed for those nuclides that are partially or completely produced through activation (^{54}Mn, ^{60}Co, ^{110m}Ag, and ^{182}Ta). Inventories were not estimated for the non-fission product transuranic ^{241}Am.

G-4.3 Fission Product Retention Results. The retention of specific fission products in the samples examined was estimated using

$$\text{Fractional Retention} \doteq C_{\text{measured}}/I_{\text{estimated}} \qquad \text{(G-7)}$$

where

C_{measured} = measured concentration of the fission product (Ci/g of $^{235}U_{eq}$)

$I_{\text{estimated}}$ = the sample-specific radionuclide inventory based on the estimated sample burnup.

The results are presented in Table G-15. Unambiguous estimates of sample burnup, inventory, and hence retention could not be provided in all cases because of the mixed irradiation history of the BR-3 fuel used in Test SFD 1-4. Eighteen of the rods in the SFD 1-4 bundle came from the B300 batch, while eight rods came from the B500 batch. As a result, in some cases retention results are presented for both a B300- and a B500-based inventory. (The B500-based values are in parentheses.) The quoted uncertainties are one estimated standard deviation of the retention percentage and are not relative values. Consequently, a quoted value of 123% ± 19% indicates a one-sigma confidence interval from 104% to 142%. Note that the retention of ^{90}Sr is about 100% in all samples, since ^{90}Sr was one of two species used as a burnup indicator.

Two of the samples obtained from the SFD 1-4 bundle were used to evaluate qualitatively the inventory estimation technique. Sample M5B was extracted from an intact fuel pellet from SFD 1-4 rod 4C at the 0.17-m elevation. Although only part of the sample was recovered during core drill sampling, the fuel material present is believed to be from rod 4C. Rod 4C was BR-3 rod I-640, a fuel rod in the B300 cycle. Sample M10A was a sample of a fuel pellet fragment from the debris bed at the 0.85-m elevation. Neither of these fuel samples exhibited morphologies indicative of high temperatures, dissolution, or melting; consequently, little or no release of fission products from these samples would be expected, and their estimated retention values can be used to judge the applicability of the inventory estimation method.

Retention results on sample M5B using the proper B300-based inventory are very good for ^{137}Cs (123% ± 19%), ^{125}Sb (119% ± 24%), and ^{155}Eu (93% ± 25%); acceptable for ^{106}Ru (166% ± 58%) and ^{154}Eu (143% ± 97%), given the large relative errors in the retention results; and appear seriously in error only for ^{144}Ce (214% ± 43%) and ^{129}I (726% ± 175%).

The actual irradiation cycle of the pellet of sample M10A is unknown. The sample exhibits complete ^{137}Cs retention (105% ± 17%). Both the B300 and B500 retention estimates for ^{125}Sb (70% ± 25% and 83% ± 22%, respectively), ^{155}Eu (87% ± 30% and 104% ± 43%, respectively) and ^{154}Eu (80% ± 41% and 96% ± 49%, respectively) are roughly 100%. The retention estimates for ^{106}Ru are strongly assumed-cycle dependent, yielding 41% ± 26% for an assumed B300 cycle and 81% ± 22% for a B500 cycle. The estimated ^{129}I retention is anomalously low at 6.5% ± 1.8%, and both the B300- and B500-based retention estimates for ^{144}Ce seem anomalous at 221% ± 44% and 652% ± 176%.

The cause of the anomalous results for ^{129}I and ^{144}Ce in both samples M5B and M10A is not known. The possibility of analytical error in the ^{129}I concentration values has been considered, since this determination requires chemical separation and activation analysis and is somewhat complicated. While this possibility remains, a review of the analytical data provided no indication of anomalies.

On the other hand, the measurement of the ^{144}Ce concentration was by gamma-ray spectroscopy, a

Table G-15. Estimated fission product retention percentages[a]

Sample		Peak Temperature (K)	Estimated Burnup (GWd/MtU)	Retention (%)								
Number	Description			$^{90}\text{Sr}^{b}$	^{106}Ru	^{125}Sb	$^{129}\text{I}^{c}$	^{134}Cs	^{137}Cs	^{144}Ce	^{154}Eu	^{155}Eu
M7C	Previously molten fuel at 0.39 m	2800	37 ± 4	87 ± 15	33 ± 8 (85 ± 48)	80 ± 26 (99 ± 27)	17 ± 4	38 ± 12 (59 ± 27)	40 ± 8	89 ± 24 (260 ± 70)	24 ± 9 (30 ± 17)	34 ± 23 (44 ± 19)
M10A	Fuel pellet fragment from 0.85 m	2200	25 ± 3	93 ± 20	40 ± 26 (81 ± 21)	70 ± 25 (83 ± 22)	6 ± 2	109 ± 51 (170 ± 75)	105 ± 17	221 ± 44 (652 ± 176)	79 ± 41 (96 ± 49)	87 ± 30 (104 ± 43)
M8C	Previously molten fuel at 0.54 m	2800	37 ± 4	97 ± 14	2 ± .6 (5 ± 6)	40 ± 11 (51 ± 14)	5 ± 1	10 ± 4 (18 ± 3)	11 ± 3	250 ± 58 (750 ± 228)	62 ± 23 (72 ± 27)	90 ± 41 (117 ± 51)
M8B	Previously molten ceramic at 0.54 m	2800	48 ± 4	98 ± 8	1 ± .3 (3 ± .7)	15 ± 4 (18 ± 4)	2 ± .4	1 ± .3 (1.6 ± .3)	1.6 ± .3	7 ± 2 (22 ± 4)	1.9 ± .5 (2.2 ± .6)	3 ± 1 (4 ± 1)
M6A	Previously molten ceramic at 0.25 m	2800	32 ± 4	88 ± 16	—[d]	13 ± 2 (16 ± 4)	—[d]	3 ± 1 (5 ± 2)	3 ± .8	9 ± 2 (26 ± 7)	4 ± 2 (5 ± 2)	6 ± 3 (8 ± 4)
M5B	Fuel pellet from rod 4D at 0.17 m[e]	2200	20 ± 2	97 ± 14	166 ± 58	119 ± 24	726 ± 175	140 ± 60	123 ± 19	214 ± 43	144 ± 97	93 ± 25
M6B	Mixed metallic-ceramic melt at 0.25 m	2800	27 ± 4	88 ± 19	152 ± 38 (420 ± 113)	123 ± 33 (146 ± 39)	4 ± 1	3 ± 2 (4 ± 2)	2.1 ± .7	218 ± 67 (671 ± 233)	93 ± 63 (100 ± 44)	107 ± 59 (132 ± 46)
M4D	Mixed metallic-ceramic melt at 0.08 m	1700	7 ± 4	69 ± 65	4042 ± 4063 (8085 ± 16190)	1915 ± 3357 (2198 ± 3758)	—[d]	197 ± 199 (—[f])	33 ± 21	314 ± 192 (1124 ± 1290)	—[e]	221 ± 222 (221 ± 222)
M2B	Silvery previously molten metallic at −0.09 m	1700	33 ± 6	105 ± 29	—[f]	140 ± 94 (166 ± 94)	2655 ± 1095	60 ± 62 (95 ± 96)	72 ± 33	138 ± 53 (403 ± 160)	15 ± 12 (17 ± 16)	31 ± 25 (39 ± 20)
M3B	Gray mixed phase previously molten metallic at 0.02 m	1700	7 ± 2	97 ± 38	—[f]	10938 ± 6923 (17500 ± 14108)	964 ± 528	330 ± 330 (—[f])	468 ± 352	—[f]	—[f]	—[f]

Table G-15. (continued)

Sample		Peak Temperature (K)	Estimated Burnup (GWd/MtU)	Retention (%)								
Number	Description			^{90}Sr^{b}	^{106}Ru	^{125}Sb	^{129}I^{c}	^{134}Cs	^{137}Cs	^{144}Ce	^{154}Eu	^{155}Eu
M4B	Previously molten control rod material at 0.08 m	1700	11 ± 4	90 ± 46	—^{f}	—^{f}	—^{f}	357 ± 359 (535 ± 538)	873 ± 584	—^{f}	—^{d}	—^{d}
M3C	Unmelted control rod material at 0.02 m	1700	<5	—^{f}	—^{f}	—^{f}	—^{f}	—^{f}	—^{f}	—^{f}	—^{f}	—^{f}
M3D	Unmelted control rod material at 0.02 m	1700	<5	—^{f}	—^{f}	—^{f}	—^{f}	—^{f}	—^{f}	—^{f}	—^{f}	—^{f}
M2D	Silvery previously molten metallic at ~0.09 m	1700	12 ± 38	100 ± 3	—^{f}	201 ± 89 (256 ± 142)	107 ± 42	21 ± 21 (31 ± 32)	76 ± 38	18 ± 6 (55 ± 26)	—^{f}	—^{f}

a. Quoted uncertainties are one estimated standard deviation developed by propagating quantified errors. Listed retention values are based on a B-300 irradiation cycle. Parenthetical values are based on a B500 irradiation cycle.

b. Complete retention assumed.

c. Poor agreement with the expected inventory of samples M5B and M10A renders the results on these nuclides suspect.

d. Not detectable.

e. Core bore failed to sample properly, and the sample was dropped.

f. Not applicable.

g. Burnup was based on ^{90}Sr content only.

measurement that is relatively free of error and interference. Isotope-specific errors in the ORIGEN2-generated burnup-dependent fission product concentration curves have also been considered as an error source. However, data[G-4] developed at the INEL comparing ORIGEN2-predicted fission product inventories with those measured on samples of BR-3 and TMI-2 fuel with known irradiation histories showed excellent agreement between measured and predicted concentrations for ^{144}Ce and ^{106}Ru and indicated that ORIGEN2-predicted ^{129}I results are biased high by around 30%. (These results showed poor agreement for ^{125}Sb and $^{154/155}$Eu.) These investigations cannot explain the anomalous ^{129}I and ^{144}Ce recoveries noted for samples M5B and M10A. Consequently, retention estimates for these two nuclides must be considered suspect in all of the retention data.

The core drilled samples were obtained from a variety of different posttest bundle structures. For the purpose of the following discussion, they will be grouped into three general categories—fuel, control rods, and melts. Fuel samples include those containing greater than 75 wt% uranium and exhibiting the apparent structure of UO_2 fuel. (Sample M5B is included on structure alone.) Control rod samples are previously molten metallic materials containing greater than 70 wt% silver. Melt samples are mixed-content previously molten materials.

G-4.3.1 Fuel—This sample group includes the two fuel pellet samples M5B and M10A discussed previously and two samples, M7C and M8C, that were identified as samples of molten fuel. The retention results for M5B and M10A have been previously discussed and generally show complete retention for all fission products other than ^{144}Ce and ^{129}I that exhibited anomalous results. This complete retention was not noted for the two fuel samples that had melted. On the contrary, generally depleted inventories for all nuclides other than isolated results for $^{154/155}$Eu were measured. Both sample M7C and M8C showed sharply reduced ^{137}Cs retentions of 40% ± 8% and 11% ± 3%, respectively. The behavior of the volatile cesium correlates well with expectations of high release from samples that experienced high temperatures. Moderate releases of the intermediate volatile antimony were expected and were noted.

G-4.3.2 Control Rod Materials—Samples M3C, M3D, and M4B consisted mainly of silver, indium, and cadmium control rod materials. Their fission product content was generally low and in most cases nondetectable. Only sample M4B had entrained or dissolved enough fuel material to allow assignment of a burnup value. (While the concept of burnup may seem unusual for control rod materials, calculation of the expected fission product content of a sample of control material based on the amount of fuel material found in the sample provides a convenient method of determining any preferential retention of a given nuclide.) Sample M4B contained more than eight times the ^{137}Cs and between two to seven times the ^{144}Ce that would be expected from it uranium and/or ^{90}Sr content. However, control rod material samples M3C and M3D showed no detectable concentration of ^{137}Cs or ^{144}Ce.

All three control rod material samples had measurable concentrations of ^{90}Sr, ^{127m}Te, and ^{110m}Ag. The ^{110m}Ag is a result of activation of the stable silver. The detection of ^{90}Sr and ^{127m}Te in samples M3C and M3D and ^{129}I in M3C, while indicative of the presence of some activity, is primarily due to the enhanced detection limit of the radiochemical methods used for these measurements.

These results indicate that while limited mixing of fission product and fuel-bearing materials with relocating molten control rod materials may occur, the overall effect is slight. No gross retention of fission products by control rod materials occurred.

G-4.3.3 Melts—The melt materials studied included those classified as ceramic melts, metallic-ceramic melts, and metallic melts. Two of the three metallic melts are further classified as mixed melts, due both to their difference in appearance from a pure silvery metallic and to their mixed composition.

The two ceramic melts (M6A and M8B) are among the highest temperature structures studied (see Table G-14). This elevated peak temperature, coupled with the grain boundary destruction that occurred during melting and oxidation, resulted in very low estimated retention of all the radionuclides measured. Less than 5% of the expected inventory of ^{137}Cs, ^{134}Cs, ^{129}I (in M8B), and ^{154}Eu was found in these samples. No detectable ^{106}Ru was measured in either sample, and ^{129}I was not detected in M6A. Estimated retention percentages for the remaining nuclides are less than 26%. These results are consistent with the high peak temperature of the samples and the ease of release of fission product material from molten, fuel-bearing materials.

The two melts identified as metallic-ceramic melts are very different in their composition and in their estimated peak temperatures. Melt M6B is a metallic-ceramic melt high in uranium and zirconium content (24 wt% and 61 wt%, respectively), while melt M4D is a metallic-ceramic melt low in uranium (1.2 wt%) but high in zirconium and silver (56 wt% and 20 wt%, respectively), with modest concentrations of stainless steel materials (iron, 7 wt%; nickel, 5 wt%; and chromium, 3 wt%). The higher uranium content melt, M6B, was one of the highest temperature structures studied, having reached an estimated peak temperature of about 2800 K; while the lower uranium content melt, M4D, was one of the lower temperature melt structures studied, having reached an estimated peak temperature of <1700 K. These differences in composition and peak temperature were expected to result in significantly different fission product retention behavior; however, the uncertainties in the estimated retention values for the low uranium content sample M4D generally preclude quantitative comparisons on isotopes other than ^{137}Cs. The lower temperature, lower uranium content melt M4D retained 33% ± 21% of its estimated ^{137}Cs inventory, while only 2% ± 0.7% of the estimated ^{137}Cs inventory of the higher temperature, higher uranium content M6B melt was retained. Melt M6B also exhibited only 4% ± 1% retention of its estimated ^{129}I inventory. (The ^{129}I retention values for the intact fuel samples were suspect, and thus may be in error throughout this work.) Complete retention of all other nuclides in both of these melts is implied; however, statistical uncertainties preclude a definitive statement.

Samples M2B, M2D, and M3B were identified as metallic melts. These melt samples vary significantly in elemental content. Melt M2B was a mixed melt primarily composed of iron (32%), silver (24%), nickel (12%), and zirconium (11%). Melt M2D was a zirconium melt (98%) with trace quantities of tin, silver, and iron. The uranium content of this melt was below the detection level of the ICP; consequently, the estimated burnup value was based solely on the ^{90}Sr content. Melt M3B was a mixed melt containing primarily zirconium (54%) and silver (29%). All three of these melts were among the lowest temperature structures studied, with estimated peak temperatures of 1700 K. All three melts had relocated from other bundle locations.

Melt M2B exhibited the highest uranium content of the three metallic melt samples, but at 0.7 wt% uranium must still be termed a minor component. The composition of this melt implies that it may have formed as the result of melting and interaction of the stainless-steel-clad Ag-In-Cd control material and the zircaloy guide tubes. During relocation, this melt material evidently interacted with a small amount of fuel material. There is no evidence for preferential retention of fission products by this melt. High uncertainties in the estimated retention values preclude quantitative conclusions; however, non-preferential retention of fuel-bearing materials is implied. It is interesting to note that ^{127m}Te was reported in this mixed melt sample.

Sample M2D, a nearly pure sample of previously molten zircaloy, picked up small amounts of fission product and fuel materials. Small amounts of ^{90}Sr, ^{125}Sb, ^{129}I, ^{134}Cs, ^{137}Cs, ^{144}Ce, and ^{154}Eu were detected. Based on a burnup estimated solely on the ^{90}Sr content, the ^{137}Cs and ^{129}I concentrations were at roughly expected levels, while the ^{125}Sb content appeared somewhat elevated. Although this sample was analyzed for ^{127m}Te, none was detected.

Although the individual uncertainties on the estimated retention percentages of melt sample M3B are too high to allow quantitative comparisons, the general trend implies either a case in which the estimated burnup method of determining inventory is in error, or it implies significant levels of fission product activity in a relocated previously molten material. Estimated retention percentages for ^{129}I, ^{125}Sb, ^{134}Cs, and ^{137}Cs were 964% ± 528%, 10938% ± 6922%, 330% ± 330%, and 468% ± 352%, respectively. (Quoted retentions are for a B300 cycle. B500 values are even higher for those isotopes that are cycle-dependent.) Some evidence of preferential retention of cesium and antimony isotopes in previously molten materials has been reported from studies of the TMI-2 core debris.[G-6]

G-5. Development of FASTGRASS Release Model

This section will describe the input used in FASTGRASS to model the steady-state BR-3 and PBF irradiations and the SFD 1-4 transient.

G-5.1 Fuel Bundle Characteristics. The SFD 1-4 fuel bundle consisted of 26 irradiated fuel rods and 2 fresh fuel rods. Of the 26 irradiated rods, 18 came from the B300 series in the BR-3 reactor while the other 8 came from the B500 series. Details about the design characteristics of the fuel and their operating history were obtained from

Reference G-2. The design details are listed in Table G-16. All the irradiated rods used in Test SFD 1-4 had an initial enrichment of 5.76%; however, the B300 and B500 rods experienced different irradiation histories in the BR-3 reactor. The B300 rods were irradiated in two cycles, whereas the B500 rods were irradiated in one cycle. The peak average linear power in the B300 rods was less on the average than the peak average linear power in the B500 rods.

G-5.2 Steady-State Irradiations. Both the BR-3 and PBF preconditioning irradiations were modeled for the SFD 1-4 FASTGRASS analysis. The details of the BR-3 irradiations were not modeled explicitly. Instead, the following approach was adopted. The peak linear powers for each rod in the SFD 1-4 bundle were time-averaged over the BR-3 irradiation to determine a rod-specific average peak linear power, <q'>. These rod-specific average peak linear powers were then averaged within each group to determine the average <q'> for the B300 rods and the B500 rods used in Test SFD 1-4. The burnup for each rod was averaged in the same manner to determine the average burnup of the batch used in PBF. The results are listed in Table G-17.

Table G-16. BR-3 fuel rod design characteristics

Parameter	Value
Fuel:	
Material	UO_2 sintered pellets
Density	95% TD
Initial enrichment	5.76%
Pellet OD	8.04 mm
Pellet length	12.0 mm
Pellet end dish (2)	1.5% of pellet cylindrical volume
Fuel stack length	1000 mm
UO_2 mass	529 g per rod
Cladding:	
Material	Zircaloy-4
Tube OD	9.50 mm
Tube ID	8.24 mm
Tube wall thickness	0.63 mm

Table G-17. Average burnup and rod average peak linear power for the BR-3 rods used in Test SFD 1-4

Cycle	Rod Average Burnup (GWd/MtU)	Rod Average Linear Power <q'> (W/cm)
B300	38.69	247.55 for cycle A 92.20 for cycle B
B500	29.93	239.71

The peak-to-average ratio of the rods changed during each irradiation cycle. Thus, an average peaking factor was calculated for the B300A, B300B, and B500 series. Based on the peaking factor and the data in Table G-17, a burnup was calculated to compare with the average burnup given in Reference G-2. The results are compared in Table G-18. In addition, examination of the detailed power history indicates that the B300A and B500 cycles lasted 563 days and the B300B cycle lasted 400 days. This is slightly less than the 640 and 463 days used in the averaging process discussed above. Use of the actual number of days would tend to cause an even greater variance between the calculated and average burnup. The reason for the discrepancy between the calculated and stated rod burnups is not clear. The variance in the calculated and predicted burnups is ∿15%, which is much larger than the variance associated with the peaking factor or the average linear power. Because of this discrepancy, the average linear powers for the average B300 and B500 rod were adjusted so that the calculated burnup listed in Reference G-2 would be achieved for the given irradiation duration. These results are shown in Table G-19.

Table G-18. Comparison of calculated and stated burnups for BR-3 rods

Cycle	Peaking Factor	Calculated Burnup (GWd/MtU)	Rod Average Burnup (GWd/MtU)
B300A	1.255		
B	1.213	34.3	38.69
B500	1.273	25.6	29.93

Table G-19. Normalized averaged linear power required to achieve rod average burnup

Cycle	Average <q'> (W/cm)	Irradiation Time (Days)
B300A	254.10	563
B	97.90	400
B500	250.35	563

Comparison of the fuel behavior parameters for the B300 and B500 rods indicates that the differences in the peak linear power and the burnup are small and should not affect the overall details of the FASTGRASS release calculation. As a result, only the B300 rods were modeled for the FASTGRASS calculation.

In the FASTGRASS analysis, a 1-m-long fuel rod was modeled using ten 0.1-m axial nodes. The local power in a given node was calculated using the B300 average linear power in Table G-19 and the peaking factors given in Table G-20. The local peaking factors were determined using the peak-to-average ratio and a chopped cosine distribution.

For the PBF steady-state irradiations, the irradiation history in Table G-21 was used for all the rods. The two PBF cycles correspond to the long-lived and short-lived fission product buildup phases. The power calibration phase has been neglected because it would have little effect on the fuel behavior and fission product release. The axial power profile for PBF as determined by reactor physics calculations (see Appendix D) is given in Table G-22.

Other inputs to FASTGRASS include grain size, fuel dimensions, and fuel temperatures during the steady-state irradiation. Dimensions are listed in Table G-16. The initial grain size, based on examinations on sibling rods and examinations of undamaged fuel in the lower portions of the SFD 1-4 bundle, was assumed to be 10 μm.[a] Temperatures during the steady-state irradiations were calculated using an INEL fuel pin conduction model that accounts for pellet cracking. Because the model was developed only for predicting fuel temperatures in low-burnup rods, the centerline temperature calculations were increased by 200 K to account for fission gas buildup in the gap which would decrease the gap conductance during the BR-3 irradiation.

Table G-20. Peaking factors for BR-3 irradiation cycles

Node	B300A	B300B	B500
1	0.654	0.704	0.624
2	0.876	0.895	0.865
3	1.053	1.046	1.057
4	1.177	1.151	1.192
5	1.240	1.204	1.261
6	1.240	1.204	1.261
7	1.177	1.151	1.192
8	1.053	1.046	1.057
9	0.876	0.895	0.865
10	0.654	0.704	0.624

Table G-21. Irradiation history for the PBF steady-state irradiations

Cycle	Rod Average Liner Power <q'> (W/cm)	Irradiation Time (h)
1	52.1	178.23
2	30.36	8.0

Table G-22. Axial power profile during the PBF irradiations

Node	Peaking Factor
1	0.627
2	0.795
3	1.040
4	1.254
5	1.284
6	1.284
7	1.254
8	1.040
9	0.795
10	0.627

---

[a] Personal communication, L. A. Neimark, Argonne National Laboratory, Argonne, Illinois.

Comparison of the release fractions of the long-lived and stable noble gases with the short- and moderate-lived isotopes indicates differences that are thought to be due to radioactive decay and changes in fuel morphology during the steady-state BR-3 irradiation. Only long-lived fission products (i.e. ^{85}Kr, ^{137}Cs, ^{90}Sr, etc) and stable elements are present in the high-burnup fuel prior to the SFD 1-4 transient because of the long decay time between the BR-3 irradiation and Test SFD 1-4. At the time of Test SFD 1-4, a portion of the BR-3-generated noble gases and volatile fission products should be on the grain boundaries. By contrast, most of the short- and moderate-lived fission products produced following the PBF irradiation would reside in the grains. Very little diffusion of these fission products to the grain boundaries would be expected due to the low temperature of the irradiation. As a result of the mixed irradiation history of the fuel, different release timings would be expected. However, the on-line gamma spectrometers can generally measure only short- and moderate-lived isotopes because of their large specific activities. As a result, a direct comparison of the differences in release timing between the BR-3-generated noble gases and the PBF-generated noble gases cannot be made. However, the integral release data suggest that the effect is important and should be modeled.

As a result, the tellurium release model in FASTGRASS was used to model the release of the PBF-generated noble gases by replacing the tellurium yield with the cumulative yield of the short- and moderate-lived noble gases. Since there is no chemistry in the code for tellurium, all the equations are the same as for the noble gases, even the diffusivity.

G-5.3 SFD 1-4 Transient Input. The SFD 1-4 transient was modeled using the SCDAP/RELAP5 best-estimate temperatures discussed in Section 8. A radial temperature gradient of 25 K was used during the entire transient. The FASTGRASS microcracking model was also invoked during the transient to model release from microcracks formed during the rapid heatup. The empirical grain growth model that is driven only by temperature was used in the calculations. To account for the ∿18% fuel dissolution during the test, the two hot nodes in the calculation (nodes 5 and 6) were assumed to begin to liquefy at 2170 K. At 2650 K, the monotectic temperature at which the solubility of UO_2 in molten zircaloy increases very drastically, the node is assumed to enter gross dissolution. Release is expected to be very large once 2650 K is reached. Details of the model and input for the transient are summarized in Table G-23.

G-6. Development of the Booth Model

The Booth diffusion model is based on the solution to the diffusion equation from a sphere of radius a. The fractional release of a fission product, FR, is given by

$$FR = 6(Dt/\pi a^2)^{1/2} - 3Dt/a^2 \qquad \text{(G-8)}$$

where

D = diffusion coefficient of the fission product (cm^2/s)

a = "equivalent radius" of the sphere (cm)

t = time (s).

The diffusion coefficient is usually given by an Arrhenius function of the form

$$D = D_0 \exp(-Q/RT) \qquad \text{(G-9)}$$

where

D_0 = preexponential factor (cm^2/s)

Q = activation energy (kcal/mole)

R = universal gas constant (kcal/mole K)

T = fuel temperature (K).

The equivalent radius is derived from the total surface area available for diffusion and the volume of the specimen. In general, the equivalent sphere radius is difficult to obtain for specimens that are poly-crystalline. As a result, many researchers correlate their results to an effective diffusion coefficient D′, where $D' = D/a^2$.

The Booth model given by Equation (G-8) is applicable for the case of a constant temperature anneal. In Test SFD 1-4, the temperatures, and hence the diffusion coefficient [Equation (G-9)], changed with time. As a result, the Booth diffusion model has been modified to account for the transient temperature response of the core. For a

Table G-23. Summary of model and input detail for the transient FASTGRASS calculation

Model or Input Variable	Description
Fuel centerline temperature	From SCDAP/RELAP5 analysis
Radial temperature gradient	25 K for all nodes
Microcracking	Invoked for transient at all nodes
Grain growth	Empirical model based on temperature
Liquefaction	Hottest two nodes. Begin liquefaction at 2170 K. Gross dissolution at 2650 K.

transient temperature, an infinite series form of the solution is used. The fractional retention, FT, is given by

$$FT = \frac{6}{\pi^2} \sum_{n=1}^{\infty} \frac{1}{n^2} \exp(-n^2\pi^2\tau) \qquad \text{(G-10)}$$

where

$$\tau = \int_0^t D[T(t')]\, dt'$$

The fractional release rate coefficient, k, is given by

$$k = \frac{d(FR)/dt}{1 - RF}$$

$$= \frac{D(t)\,\pi^2}{a^2} \frac{\sum_{n=1}^{\infty} \exp(-n^2\pi^2\tau)}{\sum_{n=1}^{\infty} \frac{\exp(-n^2\pi^2\tau)}{n^2}} \qquad \text{(G-11)}$$

The release rate coefficient, given by Equation (G-11), was used to calculate the fractional release rate from the SFD 1-4 bundle using the SCDAP/RELAP5 best-estimate temperature history and reasonable values of D and a. These results are discussed in Section 6.

G-7. References

G-1. A. G. Croft, *ORIGEN2 - A Revised and Updated Version of the Oak Ridge Isotope Generation and Depletion Code*, ORNL-5621, July 1980.

G-2. A. Charlier, J. Demeester, and M. Doucet, *Irradiated BR3 Fuel Rods for the PBF Program*, Belgonucleaire, S.A. Report BN 8306-05, 232.00,060/nc/004, June 1983.

G-3. Z. R. Martinson, D. A. Petti and B. A. Cook, *PBF Severe Fuel Damage Test 1-1 Test Results Report*, NUREG/CR-4684, EGG-2463, October 1986.

G-4. D. W. Akers and B.G. Schnitzler, "Verification of the ORIGEN2 Code Analysis for the TMI-2 Reactor Core," *Nuclear Reactor Severe Accident Chemistry Symposium, Third North American Chemical Congress, Toronto, Canada, June 5-11, 1988*.

G-5. S. E. Binney and R. L. Scherpelz, "A Review of the Delayed Fission Neutron Technique," *Nuclear Instruments and Methods, 154*, 1978, p. 413-431.

G-6. D. W. Akers and R. W. McCardell, "Fission Product Partitioning in Core Materials," *Topical Meeting on the TMI-2 Accident: Materials Behavior and Plant Recovery Technology, ANS Transactions, 57, October 31-November 4, 1988*.

APPENDIX H

FISSION PRODUCT AND AEROSOL BEHAVIOR ANALYSIS METHODS

APPENDIX H

FISSION PRODUCT AND AEROSOL BEHAVIOR ANALYSIS METHODS

Details of the various models used in the fission product and aerosol behavior analysis for Test SFD 1-4 are described in this appendix.

H-1. Vapor Condensation and Aerosol Formation Analysis

As vapors exit the hot SFD 1-4 bundle, they begin to cool and supersaturate. An estimate of the vapor supersaturation at each location in the SFD 1-4 upper plenum is needed to determine when a vapor will condense and if it will form an aerosol. The following analysis presents a methodology to determine the vapor supersaturation under conditions of constant flow rate, gas and wall temperatures, and material release rate from the bundle. Although conditions during Test SFD 1-4 were transient in nature, the use of constant boundary conditions in the approach presented here is intended to bracket the condensation and nucleation behavior in the experiment.

Consider a volume of size V at a bulk temperature of T_b. The volume has a wall with surface area of A_w at a constant temperature of T_w. A vapor enters at a rate $\dot{m}_{in}$. A mass balance on the vapor in the volume yields

$$\frac{dm}{dt} = \dot{m}_{in} - \dot{m}_{cond} - \dot{m}_{out} \qquad \text{(H-1)}$$

where

$\dot{m}_{in}$ = source rate of vapor entering volume (kg/s)

$\dot{m}_{cond}$ = rate of vapor condensation onto the wall (kg/s)

$\dot{m}_{out}$ = rate of vapor leaving the volume (kg/s).

The rate of condensation onto the wall is given by

$$\dot{m}_{cond} = h_D A_w \left(\frac{p_b}{RT_b} - \frac{p_w}{RT_w} \right) MW \qquad \text{(H-2)}$$

where

h_D = mass transfer coefficient (m/s)

A_w = surface area of the wall (m^2)

p_t = partial pressure of vapor in bulk gas (Pa)

p_w = vapor pressure of vapor at wall temperature (Pa)

T_b = bulk gas temperature (K)

T_w = wall temperature (K)

MW = molecular weight (kg/kgmole)

R = gas constant (Pa-m^3/kgmole-K).

Because the flow in the SFD 1-4 upper plenum is laminar ($Re < 2200$), the mass transfer coefficient is given by[H-1]

$$h_D = 3.56\ D/d_e \qquad \text{(H-3)}$$

where

D = diffusion coefficient of vapor in the effluent (m^2/s)

d_e = hydraulic diameter of the volume (m).

The diffusion coefficient is given by[H-2]

$$D = 9.8\ E-05\ T^{1.75}/p \qquad \text{(H-4)}$$

where

D = diffusion coefficient (m^2/s)

T = gas temperature (K)

p = gas pressure (Pa).

The rate of vapor leaving the volume is calculated using a donor cell approach

$$\dot{m}_{out} = \frac{Q\ MW\ p_b}{RT_b} \qquad \text{(H-5)}$$

where

Q = the volumetric flow of effluent (m^3/s).

The supersaturation of the vapor is defined as the mass of vapor in the volume to that at equilibrium

$$S = \frac{p_b}{p_v(T_b)} = \frac{m_v}{m_{eq}} \qquad \text{(H-6)}$$

where

$p_v(T_b)$ = the vapor pressure of vapor at bulk gas temperature, T_b (Pa).

A vapor can condense onto aerosols if the supersaturation is greater than 1.0. Substituting Equations (H-2) through (H-6) into Equation (H-1) yields a differential equation for the supersaturation of the vapor

$$\frac{dS}{dt} = \frac{\dot{m}_{in} RT_b}{V\ MW\ p_v} - \left(\frac{h_D A_w + Q}{V}\right) S + \left(\frac{p_w T_b}{p_v T_w}\right)\left(\frac{h_D A_w}{V}\right) \quad . \qquad \text{(H-7)}$$

The solution to Equation (H-7) is given by

$$S = S_\infty [1 - \exp(-At)] \qquad \text{(H-8)}$$

where

$A = (h_D A_w + Q)/V$

and S_∞, the steady-state value of S, is given by

$$S_\infty = \left(\frac{\dot{m}_{in} RT_b}{V\ MW\ p_v} + \frac{p_w T_b\ h_D A_w}{p_v T_w V}\right) \Big/ A. \qquad \text{(H-9)}$$

Examination of Equation (H-9) indicates that the steady-state supersaturation is a function of the source rate of vapor into the volume, the surface-to-volume ratio of the volume, the volumetric flow rate in the volume, and the bulk and gas surface temperatures. Equation (H-9) gives the steady-state supersaturation in a volume accounting for wall condensation. If there were no wall (i.e., $A_w = 0.0$), then the supersaturation would be simply a function of the source rate and the volumetric source rate

$$S\ (\text{no walls}) = \frac{\dot{m}_{in} RT_b}{Q\ MW\ p_v} \quad . \qquad \text{(H-10)}$$

Since, for each volume, the source rate of material entering the volume is given by the rate of material exiting the previous volume, Equation (H-9) is used to determine the local supersaturation in each section of the SFD 1-4 upper plenum. Equation (H-9) has been applied to cadmium, silver, tin, and cesium iodide using the range of release rates, the thermal-hydraulic conditions, and the SFD 1-4 upper plenum geometry presented in Section 7. By using a range of bundle material release rates, this analysis determined the supersaturation range of each specie as it travels through the upper plenum, taking into account wall condensation. The supersaturation estimated with this model was then compared to that required to form an aerosol.

H-2. Aerosol Settling Calculations

The settling velocity of an aerosol particle of diameter d can be calculated using Stoke's law modified to account for particle slip at small aerosol sizes. The terminal settling velocity is determined by balancing the drag and gravity forces on the particles.[H-3] Thus

$$F_{drag} = F_{gravity}$$

$$\rho_p \frac{\pi d^2 C_D V}{8} = \frac{(\rho_p - \rho_g)\pi d^3 g C_c}{6} \qquad \text{(H-11)}$$

where

ρ_p = density of particle (kg/m^3)

ρ_g = density of gas (kg/m^3)

d = diameter of aerosol particle (m)

V = settling velocity (m/s)

g = acceleration due to gravity (m/s^2)

C_D = drag coefficient on aerosol particle

C_c = Cunningham slip correction factor.

The drag coefficient is related to the particle Reynolds number by[H-3]

$$C_D = \frac{24(1 + 0.158\mathrm{Re}_p^{2/3})}{\mathrm{Re}_p} \qquad \text{(H-12)}$$

where $\mathrm{Re}_p = \rho V d/\mu$. The Cunningham slip correction factor is used to account for "slip" between the aerosol particle and the gas molecules. It is given by

$$C_c = \{1 + (\lambda/d)^*[2.514 + 0.8 \exp(-0.55d/\lambda)]\} \qquad \text{(H-13)}$$

where λ is the mean free path of the gas. For large particles, C_c approaches unity. Substitution of Equations (H-12) and (H-13) into Equation (H-11) yields an equation for the settling velocity, V, as a function of particle diameter

$$V[1 + 0.158(\rho V d/\mu)^{2/3}] = \frac{\rho d^2 g}{18\mu}\{1 + (\lambda/d)[2.514 + 0.8 \exp(-0.55d/\lambda)]\} \ . \qquad \text{(H-14)}$$

The results of solving this equation are presented in Section 7.

H-3. Aerosol Monitor Analysis

The aerosol monitor in Test SFD 1-4 consisted of two optical cells connected in series. The monitor was designed to measure the attenuation of a light beam due to the presence of aerosols. This section discusses details of the methodology used to obtain number concentration, mass concentration, and total aerosol mass using the aerosol monitor responses and the particle size and composition information from the effluent filtered grab samples.

The beam attenuation of the 1- and 4-cm optical paths is related to the size and number concentration of a monodisperse aerosol by the Lambert-Beer relation[H-4]

$$I/I_0 = \exp(-N\pi d_m^2 L Q_{ext}/4) \qquad \text{(H-15)}$$

where

I = intensity of light traversing the aerosol

I_0 = intensity of incoming light beam

N = particle number concentration (p/cm^3)

d_m = diameter of average mass (cm)

L = path length of monitor (cm)

Q_{ext} = extinction efficiency.

The extinction efficiency is a relative measure of a particle's ability to remove light from a beam compared to simple blocking by its projected area. Thus, a value of $Q_{ext} = 2$ indicates that a particle can remove twice as much light as it would by simple projected area blocking due to scattering and absorption. The value of Q_{ext} depends on the particle refractive index, shape, and size relative to the wavelength of light.[H-4] For a polydisperse system, the Lambert-Beer law is still valid. However, an effective extinction efficiency is given by

$$Q_{ext} = \frac{\int N(d')\, d'^2\, Q(d')\, dd'}{\int N(d')\, d'^2\, dd'} \ . \qquad \text{(H-16)}$$

Aerosol characteristics, such as number and mass concentration, cannot usually be calculated from Equation (H-15) because N, d_m, and Q_{ext} are not all known. However, atmospheric aerosol researchers have been able to use correlations and assumptions to obtain aerosol characteristics from the Lambert-Beer relation. When the aerosol system is less characterized, like that resulting from a severe reactor accident, the conventional light extinction measurement alone cannot yield information on the mass or number concentration of the aerosol because of the difficulty in obtaining values for Q_{ext}. Fortunately, the design of the aerosol monitor in Test SFD 1-4 allows a determination of the aerosol number concentration independent of the value of the extinction coefficient.[H-5]

The SFD 1-4 aerosol monitor consists of two optical cells in series. The optical paths are separated by a volume of approximately 236 cm^3. Based on the effluent flow rate through the sampling system, the delay time between the two cells varies between 4 and 10 s. As a result, it is assumed that the extinction coefficient, Q_{ext}, and the diameter of average mass, d_m, did not change as the aerosol passed from cell 1 (1 cm) to cell 2 (4 cm). This assumption is valid as long as agglomeration and particle deposition do not appreciably change the particle size and the aerosol size distribution. Based on these assumptions, the ratio of the beam attenuations is given by

$$\frac{(I_2/I_{20})}{(I_1/I_{10})} = \left[\frac{\exp(L_2\ N_2)}{\exp(L_1\ N_1)}\right] \qquad \text{(H-17)}$$

where

(I_1/I_{10}) = attenuation ratio for cell 1

(I_2/I_{20}) = attenuation ratio for cell 2

L_1 = path length for cell 1 (= 1 cm)

L_2 = path length for cell 2 (= 4 cm)

N_1 = particle number concentration at cell 1 (p/cm^3)

N_2 = particle number concentration at cell 2 (p/cm^3).

This equation relates the measured values of the attenuation ratios to the number concentration at each cell. The [illegible]ly process that could alter the number concentration between the cells is assumed to be agglomeration. Particle size analysis of filters from the effluent filtered samples indicates that the aerosol is too small to settle significantly during transit between the cells. In addition, diffusional deposition is unimportant[H-5] for the conditions at the monitor. Thus, for a monodisperse aerosol undergoing agglomeration, the number concentration, N, as a function of time is given by[H-3]

$$N(t)/N(O) = 1/[1 + 0.5\beta t N(O)] \qquad \text{(H-18)}$$

where

β = agglomeration coefficient (cm^3/s)

t = time (s).

The agglomeration coefficient for an aerosol particle of size v_i agglomerating with an aerosol particle of size v_j where v_i and v_j are much greater than the mean free path of the gas is given by[H-3]

$$\beta = \frac{2kT}{3\mu}\left(\frac{1}{v_i^{1/3}} + \frac{1}{v_j^{1/3}}\right)\left(v_i^{1/3} + v_j^{1/3}\right) \qquad \text{(H-19)}$$

where

k = Boltzman's constant (J/K)

μ = gas viscosity (kg/m-s).

For a monodisperse aerosol, $v_i = v_j$. Thus, Equation (H-19) reduces to

$$\beta = 8kT/3\mu \ . \qquad \text{(H-20)}$$

Although the aerosol generated during Test SFD 1-4 is not monodisperse, Reference H-5 indicates that the uncertainty introduced by using the simple monodisperse agglomeration coefficient [as given by Equation (H-20)] as opposed to a more complex expression for a polydisperse system is about 15%. As a result, the monodisperse expression will be used for simplicity; and 15% will be the assumed uncertainty in the value of β.

Equation (H-18) can be applied to the dual cell aerosol monitor by assuming that t represents the transit time between the two cells, N(0) is the particle number concentration at the 1-cm cell (cell 1), and N(t) is the particle concentration at the 4-cm cell (cell 2). Thus, combining Equations (H-17) and (H-18) yields

$$\left[\frac{(L_2)\ln(I_1/I_{10})}{(L_1)\ln(I_2/I_{20})}\right] = 1 + ktN_1 \quad . \qquad \text{(H-21)}$$

Equation (H-21) was used to calculate the number concentration at the 1-cm cell as a function of time based solely on the measured attenuation ratios, the agglomeration coefficient given by Equation (20), and the thermal-hydraulic conditions in the experiment. The effluent line entering the monitor was heat-traced to provide a constant temperature of 644 K. The effluent gas viscosity was calculated based on the viscosities of steam, argon, and hydrogen (at 6.8 MPa and 644 K) and the gas composition given by the effluent transit analysis. The delay time through the monitor was calculated using the effluent flow rate and the system volume between the two cells.

The uncertainty in the number concentration was calculated by propagating the individual uncertainties in the 1-cm and 4-cm cell responses and the uncertainty in the agglomeration coefficient. As discussed in Appendix B, aerosol deposition on the windows of the monitor resulted in constant 12% and 4% attenuation signals for the 1-cm and 4-cm cells at the end of the experiment. It was assumed that this deposition was due to a linear buildup of material over time starting at 1760 s, the time at which both monitors first detected aerosols, and ending at 4000 s. This linear buildup was assumed to represent the absolute uncertainty in the response of each cell at any given time between 1760 and 4000 s. The excellent stability of the monitor during the transient suggested that uncertainties due to noise, instrument drift, and random fluctuations were much less than the bias due to deposition. As discussed earlier, the uncertainty in the agglomeration coefficient was assumed to be 15%. The uncertainty in the aerosol number concentration was determined using the standard error propagation expression:

$$\sigma_N^2 = \left(\frac{\partial N}{\partial A}\right)^2 \sigma_A^2 + \left(\frac{\partial N}{\partial B}\right)^2 \sigma_B^2 + \left(\frac{\partial N}{\partial kt}\right)^2 \sigma_{kt}^2 \qquad \text{(H-22)}$$

where A is the attenuation ratio for cell 1 and B is the attenuation ratio for cell 2. Evaluating the partial derivatives of Equation (H-22) yields

$$\left(\frac{\sigma_N}{N}\right)^2 = \left(\frac{\sigma_A}{A}\right)^2 \frac{16}{[\ln(A/B)^2]} + \left(\frac{\sigma_B}{B}\right)^2 \frac{16}{[\ln(A/B)^2]} + \left(\frac{\sigma_{kt}}{kt}\right)^2 \ . \qquad \text{(H-23)}$$

Size, mass, and elemental characteristics of the aerosol were determined using the calculated number concentration and aerosol size and composition information obtained from the effluent filtered samples discussed in Section 7. Particle size statistics from the analysis of the effluent filtered samples were used to determine the diameter of average mass at six times during the transient. Straight-line interpolations were used to construct the diameter of average mass of the aerosol as a function of time. Although the uncertainty in the particle size results is much less than 5%, an uncertainty of 20% was assigned to these data to represent the fact that the detailed time-dependent history of d_m is not known.

The aerosol mass concentration at the aerosol monitor in Test SFD 1-4 is given by

$$m = \pi d_m^3 \rho N/6 \qquad \text{(H-24)}$$

where ρ is the density of the aerosol material. Since the aerosol is predominantly tin and cadmium, a density of 7 g/cm^3 was used in the calculation. The uncertainty in the mass concentration is given by

$$\left(\frac{\sigma_m}{m}\right)^2 = 3\left(\frac{\sigma_{dm}}{d_m}\right)^2 + \left(\frac{\sigma_N}{N}\right)^2 \ . \qquad \text{(H-25)}$$

The aerosol mass flow rate, w, and total aerosol mass were calculated using the aerosol mass concentration data between 2300 and 3500 s. The data outside of this range are too uncertain to allow an estimate to be made of the mass flow of aerosol. The aerosol mass flow is given by

$$w = mQ \qquad \text{(H-26)}$$

where m is the mass concentration of the aerosol and Q is the effluent flow rate in cm^3/s at the monitor conditions (644 K, 6.8 MPa). The results were combined with the compositional information of the aerosol from the effluent filtered grab samples and integrated to obtain the total mass of aerosol that passed the monitor. The results of this analysis are presented in Section 7.

H-4. VAPOR Calculation

The VAPOR model was used to provide an estimate of the release of silver, indium, and cadmium vapors from the control rods during Test SFD 1-4. VAPOR models the simultaneous vaporization and downward relocation of control rod material during a severe reactor accident. A complete description of the model is provided in Reference H-6. Two separate calculations were performed for Test SFD 1-4. One calculation was performed using the results of the SCDAP/RELAP5 best-estimate analysis. In addition, an improved calculation was performed where boundary conditions were changed to more accurately represent the melt progression scenario in the experiment.

The thermal-hydraulic input needed in the VAPOR calculation was provided by the best-estimate SCDAP/RELAP5 analysis of Test SFD 1-4 (see Section 8). Specifically, VAPOR requires the control rod and bulk coolant temperatures and the bundle effluent flow as functions of elevation and time. Because VAPOR considers only a two-component carrier gas, argon and hydrogen were assumed to be the major constituents of the effluent. As a result, the input flow of steam, calculated by SCDAP/RELAP5, was converted to an equivalent hydrogen flow rate, assuming total conversion of steam to hydrogen via oxidation. The results of the effluent transit analysis indicate that this is a good assumption.

The VAPOR calculation begins at 1900 s, the time at which the first control rod node (Node 6) reaches stainless steel melting. (The early failure of instrumented control rod 5E is not considered in the calculation. Its vaporization and melt progression behavior is assumed to be identical to the remaining noninstrumented rods.) Because SCDAP/RELAP5 predicts stainless steel melting at node 6, the five axial nodes (each 0.1-m long) below this elevation were used in the analysis. Details of the input to VAPOR are shown in Table H-1.

The first calculation used the SCDAP/RELAP5 results discussed above to calculate the vaporization and downward relocation behavior of the alloy in the experiment. The silver, indium, and cadmium release rates per control rod calculated using VAPOR for this case are shown in Figure H-1. The VAPOR calculation indicates that the release of cadmium is much greater than silver or indium due to its higher vapor pressure. All three release rate curves show two peaks at 1938 and 1990 s. These peaks correspond to the times at which the top two nodes below the failure plane are calculated to reach stainless steel melting. Despite the similarities in the release rates, closer examination of the results indicates that cadmium is behaving quite differently than silver and indium due to the differences in volatility of the species. In general, the silver and indium release rates increase with time due to the increasing temperature of the control rod guide tube. At stainless steel melting, the control rod alloy inside a node is allowed to relocate downward to the node below it. Because the node temperature below is lower, the vaporization rate of silver and indium decreases at the time each node reaches stainless steel melting.

By contrast, the cadmium release rate decreases slightly with time. Examination of the detailed output indicates that the cadmium release rate from the bundle decreases for two reasons: (a) the preferential vaporization of cadmium from the alloy causes its mole fraction in the liquid to decrease which, in turn, reduces its vapor pressure via Raoult's law; and (b) the low effluent flow rate in the bundle causes the cadmium release to be mass-transfer limited at the hot node in the calculation. For cadmium, upon stainless steel melting at a node, the release rate increases because the node that was mass-transfer limited has relocated downwards.

The results in the figure also indicate that the duration of the release is quite short. VAPOR calculates that the release terminates after 150 s because the control rod material is predicted to relocate rapidly down to cooler portions of the rod and into the lower plenum. These results do not agree with the data. Elemental analysis of the aerosol filters downstream of the aerosol monitor indicates that cadmium was a major constituent of the aerosol throughout the entire transient. Based on the posttest bundle configuration, it is believed that this continuous source of cadmium was due to holdup and continued heating of the alloy at the spacer grid location.

For the improved calculation, the VAPOR model was modified to account for this continued long-term vaporization of relocated control rod material. The material relocating to the spacer grid (approximately node 2 in the calculation) was allowed to collect there and continue to vaporize. In addition, the best-estimate temperature at node 2 was modified to account for the reheating of control rod material that is thought to have occurred between 2800 and 3000 s as a result of ceramic melt relocation and interaction with the absorber alloy. The modified temperature is shown in Figure H-2. The results of the best-estimate calculation accounting for reheat are shown in Figure H-3. The release up to 2050 s is identical to the base-case results. However, because material is allowed to collect at the spacer grid and continue to vaporize, release is calculated to occur until the end of the transient. The silver and indium release rates increase from 2000 to 2140 s as the temperature of the third node in the calculation increases. At 2140 s, node 3 reaches stainless steel melting and relocates downward. The release rates drop dramatically because node 2 remains at ~1000 K until 2800 s, at which time reheat begins. The cadmium release rate remains constant between 2000 and 2800 s. Cadmium release from the bundle does not respond to the melting of node 3 because all of the cadmium is calculated to have been vaporized from the surface of node 3 prior to stainless steel

Table H-1. Test SFD 1-4 geometrical input to the VAPOR code

Parameter	Value
Flow area, A_{flow}	8.46 E − 04 m^2
Axial length of node, ΔZ	1.00 E − 01 m^2
Volume of node, V	8.46 E − 05 m^3
Surface area of liquid node, SA	3.85 E − 03 m^2
Equivalent diameter, D_e	1.13 E − 02 m
Rod outer diameter, D_{rod}	1.22 E − 02 m
Rod inner diameter, D_{in}[a]	8.74 E − 03 m
Area of hole, A_{fail}	1.00 E − 05 m^2
Initial height of alloy above the break, h_0[b]	4.67 E − 01 m

---

[a] This is the inner diameter of the stainless steel cladding. It is assumed that on melting the alloy will fill the gap.

[b] This initial height reflects the fact that the alloy has relocated somewhat on melting. Thus, h_0 is not equal to 0.5 m.

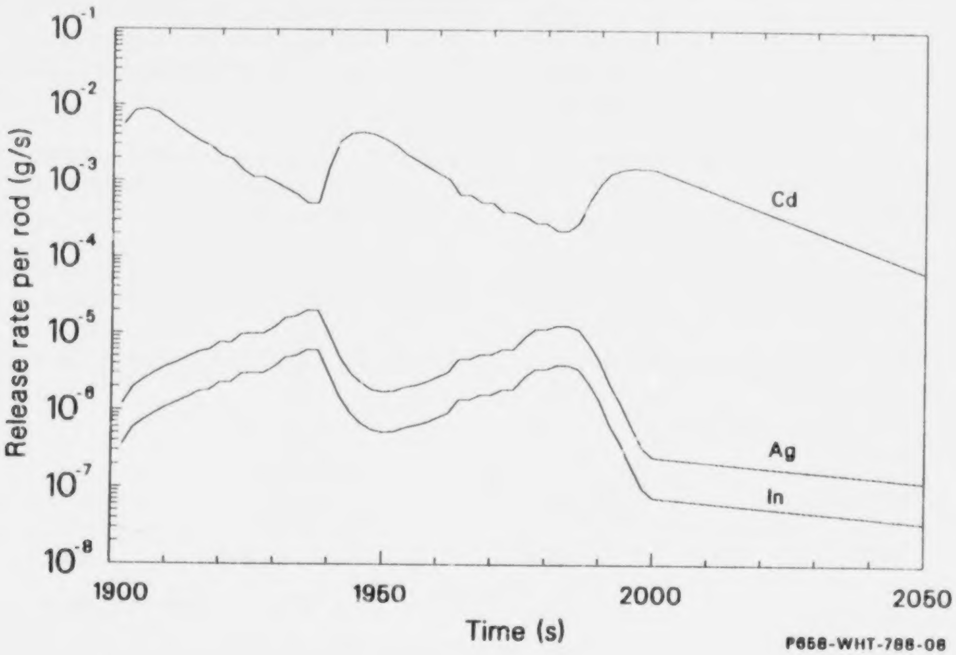

P658-WHT-788-06

Figure H-1. Silver, indium, and cadmium release rate predictions from VAPOR (base-case calculation).

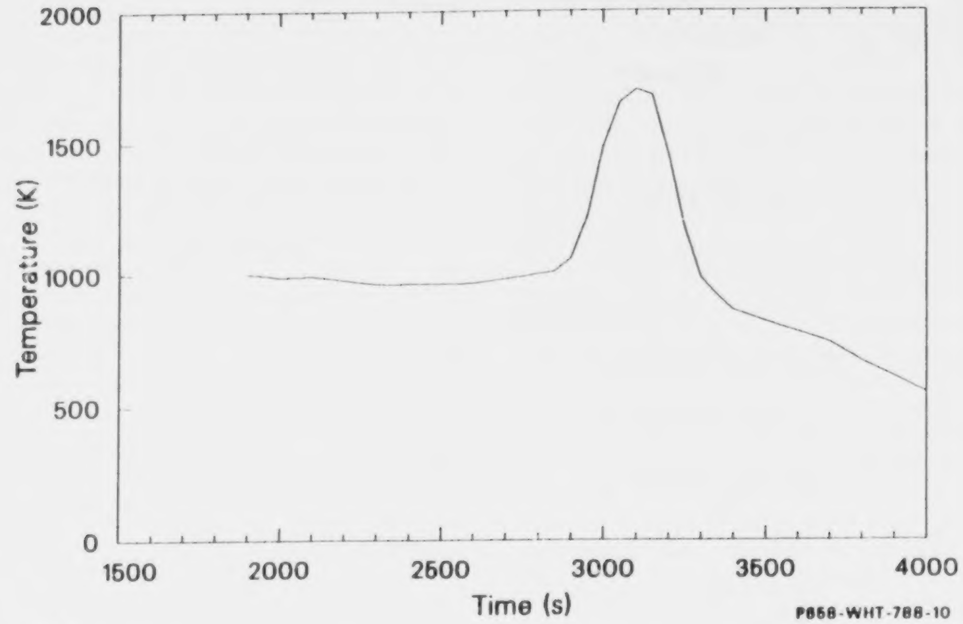

Figure H-2. Modified temperature at Node 2 used for the VAPOR reheat calculation.

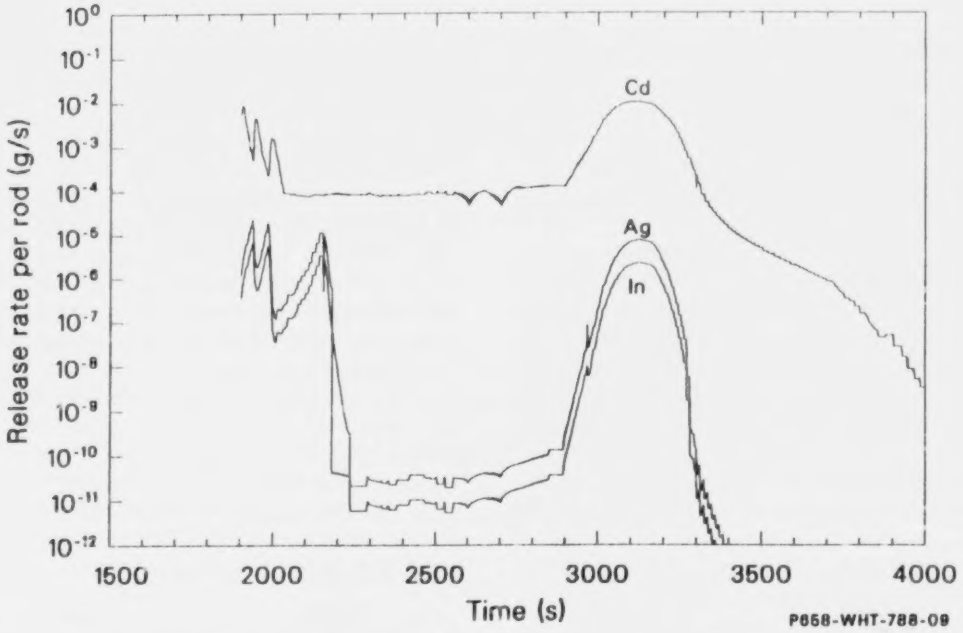

Figure H-3. Silver, indium, and cadmium release rate predictions from VAPOR, accounting for reheat.

melting. The increase in temperature at node 2 starting at 2800 s, to simulate reheating of the relocated control rod material, causes the release rates of all three elements to increase dramatically.

Integral release of control rod material for both VAPOR calculations are compared to the data in Table H-2. As expected, the improved calculation that accounts for control rod reheat is in better agreement with the data. Both calculations underpredict the release of silver and indium in Test SFD 1-4. The silver and indium releases in Test SFD 1-4 may be dominated by release of the alloy during rupture of the instrumented control rod which was not accounted for in the analysis.

H-5. Input Used for PULSE Code Analysis

The data required for the PULSE computer code analysis of fission product and aerosol transport in Test SFD 1-4 are: (a) system dimensions and wall material; (b) isotopic fractions for the chemical elements of the fission product species considered; (c) source rates of structural materials which may form or affect an aerosol (e.g., tin from cladding and silver and cadmium from control rod material); (d) flow rates of argon, hydrogen, and steam; (e) system pressure; (f) wall temperatures; (g) initial fluid temperatures, and (h) a time constant for the rate of change of the system boundary conditions (required to determine the size of the fluid slug).

H-5.1 System Geometry and Thermal-Hydraulic Input Data. Table H-3 lists the system dimensions and wall material designations that were used. Segments 1 to 5 represent the heat shield cone and tube, a region where considerable heat was transferred to the walls by both convection and radiation as the effluent moved from the fuel bundle toward the cooler deposition rod region. During the experiment, wall temperatures at segment 1 were approximately 1300 K; and those at segment 5 were typically 950 K. Segments 6 through 10 represent the deposition rod region. Segments 6 and 7 did not have temperature controls, but the wall temperatures of segments 8, 9, and 10 were controlled by heaters to be approximately 700, 730, and 580 to 640 K, respectively. Segments 11 through 14 represent the effluent line from the top of the deposition rod to the aerosol monitor. The last three segments, 15 through 17, represent sections of the aerosol monitor.

Hydrogen, steam, and argon source rates were taken from the effluent transit analysis results discussed in Appendix E. Figure H-4 is a plot of the total molar flow and mole fractions of these gases. The figure shows that the effluent was a mixture of hydrogen and argon for most of the time span modeled. The increase in molar flow near 3200 s represents the increase in argon flow rate that concluded the high-temperature portion of the experiment.

Figure H-5 shows the gas temperature in the heat shield cone assumed for the fission product transport analysis. The temperatures were obtained from the tin release analysis.

Figures H-6 through H-8 display the wall temperatures used for the fission product and aerosol transport analysis. The temperatures are best estimates and were obtained from thermocouple data at the entrance to the heat shield at 1.14 m and at coupon holder two on the deposition rod at 1.57 m with interpolation as necessary. Figure H-6 shows the decrease in the wall temperatures encountered by the effluent as it moved from the heat shield cone (segments 1 through 4) to the heat shield tube (segment 5). Figure H-7 illustrates the wall temperatures in the regions of the deposition rod.

Table H-2. Comparison of SFD 1-4 control rod material release fractions with the VAPOR code

Element	Measured Total	VAPOR without Holdup and Reheat	VAPOR with Holdup and Reheat
Silver	2.69 E – 04	1.89 E – 06	5.98 E – 06
Indium	8.79 E – 04	3.04 E – 06	9.57 E – 06
Cadmium	6.18 E – 02	1.18 E – 02	9.85 E – 02

Table H-3. System dimensions and wall materials

Segment Number	Description	Length (m)	Cross Section (m²)	Wall Surface (m²)	Horizontal Surface (m²)	Wall Type	Pipe Bend
1	Heat shield cone	0.020	5.15 E – 03	5.45 E – 03	0	Zircaloy	0
2	Heat shield cone	0.020	5.15 E – 03	5.45 E – 03	0	Zircaloy	0
3	Heat shield cone	0.020	5.15 E – 03	5.45 E – 03	0	Zircaloy	0
4	Heat shield cone	0.020	5.15 E – 03	5.45 E – 03	0	Zircaloy	0
5	Heat shield tube	0.111	3.88 E – 04	1.33 E – 02	0	Zircaloy	0
6	Deposition rod tip	0.140	2.96 E – 04	3.35 E – 02	7.28 E – 05	SS	0
7	Deposition rod (DC-2)	0.203	3.30 E – 04	1.99 E – 02	7.28 E – 05	SS	0
8	Deposition rod heater 1 (DC-2 to DC-8)	1.137	3.30 E – 04	1.12 E – 01	4.07 E – 04	SS	0
9	Deposition rod heater 2 (DC-9 to DC-12)	0.840	3.30 E – 04	8.24 E – 02	3.01 E – 04	SS	0
10	Deposition rod heater 3 (DC-13 to DC-20)	1.681	3.30 E – 04	1.65 E – 01	6.02 E – 04	SS	0
11	Deposition rod above DC-20	0.169	3.69 E – 04	1.43 E – 02	0	SS	90°
12	Bend to top of deck plates	0.860	3.87 E – 04	6.00 E – 02	2.44 E – 03	SS	90°
13	Top of deck to transition 1	0.760	3.87 E – 04	5.30 E – 02	1.69 E – 02	SS	90°
14	Transition 1 to main floor gamma spec.	3.490	5.65 E – 05	9.30 E – 02	2.87 E – 02	SS	0
15	Aerosol monitor 1-cm path	0.173	7.85 E – 05	5.43 E – 03	1.73 E – 03	SS	0
16	Aerosol monitor transition	0.251	5.49 E – 04	1.97 E – 02	6.10 E – 03	SS	0
17	Aerosol monitor 4-cm path	0.152	1.26 E – 03	1.92 E – 02	6.10 E – 03	SS	0

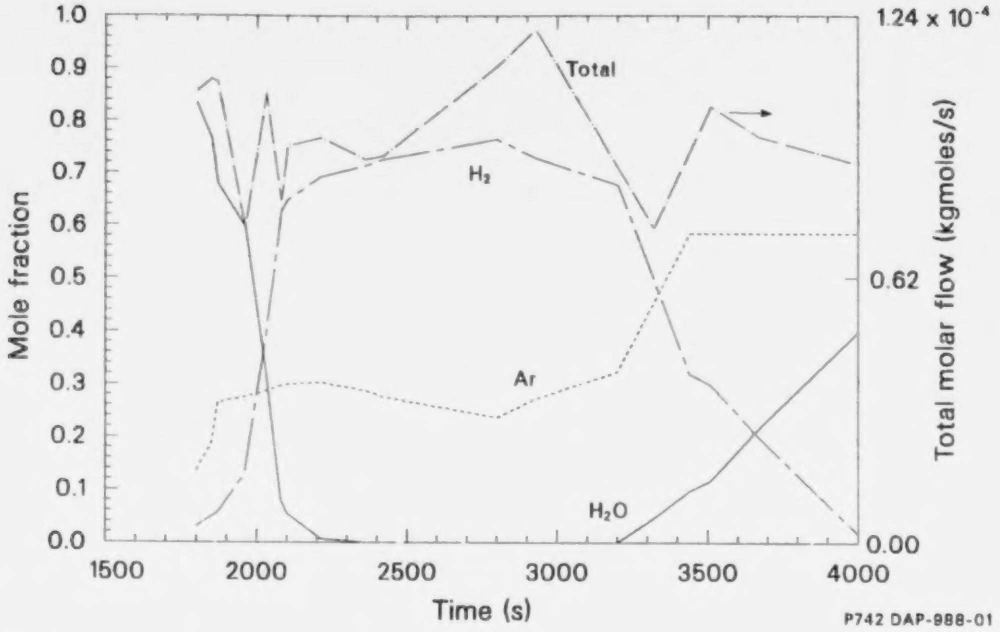

Figure H-4. Mole fractions of steam, hydrogen, and argon; and total molar flow rate.

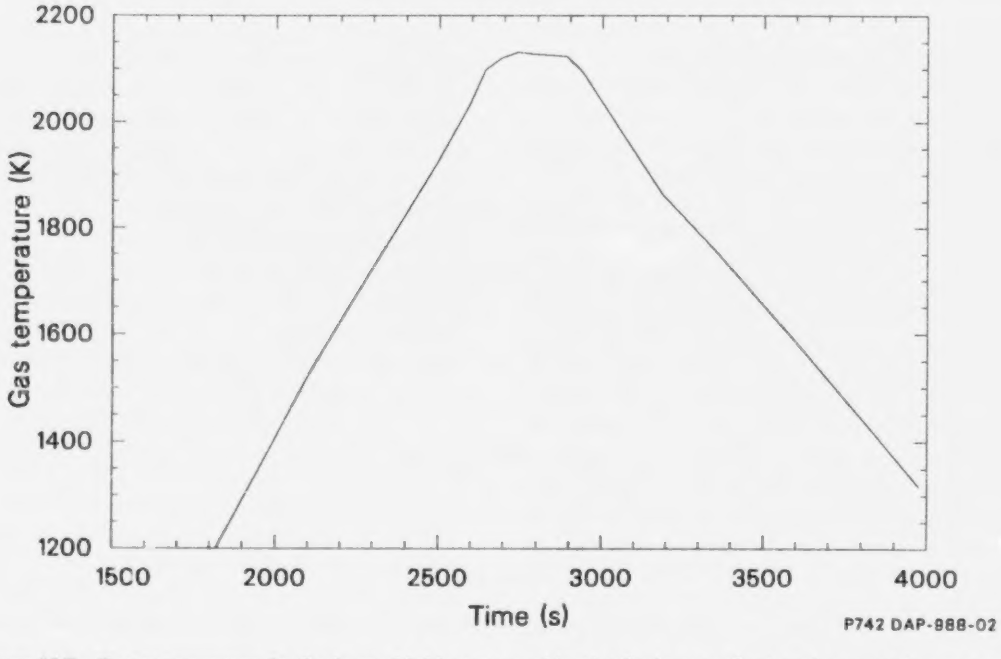

Figure H-5. Gas temperature in the heat shield cone used in the fission product and aerosol transport analysis.

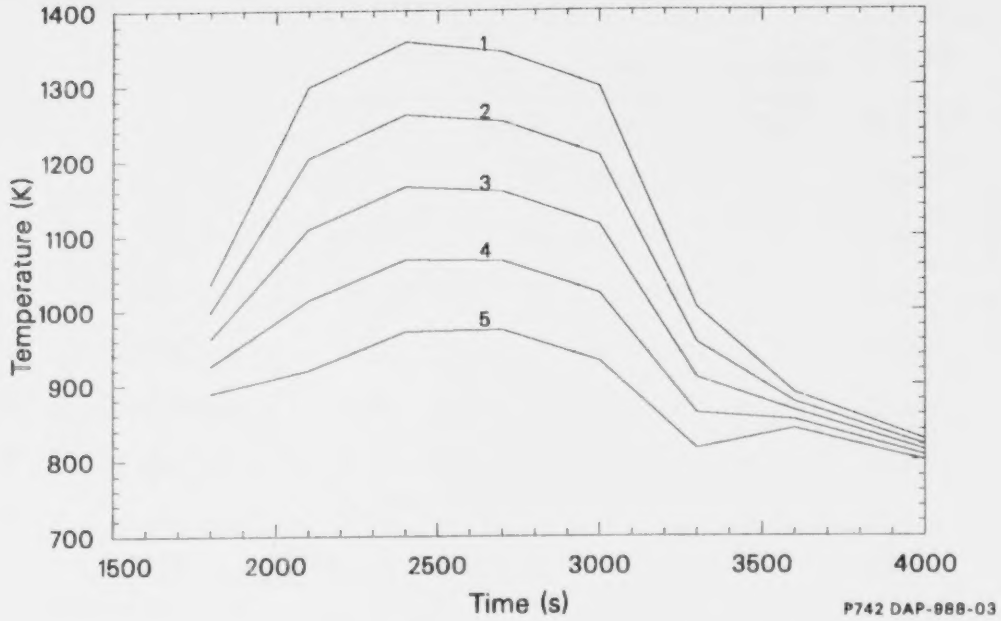

Figure H-6. Wall temperature in the heat shield cone (1 through 4) and heat shield tube (5) used in the fission product and aerosol transport analysis.

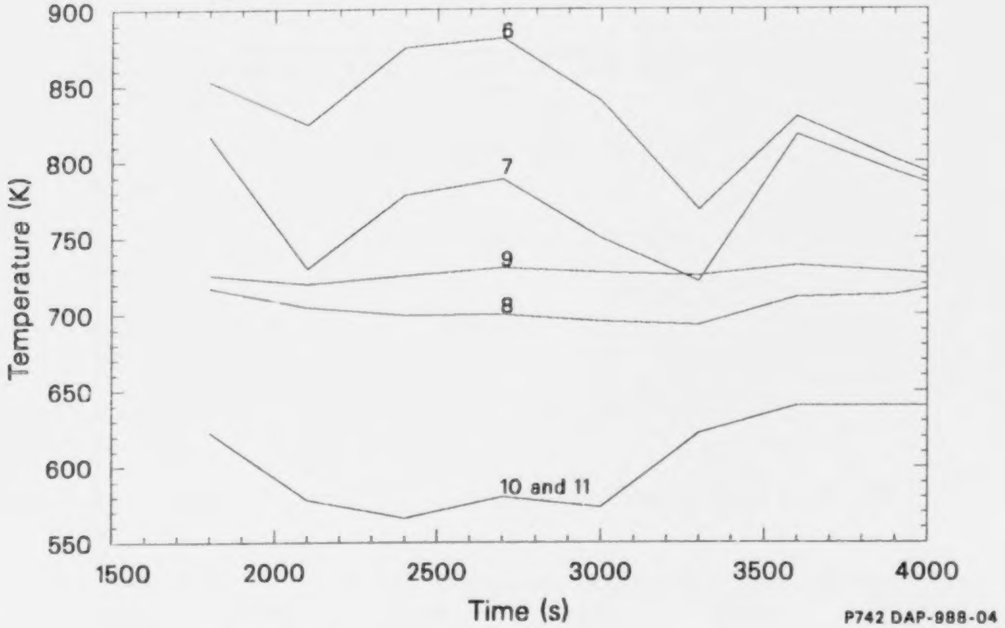

Figure H-7. Wall temperatures of the deposition rod (6 through 11) used in the fission product and aerosol transport analysis.

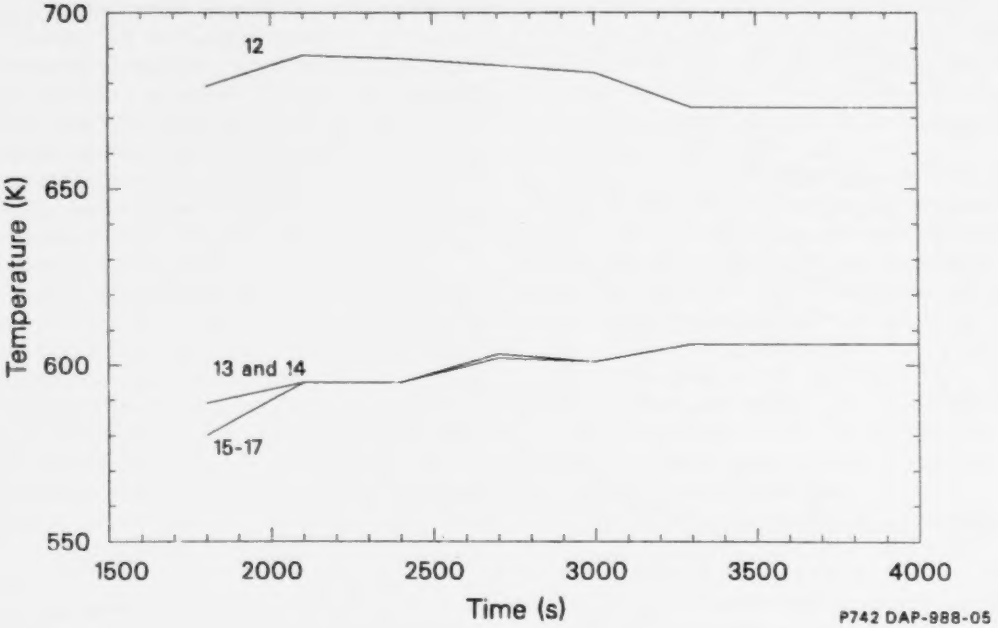

Figure H-8. Wall temperature of effluent line (12 through 14) and aerosol monitor (15 through 17) used in the fission product and aerosol transport analysis.

Segment 6 represents the lower end of the deposition rod tip, which was heated significantly by the effluent during the high-temperature portions of the experiment. Segment 7 represents the portion of the deposition rod between the tip and the first electric heater that was used to maintain wall temperatures. Wall heaters were used to set the temperatures of segments 8 to 10 at 800, 750, and 700 K, respectively. The figure shows that the best-estimate wall temperatures did not follow the orderly progression to cooler temperatures that was attempted with the heating tapes. In particular, the heater for segment 8 appears not to have held that segment at the 800-K temperature desired. Segment 10 is also estimated to have been cooler than the desired temperature. Segment 11 represents the deposition rod above coupon DC-20, a region of the rod that was not heated by external sources. Figure H-8 displays the temperatures of the sample line (segments 12 through 14) and the aerosol monitor (segments 15 through 17).

As discussed in Section 4, the system pressure was controlled to within ±0.02 MPa of 6.98 MPa for most of the 1800- to 4000-s time span of interest. A table approximating the minor variations in pressure during the experiment was used to represent the system pressure for the fission product transport analysis.

H-5.2 Fission Product Sources. Determining fission product release rates from the fuel bundle is complicated by the fact that radionuclide concentrations had to be measured at considerable distance from the bundle, beyond locations where some reactive species condensed. As a result, noble gas fractional release rates discussed in Section 6 and Appendix G were employed to estimate release rates for all species. Figure H-9 shows the noble gas fractional release rates expressed as a fraction of the initial inventory per second. The cesium and iodine fractional release rates were assumed to be equal to those of the noble gases because no better estimate was available and because evidence shows release rates for these elements to be similar to the rates for the noble gases. These fractional release rates were multiplied by the initial inventories shown in Table H-4 to estimate a source rate for each species. Elemental inventories were obtained from the ORIGEN2 calculation discussed in Section 6 and Appendix G. Isotopic fractions required for the fission product heating estimates calculated by the analysis tool were also determined from isotopic distributions calculated using the ORIGEN2

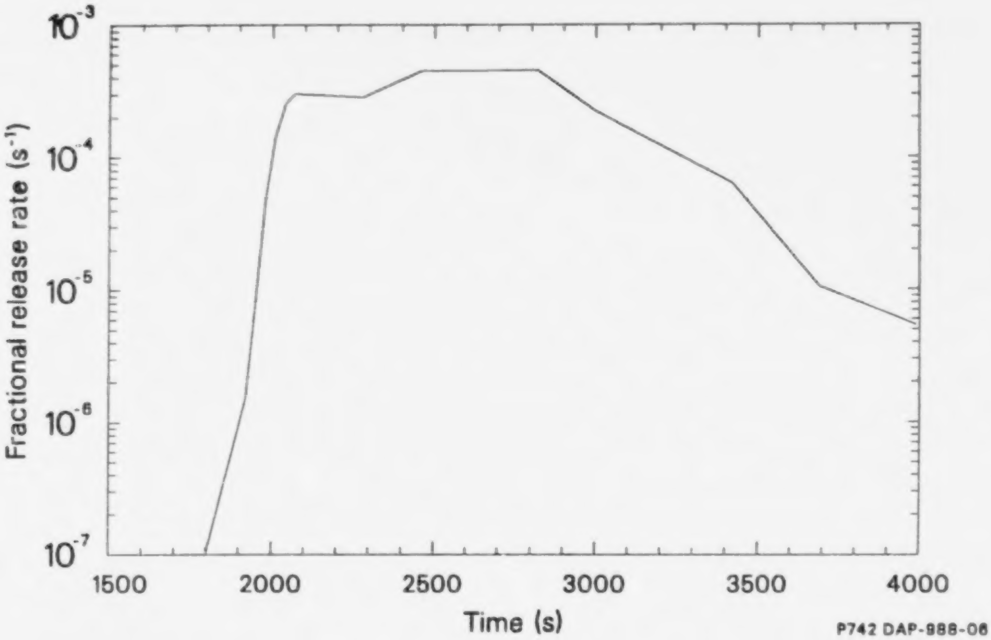

Figure H-9. Fission product fractional release rate used in the fission product and aerosol transport analysis.

computer code. The fractions were assumed to be constant throughout the experiment.

The distribution of the elements among chemical species shown in the table was based on equilibrium calculations for the Cs-I-O-H system. These calculations are discussed in Section H-5.5.

H-5.3 Control Rod Release. The VAPOR model has been used to provide an estimate of the release of silver, indium, and cadmium vapors from the control rods during Test SFD 1-4. VAPOR models the simultaneous vaporization and downward relocation of control rod material during a severe reactor accident.[H-6] Two separate calculations were performed for Test SFD 1-4. One calculation was performed using the results of the SCDAP/RELAP5 best-estimate analysis. In addition, an improved calculation was performed where boundary conditions were changed to more accurately represent the melt progression scenario in the experiment. The results of the improved calculation, shown in Figure H-3, were used in the fission product and aerosol transport analysis. Details of the VAPOR calculation are given in Section H-4.

H-5.4 Tin Release Calculation. The tin release rate from the bundle was calculated with a model that accounted for tin vaporization from the

Table H-4. Initial inventories

Element	Element Inventory (kg)	Chemical Distribution	Compound Inventory (kg)
Iodine	2.665 E − 03	CsI	5.456 E − 03
Cesium	3.441 E − 02	All not in CsI as CsOH	3.567 E − 02

unoxidized portion of the zircaloy cladding into a slug of coolant which was heated in the bundle. As the coolant left the bundle region, it was cooled very rapidly by both convection and radiation in the upper fuel rod and heat shield region just above the bundle. Radiation heat transfer to the cooler walls of these regions exceeded the convective heat transfer by a factor of five and caused the tin vapor to become supersaturated and form an aerosol before the tin could condense on the walls. Details of aerosol formation were discussed in Section H-1.

Since the initial size of the aerosol was not measured, the diameter of the newly formed aerosol was treated as a parameter. Sizes from 0.01 to 10 μm were assumed, and the calculated aerosol number density and size were compared with the aerosol monitor data and the pattern of horizontal and vertical surface deposition on the deposition rod to determine a best-estimate geometric mean aerosol diameter of 0.01 to 0.1 μm in the heat shield region. The larger size was used during the greatest source rate, from 2400 to 3200 s. The particle concentration was assumed to be sufficient to return the tin vapor to saturation after formation of the aerosol.

H-5.5 Chemical Speciation. Thermochemical equilibrium calculations for the dominant chemical forms of cesium, iodine, and tellurium were performed using the SOLGAS3 code.$^{H-7}$ The equilibrium concentrations of the 9 species and 5 elements listed in Table H-5 for the Cs-I-Ag-H-O system were predicted. Because the actual thermal-hydraulic and chemical conditions varied during Test SFD 1-4, SOLGAS3 was used to bracket the potential chemical forms expected in the experiment. The calculations were performed at a pressure of 6.95 MPa and temperatures between 900 and 2100 K. Fission product and bundle material release rates were varied to represent releases during rapid heatup and the high-temperature portion of the experiment. Thermal-hydraulic and postirradiation examination data indicate that Test SFD 1-4 was steam-starved. However, the exact value of the H_2/H_2O ratio depended on the steaming rate, which is uncertain. As a result, calculations were performed at H_2/H_2O ratios of 30, 100, and 200 to determine the effect of a reducing environment on the dominant fission product chemical forms in Test SFD 1-4. The initial conditions for the various cases are shown in Table H-6. The free energies of formation used in the calculation are presented in Table H-7.

The calculations indicate that CsI is the dominant chemical form of iodine at all temperatures. Very little HI and no AgI are predicted to form. These results are quite different than those calculated for Test SFD 1-1.$^{H-8}$ The iodine and cesium concentrations in Test SFD 1-4 are about two to three orders of magnitude greater than those in Test SFD 1-1 because of the high-burnup fuel used in Test SFD 1-4. The higher concentrations favor the formation of CsI over HI at high temperatures, and AgI is less stable than CsI at the silver concentrations used in the calculations.

Figure H-10 presents the calculated mole fraction of the dominant cesium species at thermochemical equilibrium for the base-case conditions listed in Table H-6 at temperatures between 900 and 2100 K. The dominant chemical forms in Test SFD 1-4 are predicted to be CsOH, CsI, and elemental cesium. At 1500 K, 75% of the cesium is in the form of CsOH, 8% is CsI, and 17% is elemental cesium. At temperatures above 1500 K, the elemental cesium concentration increases, whereas at temperatures less than 1100 K very little elemental cesium is predicted to be present.

The dominant chemical form of tellurium released from the SFD 1-4 bundle is SnTe. The low release of tellurium and steam-starved nature of the test are consistent with the theory that tellurium is scavenged by the unoxidized cladding^{H-9} to form zirconium and tin tellurides. Because these tellurides have low vapor pressures and form an alloy solution with the zircaloy, their release from unoxidized regions of the bundle would be small. As a result, most of the released tellurium in the experiment is believed to be from regions of the core which were heavily oxidized in which the SnTe in the cladding could vaporize.

The results of the other bounding cases indicate that decreasing the concentration of fission

Table H-5. Principal species of the I-Cd-Ag-H-O system

Elemental components (5):	Cesium, iodine, silver, hydrogen, oxygen
Reaction species (9):	H_2O, H_2, O_2, Cs, I_2, CsI, AgI, HI, CsOH

Table H-6. Initial conditions for Test SFD 1-4 thermochemical calculations[a]

Case	H_2/H_2O Ratio	Fractional Release Rate (s^{-1})
Base case	100	4.82 E – 04 for Cs and I 9.40 E – 08 for Ag
Case 2	30	Same as base case
Case 3	200	Same as base case
Case 4	100	One-tenth base case
Case 5	30	One-tenth base case
Case 6	200	One-tenth base case

---

a. Temperatures in all calculations varied between 900 and 2100 K. Concentrations were based on the following inventories and flow rates:

Cesium: 34.5 g
Iodine: 2.66 g
Silver: 1372 g
Hydrogen flow rate: 0.08 g/s
Argon flow rate: 0.58 g/s

products and bundle materials by an order of magnitude and varying the H_2/H_2O ratio between 30 and 200 have no significant effect on the base-case equilibrium concentrations.

H-5.6. Species Release Rates Used for Transport Analysis. Figures H-11 and H-12 show the release rates of CsI, CsOH, cadmium, tin vapor, and tin aerosol used for the fission product and aerosol transport analysis. As discussed in Section H-5, the first peak in the cadmium release rate is associated with the early release as the control rods fail and relocate, while the second peak is caused by reheating of control rod material by hotter melts that flowed after the initial relocation of the control rod material.

Tin release rates for both vapor and aerosol do not rise as rapidly as the release rates for CsOH and CsI. This is because the tin release rate is calculated as vaporization from a simple metal surface. Unlike fission product release from high-burnup fuel, the tin release process does not have the history of buildup of material on ceramic grain boundaries during irradiation followed by a more sudden release from these reservoirs as the grain boundaries become permeable that characterizes release of fission products from the fuel. At maximum temperature, the tin release rate is comparable to that of CsOH; but most of the tin is an aerosol because of the low equilibrium vapor pressure of tin. The CsOH, CsI, and cadmium are all unsaturated vapors at the heat shield.

H-5.7 Boundary Condition Time Constants. The final set of input data to be discussed are the boundary condition time constants employed. The time constants were selected to sample the boundary conditions every 50 s from 1800 through 3000 s and to sample the boundary conditions every 100 s from 3001 to 4000 s. The constants were selected by inspection of the thermal-hydraulic and fission product input data.

Results of the fission product and aerosol transport calculation are discussed in Section 7.

Table H-7. Free energies of formation used in the SOLGAS analysis

Species		A	B	C
H_2	G	0.000 E+00	0.000 E+00	0.000 E+00
H_2O	G	−0.251 E+06	0.577 E+02	0.000 E+00
I	G	0.785 E+05	−0.541 E+02	0.000 E+00
I_2	G	0.000 E+00	0.000 E+00	0.000 E+00
HI	G	−0.679 E+04	−0.722 E+01	0.000 E+00
HOI	G	−0.122 E+06	0.552 E+02	0.000 E+00
CsI	G	−0.267 E+06	0.337 E+02	0.000 E+00
Cs_2I_2	G	−0.672 E+06	0.176 E+03	0.000 E+00
Cs	G	0.000 E+00	0.000 E+00	0.000 E+00
CsOH	G	−0.339 E+06	0.861 E+02	0.000 E+00
$Cs_2O_2H_2$	G	−0.838 E+06	0.329 E+03	0.000 E+00
Cs_2O	G	−0.248 E+06	0.138 E+03	0.000 E+00
CsO	G	−0.142 E+05	0.223 E+02	0.000 E+00
Cs_2	G	−0.493 E+05	0.708 E+02	0.000 E+00
O_2	G	0.000 E+00	0.000 E+00	0.000 E+00
H	G	0.226 E+06	−0.598 E+02	0.000 E+00
O	G	0.254 E+06	−0.664 E+02	0.000 E+00
OH	G	0.370 E+05	−0.138 E+02	0.000 E+00
O_2H	G	−0.188 E+04	0.486 E+02	0.000 E+00
CsI	L	−0.416 E+06	0.129 E+03	0.000 E+00
CsOH	L	−0.458 E+06	0.185 E+03	0.000 E+00
H_2O	L	−0.283 E+06	0.154 E+03	0.000 E+00
Cs_2TeO_3	L	−0.110 E+07	0.478 E+03	0.000 E+00
Cs_2Te	C	−0.438 E+06	0.226 E+03	0.000 E+00
Ag	L	0.000 E+00	0.000 E+00	0.000 E+00
AgI	G	0.881 E+05	−0.143 E+03	0.984 E+01
AgI	L	0.898 E+05	0.978 E+02	−0.900 E+01

a. Free energies of the form $\Delta G = A + B/T + CT\ln T$.

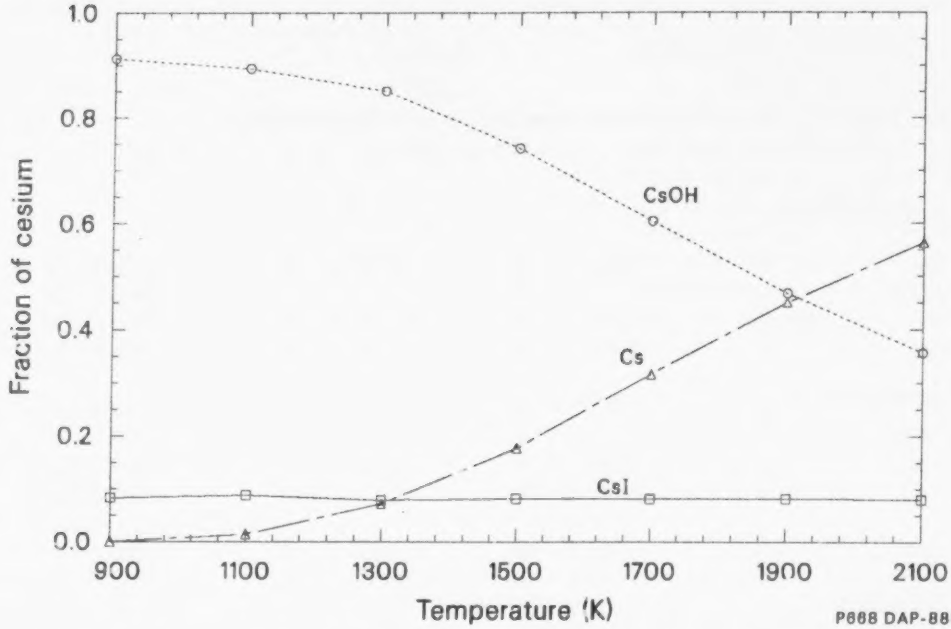

P688 DAP-888-84

Figure H-10. Calculated mole fraction of the dominant cesium chemical species at thermochemical equilibrium for the base-case conditions at temperatures between 900 and 2100 K.

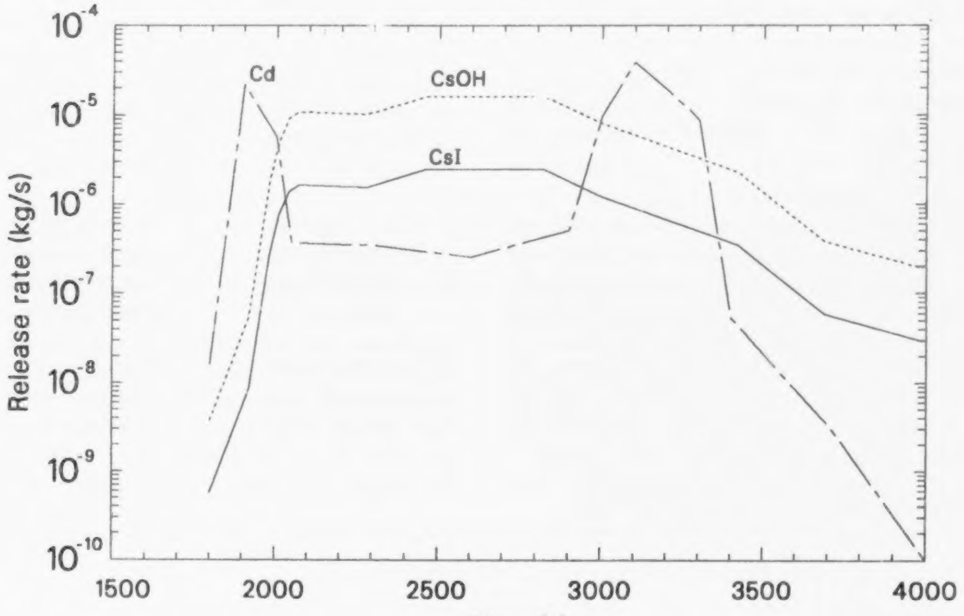

P742 DAP-888-07

Figure H-11. Source rates of cadmium, cesium hydroxide, and cesium iodide to the heat shield used in the fission product and aerosol transport analysis.

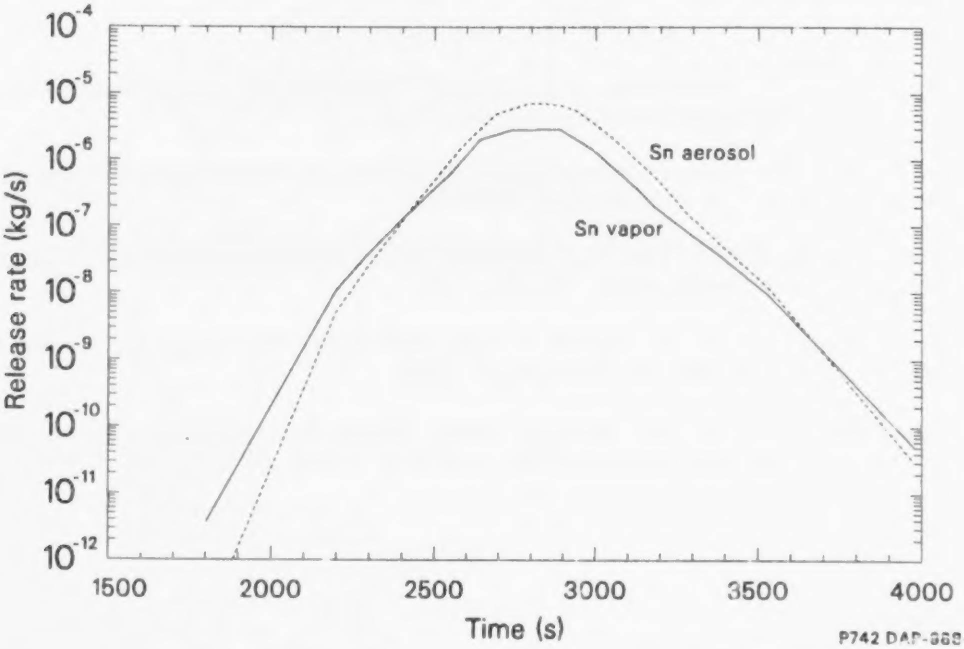

P742 DAP-368-08

Figure H-12. Source rates of tin vapor and tin aerosol to the heat shield used in the fission product and aerosol transport analysis.

H-6. References

H-1. R. B. Bird, W. E. Stewart, and E. N. Lightfoot, *Transport Phenomena*, New York: Wiley and Sons, 1960.

H-2. H. Jordan, J. A. Gieseke, and P. Baybutt, *TRAP-MELT User's Manual*, NUREG/CR-0632, 1979.

H-3. S. K. Friedlander, *Smoke, Dust and Haze: Fundamentals of Aerosol Behavior*, New York: John Wiley and Sons, 1977.

H-4. W. Hinds, *Aerosol Technology*, New York: Wiley Interscience, 1982.

H-5. V. J. Novick, "The Use of Series Light Extinction Cells to Determine Aerosol Number Concentration," *Aerosol Science and Technology*, December 1988.

H-6. D. A. Petti, *Silver-Indium-Cadmium Control Rod Behavior and Aerosol Behavior in Severe Reactor Accidents*, NUREG/CR-4876, EGG-2501, April 1987.

H-7. T. M. Besmann, *SOLGASMIX-PV, A Computer Program to Calculate Equilibrium Relationships in Complex Chemical Systems*, ORNL/TM-5775, 1977.

H-8. Z. R. Martinson, D. A. Petti, and B. A. Cook, *PBF Severe Fuel Damage Test 1-1 Test Results Report*, NUREG/CR-4684, EGG-2463, October 1986.

H-9. J. L. Collins, M. F. Osborne, and R. A. Lorenz, "Fission Product Tellurium Release Behavior Under Severe Light Water Reactor Accident Conditions," *Nuclear Technology*, 77, 1, April 1987.

APPENDIX I

POSTIRRADIATION EXAMINATION RESULTS

APPENDIX I

POSTIRRADIATION EXAMINATION RESULTS

A discussion of the data obtained from the postirradiation examination (PIE) of the fuel bundle that are used to support the description of the accident scenario is presented in this appendix. The objectives of the PIE were to determine the physical and chemical state of the major bundle components (fuel, cladding, spacer grids, zircaloy inner liner, ZrO_2 insulation material, and zircaloy saddle) and to quantify material relocation, bundle end-state geometry, oxidation, and peak temperatures reached. In addition, obtaining evidence of the mechanisms of material interactions is important for evaluating the relocation and interaction models used by severe accident computer codes; and identifying changes in fuel morphology that occurred during the experiment is important for understanding fission product release.

Information on the overall condition of the fuel bundle obtained by gross gamma scanning and neutron radiography is presented in the first section of the appendix. The techniques employed to obtain data on the physical, chemical, and metallurgical properties of the bundle are described in the second section, along with compilations of these data as a function of axial elevation within the bundle. The third section contains a description of the properties and damage state of each of the nine cross sections removed from the bundle for examination.

I-1. Overall Condition of the Test Bundle

Gross gamma scanning and neutron radiography were used to obtain information on the overall condition of the test bundle. The results of these methods were used to guide subsequent microexaminations.

I-1.1 Gross Gamma Scanning. The SFD 1-4 test train was transferred in the vertical orientation from the PBF reactor to the adjacent canal and gross (non-spectral) gamma scanned to determine the axial fuel distribution before the fuel assembly was tipped for horizontal transport to the hot cells. The scanning was performed approximately five months after the experiment and after the test train had been flushed with water and the deposition rod had been removed from the plenum above the fuel assembly. During the measurement, the test train was held in a vertical position while the gamma scanner and the shielded ion chamber were elevated by a crane fixture.

The axial gross gamma scan of the test train presented in Figure I-1 shows that gamma-active material had migrated from the center of the fuel bundle to locations both lower and higher in the bundle and in the upper plenum deposition rod region. The piping surrounding the upper plenum was less massive than the several materials surrounding the fuel assembly. As a result, the shielding of gamma rays is less in the plenum; and the gamma activity recorded there is somewhat larger relative to that in the fuel assembly region. The gamma activity is most likely associated with the long-lived isotopes of the fission product cesium (such as ^{134}Cs and ^{137}Cs) which were found to be present on the deposition rod. Although evidence of iodine was found on the deposition rod, the gamma-active iodine isotopes (such as ^{131}I and ^{133}I) had decayed significantly by the time of the gross gamma measurement.

The relatively short PBF irradiation produced predominantly short-lived fission products which decayed away prior to the gamma scanning. Therefore, the gamma measured activity was primarily from long-lived radioisotopes produced during the much longer BR-3 irradiation. An expanded and normalized plot of the posttest gamma scan over the fuel assembly is calculated for the BR-3 irradiation in Figure I-2. The burnup profile reflects the distribution of long-lived isotopes and is consistent with gamma scans and burnup measurements of BR-3 rods. This plot indicates that there has been considerable migration of long-lived fission products from the center of the bundle toward the upper and lower ends. However, results from the neutron radiograph and the metallographic cross sections discussed in subsequent sections indicate that fuel material accumulated in the lower third of the bundle, but there was no evidence of fuel material accumulation in the upper third of the bundle. Therefore, it is thought that the peak in gamma activity in the lower third of the bundle is associated with the relocation of molten bundle materials, including liquefied fuel. The peak in the upper third of the bundle is most likely associated with

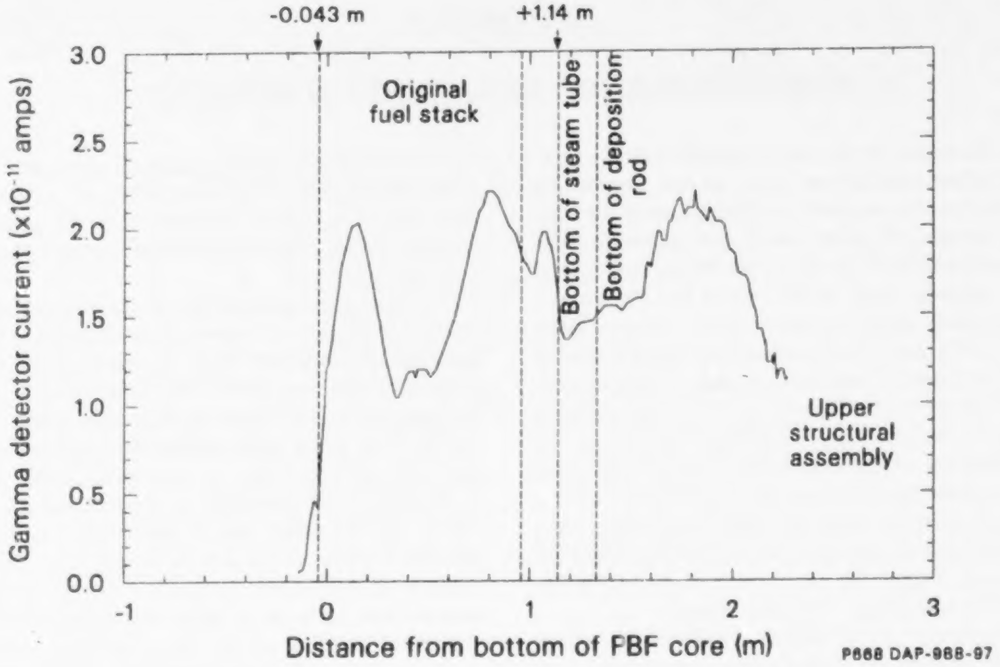

Figure I-1. Axial gross gamma scan of the SFD 1-4 test train posttest.

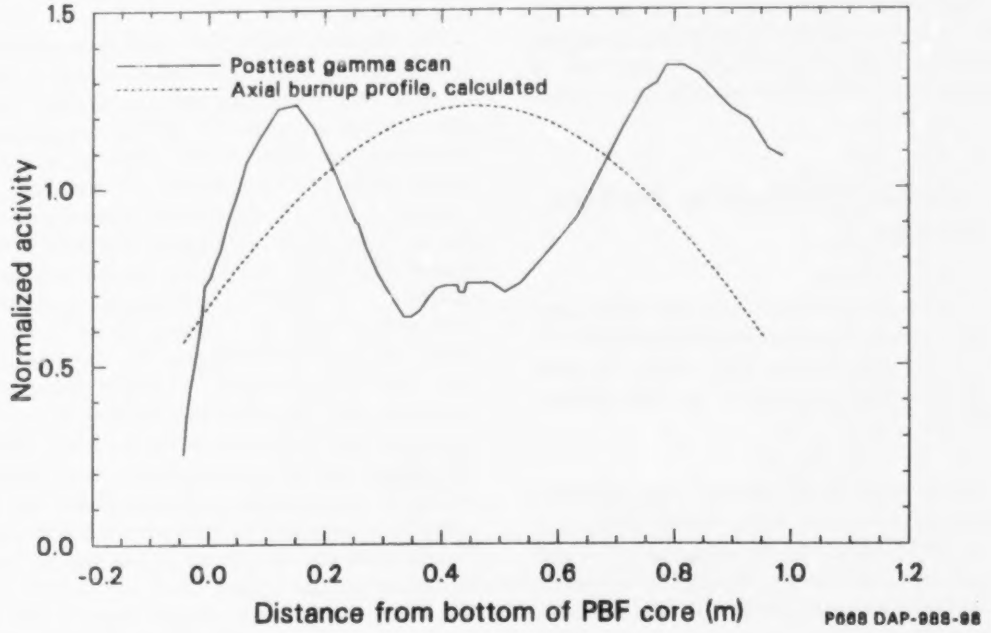

Figure I-2. Comparison of the posttest gamma scan from test bundle SFD 1-4 with calculated burnup profile (from irradiation in the BR-3 reactor prior to PBF operation).

either the transport and deposition of fission products released from the fuel or greater transmission due to relocation of metallic material (zircaloy, Ag-In-Cd) from the upper bundle.

I-1.2 Neutron Radiography. The SFD 1-4 fuel bundle was separated from the test train in the PBF canal and transported horizontally to a hot cell facility where it was dried and then transported horizontally to Argonne National Laboratory-West where neutron radiography was performed with the bundle in a vertical position. Neutron radiographs (neutrographs) of the bundle were obtained at two orientations (135 and 225 degrees) and are shown in Figure I-3. The neutrographs show a region of loose debris in the top third of the bundle above which are intact rod upper plenum sections containing upper end caps and plenum springs. The middle third of the bundle consists of material in more rod-like geometry containing debris in the cooling channels. The lower third of the bundle is opaque to neutrons due to the accumulation of fuel and control materials that had melted and relocated to this region from locations higher in the bundle. The materials that had relocated to the bottom of the fuel rods and to the tie plate below the fuel rods were identified by destructive examination to contain considerable amounts of the control rod alloy materials (silver, indium, and cadmium), which are strong neutron absorbers and therefore appear dark in the neutrograph. The locations of cross sections removed from the bundle for metallographic, scanning electron microscopic (SEM), chemical, and radiochemical analyses are also shown in Figure I-3.

I-2. Experimental Methods and Summary Data

A brief description of the experimental methods used to examine the bundle is presented in this section, along with results that describe the bundle material composition and component redistribution as a function of axial elevation.

I-2.1 Experimental Methods. Based on the experience with fuel rod bundles from previous tests,[I-1,I-2] Dow Epoxy resin 332 and Jeffamine T-403[a] mixed in a ratio of 100 to 45 g, respectively, were used as the SFD 1-4 bundle encapsulant. This epoxy exhibited good debris penetration and polishing characteristics and also showed little heating during the curing stage. The volume of epoxy needed was calculated prior to encapsulation to be approximately 7 L, based on the assumption that the insulating region would not fill with epoxy. However, during the potting operation, about 9.5 L of epoxy were required to fill the bundle, implying nearly complete epoxy penetration of the insulation region and voids in the bundle. Sectioning of the bundle confirmed this result.

The sectioning saw was manufactured by Felker and included a 0.355-m-dia by 0.0023-m-thick, diamond-embedded steel blade. The saw had a traversing table with an average manual feed rate of 0.00071 m per minute and a blade speed of about 1600 rpm. Ten 0.025-m-thick metallographic sections were cut and vacuum-impregnated with epoxy into the metallographic mounts. Examination of these sections showed excellent penetration of the epoxy into the debris and insulation. Nine cross sections, representative of all the major regions in the bundle, were examined and are discussed in this appendix. The bottom of the PBF active core was used as the zero reference for the elevations of the cross sections. The bottom surface of the mounts was examined in the upper seven cross sections, and the top surface was examined in the lower two cross sections.

Low magnification photographs (photomacrographs) were taken through the hot cell periscope to document the overall features of the cross sections. The photomacrographs of the two lower cross sections were intentionally reversed in the figures presented in this report to be consistent with the orientation notches (a "V" at 0 degrees and a "U" at 90 degrees) inscribed along the length of the bundle prior to sectioning.

All nine cross sections were examined in the as-polished condition; some were examined in the etched condition under bright field illumination, and some were examined under polarized light. Magnifications ranging from 50 to 500X were used. The following techniques were used to etch cross sections after examination in the as-polished condition:

Fuel and ceramic materials:	Cotton swab etching for 90 s with an 85 vol.% hydrogen peroxide, 15 vol.% sulfuric acid solution.
Cladding and metallic materials:	Cotton swab etching for about 30 s with a 55% lactic acid, 19% water, 19% nitric acid, and 7% hydrofluoric acid solution, by volume.

---

[a] Dow Epoxy Resin 332 is manufactured by Dow Chemical Co., Midland, MI; Jeffamine T-403 is manufactured by Jefferson Chemical Co., a subsidiary of Texaco, BelAire, TX.

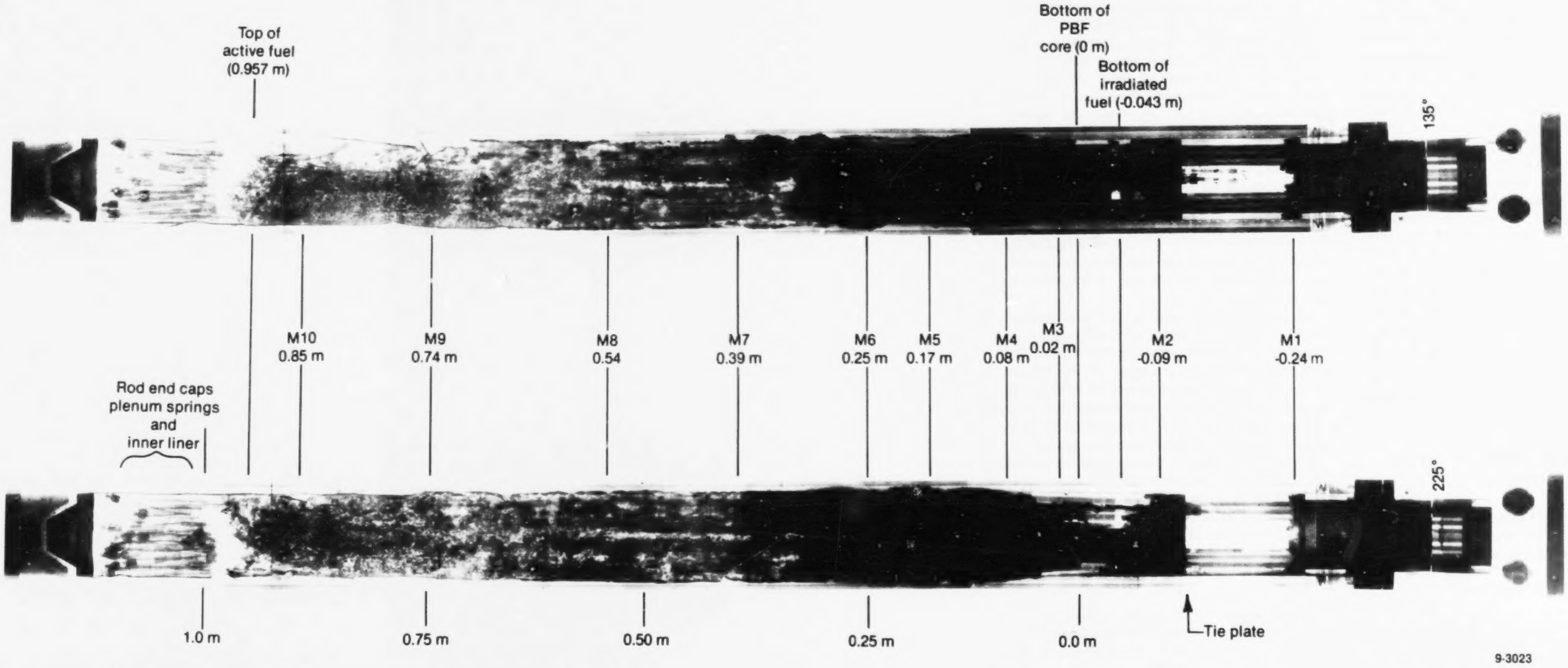
Top of active fuel (0.957 m)
Bottom of PBF core (0 m)
Bottom of irradiated fuel (-0.043 m)
135°
M10 0.85 m
M9 0.74 m
M8 0.54
M7 0.39 m
M6 0.25 m
M5 0.17 m
M4 0.08 m
M3 0.02 m
M2 -0.09 m
M1 -0.24 m
Rod end caps plenum springs and inner liner
225°
1.0 m
0.75 m
0.50 m
0.25 m
0.0 m
Tie plate
9-3023

Figure I-3. Overall axial neutron radiographs of the Test SFD 1-4 bundle, showing relative locations of sections.

After etching, the specimens were rinsed in water and dried.

Five-millimeter core-drilled samples were removed from the cross sections for chemical and/or SEM analysis. SEM included energy dispersive X-ray spectroscopy (EDS) and wave-length dispersive X-ray spectroscopy (WDS) for microelemental analysis down to atomic number 5 (boron). Chemical analysis of core bores included induction coupled plasma spectroscopy (ICP) for elemental composition (excluding oxygen), gamma spectroscopy, beta spectroscopy, and neutron activation analysis for fission products and fissile analysis for fuel materials.

I-2.2 Summary of Data as a Function of Bundle Elevation. The photomacrographs of each bundle cross section were analyzed to determine the cross-sectional areas occupied by various features. This was done by tracing and blackening the areas of the features of interest and measuring the areas with an image analyzer. A reference area was used for calibration.

Features of interest include the various intact bundle components and different categories of previously molten material that could be distinguished. At each elevation, all the area inside of the saddle was included in the features that were measured. The intact bundle components consisted of ZrO_2 insulation, zircaloy liner and cladding, UO_2 fuel, control rod components (zircaloy guide tube, stainless steel cladding, and Ag-In-Cd alloy), and miscellaneous zircaloy and stainless steel or Inconel structural components. The melt features were divided into three categories according to visual appearance: bright metallic,[a] dense gray,[b] and foamy ceramic. At 0.17 and 0.25 m, an interaction region was observed in the insulation and measured separately. At 0.08 m, much of the liner was heavily interacted but distinguishable from the melt and hence measured separately. At 0.25 m, fuel well along in the process of dissolution was distinguishable from the surrounding melt in color photographs of the cross section and was measured separately. In addition to the features mentioned above, open flow area and the entire area inside the saddle were measured separately at each elevation.

The individual area measurements were summed and compared with the independently measured area inside of the saddle at each elevation. The ratio between the summed areas and the measured saddle interior for all cross sections averaged 0.998, with a standard deviation of 0.03. Due to a lack of damage for many features in the lower elevations (0.08 m and below), some areas could be calculated from as-fabricated dimensions or easily measured with a planimeter. A bias was discovered in the area measurements of thin areas such as cladding and liner. A correction factor was determined, based on comparisons with calculations and other measurements, and applied to all thin areas at all elevations. The areas in lower elevations for which there was confidence in the calculated or measured (planimeter) values were also corrected. This correction for measurement bias typically amounted to about 10%. Finally, all areas at an elevation were normalized so that the sum of all areas equaled the measured total area. Overall uncertainties of the area measurements are estimated to be 10% for individual elements, but only 5% summed over the entire cross section. The resultant absolute area measurements are presented in Table I-1.

Area measurements of various bundle components from Table I-1 are displayed in Figures I-4 through I-6. The posttest intact fuel and flow area distributions are compared to their pretest values in Figures I-4 and I-5. Integration of the unreacted fuel distribution in Figure I-4 suggests that ~18% of the fuel was liquefied during the tests. The posttest distribution of intact zircaloy, both oxidized and unoxidized, is shown in Figure I-6. Area measurements of the metallic, mixed, and ceramic melts are shown in Figure I-7. The metallic melt includes the data from the column labeled "bright metallic" and molten control rod cladding and alloy measured at 0.8 m. The mixed melt includes the "gray" melt listed in Table I-1, the molten liner at 0.08 m, and the insulation interaction measured at 0.17 and 0.25 m. The ceramic melt includes the "foamy" melt listed in Table I-1 and the dissolved fuel at 0.25 m. In general, a straight-line interpolation was used between elevations for the purpose of volume integrations. The exception to this was in the lower elevations, where neutron radiographs were used to limit the extent of relocated material below the fuel rods and known end points of components such as fuel rods were incorporated for better estimates.

The compositions of the various melts were determined from the analysis of core bores taken from melt regions. SEM/WDS analysis yielded qualitative

---

[a] At 0.08 m and below, these areas are strictly metallic; but at 0.25 m, these areas contain a mixture of phases dominated by metallic phases.

[b] These areas are primarily a complex mixture of metallics below 0.17 m, becoming mostly oxidized at 0.25 m.

Table I-1. Measured cross-sectional area of bundle components (cm^2)[a]

	Sample ID[b]									
Component	M1	M2	M3	M4	M5	M6	M7	M8	M9	M10
Insulation	22.14	24.02	23.00	17.80	17.80	15.99	25.56	26.39	21.98	13.82
Liner	2.44	2.41	2.44	0.62	0.17	0.78	0.96	0.40	1.53	2.71
Unreacted fuel	0.00	0.00	13.20	14.20	14.04	8.92	8.79	7.10	16.44	17.14
Insulation interaction	0.00	0.00	0.00	0.00	5.09	5.06	0.00	0.00	0.00	0.00
Liner interaction	0.00	0.00	0.00	1.28	0.00	0.00	0.00	0.00	0.00	0.00
Dissolved fuel	0.00	0.00	0.00	0.00	0.00	3.65	0.00	0.00	0.00	0.00
Control rod materials:										
Guide tube	0.00	0.00	0.61	0.00	0.00	0.00	0.00	0.00	0.00	0.00
Cladding	0.00	0.00	0.54	0.51	0.00	0.00	0.00	0.00	0.00	0.00
Alloy	0.00	0.00	2.48	1.71	0.00	0.00	0.00	0.00	0.00	0.00
Melts:										
Bright	0.82	11.10	2.40	4.81	0.00	4.89	0.00	0.00	0.00	0.00
Gray	1.27	6.02	3.68	39.02	16.81	30.82	0.00	0.00	0.00	0.00
Foamy	0.00	0.00	0.00	0.00	6.58	4.75	14.71	15.33	0.00	0.00
Miscellaneous	9.38[c]	26.05[c]	3.26	2.26	0.00	0.00	0.00	0.00	3.88	4.79
Measured flow area	49.47	18.30	31.54	4.53	24.37	10.33	34.86	36.40	42.26	47.09
Total area inside saddle	85.52	87.89	87.78	87.81	88.32	87.61	87.01	86.20	86.30	85.78

---

a. Original component cross-sectional areas (in cm^2): fuel, 14.27; cladding, 4.9; liner, 2.44; insulation, 24.77; control rod alloy, 1.85; stainless steel cladding, 0.47; zircaloy guide tube, 0.60; flow area, 34.5; total, 86.0.

b. Sample elevations (in meters) by ID: M1, -0.24; M2, -0.09; M3, 0.02; M4, 0.08; M5, 0.17; M6, 0.25; M7, 0.39; M8, 0.54; M9, 0.74, and M10, 0.85.

c. Represents undamaged structural material below the active fuel region.

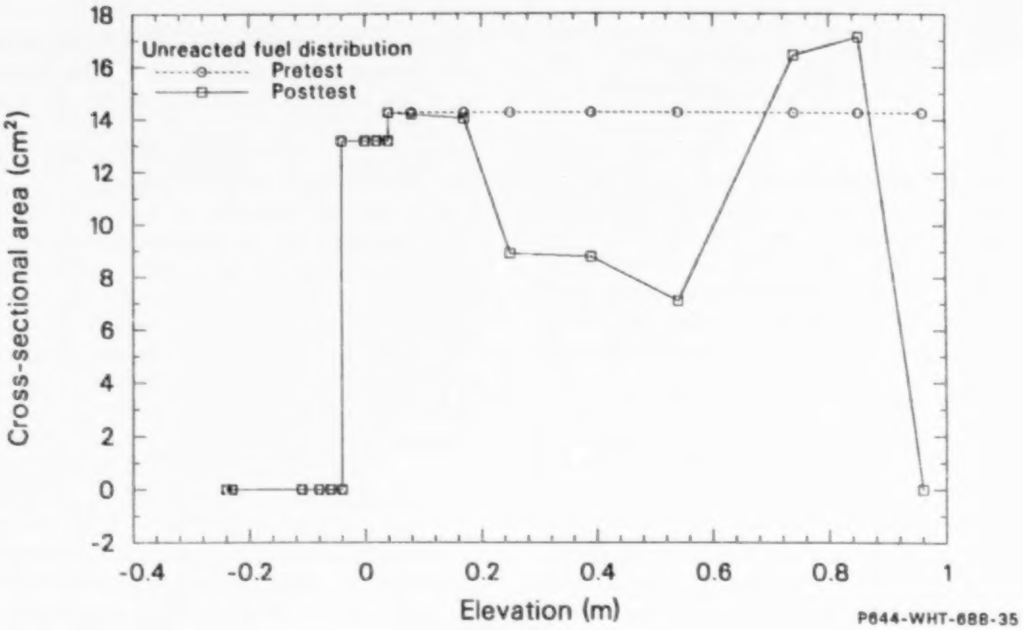

Figure I-4. Comparison of pretest and posttest unreacted fuel distribution.

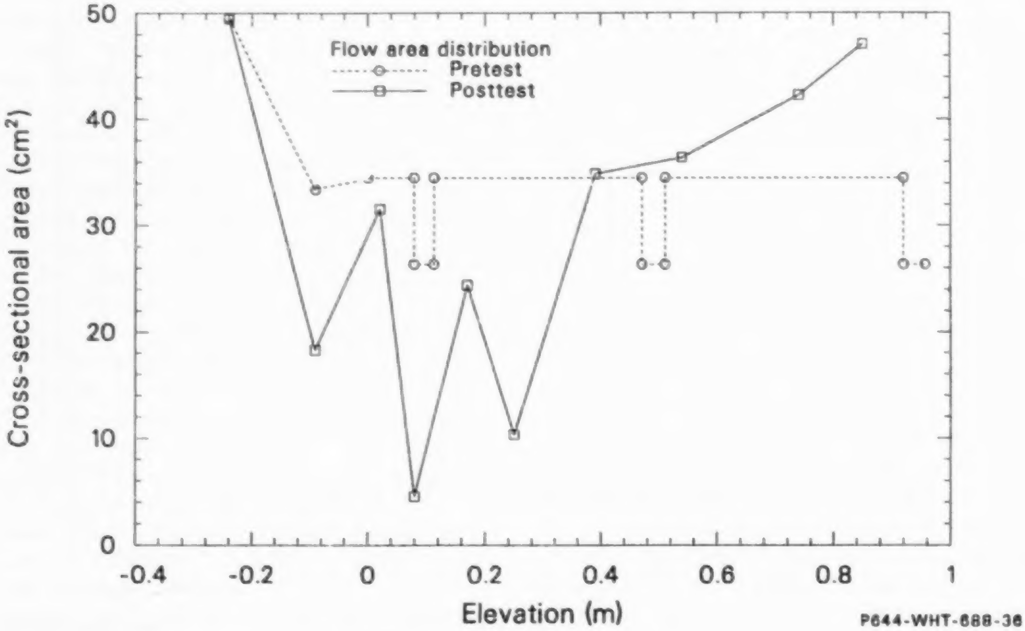

Figure I-5. Comparison of pretest and posttest flow area distribution.

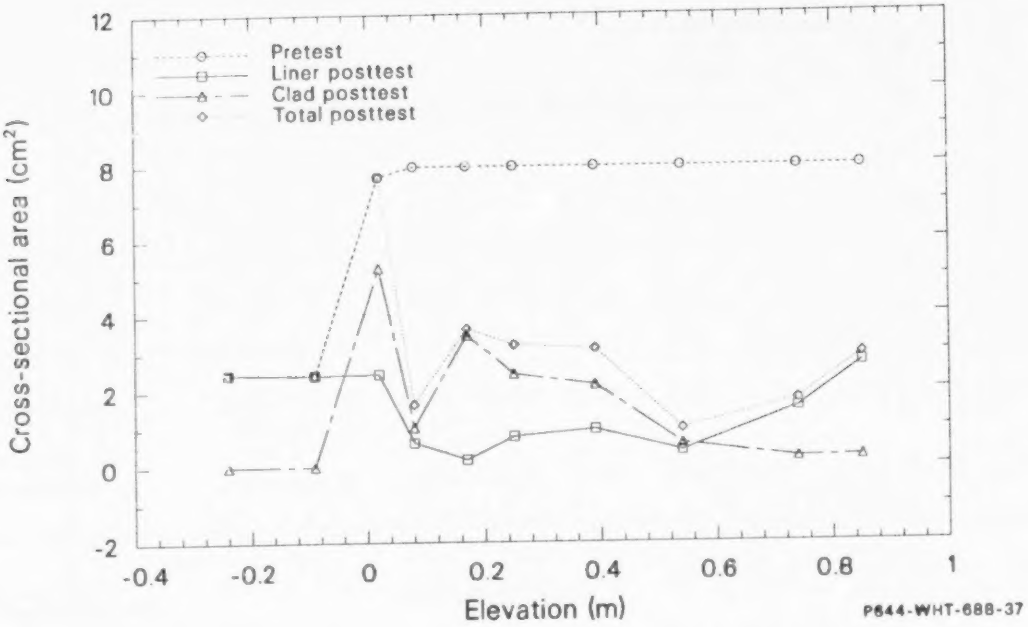

Figure I-6. Posttest distribution of zircaloy components in the SFD 1-4 bundle.

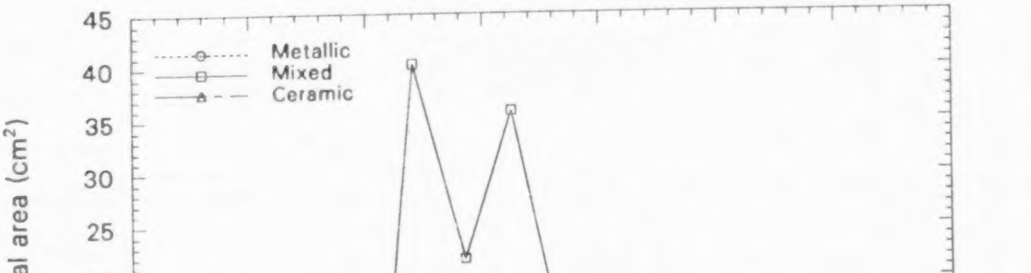

Figure I-7. Distribution of different melts in the SFD 1-4 bundle.

information on a microscopic scale. These results are discussed later in this appendix in conjunction with descriptions of the microstructures exhibited by the various features in the bundle. The results of ICP analysis of core bore samples from the bundle cross sections are presented in Table I-2. The data have been normalized to sum to 100 at.%, ignoring oxygen which is not measurable by ICP. The uncertainty of the ICP technique is 10% for all the elements except tin and indium, which have a 20% uncertainty. (The data for sample M5A from the 0.17-m elevation are somewhat more uncertain due to the very high dilution factor that was required for this sample.) The SEM/WDS data and ICP data were used to estimate the average composition of the various melts at each elevation. These estimates are displayed in Table I-3.

Optical examinations were used to estimate the extent of zircaloy oxidation in the melts and intact structures. A wide variation in composition existed on both a microscopic and macroscopic scale. As a result, the uncertainties of these estimates are believed to be on the order of 50 to 100%. The percent of intact zircaloy (liner, cladding, and guide tubes) that was oxidized at each elevation is shown in Table I-4. When combined with the total amount of intact zircaloy remaining in the bundle (see Figure I-6), these results yield the area of intact zircaloy that was oxidized, shown in Figure I-8. Oxidation estimates for the zircaloy in melts were based on the compositional information in Table I-3 and the cross-sectional area of melt measured posttest. The area of molten zircaloy in melts that was oxidized is shown in Figure I-9.

Estimates of posttest distributions of total fuel and control rod alloy were made by combining the composition estimates shown in Table I-3 with the area measurements shown in Table I-1. Plots of posttest fuel and control alloy distributions are shown in Figures I-10 and I-11. The calculated fuel inventory is 1450 cm^3, compared with the pretest inventory of 1418 cm^3; and the calculated control alloy inventory is 189 cm^3, compared with the pretest inventory of 177 cm^3. The fuel and control alloy distributions were not normalized because of uncertainty in the amount of upper end fittings and ZrO_2 insulation that were involved in the melts. The calculated zircaloy inventory accounting for expansion due to oxidation is 911 cm^3, compared with 794 cm^3 of zircaloy in the active core region and 935 cm^3 including end fittings.

Minimum peak temperatures were estimated from microstructural and elemental chemistry information in conjunction with appropriate phase diagrams and past experiments.[I-1,I-2,I-3] Peak temperatures as a function of elevation for both intact and relocated material are shown in Figure I-12.

I-3. Description of Bundle Cross Sections

The damage state and the chemical and physical properties of the nine cross sections of the SFD 1-4 fuel bundle that were examined are described in this section. Results from optical metallography, SEM, and chemical analysis are discussed. The results of examining the cross sections are discussed in order of descending bundle elevation.

I-3.1 Bundle Cross Section at 0.85 m. The fuel bundle at the 0.85-m elevation, shown in cross section in Figure I-13, is a debris bed of UO_2 fuel fragments with little of the zircaloy fuel rod cladding remaining. The zircaloy inner liner was deformed and disrupted; much of the ZrO_2 insulation was disrupted, and large portions were no longer present at this elevation. The zircaloy saddle was unaffected. Chemical analysis of a sample from the debris (sample 10A, see Table I-1) confirmed the depletion of zircaloy and indicated that silver control materials were also strongly depleted from the debris.

What little zircaloy remaining at this elevation was molten and had been partially oxidized, as is shown in the photomicrograph in Figure I-14. The low contact angle between the previously molten zircaloy and the UO_2 fuel pieces in this figure indicates that the melt had wet the surface of the fuel. The wetting of the fuel allowed the molten zircaloy to remain long enough to either partially oxidize in steam and solidify at this location or solidify and then partially oxidize. It is not possible to determine from this photomicrograph if the zircaloy was solid or liquid during the oxidation process. Either is possible. In either case, minimum interaction between UO_2 and zircaloy took place.

The photomicrographs of the cross section of the zircaloy inner liner in Figure I-15 show a microstructure that has been interpreted as molten zircaloy within oxide layers on both surfaces. The microstructure of the metallic material (a two-phase mixture of α-Zr(O) and ZrO_2) is consistent with a hypoeutectic composition identified by position 3 in the Zr-O phase diagram presented in Figure I-16. This material would embrittle the liner despite ZrO_2 layers only 15% of the wall thickness and is therefore consistent with the observed fragmentation of the liner.

Using oxygen densities of 0.5 g O_2/cm^3 for α-Zr(O) and 1.53 g O_2/cm^3 for ZrO_2 [ignoring the small amount of ZrO_2 in the two-phase mixture

Table I-2. ICP results

Sample Elevation (m)	Sample No.	Normalized at.% U	Zr	Sn	Ag	In	Cd	Fe	Cr	Ni
.85	M10A	69.8	13.9	0.0	0.4	0.0	1.6	7.7	0.0	6.6
.54	M8B	40.4	27.9	0.0	3.1	0.2	6.0	13.9	0.0	8.5
.54	M8C	57.9	31.7	0.0	0.8	0.0	6.0	3.6	0.0	0.0
.39	M7A	74.0	11.4	0.0	0.6	3.8	1.7	2.3	0.0	6.3
.25	M6A	37.8	57.5	0.0	0.4	0.0	1.1	2.5	0.7	0.0
.25	M6B	10.7	70.2	0.8	7.1	0.2	1.9	3.7	1.5	3.9
.17	M5A	16.8	39.5	0.0	9.1	0.9	9.3	6.8	0.0	17.7
.08	M4B	0.1	6.6	0.0	74.8	11.9	4.9	1.1	0.5	0.3
.08	M4D	0.5	54.1	2.0	16.1	3.0	0.9	11.4	4.5	7.6
.02	M3B	0.3	55.2	1.5	24.8	4.3	1.8	7.5	1.5	3.1
.02	M3C	0.0	1.1	0.0	76.1	17.4	5.3	0.0	0.0	0.0
.02	M3D	0.0	1.3	0.0	75.4	17.9	5.4	0.0	0.0	0.0
−.09	M2B	0.3	8.6	0.2	16.0	2.9	2.8	41.3	13.9	13.9
−.09	M2D	0.0	98.2	1.0	0.2	0.0	0.0	0.4	0.2	0.0

Table I-3. Average composition of molten material

Description	Sample ID	UO_2	Zry	Control Rod	SS	Oxidation Fraction[a]
Bright melt	M1	0	55	30	15	0
	M2	0	55	25	20	0
	M3	0	55	25	20	0
	M4	0	30	40	30	0
	M6	10	70	10	10	20
Molten control rod cladding	M4	0	5	5	90	0
Molten control rod alloy	M4	0	3	96	1	0
Gray melt	M1	40	24	20	16	15
	M2	3	40	30	27	15
	M3	3	40	30	27	15
	M4	3	55	30	12	15
	M5	5	70	5	20	20
	M6	15	65	3	17	75
Molten liner	M4	0	66	10	24	20
Insulation interaction	M5[b]	0	70	5	5	60
	M6[b]	0	70	5	5	60
Foamy melt	M5	10	70	5	15	100
	M6	15	65	3	17	100
	M7[b]	40	30	1	9	100
	M8[b]	40	30	1	9	100
Dissolved fuel	M6	80	20	0	0	100

---

[a] Fraction of zircaloy in melt that is oxidized.

[b] Material composition calculation assumes 20% porosity.

Table I-4. Percent of intact zircaloy components that are oxidized

Sample ID	Liner	Guide Tube and Cladding
M1	0	0
M2	0	0
M3	0	0
M4	17	17
M5	98	98
M6	98	98
M7	100	100
M8	100	100
M9	40	60
M10	20	40

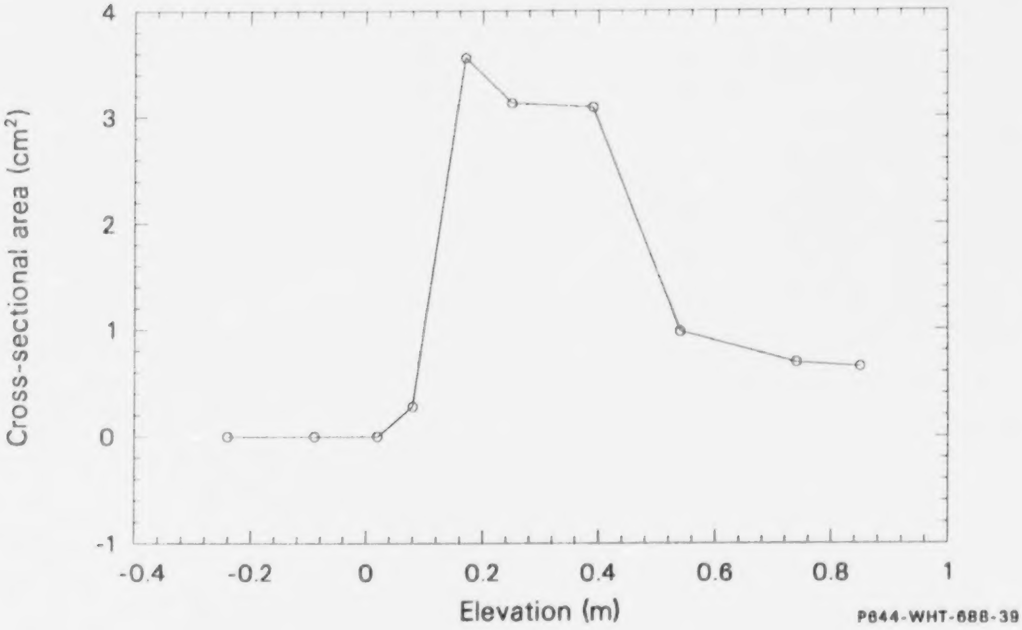

Figure I-8. Cross-sectional area of oxidized zircaloy components in the SFD 1-4 bundle.

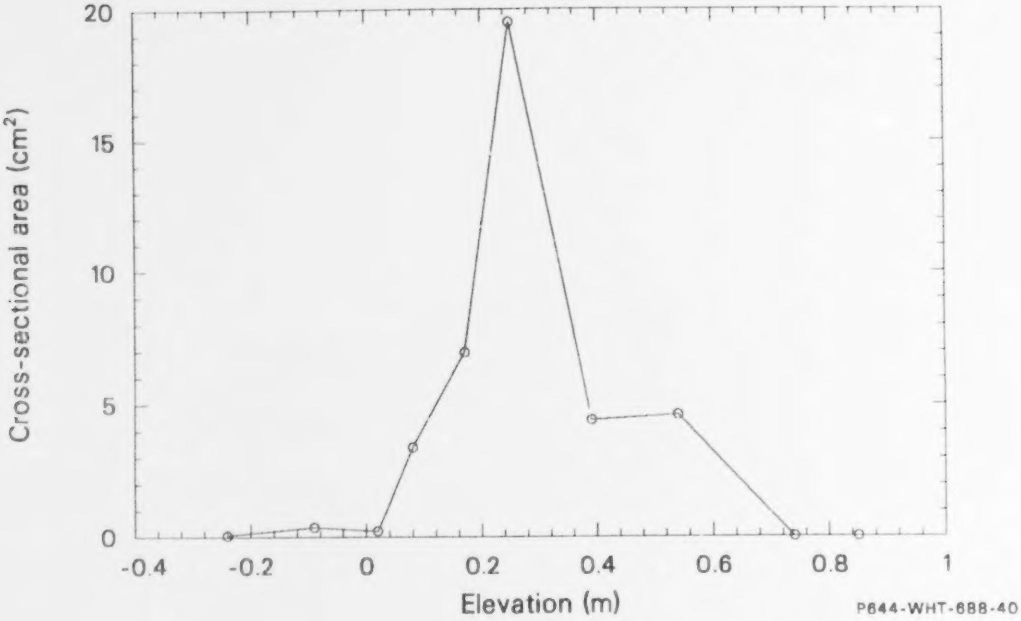

Figure I-9. Cross-sectional area of molten zircaloy in the SFD 1-4 bundle that was oxidized.

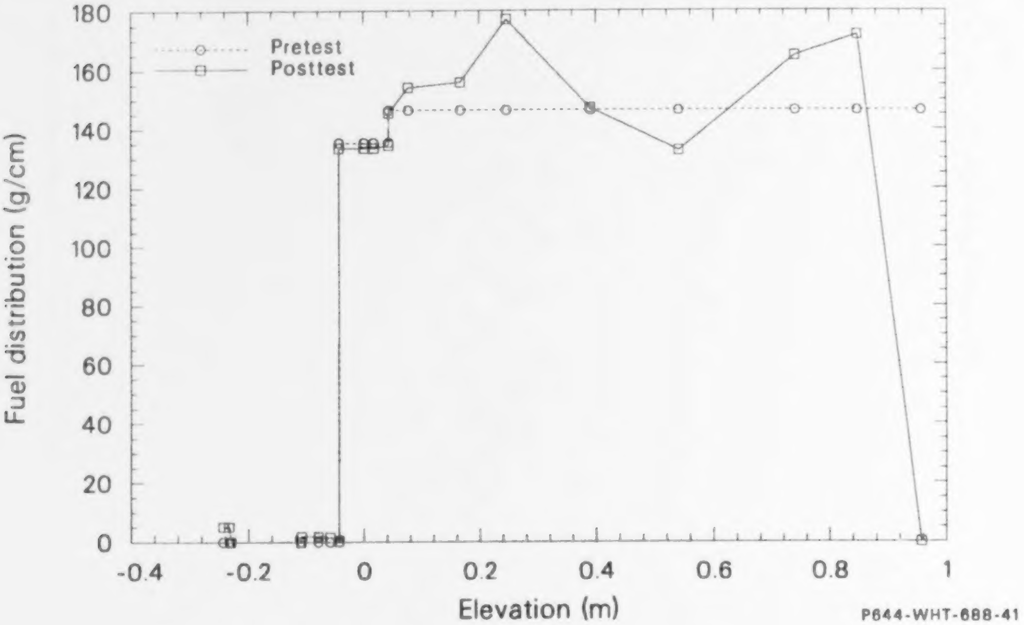

Figure I-10. Pre- and posttest axial fuel distribution in the SFD 1-4 bundle.

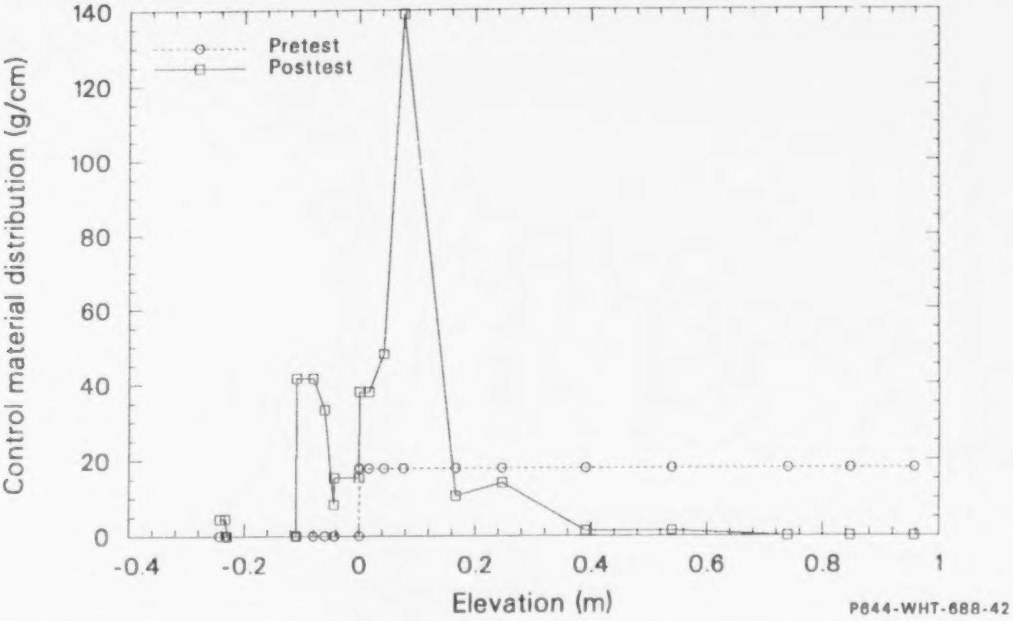

Figure I-11. Pre- and posttest axial control rod material distribution in the SFD 1-4 bundle.

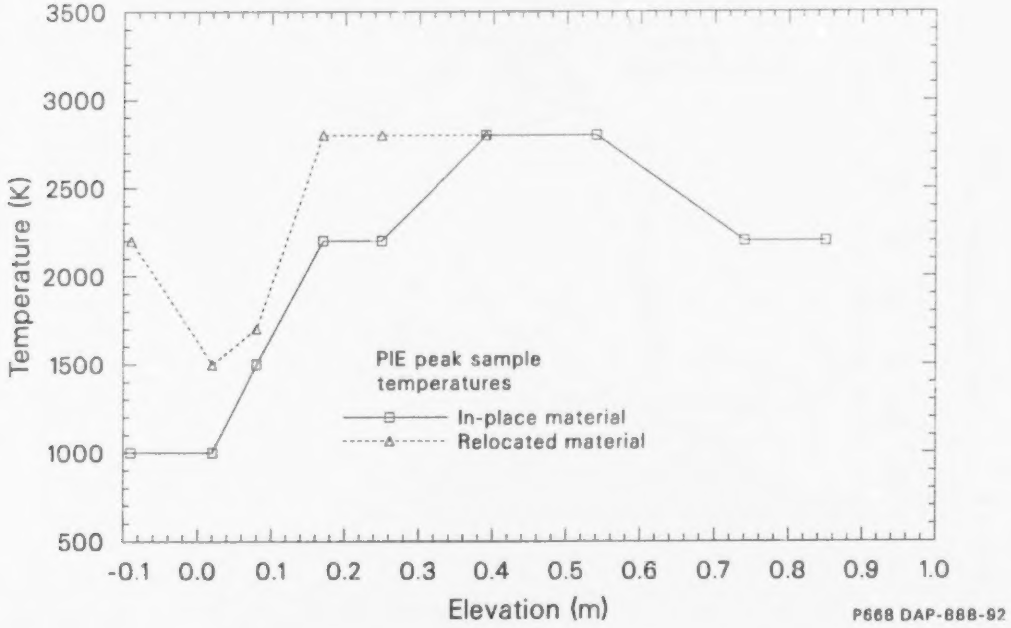

Figure I-12. Minimum peak temperature of in-place and relocated materials.

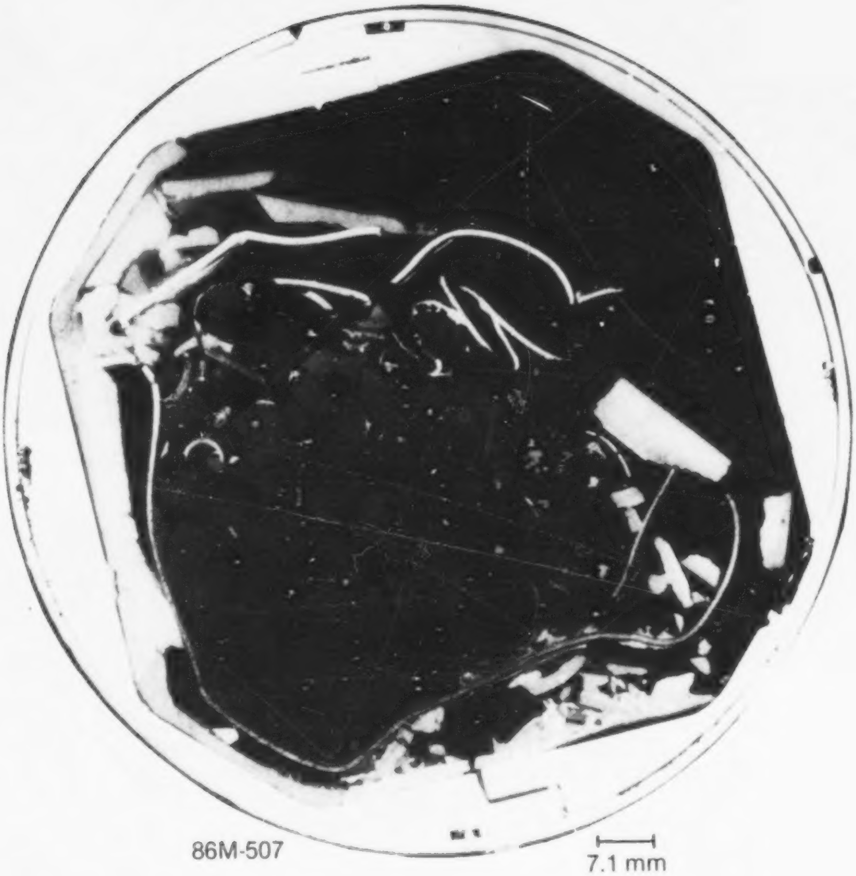
86M-507
7.1 mm

Figure I-13. SFD 1-4 bundle cross section at 0.85 m.

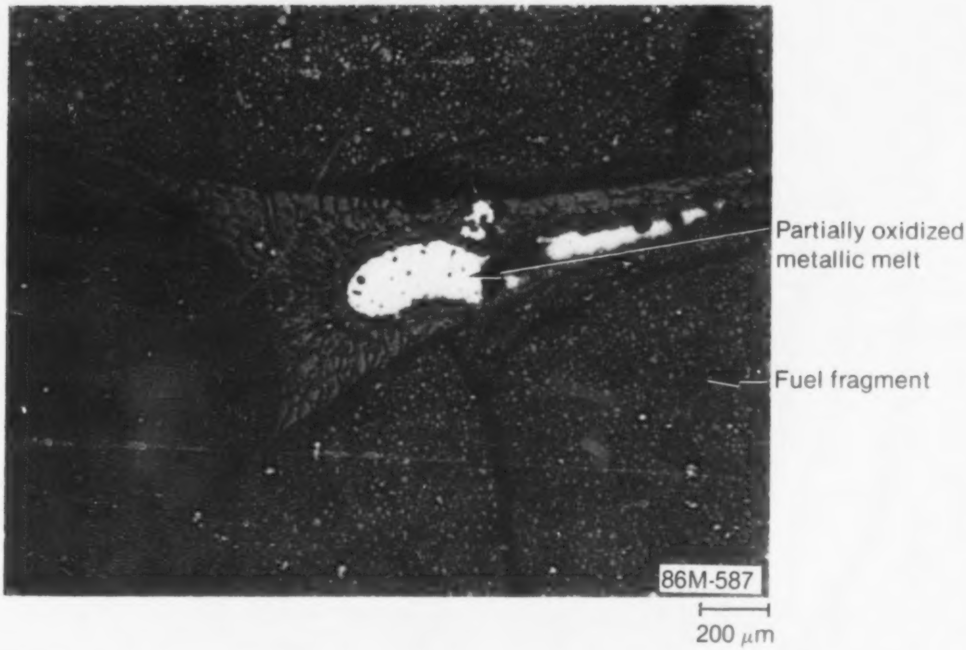
Partially oxidized metallic melt
Fuel fragment
86M-587
200 μm

Figure I-14. Partially oxidized metallic melt between two fuel fragments at 0.85 m.

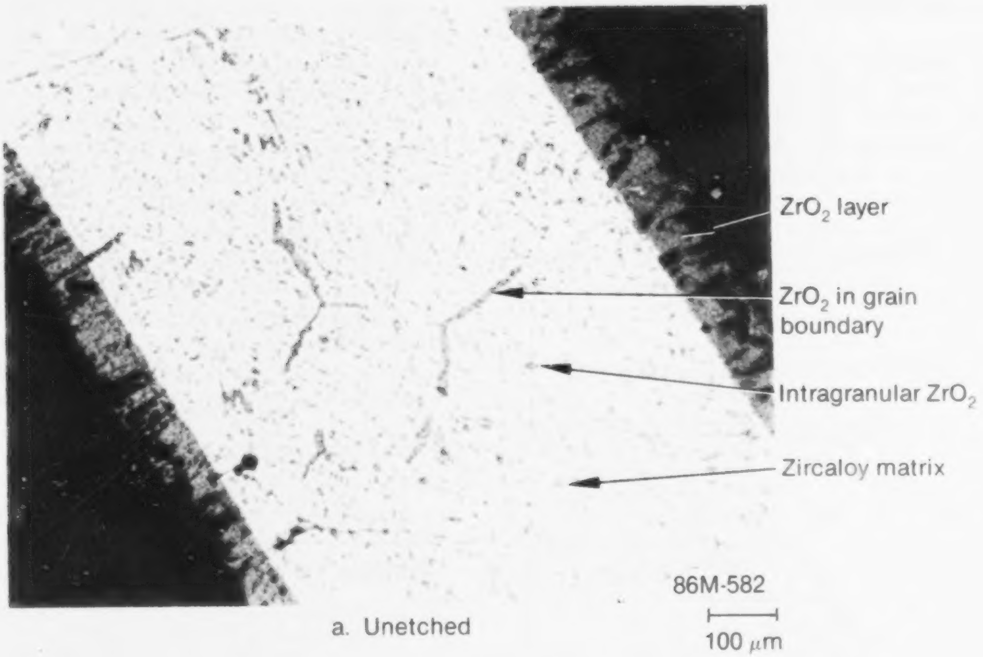
ZrO$_2$ layer
ZrO$_2$ in grain boundary
Intragranular ZrO$_2$
Zircaloy matrix
86M-582
100 μm

a. Unetched

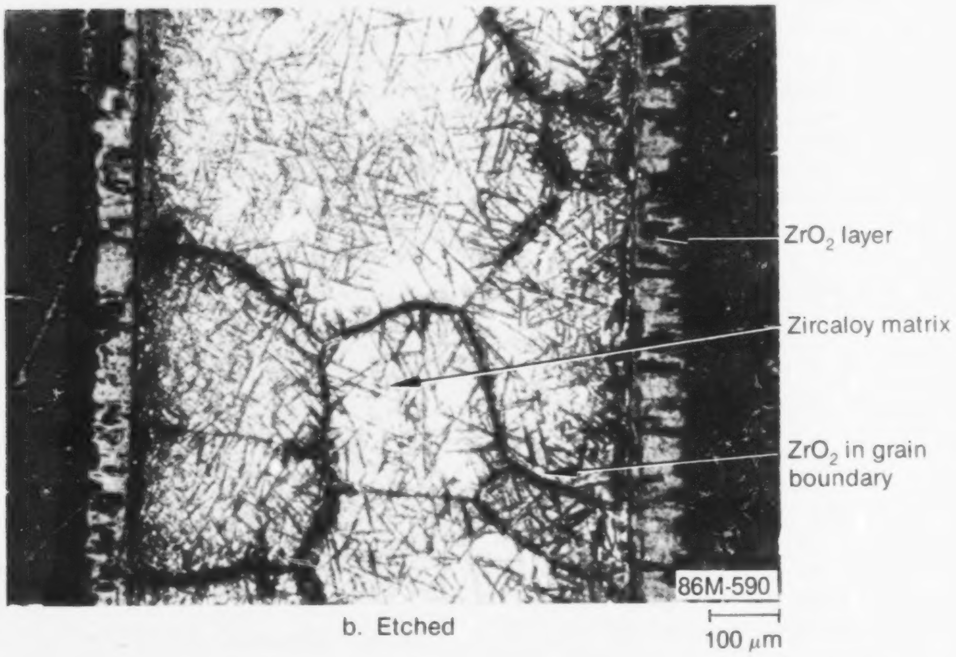
ZrO$_2$ layer
Zircaloy matrix
ZrO$_2$ in grain boundary
86M-590
100 μm

b. Etched

Figure I-15. Photomicrographs showing oxidized and previously molten inner liner at 0.85 m.

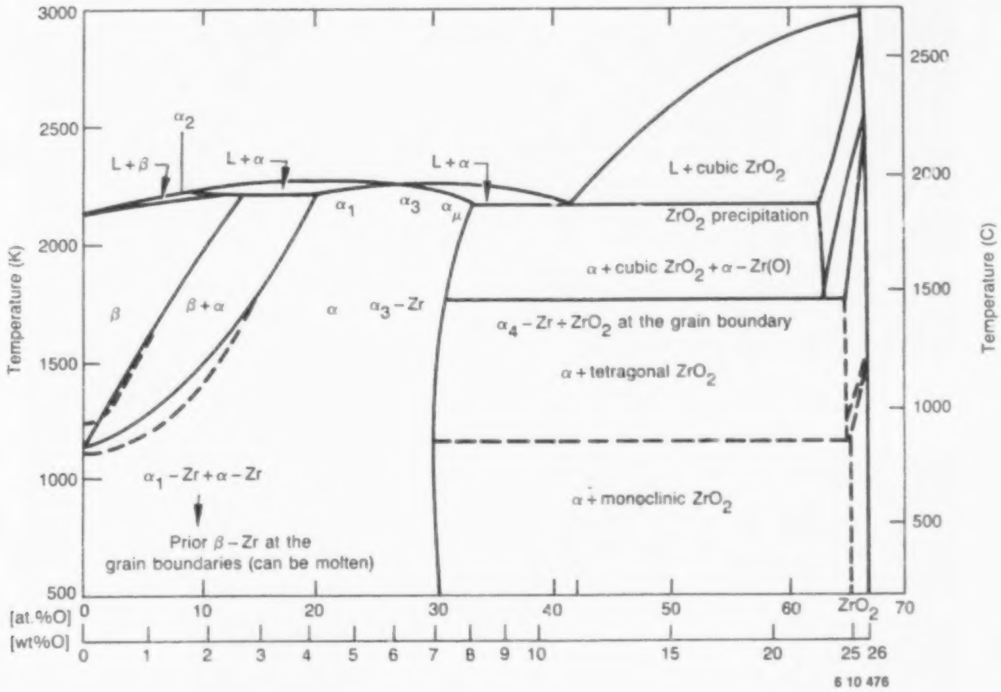

Figure I-16. Zirconium-oxygen equilibrium phase diagram (Ref. I-3).

with the α-Zr(O)] and the oxidation kinetics of Prater and Courtright,[I-4] an exposure time in steam of only 5 s at 2200 K was calculated to be required to account for the oxygen pickup in the liner. Because the bundle was at high temperature for much longer than 5 s, the analysis of oxygen weight gain in the liner suggests that if the liner was above the melting temperature of α-Zr(O), it must have been under steam-starved conditions much of the time that the bundle was at elevated temperatures. For an exposure time in steam of 680 s, a temperature of 1564 K would be sufficient to account for the oxygen weight gain derived from the observed layer thicknesses in the liner. However, the layer thicknesses would be much different than those observed: 161 μm calculated for ZrO_2 versus 90 μm measured and 171 μm calculated for α-Zr(O) versus 365 μm measured. Clearly, dissolution of ZrO_2 by molten zircaloy had taken place during a period of steam starvation.

The microstructure in Figure I-15 is also consistent with exposure of the liner to steam-starved conditions following oxidation at temperatures below the melting point of α-Zr(O). Since previously molten zircaloy has been identified in the bundle (Figure I-14), it is likely that the liner was near the melting point of zircaloy. In any case, it is clear that the liner was steam-starved for much of the high-temperature portion of the transient. Similarly, for the previously molten zircaloy in Figure I-14, the measured ZrO_2 thickness could be produced in 8 s at 2200 K or, if the melt froze before oxidation, 29 s at 2000 K.

The fuel microstructure at this elevation shows grain sizes in the range 15 to 20 μm and zones of both intragranular and intergranular porosity (Figure I-17). These circumferential zones or bands of differing porosity distribution in the fuel are seen throughout the bundle and are of unknown origin. The grain sizes are similar to those measured after BR-3 irradiation and before the SFD 1-4 transient (13 μm for low-power rods and 26 μm for high-power rods). The lack of grain growth in the SFD 1-4 transient is likely related to pinning of the grain boundaries by the porosity in this high-burnup fuel.

Little evidence of material interactions remained at this elevation because so much of the fuel rod cladding and control material had melted and relocated to lower bundle elevations. The flow area at this elevation was larger than the flow area in the intact bundle (see Figure I-5) due to the relocation of bundle materials, including control rods, fuel rod cladding, and segments of the inner liner and the ZrO_2 insulation.

In summary, the debris bed of UO_2 fuel fragments was formed due to the melting and relocation of zircaloy fuel rod cladding. The control rods also melted and relocated. Peak temperatures were at least 2200 K based on cladding melting. There was no reduction in flow area at this elevation, and there was little evidence of fuel liquefaction. The remaining zircaloy was partially oxidized, and there was evidence of steam starvation.

I-3.2 Bundle Cross Section at 0.74 m. The cross section at 0.74 m, shown in Figure I-18, is in the upper debris bed and is similar in appearance to the cross section at 0.85 m. Fuel liquefaction by interaction of molten zircaloy with UO_2 is more evident at this elevation, although it is still quite limited by relocation of molten zircaloy (Figure I-19). In Figure I-19, metallic melt in a fuel crack attacked UO_2 but subsequently was oxidized to a large extent.

The liner was oxidized to a greater extent at this elevation (40% conversion to ZrO_2) than at the higher-elevation cross section (20% conversion to ZrO_2). The liner was fractured; some of the fracture surfaces were oxidized and some were not, indicating that fracturing took place both before and after oxidation ceased. The metallic zircaloy within the oxide was molten, and the structure appears to be a two-phase mixture of α-Zr(O) and ZrO_2 (Figure I-20). Analysis of the oxide layers indicates that at 2200 K, 11 s would be required to produce the thick oxide on the inner surface of the liner and 3 s would be needed to produce the thinner oxide on the outer surface. If both sides of the liner were exposed to steam for 11 s, a temperature of 2000 K would be needed to produce the thin oxide. It seems unlikely that a temperature gradient of 200 K could have existed across molten, or nearly molten, zircaloy of less than 0.76 mm thickness (original thickness of liner). It seems more likely that the outside surface of the liner saw steam for a shorter period of time than the inside surface. In either case, the implication is that this region of the rubble bed, as with the higher-elevation cross section, was steam-starved over a long period of the high-temperature transient.

An example of the interaction of molten zircaloy with ZrO_2 insulation is presented in Figure I-21. The microstructure shows the formation of a two-phase mixture of α-Zr(O) and ZrO_2 as a result of the dissolution of ZrO_2 by metallic zircaloy. A temperature above 2170 K was required to generate the

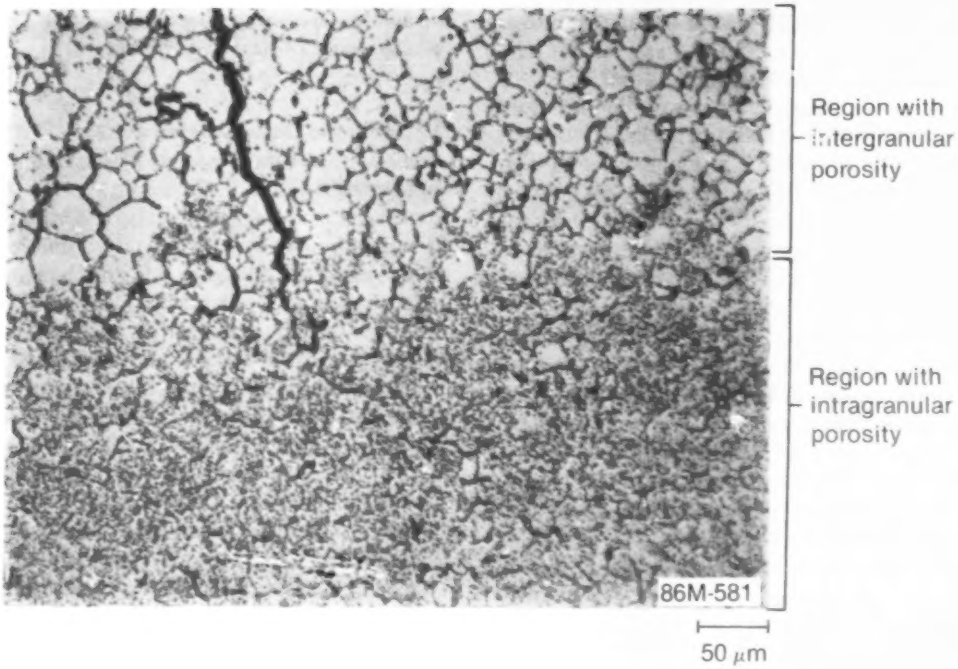
Region with intergranular porosity
Region with intragranular porosity
86M-581
50 μm

Figure I-17. Photomicrograph showing fuel microstructure typical of the 0.85-m elevation.

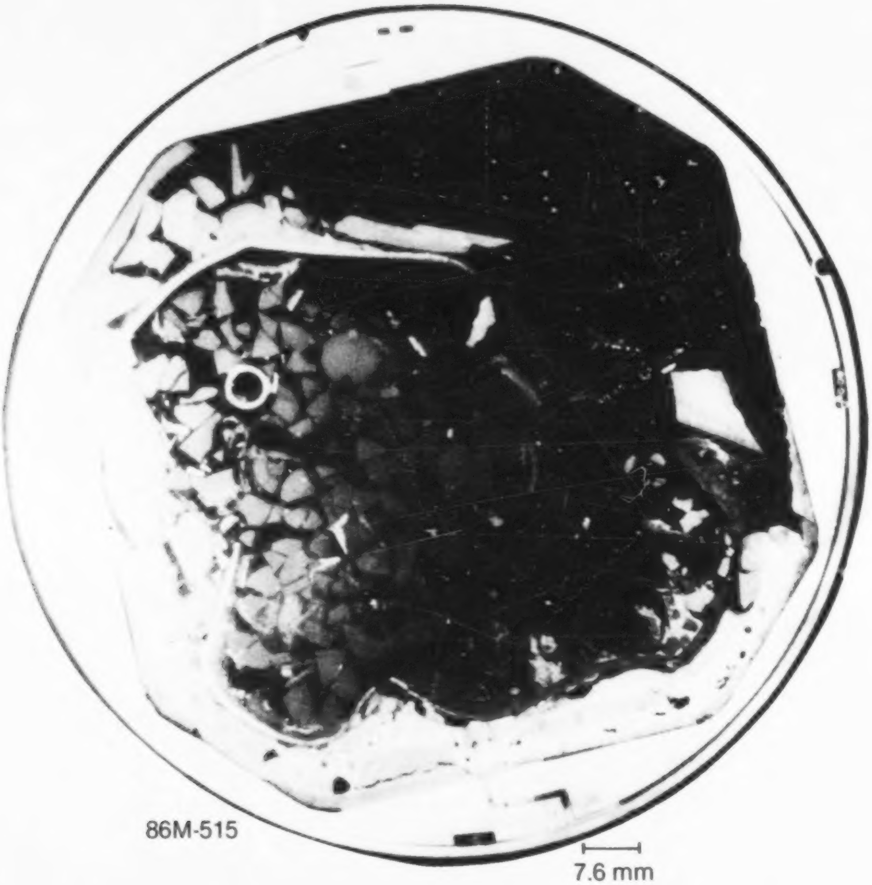
86M-515
7.6 mm

Figure I-18. SFD 1-4 bundle cross section at 0.74 m.

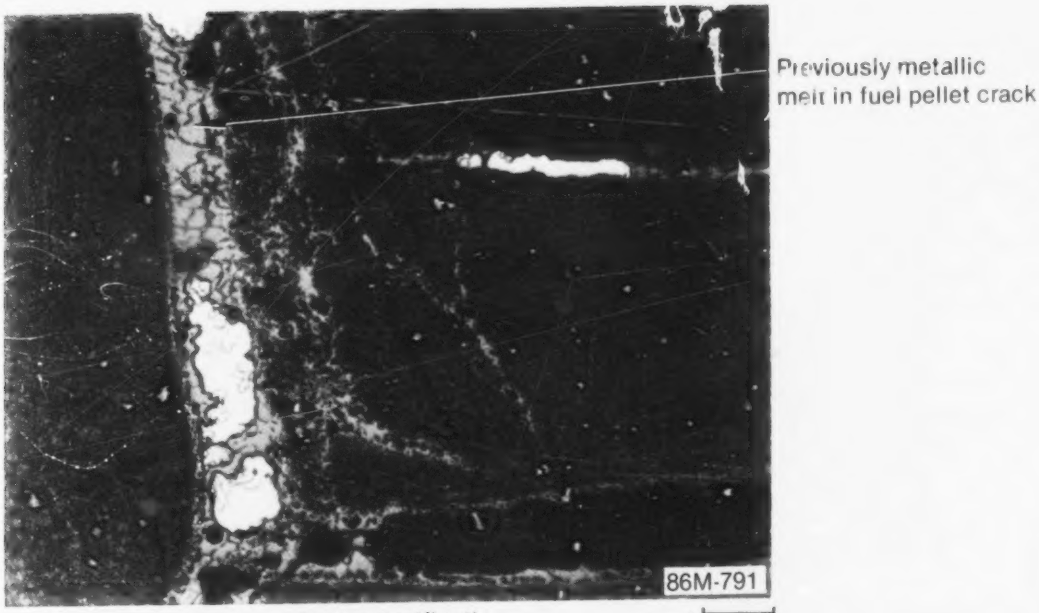
Previously metallic melt in fuel pellet crack
86M-791
200 μm

a. Low magnification

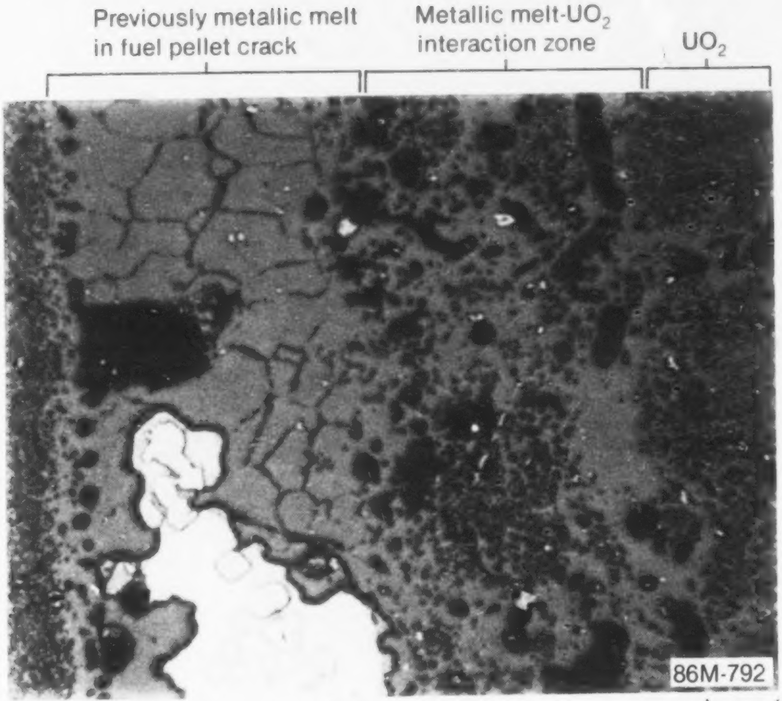
Previously metallic melt in fuel pellet crack
Metallic melt-UO_2 interaction zone
UO_2
86M-792
50 μm

b. Higher magnification

Figure I-19. Unetched photomicrographs showing attack of UO_2 by previously metallic melt in pellet crack at 0.74 m.

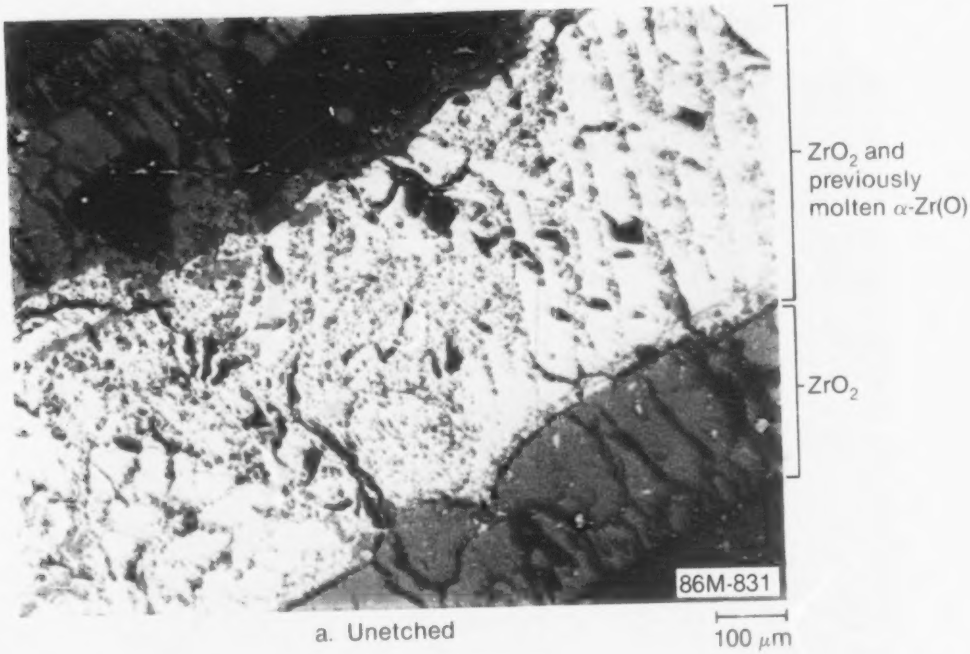
ZrO$_2$ and previously molten α-Zr(O)
ZrO$_2$
86M-831
100 μm

a. Unetched

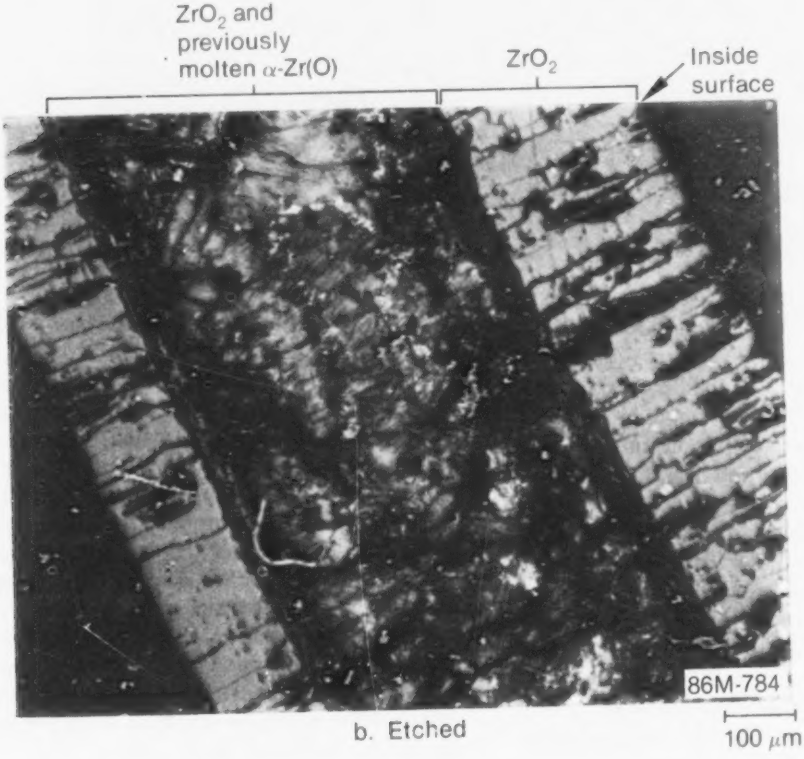
ZrO$_2$ and previously molten α-Zr(O)
ZrO$_2$
Inside surface
86M-784
100 μm

b. Etched

Figure I-20. Photomicrograph showing oxidized and previously molten inner liner at 0.74 m.

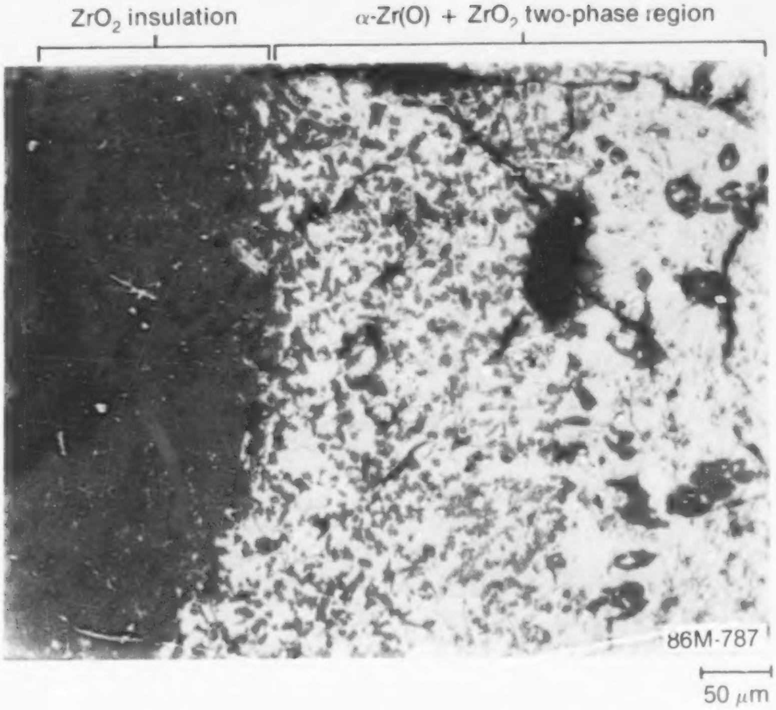

Figure I-21. Unetched photomicrograph showing dissolution of ZrO_2 insulation by molten zircaloy at 0.74 m.

interactions of molten zircaloy with UO_2 and ZrO_2 discussed above.

The microstructure of the fuel (Figure I-22) is similar to that at the 0.85-m elevation, with grain sizes about 23 μm.

As is shown in Figure I-5, the flow area at this elevation increased relative to that for an intact cross section because of the relocation of bundle components such as fuel rod cladding, control rods, liner, and ZrO_2 insulation.

In summary, the cross section at the 0.74-m elevation was a debris bed similar to that at the 0.85-m elevation. The extent of metallic melt interaction with ceramics (UO_2 and ZrO_2) was limited at the 0.74-m elevation, but was greater than at the 0.85-m elevation. The extent of steam oxidation was greater at the 0.74-m elevation than at the higher cross section, but the fuel microstructure was similar at the two elevations. It would appear that peak temperatures at the 0.74-m elevation were at least 2200 K and that steam was more plentiful than at the 0.85-m elevation.

I-3.3 Bundle Cross Section at 0.54 m. The photomacrograph of the cross section at 0.54-m elevation in Figure I-23 shows that strong fuel dissolution occurred and much of the cladding and some of the fuel have relocated downward. No traces of the four control rods and their guide tubes are apparent. Most of the liner melted, and some of it interacted with the insulation. Only about 10% of the cladding and liner remain, and this material was oxidized to ZrO_2. Some unreacted fuel remains as declad pellet fragments at the periphery of the bundle. The central region of the bundle principally contains previously molten ceramic material, a result of UO_2-molten metal interactions. The flow area at this cross section is about 6% greater than in the intact bundle (see Table I-1).

The photomicrograph in Figure I-24 shows previously molten material containing large pores and

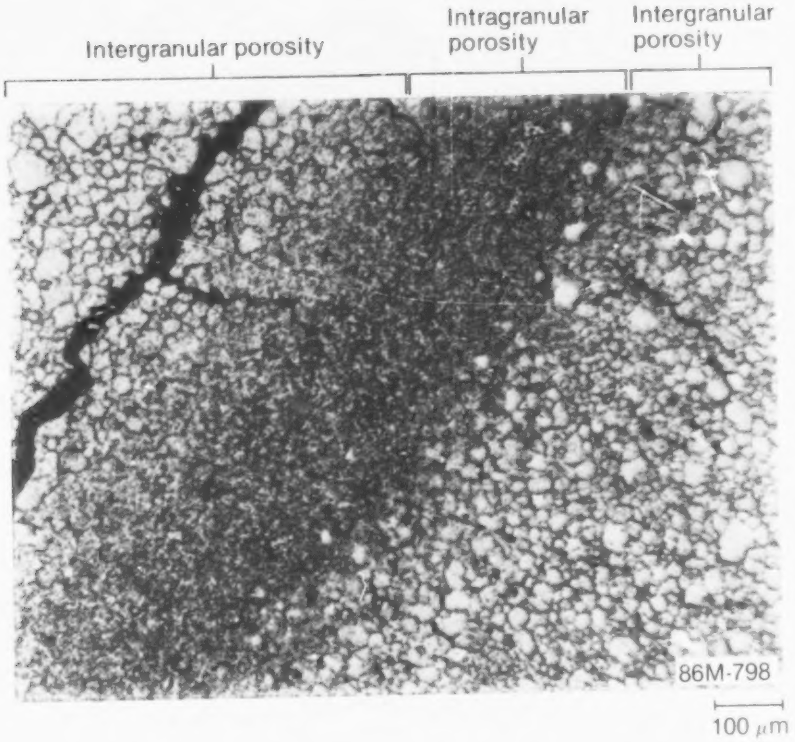
Intergranular porosity
Intragranular porosity
Intergranular porosity
86M-798
100 μm

Figure I-22. Unetched photomicrograph showing UO_2 fuel microstructure at 0.74 m.

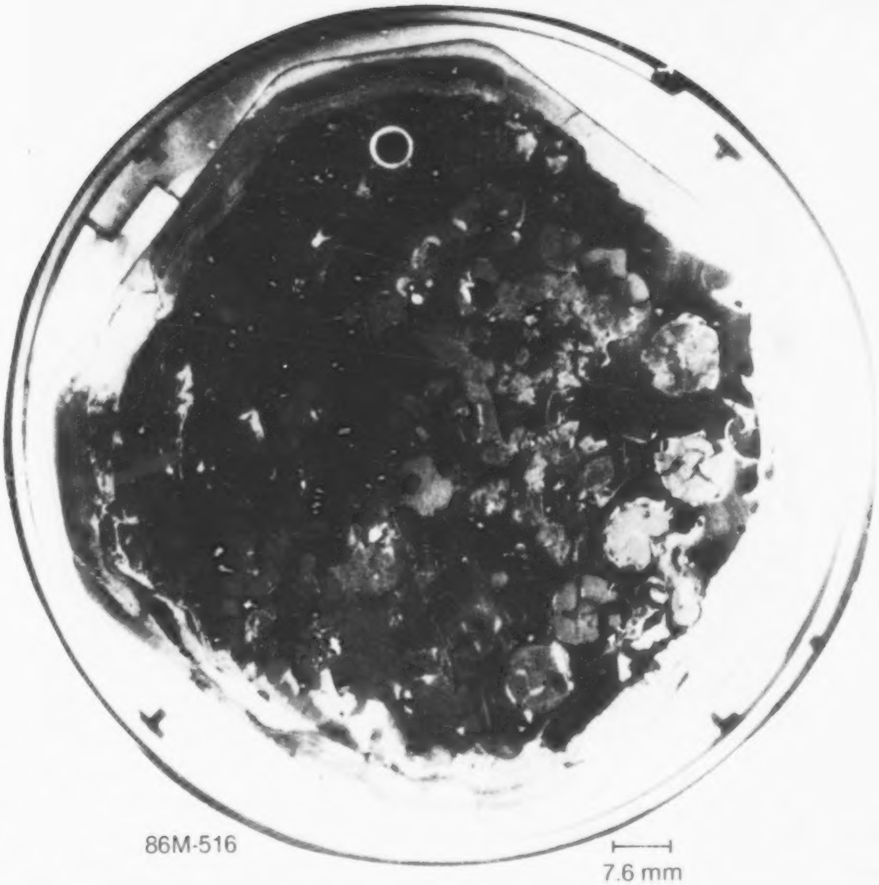
86M-516
7.6 mm

Figure I-23. SFD 1-4 bundle cross section at 0.54 m.

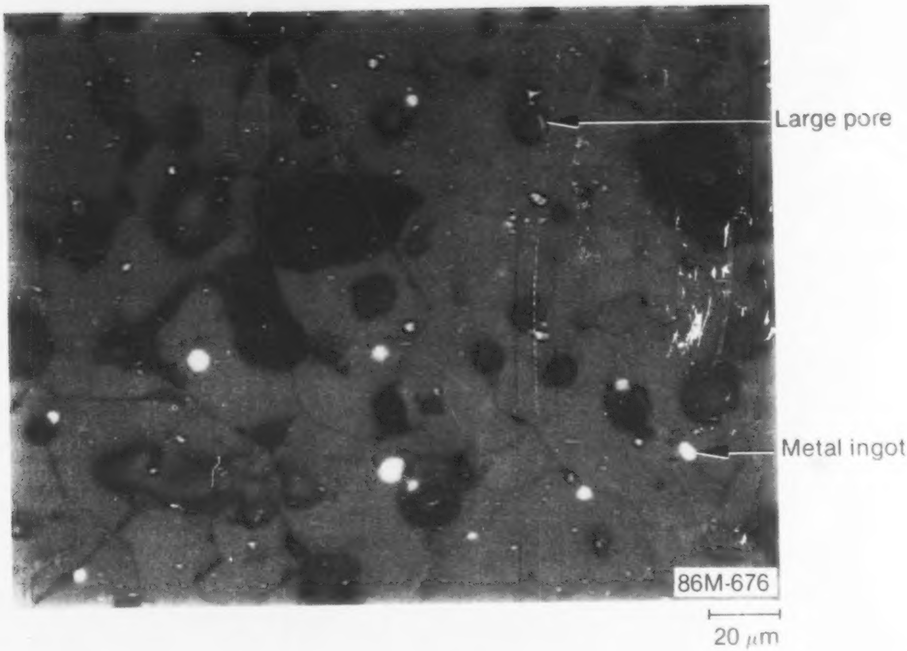

Figure I-24. Photomicrograph showing microstructure in reacted portion of rod 5A fuel pellet at 0.54 m.

large metal ingots in a reacted zone in the partially liquefied fuel of rod 5A. A SEM photomicrograph, using a secondary electron image, in Figure I-25a shows wide grain boundaries. An X-ray dot map in Figure I-25b shows that iron is present in these grain boundaries. An oxygen dot map shows uniform oxygen concentration across this region, indicating Fe_3O_4 as the probable chemical form of the iron. A secondary electron image in Figure I-26 demonstrates that the microstructure of the fuel in the unreacted region of rod 5A is similar to that observed in the fuel in the cross sections at the higher elevations already discussed; i.e., grains of approximately 20 μm in diameter with porosity primarily in the grain boundaries. Bulk chemical analysis from a core bore taken from the area of rod 5A indicated uranium with significant amounts of zirconium and smaller amounts of iron, silver, and cadmium (see sample M8C in Table I-1). SEM microchemical analysis indicated that the unreacted regions contained solely UO_2, whereas the reacted regions contained $(U,Zr)O_2$ with oxidized iron in the grain boundaries.

A core bore for chemical analysis (M8B) was also taken from the center of the bundle. This region was examined by SEM and found to contain a similar structure (shown in Figure I-27) of previously molten $(U,Zr)O_2$, with oxidized iron in the grain boundaries as in the reacted zones of fuel rod 5A. The chemical analysis of the core bore (see Table I-1) again indicated primarily uranium with significant zirconium but with somewhat greater amounts of iron, silver, cadmium (in comparison with rod 5A at the bundle periphery), and some nickel.

According to the phase diagram^{I-5} for Fe_3O_4 and ZrO_2 (Figure I-28), Fe_3O_4 in the ceramic melt can be expected to lower the liquidus temperature and to form a low melting eutectic which freezes in the grain boundaries. Because UO_2 and ZrO_2 are miscible in both the liquid and solid states at elevated temperatures, it is probably reasonable to assume that the phase diagram in Figure I-28 applies in a general way to $(U,Zr)O_2$. A Fe_3O_4 content of about 5% (based on the M8B core bore) would tend to reduce the liquidus of the ceramic by about 30 K from the 2800 K minimum for mixtures of UO_2 and ZrO_2. Given that the composition of the $(U,Zr)O_2$ ceramic probably does not correspond to that for minimum melting in the system, the 30-K decrement can be ignored.

An example of UO_2 attack by molten metal (subsequently oxidized) on a fuel fragment near the bundle periphery is shown in Figure I-29.

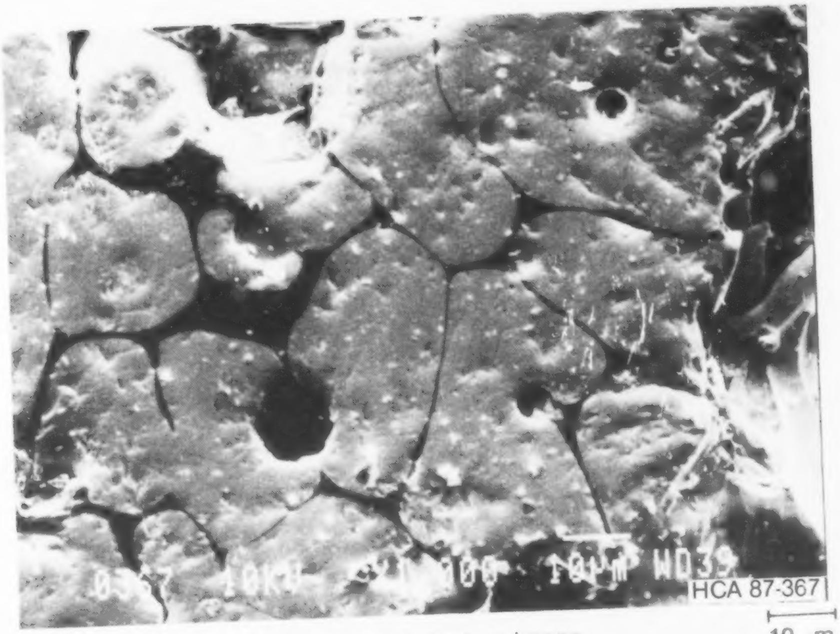
10KV X1,000 10μm WD39
HCA 87-367
10 μm

a. Secondary electron image

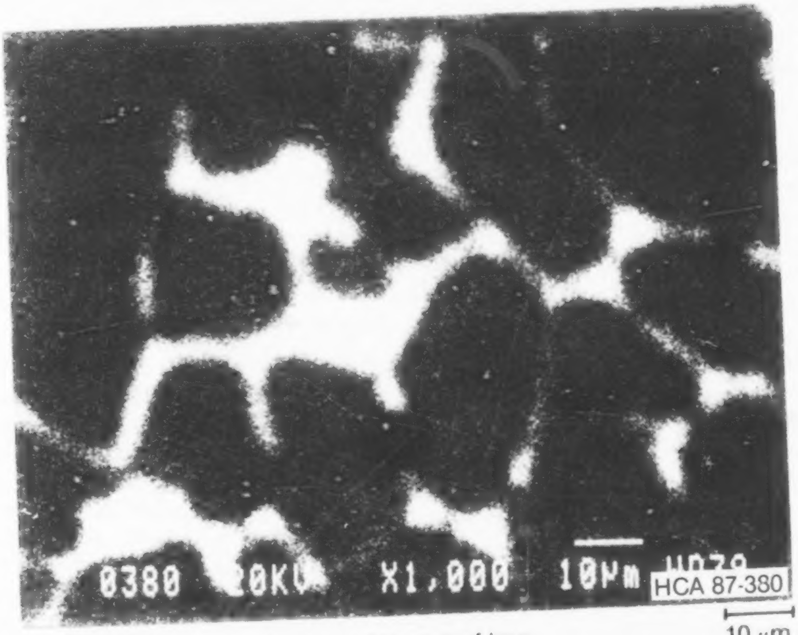
0380 20KV X1,000 10μm
HCA 87-380
10 μm

b. X-ray dot map of iron

Figure I-25. Secondary electron image and X-ray dot map showing wide grain boundaries filled with iron oxide in reacted region of fuel rod 5A at 0.54 m.

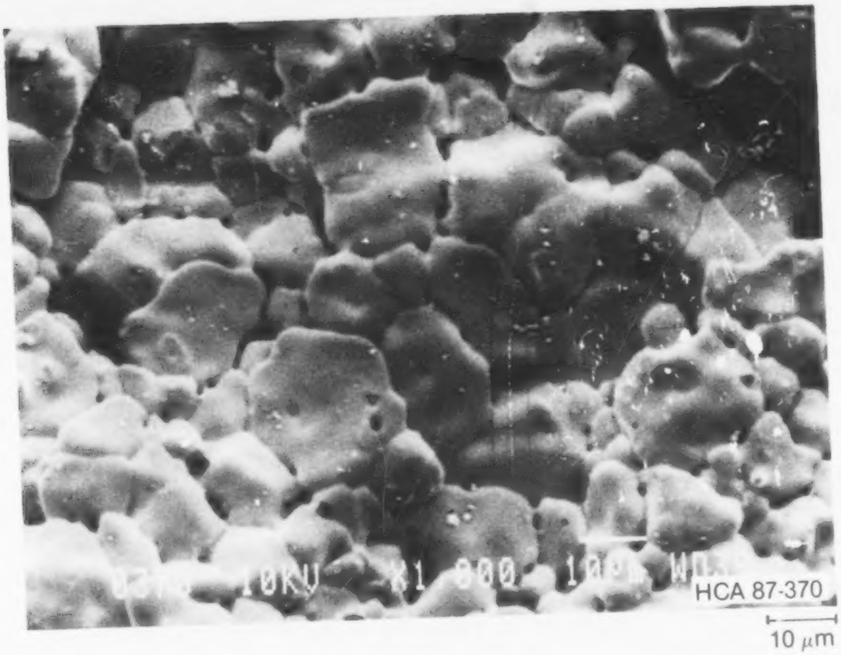
HCA 87-370
10 μm

Figure I-26. Secondary electron image showing fuel microstructure in unreacted region of fuel rod 5A at 0.54 m.

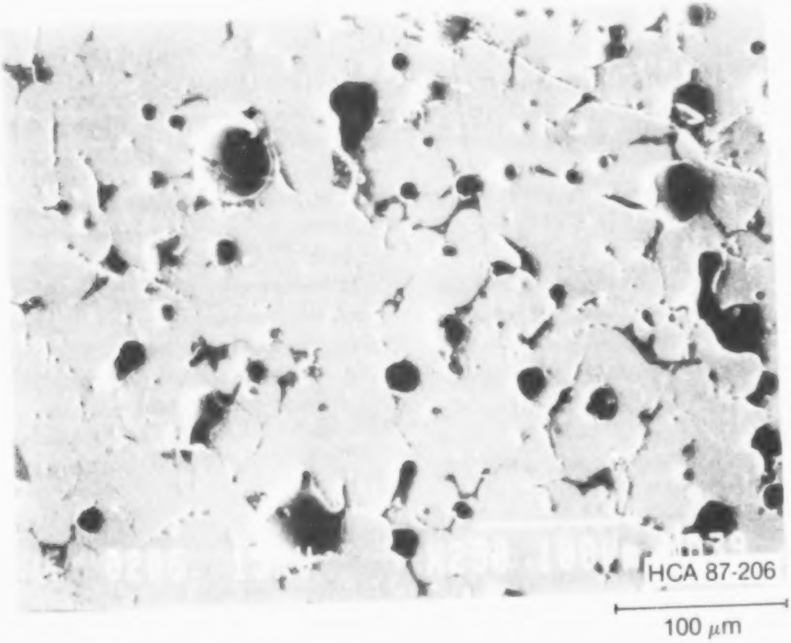
HCA 87-206
100 μm

Figure I-27. Secondary electron image showing microstructure of reacted fuel in the center of the bundle at 0.54 m.

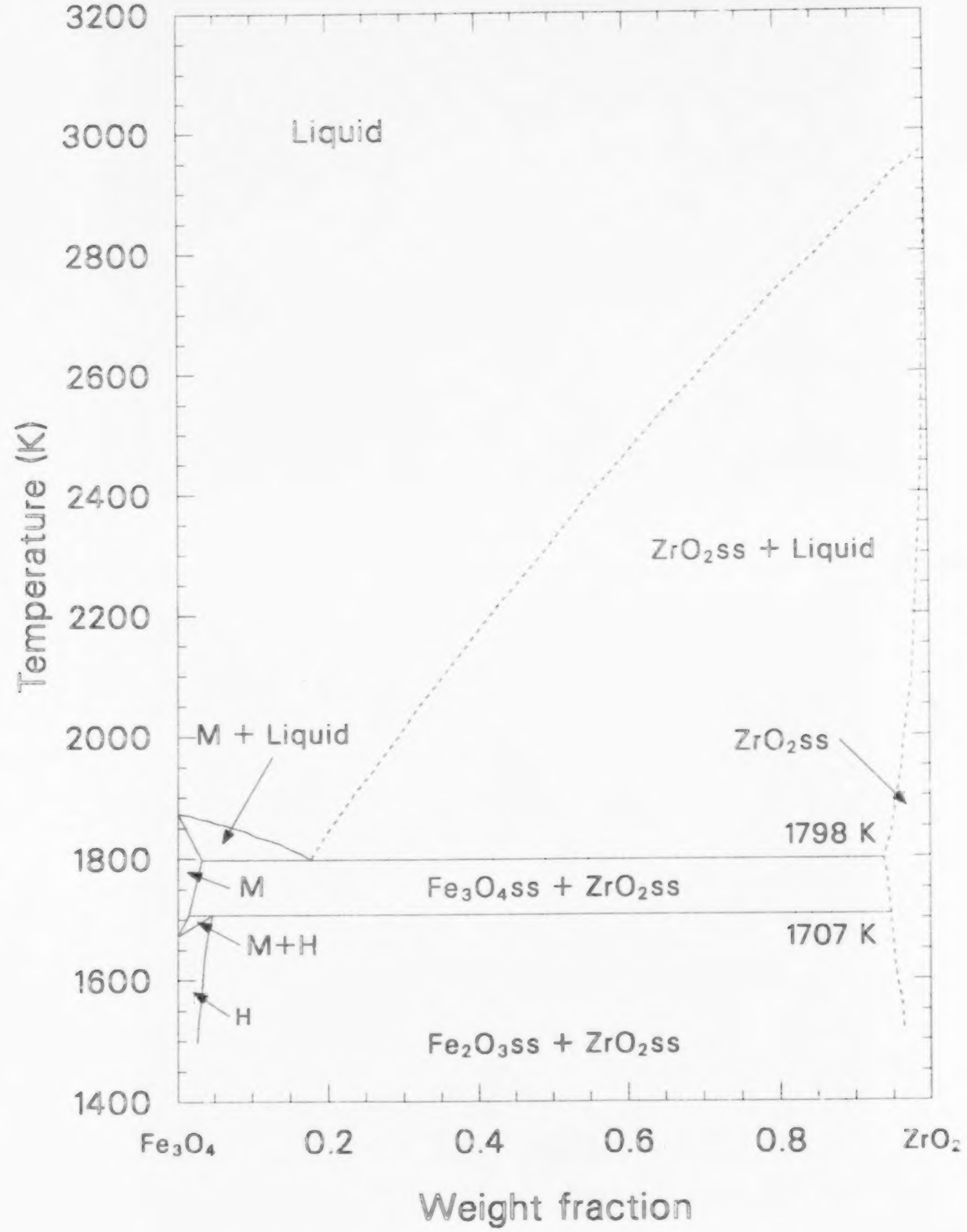

Figure I-28. Fe_3O_4—ZrO_2 phase diagram (Reference I-4).

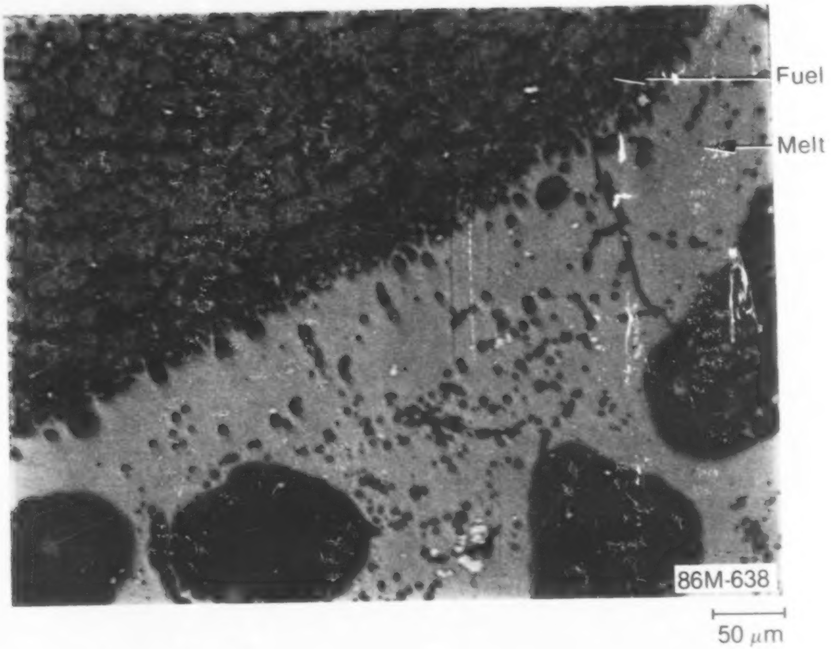

Figure I-29. Photomicrograph showing melt/fuel interaction at the bundle periphery, rod 6C, at 0.54 m.

In summary, the cross section of the bundle at the 0.54-m elevation contains molten ceramic $(U,Zr)O_2$ in the center of the bundle and partially liquefied fuel and unreacted fuel fragments near the bundle periphery. What little cladding and liner remained were fully oxidized, as were the metallic melts that had attacked the UO_2 fuel and the ZrO_2 insulation. Some control and structural materials were found to be remaining at this elevation. The flow area was somewhat greater than that of an intact bundle geometry. Peak temperatures are estimated to have exceeded 2800 K.

I-3.4 Bundle Cross Section at 0.39 m. The cross section at the 0.39-m elevation (Figure I-30) shows evidence of strong fuel dissolution in the central region of the bundle, with partially reacted and some unreacted fuel at the bundle periphery. All four control rods are missing, but portions of oxidized zircaloy guide tubing remain in two locations. Much of the zircaloy cladding and liner has melted, reacted with fuel and insulation, and relocated. The zircaloy remaining at this elevation (about 40%) was completely oxidized, with the exception of some metallic zircaloy interacting with insulation which is believed to have relocated to this region from higher in the bundle late in the transient. The flow area at this elevation is approximately equal to that in a cross section of the intact bundle.

The interior rods at this elevation all were at least partially dissolved as a result of molten metal-UO_2 interactions. Some rods are completely missing, and other rods are missing portions of the fuel. In addition, some ceramic melt has relocated into this cross section from above. Figure I-31 is a

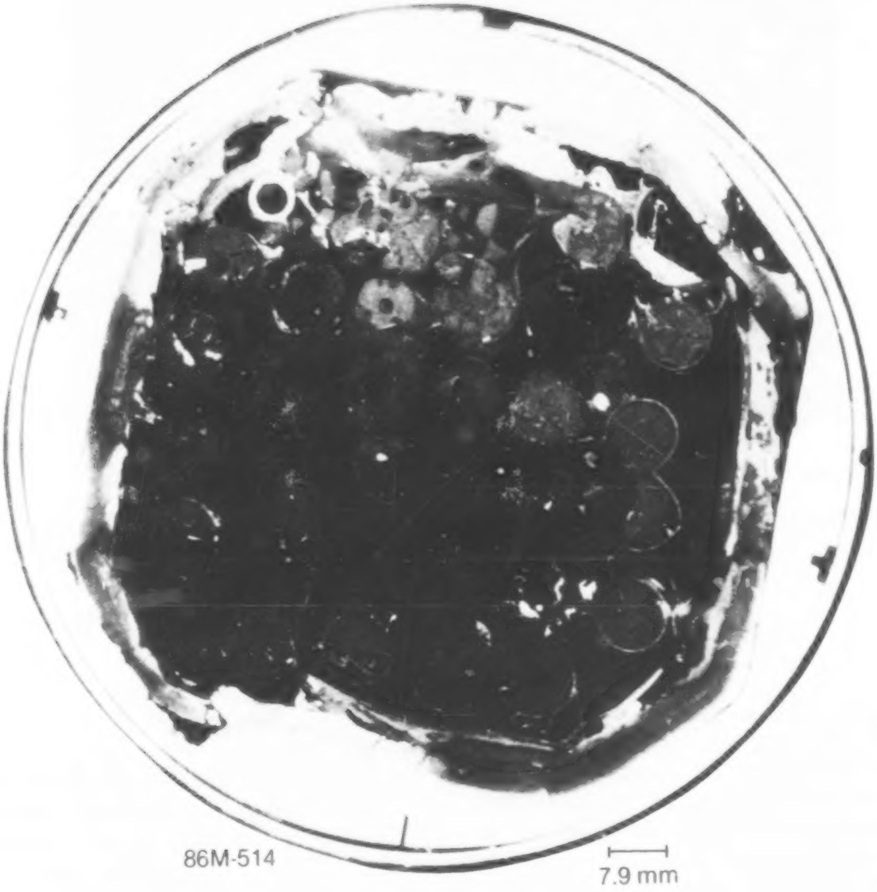
86M-514
7.9 mm

Figure I-30. SFD 1-4 bundle cross section at 0.39 m.

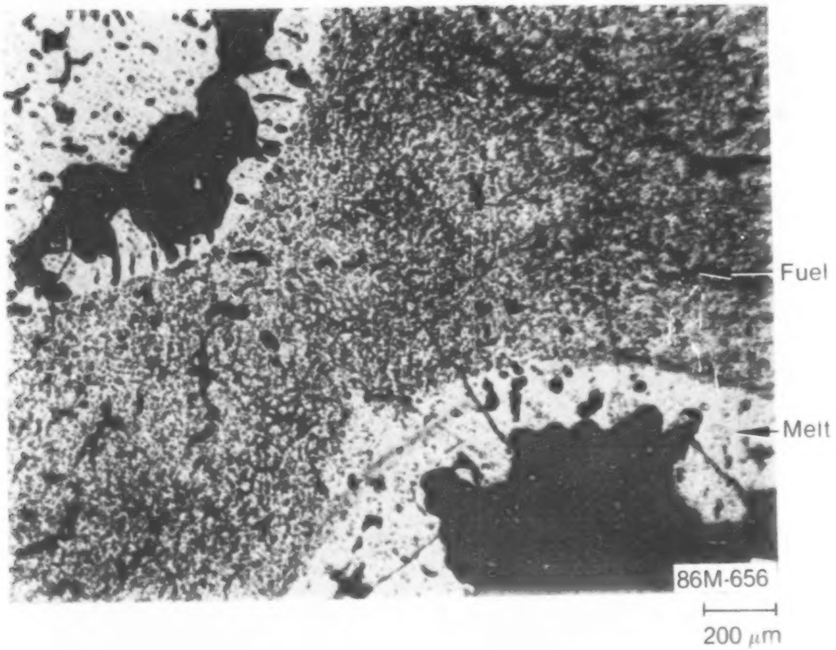

Figure I-31. Photomicrograph showing melt attack on fuel in rod 3B at 0.39 m.

photomicrograph that shows fuel in rod 3B under attack by a previously molten metal which subsequently oxidized. Part of rod 3C appears to have relocated away, and most of the remaining portion has been liquefied by interaction with a previously metallic melt. This interaction is displayed in a photomicrograph in Figure I-32. Examples of ceramic melts that have relocated into this cross section from above are shown in the photomicrographs in Figure I-33. Areas that were unaffected by the fuel etch are believed to be previously molten $(U,Zr)O_2$, which has a minimum melting temperature of 2800 K. Areas that were affected by the etch are believed to contain impurities or to be incompletely oxidized and have somewhat lower melting temperatures.

Photomicrographs of two regions of rod 6B, that is on the periphery of the fuel bundle, are presented in Figures I-34 and I-35. The microstructure in Figure I-34 is from the center of the pellet and appears to represent previously molten ceramic containing large pores and metal ingots. Figure I-35 is from a region of the pellet facing away from the center of the bundle and displays fuel grains with diameters up to 40 μm and porosity on the grain boundaries. A core bore removed from the fuel pellet of rod 6B indicated predominantly uranium, with about 5% zirconium and smaller amounts of iron, nickel, indium, cadmium, and silver. The melting point of the ceramic material in position 6B is probably at least 2800 K, given the small material additions to the UO_2.

In summary, the cross section of the bundle at the 0.39-m elevation is similar to the cross section at the 0.54-m elevation, with molten ceramic $(U,Zr)O_2$ in the center of the bundle and partially liquefied fuel and unreacted fuel fragments near the bundle periphery. Somewhat more zircaloy remained in this cross section than at 0.54 m; but, again, the remaining zircaloy was totally oxidized except for some metallic zircaloy that had relocated from above and had begun to interact with the insulation. Also at this elevation, some ceramic melt seemed to have relocated from above. Smaller amounts of control rod and structural materials were found in the one core bore sample at this elevation than in the two samples from 0.54 m. The net result of material relocation to and from this elevation was a flow area roughly equivalent to that of an intact cross section. Peak temperatures at this elevation were at least 2800 K.

I-3.5 Bundle Cross Section at 0.25 m. As shown in Figures I-36 and I-37, the fuel rods,

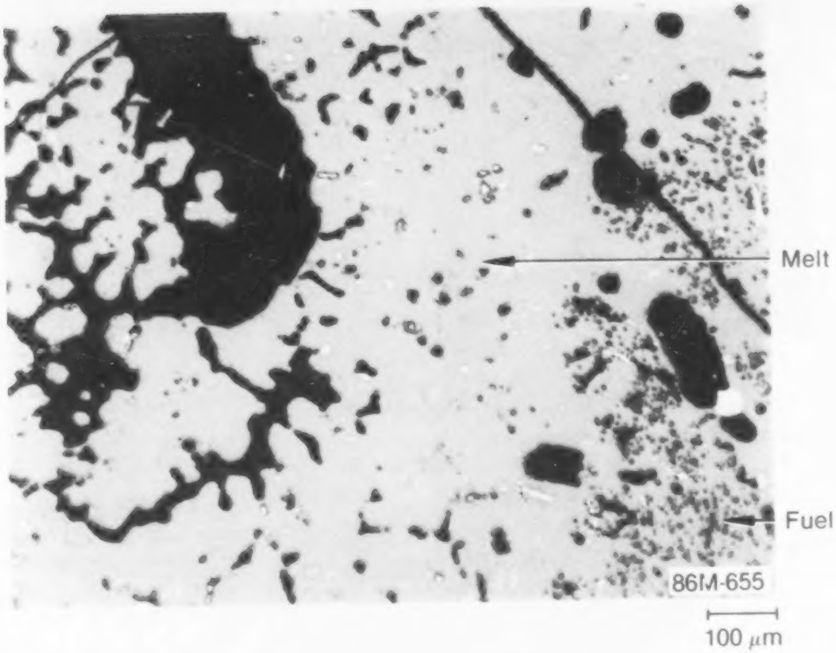
Melt
Fuel
86M-655
100 μm

Figure I-32. Photomicrograph showing melt interaction with fuel in rod 3C at 0.39 m.

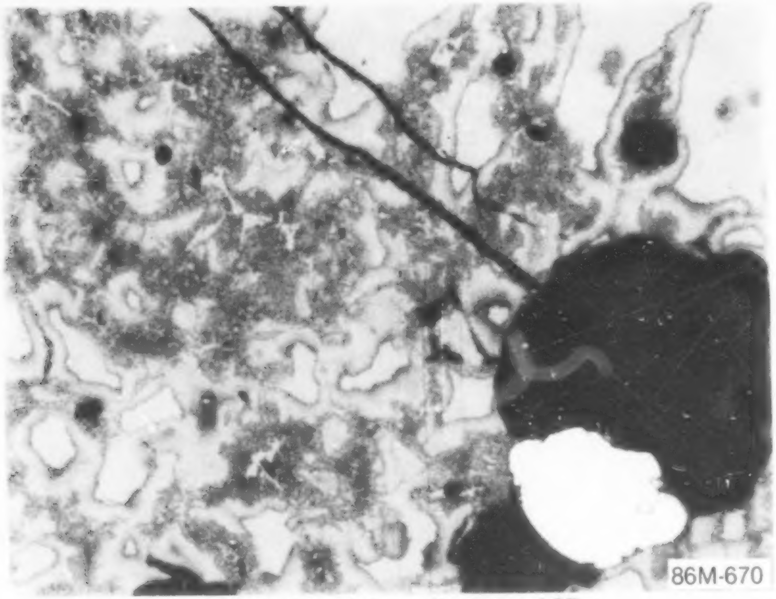
86M-670
50 μm

a. Affected by etch, melt near rod 6D

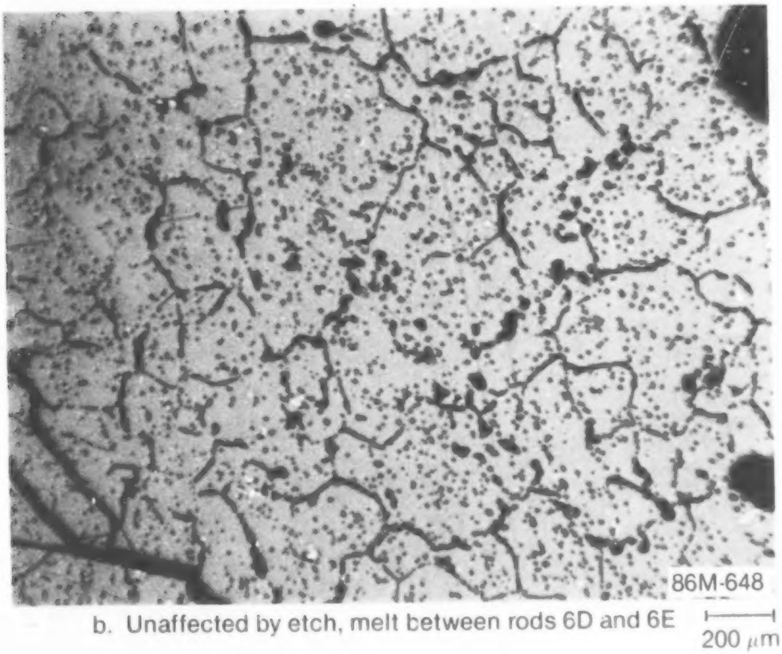
86M-648
200 μm

b. Unaffected by etch, melt between rods 6D and 6E

Figure I-33. Photomicrographs showing effects of fuel etch on ceramic melts at 0.39 m.

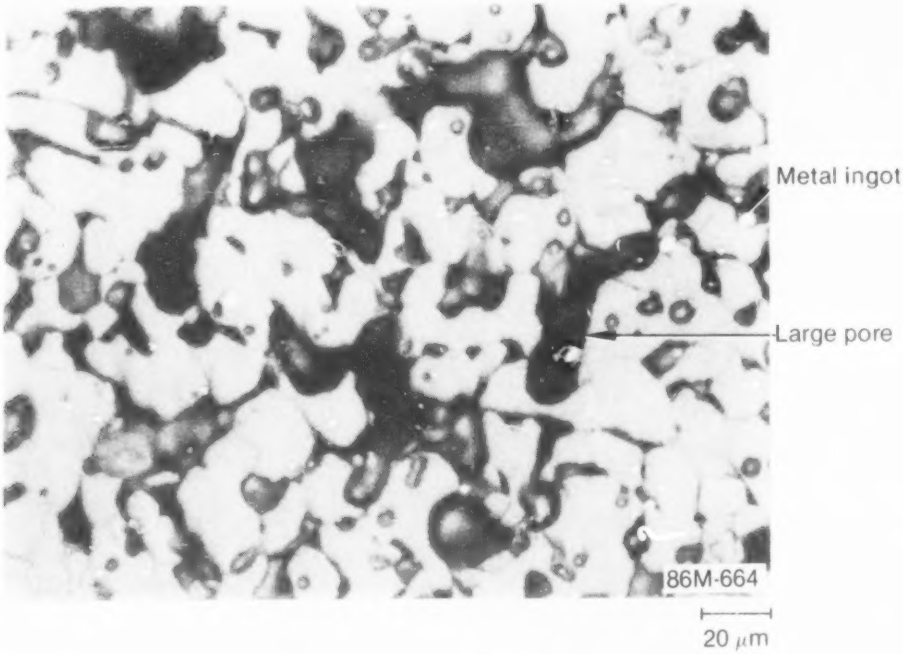
Metal ingot
Large pore
86M-664
20 μm

Figure I-34. Photomicrograph showing microstructure of reacted/melted fuel in center of rod 6B at 0.39 m.

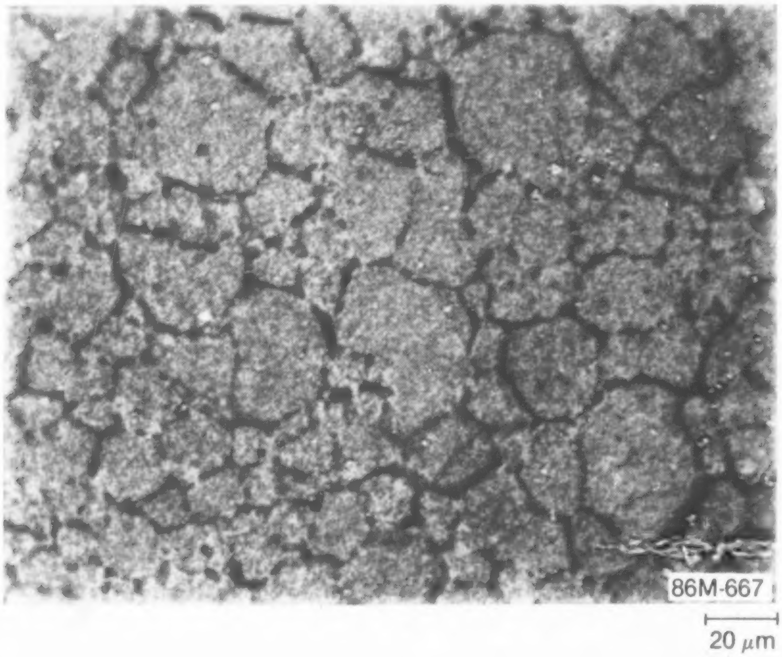
86M-667
20 μm

Figure I-35. Photomicrograph showing fuel microstructure in unreacted portion of rod 6B at 0.39 m.

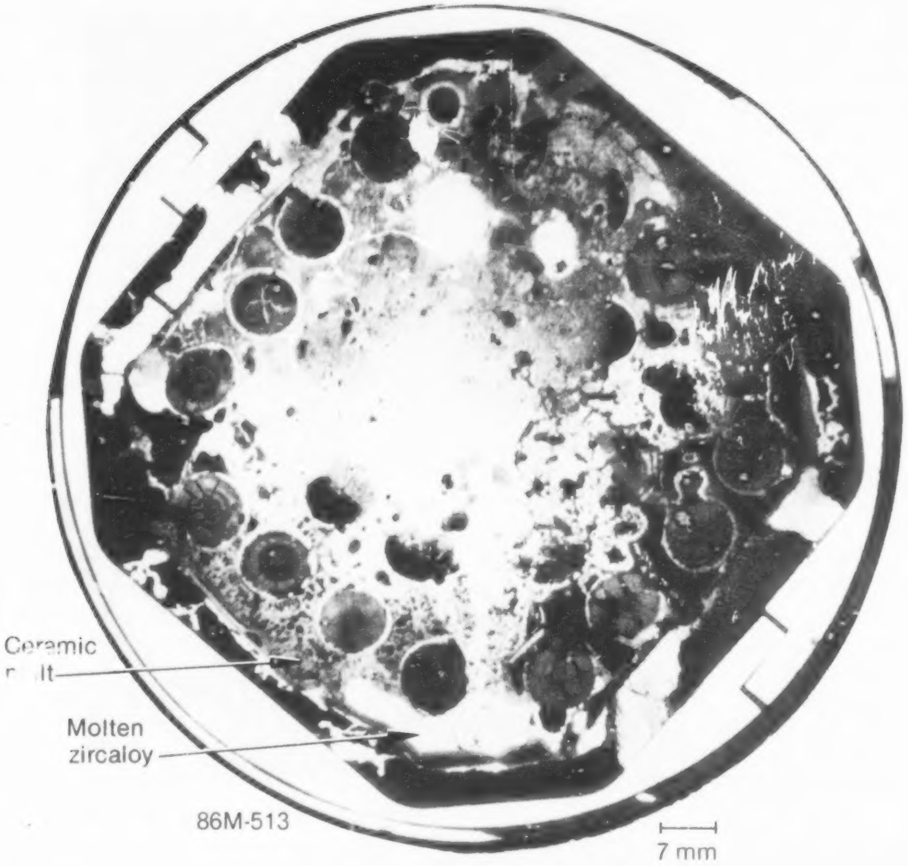
Ceramic melt
Molten zircaloy
86M-513
7 mm

Figure I-36. SFD 1-4 bundle cross section at 0.25 m.

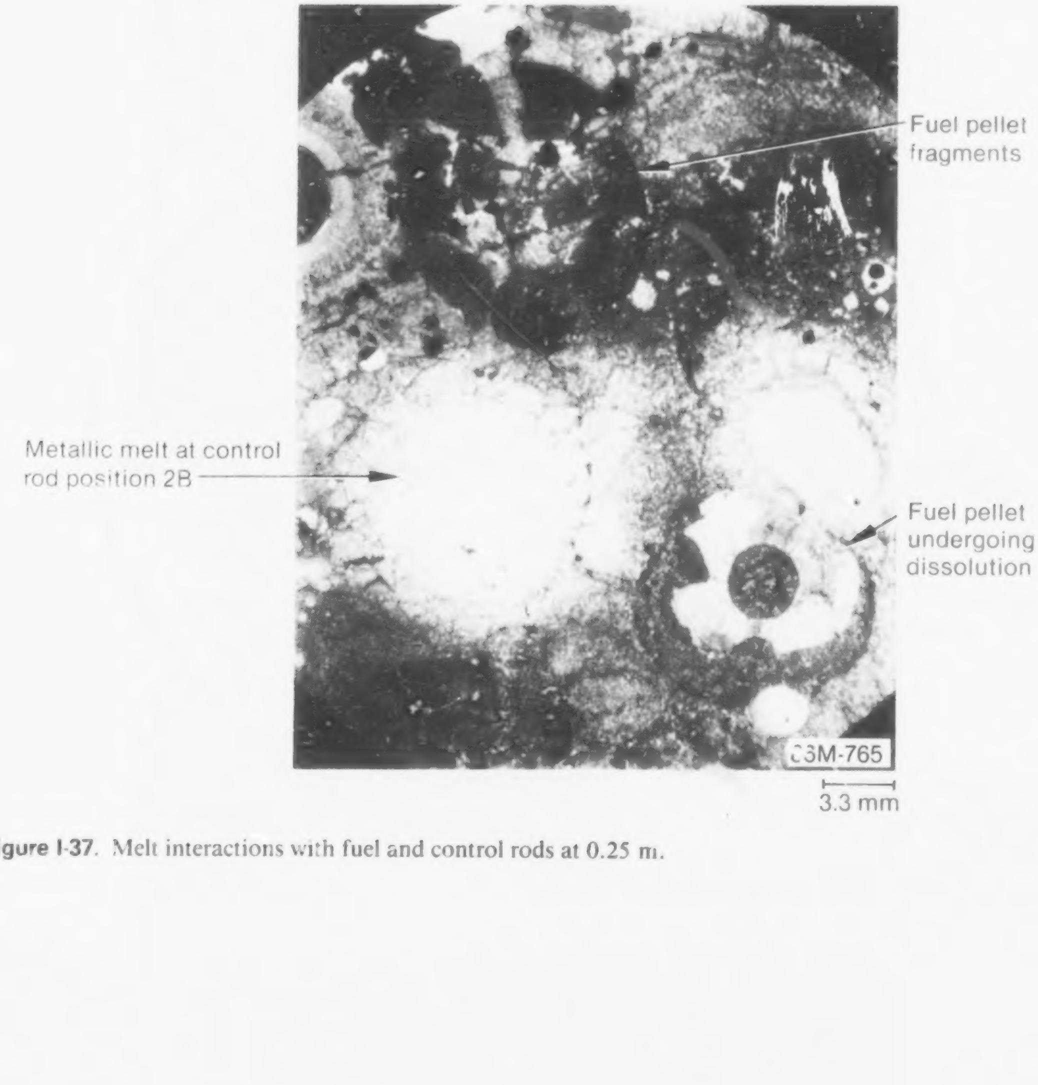
Fuel pellet fragments
Metallic melt at control rod position 2B
Fuel pellet undergoing dissolution
83M-765
3.3 mm

Figure I-37. Melt interactions with fuel and control rods at 0.25 m.

insulation, and liner at the 0.25-m elevation have undergone strong attack by metallic melt. Fourteen of the fuel rod positions contain damaged but recognizable fuel rod cross sections. Where fuel rod cladding and liner exist, they are fully oxidized. Ten other positions contain fuel pieces and/or parts of oxidized cladding, and in four positions no recognizable fuel rod pieces remain in the photograph in Figure I-36. All four control rods are missing, and there is evidence remaining of metallic melt in two of the four control rod positions [2B (see Figure I-37) and 2E]. Both metallic and ceramic melts have relocated to this elevation, resulting in a 70% reduction in the flow area relative to the intact bundle flow area.

As a result of melt interaction with the fuel rods, a heterogeneous melt has formed over the central portion of the bundle cross section that contains both metallic and ceramic components. A ceramic-appearing melt between rods 2F, 3F, 4F, and the shroud inner liner did not react with the oxidized cladding and liner. However, the chemically aggressive melt in the center of the cross section initially contained metallic zircaloy which dissolved UO_2 and ZrO_2. The ceramic portions of this melt contain uranium, zirconium, and oxygen. Elemental composition results from the SEM indicate that the ceramic portion of the melt contains uranium in amounts that vary from about 15 to 77 at%, ignoring the oxygen content. Results shown in Table I-1 of the elemental analysis of two samples removed from the melt in this cross section indicate uranium contents in the range of 11 to 38 at%. The minimum melting point for solutions of UO_2 and ZrO_2, termed $(U,Zr)O_2$, is 2800 K.

The microstructure of a melt that is principally a ceramic $(U,Zr)O_2$ phase with small metallic inclusions is shown in the SEM photomicrograph in Figure I-38. Point elemental analysis of the metallic inclusions indicate that they are primarily zirconium with, in some cases, tin from the zircaloy and, in other cases, iron, nickel, and chromium from the stainless steel. In comparison, as shown in Figure I-39, the microstructure of a melt in which the ceramic phase is less dominant exhibits a more complex structure. Several metallic phases make up a large portion of the melt, along with some undissolved UO_2 particles. The metallic phases are quite variable in composition but generally contain principally zirconium, iron, nickel, and chromium, with smaller amounts of tin, silver, and indium.

In the vicinity of the 2B control rod position, SEM investigations revealed the presence primarily of a metallic melt of zirconium, iron, nickel, chromium, and tin that contained an intimate mixture of silver and UO_2. This microstructure is displayed in Figure I-40.

The ZrO_2 in the cladding of rod 1C (Figure I-41) exhibits microstructural evidence of the cubic-to-tetragonal eutectoid transformation at 1770 K (see Zr-O phase diagram, Figure I-15), indicating that fuel rod temperatures were at least this high at the bundle periphery. The rounded cavity in the oxidized cladding may be the result of cladding melting prior to oxidation or eutectic reaction with metallic zirconium (since relocated metallic melt was present in this area) and drainage of the melt at temperatures in excess of 2170 K. Fuel that did not interact with the melt appears to be fractured at grain boundaries and to have a grain size of about 20 μm, as shown in Figure I-42.

The inner liner remaining at this elevation is completely oxidized. The interaction of metallic melt with the oxidized liner and with the ZrO_2 insulation is shown in Figure I-43. The metallic zircaloy relocated from above after oxidation at the 0.25-m elevation had taken place. The saddle shows an equiaxed α-zircaloy microstructure (Figure I-44) that has a temperature range from 920 to 1105 K and contains hydrides [evaluated metallographically^{I-6} at a level of about 150 ppm (Figure I-45)]. This is the highest level of hydriding in the bundle. Measurements of hydriding in the saddle as a function of elevation are presented in Table I-5. The general lack of zircaloy melting, combined with the total conversion to ZrO_2 in structures originally present at the 0.25-m elevation, suggests that temperatures were between 1900 to 2200 K prior to relocation of molten debris from above.

In summary, the bundle cross section at the 0.25-m elevation experienced an influx of metallic and ceramic melts from above and a depletion of control materials, zircaloy, and structural materials. The net accumulation of materials caused a 70% reduction in flow area at this elevation relative to intact bundle geometry. The metallic melts arrived after complete oxidation of the zircaloy present at this elevation and caused considerable dissolution of ZrO_2 and UO_2. It is estimated that temperatures were between 1900 and 2200 K before melts of temperatures up to 2800 K relocated to this elevation. Some control materials were trapped in this high-temperature zone.

I-3.6 Bundle Cross Section at 0.17 m. The photomacrograph of the cross section at the 0.17-elevation in Figure I-46 shows that all but one of

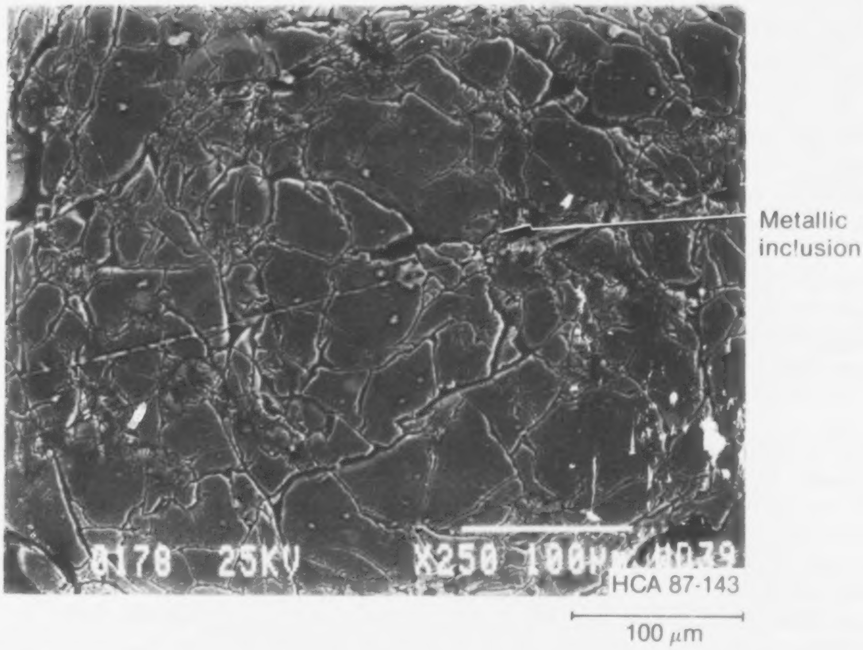
Metallic inclusion
0178 25KV X250 100µm WD39
HCA 87-143
100 µm

Figure I-38. SEM photomicrograph showing ceramic melt with metallic inclusions at 0.25 m.

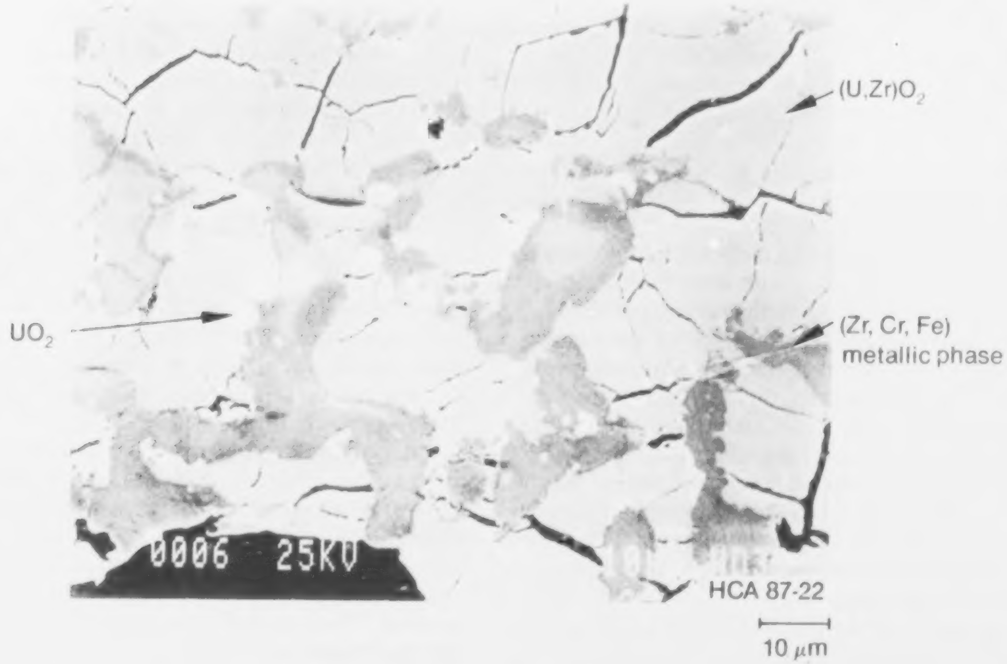
(U,Zr)O$_2$
UO$_2$
(Zr, Cr, Fe) metallic phase
0006 25KV
HCA 87-22
10 µm

Figure I-39. SEM photomicrograph showing ceramic and metallic phases in melt at 0.25 m.

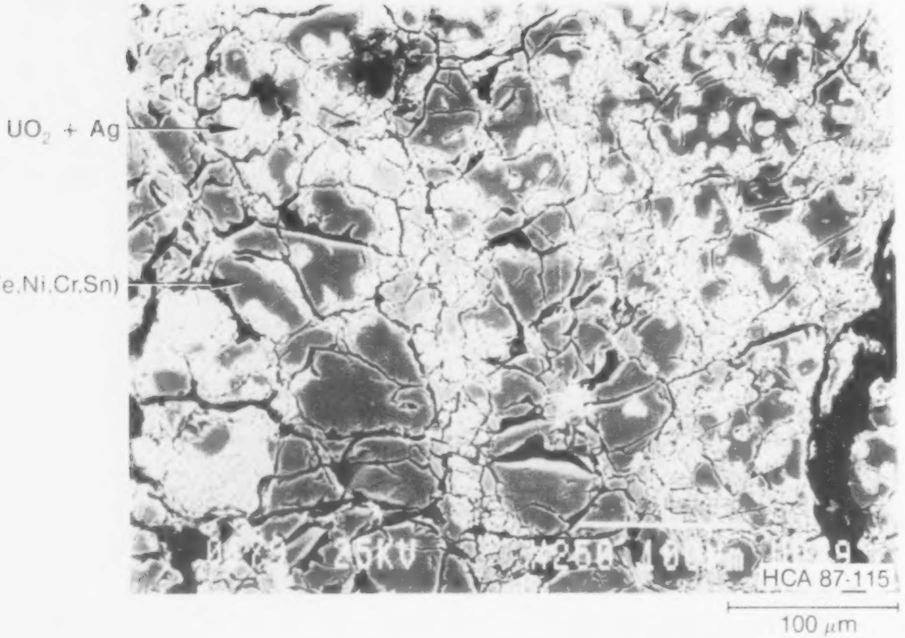
UO_2 + Ag
(Zr,Fe,Ni,Cr,Sn)
25KV
HCA 87-115
100 μm

Figure I-40. SEM photomicrograph at control rod position 2B at 0.25 m showing mixture of UO_2 and silver.

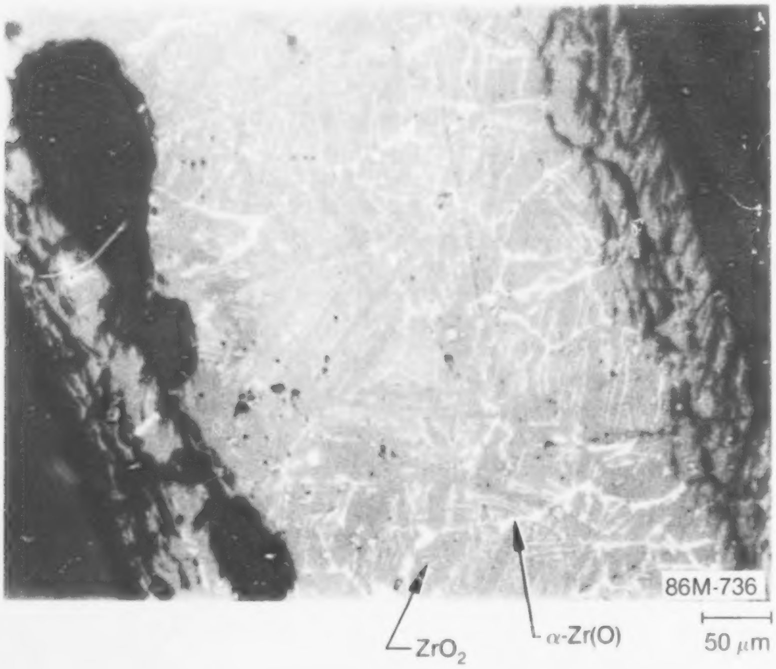
86M-736
ZrO_2
α-Zr(O)
50 μm

Figure I-41. Photomicrograph showing eutectoid transformation at 1770 K in ZrO_2 in the oxidized cladding of fuel rod 1C at the periphery of the bundle at 0.25 m.

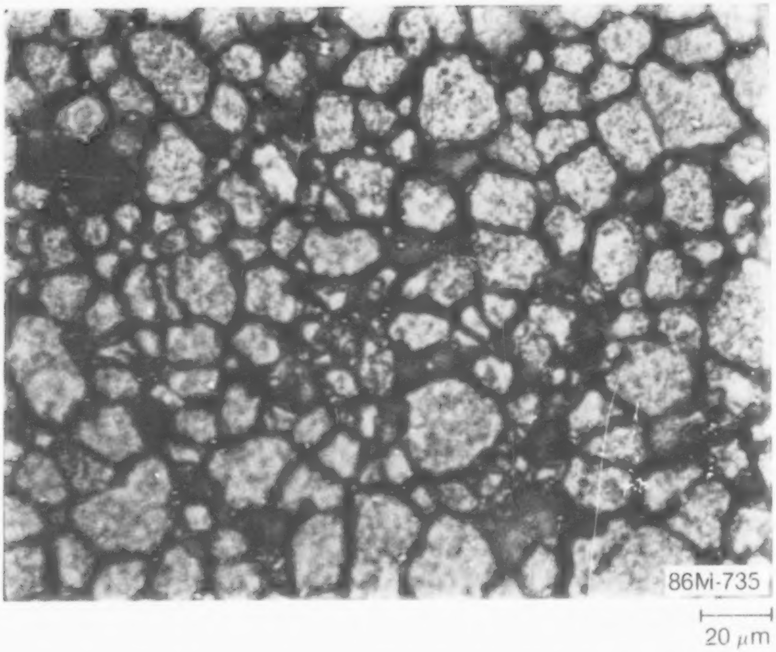
86M-735
20 μm

Figure I-42. Photomicrograph showing fuel unreacted with melt and with grain boundary shattering at 0.25 m.

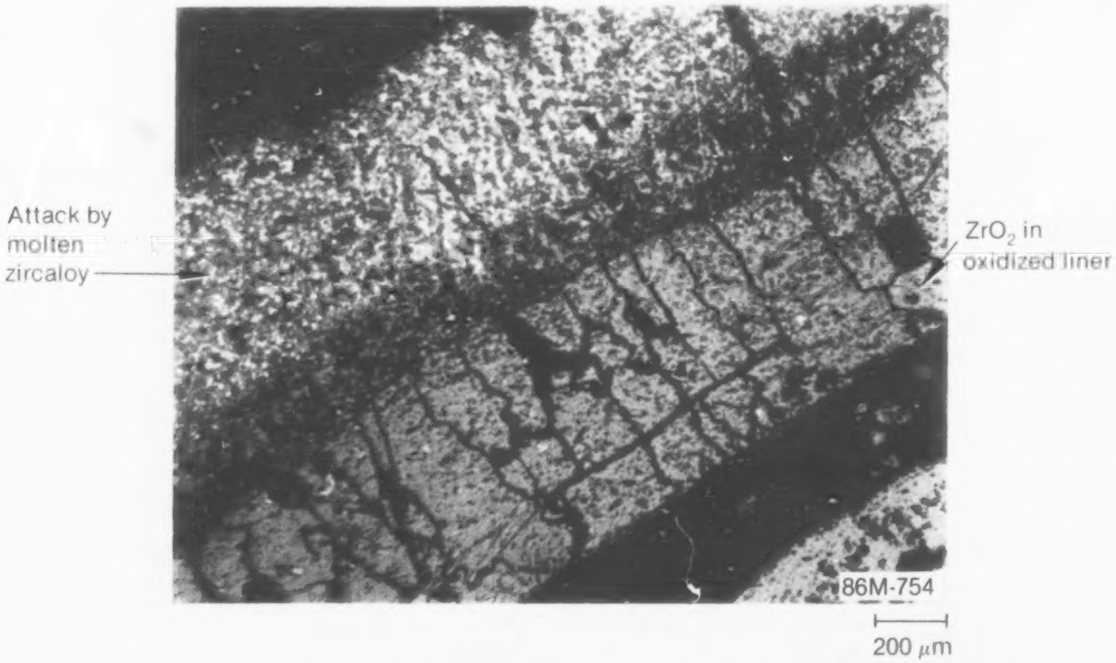
Attack by molten zircaloy
ZrO_2 in oxidized liner
86M-754
200 μm

Figure I-43. Photomicrograph showing the attack of molten zircaloy on ZrO_2 in the oxidized liner at 0.25 m.

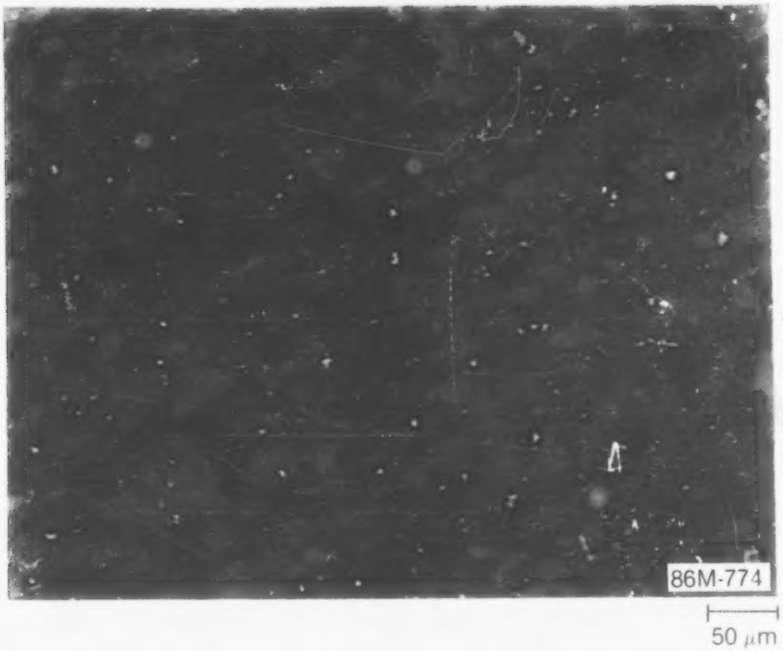
86M-774
50 μm

Zr etch, polarized light

Figure I-44. Photomicrograph showing the equiaxed α-zircaloy microstructure in the saddle at 0.25 m.

86M-773
50 μm

Figure I-45. Photomicrograph showing the hydriding (about 150 ppm) in the saddle at 0.25 m.

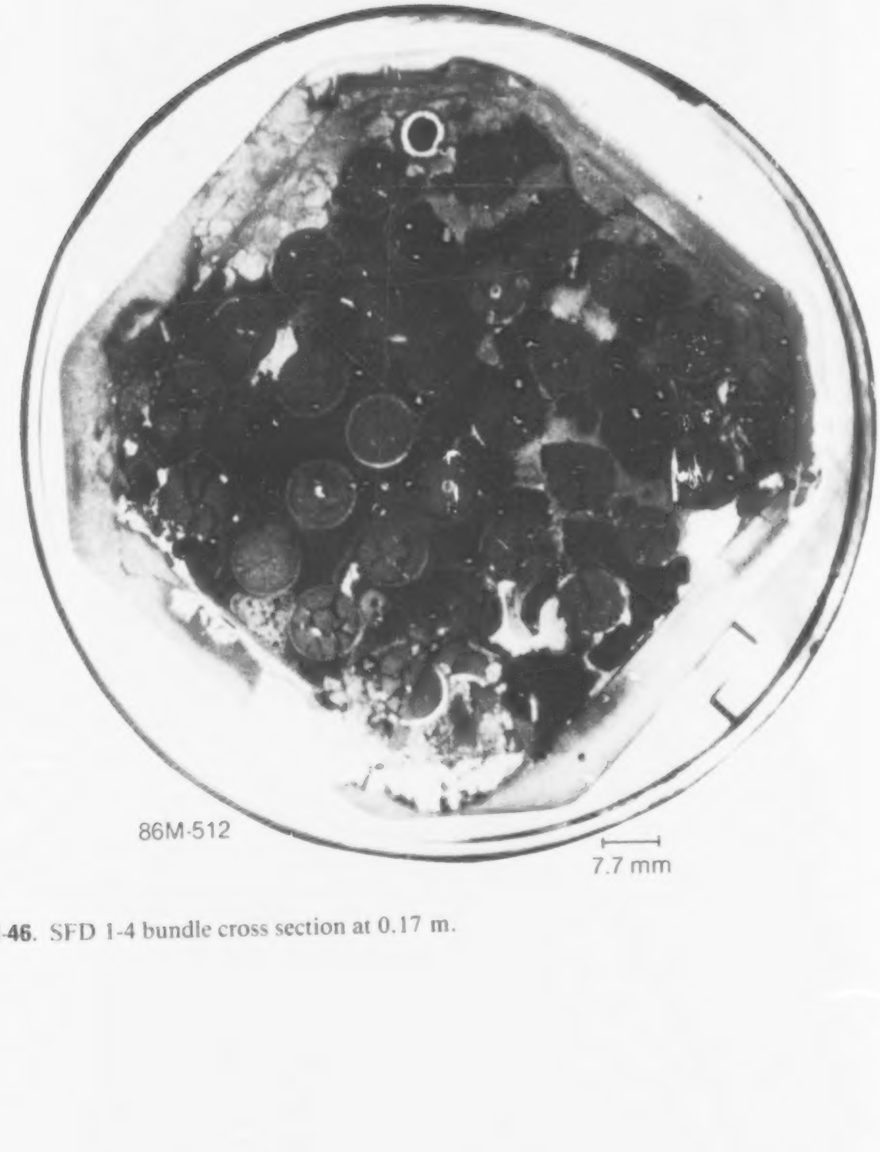
86M-512
7.7 mm

Figure I-46. SFD 1-4 bundle cross section at 0.17 m.

Table I-5. Hydriding in the zirconium saddle

Elevation (m)	Hydride Concentration (ppm)
0.85	—
0.74	<25
0.54	50
0.39	75
0.25	150
0.17	100
0.08	25
0.02	25
−0.09	25

the 28 fuel rods are present in roughly their as-assembled locations in the bundle, and fuel fragments and pieces of cladding from the missing rod are visible in the vicinity of its initial location (6E). The four control rods are absent, although oxidized shells of the zircaloy guide tubes remain at two positions (2B and 2E). Portions of the liner and of the cladding have relocated from this elevation. With one or two exceptions, the remaining zircaloy is fully oxidized. Metallic and ceramic melts have relocated to this elevation. The metallic melts have attacked ZrO_2 in the insulation and oxidized cladding and liner, but no significant dissolution of fuel has taken place at this elevation. The accumulation of melts has more than compensated for the loss of the control rods and some liner and cladding material so that the flow area at this elevation has been reduced by approximately 30% relative to that of an intact bundle geometry.

Two examples of metallic melts found at this elevation are described. One of these melts, shown in Figure I-47, was located primarily at the periphery of the bundle and attacked the insulation, oxidized liner, and oxidized cladding of peripheral rods. This melt was examined by SEM/WDS microelemental analysis and found to contain predominantly zirconium with tin and trace amounts (generally less than 0.5 wt.%) of uranium, iron, nickel, chromium, and silver. The oxygen content was measured to be very low, about 0.1 wt.%. This material appears to be basically zircaloy that relocated after most of the oxidation had taken place at this elevation. The relatively thin oxide on the surfaces of the melt indicates that this material arrived at this elevation rather late in the transient.

Another primarily metallic melt observed at this elevation was found between rods in the bundle. This melt is actually a mixed melt containing both ceramic and metallic components and having a gray appearance. An example of this melt adjacent to rods 5C, 6B, and 6C is shown in Figure I-48. This melt reacted with oxidized cladding on rod 6C, as shown in the photomicrograph of Figure I-49. A ceramic phase can be seen in the microstructure, indicating that the oxygen content of the melt is fairly high. A backscattered electron image from a sample of this melt, shown in Figure I-50(a), indicates that several metallic phases, as well as ceramic materials, are present. X-ray dot maps used to interpret the structure are presented in Figures I-50(b) through (k). One of the keys to interpreting the structure is the UO_2 particles observable in Figures I-50(a) and I-50(b). The dark, elongated particles at the bottom of Figure I-50(a) contain zirconium and uranium and about the same level of oxygen as the UO_2 particles, indicating that these particles are $(U,Zr)O_2$. The broad gray phase in Figure I-50(a) consists of the transition metals (iron, nickel, and chromium) and zirconium, uranium, and tin and is low in oxygen. The x-ray dot map for silver [Figure I-50(i)] indicates that this element is present primarily as silver-rich particles in the gray metallic region but also it is distributed at a lower concentration level throughout this region. Cadmium appears to be associated with silver, and indium is both concentrated in the silver-rich particles and distributed throughout the metallic region. This melt clearly relocated to this elevation after cladding oxidation was complete, and the surface of the melt shows evidence of a thin oxide (Figure I-48).

Multiple oxide layers were found within metallic melts low in the bundle, indicating continual oxidation after relocation, multiple relocation events, and/or relocation of oxidized cladding pieces into metallic melt. The thicknesses of these multiple oxide layers suggest relocation events at 5- to 60-s intervals. A photomicrograph demonstrating this effect is presented in Figure I-51.

Ceramic melt that relocated to this elevation is visible in Figure I-52(a). The photomacrograph in Figure I-52(a) shows that this melt arrived after oxidation was complete and that it did not interact with the oxidized cladding of rods 3F and 4F or with the adjacent oxidized liner. The photomicrograph in Figure I-52(b) shows an unidentified, lighter-colored phase within the gray colored matrix brought out by an etch normally used for zircaloy.

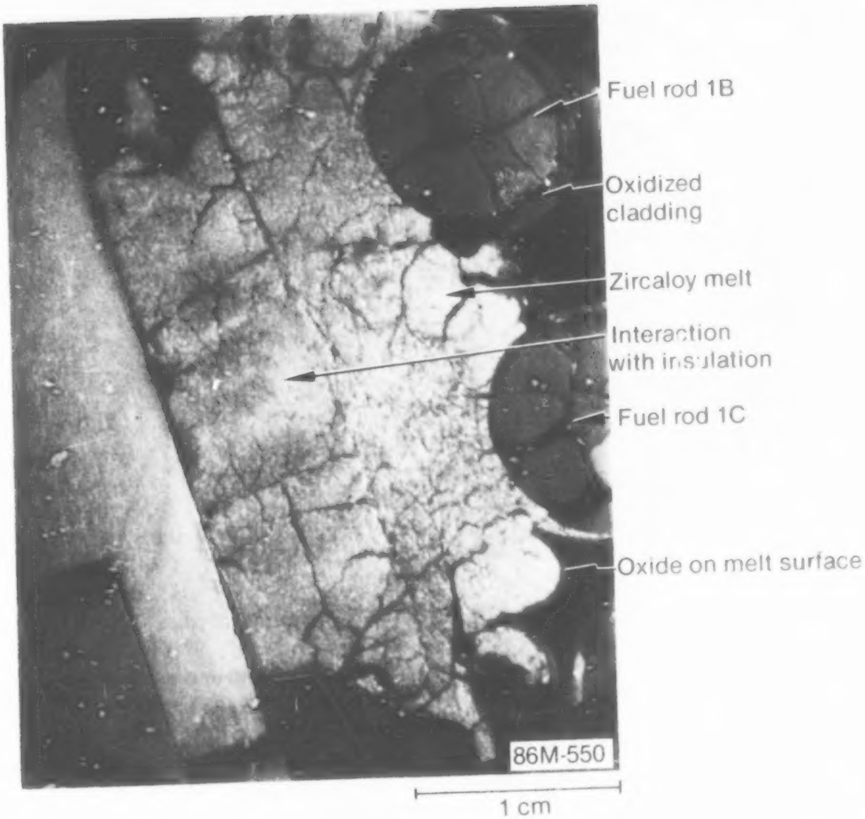
Fuel rod 1B
Oxidized cladding
Zircaloy melt
Interaction with insulation
Fuel rod 1C
Oxide on melt surface
86M-550
1 cm

Figure I-47. Photomacrograph showing molten zircaloy attack on oxidized cladding and bundle insulation, locations 1B and 1C, at 0.17 m.

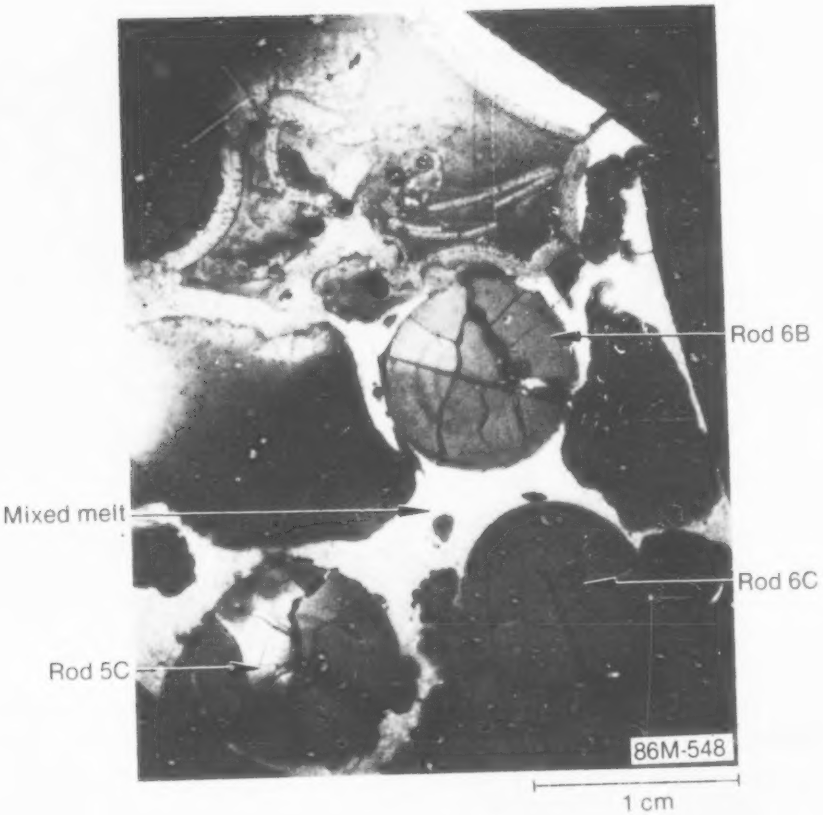
Rod 6B
Mixed melt
Rod 6C
Rod 5C
86M-548
1 cm

Figure I-48. Photomacrograph showing metallic melt between rods 5C, 6B, and 6C at 0.17 m.

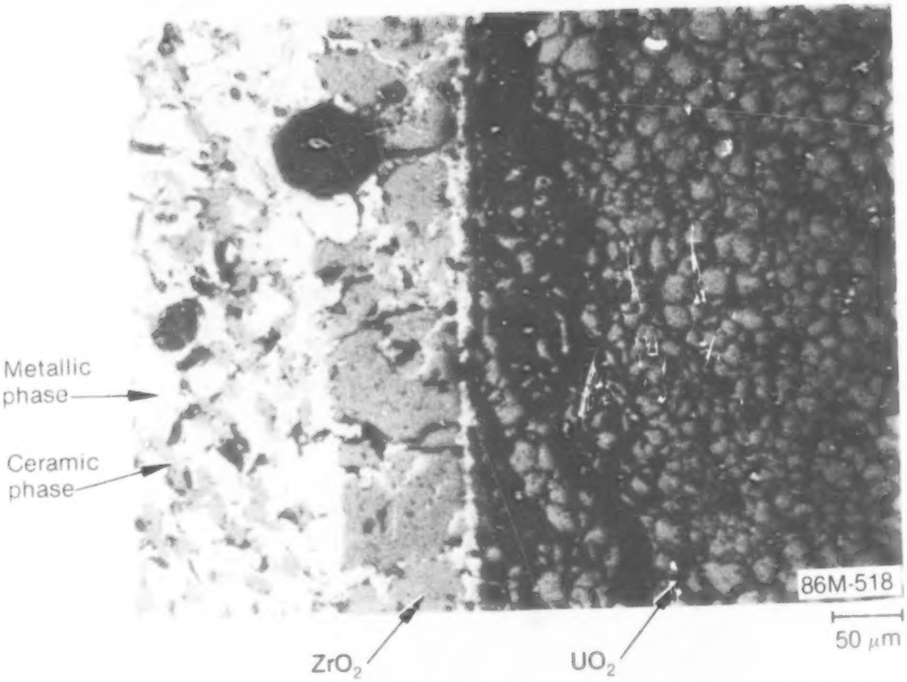
Metallic phase
Ceramic phase
ZrO_2
UO_2
86M-518
50 μm

Figure I-49. Photomicrograph of metallic melt attacking oxidized cladding on rod 6C at 0.17 m.

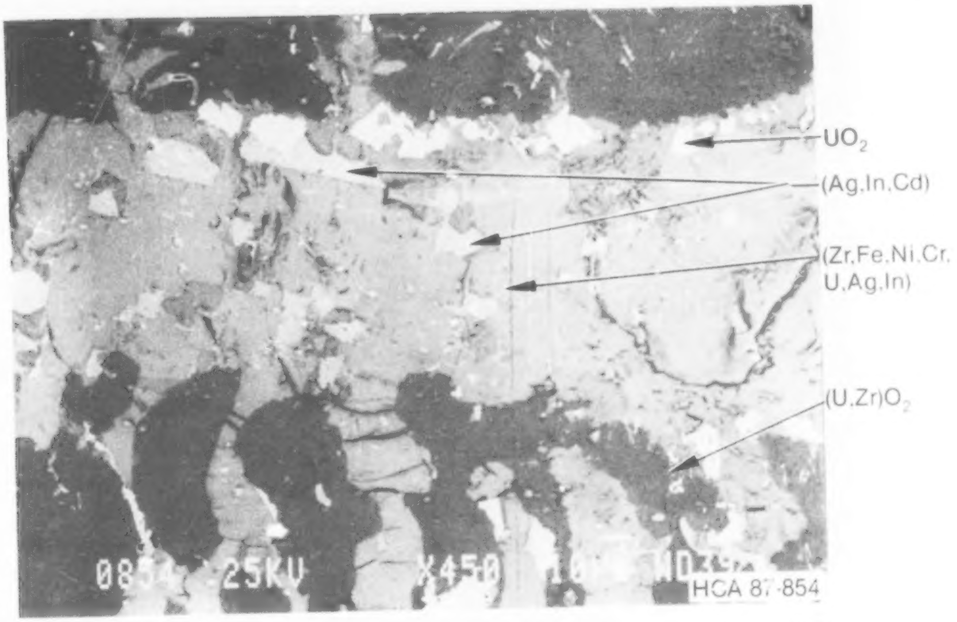
UO$_2$
(Ag,In,Cd)
(Zr,Fe,Ni,Cr,
U,Ag,In)
(U,Zr)O$_2$
0854 25KU X450
HCA 87-854

a. Backscattered electron image

10 μm

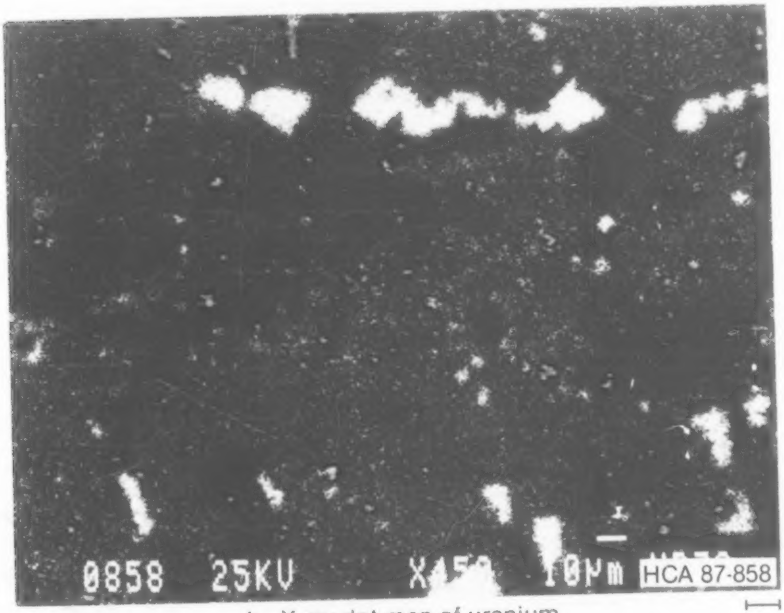
0858 25KU X450 10μm
HCA 87-858

b. X-ray dot map of uranium

10 μm

Figure I-50. Backscattered electron image and x-ray dot maps of a sample of metallic melt between rods 5C, 6B, and 6C at 0.17 m.

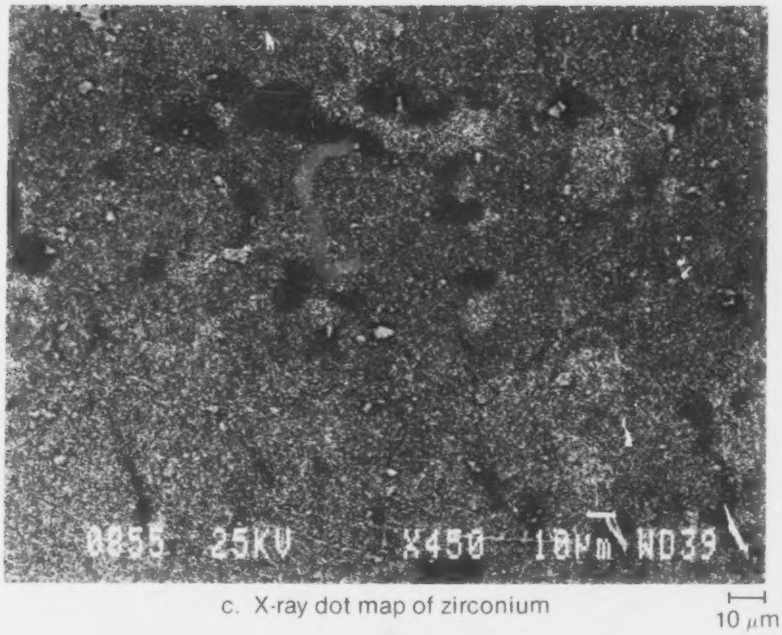
0855 25KV X450 10μm WD39
10 μm

c. X-ray dot map of zirconium

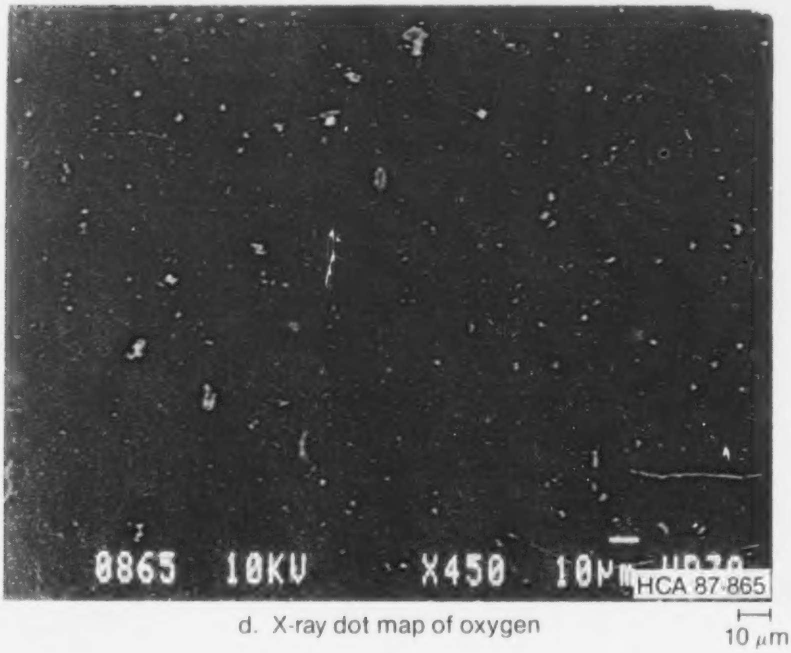
0865 10KV X450 10μm
HCA 87-865
10 μm

d. X-ray dot map of oxygen

Figure I-50. (continued).

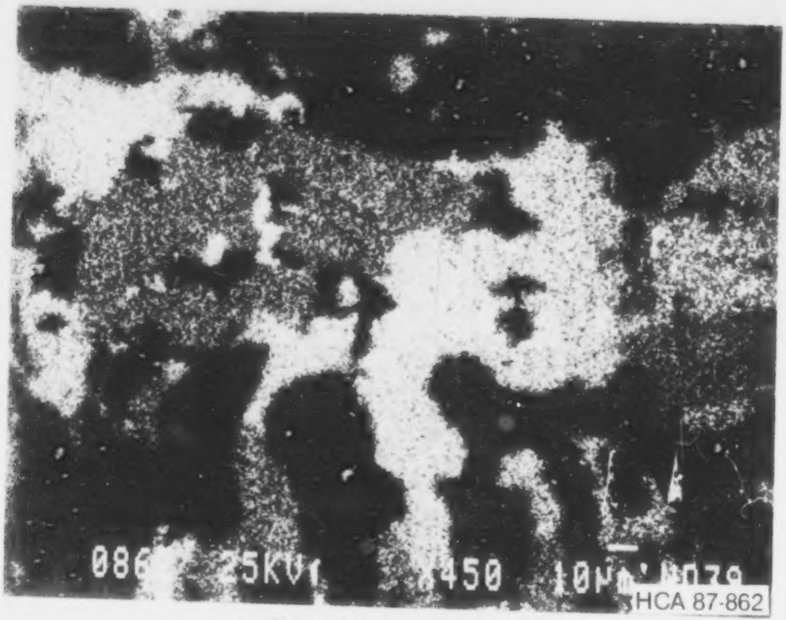
086
25KV
450
10µm
HCA 87-862

e. X-ray dot map of nickel

10 μm

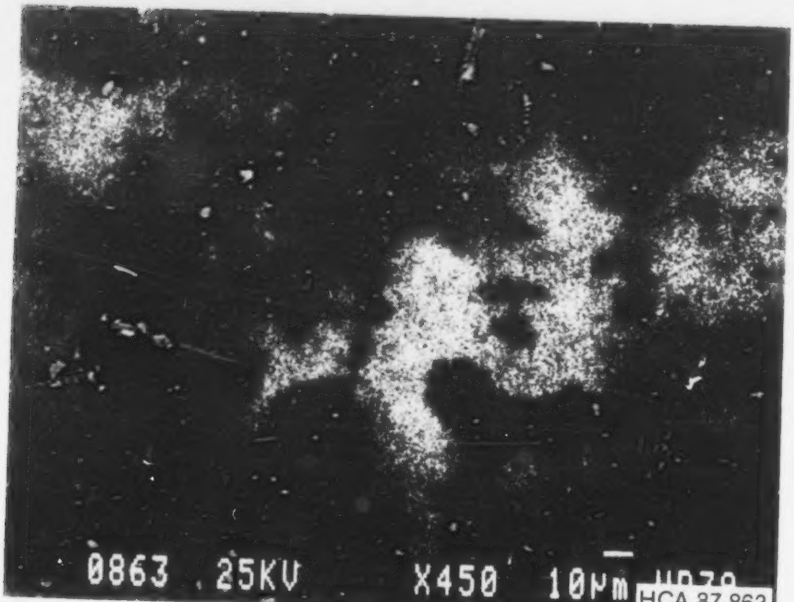
0863
25KV
X450
10µm
HCA 87-863

f. X-ray dot map of iron

10 μm

Figure I-50. (continued).

best copy available

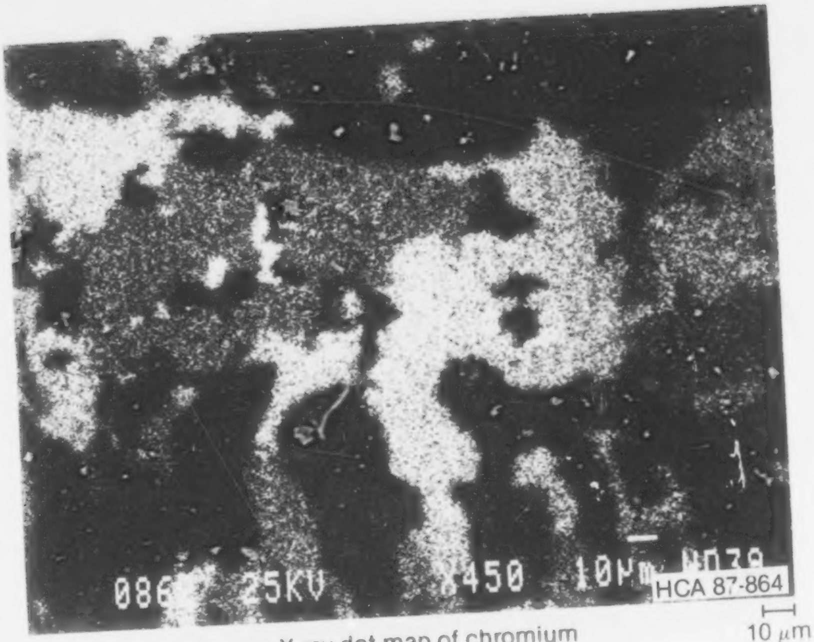
0860 25KV X450 10Pm WD39
HCA 87-864
10 μm

g. X-ray dot map of chromium

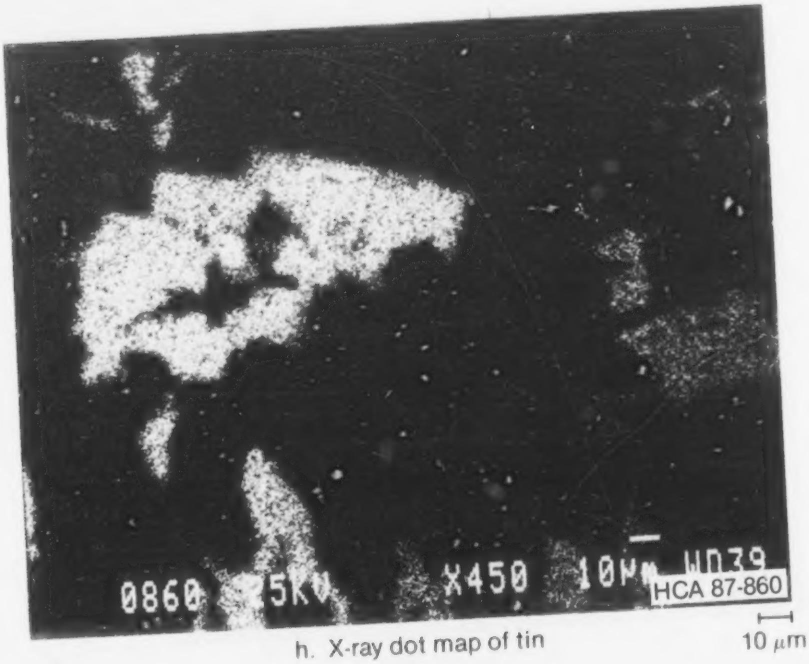
0860 25KV X450 10Pm WD39
HCA 87-860
10 μm

h. X-ray dot map of tin

Figure I-50. (continued).

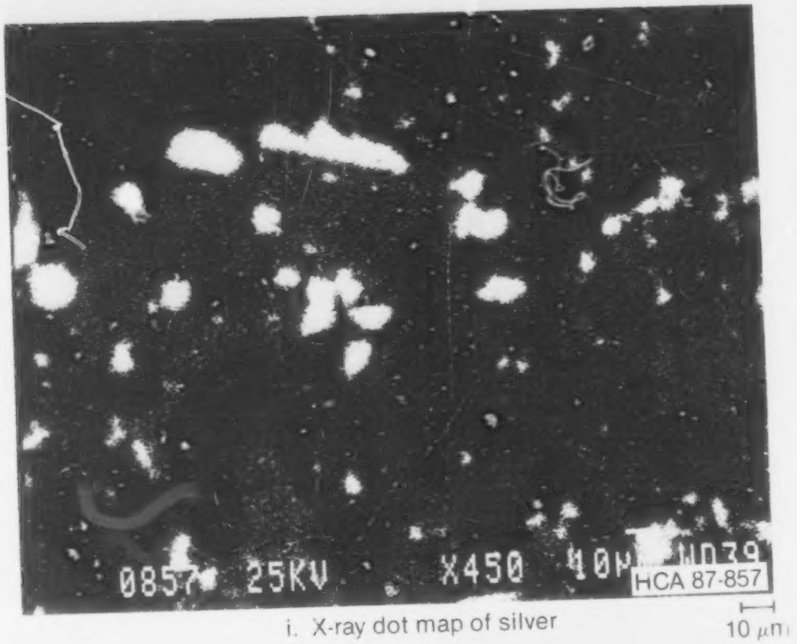
0857 25KV X450 10Pm WD39
HCA 87-857
10 μm

i. X-ray dot map of silver

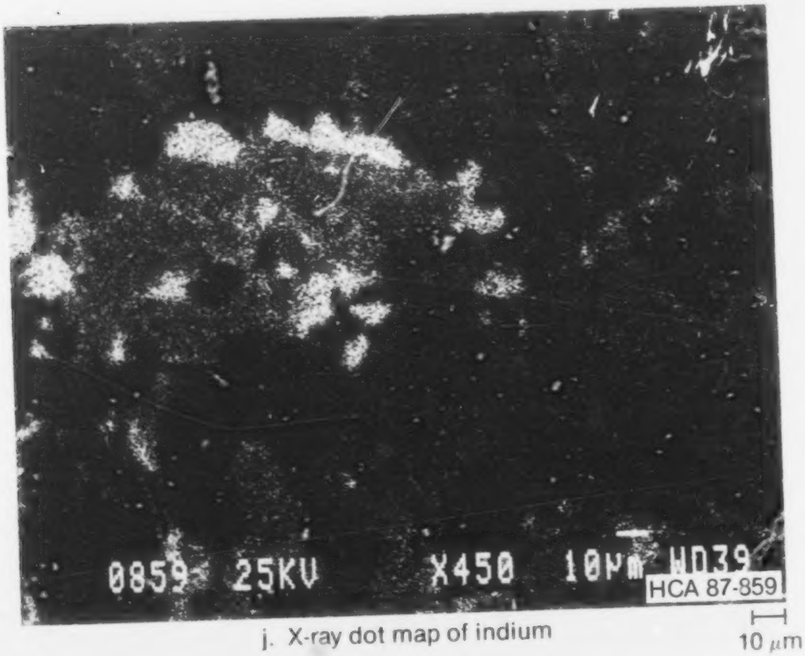
0859 25KV X450 10Pm WD39
HCA 87-859
10 μm

j. X-ray dot map of indium

Figure I-50. (continued).

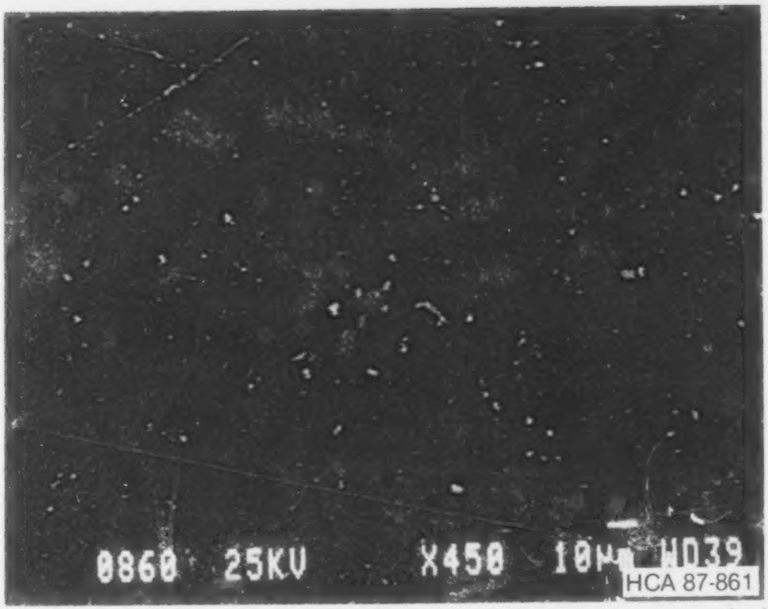
0860 25KV X450 10μm WD39
HCA 87-861

k. X-ray dot map of cadmium

10 μm

Figure I-50. (continued).

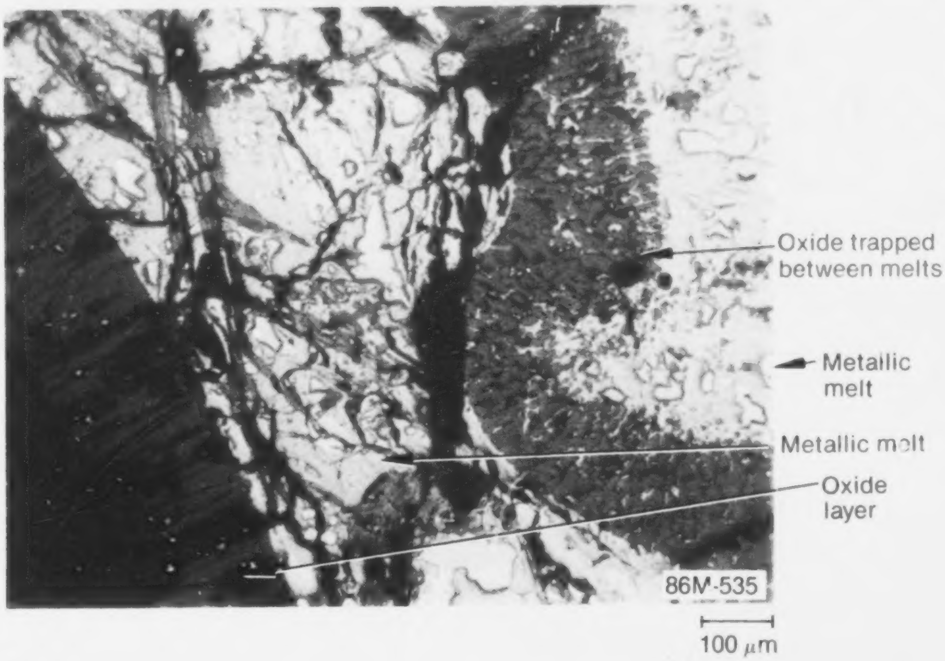
Oxide trapped between melts
Metallic melt
Metallic melt
Oxide layer
86M-535
100 μm

Figure I-51. Photomicrograph showing multiple oxide layers in melt at 0.17 m.

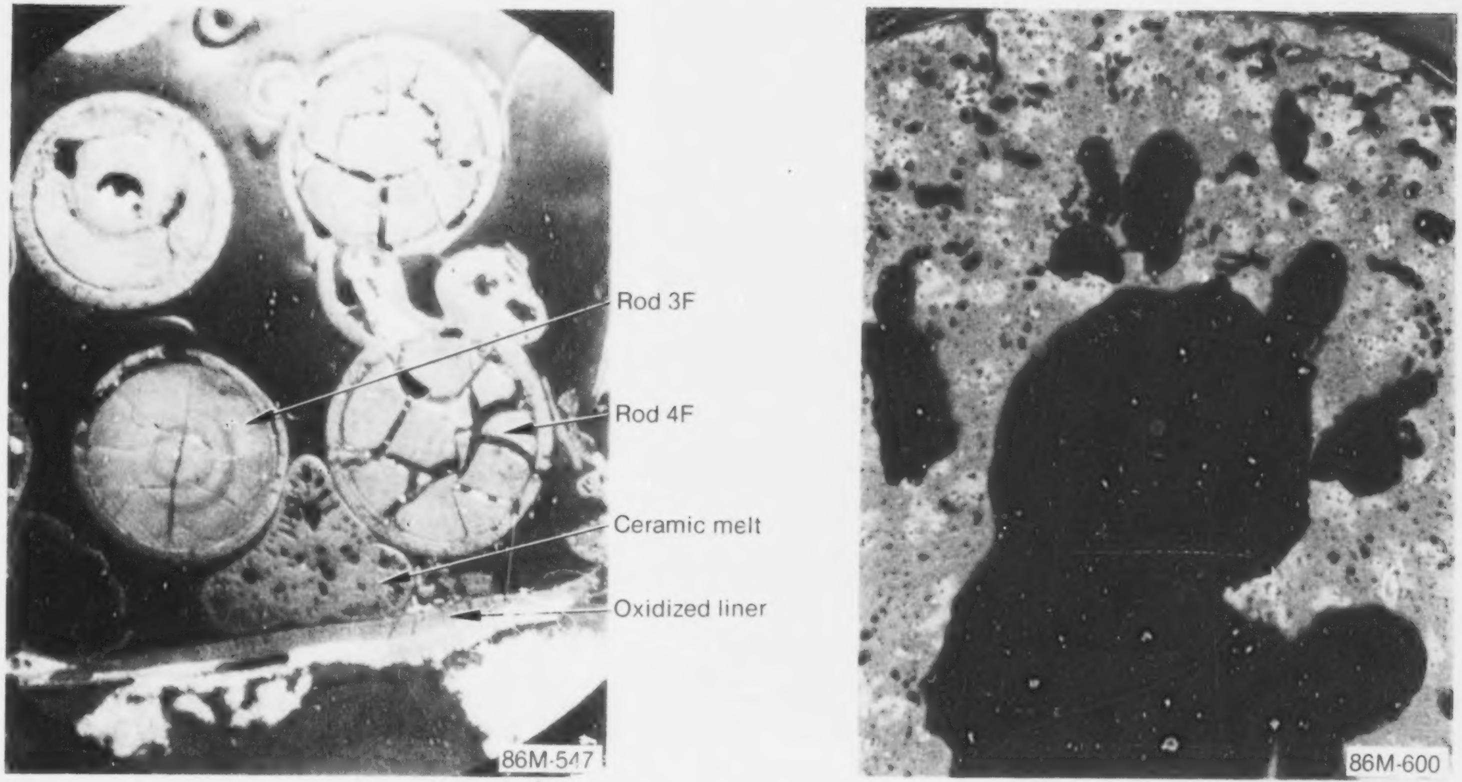
Rod 3F
Rod 4F
Ceramic melt
Oxidized liner
86M-547
3.3 mm
86M-600
100 μm

a. Photomicrograph of ceramic melt

b. Photomicrograph of surface ceramic melt etched for zircaloy

Figure I-52. Ceramic melt between rods 3F and 4F at 0.17 m.

The fuel structure of rod 5C near the pellet periphery shows a succession of light and dark colored bands (Figure I-53). This band structure was observed a number of times at widely varying elevations during the postirradiation examination. The dark bands appear to be associated with intragranular porosity, such as is displayed in Figure I-54(a); whereas the light bands appear to be associated with intergranular porosity, such as is displayed in Figure I-54(b), and are typical of the fuel structure near the pellet center. This banded structure and the intergranular porosity near the pellet center are thought to be the result of the BR-3 irradiation. Grain growth during the SFD 1-4 transient was severely limited by the pinning of the grain boundaries by the accumulated porosity.

An example of an unusual fuel structure not observed elsewhere in the SFD 1-4 bundle is the central void in the center of rod 3E shown in Figure I-55. The void is partially filled with melt having a metallic appearance and is surrounded by a ring of large, equiaxed grains 100 to 200 μm in diameter, with well-developed grain boundary porosity and a broad band of grains 20-40 μm in diameter that appear to be well separated along the boundaries. The ring structure including the central void is probably the result of an anomalously high fuel centerline temperature during the BR-3 irradiation. The grain boundary separation revealed in this fuel microstructure was also observed at the 0.25-m elevation and may have occurred during cooldown in the SFD 1-4 transient. However, this mechanism is not expected to strongly influence fission product release from the fuel because the grain boundaries are already fairly open with accumulated porosity in this high-burnup fuel.

As mentioned earlier, with a few exceptions the cladding remaining at this elevation was completely oxidized. The structure of incompletely oxidized cladding is shown in Figure I-56. The photomicrographs reveal a thick layer of ZrO_2 from steam oxidation on the outside of the cladding containing a two-phase mixture of previously molten α-Zr(O) and ZrO_2 which has reacted with the UO_2 fuel on the inside of the cladding. This structure indicates that temperatures were at least as high as 2170 K in this region prior to the relocation of melts from above. Apparently, slow oxidation produced thick oxide layers before the zircaloy melting temperature was reached and prevented the relocation of this and other cladding at this elevation.

The photomicrographs in Figure I-57 reveal that the temperature in one area of the saddle was in the range of the $\alpha + \beta$ two-phase region (1105 to 1245 K), although typically the saddle exhibited equiaxed α-zircaloy microstructure indicative of temperatures in the range of 920 to 1105 K. The level of hydriding in Figure I-58 is about 100 ppm.

In summary, the bundle cross section at the 0.17-m elevation experienced an influx of metallic and ceramic melts from above and a depletion of control and structural materials. The net accumulation of materials caused a 30% reduction in the flow area at this elevation relative to intact bundle geometry. The melts relocated to this elevation after the oxidation of the zircaloy remaining at this elevation was complete. The metallic melts interacted with ZrO_2 on the cladding and liner and in the insulation, but little dissolution of UO_2 occurred. It is estimated that temperatures were as high as 2200 K before melts of temperatures up to 2800 K relocated to this elevation.

I-3.7 Bundle Cross Section at 0.08 m. The cross section of the bundle at the 0.08-m elevation (Figure I-59) is characterized by the accumulation of metallic melts at the location of the lowest spacer grid. The melt accumulation has reduced the flow area by 87% with respect to the flow area in an intact bundle geometry. The melt has attacked the spacer grid and the fuel rod cladding but not the fuel. The control alloy has melted but has been retained in the vicinity of the control rods in three of the four positions.

Damage in the vicinity of control position 5E is shown in Figure I-60. Intact spacer grid material, spacer grid material that has reacted with the melt, reacted fuel rod cladding, reacted control rod cladding and guide tube, and molten control materials at the control position are all evident. The intact spacer grids indicate that temperatures were below the melting point of Inconel (1700 K), and the melting of the control materials indicates temperatures above 1070 K. In Figure I-61, the molten control material in rod 2E appears to be contained by a thin oxide, probably on the zircaloy guide tube that had interacted with the stainless steel control rod cladding. Thin oxides which were noticeable on the melts in Figure I-60 are more evident in Figure I-61. In Figure I-60, the liner, as well as fuel rod cladding and the spacer grid, has been strongly attacked by metallic melt. Melt is present in cracks in fuel pellets in Figure I-62, but there is no evidence of attack on the UO_2. The microstructure of unreacted liner (Figure I-63) shows a low-temperature, β-phase zircaloy with a thin oxide (25 μm) and indicates temperatures only slightly

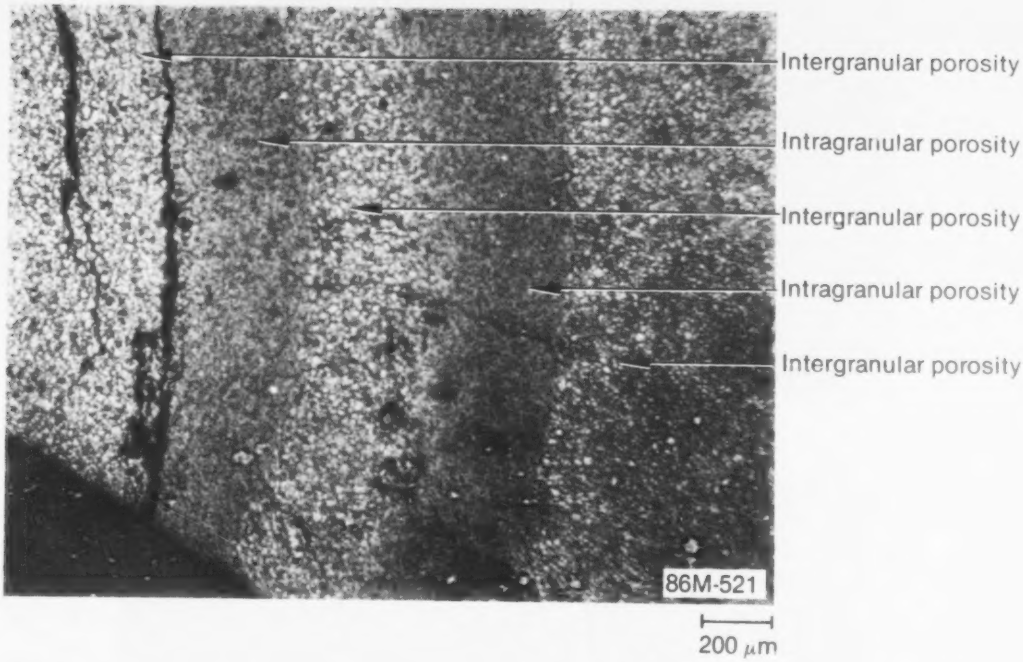
Intergranular porosity
Intragranular porosity
Intergranular porosity
Intragranular porosity
Intergranular porosity
86M-521
200 μm

Figure I-53. Photomicrograph showing unetched fuel microstructure near the periphery of rod 5C at 0.17 m.

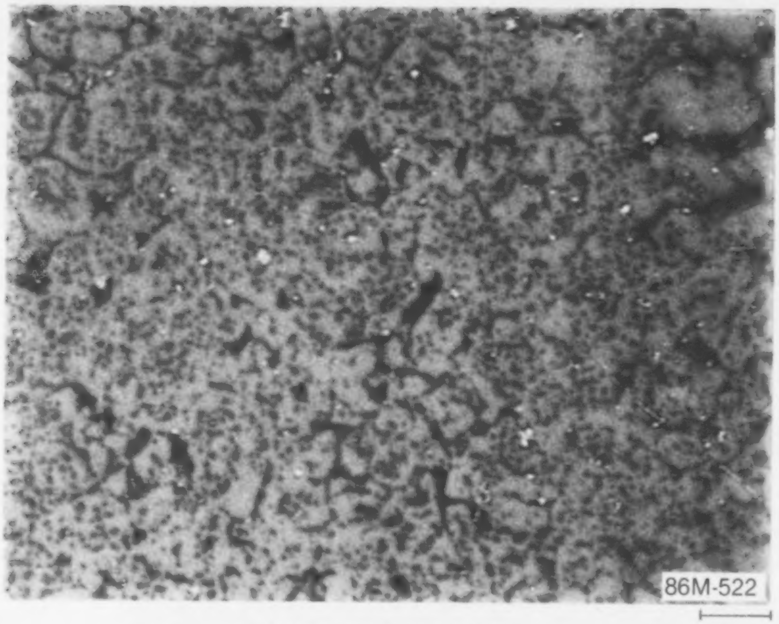
86M-522
20 μm

a. Intragranular porosity

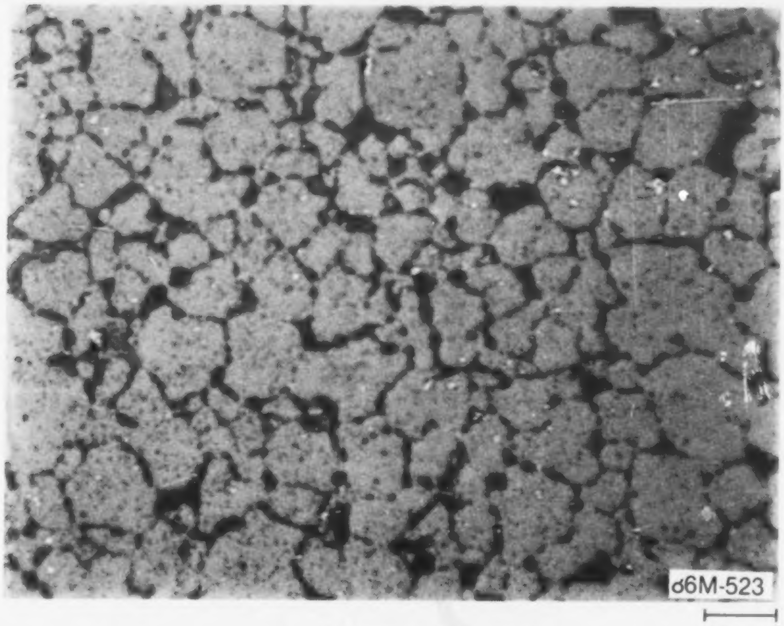
86M-523
20 μm

b. Intergranular porosity

Figure I-54. Photomicrograph showing unetched fuel microstructure near the center of rod 5C at 0.17 m.

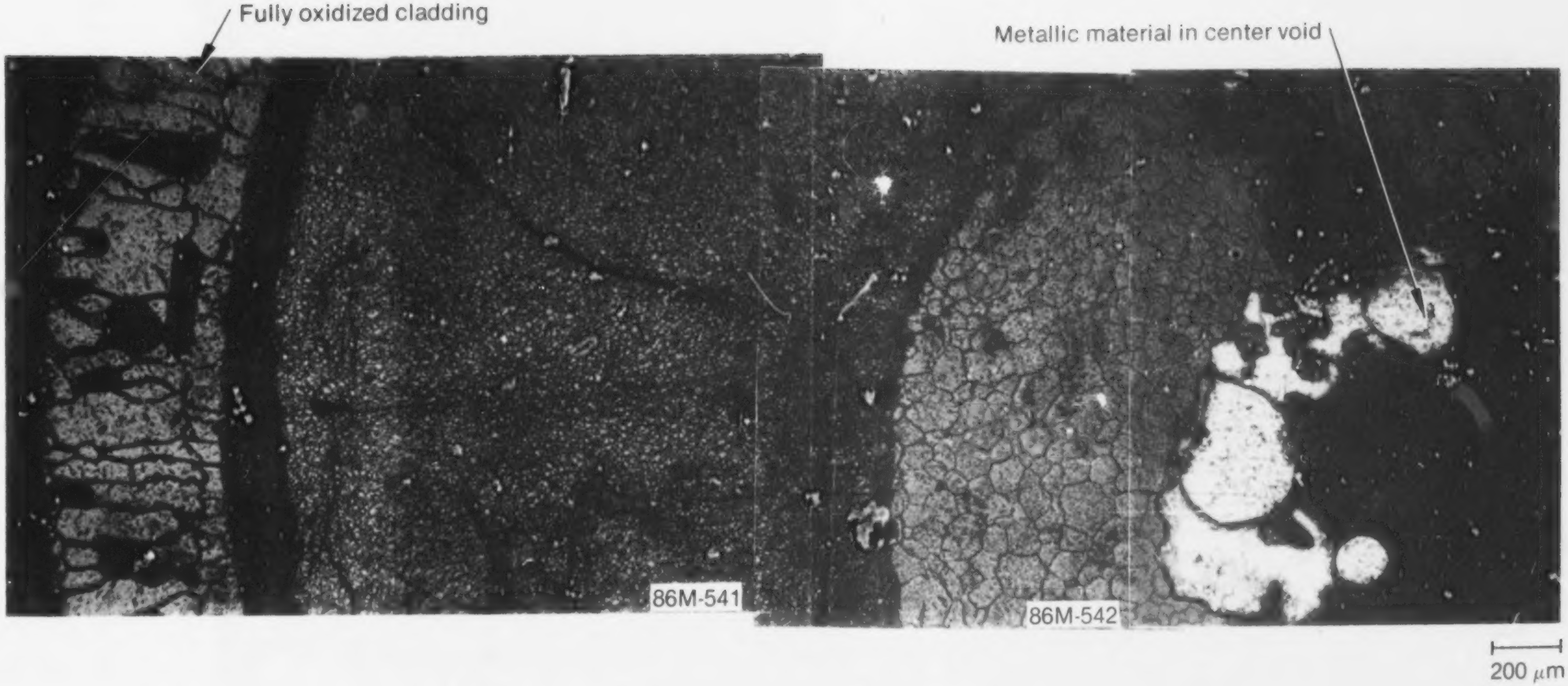
Fully oxidized cladding
Metallic material in center void
86M-541
86M-542
200 μm

Figure I-55. Composite photomicrograph of the fuel structure in rod 3E showing grain boundary separation in the outer ring of the fuel, large equiaxed grains in the inner ring, and metallic material relocated and frozen in the central void at 0.17 m.

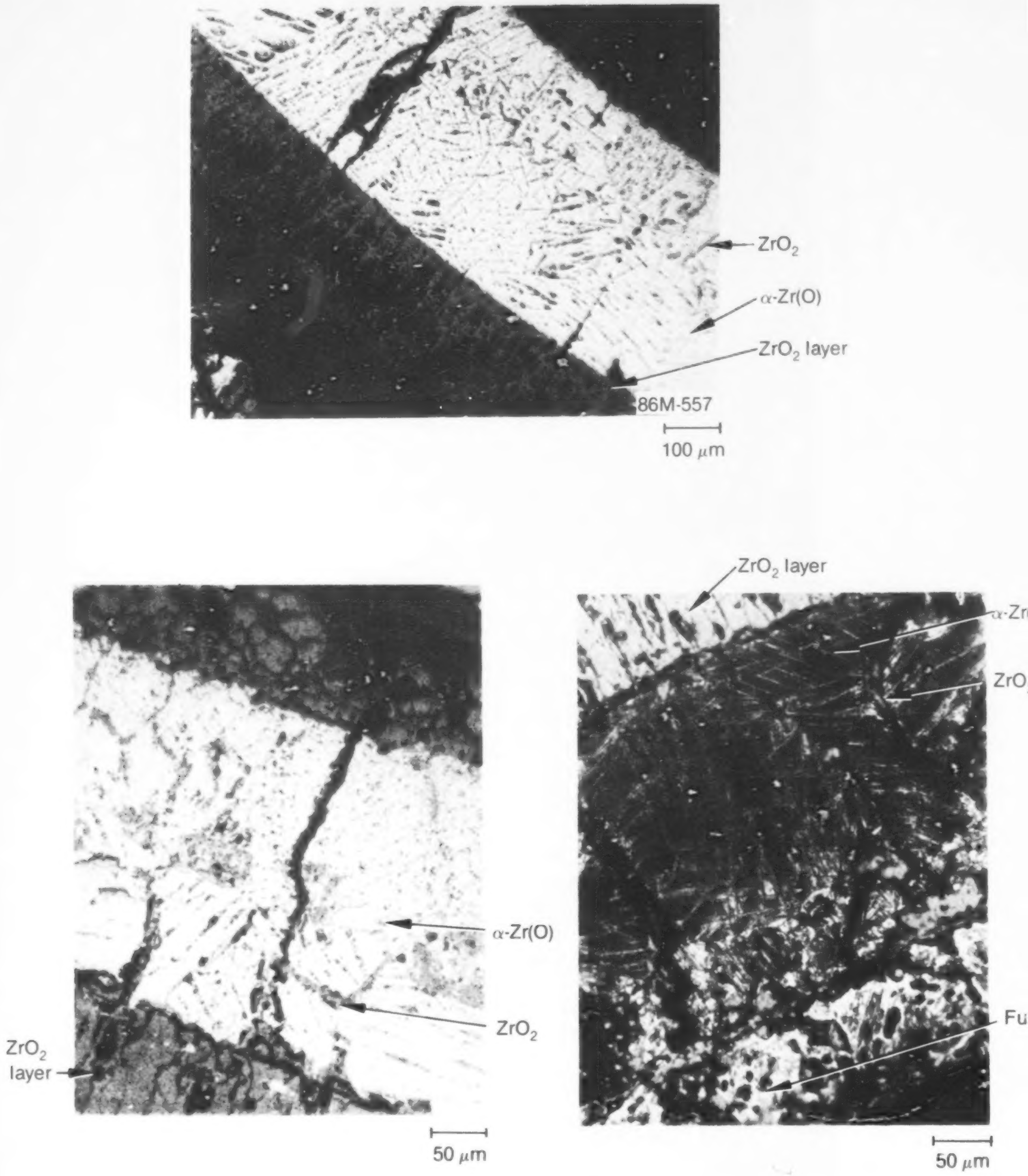
ZrO$_2$
α-Zr(O)
ZrO$_2$ layer
86M-557
100 μm
ZrO$_2$ layer
α-Zr
ZrO
α-Zr(O)
ZrO$_2$
ZrO$_2$ layer
Fu
50 μm
50 μm

Figure I-56. Photomicrographs showing the cladding at control rod position 5F, as polished, at 0.17 m.

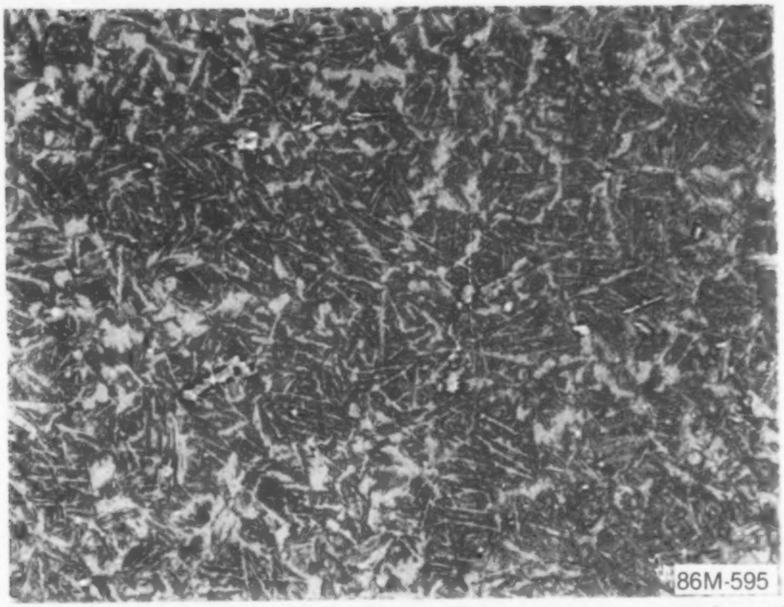

a. $\alpha + \beta$ two-phase zircaloy region

50 μm

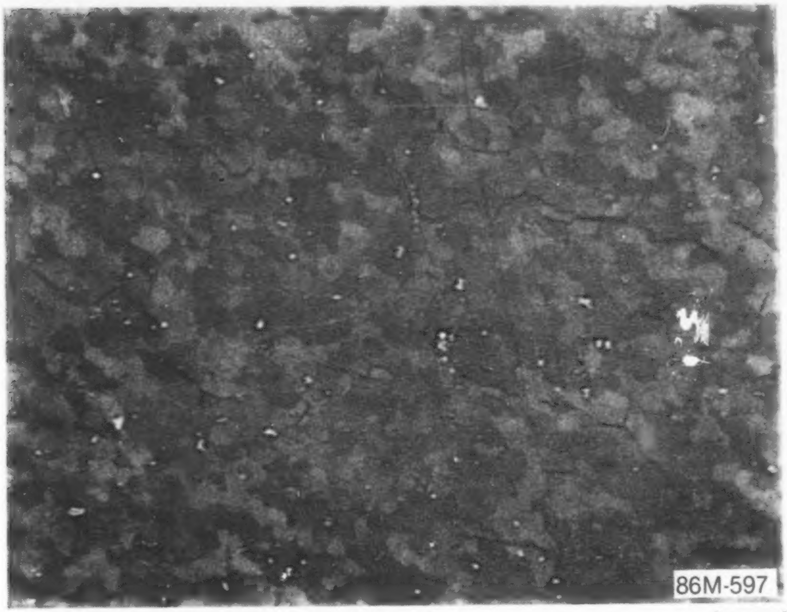

b. Equiaxed α-zircaloy region

50 μm

Figure I-57. Photomicrograph showing the heat-affected region in the saddle at 0.17 m.

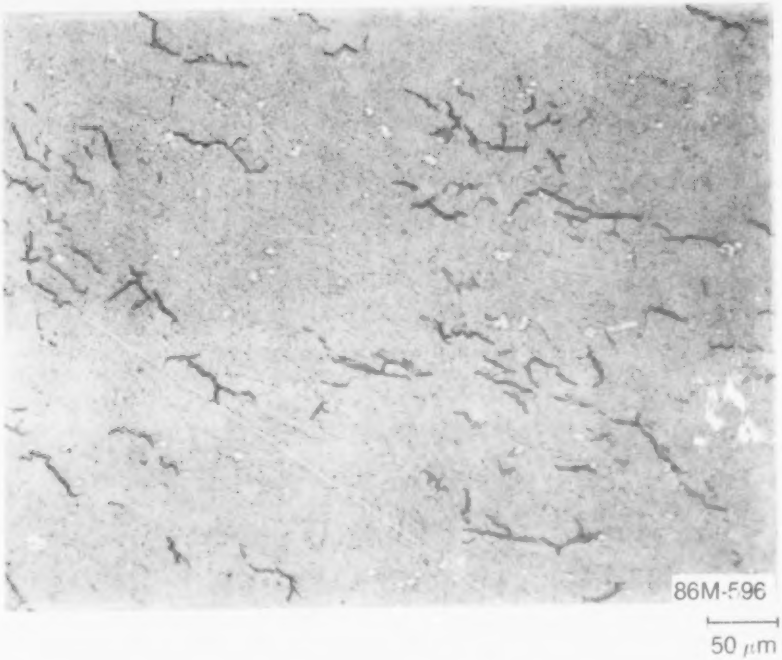
86M-596
50 μm

Figure I-58. Photomicrograph showing hydriding typical of the saddle at 0.17 m.

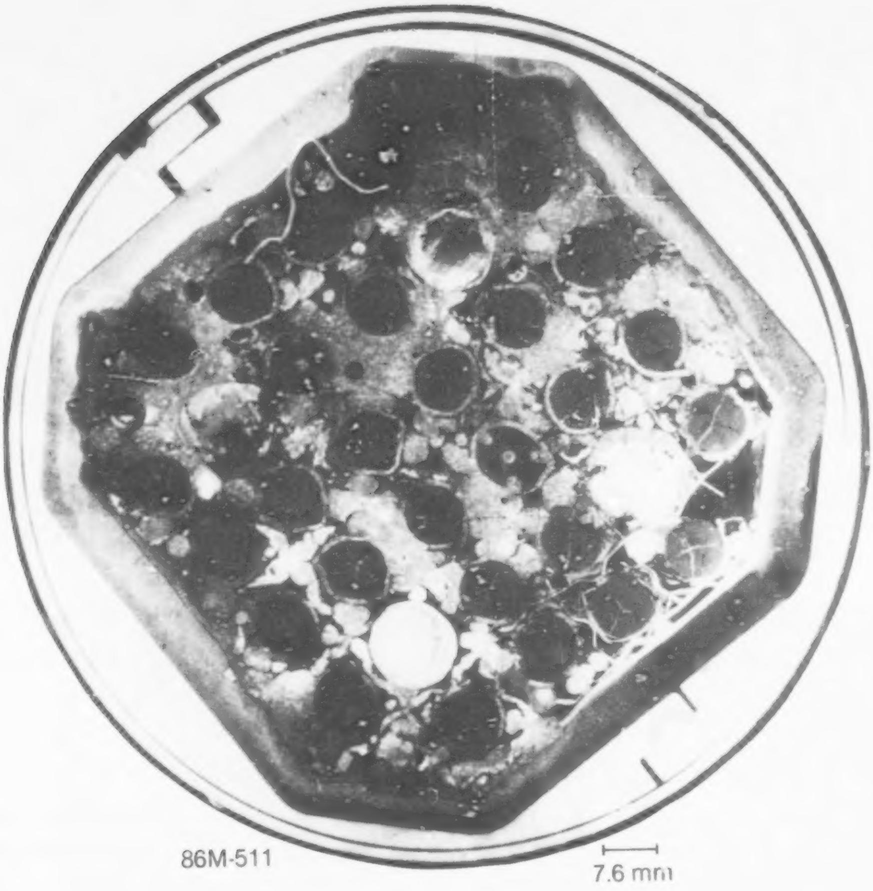
86M-511
7.6 mm

Figure I-59. SFD 1-4 bundle cross section at 0.08 m.

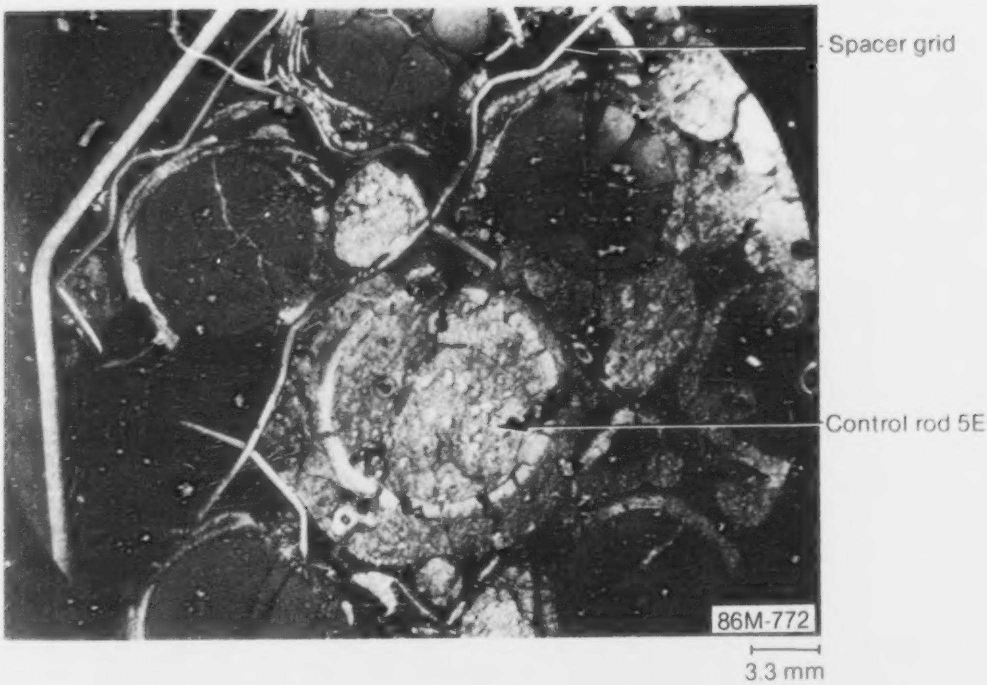
Spacer grid
Control rod 5E
86M-772
3.3 mm

Figure I-60. Photomicrograph showing damage in the vicinity of control rod position 5E at 0.08 m.

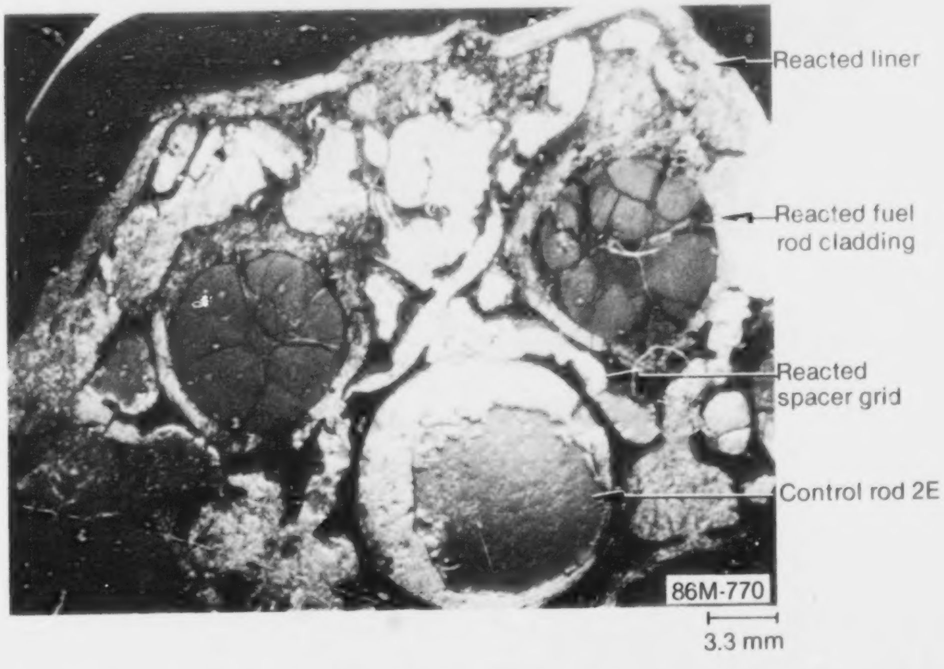
Reacted liner
Reacted fuel rod cladding
Reacted spacer grid
Control rod 2E
86M-770
3.3 mm

Figure I-61. Photomicrograph showing molten control material contained by the ZrO_2 shell of the oxidized guide tube at 0.08 m.

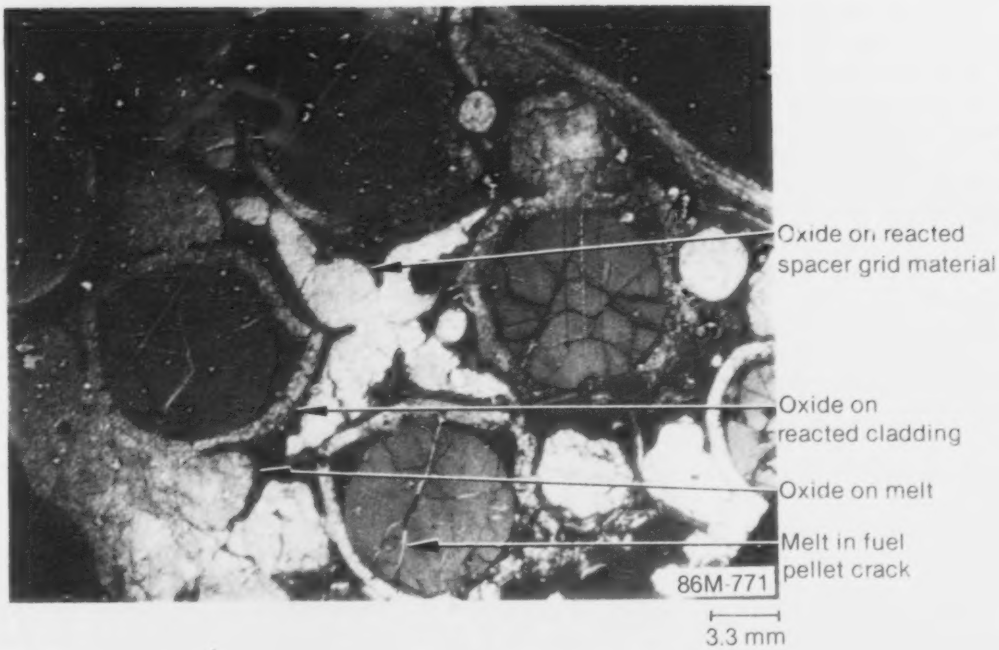
Oxide on reacted spacer grid material
Oxide on reacted cladding
Oxide on melt
Melt in fuel pellet crack
86M-771
3.3 mm

Figure I-62. Photomicrograph showing oxides on materials that have interacted with the melt at 0.08 m.

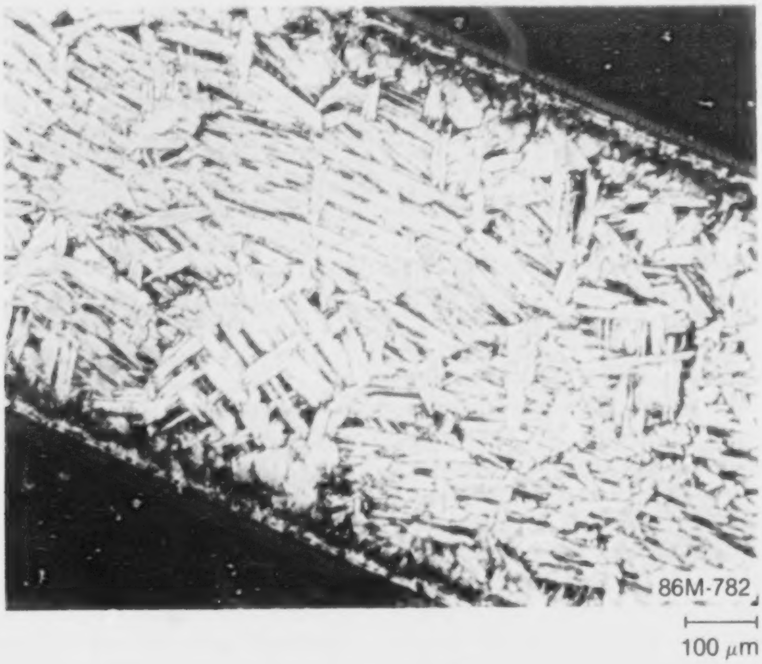
86M-782
100 μm

Figure I-63. Photomicrograph showing prior β-zircaloy microstructure of unreacted liner at 0.08 m.

above 1245 K. The unreacted liner suggests a temperature of ~1300 K at the periphery in the absence of interaction with relocated melts.

The photomicrograph in Figure I-64 shows chemical attack of the cladding by the metallic melt. The oxide (90 μm) on the cladding did not protect the cladding from attack by the melt. There appears to have been no significant reaction of the fuel with the melt. The composite photomicrograph in Figure I-65 shows the retention of melt inside a control rod by a 90-μm oxide layer on the guide tube. The flow channel is filled with metallic melt that has interacted with a spacer grid and the cladding of the adjacent fuel rod. The oxide layers on the guide tube and cladding do not appear to have been chemically attacked by the melt.

Chemical analysis of a core bore (see Table I-1, sample M4D) and SEM/WDS results indicate that the melt consists primarily of zirconium and silver, with some iron, nickel, chromium, indium, and cadmium. Both methods also indicate that within the control rods the melt contains primarily silver, indium, and cadmium with roughly the initial composition of the control alloy (80% Ag, 15% In, 5% Cd) with, in some cases, zirconium. The relocated melt is quite heterogeneous and exhibits a variety of phases with different compositions. Phases with the following elemental constituents were found: (Ag,In,Cd), (Fe,Ni,Cr,Zr), (Ni,In,Zr), (Ag,Cd), (Ag,Zr), and (U,O,Ag). The (U,O,Ag) material was also observed at the 0.25-m elevation and is thought to be an intimate mixture of two phases, UO_2 and silver. Zircaloy is found with all the remaining phases except for unreacted control material, (Ag,In,Cd). Indium shows a tendency to separate from silver and cadmium and form an alloy containing nickel and zirconium. In the molten control rods, the phases (Ag,In,Cd), (Ag,In,Cd,Zr), and (In,Zr) have been identified. The lack of chemical attack on UO_2 and ZrO_2 by melt which is rich in zirconium suggests that the temperatures of the melt must have been relatively low, much less than 2200 K. (Ten minutes at 1500 K is calculated by Cathcart-Pawel kinetics[I-7] to give 90 μm of ZrO_2.) Temperatures at this elevation were between 1300 and 1700 K before the metallic melt arrived, and the temperature likely did not exceed about 1700 K after arrival of the melt, otherwise the spacer grid would have melted away. The temperatures of the relocating melts could have been anywhere in the range from 1300 to 2200 K, but were most likely between 1500 to 1700 K.

The bundle cross section in Figure I-59 reveals that relocation occurred in the form of many separate melts. The metallographic and SEM examinations confirm that numerous metallic melts with varying compositions relocated to this elevation. This is evidence of the incoherent nature of the core melt progression process.

The fuel in rod 3C has a grain size of about 20 μm. Although there is considerable grain boundary separation in this fuel, the fuel shows no effect of contact with metallic melt which has filled cracks in the pellet (Figure I-66.) The microstructure of the saddle indicates the onset of recrystallization of residual cold work. This phenomenon places the maximum temperature of the saddle above 920 K but below 1105 K.

In summary, considerable metallic melt collected on the spacer grid at the 0.08-m elevation. The melt was primarily zircaloy and control alloy material, with some stainless steel components as well. The melt interacted with the fuel rod cladding, the control rod guide tubes, and the Inconel spacer grid, but did not attack the fuel or zirconium dioxide. The temperature before arrival of the melt was probably ~1500 K; after melt arrival (maximum melt temperature of ~1700 K), the temperature was probably between 1600 and 1700 K. The flow area was reduced by 87% relative to that of an intact bundle geometry.

I-3.8 Bundle Cross Section at 0.02 m. As can be seen in Figure I-67, a small amount of metallic melt relocated and froze in the cross section at 0.02 m. As a result, the flow area was reduced by about 8% relative to that of an intact bundle geometry. The relocated melt chemically attacked and penetrated the zircaloy guide tube at three control rod locations, but the stainless steel control rod cladding remained intact at this elevation.

Chemical analysis of a core bore and SEM/WDS indicate that one sample of the melt (sample M3B, Table I-1) has essentially the same composition as the zircaloy, silver, indium, cadmium, iron, nickel, and chromium melt found at the 0.08-m elevation. The penetration of a zircaloy guide tube by a multiphase metallic melt is shown in Figure I-68. Neither the guide tube nor the melt has a measurable oxide, suggesting a very low temperature interaction.

Primarily (Ag,In,Cd) melt is visible in the gap between solid control rod alloy and the stainless steel cladding and between the cladding and the zircaloy guide tube, and outside of the guide tube in position 5B in Figure I-69. The control rod and its guide tube are intact at this elevation, indicating

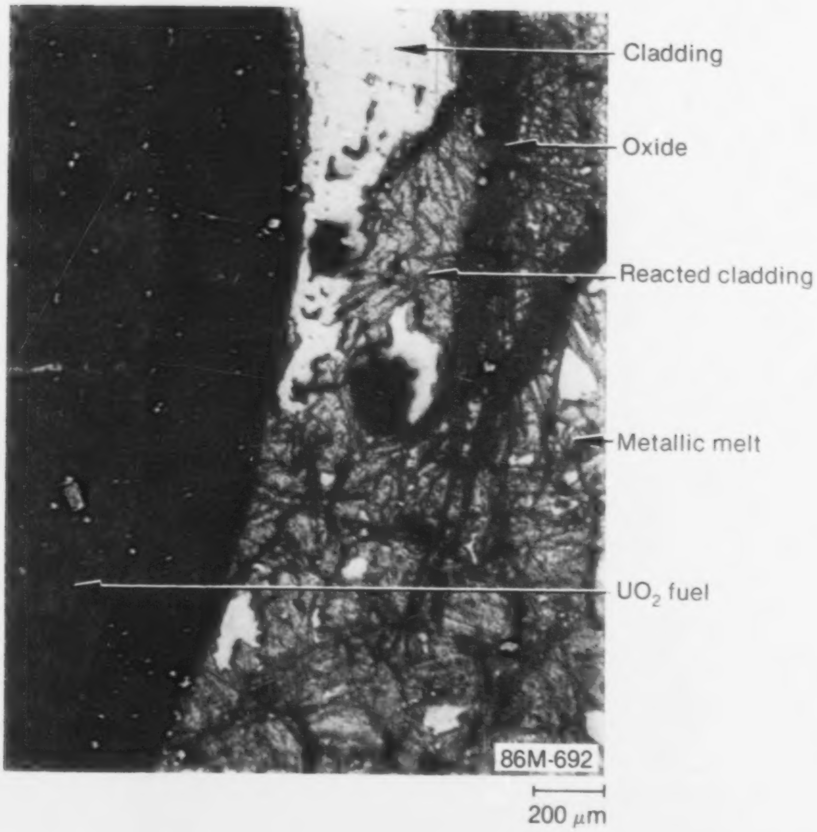
Cladding
Oxide
Reacted cladding
Metallic melt
UO2 fuel
86M-692
200 μm

Figure I-64. Photomicrograph showing melt attack on cladding at 0.08 m.

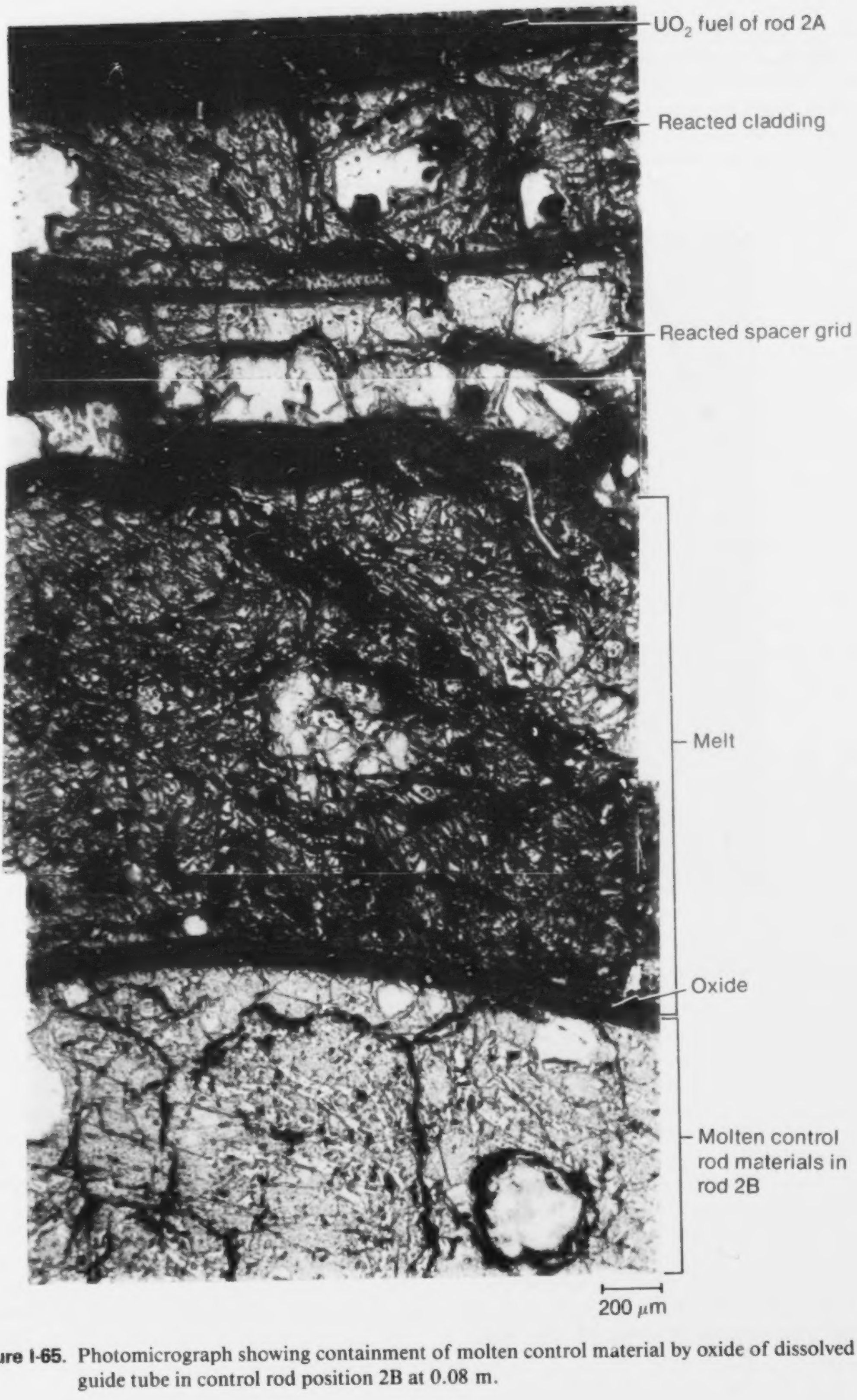
UO$_2$ fuel of rod 2A
Reacted cladding
Reacted spacer grid
Melt
Oxide
Molten control rod materials in rod 2B
200 μm

Figure I-65. Photomicrograph showing containment of molten control material by oxide of dissolved guide tube in control rod position 2B at 0.08 m.

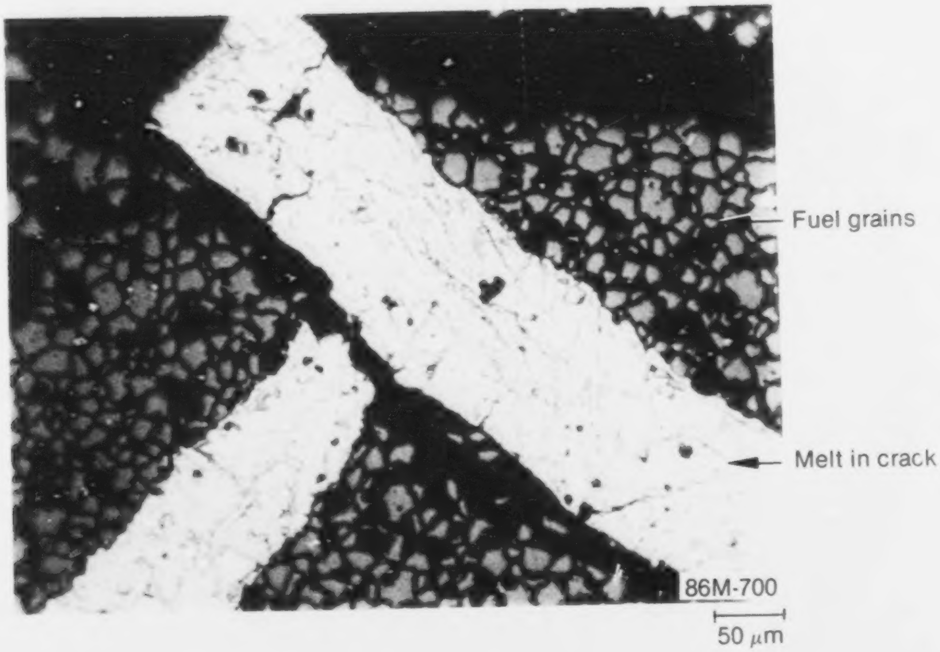
Fuel grains
Melt in crack
86M-700
50 μm

Figure I-66. Photomicrograph showing melt in fuel cracks in rod 3C at 0.08 m.

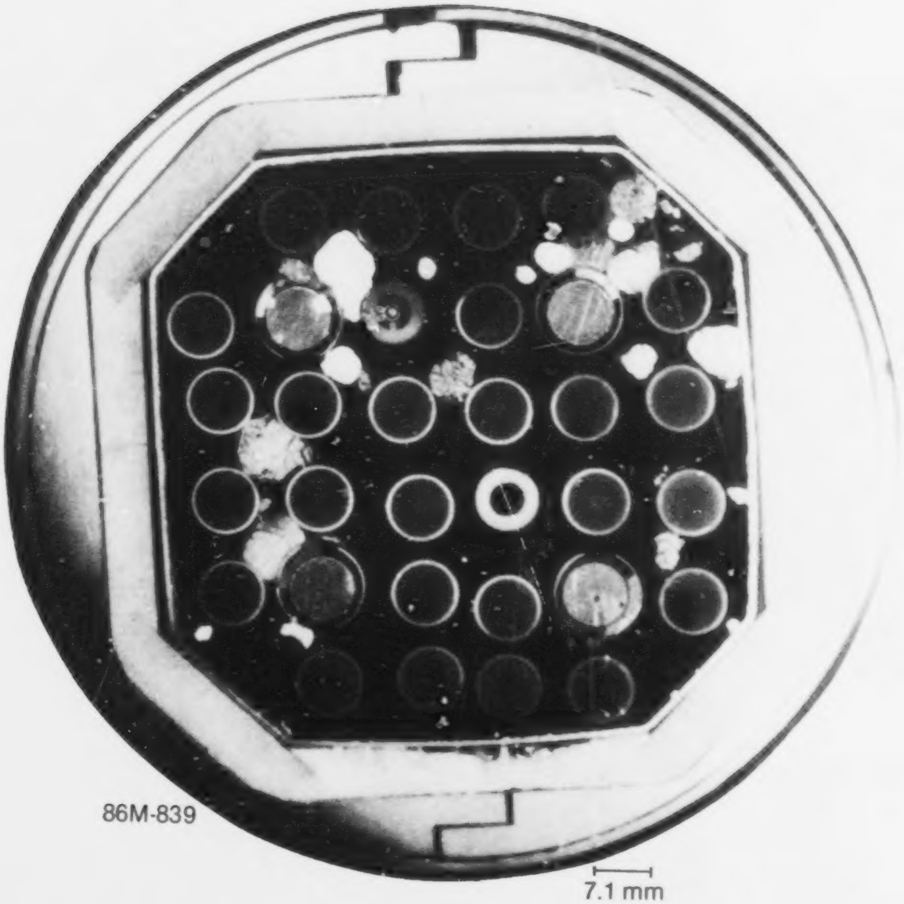
86M-839
7.1 mm

Figure I-67. SFD 1-4 bundle cross section at 0.02 m.

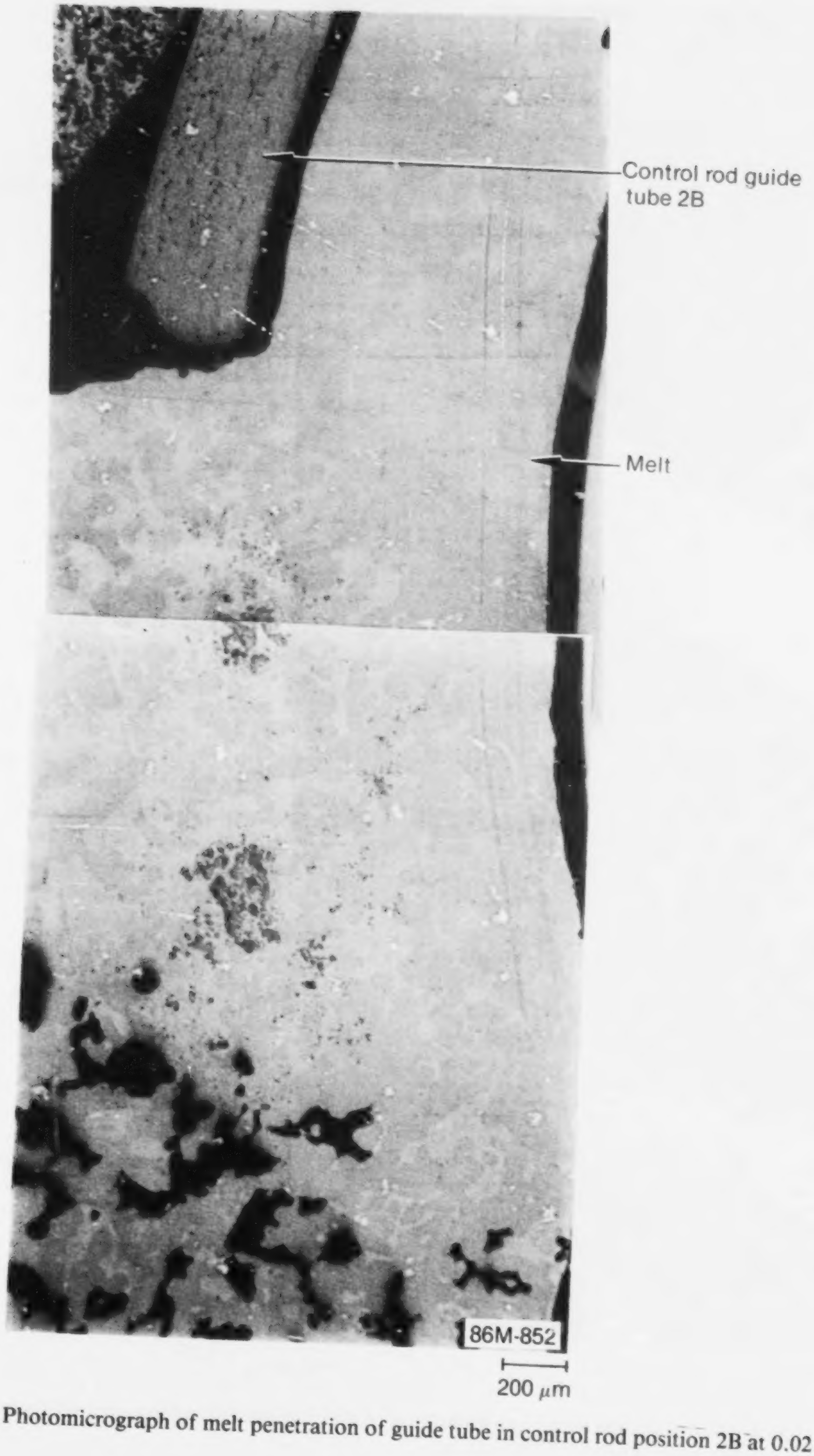
Control rod guide tube 2B
Melt
86M-852
200 μm

Figure I-68. Photomicrograph of melt penetration of guide tube in control rod position 2B at 0.02 m.

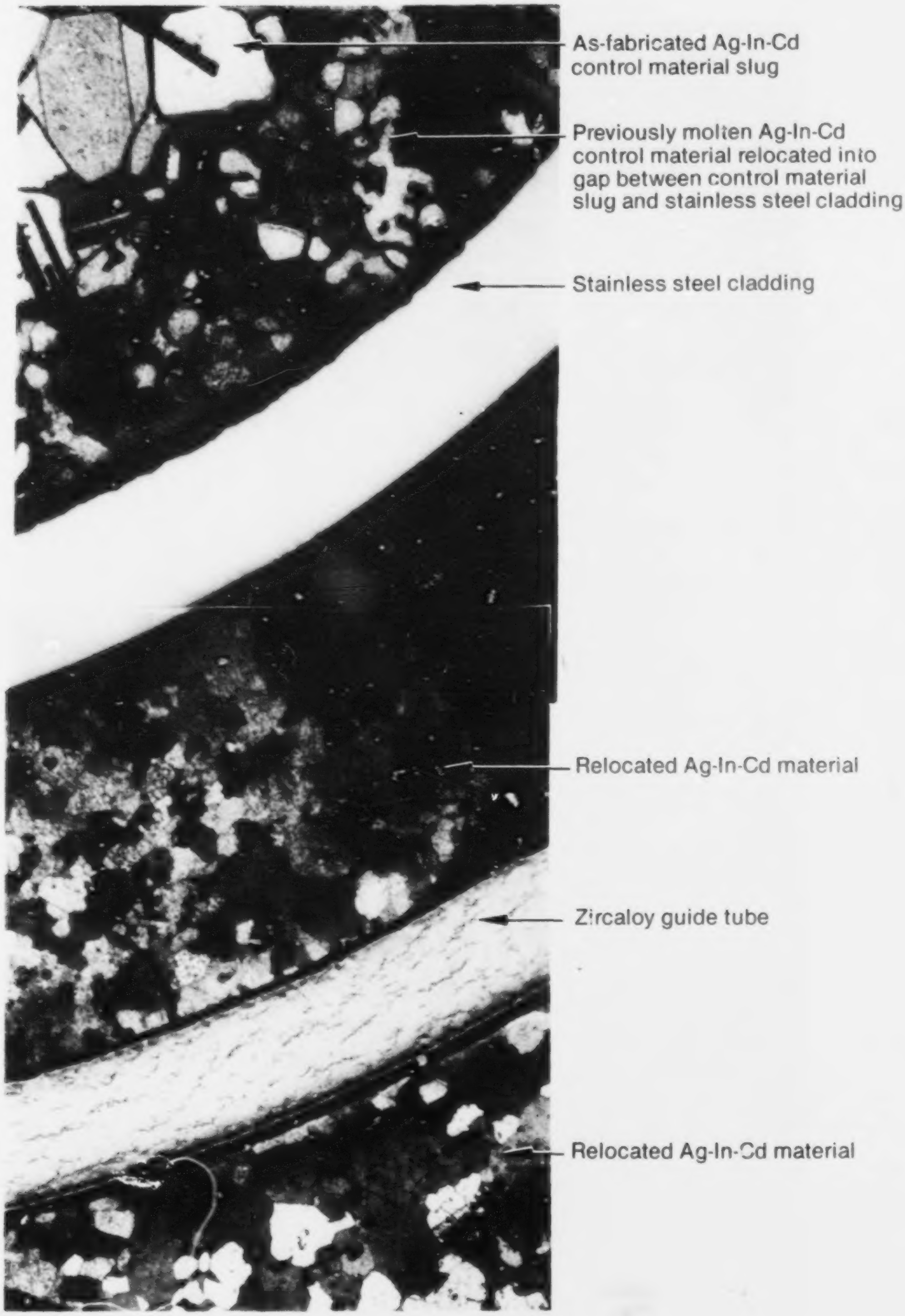

As-fabricated Ag-In-Cd control material slug
Previously molten Ag-In-Cd control material relocated into gap between control material slug and stainless steel cladding
Stainless steel cladding
Relocated Ag-In-Cd material
Zircaloy guide tube
Relocated Ag-In-Cd material
Etched
200 μm

Figure I-69. Photomicrograph showing relocation of Ag-In-Cd control rod material within and outside of control rod position 5B at 0.02 m.

that the melt relocated from above in all these regions of the control position. The temperatures of the original materials at this elevation are quite low, as demonstrated by the solid control rod alloy (less than 1070 K) in Figure I-69 and the equiaxed α-zircaloy structures (920 to 1105 K) of fuel rod cladding (Figure I-70), liner (Figure I-71), and saddle (Figure I-72). There is no measurable oxide on the zircaloy structures. The temperature of the relocated melt that penetrated the zircaloy guide tube is not known, but meltings points of binary alloys of zirconium with silver are as low as 1465 K, and with iron are as low as 1207 K, on the zirconium-rich side. The lack of oxidation of the relocated melt suggests that temperatures of the melt were no greater than ∿1500 K.

The chemical composition of the control rod alloy in position 2E was measured (see sample M3C in Table I-1) and found to be very nearly the as-fabricated composition.

A photomicrograph of the fuel in rod 6B (Figure I-73) shows the grain size to be 18.4 μm. Similar measurements at another location in rod 6B and in rod 5D give grain sizes of 17.5 and 16.1 μm.

In summary, the cross section at the 0.02-m elevation was quite cool, about 1000 K, and received an influx of metallic melt (<1500 K) that chemically attacked and penetrated three of the four zircaloy guide tubes but did not penetrate the stainless steel control rod cladding. Silver, indium, and cadmium from molten control rod alloy relocated from above and froze within the control rods at this elevation.

I-3.9 Bundle Cross Section at −0.09 m. This cross section is below the fueled region of the bundle; but, as can be seen in Figure I-74, metallic melts relocated and froze in this region without interactions with existing structures. The accumulation of relocated melts reduced the flow area in this region by about 48% relative to that of the undisturbed bundle geometry at this elevation.

Two melts were sampled and analyzed for elemental composition. These samples are listed in Table I-1 as samples M2B and M2D. Sample M2B, taken from the melt in the flow channel between rods 5C, 5D, 6C, and 6D, was found to consist of a mixture of control materials, stainless steel components, zircaloy, and a small amount of uranium. The second sample was taken from the melt between the liner and positions 2A and 3A and was found to be essentially pure zircaloy.

Several different kinds of melts that were not analyzed for elemental composition were observed to have frozen at the −0.09-m elevation. The melt in Figure I-75 was found between rods 3C and 3D and appears to contain two phases and to have a thin surface oxide. The melt in Figure I-76 was found between rods 3F and 4F and is circular in cross section with a diameter of about 1 mm. The structure appears multiphase and has a surface oxide layer about 100 μm thick.

Fuel rod cladding and liner show recrystallized α-zircaloy structures, indicating temperatures in the range from 920 to 1105 K, probably about 1000 K. The 100-μm-thick oxide on the melt in Figure I-69 suggests a temperature of about 1530 K for a 10-min exposure based on calculations using Cathcart-Pawel[I-7] zircaloy oxidation kinetics. The temperature of the molten zircaloy is assumed to be in the neighborhood of 2200 K.

The relocation of these various melts with quite different compositions and melting temperatures to an elevation below the fueled region in the bundle is an indication of the heterogeneous nature of the melts and the incoherent nature of the core melt process.

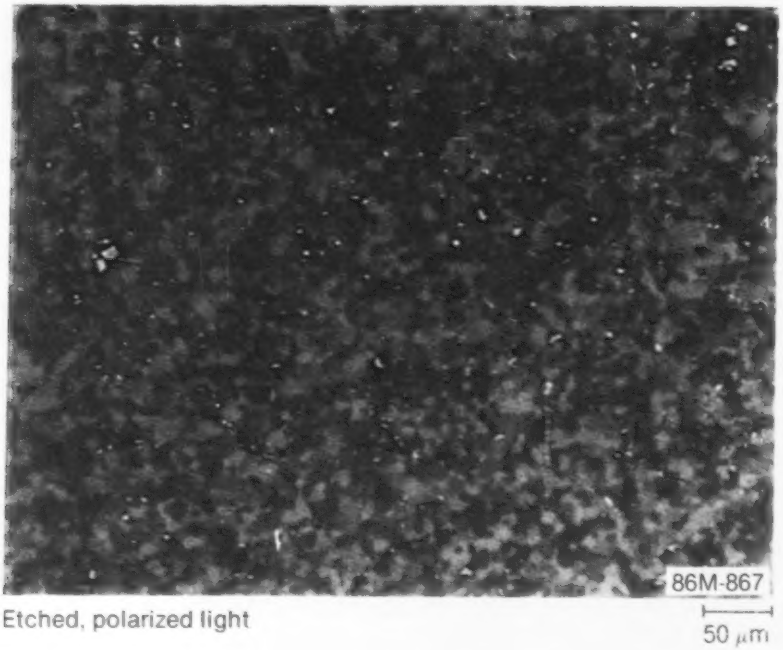
86M-867
Etched, polarized light
50 μm

Figure I-70. Photomicrograph showing equiaxed α-zircaloy microstructure typical of fuel rod cladding at 0.02 m.

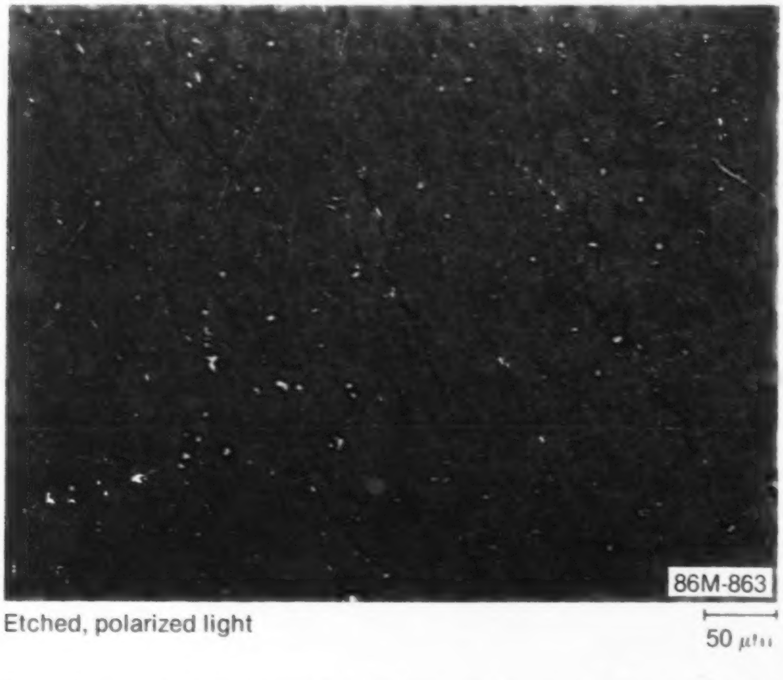
86M-863
Etched, polarized light
50 μm

Figure I-71. Photomicrograph showing equiaxed α-zircaloy microstructure typical of the liner at 0.02 m.

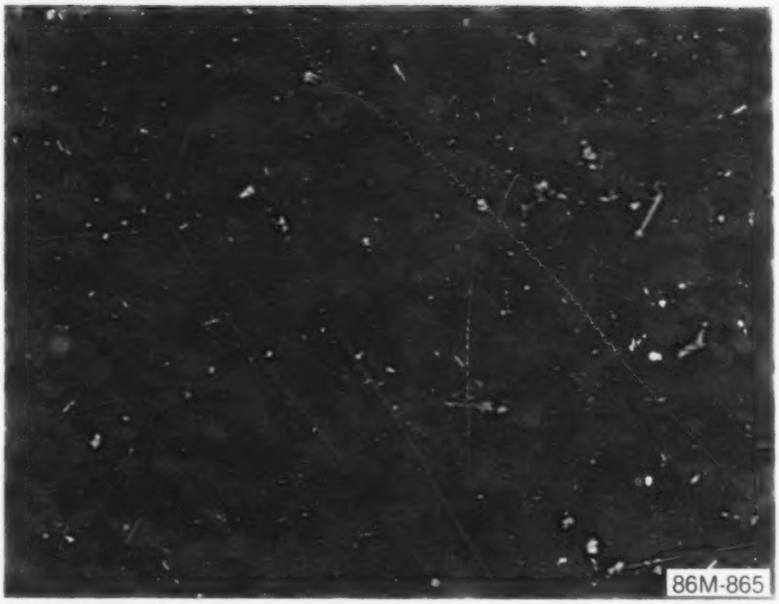
86M-865
Etched, polarized light
50 μm

Figure I-72. Photomicrograph showing equiaxed α-zircaloy microstructure typical of the saddle at 0.02 m.

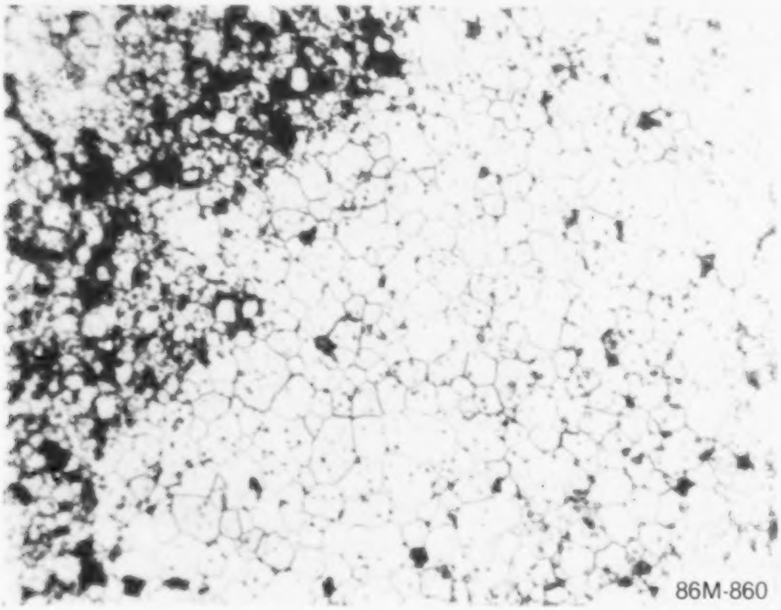
86M-860
50 μm

Figure I-73. Photomicrograph showing fuel grain size of 18.4 μm in rod 6B at 0.02 m.

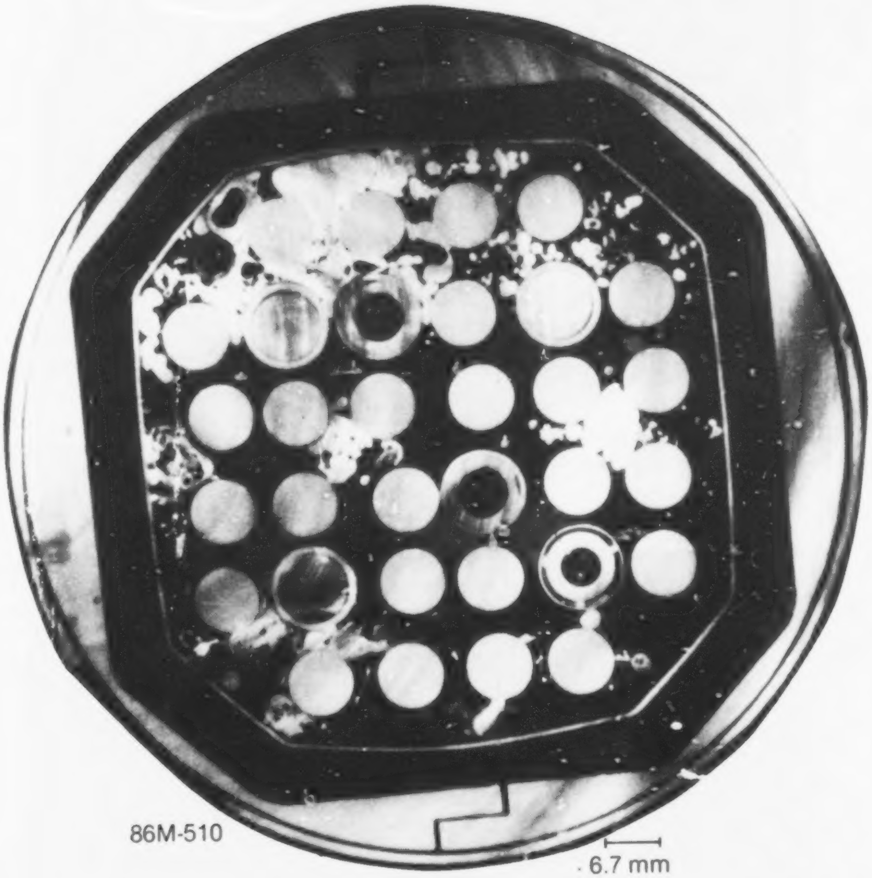
86M-510
6.7 mm

Figure I-74. SFD 1-4 bundle cross section at −0.09 m.

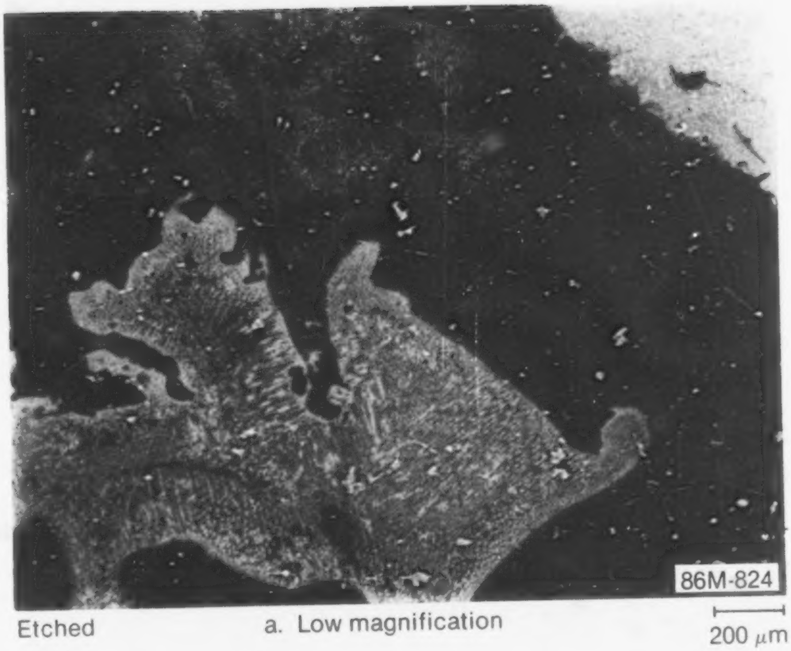
86M-824
200 μm

Etched a. Low magnification

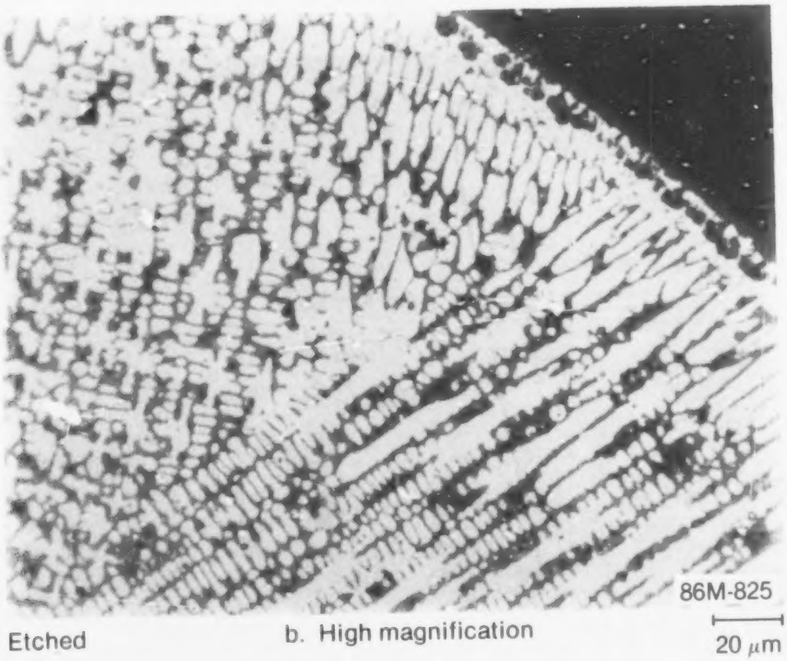
86M-825
20 μm

Etched b. High magnification

Figure I-75. Photomicrographs showing two-phase melt between rods 3C and 3D at −0.09 m.

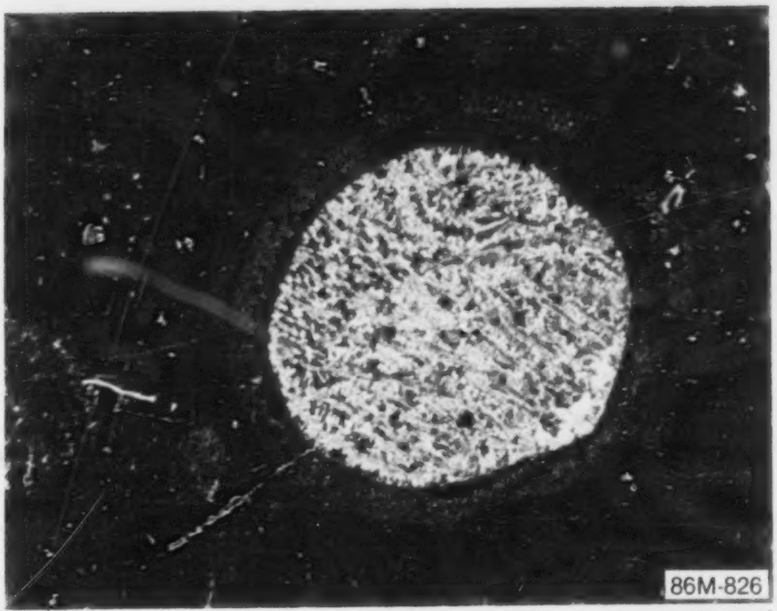

Etched a. Low magnification 200 μm

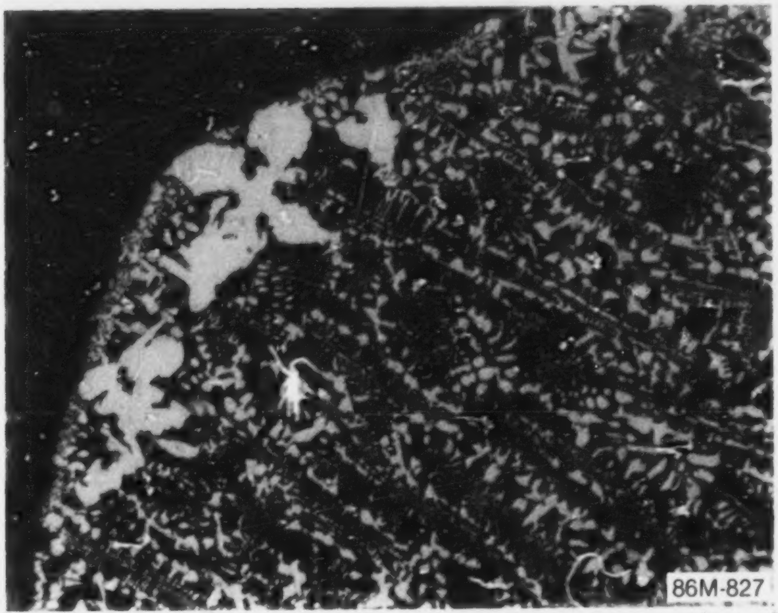

Etched b. High magnification 50 μm

Figure I-76. Photomicrographs of multiphase melt surrounded by oxide layer between rods 3F and 4F at −0.09 m.

I-4. REFERENCES

I-1. A. D. Knipe, S. A. Ploger, and D. J. Osetek, *PBF Severe Fuel Damage Scoping Test—Test Results Report*, NUREG/CR-4683, EGG-2413, August 1986.

I-2. Z. R. Martinson, D. A. Petti and B. A. Cook, *PBF Severe Fuel Damage Test 1-1 Test Results Report*, NUREG/CR-4684, EGG-2463, October 1986.

I-3. P. Hofmann, *Metallographic Examination of the Severe Fuel Damange Scoping Test (SFD-ST) Fuel Rod Bundle Cross Sections*, NUREG/CR-5229, EGG-2537, July 1988.

I-4. J. T. Prater and E. L. Courtright, *Properties of Reactor Fuel Rod Materials at High Temperatures*, NUREG/CR-4891, PNL-6164, July 1987.

I-5. E. M. Levin et al., National Bureau of Standards, *Phase Diagrams for Ceramists*, American Ceramic Society, 1969.

I-6. B. Z. Hyatt, *Metallographic Hydride Standards for LWBR Zircaloy 4-Seed Tubing Based on Out-of-Pile Corrosion Tests*, WAPD-LC(BB)-89, February 1974.

I-7. J. V. Cathcart and R. E. Pawel, *Zirconium Metal-Water Oxidation Kinetics, IV: Reaction Rate Studies*, ORNL-NUREG-17, August 1977.

APPENDIX J

SCDAP/RELAP5 ANALYSIS MODEL

APPENDIX J

SCDAP/RELAP5 ANALYSIS MODEL

Analysis of Test SFD 1-4 was performed with Cycle 5 of the SCDAP/RELAP5/MOD1 code, which is a computer code designed to characterize and quantify fuel damage processes in a reactor vessel during severe accidents. The code can be applied to the analysis of an individual fuel bundle, such as is the case for Test SFD 1-4, or to the analysis of an entire primary coolant system.

This appendix briefly describes the SCDAP/RELAP5 models and provides a listing of the code calculations. The listing is on microfiche attached to the back cover of the report.

SCDAP/RELAP5 calculates the fuel bundle temperature response, cladding ballooning, oxidation, liquefaction, meltdown, and fission gas release. The code has models for all of the major relevant phenomena occurring in a fuel bundle during a severe accident. A short description of the code models is given in Table J-1.

Table J-1. Description of the SCDAP model

Phenomenon	Description of SCDAP Model
Thermal-hydraulics	One-dimensional, transient, two-fluid model for flow of a two-phase steam-water mixture that can contain noncondensible components in the steam phase and/or a nonvolatile component in the water phase; axially varying geometry with consideration of cladding ballooning and fuel rod meltdown.
Fission product release from fuel	PARAGRASS model, which is an empirical model derived from mechanistically based GRASS model.
Cladding oxidation	Cartcart-Pawel (temperature < 1850 K) and Urbanic parabolic rate equations. Model takes into account oxidation limitation due to oxygen starvation.
Dissolution of UO_2 by liquefied zircaloy	Transient dissolution calculated by Hofmann and Vetsuka model; saturation dissolution is modeled by MATPRO.
Dissolution of ZrO_2 by liquefied zircaloy	If temperature is below user-specified value, no dissolution occurs. If temperature is greater than user-specified value and the extent of cladding oxidation is less than a user-specified value, then complete dissolution instantly occurs.
Relocation of liquefied Zr-U-O mixture flowing through breach in ZrO_2 shell and downward along the outside of fuel rod	Motion of Zr-U-O mixture is calculated, taking into account gravity and friction forces. Cooling and solidification of Zr-U-O mixture is calculated, taking into account heat conduction from mixture into fuel rod.
Heat conduction in fuel rods and control rods	Stacked one-dimensional (radial) heat conduction is modeled, using finite element method. Maximum of six radial nodes in fuel and cladding. Maximum of 20 radial nodes in shroud.
Heat transfer at surface of fuel rods and control rods	Heat transfer by convection and radiation between fuel rods and coolant mixture is modeled. In addition, heat transfer by radiation between fuel rods and control rods is modeled.
Cladding ballooning and rupture	Anisotropic cladding material properties and strain rate and temperature-dependent stress-strain relations are used.
Pressure change in fuel rods	Perfect gas law is employed, using current values for fuel rod internal void volume, temperature distribution, and gas inventory.

NRC FORM 335
(9-87)
NRCM 1102
3201, 3202

U.S. NUCLEAR REGULATORY COMMISSION

BIBLIOGRAPHIC DATA SHEET

SEE INSTRUCTIONS ON THE REVERSE

1. REPORT NUMBER (Assigned by PPMB, DPS, add Vol. No., if any)
NUREG/CR-5163
EGG-2542

2. TITLE AND SUBTITLE
Power Burst Facility (PBF) Severe Fuel Damage Test 1-4
Test Results Report

3. LEAVE BLANK

4. DATE REPORT COMPLETED
MONTH: February
YEAR: 1989

5. AUTHOR(S)
D.A. Petti, Z.R. Martinson, R.R. Hobbins, C.M. Allison,
E.R. Carlson, D.L. Hagrman, T.C. Cheng, J.K. Hartwell,
K. Vinjamuri, L.J. Seifken

6. DATE REPORT ISSUED
MONTH: April
YEAR: 1989

7. PERFORMING ORGANIZATION NAME AND MAILING ADDRESS (Include Zip Code)
EG&G Idaho, Inc.
Idaho Falls, ID 83401

8. PROJECT/TASK/WORK UNIT NUMBER

9. FIN OR GRANT NUMBER
A6305, A6321

10. SPONSORING ORGANIZATION NAME AND MAILING ADDRESS (Include Zip Code)
Division of Systems Research
Office of Nuclear Regulatory Research
U.S. Nuclear Regulatory Commission
Washington, DC 20555

11a. TYPE OF REPORT

b. PERIOD COVERED (Inclusive dates)

12. SUPPLEMENTARY NOTES

13. ABSTRACT (200 words or less)

An evaluation of the Severe Fuel Damage (SFD) Test 1-4 performed in the PBF at the INEL is presented. The objective of the test was to contribute to the understanding of fuel and control rod behavior, aerosol and hydrogen generation, and fission product release and transport during a high-temperature, SFD transient.

A test bundle, comprised of 26 previously irradiated PWR-type fuel rods, 2 fresh instrumented fuel rods, and 4 Ag-In-Cd control rods, was surrounded by an insulating shroud and contained in a pressurized in-pile tube. The experiment consisted of a 1.3-h transient at a coolant pressure of 6.95 MPa in which the inlet coolant flow was reduced to 0.6 g/s while fission power was gradually increased until dryout, heatup, cladding rupture, and oxidation occurred. With sustained fission power and heat from oxidation, temperatures rose rapidly, resulting in zircaloy and control rod absorber alloy melting, fuel liquefaction, material relocation, and hydrogen, aerosol, and fission product release. The transient was terminated over 2100 s by slowly reducing reactor power and cooling the damaged bundle with argon gas.

A description and evaluation of major phenomena, based upon on-line instrumentation response, fission product and aerosol data analysis, fuel bundle PIE, and SCDAP/RELAP5 computer code calculations, are presented.

14. DOCUMENT ANALYSIS – a. KEYWORDS/DESCRIPTORS
Power Burst Facility (PBF)
Severe Fuel Damage (SFD) Test
light water reactor (LWR)
severe accident research

b. IDENTIFIERS/OPEN ENDED TERMS

15. AVAILABILITY STATEMENT
unlimited

16. SECURITY CLASSIFICATION
(This page)
unclassified
(This report)
unclassified

17. NUMBER OF PAGES

18. PRICE

☆ U.S. GOVERNMENT PRINTING OFFICE : 1989 0 - 235-009

UNITED STATES
NUCLEAR REGULATORY COMMISSION
WASHINGTON, D.C. 20555

OFFICIAL BUSINESS
PENALTY FOR PRIVATE USE, $300

SPECIAL FOURTH-CLASS RATE
POSTAGE & FEES PAID
USNRC

PERMIT No. G-67